HELLENIC REPUBLIC
UNIVERSITY OF IOANNINA
SCHOOL OF ENGINEERING
DEPARTMENT OF MATERIALS SCIENCE AND ENGINEERING

"Characterization of atmospheric aerosol composition and sources of pollution with X- ray spectrometry techniques"

Stefanos Papagiannis

DOCTORAL THESIS

Ioannina, 2026

ΕΛΛΗΝΙΚΗ ΔΗΜΟΚΡΑΤΙΑ
ΠΑΝΕΠΙΣΤΗΜΙΟ ΙΩΑΝΝΙΝΩΝ
ΠΟΛΥΤΕΧΝΙΚΗ ΣΧΟΛΗ
ΤΜΗΜΑ ΜΗΧΑΝΙΚΩΝ ΕΠΙΣΤΗΜΗΣ ΥΛΙΚΩΝ

" Χαρακτηρισμός των συστατικών ατμοσφαιρικού αερολύματος και των πηγών ρύπανσης με τεχνικές φασματομετρίας ακτίνων-Χ"

Στέφανος Παπαγιάννης

ΔΙΔΑΚΤΟΡΙΚΗ ΔΙΑΤΡΙΒΗ

Ιωάννινα, 2026

«Η έγκριση της διδακτορικής διατριβής από το Τμήμα Μηχανικών Επιστήμης Υλικών της Πολυτεχνικής Σχολής του Πανεπιστημίου Ιωαννίνων δεν υποδηλώνει αποδοχή των γνωμών του συγγραφέα Ν. 5343/32, άρθρο 202, παράγραφος 2».

Date of application of Mr. Stefanos Papagiannis: 07-04-2020

Date of appointment of the three-membered advisory committee: 08-04-2020

Members of the three-membered advisory committee:

Supervision

Dimitrios Anagnostopoulos: Professor in the Department of Materials Science and Engineering of the School of Engineering at the University of Ioannina.

Members

Konstantinos Eleftheriadis, Researcher A' (First-Grade Researcher), Research Director at the Institute of Nuclear & Radiological Sciences & Technology, Energy & Safety, N.C.S.R. "Demokritos"

Andreas-Germanos Karydas: Researcher A' (First-Grade Researcher), Research Director at the Institute of Nuclear and Particle Physics, N.C.S.R. "Demokritos".

Thesis definition date: 08-04-2020

"Characterization of atmospheric aerosol composition and sources of pollution with X- ray spectrometry techniques"

Date of reconstitution of the three-member advisory committee: 23-03-2021

Supervision

Dimitrios Anagnostopoulos: Professor in the Department of Materials Science and Engineering of the School of Engineering at the University of Ioannina.

Members

Evangelia Diapouli: Researcher B' (Second-Grade Researcher), Principal Researcher at the Institute of Nuclear & Radiological Sciences & Technology, Energy & Safety, N.C.S.R. "Demokritos".

Andreas-Germanos Karydas: Researcher A' (First-Grade Researcher), Research Director at the Institute of Nuclear and Particle Physics, N.C.S.R. "Demokritos".

APPOINTMENT OF SEVEN-MEMBERED EXAMINATION COMMITTEE: 10-12-2025

1. Dimitrios Anagnostopoulos	Professor in the Department of Materials Science and Engineering of the School of Engineering at the University of Ioannina.
2. Andreas-Germanos Karydas	Researcher A' (First-Grade Researcher), Research Director at the Institute of Nuclear and Particle Physics, N.C.S.R. "Demokritos".
3. Evangelia Diapouli	Researcher B' (Second-Grade Researcher), Principal Researcher at the Institute of Nuclear & Radiological Sciences & Technology, Energy & Safety, N.C.S.R. "Demokritos".
4. Mihalis Karakasidis	Professor in the Department of Materials Science and Engineering of the School of Engineering at the University of Ioannina.
5. Nikolaos Zafeiropoulos	Professor in the Department of Materials Science and Engineering of the School of Engineering at the University of Ioannina
6. Konstantinos Spyrou	Ass. Professor (Assistant Professor) in the Department of Materials Science and Engineering of the School of Engineering at the University of Ioannina.
7. Konstantinos Eleftheriadis	Researcher A' (First-Grade Researcher), Research Director at the Institute of Nuclear & Radiological Sciences & Technology, Energy & Safety, N.C.S.R. "Demokritos".

Approval of doctoral thesis with grade: "EXCELLENT" on 24-02-2026

The Head of the Department

Simeon Agathopoulos
Professor

ΤΜΗΜΑ ΜΗΧΑΝΙΚΩΝ ΕΠΙΣΤΗΜΗΣ ΥΛΙΚΩΝ
ΠΑΝΕΠΙΣΤΗΜΙΟ ΙΩΑΝΝΙΝΩΝ

The Secretary of the Department

Maria Kontou

Ημερομηνία αίτησης του κ. Στέφανου Παπαγιάννη: 07-04-2020

Ημερομηνία ορισμού Τριμελούς Συμβουλευτικής Επιτροπής: 08-04-2020

Μέλη Τριμελούς Συμβουλευτικής Επιτροπής:

Επιβλέπων

Δημήτριος Αναγνωστόπουλος: Καθηγητής του Τμήματος Μηχανικών Επιστήμης Υλικών της Πολυτεχνικής Σχολής του Πανεπιστημίου Ιωαννίνων.

Μέλη

Κωνσταντίνος Ελευθεριάδης: Ερευνητής Α' (Διευθυντής Ερευνών) του Ινστιτούτου Πυρηνικών & Ραδιολογικών Επιστημών & Τεχνολογίας, Ενέργειας & Ασφάλειας, Ε.Κ.ΕΦ.Ε «Δημόκριτος».

Ανδρέας-Γερμανός Καρύδας: Ερευνητής Α' (Διευθυντής Ερευνών) του Ινστιτούτου Πυρηνικής και Σωματιδιακής Φυσικής, Ε.Κ.ΕΦ.Ε «Δημόκριτος».

Ημερομηνία Ορισμού Θέματος: 08-04-2020

"Χαρακτηρισμός των συστατικών ατμοσφαιρικού αερολύματος και των πηγών ρύπανσης με τεχνικές φασματομετρίας ακτίνων-Χ"

Ημερομηνία Ανασυγκρότησης Τριμελούς Συμβουλευτικής Επιτροπής: 23-03-2021

Επιβλέπων

Δημήτριος Αναγνωστόπουλος: Καθηγητής του Τμήματος Μηχανικών Επιστήμης Υλικών της Πολυτεχνικής Σχολής του Πανεπιστημίου Ιωαννίνων.

Μέλη

Ευαγγελία Διαπούλη: Ερευνήτρια Β' (Κύρια Ερευνήτρια) στο Ινστιτούτο Πυρηνικών & Ραδιολογικών Επιστημών & Τεχνολογίας, Ενέργειας & Ασφάλειας, Ε.Κ.ΕΦ.Ε «Δημόκριτος».

Ανδρέας-Γερμανός Καρύδας: Ερευνητής Α' (Διευθυντής Ερευνών) του Ινστιτούτου Πυρηνικής και Σωματιδιακής Φυσικής, Ε.Κ.ΕΦ.Ε «Δημόκριτος».

ΣΥΣΤΑΣΗ ΤΗΣ ΕΠΤΑΜΕΛΟΥΣ ΕΞΕΤΑΣΤΙΚΗΣ ΕΠΙΤΡΟΠΗΣ: 10-12-2025

1. Δημήτριος Αναγνωστόπουλος	Καθηγητής του Τμήματος Μηχανικών Επιστήμης Υλικών της Πολυτεχνικής Σχολής του Πανεπιστημίου Ιωαννίνων.
2. Ανδρέας-Γερμανός Καρύδας	Ερευνητής Α' (Διευθυντής Ερευνών) του Ινστιτούτου Πυρηνικής και Σωματιδιακής Φυσικής, Ε.Κ.ΕΦ.Ε «Δημόκριτος».
3. Ευαγγελία Διαπούλη	Ερευνήτρια Β' (Κύρια Ερευνήτρια) στο Ινστιτούτο Πυρηνικών & Ραδιολογικών Επιστημών & Τεχνολογίας, Ενέργειας & Ασφάλειας, Ε.Κ.ΕΦ.Ε «Δημόκριτος».
4. Μιχάλης Καρακασίδης	Καθηγητής του Τμήματος Μηχανικών Επιστήμης Υλικών της Πολυτεχνικής Σχολής του Πανεπιστημίου Ιωαννίνων.
5. Νικόλαος Ζαφειρόπουλος	Καθηγητής του Τμήματος Μηχανικών Επιστήμης Υλικών της Πολυτεχνικής Σχολής του Πανεπιστημίου Ιωαννίνων.
6. Κωνσταντίνος Σπύρου	Επίκ. Καθηγητής (Επίκουρος Καθηγητής) του Τμήματος Μηχανικών Επιστήμης Υλικών της Πολυτεχνικής Σχολής του Πανεπιστημίου Ιωαννίνων.
7. Κωνσταντίνος Ελευθεριάδης	Ερευνητής Α' (Διευθυντής Ερευνών) του Ινστιτούτου Πυρηνικών & Ραδιολογικών Επιστημών & Τεχνολογίας, Ενέργειας & Ασφάλειας, Ε.Κ.ΕΦ.Ε «Δημόκριτος».

Έγκριση Διδακτορικής Διατριβής με Βαθμό: «ΑΡΙΣΤΑ» στις 24-02-206

Ο πρόεδρος του Τμήματος

Συμεών Αγαθόπουλος
Καθηγητής

ΤΜΗΜΑ ΜΗΧΑΝΙΚΩΝ ΕΠΙΣΤΗΜΗΣ ΥΛΙΚΩΝ
ΛΟΓΟΣ ΕΡΓΟΥ
ΠΑΝΕΠΙΣΤΗΜΙΟ ΙΩΑΝΝΙΝΩΝ

Η Γραμματέας του Τμήματος

Μαρία Κόντου

Acknowledgements

I would like to express my deepest gratitude to all those who supported, guided, and encouraged me throughout the journey of this doctoral thesis.

I owe my sincerest thanks to my supervisor, **Professor Dimitrios F. Anagnostopoulos**. I am profoundly grateful for his trust, his guidance, and the unwavering support he has offered me for more almost a decade. From my undergraduate studies through my Master's degree and now my PhD, he has been not only a teacher, but a mentor, advisor, and constant source of motivation. His scientific insight, calm leadership, and genuine interest in my development shaped this work and my academic path. This dissertation would simply not have been possible without him, and for that, I thank him from the bottom of my heart.

I extend my heartfelt appreciation to **Dr. Andreas G. Karydas** for his invaluable mentorship and scientific advice. His deep expertise in X-ray Fluorescence (XRF) spectrometry and Particle Induce X-Ray Emision (PIXE) was a cornerstone of this research. During my time at the XRF laboratory at the Institute of Nuclear and Particle Physics, Dr. Karydas provided constant guidance, always making himself available to offer advice and assistance whenever needed. I am deeply grateful for the generous amount of time he dedicated to passing on his knowledge to me; his technical direction and supportive presence significantly enriched this thesis.

I am equally indebted to **Dr. Evaggelia Diapouli** for her continuous support and for being an exceptional educator. Her guidance was fundamental in helping me master the physical and chemical processes of atmospheric aerosols. When I arrived at the laboratory, concepts such as aerosol science and source apportionment were entirely new to me. Dr. Diapouli patiently bridged that gap, spending countless hours in her office with me running PMF models and discussing the results in depth. Her constructive feedback and willingness to teach were instrumental in the completion of this thesis.

I would also like to express my sincere gratitude to **Dr. Manousos I. Manousakas**, whose contribution has been fundamental. Throughout this work, he has been a constant source of support—always available to guide, teach, and offer practical and scientific help whenever needed. His mentoring, patience, and personal encouragement have played a major role in shaping both this dissertation and my growth as a researcher.

My warmest thanks are also extended to **Dr. Konstantinos Eleftheriadis** for his trust, support, and continuous interest in my work over the years. His guidance, encouragement, and confidence in my abilities have been truly invaluable. He has consistently offered me opportunities to grow, challenged me to become better, and entrusted me with

responsibilities—including the preparation of scientific proposals—that significantly shaped my development as a researcher. I am deeply grateful for his support throughout this journey.

I am deeply thankful to **Dr. Anastasios Lagogiannis** and **Dr. Mihail Axiotis** for their essential assistance with all experimental work performed at the NCSR "Demokritos" accelerator facilities. Their technical expertise and personal willingness to help at every step greatly supported the progress of this thesis.

My sincere thanks go to all my colleagues whose collaboration made this journey meaningful. I warmly thank **Ms. Kalliopi Tsampa**, for her daily support, cooperation, and positive spirit in the laboratory; **Dr. Olga Zografou**, **Mr. Konstantinos Granakis**, and **Mrs. Stavroula Katsikari** for their encouragement and helpful presence throughout these years. I also thank **Dr. Vasiliki Vasilatou** for our excellent collaboration in the ENRACT laboratory, **Dr. Maria Gini** for her guidance and scientific advice, and **Mr. Panagiotis Karkavitas** for his continuous technical support.

I also wish to thank my colleagues at the University of Ioannina, **Mr. Anastasios Asvestas** and **Mrs. Ioanna Patakiouta**, for their unwavering support and collaboration throughout the entire duration of this thesis. Their contribution went far beyond scientific support; they assisted me consistently with every task and challenge that arose, always with kindness and dedication. I am deeply grateful for the time they devoted—often sacrificing their weekends—to help ensure the successful completion of this work. Additionally, I would like to extend my gratitude to **Dr. Anastasia Tzima**, for her constant guidance in the lab, her willingness to answer my every question, and her invaluable mentorship.

I also am grateful to **Professor Emanouela Remoundaki** for granting me access to scientific equipment at the School of Mining and Metallurgical Engineering at the National Technical University of Athens, and for her kind assistance whenever needed.

Finally, I would like to express my deepest love and gratitude to my family. Their patience, encouragement, and unwavering support have sustained me through every challenge of this long journey. Nothing would have been possible without them.

Abstract

The primary objective of this doctoral dissertation is to advance and validate non-destructive X-ray analytical techniques for the quantitative chemical characterization of atmospheric aerosol filters. While traditional air quality monitoring relies heavily on bulk mass concentrations (PM_{10}, $PM_{2.5}$), this work addresses the critical need for detailed elemental data by optimizing a suite of complementary spectroscopic methods—ranging from Energy-Dispersive X-ray Fluorescence (ED-XRF), Wavelength-Dispersive X-ray Fluorescence (WD-XRF), micro-XRF Imaging, Near Real-Time XRF (NRT-XRF), and Particle-Induced X-ray Emission (PIXE). A central contribution of this research is the rigorous development of analytical protocols that overcome existing limitations regarding calibration, spatial heterogeneity, and instrument intercomparability. By systematically cross-validating these techniques, the study establishes a robust framework for obtaining reliable and high-resolution chemical data essential for understanding aerosol composition.

Beyond methodological innovation, the research aims to bridge the gap between instrumental development and practical environmental application through determining the sources of particulate pollution in diverse and under-studied environments. The optimized analytical protocols were applied to real-world case studies, enabling a harmonized source identification across six diverse sites in Greece and the first multi-year source apportionment in a heavily polluted city in Central Asia. These applications demonstrate the capability of the developed methods to identify specific anthropogenic drivers, such as residential biomass burning and industrial emissions, thereby providing the scientifically grounded evidence required for policymakers to design effective, targeted air quality mitigation strategies.

Airborne particulate matter (PM) remains one of the most pressing environmental challenges and threats to public health worldwide. Fine and coarse particles not only degrade air quality and visibility but also contribute to adverse health effects, including respiratory and cardiovascular diseases. The chemical composition of PM reflects a complex mixture of natural and anthropogenic sources, atmospheric processes, and long-range transport; therefore, its characterization is fundamental for understanding impacts and supporting mitigation policies.

Despite significant progress, major challenges remain in the quantitative chemical analysis of aerosol samples. Traditional monitoring networks provide information on mass concentrations (PM_{10}, $PM_{2.5}$); however, these data are insufficient for source identification and process understanding. Instead, detailed elemental and compositional data are required. In this context, non-destructive, multi-element techniques such as X-ray fluorescence (XRF) and

particle-induced X-ray emission (PIXE) have become essential tools in atmospheric sciences. Nevertheless, the application of these techniques to thin aerosol deposits collected on filters requires careful calibration, rigorous uncertainty estimation, and systematic intercomparison.

This Doctoral Dissertation addresses these challenges by combining advanced X-ray fluorescence (XRF) methods with ion-beam analysis (PIXE) for the chemical characterization of atmospheric aerosols. To this end, several complementary spectrometers were employed, including a secondary-target ED-XRF, a high-resolution WD-XRF, a portable ED-XRF (HH-XRF), a micro-XRF scanner for spatially resolved analysis of multi-stage impactor filters, a near real-time XRF spectrometer (NRT-XRF) evaluated through direct comparison with a laboratory ED-XRF, as well as a dedicated PIXE setup at the Institute of Nuclear and Particle Physics (INPP) of NCSR "Demokritos". Through careful optimization and cross-validation, these methodologies were adapted to deliver reliable quantitative analysis of aerosol filters.

The central objective of this dissertation is twofold: (a) the advancement and application of non-destructive analytical techniques for the quantitative determination of aerosol elemental composition, and (b) the use of these techniques to improve the understanding of particulate pollution sources in diverse environments. The work contributes both to the optimization of analytical protocols and to the broader effort of investigating pollution sources, with the aim of providing accurate public information and supporting effective mitigation strategies.

The **first part** of the dissertation (Chapters 1–7) provides the scientific foundation for studying atmospheric particulate matter (PM). It begins with the definition and physical characteristics of aerosols, highlighting their size range, formation mechanisms, and ability to undergo transformations and long-range transport. It then examines filter-based sampling methodologies, emphasizing the advantages and limitations of different substrates and their implications for subsequent chemical analysis. A detailed overview of the chemical composition of atmospheric PM follows, covering crustal, marine, secondary inorganic, carbonaceous components, and trace elements, linking them to environmental and health impacts. Finally, Positive Matrix Factorization (PMF), the main receptor model used in this dissertation, is presented, focusing on its mathematical framework, treatment of uncertainty, and diagnostic tools.

The **second part** (Chapters 8–10) is dedicated to the analytical foundations of the applied X-ray methods. It introduces the physical principles of X-ray fluorescence (XRF), including excitation processes, attenuation, and quantification strategies, with particular emphasis on thin targets such as aerosol filters. Complementarily, the fundamental principles of particle-induced X-ray emission (PIXE) are described, outlining ion–matter interactions, geometries, and calibration requirements for aerosol analysis. Together, these chapters establish the theoretical basis for the quantitative interpretation of spectra obtained with different

instruments and provide the framework necessary to adapt XRF and PIXE techniques to the specific challenges of environmental aerosol research.

The **third part** (Chapters 11–12) presents the experimental setups used. These include the secondary-target ED-XRF spectrometer (Epsilon 5, PANalytical), the portable HH-XRF analyzer (Tracer 5i, Bruker), the large-area μ-XRF scanner (M6 Jetstream, Bruker), the WD-XRF spectrometer (ZSX Primus IV, Rigaku), and the near real-time XRF spectrometer (NRT-XRF) (Xact 625i, SailBri Cooper) for automated hourly elemental monitoring. In addition, the specialized external-beam PIXE facility of the Institute of Nuclear and Particle Physics (INPP), NCSR "Demokritos", is described.

The **fourth part** of the dissertation (Chapters 13–19) presents the experimental results, beginning with the X-ray analytical methodologies (Chapters 13–17) and continuing with their application in source apportionment studies (Chapters 18–19).

Initially, the methodological performance of the new analytical tools was investigated. The portable **HH-XRF** spectrometer (Tracer 5i, Bruker) was optimized for aerosol filter analysis, calibrated against thin-film standards, and compared with the laboratory ED-XRF system (Epsilon 5, PANalytical). The results demonstrate strong performance across 24 elements.

Additionally, an analytical protocol using **μ-XRF** (M6 Jetstream, Bruker) was developed for filters from a multi-stage impactor, providing spatially resolved quantification of elements across different particle size fractions. In this context, the spatial heterogeneity of aerosol deposition on filters was systematically examined.

Further enhancement of laboratory instrumentation was achieved through the calibration of a **WD-XRF** spectrometer (ZSX Primus IV, Rigaku). Using thin-film standards and reference filters, the WD-XRF proved to be a reliable and complementary tool, offering superior energy resolution.

An additional methodological contribution is the development of a quantitative external-beam PIXE protocol. Using two SDD detectors, calibration for aerosol filters was successfully achieved.

Finally, an intercomparison was performed between the benchtop ED-XRF spectrometer (Epsilon 5, PANalytical) and the **NRT-XRF** instruments (Xact 625i and Xact 625, SailBri Cooper) in three European cities. The study highlights the complexity of intercomparisons between different XRF instrument types and substrates.

After the development and evaluation of the X-ray methodologies, they were applied to real-world case studies in different geographical contexts.

The first study focuses on Central Asia, presenting the first multi-year $PM_{2.5}$ source apportionment in Dushanbe, Tajikistan. Using gravimetric elemental analysis with ED-XRF and black carbon (BC) measurements, the results reveal persistently high $PM_{2.5}$ levels, far exceeding European standards and World Health Organization (WHO) guidelines. The Positive Matrix Factorization (**PMF**) model identified eight pollution sources, including coal burning, biomass burning, emissions from cement industries, crustal dust, secondary aerosols, and emissions from power plants. Strong seasonality in source contributions was observed, with residential coal burning dominating in winter and power-plant emissions increasing during warmer months.

In the European context, a comprehensive study was conducted in **Greece** within the PANACEA project. Six stations representing urban, suburban, and rural environments were monitored using ED-XRF, carbon analyses (OC and EC), and ion chromatography. The resulting source apportionment highlights the interplay among traffic emissions, biomass burning, secondary aerosols, and natural sources, with site-specific contributions reflecting local conditions and meteorology. This work establishes a coherent national dataset that can inform targeted mitigation strategies.

Finally, the **fifth part** summarizes the main conclusions of the dissertation, emphasizing the successful bridging of instrumental development and environmental application.

Περίληψη

Ο πρωταρχικός στόχος αυτής της διδακτορικής διατριβής είναι η εξέλιξη και η επικύρωση μη καταστροφικών τεχνικών ανάλυσης ακτίνων-Χ για τον ποσοτικό χημικό χαρακτηρισμό φίλτρων ατμοσφαιρικών αερολυμάτων. Ενώ η παραδοσιακή παρακολούθηση της ποιότητας του αέρα βασίζεται σε μεγάλο βαθμό στις συγκεντρώσεις μάζας (PM_{10}, $PM_{2.5}$), η παρούσα εργασία αντιμετωπίζει την κρίσιμη ανάγκη για λεπτομερή στοιχειακά δεδομένα, βελτιστοποιώντας μια σειρά συμπληρωματικών φασματοσκοπικών μεθόδων — οι οποίες κυμαίνονται από τον φθορισμό ακτίνων-Χ ενεργειακής Διασποράς (ED-XRF), τον φθορισμό ακτίνων-Χ διασκεδασμού μήκους κύματος (WD-XRF), την απεικονιστική φασματομετρία micro-XRF, XRF σχεδόν πραγματικού χρόνου (NRT-XRF) και την εκπομπή ακτίνων-Χ από επαγόμενα από σωματίδια (PIXE). Μια κεντρική συνεισφορά αυτής της έρευνας είναι η αυστηρή ανάπτυξη αναλυτικών πρωτοκόλλων που υπερβαίνουν τους υπάρχοντες περιορισμούς σχετικά με τη βαθμονόμηση, τη χωρική ανομοιογένεια και τη συγκρισιμότητα των οργάνων. Μέσω της συστηματικής διασταυρούμενης επικύρωσης αυτών των τεχνικών, η μελέτη καθιερώνει ένα ισχυρό πλαίσιο για την απόκτηση αξιόπιστων χημικών δεδομένων υψηλής ανάλυσης, τα οποία είναι απαραίτητα για την κατανόηση της σύνθεσης των αερολυμάτων.

Πέρα από τη μεθοδολογική καινοτομία, η έρευνα στοχεύει να γεφυρώσει το χάσμα μεταξύ της ανάπτυξης οργάνων και της πρακτικής περιβαλλοντικής εφαρμογής, προσδιορίζοντας τις πηγές σωματιδιακής ρύπανσης σε ποικίλα και ελλιπώς μελετημένα περιβάλλοντα. Τα βελτιστοποιημένα αναλυτικά πρωτόκολλα εφαρμόστηκαν σε μελέτες επιμερισμού πηγών ρύπανσης, επιτρέποντας τον εναρμονισμένο προσδιορισμό πηγών σε έξι διαφορετικές τοποθεσίες στην Ελλάδα, καθώς και την πρώτη πολυετή κατανομή πηγών (source apportionment) σε μια βαριά ρυπασμένη πόλη της Κεντρικής Ασίας. Οι εφαρμογές αυτές καταδεικνύουν την ικανότητα των αναπτυγμένων μεθόδων να εντοπίζουν συγκεκριμένους ανθρωπογενείς παράγοντες, όπως η καύση βιομάζας για οικιακή χρήση και οι βιομηχανικές εκπομπές, παρέχοντας έτσι τα επιστημονικά τεκμηριωμένα στοιχεία που απαιτούνται ώστε οι φορείς χάραξης πολιτικής να σχεδιάσουν αποτελεσματικές και στοχευμένες στρατηγικές μετριασμού για την ποιότητα του αέρα.

Τα αιωρούμενα σωματίδια (ΑΣ) παραμένουν μία από τις πιο πιεστικές περιβαλλοντικές προκλήσεις και απειλές για τη δημόσια υγεία παγκοσμίως. Τα λεπτόκοκκα και χονδρόκοκκα σωματίδια όχι μόνο υποβαθμίζουν την ποιότητα του αέρα και την ορατότητα, αλλά συμβάλλουν επίσης σε δυσμενείς επιπτώσεις για την υγεία, συμπεριλαμβανομένων των αναπνευστικών και καρδιαγγειακών παθήσεων. Η χημική σύσταση των ΑΣ αντικατοπτρίζει ένα πολύπλοκο μείγμα φυσικών και ανθρωπογενών

πηγών, ατμοσφαιρικών διεργασιών και μεταφοράς μεγάλων αποστάσεων, και ως εκ τούτου, ο χαρακτηρισμός της είναι θεμελιώδης για την κατανόηση των επιπτώσεων και την υποστήριξη πολιτικών μετριασμού.

Παρά τις σημαντικές προόδους, παραμένουν σημαντικές προκλήσεις στην ποσοτική χημική ανάλυση των δειγμάτων αερολυμάτων. Τα παραδοσιακά δίκτυα παρακολούθησης παρέχουν πληροφορίες σχετικά με τις συγκεντρώσεις μάζας (PM_{10}, $PM_{2.5}$), ωστόσο τα δεδομένα αυτά είναι ανεπαρκή για την ταυτοποίηση των πηγών και την κατανόηση των μηχανισμών. Αντ' αυτού, απαιτούνται λεπτομερή στοιχειακά δεδομένα και δεδομένα σύστασης. Σε αυτό το πλαίσιο, οι μη καταστροφικές, πολυ-στοιχειακές τεχνικές, όπως ο φθορισμός ακτίνων-Χ (XRF) και η εκπομπή ακτίνων-Χ από επαγόμενα σωματίδια (PIXE), έχουν καταστεί απαραίτητα εργαλεία για τις ατμοσφαιρικές επιστήμες. Ωστόσο, η εφαρμογή αυτών των τεχνικών σε λεπτές εναποθέσεις αερολυμάτων που συλλέγονται σε φίλτρα απαιτεί προσεκτική βαθμονόμηση, αυστηρή εκτίμηση της αβεβαιότητας και συστηματική δια-σύγκριση.

Η παρούσα Διδακτορική Διατριβή αντιμετωπίζει αυτές τις προκλήσεις συνδυάζοντας σύγχρονες μεθόδους φθορισμού ακτίνων-Χ (XRF) με ανάλυση ιόντων-ακτίνων (PIXE) για τη χημική ταυτοποίηση των ατμοσφαιρικών αερολυμάτων. Για το σκοπό αυτό χρησιμοποιήθηκαν διάφορα συμπληρωματικά φασματόμετρα, όπως δευτερογενών στόχων ED-XRF, WD-XRF υψηλής διακριτικής ικανότητας, φορητό ED-XRF (HH-XRF), μικρο-XRF για χωρικά διακριτή απεικόνιση δειγμάτων από δειγματολήπτη πολλαπλών σταδίων, φασματόμετρο XRF σε σχεδόν πραγματικό χρόνο (NRT-XRF) που αξιολογήθηκε μέσω άμεσης σύγκρισης με εργαστηριακό ED-XRF, καθώς και ειδική διάταξη PIXE στο Ινστιτούτο Πυρηνικής και Σωματιδιακής Φυσικής (INPP), ΕΚΕΦΕ «Δημόκριτος». Μέσω προσεκτικής βελτιστοποίησης και διασταυρούμενης επικύρωσης, οι μέθοδοdολογίες αυτές προσαρμόστηκαν ώστε να παρέχουν αξιόπιστη ποσοτική ανάλυση φίλτρων αερολυμάτων.

Ο κεντρικός στόχος της παρούσας διατριβής είναι διττός: (α) η προώθηση και εφαρμογή μη καταστροφικών αναλυτικών τεχνικών για τον ποσοτικό προσδιορισμό της στοιχειακής σύστασης των αερολυμάτων και (β) η αξιοποίηση αυτών των τεχνικών για την πληρέστερη κατανόηση των πηγών σωματιδιακής ρύπανσης σε διαφορετικά περιβάλλοντα. Η εργασία συμβάλλει τόσο στη βελτιστοποίηση αναλυτικών πρωτοκόλλων όσο και στη συνολικότερη προσπάθεια διερεύνησης των πηγών ρύπανσης, με στόχο την έγκυρη ενημέρωση των πολιτών και τη διαμόρφωση αποτελεσματικών στρατηγικών για τον περιορισμό της.

Το **πρώτο μέρος** της διατριβής (Κεφάλαια 1–7) παρέχει την επιστημονική βάση για τη μελέτη των ατμοσφαιρικών σωματιδίων (ΑΣ). Ξεκινά με τον ορισμό και τα φυσικά χαρακτηριστικά των αερολυμάτων, επισημαίνοντας το εύρος μεγεθών, τους

μηχανισμούς σχηματισμού και την ικανότητά τους να υφίστανται μετασχηματισμούς και μεταφορά σε μεγάλες αποστάσεις. Στη συνέχεια εξετάζονται οι μεθοδολογίες δειγματοληψίας σε φίλτρα, με έμφαση στα πλεονεκτήματα και τους περιορισμούς των διαφορετικών υποστρωμάτων και τις επιπτώσεις στη μετέπειτα χημική ανάλυση. Ακολουθεί μια λεπτομερής επισκόπηση της χημικής σύστασης των ατμοσφαιρικών ΑΣ, καλύπτοντας εδαφικά, θαλάσσια, δευτερογενή ανόργανα, ανθρακούχα συστατικά και ιχνοστοιχεία, συνδέοντάς τα με περιβαλλοντικές και υγειονομικές επιπτώσεις. Τέλος, παρουσιάζεται το μοντέλο της Παραγοντοποίησης Θετικής Μήτρας (PMF) ως το κύριο μοντέλο αποδέκτη που χρησιμοποιείται στη διατριβή για τον επιμερισμό πηγών ρύπανσης, εστιάζοντας στο μαθηματικό πλαίσιο, τον χειρισμό της αβεβαιότητας και τα διαγνωστικά εργαλεία.

Το **δεύτερο μέρος** (Κεφάλαια 8–10) αφιερώνεται στα αναλυτικά θεμέλια των μεθόδων ακτίνων-Χ που εφαρμόζονται. Εισάγει τις φυσικές αρχές του φθορισμού ακτίνων Χ (XRF), συμπεριλαμβανομένων των διεργασιών διέγερσης, της εξασθένησης, και των στρατηγικών ποσοτικοποίησης, με ιδιαίτερη επισήμανση στους λεπτούς στόχους, όπως είναι και τα φίλτρα αερολύμάτων. Συμπληρωματικά, περιγράφονται οι θεμελιώδεις αρχές της εκπομπής ακτίνων-Χ από επαγόμενα σωματίδια (PIXE), περιγράφοντας τις αλληλεπιδράσεις ιόντων-ύλης, τις γεωμετρίες, και τις απαιτήσεις βαθμονόμησης για ανάλυση αερολυμάτων. Μαζί, τα κεφάλαια αυτά θεμελιώνουν τη θεωρητική βάση για την ποσοτική ερμηνεία των φασμάτων που λαμβάνονται με διαφορετικά όργανα και παρέχουν το απαραίτητο πλαίσιο για την προσαρμογή των τεχνικών XRF και PIXE στις ειδικές προκλήσεις της έρευνας περιβαλλοντικών αερολυμάτων.

Το **τρίτο μέρος** (Κεφάλαια 11–12) παρουσιάζει τις πειραματικές διατάξεις που χρησιμοποιήθηκαν. Αυτές περιλαμβάνουν το φασματόμετρο ED-XRF με δευτερογενες στόχους (Epsilon 5, PANalytical), τον φορητό αναλυτή HH-XRF (Tracer 5i, Bruker), τον σαρωτή μ-XRF μεγάλων επιφανειών (M6 Jetstream, Bruker), το φασματόμετρο WD-XRF (ZSX Primus IV, Rigaku) και το φασματόμετρο XRF σχεδόν πραγματικού χρόνου (NRT-XRF) (Xact 625i, SailBri Cooper) για αυτοματοποιημένη, ωριαία στοιχειακή παρακολούθηση. Επιπλέον, περιγράφεται η εξειδικευμένη εγκατάσταση εξωτερικής δέσμης PIXE του Ινστιτούτου Πυρηνικής και Σωματιδιακής Φυσικής (INPP), ΕΚΕΦΕ «Δημόκριτος» ΕΚΕΦΕ «Δημόκριτος».

Το **τέταρτο μέρος** της διατριβής (Κεφάλαια 13–19) παρουσιάζει τα πειραματικά αποτελέσματα, ξεκινώντας με τις αναλυτικές μεθοδολογίες ακτίνων-Χ (Κεφάλαια 13–17) και συνεχίζοντας με την εφαρμογή τους σε μελέτες επιμερισμού πηγών (Κεφάλαια 18–19).

Αρχικά, διερευνήθηκε η μεθοδολογική δυναμική των νέων αναλυτικών εργαλείων. Το φορητό φασματόμετρο **HH-XRF** (Tracer 5i, Bruker) βελτιστοποιείται για ανάλυση

αερολυμάτων σε φίλτρα, βαθμονομείται έναντι προτύπων λεπτού υμενίου και συγκρίνεται με το επιτραπέζιο συστημά ED-XRF (Epsilon 5, PANalytical). Τα αποτελέσματα δείχνουν ισχυρή απόδοση για 24 στοιχεία.

Επιπρόσθετα, αναπτύχθηκε ένα πρωτόκολλο ανάλυσης με τη χρήση **μ-XRF** (M6 Jetstream, Bruker) για φίλτρα από δειγματολήπτη πολλαπλών σταδίων, παρέχοντας χωρικά αναλυμένη ποσοτικοποίηση στοιχείων στα διάφορα κλάσματα μεγέθους σωματιδίων. Στο πλαίσιο αυτό εξετάστηκε συστηματικά η χωρική ανομοιογένεια της εναπόθεσης αερολυμάτων στα φίλτρα.

Περαιτέρω βελτίωση της εργαστηριακής οργανολογίας επιτεύχθηκε μέσω της βαθμονόμησης ενός φασματομέτρου **WD-XRF** (ZSX Primus IV, Rigaku). Με τη χρήση προτύπων λεπτών υμενίων και φίλτρων αναφοράς, το WD-XRF αποδεικνύεται αξιόπιστο και συμπληρωματικό εργαλείο, προσφέροντας ανώτερη ενεργειακή διακριτική ικανότητα.

Μια επιπλέον μεθοδολογική συνεισφορά είναι η ανάπτυξη ενός ποσοτικού πρωτοκόλλου **PIXE** εξωτερικής δέσμης. Χρησιμοποιώντας δύο ανιχνευτές SDD επιτεύχθηκε η βαθμονόμηση για φίλτρα αερολύμάτων.

Τέλος, πραγματοποιήθηκε διασύγκριση μεταξύ του επιτραπέζιου φασματομέτρου ED-XRF (Epsilon 5, PANalytical) και **NRT-XRF** (Xact 625i και Xact 625 , SailBri Cooper) σε τρεις ευρωπαικές πόλεις. Η μελέτη υπογραμμίζει την πολυπλοκότητα των διασυγκρίσεων μεταξύ διαφορετικών τύπων XRF και υποστρωμάτων.

Μετά την ανάπτυξη και αξιολόγηση των μεθοδολογιών με ακτίνες-Χ, αυτές εφαρμόστηκαν σε πραγματικές περιπτωσιολογικές μελέτες σε διαφορετικά γεωγραφικά πλαίσια.

Η πρώτη μελέτη εστιάζει στην Κεντρική Ασία, παρουσιάζοντας τον πρώτο πολυετή επιμερισμό πηγών $PM_{2.5}$ στην Ντουσαμπέ του Τατζικιστάν. Χρησιμοποιώντας σταθμικό στοιχειακή ανάλυση με ED-XRF και αναλύση σε μάυρο άνθρακα (BC), τα αποτελέσματα αποκαλύπτουν σταθερά υψηλά επίπεδα $PM_{2.5}$, πολύ πάνω από τα ευρωπαϊκά πρότυπα και τις οδηγίες του Παγκόσμιου Οργανισμού Υγείας (WHO). Το μοντέλο της παραγοντοποίησης θετικής μήτρας (**PMF**) εντόπισε οκτώ πηγές ρύπανσης, περιλαμβάνοντας καύση καύρβουνου, καύση βιομάζας, εκπομπές από τσιμεντοβιομηχανίες , εδαφική σκόνη, δευτερογενή αερολύματα και εκπομπές από το σταθμούς παραγωγής ενέργειας. Η εποχικότητα στις συνεισφορές των πηγών ήταν έντονη, με την οικιακή καύση άνθρακα να κυριαρχεί τον χειμώνα και τις εκπομπές από σταθμούς παραγωγής ενέργειας να αυξάνονται κατά τους θερμότερους μήνες.

Στο ευρωπαϊκό πλαίσιο, διεξήχθη μια ολοκληρωμένη μελέτη στην Ελλάδα στο πλαίσιο του έργου PANACEA. Έξι σταθμοί που αντιπροσωπεύουν αστικά, προαστιακά και αγροτικά περιβάλλοντα παρακολουθήθηκαν χρησιμοποιώντας ED-XRF, ανάλυσεις άνθρακα (OC και EC) και ιοντική χρωματογραφία. Τα αποτελέσματα επιμερισμού πηγών καταδεικνύουν την αλληλεπίδραση των εκπομπών κυκλοφορίας, της καύσης βιομάζας, των δευτερογενών αερολυμάτων και των φυσικών πηγών, με τις ειδικές συνεισφορές ανά περιοχή να αντικατοπτρίζουν τις τοπικές συνθήκες και τη μετεωρολογία. Η εργασία αυτή καθιερώνει ένα συνεκτικό εθνικό σύνολο δεδομένων που μπορεί να ενημερώσει στοχευμένες στρατηγικές μετριασμού.

Τέλος, το **πέμπτο μέρος** συνοψίζει τα γενικά συμπεράσματα της διατριβής, τονίζοντας την επιτυχή γεφύρωση μεταξύ της οργανολογικής ανάπτυξης και της περιβαλλοντικής εφαρμογής.

Table of Contents

List Of Figures

List Of Tables

Section A. Introduction to Atmospheric Aerosols

1. Definition and Characteristics of Atmospheric Suspended Particulate Matter

1.1 Introduction

Atmospheric aerosols, also known as suspended particulate matter (PM), are a complex and dynamic mixture of solid and liquid particles dispersed in the air. Despite making up only a small fraction of the atmospheric mass, these microscopic particles exert a substantial influence on Earth's climate, weather systems, and air quality. Aerosols range in size from just a few nanometers to over 100 micrometers and are present across the globe, arising from a wide variety of natural and anthropogenic sources. Their significance lies in their ability to interact with both solar and terrestrial radiation, act as cloud condensation nuclei, and participate in diverse chemical reactions within the atmosphere.
Particulate matter can be classified as either primary PM, which is directly emitted from sources such as combustion or dust, or secondary PM, which forms through chemical and physical transformations in the atmosphere. The composition of PM is highly variable and depends on its origin and the processes by which it was emitted or formed. These particles undergo a range of physical and chemical transformations, and they are eventually removed from the atmosphere via wet or dry deposition. However, depending on atmospheric conditions and their residence time, aerosols can travel long distances from their source, impacting regions far from where they were initially generated.

Depending on their distinct characteristics, particulate matter (PM) can be described using a variety of terms (Seinfeld and Pandis, 1998):

- **Aerosol**: A general term referring to solid or liquid particles suspended in a gas.
- **Fog**: A visible suspension of liquid droplets, typically water, near the Earth's surface. It is a natural meteorological phenomenon whose presence is highly dependent on atmospheric conditions.
- **Dusts**: Solid airborne particles generated primarily through mechanical processes.
- **Haze**: A mixture of fine particles that scatter light and reduce visibility. It can consist of water droplets, pollutants, and dust.
- **Particle**: A physical unit of matter, which may be solid or liquid, composed of a large number of molecules held together by intermolecular forces. A particle may be formed from several smaller particles that are joined together and behave as a single unit.
- **Smog**: A compound term derived from “smoke” and “fog,” used to describe dense atmospheric pollution events characterized by elevated particle concentrations.
- **Soot**: Carbonaceous aggregates formed during the incomplete combustion of carbon-containing materials.

- **Bioaerosol**: Particulate matter of biological origin, such as pollen, viruses, bacteria, and fragments of biological organisms.
- **Cloud**: A suspension of water droplets or ice crystals in the atmosphere, generally occurring at higher altitudes and with defined spatial boundaries.
- **Particulate**: A term used to denote matter with particulate characteristics, often in reference to its behavior or measurement as discrete particles.
- **Nanoparticle**: A particle with at least one dimension in the range of 1–100 nanometers.

In addition to the general classifications, several terms are used to describe particle morphology and origin within an aerosol:

- **Aggregate**: A heterogeneous particle in which components are tightly bound together.
- **Agglomerate**: A loosely bound collection of particles, held together primarily through weak van der Waals forces.
- **Primary particles**: Particles directly emitted from a source into the atmosphere.
- **Secondary particles**: Particles that form in the atmosphere through chemical reactions or transformations, rather than direct emission.

1.2 Equivalent Diameter

The size of airborne particles is typically the key parameter used to characterize particulate matter (PM), as commonly indicated in classifications such as PM_{10}. This parameter is far from arbitrary—particle size plays a pivotal role in governing numerous properties and effects of PM. These include, but are not limited to, their environmental impact, health implications for humans, and atmospheric residence time.

As previously discussed, PM encompasses a wide range of shapes and sizes. This morphological variability poses a challenge when attempting to assign a single representative size to particles, especially those with irregular or undefined geometries. To address this issue, the concept of equivalent diameter is employed.

When a particle's size is determined through a specific measurement technique, the result typically reflects a physical property relevant to that method. The equivalent diameter is thus defined as the diameter of a hypothetical spherical particle that exhibits the same measurable physical characteristic as the actual, often non-spherical, particle. For instance, if optical properties are the basis for measurement, the equivalent optical diameter corresponds to that of a sphere with identical optical behavior to the particle under examination.

Among the various equivalent diameters, two are most frequently used**:** the aerodynamic diameter and the Stokes diameter. The aerodynamic diameter (commonly denoted d_a) refers to the diameter of a sphere with a standard density of 1 g/cm³ that settles through the air at the same terminal velocity as the particle being measured. The Stokes

diameter (d_s), on the other hand, is defined as the diameter of a sphere with the same density and settling velocity as the test particle.
Throughout this dissertation, any reference to particle size will specifically refer to the aerodynamic diameter, unless otherwise noted.

For particles with a known aerodynamic diameter (d_a), it is possible to estimate their actual physical diameter (d_ρ) using the following expression:

$$d_a = d_\rho \left(\frac{\rho_p}{\rho_0}\right)^{\frac{1}{2}} \quad (1)$$

This equation assumes that the true density of the particle (ρ_p) does not deviate significantly from the reference density (ρ_0).

Equation (1) essentially links the aerodynamic behavior of a particle—how it settles under gravity or behaves under aerodynamic forces—to its intrinsic geometric size and material density. It is particularly useful when analyzing particles of spherical geometry and uniform composition, where this approximation remains valid.

1.3 Sources of PM Emissions and Formation Mechanisms

Particulate matter (PM) can be classified based on how it is introduced into the atmosphere. This classification distinguishes between primary particles, which are directly emitted, and secondary particles, which form through atmospheric processes. This distinction is particularly important, as the origin of the particles influences their size, composition, and physicochemical behavior.

Primary particles are typically generated through mechanical processes and are generally larger in size, falling into the coarse particle category. These particles may arise from natural sources, such as soil dust, sea spray, volcanic ash, and biological materials (e.g., pollen or viruses), or from anthropogenic activities, including industrial processes, construction work, and combustion operations (Viana et al., 2008).

In contrast, secondary particles are not directly emitted into the atmosphere. Instead, they are formed through physical or chemical transformations of gaseous precursors or pre-existing particles. These are usually found in the fine or ultrafine size range. Two major mechanisms govern the formation of secondary particles:

- **Nucleation**: The initial generation of new particles from supersaturated vapors, which may occur either **homogeneously**, without the presence of existing surfaces, or **heterogeneously**, with **condensation** onto pre-existing particles.
- **Coagulation**: The process by which smaller particles collide and combine to form larger aggregates.

The distinction between primary and secondary PM is essential for understanding their behavior in the atmosphere, as it affects not only their size distribution, but also their chemical composition, reactivity, and impact on health and the environment.

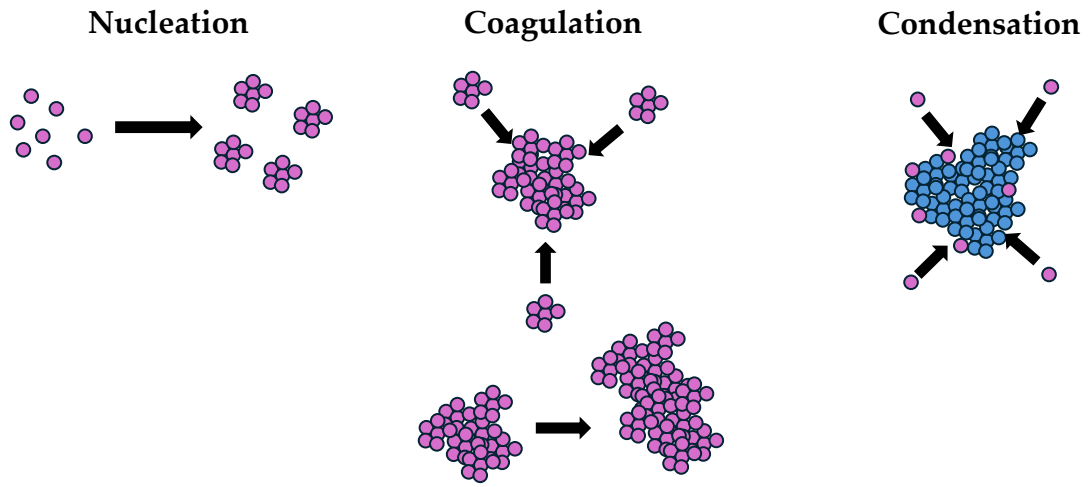

Figure 1. *Schematic representation of secondary aerosol particle growth mechanisms: nucleation, coagulation, and condensation.*

1.3.1 Homogeneous Nucleation

Homogeneous nucleation refers to the process through which clusters—i.e., aggregates of fundamental molecular units—form a new phase within a continuous medium without the presence of any foreign surfaces or materials. This transformation occurs when the supersaturation ratio (S) of the system exceeds unity ($S > 1$), indicating a condition of supersaturation.

Under such conditions, an excess of monomeric molecules is present in the vapor phase compared to equilibrium. These monomers randomly collide with molecular clusters, leading to their growth. Once a cluster reaches a certain threshold—termed the **critical size**—it becomes energetically favorable for it to continue growing into a stable, macroscopically observable particle, effectively initiating the emergence of a new phase.

The critical cluster size is defined as the size at which the rate of cluster growth equals the rate of its dissociation. Clusters smaller than this threshold typically evaporate or shrink back into the vapor phase, whereas those exceeding it are more likely to continue growing.
The rate of homogeneous nucleation is expressed as the number of clusters surpassing the critical size per unit time, and it strongly depends on factors such as temperature, saturation ratio, and molecular properties of the condensing species (Wyslouzil et al., 2016).

1.3.2 Heterogeneous Nucleation or Condensation

Heterogeneous nucleation is generally a more common pathway than its homogeneous counterpart. It involves the condensation of gaseous species onto existing particles, typically smaller than 1 μm in diameter, known as condensation nuclei.
These nuclei can be classified into two main categories:

- Water-soluble nuclei
- Insoluble (hydrophobic) nuclei

Insoluble particles act as passive condensation sites, particularly under conditions of supersaturation. When the diameter of a nucleus exceeds the Kelvin diameter—a critical size related to surface curvature and saturation conditions—it behaves similarly to a liquid droplet, promoting vapor condensation on its surface. Once the condensation process begins, particle growth is self-sustaining and continues as long as supersaturated vapor remains available.

Heterogeneous nucleation involving water-soluble nuclei is considerably more complex. In the atmosphere, a significant number of such nuclei exist, often formed from evaporated aqueous droplets containing dissolved substances. When the water evaporates, it leaves behind residual solutes that serve as condensation seeds. Because these water-soluble nuclei have a strong chemical affinity for water, condensation can initiate even at lower levels of supersaturation. In general, dissolved salts facilitate faster droplet growth while also suppressing evaporation rates compared to droplets composed solely of pure liquid.

Evaporation, conversely, is essentially the reverse process of condensation: it occurs when the partial pressure of the condensed phase falls below its saturation vapor pressure, leading to mass loss from the droplet (Smorodin et al., 2006).

1.3.3 Coagulation

Coagulation refers to the process by which particles grow in size through collisions and subsequent adhesion. These collisions can occur due to two primary mechanisms:

- Brownian motion, in which case the process is termed thermal coagulation (Patra and Roy, 2022).
- External forces (e.g., turbulence, electrical or gravitational fields), resulting in kinematic coagulation.

Although coagulation is conceptually similar to growth by condensation, the key difference lies in the interacting species—in coagulation, entire particles collide and merge, whereas in condensation, growth occurs via the addition of gas-phase molecules.

Unlike nucleation or condensation, coagulation does not require supersaturation conditions, and it is typically irreversible. As particles collide and merge, the total number of particles in the system decreases, while their average size increases. Importantly, if no particle removal processes are active, the total mass of the particulate system remains constant. In

systems where particle growth is diffusion-limited, the coagulation rate is generally proportional to the square of the particle concentration. This means that coagulation is more rapid in environments with high particle number density and considerably slower in cleaner or more dilute systems. Kinematic coagulation follows different dynamic mechanisms compared to thermal coagulation, but in both cases, the rate of coagulation increases with increasing particle concentration.

1.4 PM classification of Based on Size

Particle size is arguably the most critical property of PM, as it governs not only its environmental behavior but also its health impact and atmospheric lifetime. The size range of PM spans from just a few nanometers up to approximately 100 micrometers. This wide variability is determined primarily by the emission source and the physical and chemical processes acting upon the particles once they are airborne.

1.4.1 Fine Mode Particles

Fine particles are defined as those with an aerodynamic diameter of 2.5 μm or smaller ($PM_{2.5}$). These particles are typically formed secondarily in the atmosphere, as a result of gas-to-particle conversion processes. The fine fraction can be further subdivided into two categories, based on particle origin and formation mechanism:

i) Nuclei Mode Subcategory (Nuclei Range)

The nuclei mode includes ultrafine particles ranging in size from approximately 0.01 to 0.05 μm (10–50 nm). These particles may originate directly from combustion sources or may form as condensates of combustion by-products. Due to their extremely small size, they exhibit short atmospheric lifetimes, as they are highly reactive and tend to rapidly coagulate with each other or with slightly larger particles. This leads to the formation of larger-sized particles through growth processes (Hinds, 1999). The nuclei mode is further divided into two subgroups:

- Aitken Nuclei: This subgroup includes particles that exhibit a local maximum in number distribution above 15 nm. These particles often represent the early stages of particle growth following nucleation and are involved in subsequent coagulation and condensation processes.
- Ultrafine Nuclei: This category comprises the smallest particles in the nuclei range, typically below 15 nm in diameter, and shows a local peak in number concentration within this lower range. These particles are freshly formed and highly transient, often representing the initial outcome of homogeneous nucleation events.

ii) Accumulation Mode Subcategory (Accumulation Range)

The accumulation mode includes particles with aerodynamic diameters ranging from approximately 0.05 to 2.5 μm. These particles are typically formed through the coagulation of smaller particles (primarily from the nuclei mode), as well as through condensation of vapors onto existing particles, resulting in progressive growth (Hinds, 1999). Particles in the accumulation range generally exhibit longer atmospheric lifetimes, typically from 7 to 30 days, due to their relatively low settling velocities and slower removal rates. This allows them to travel long distances and participate in various atmospheric processes. The accumulation mode is further divided into two characteristic groups:

- Droplet Mode: This group forms under high relative humidity conditions, such as in clouds, fog, or during aqueous-phase reactions. Condensation and chemical transformations occur on the surface of suspended particles, leading to the formation of larger hygroscopic droplets. These particles often serve as cloud condensation nuclei (CCN).
- Condensation Mode: These are smaller particles within the accumulation range that originate from the coagulation of non-hygroscopic nuclei-mode particles or from direct vapor condensation without significant liquid-phase interactions. They represent a transitional growth phase and may eventually evolve into larger droplet-mode particles under suitable environmental conditions.

1.4.2 Coarse Mode Particles

Coarse particles are defined as those with an aerodynamic diameter greater than 2.5 μm. They are primarily produced by mechanical processes, such as wind-driven resuspension of soil dust, sea spray, abrasion, and industrial activity. Larger particles—such as those around 10 μm in diameter—have relatively short atmospheric lifetimes, typically 10 to 20 hours, before settling under gravity within the lower troposphere. Assuming an average wind speed of approximately 7 m/s, such particles can be transported up to 20–30 kilometers from their emission source before deposition occurs.

In contrast, smaller particles (e.g., 0.1 to 1 μm) are less affected by gravitational forces and can remain suspended for significantly longer durations, enabling them to travel hundreds of kilometers under favorable meteorological conditions.

A small fraction of airborne particles, particularly those in the fine or ultrafine range, can ascend to the upper troposphere (altitudes of 8–15 km) and remain suspended for extended periods, even up to one year, depending on atmospheric dynamics and vertical mixing processes (EPA, 2021; Toohey et al., 2025).

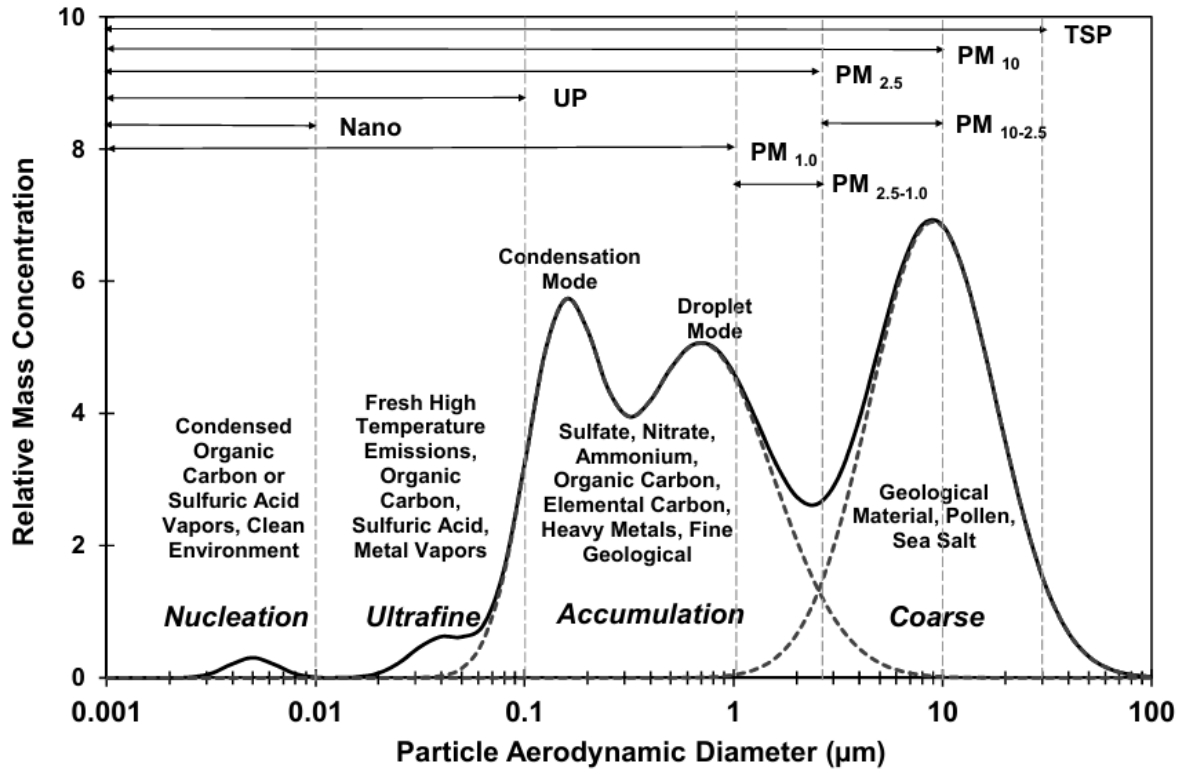

***Figure 2**. Typical particle size distribution in the atmosphere. Total Suspended Particles (TSP) span a size range from about 0 up to ~30–50 µm. The nucleation mode refers to particles smaller than 0.01 µm, while ultrafine particles are those below 0.1 µm. The accumulation mode primarily includes fine particles between ~0.1 and ~2 µm. Within this range, a condensation peak appears near 0.2 µm due to gas-phase reaction products, and a droplet mode around 0.7 µm arises from reactions occurring in aqueous droplets. Coarse particles generally fall between ~2–3 µm and 100 µm. UP corresponds to Ultrafine Particles, and Nano denotes nanoparticles (Cao et al., 2013) .*

2. Filter-Based Sampling of PM

2.1 PM Sampling Introduction

Although continuous monitoring techniques for PM concentrations—and to a lesser extent, for PM composition—are gaining ground in environmental research, filter-based sampling remains the most fundamental method for PM collection and analysis (Patel and Aggarwal 2022).

Sampling is typically the first step in any environmental investigation, and its quality has a decisive impact on the reliability of all subsequent analytical results. For this reason, it is essential that sampling procedures are conducted with strict attention to protocol and precision.

A wide variety of commercial PM samplers are available, each operating on distinct physical principles, depending on the design and intended application. Among these, inertial samplers are among the most widely used, especially for size-segregated collection. The use of filters is arguably the most common and well-established approach for both the collection and mass determination of PM (Dzubay et al., 1991;). The basic principle involves capturing a representative sample of airborne particulate matter on a porous substrate or filter membrane. The procedure generally involves two main stages:

1. Collection Stage – The airborne particles are extracted from the atmosphere and deposited onto a filter medium by drawing air through it.
2. Post-collection Analysis – The mass of the collected particles is determined gravimetrically. This may be followed by more advanced chemical or elemental analysis, depending on the scope of the study.

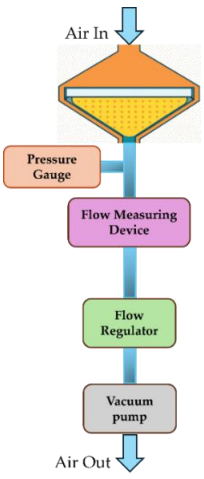

Figure 3. *Schematic of a filter-based PM sampling system, illustrating the main components including the sampling probe, filter holder, flow measurement and regulation units, and vacuum pump.*

Initially, ambient aerosol-laden air enters the sampler through the inlet, which is specifically designed to ensure isokinetic sampling. The air is then directed through a pre-selected filter medium, chosen according to the type and size of particulate matter (PM) targeted for collection. After passing through the filter, the air continues into a flow measurement device, which quantifies the volumetric air flow rate. Airflow through the system is actively driven by a vacuum pump, connected downstream. A flow controller (such as a critical orifice or flow-regulating valve) is placed between the filter and the pump to maintain a stable and controlled flow rate. These components form the essential configuration of a filter-based PM sampling unit. Optional components may include:

- A pressure gauge, which measures the pressure drop across the filter (indicative of filter loading),
- And sensors for temperature and relative humidity, which can affect PM characteristics and mass.

This type of sampler is generally suitable for the collection of total suspended particulates (TSP), as it lacks any particle size-selective inlet (e.g., impactor, cyclone, or virtual impactor). In order to isolate specific PM fractions (such as PM_{10} or $PM_{2.5}$), a size-segregating pre-separator must be added upstream of the filter.

The efficiency of sampling depends largely on:

- The suction performance (ability of the pump to maintain stable airflow),
- And the transport efficiency, defined as the ratio of PM that reaches the filter to the total amount entering the sampler.

Achieving high sampling efficiency is particularly challenging because it varies with particle size. In general, minimizing the distance between the inlet and the filter reduces deposition losses along the flow path and increases collection efficiency.

2.2 Types of Filters Used in PM Sampling

As mentioned in the previous section, the collection of particulate matter (PM) requires a collection medium, commonly referred to as a filter. A wide variety of filter types exist, differing in terms of material composition, geometry, dimensions, and cost (Lindsley, n.d.). The choice of filter depends on several key factors:

- The PM size fraction being targeted,
- The sampling device being used,
- And the type of analysis intended for the collected sample (e.g. gravimetric, elemental, organic, or microscopy).

Filters are typically categorized into three major classes:

1. Fibrous Filters: Composed of a network of interwoven or randomly arranged fibers that trap particles as air flows through.

2. Membrane Filters: These consist of a thin, continuous film with microscopic pores and offer precise control over particle retention by size. They are often used in microscopy or chemical analysis.
3. Porous (or Depth) Filters: Characterized by an internal pore structure, allowing particles to be retained throughout the depth of the filter matrix. These filters are often used when high particle loading is expected.

2.2.1 Membrane Filters

Membrane filters are commonly manufactured from materials such as polyvinyl chloride (PVC), polytetrafluoroethylene (PTFE, also known as Teflon®), and other synthetic polymers. They often consist of multiple layers with distinct structural or functional characteristics. Although these filters typically exhibit a relatively high pressure drop during sampling, they offer high collection efficiency, even for particles significantly smaller than their nominal pore size (Lindsley, n.d.). Particle retention on membrane filters primarily occurs through mechanisms such as:

- Inertial impaction, where larger particles deviate from the air stream and impact the filter surface,
- And Brownian diffusion, which facilitates the capture of ultrafine particles due to their random motion.

These filters are frequently used in applications requiring chemical analysis, microscopy, or low blank background, due to their uniform structure and compatibility with analytical techniques.

2.2.2 Fibrous Filters

Fibrous filters are composed of densely entangled fibers forming a porous structure. Their porosity typically ranges between 0.600 and 0.999, depending on the fiber packing density. Further compaction to reduce porosity is often not possible due to structural limitations of the medium. The diameter of individual fibers can vary significantly—from approximately 1 μm to several hundred micrometers—depending on the manufacturing process and filter type. While most fibrous filters exhibit a range of fiber diameters, uniform-fiber filters also exist for specific applications. To enhance the mechanical stability of the filter matrix, binding agents are often added to the structure, sometimes comprising up to 10% of the total filter mass. Fibers used in these filters may be made from: Cellulose, Glass, Quartz and Polystyrene. Each fiber type has distinct advantages and disadvantages, depending on its composition and intended analytical application:

- Quartz Fiber Filters: Quartz filters are chemically inert, contain minimal elemental background, and are well suited for elemental analysis. They are ideal for organic

carbon (OC) and elemental carbon (EC) measurements, as they can be pre-fired at high temperatures to remove organic contaminants (Hopke et al., 2023). Additionally, quartz filters are non-hygroscopic, minimizing interference from ambient humidity (Subramanian et al., 2004). However, they are fragile, making them more difficult to handle and prone to breakage.

- Cellulose Filters: These filters offer good mechanical strength, are cost-effective, and impose a relatively low pressure drop during sampling (Chow et al., 2022). Their main disadvantage is their low efficiency in capturing submicron particles, particularly those with diameters <1 μm.
- Glass Fiber Filters: While these filters result in higher pressure drops compared to cellulose filters, they offer excellent collection efficiency, typically exceeding 99% for particles >0.3 μm (Chow et al., 2022). They are also relatively unaffected by moisture, making them reliable under varying humidity conditions.

2.2.3 Pore-Through Filters (Nucleopore Filters)

Nuclepore filters, also referred to as track-etched polycarbonate membranes, are widely used in aerosol science and microbiological applications due to their precise pore structure and smooth surface. These filters are manufactured by irradiating a thin polymer film (typically polycarbonate) with high-energy particles such as neutrons or heavy ions, followed by chemical etching to create cylindrical pores of uniform diameter.

In contrast to fibrous or tortuous-pore filters, Nuclepore membranes feature straight, through-pores that allow for well-defined particle size selection and minimal particle loss due to diffusion or retention within the matrix. Their smooth, flat surface makes them particularly suitable for applications involving microscopic analysis or quantitative particle counting. Despite their high resolution and analytical suitability, these filters are mechanically fragile and often require careful handling during sampling and analysis. Due to their chemically inert nature and low background contamination, they are commonly employed in studies involving trace elemental analysis. (Mateus et al., 2006; Ghermandi et al., 2005).

2.3 Inertial Particle Size Classifiers

In many cases it is necessary to isolate a specific fraction of PM and the sampling device must incorporate a mechanism capable of selectively capturing only that target size range (Hinds, 1999). This is typically accomplished using a device designed to separate particles according to their aerodynamic diameter. Most such devices operate on the principle of particle inertia. Among them, inertial impactors are the most prevalent, with cyclones also being commonly employed but to a lesser extent impactors exploit the inertia-based separation principle, whereby particles of differing sizes possess distinct inertial responses

(Marple and Willeke, 1976). In such devices, an alteration of the aerosol flow path causes particles with sufficient inertia to deviate from the airflow, enabling their capture while smaller particles follow the redirected streamlines.

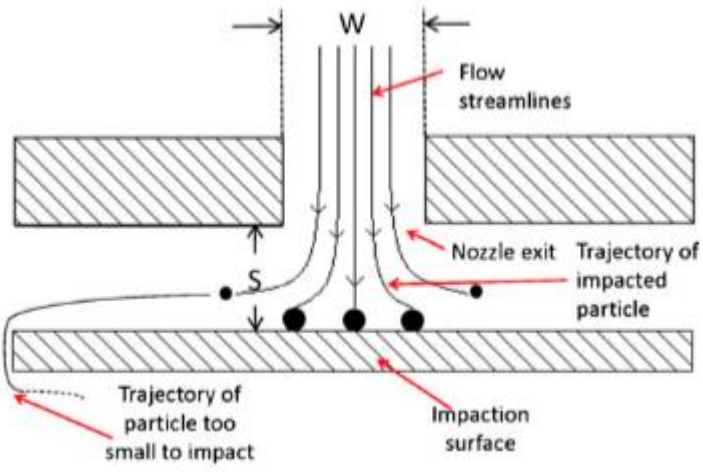

Figure 4. *Operation of an impactor (Nichols et al., 2013)*

2.3.1 Stokes Number and Its Role in Impactor Performance

The Stokes number (St_k) is a dimensionless quantity that indicates whether a particle approaching an obstacle will collide with it or be carried along by the surrounding airflow (Baron and Willeke 2001). It represents the ratio of the particle's stopping distance to the characteristic size of the obstacle.

$$St_k = \frac{\rho_p C_c U d_p^2}{18 \mu d_b} \tag{2}$$

In this expression:

- ρ_p is the particle density which directly affects the particle's inertia; denser particles are less easily decelerated by air drag.
- C_c is the slip correction factor, a dimensionless coefficient that compensates for deviations from continuum flow when particle diameters are on the order of the mean free path of air molecules. This factor is especially relevant for submicron particles.
- U represents the relative air velocity, determined by the flow rate and the geometry of the sampling system. Higher velocities impart greater momentum to particles, increasing their likelihood of deviating from streamlines.
- d_p is the particle diameter, which may be specified as aerodynamic or geometric, depending on the application. Larger particles possess greater inertia and are thus more prone to impact.

- μ denotes the dynamic viscosity of air (Pa·s), a measure of the internal resistance of air to flow. Higher viscosity increases the drag force on moving particles, reducing their stopping distance.
- d_b is the obstacle diameter, representing the characteristic size of the target, such as the collection plate, against which particles may collide.

When $Stk>1$, the particle retains enough inertia to impact the obstacle rather than follow the deflected airflow. For inertial impactors, it is often more convenient to relate the stopping distance to the radius of the nozzle rather than the obstacle diameter, giving the form:

$$St_k = \frac{\rho_p C_c U d_p^2}{9\mu W} \quad (3)$$

where W is the nozzle diameter. A useful benchmark in characterizing inertial separators is the cut-off Stokes number (Stk_{50}) defined as the Stokes number corresponding to particles that are collected with 50% efficiency. The square root of the Stokes number is also a dimensionless indicator of particle size, providing a convenient way to relate particle properties to the separation performance of the device.

2.3.2 Impactors

A typical impactor consists of one or more nozzles through which air is drawn and directed toward a flat surface known as the impaction plate. Particles larger than the impactor's cut-off size cannot follow the abrupt change in airflow direction and thus collide with and are retained on this plate. Conversely, smaller particles remain entrained in the airflow and continue onward to the filter downstream.

The key performance metric of an impactor is its collection efficiency curve, which quantifies the percentage of particles captured relative to the total particle count. Ideally, an impactor selectively collects only those particles exceeding its designated size threshold. A single-stage impactor is useful when the objective is to isolate a single size fraction. However, when multiple particle size ranges must be separated, a multi-stage cascade impactor is employed. This device comprises several impactor stages arranged sequentially, each referred to as a "stage". As the aerosol passes through successive stages, the gas velocity increases, enabling the collection of progressively smaller particles at each subsequent plate (Roberts et al., 2009; Stefancova et al., 2011; Wang et al., 1998).

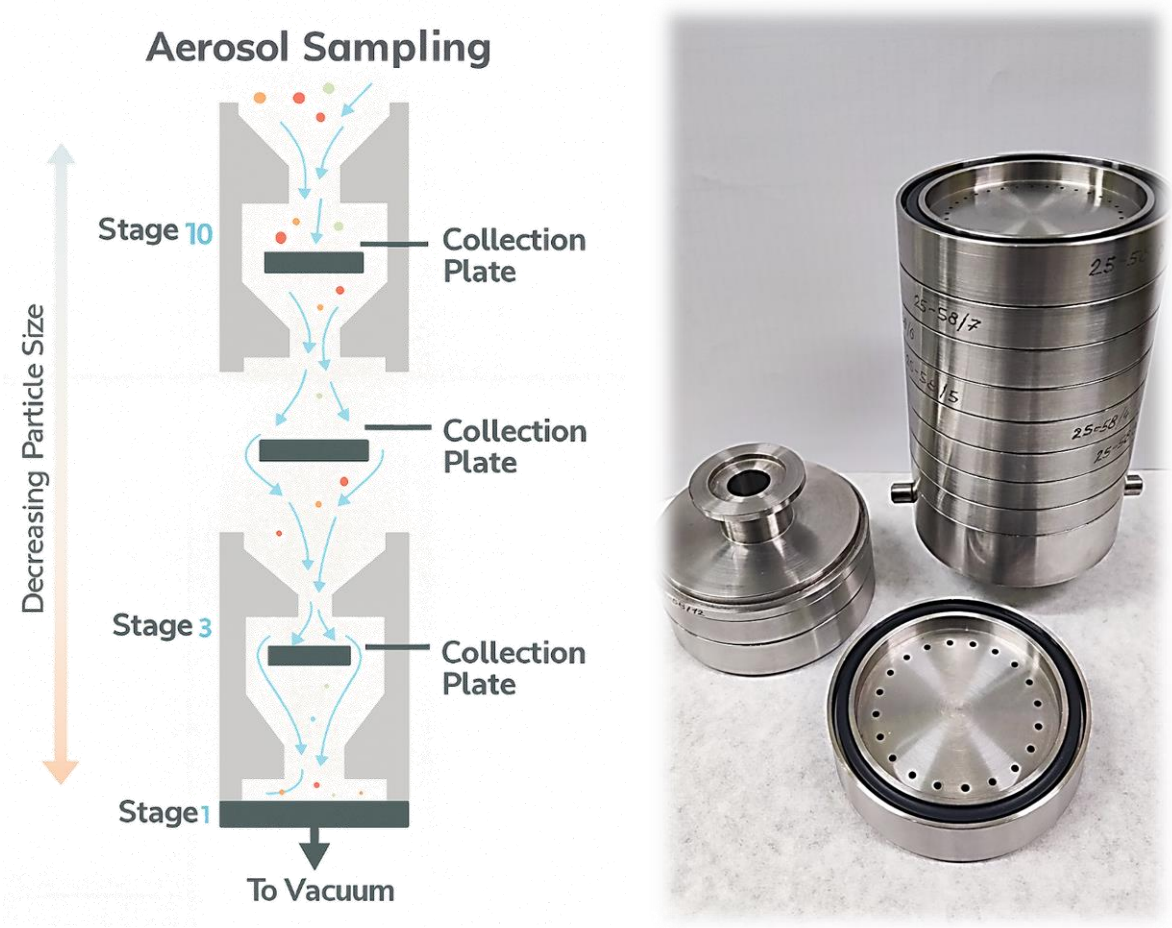

Figure 5. *Left)* *Operation principle of a multi-stage cascade impactor. Right) The 10-Stage Berner multi-nozzle cascade impactor.*

3. Chemical Composition of PM

The chemical composition of airborne particulate matter (PM) is highly variable and influenced by both the origin of the particles and the location of observation. Even particles emitted from a common source may exhibit distinct chemical profiles when sampled in different geographic regions, due to local environmental conditions and atmospheric processes (Seinfeld and Pandis, 1998; Amato et al., 2016; Almeida et al., 2020). Despite this variability, several major component groups are consistently identified across numerous studies. These typically include secondary inorganic ions—such as sulfates, nitrates, ammonium, and chloride—as well as carbonaceous species, namely organic carbon (OC) and elemental carbon (EC). In addition, PM contains trace elements, crustal materials, heavy metals, biological matter, and, in coastal or marine-influenced areas, significant amounts of sea salt.

3.1 Organic Carbon (OC)

Organic carbon (OC) constitutes a significant fraction of atmospheric particulate matter (PM) and is derived from both primary emissions and secondary formation processes. Primary OC originates from combustion-related activities, including the burning of fossil fuels, biomass, and waste, as well as from biological sources and resuspended road or soil dust. Secondary OC, by contrast, is formed in the atmosphere via photochemical reactions involving volatile organic compounds (VOCs), which oxidize and condense to produce low-volatility organic species. The extent of secondary organic aerosol (SOA) formation is often evaluated by the organic carbon to elemental carbon (OC/EC) ratio, with values exceeding 2 typically indicating a dominant secondary origin (Pio et al., 2016).

The organic fraction in PM comprises a wide spectrum of chemical species, including aliphatic hydrocarbons (such as n-alkanes), aromatic and oxygenated compounds (e.g., aldehydes, ketones, esters, and epoxides), and organic acids (e.g., palmitic, oleic, linoleic acids) (Mendonça da Silva et al., 2025).

An especially toxic subset of OC includes polycyclic aromatic hydrocarbons (PAHs), which are primarily generated through pyrosynthesis during incomplete combustion. These compounds are of concern due to their known carcinogenic and mutagenic properties (Moubarz et al., 2022).

From an analytical perspective, OC is quantified alongside elemental carbon (EC), with the sum of the two representing the total carbon (TC) content of PM. The fraction attributed to OC is estimated as the difference between TC and EC, typically determined using thermal or thermo-optical methods, where carbon is oxidized and measured as CO_2 or CH_4 (Rauber et al., 2023). Since OC consists not only of carbon but also of oxygen, hydrogen, and nitrogen atoms, the total organic matter (OM) is calculated using a conversion factor, generally

ranging from 1.4–1.8 for fresh aerosols and 1.9–2.3 for aged, more oxidized particles (Turpin et al., 2000; Pang et al., 2006).

OC plays a key role in climate and atmospheric chemistry, contributing to the scattering of solar radiation, altering cloud condensation properties, and influencing surface tension in cloud droplets (Bahadur et al., 2009). Its variability across locations and sources highlights its importance in both source apportionment and air quality assessments.

3.2 Elemental Carbon (EC)

Elemental carbon (EC) is a major component of carbonaceous PM and is predominantly produced through incomplete combustion of carbon-containing fuels, including fossil fuels and biomass. It is primarily emitted in the form of soot particles, which consist of solid, refractory carbonaceous cores. These cores may contain graphitic structures or non-volatile high molecular weight materials such as tar or coke. A characteristic feature of these soot particles is that their solid carbon cores are often coated with semi-volatile organic compounds, which condense from combustion gases as the aerosol cools. These organic coatings frequently include functional groups such as hydroxyls, phenols, carbonyls, and carboxylic acids, altering the surface chemistry of the particles and influencing their environmental interactions.

In the literature, the terms elemental carbon (EC) and black carbon (BC) are often used interchangeably, but they refer to different operational definitions of the same general class of material. EC is typically defined based on its chemical composition, and is quantified using thermal or thermo-optical methods, where carbon is combusted and detected as CO_2 or CH_4. BC, on the other hand, is defined based on its optical properties, specifically its strong light-absorbing ability across the visible spectrum.

Due to its stability in the atmosphere and relatively limited chemical reactivity, elemental carbon is considered a robust tracer for primary anthropogenic pollution, especially from traffic emissions and other combustion sources (Manousakas et al., 2020; Diapouli et al., 2022). Furthermore, its climatic impact is significant, as EC (or BC) strongly absorbs solar radiation, contributing to atmospheric warming, cloud property alterations, and surface darkening when deposited on snow or ice.

In summary, elemental or black carbon is both a chemically and optically significant pollutant, and its accurate measurement is essential for understanding source contributions, radiative forcing, and air quality.

3.3 Secondary Inorganic Ions

Secondary inorganic ions are key constituents of fine PM and are primarily formed in the atmosphere through chemical transformations of gaseous precursor species (Pecorari et al., 2014). The most abundant of these ions include sulfates (SO_4^{2-}), nitrates (NO_3^-), and

ammonium (NH_4^+). These species are highly water-soluble and largely present in the $PM_{2.5}$ size fraction, often forming internally mixed particles with organic or elemental carbon.

3.3.1 Sulfates (SO_4^{2-})

Sulfate ions in the atmosphere are predominantly formed through the oxidation of sulfur dioxide (SO_2), a gas mainly emitted by anthropogenic sources, especially the combustion of fossil fuels (Viana et al., 2008; Hopke et al., 2020). The oxidation process occurs through various pathways:

- In the gas phase, via reaction with hydroxyl radicals (•OH),
- In the aqueous phase (cloud droplets or fog), through reactions with H_2O_2 or O_3,
- And on the surface of pre-existing aerosols, facilitating heterogeneous conversion (Seinfeld and Pandis, 1998; Wang et a., 2022).

These reactions result in the formation of sulfuric acid (H_2SO_4), which, due to its low vapor pressure, either condenses onto existing particles or participates in new particle formation. Most atmospheric sulfates are found as ammonium sulfate ($(NH_4)_2SO_4$), though in marine environments, sodium sulfate (Na_2SO_4) may also form through the neutralization of H_2SO_4 by sea salt (NaCl). While sulfates may also occur in mineral forms such as gypsum, these are typically less soluble and are classified as part of the crustal material fraction (Miyamoto et al., 2022).

3.3.2 Nitrates (NO_3^-)

Nitrate ions are formed primarily from the oxidation of nitrogen dioxide (NO_2), which is largely emitted by combustion processes including traffic and industrial activity (Viana et al., 2008; Hopke et al., 2020). The key intermediate product is nitric acid (HNO_3), which forms via reaction with hydroxyl radicals and rapidly partitions to particle surfaces or dissolves in cloud water and fog. In ambient aerosols, nitrates are often found as ammonium nitrate (NH_4NO_3), a semi-volatile salt that exists in thermodynamic equilibrium with its precursors NH_3 and HNO_3 (Lunden et al., 2003).

The formation of nitrate is influenced by temperature and humidity. At elevated temperatures, NH_4NO_3 tends to volatilize, resulting in lower concentrations during summer (Neuman et al., 2003). In addition to NH_4NO_3, sodium nitrate ($NaNO_3$) may dominate in coastal regions or environments rich in sea salt (Athanasopoulou et al., 2008).

3.3.3 Ammonium (NH_4^+)

Ammonium ions form through the neutralization of acidic species, specifically sulfuric acid (H_2SO_4) and nitric acid (HNO_3), by gaseous ammonia (NH_3). Ammonia is the most abundant basic gas in the atmosphere and is primarily emitted from agricultural and livestock

activities, as well as biomass burning and marine sources. NH_3 readily reacts with available acids to form stable salts such as ammonium nitrate (NH_4NO_3) and ammonium sulfate ($(NH_4)_2SO_4$). The sequence of neutralization typically begins with H_2SO_4, followed by HNO_3, as shown in the reversible equilibrium: NH_3 (g) + HNO_3 (g) ⇌ NH_4NO_3 (s) (Seinfeld and Pandis, 1998).

3.4 Sea Spray Aerosols

Sea spray aerosols originate from the mechanical action of wind and waves over the ocean surface, which leads to the ejection of seawater droplets into the atmosphere. As these droplets evaporate, they leave behind PM composed primarily of inorganic sea salts. These particles can exist in both solid and liquid forms, depending on ambient relative humidity (Su et al., 2022).

The composition of sea spray aerosols closely mirrors that of seawater, including ions such as Na^+, Cl^-, SO_4^{2-}, Mg^{2+}, Ca^{2+}, K^+, and CO_3^{2-}, along with various organic compounds derived from marine biological activity (Bertram et al., 2018). Sea-spray aerosols exhibit a multimodal size distribution, dominated in number by submicron particles (~0.1–0.3 μm) produced from film and jet drops, while the mass is concentrated in supermicron particles (~1–10 μm) arising from jet and spume drops (Deike et al., 2022; Wang et al., 2017).

While primarily composed of sodium chloride (NaCl), these particles can undergo heterogeneous reactions with atmospheric acidic species such as sulfuric acid (H_2SO_4) and nitric acid (HNO_3)(Seinfeld and Pandis, 1998):

Nitrate substitution reaction (heterogeneous displacement of chloride by nitric acid):

$$HNO_3(g)+NaCl(s)\leftrightarrow NaNO_3(s)+HCl(g) \quad (4)$$

Sulfate substitution reaction (heterogeneous displacement of chloride by sulfuric acid):

$$H_2SO_4(g)+2NaCl(s)\leftrightarrow Na_2SO_4(s)+2HCl \quad (5)$$

These reactions, especially efficient under high humidity when particles are in aqueous form, release hydrogen chloride (HCl) into the gas phase and result in chloride depletion from the particulate phase (Su et al., 2022). Additional chloride in the particulate phase can also originate from anthropogenic sources, including road de-icing salts in winter and HCl emissions from incinerators and power plants. Secondary reactions with ammonia (NH_3) can form ammonium chloride (NH_4Cl), typically found in the fine fraction of aerosols (Ianniello et al., 2011).

3.5 Crustal and Geological Material

PM originating from crustal and geological sources is primarily composed of wind-blown soil dust and weathered mineral fragments that are resuspended into the atmosphere. These materials are collectively classified as geological aerosols and are recognized for their significant contribution to the coarse fraction of atmospheric particles.

Their chemical composition is inherently variable and reflects the local geological characteristics and surface conditions of the source region. As such, mineral dust sampled in different geographical areas can exhibit markedly different elemental profiles. Key factors influencing their atmospheric concentration include meteorological conditions such as wind speed and precipitation, as well as anthropogenic activities like agriculture, grazing, industrial processes, and mining, which enhance surface erosion and dust mobilization (Adebiyi et al., 2023).

Coarse and super-coarse dust aerosols together account for the majority of atmospheric dust mass (~85%), with the global coarse dust load (2.5–10 μm; ~14 Tg) exceeding fine dust by more than a factor of three, while super-coarse dust (10–20 μm; ~10 Tg) and giant dust (>20 μm; ~0.3 Tg) also make measurable contributions (Adebiyi & Kok, 2020; Adebiyi et al., 2023).

The primary elemental constituents of these aerosols—commonly referred to as major crustal elements—include silicon (Si), aluminum (Al), iron (Fe), calcium (Ca), magnesium (Mg), sodium (Na), potassium (K), titanium (Ti), and oxygen (O). These are typically present as naturally occurring minerals such as: Quartz (SiO_2), Calcite ($CaCO_3$), Gypsum ($CaSO_4 \cdot 2H_2O$), Feldspars (e.g., $KAlSi_3O_8$), Magnesium salts like epsomite ($MgSO_4 \cdot 7H_2O$), Clay minerals including chlorite, kaolinite, and montmorillonite, Iron oxides such as hematite (Fe_2O_3) (Nowak et al., 2018). The specific mineralogical makeup of the dust strongly influences the particles' hygroscopicity, reactivity, and optical properties, thereby playing an important role in atmospheric chemistry and radiative forcing.

3.6 Trace elements

PM often contains a wide range of trace elements, typically present in very low concentrations but of significant environmental and health concern. These elements include transition metals and metalloids such as vanadium (V), chromium (Cr), manganese (Mn), cobalt (Co), nickel (Ni), copper (Cu), zinc (Zn), arsenic (As), cadmium (Cd), barium (Ba), selenium (Se), tin (Sn), strontium (Sr), mercury (Hg), and lead (Pb) (Viana et al., 2008; Kumar et al., 2018).

The origin of trace elements in PM is both natural and anthropogenic. Natural sources include soil resuspension, volcanic activity, oceanic spray, and wildfires, with mineral dust playing a dominant role, especially for elements such as Cr, Mn, and V. Volcanic emissions

contribute notably to global loads of Cd, Hg, As, and Pb, while sea spray can account for a modest fraction (~10%) of total trace element emissions. Additionally, some biologically derived particles may contain trace metals, especially in forested environments. Anthropogenic contributions, however, are generally more dominant in urban and industrial settings. Combustion of fossil fuels and biomass, metal smelting, waste incineration, and vehicular traffic are major contributors. Specifically:

- Coal combustion and heavy oil combustion release metals like V and Ni.
- Traffic-related emissions include direct exhaust contributions of Fe, Zn, Cu, Ni, and Cd, along with indirect releases from abrasion of brakes, tires, and road surfaces, which emit elements such as Sb, Ba Fe and Cu.
- Industrial metallurgy is a major source of As, Cd, Zn, and Cu.

Although trace elements account for a small fraction of PM mass, many exhibit toxicological relevance even at low concentrations.

4. Impacts of Particulate Matter

4.1 Health Effects of PM

PM poses one of the most serious risks to human health among all air pollutants. The extent of its impact depends both on particle size and chemical composition. Fine particles ($PM_{2.5}$) and ultrafine particles (UFPs) are of particular concern, as their small size allows them to penetrate deep into the respiratory tract, reaching the alveolar region and, in some cases, entering the bloodstream. Larger particles (PM_{10}) tend to deposit in the upper respiratory tract due to inertial impaction in the nasal cavity and trachea, whereas particles smaller than 2.5 μm often evade these defenses and deposit in the terminal bronchioles and alveoli, especially via Brownian motion in low-flow regions (Kim et al., 2015).

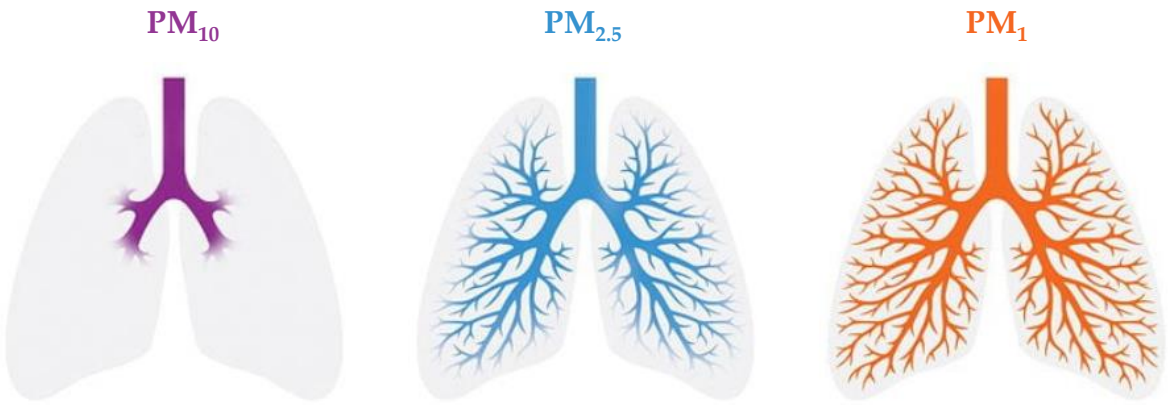

Figure 6. *Schematic representation of the deposition pattern of different PM size fractions in the human respiratory system. Larger particles (PM_{10}, left) tend to deposit in the upper airways (nasal passages and bronchi), while finer particles ($PM_{2.5}$, center) penetrate deeper into the bronchial tree. Ultrafine particles (PM_1, right) can reach the alveolar region, potentially leading to more severe health effects. The illustration highlights the increasing penetration depth of smaller PM fractions within the lungs (Safera, 2025).*

Numerous epidemiological studies have demonstrated a robust association between PM exposure and a range of adverse health outcomes, including respiratory and cardiovascular diseases, exacerbation of asthma, lung tissue damage, and even premature mortality (Sangkham et al., 2024; WHO, 2024).

The chemical composition of inhaled particles plays a crucial role in their toxicity. Certain constituents—such as elemental carbon (EC), organic compounds (OC), sulfate ions (SO_4^{2-}), and transition metals—have been linked with elevated health risks, including inflammation, oxidative stress, and increased cardiovascular hospital admissions (Morakinyo et al., 2016).

The short-term effects of exposure to elevated PM concentrations have also been widely investigated. Brief but intense episodes of PM pollution have been shown to trigger acute respiratory symptoms, reduced pulmonary function, cardiovascular stress, and hospital admissions (Han et al., 2022). Additionally, certain vulnerable groups are more susceptible to

PM exposure which include the elderly, individuals with pre-existing respiratory or cardiovascular diseases, and, notably, children (Amnuaylojaroen and Parasin (2024)).

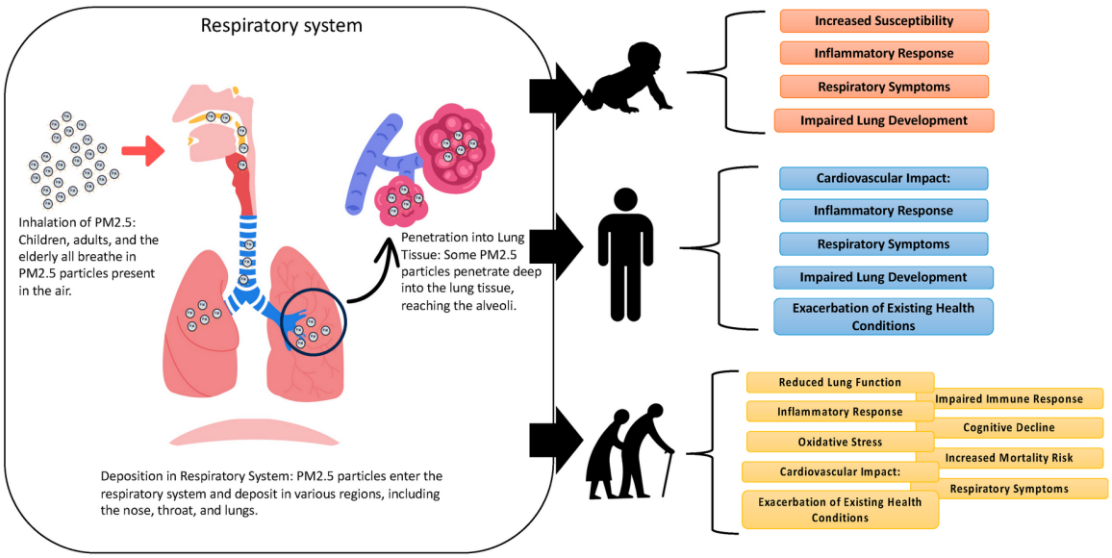

Figure 7. *Age-related differences in the toxic effects of $PM_{2.5}$: from childhood to old age. Image from (Amnuaylojaroen and Parasin (2024)).*

Children's heightened sensitivity is attributed to their developing respiratory and immune systems, as well as their higher air intake per body weight compared to adults. Their smaller lungs lead to a larger depositional surface area relative to inhaled volume, increasing the effective dose of inhaled particles (Chong-Neto and Filho (2025)). This underscores the importance of minimizing children's exposure to air pollution, particularly in areas of high vehicular traffic.

In summary, the body of evidence clearly supports the conclusion that exposure to atmospheric PM—particularly fine and ultrafine particles—is harmful to human health. Both acute and chronic exposures are implicated, and their effects are mediated not only by particle size but also by specific toxic components. Protecting vulnerable populations and reducing PM levels remains a crucial public health goal.

4.2 Environmental and Climatic Effects of PM

PM plays a complex role in the environment, influencing atmospheric visibility, climate processes, and material degradation. These effects vary depending on the physical and chemical characteristics of the particles, as well as their interaction with solar radiation and other atmospheric components.

4.2.1 Visibility and Light Scattering

One of the most immediate and noticeable environmental consequences of PM is the reduction in atmospheric visibility. Fine particles (especially $PM_{2.5}$) effectively scatter and absorb sunlight, diminishing the clarity of the atmosphere and altering the perception of natural colors and landscape features. These particles act like a veil, filtering solar radiation and leading to hazy conditions. This effect not only impacts human well-being but can also pose safety risks in transportation (Jeong et al., 2022)

4.2.2 Influence on Climate and Radiation Balance

PM affects the Earth's radiative balance in both direct and indirect ways. Direct effects include the scattering and absorption of incoming solar radiation. Bright, reflective particles such as sulfates and sea salt tend to cool the atmosphere by increasing Earth's albedo, while darker particles like black carbon absorb sunlight and contribute to atmospheric warming (Chen et al., 2021).

Indirectly, PM influences cloud properties by acting as cloud condensation nuclei (CCN). An increased number of CCN can lead to the formation of more numerous but smaller cloud droplets, which enhances cloud reflectivity (albedo) and prolongs cloud lifetime—a phenomenon known as the "Twomey effect". These changes can suppress precipitation and further affect regional and global climate systems. Moreover, particles such as mineral dust can absorb both incoming solar and outgoing terrestrial radiation, leading to localized heating or cooling effects depending on altitude and surface conditions (Adebiyi et al., 2023).

4.2.3 Effects on Agriculture and Ecosystem

By reducing the amount of solar radiation reaching the Earth's surface, PM can indirectly hinder photosynthesis and affect agricultural productivity, particularly in regions where light availability is already a limiting factor. The deposition of particles onto leaf surfaces can also interfere with gas exchange and water retention in plants, potentially impacting plant health and crop yields. (Roy et al., 2024). Furthermore, the chemical composition of particles can lead to the formation of acid rain through the atmospheric conversion of sulfur and nitrogen oxides into sulfuric and nitric acid. This acid deposition alters soil pH, depletes essential nutrients, and harms sensitive ecosystems such as forests and freshwater bodies (Bhargava 2013).

5. Sources of Particulate Matter

The sources of PM can be broadly classified into natural sources—such as dust storms, sea spray, and biological emissions—and anthropogenic sources, including traffic emissions, industrial activities, and biomass burning. Importantly, the size of the particles plays a crucial role in determining their origin, atmospheric behavior, and health effects.

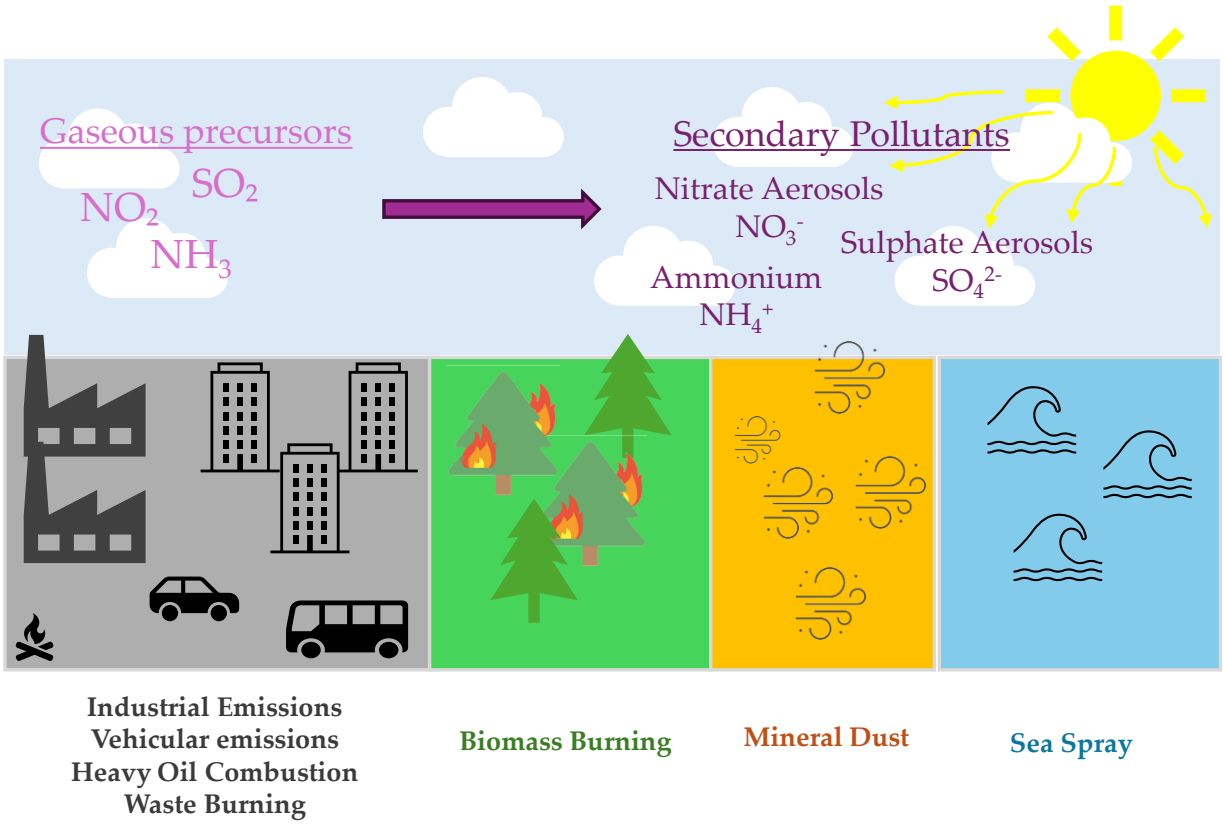

Figure 8. Major Sources of Particulate Matter.

5.1 Biomass Burning

Common Tracers: Organic Carbon (OC), Elemental Carbon (EC), Potassium (K), Levoglucosan, Chloride (Cl)

Biomass burning is a major source of PM, arising from the combustion of plant-based materials such as wood, agricultural residues, and forest vegetation. It encompasses a variety of activities, including residential heating with wood, open field burning of crop residues and forest fires. The contribution of biomass burning to ambient PM levels is especially significant during colder months (due to residential heating) and in regions where agricultural burning is seasonally practiced (Jiang et al., 2024).

The particles emitted from biomass combustion typically fall in the fine ($PM_{2.5}$) and ultrafine ($PM_{0.1}$) ranges and are rich in carbonaceous material. Two primary components—

OC and EC—serve as key indicators of combustion processes. A widely used elemental tracer for biomass burning is potassium (K), particularly in its soluble form (K^+), which is abundant in plant tissues and volatilizes during combustion. Its presence in the fine PM fraction, especially when correlated with OC and EC, strongly suggests biomass combustion as a source (Viana et al., 2008; Hopke et al., 2020; Amato et al., 2016; Almeida et al., 2020).

In addition to inorganic tracers, specific molecular markers such as levoglucosan—a monosaccharide anhydride produced from the pyrolysis of cellulose—provide robust evidence for biomass burning. Levoglucosan is particularly valuable due to its specificity and stability under atmospheric conditions. Chloride (Cl^-), when detected in elevated concentrations, can also indicate biomass burning, especially when derived from vegetation or salt-containing biomass (Giannoni et al., 2012).

Another key element is sulfur (S), whose role becomes more prominent in the context of aged smoke. While S is not typically abundant in freshly emitted particles from biomass combustion, it can increase through atmospheric processing. Li et al. (2003) described how smoke aging results in the transformation of potassium chloride (KCl)—a component of fresh biomass emissions—into potassium sulfate (K_2SO_4) and potassium nitrate (KNO_3). These transformations occur via heterogeneous reactions with sulfur- and nitrogen-bearing species in the atmosphere, including those from the same combustion source or from background urban pollution. Thus, aged biomass burning aerosols tend to show depleted Cl^- levels and enhanced sulfate and nitrate, alongside persistent K. Almeida et al., 2020 also emphasized sulfur's utility as an indicator of aged biomass burning in urban receptor profiles where elevated S concentrations coincided with biomass-related organic markers.

5.2 Heavy Oil Combustion

Common Tracers: Vanadium (V), Nickel (Ni), Sulfate (SO_4^{2-}), Elemental Carbon (EC)

Heavy oil combustion refers to the burning of residual fuels such as bunker oil or heavy fuel oil (HFO), commonly used in shipping, power generation, and some industrial processes. These fuels are characterized by high viscosity, high sulfur content, and elevated concentrations of trace metals, resulting in distinct emission profiles when combusted (Viana et al., 2008).

Emissions from heavy oil combustion are predominantly composed of fine particles ($PM_{2.5}$), many of which are formed through the condensation of vaporized compounds or via gas-to-particle conversion. A key feature of heavy oil combustion is the release of transition metals, particularly vanadium (V) and nickel (Ni), which are naturally enriched in the residual fractions of crude oil. These metals are emitted in both particulate and gaseous forms and are commonly used as tracers due to their abundance and relative specificity to heavy fuel oil combustion (Corbin et al., 2018).

In coastal or port cities, elevated concentrations of V and Ni in ambient air are often attributed to marine traffic, with emission profiles typically showing a V:Ni ratio in the range of 1.8–3.5, depending on fuel composition and combustion conditions. These elements are generally found in the ultrafine to fine mode, either in soluble form or bound to carbonaceous or sulfate particles (Jang et al., 2023).

Sulfate (SO_4^{2-}) is another key tracer associated with heavy oil combustion, particularly due to the high sulfur content of bunker fuels. Sulfur dioxide (SO_2), a primary combustion product, undergoes atmospheric oxidation to form sulfate aerosols, which can dominate the non-carbonaceous fraction of $PM_{2.5}$ in shipping-influenced areas(Jang et al., 2023).

Elemental carbon (EC) is also commonly present, although in lower concentrations compared to diesel or biomass burning. Its presence in conjunction with high sulfate and metal content helps differentiate heavy oil combustion from other combustion sources. Given the increasing attention to air quality in port areas, these tracers are vital for identifying and regulating ship-related emissions (Bučinskas et al., 2024).

5.3 Mineral Dust

Common Tracers: Silicon (Si), Aluminum (Al), Iron (Fe), Calcium (Ca), Titanium (Ti), Magnesium (Mg), Potassium (K), Manganese (Mn)

Mineral dust is a major component of atmospheric particulate matter, particularly in arid and semi-arid regions, but also significantly contributes to PM levels in urban environments through resuspension mechanisms. It originates primarily from the mechanical breakdown and wind erosion of soil, rock, and crustal surfaces, and is typically emitted in the coarse mode (PM_{10}), although smaller particles can remain airborne and travel over long distances (Viana et al., 2008; Adebiyi et al., 2023).Natural sources of mineral dust include deserts, dry lake beds, and bare soils, while anthropogenic activities such as construction, agriculture, road traffic, and mining can also generate large quantities of dust through resuspension. Urban road dust, for instance, is a complex mixture of crustal material and anthropogenic pollutants, influenced by land use and human activity.

The chemical composition of mineral dust reflects the geological characteristics of the source region but generally consists of oxides and carbonates of silicon (Si), aluminum (Al), calcium (Ca), iron (Fe), and magnesium (Mg). Among these, Si and Al are primary components of silicate minerals like quartz and feldspars and are thus considered core tracers for mineral dust. Fe and Ti, though present in smaller quantities, are also robust indicators, often associated with minerals such as hematite and rutile(Nowak et al., 2018).

In areas influenced by desert dust outbreaks (e.g., the Mediterranean, Middle East, and Asia), the contribution of mineral dust to total PM can become dominant, with episodic increases in coarse mode concentrations and elevated levels of crustal elements. These events

are often identifiable in ambient datasets by sudden peaks in Si, Al, and Ca concentrations (Vasilatou et al., 2017).

5.4 Sea Spray

Common Tracers: Sodium (Na), Chloride (Cl^-), Magnesium (Mg), Potassium (K), Calcium (Ca), Sulfate (SO_4^{2-})

Sea spray, also referred to as marine aerosol, is a major natural source of atmospheric PM, particularly in coastal areas and over open oceans. It is produced primarily through the mechanical action of wind and waves at the ocean surface, which leads to the formation of sea spray droplets. These droplets are generated when air bubbles formed by breaking waves burst at the sea surface, ejecting a range of particle sizes into the atmosphere (Su et al., 2022).

Marine aerosols are predominantly found in the coarse fraction (PM_{10}), though fine and even ultrafine particles can result from the evaporation of smaller droplets. Their chemical composition closely mirrors that of seawater, making them distinguishable by their characteristic ionic profile. The primary tracers for sea spray are sodium (Na) and chloride (Cl^-), which are the most abundant ions in seawater and are typically emitted in a near 1:1 molar ratio. Magnesium (Mg), potassium (K), and calcium (Ca) are also present in marine particles at proportions consistent with seawater composition and can be used in conjunction with Na and Cl^- to confirm a marine origin (Viana et al., 2008; Su et al., 2022).

Sulfate (SO_4^{2-}) in marine aerosol can originate from both primary and secondary processes. A portion is directly emitted with sea spray, while a significant fraction may form secondarily from the atmospheric oxidation of dimethyl sulfide (DMS), a sulfur-containing compound released by marine phytoplankton. This secondary sulfate, often found in the submicron fraction, can complicate the apportionment of marine aerosol if not carefully distinguished from anthropogenic sulfate sources.

In atmospheric monitoring, a useful diagnostic approach is to examine the Na:Cl ratio. Deviations from the typical seawater ratio—often due to the chloride depletion phenomenon—indicate chemical aging of marine particles (Su et al., 2022). This occurs when Cl^- is displaced by atmospheric acids such as nitric acid (HNO_3) or sulfuric acid (H_2SO_4), forming sodium nitrate ($NaNO_3$) and sodium sulfate (Na_2SO_4). Such changes are more pronounced in polluted coastal environments and can signal the interaction between natural and anthropogenic processes.

5.5 Vehicular Emissions

5.5.1 Vehicular Non-Exhaust Emissions

Common Tracers: Iron (Fe), Copper (Cu), Barium (Ba), Zinc (Zn), Antimony (Sb), Tin (Sn), Titanium (Ti), Manganese (Mn), Silicon (Si), Aluminum (Al), Calcium (Ca), Organic Carbon (OC)

Vehicular non-exhaust emissions refer to PM generated by mechanical and wear-related processes from vehicles, excluding fuel combustion. These include brake wear, tire wear, road surface abrasion, and resuspension of road dust. In recent years, non-exhaust sources have emerged as dominant contributors to traffic-related PM (He et al., 2024).

Brake wear is a major source of trace metals in urban air. Particles generated through braking contain high concentrations of iron (Fe)—from rotors and pads—as well as copper (Cu), barium (Ba), antimony (Sb), and tin (Sn), all originating from metallic additives used in brake linings. These particles are generally in the coarse and fine modes and have a characteristic metallic profile (Grigoratos and Martini, 2015).

Tire wear emits particles rich in zinc (Zn)—primarily from the vulcanization agent zinc oxide—as well as organic carbon (OC) and trace elements such lead (Pb). Tire wear particles often include carbonaceous rubber fragments, which can be difficult to differentiate from other carbon-rich PM without detailed molecular analysis (Li et al., 2023).

Road surface abrasion and resuspension contribute to ambient PM via the mechanical disturbance of road material and previously deposited dust. These processes introduce crustal elements such as silicon (Si), aluminum (Al), calcium (Ca), and titanium (Ti) into the air, often in the coarse fraction (PM_{10}). Resuspension is influenced by vehicle speed, weather conditions, and road cleanliness (Harrison et al., 2021).

Collectively, non-exhaust emissions result in a complex mix of metals, crustal materials, and carbonaceous compounds, and their contribution to total PM concentrations is often underestimated. Importantly, these emissions are unregulated in many jurisdictions and are likely to increase in relative importance as electric vehicles become more widespread.

5.5.2 Vehicular Exhaust Emissions

Common Tracers: Elemental Carbon (EC), Organic Carbon (OC), Polycyclic Aromatic Hydrocarbons (PAHs), Sulfate (SO_4^{2-}), Nitrate (NO_3^-), Zinc (Zn), Lead (Pb), Nickel (Ni), Vanadium (V), Iron (Fe), Nitrogen Oxides (NO_x)

Vehicular exhaust emissions result from the combustion of fuels in internal combustion engines, including gasoline, diesel, biodiesel, and alternative fuels. These emissions are a primary source of fine ($PM_{2.5}$) and ultrafine ($PM_{0.1}$) particles in urban air and

are composed of a complex mixture of carbonaceous and inorganic material (Viana et al., 2008).

Elemental carbon (EC), also referred to as black carbon, is a major marker of diesel combustion and is often used to quantify traffic-related PM. EC is highly light-absorbing and contributes to both health risks and climate warming. Organic carbon (OC) is emitted from both gasoline and diesel vehicles and includes a wide array of hydrocarbons and semi-volatile compounds. A significant fraction of OC is composed of polycyclic aromatic hydrocarbons (PAHs), many of which are carcinogenic. Sulfate (SO_4^{2-}) and nitrate (NO_3^-) are secondary components formed from the oxidation of sulfur dioxide (SO_2) and nitrogen oxides (NO_x), respectively, both of which are emitted in substantial amounts from vehicle exhaust, especially diesel engines. Trace metals, such as zinc (Zn), lead (Pb) (especially in areas still impacted by legacy leaded fuels), nickel (Ni), vanadium (V), and iron (Fe), may also be present, either from fuel impurities, lubricating oils, or engine wear (Charron et al., 2019; Kumar et al., 2024).

The composition of exhaust emissions varies with fuel type, engine technology, after-treatment systems, and driving conditions. While modern regulations (e.g., Euro 6/VI, Tier 3) have drastically reduced exhaust-related PM, it remains a significant source in many urban and developing regions (Hooftman et al., 2018).

5.6 Industrial Emissions

Common Tracers: Iron (Fe), Zinc (Zn), Lead (Pb), Chromium (Cr), Vanadium (V), Nickel (Ni), Manganese (Mn), Copper (Cu), Calcium (Ca), Silicon (Si), Sulfur (S)

Industrial processes are a major source PM, contributing significantly to atmospheric pollution. Emissions stem from a diverse range of sectors including metallurgy, cement production, chemical manufacturing, waste incineration, petroleum refining, and power generation. The physical and chemical characteristics of industrial PM emissions vary widely depending on the type of process, raw materials, fuel composition, and pollution control technologies in place (Viana et al., 2008).

Generally, industrial PM tends to include both coarse particles from mechanical activities (e.g., crushing, grinding, and material handling) and fine particles from high-temperature processes like combustion, smelting, and sintering. Key chemical tracers for industrial emissions include a range of metals and oxides, often present in enriched concentrations (Papagiannis et al., 2024).

Iron (Fe), zinc (Zn), copper (Cu), lead (Pb), chromium (Cr), nickel (Ni), and manganese (Mn) are commonly emitted from steel plants, metal smelters, electroplating, and battery recycling facilities. These elements can be found in both coarse and fine PM fractions, often as oxides or metal-containing aerosols. Calcium (Ca) and silicon (Si) are dominant in emissions from cement kilns, lime production, and ceramic industries, where they are often

associated with coarse mineral dust. However, fine Ca-containing particles can also result from high-temperature kiln emissions (Viana et al., 2008).

5.7 Secondary Aerosol Sources

Common Tracers: Sulfate (SO_4^{2-}), Nitrate (NO_3^-), Ammonium (NH_4^+)

Secondary aerosols are not emitted directly into the atmosphere but are formed through chemical transformations of gaseous precursors. They constitute a major fraction of fine particulate matter ($PM_{2.5}$), often dominating during periods of atmospheric stagnation and in polluted environments. Among these, secondary inorganic aerosols (SIA)—composed of sulfate (SO_4^{2-}), nitrate (NO_3^-), and ammonium (NH_4^+)—are the most abundant and widely studied (Seinfeld and Pandis, 1998).

Sulfate is primarily formed by the atmospheric oxidation of sulfur dioxide (SO_2), a gas emitted during the combustion of coal, heavy oil, and industrial processes. This oxidation occurs via gas-phase reactions with hydroxyl radicals (OH), or aqueous-phase reactions in cloud droplets, especially under high relative humidity. Once formed, sulfate exists almost exclusively in the fine fraction, contributing significantly to aerosol acidity and hygroscopic growth. Sulfate is also a key player in the formation of ammonium sulfate ($(NH_4)_2SO_4$) when neutralized by ammonia (Ye et al., 2023).

Nitrate in the atmosphere is predominantly formed through the oxidation of nitrogen oxides (NO_x), emitted by vehicle exhaust, industrial activity, and power generation. During the day, NO_2 reacts with hydroxyl radicals (OH) to produce nitric acid (HNO_3), which partitions into the particle phase under suitable conditions (Zhu et al., 2025). At night, NO_2 interacts with ozone to generate nitrate radicals (NO_3) and subsequently N_2O_5, which undergoes heterogeneous hydrolysis on aerosol surfaces, significantly contributing to secondary nitrate formation (Ma et al., 2023). Nitrate, especially as ammonium nitrate (NH_4NO_3), exhibits semi-volatile behavior and is temperature-dependent—favoring the gas phase at higher temperatures and reforming particles during cooler periods (winter, nighttime) (Dai et al., 2024).

Ammonium derives from ammonia (NH_3), a gas predominantly emitted from agricultural activities such as livestock operations and fertilizer application. In the atmosphere, ammonia reacts readily with sulfuric and nitric acids to form ammonium sulfate ($(NH_4)_2SO_4$) and ammonium nitrate (NH_4NO_3) (Wyer et al., 2022).

6. Source Apportionment by Positive Matrix Factorization (PMF)

As mentioned in previous chapters, PM is a complex mixture of airborne particles originating from a wide range of natural and anthropogenic sources. Its chemical composition varies substantially depending on emission sources, atmospheric transport, and transformation processes. Understanding the contribution of different sources to measured PM levels is essential for developing effective air quality management strategies and for assessing the associated health and environmental impacts. While direct measurement of emissions is often impractical, receptor modelling provides a robust approach to infer source contributions from ambient concentration data.

Positive Matrix Factorization (PMF) is one of the most widely applied receptor models for source apportionment of atmospheric aerosols. It is a multivariate factor analysis method that resolves a matrix of observed concentrations into factor profiles (source chemical signatures) and factor contributions (temporal variation of each source) under the constraint of non-negativity. PMF uses uncertainty estimates for each observation, allowing the model to weight data appropriately and to handle below-detection-limit values more effectively than traditional factor analysis methods. Its flexibility and ability to incorporate error structures have made it a preferred choice in air quality studies worldwide (Paatero, 1999; Paatero and Tapper 1994).

A major advantage of PMF is that it does not require prior knowledge of source profiles, making it suitable for complex urban and regional environments with diverse and variable emissions. It has been successfully applied in numerous studies to identify sources such as traffic, biomass burning, industrial activities, sea salt, and secondary aerosol formation. The interpretability of PMF results often benefits from auxiliary data such as meteorological parameters, gaseous pollutants, and emission inventories, which assist in source identification.

6.1 PMF chemical mass balance equation

PMF receptor modelling technique decomposes a matrix of observed species concentrations into two non-negative matrices: source contributions and source profiles. The fundamental chemical mass balance equation in PMF can be expressed as (Paatero, 1999):

$$x_{ij} = \sum_{k=1}^{p} g_{ik} \cdot f_{kj} + e_{ij} \quad (6)$$

where x_{ij} represents the measured concentration of species j in sample i; g_{ik} denotes the contribution of source k to sample i; f_{kj} is the mass fraction of species j in the profile of source

k; and e_{ij} represents the residual, i.e., the unexplained portion of the measured concentration. The model estimates g_{ik} and f_{kj} by minimizing the objective function Q (Paatero and Tapper 1994):

$$Q = \sum_{m=1}^{\nu} \sum_{n=1}^{\mu} \frac{{e_{mn}}^2}{{s_{mn}}^2} \quad (7)$$

Here, ν and μ denote the total number of samples and species, respectively; e_{mn} is the residual for species n in sample mmm; and s_{mn} is the associated measurement uncertainty. The formulation ensures that both the magnitude of the residual and the reliability of the measurement are taken into account during the fitting process. The minimization of Q results in a solution where the modelled concentrations optimally reproduce the observations within their stated uncertainties.

6.2 Model Performance Indicators: Q_{true} and Q_{robust}

The PMF (EPA-PMF 5.0) model evaluates the quality of its fit using a statistic called Q. Two versions are reported: Qtrue , calculated using all data points, and Qrobust , calculated after excluding data points with very large scaled residuals. These excluded points often correspond to unusual events, analytical errors, or measurements with large deviations from the modelled values. If the two Q values differ substantially, it indicates that a small number of extreme observations are strongly influencing the solution and should be examined further. Scaled residual analysis therefore plays an important role in identifying such anomalies and assessing the reliability of the PMF results (U.S. Environmental Protection Agency [EPA], 2014).

6.3 Rotational Ambiguity and Diagnostic Tools

"Rotational ambiguity" refers to a situation where the model can produce different solutions that are equally good at explaining the observed data. These solutions might look different in terms of the contributions from different sources, but they all result in a similar level of agreement with the measured concentrations. To understand this concept, imagine a jigsaw puzzle with several pieces that could fit together in different ways to form a complete picture. In a similar manner, in PMF, there may be multiple combinations of source contributions and profiles that can explain the observed pollution levels equally well. To evaluate the stability and uniqueness of the solution, two diagnostic tools are commonly applied: Bootstrap (BS) and Displacement (DISP) analyses (Hopke et al., 2025).

- Bootstrap (BS) checks how stable the PMF results are when the dataset changes slightly. It creates many new datasets by randomly reselecting samples (with replacement) from the original data and runs PMF on each one. The new factors are then compared to the original run to see how often they match. High matching percentages (usually >80%) mean the factors are stable and reliable, while low matches suggest the factor may be less well-resolved.
- Displacement (DISP) tests how much the PMF solution can change due to rotational ambiguity without losing its fit quality. It does this by slightly changing (perturbing) the source profiles and measuring how much the Q value increases for a given allowed limit (ΔQ_{max}). Smaller ΔQ_{max} values keep the solution close to the best fit, while large allowable changes may mean the solution is less stable and could require constraints or adjustments.

6.4 The Role of Constraints in PMF

Constraints in PMF help make the solution more realistic, easier to interpret, and more stable, while also reducing rotational ambiguity. The effect of constraints is checked by comparing Q_{robust} from the constrained run to that of the unconstrained run. An increase of up to about 1% is generally acceptable, meaning the constraints improve interpretation without significantly reducing the quality of fit. Using constraints together with Bootstrap and DISP diagnostics allows PMF to produce results that are both statistically reliable and chemically meaningful (Manousakas et al., 2017).

6.5 Preliminary Data Analysis, Missing Values, Uncertainties, and Below Detection Limit Values in PMF Pre-treatment

6.5.1 Preliminary Data Analysis

Before performing PMF, a detailed preliminary analysis of the input dataset is essential to ensure quality, identify anomalies, and gain initial insight into possible sources (U.S. Environmental Protection Agency [EPA], 2014). This process typically includes:

- Exploring species relationships through tools such as linear regression (to identify associations and outliers) and correlation matrices (e.g., Pearson coefficients).
- Examining temporal patterns to detect seasonal, diurnal, or day-of-week variability, and to flag short-term events such as dust transport, biomass burning, or industrial incidents.
- Spatial comparison when multiple sites are included, to reveal regional patterns.
- Mass closure analysis to verify consistency between gravimetric PM mass and the sum of quantified chemical components. This also provides an early view of source

categories (e.g., secondary inorganic aerosols, carbonaceous material, mineral dust, sea salt, trace metals).

- Ion balance checks for ionic components, identifying days with atypical composition or invalid values.

Outliers must be carefully evaluated. While some may result from measurement errors and should be excluded, others may reflect real and important pollution events.

6.5.2 Missing Values

PMF models cannot process blank cells. Handling missing data requires a balance between retaining samples and maintaining dataset reliability (U.S. Environmental Protection Agency [EPA], 2014). Common approaches include:

- Substitution with statistical measures such as the mean, median, or geometric mean for the given species, assigning the corresponding uncertainty as four times the substituted concentration.
- Model-handled replacement by defining a missing value indicator (e.g., -999). EPA PMF can replace missing values internally using the median and adjusting uncertainties accordingly.
- Limit on substitution: Missing values for a species should not exceed 50% of total samples, as excessive replacement increases uncertainty and may bias source identification .

6.5.2 Below Detection Limit (BDL) Values

BDL concentrations should be retained rather than removed, as they still carry valuable information (U.S. Environmental Protection Agency [EPA], 2014). The most widely used approach is:

- Replace BDL values with ½ of the Detection Limit (DL).
- Assign uncertainties as 5/6 of the DL.

If a large proportion of a species' data is BDL, its inclusion should be reconsidered unless it serves as a key tracer. High BDL frequencies across several trace species can artificially create PMF factors dominated by these low values. Zero or negative concentrations may occasionally be valid (true near-zero levels), but uncertainties must always be positive. Zero or negative uncertainties should be replaced with reasonable estimates.

6.5.3 Analytical Uncertainty Estimation for PMF Input

Uncertainty directly affects PMF weighting, influencing the model's interpretation of the data. The simplest estimate is the analytical uncertainty from repeated measurements or

reference material comparisons. However, most PMF studies incorporate both measurement variability and detection limit information using formulas such as (Reff et al., 2007):

$$\sigma_{ij} = s_{ij} + C_3 \cdot | x_{ij} |$$

$$\sigma_{ij} = 0.05 \cdot x_{ij} + DL_{ij}$$

$$\sigma_{ij} = s_{ij} + \frac{DL_{ij}}{3}$$

$$\sigma_{ij} = s_{ij} + 0.2 \cdot DL_{ij}$$

$$\sigma_{ij} = 0.3 + DL_{ij}$$

$$\sigma_{ij} = k_j \cdot x_{ij} + \frac{DL_{ij}}{3} \quad (8)$$

$$\sigma_{ij} = \sqrt{a_j \cdot s_{ij}^2 + bj \cdot DL_{ij}^2}$$

$$\sigma_{ij} = \sqrt{REP^2 + (0.05 \cdot x_{ij})^2}$$

$$\sigma_{ij} = \sqrt{3 \cdot s_{ij}^2 + DL_{ij}^2}$$

In the above equations, σ_{ij} denotes the estimated analytical uncertainty for species *j* in sample *i*, which is provided as input to the PMF model for weighting. The term s_{ij} corresponds to the analytical uncertainty of species *j* in sample *i*, while DL_{ij} represents the method detection limit. The constant C_3 takes values between 0.1 and 0.2, and k_j is a species-specific fraction determined from uncertainty–concentration plots. The parameters a_j and b_j are empirical scaling factors, and Rep denotes the reproducibility of the analytical method for species *j*. The notation $\bar{s_j}$ refers to the mean analytical uncertainty for species *j* across replicate analyses.

7. References for Section A

Adebiyi, A. A., & Kok, J. F. (2020). Climate models miss most of the coarse dust in the atmosphere. *Science Advances*, *6*(15). https://doi.org/10.1126/SCIADV.AAZ9507/SUPPL_FILE/AAZ9507_SM.PDF

Adebiyi, A., Kok, J. F., Murray, B. J., Ryder, C. L., Stuut, J. B. W., Kahn, R. A., Knippertz, P., Formenti, P., Mahowald, N. M., Pérez García-Pando, C., Klose, M., Ansmann, A., Samset, B. H., Ito, A., Balkanski, Y., Di Biagio, C., Romanias, M. N., Huang, Y., & Meng, J. (2023). A review of coarse mineral dust in the Earth system. *Aeolian Research*, *60*, 100849. https://doi.org/10.1016/J.AEOLIA.2022.100849

Almeida, S. M., Manousakas, M., Diapouli, E., Kertesz, Z., Samek, L., Hristova, E., Šega, K., Alvarez, R. P., Belis, C. A., Eleftheriadis, K., Albania, Civici, N., Radic, R., Vukic, L., Hristova, E., Veleva, B., Šega, K., Bešlic, I., Davila, S., … Karydas, A. G. (2020). Ambient particulate matter source apportionment using receptor modelling in European and Central Asia urban areas. *Environmental Pollution*, *266*. https://doi.org/10.1016/J.ENVPOL.2020.115199

Amato, F., Alastuey, A., Karanasiou, A., Lucarelli, F., Nava, S., Calzolai, G., Severi, M., Becagli, S., Gianelle, V. L., Colombi, C., Alves, C., Custódio, D., Nunes, T., Cerqueira, M., Pio, C., Eleftheriadis, K., Diapouli, E., Reche, C., Minguillón, M. C., … Querol, X. (2016). AIRUSE-LIFE+: A harmonized PM speciation and source apportionment in five southern European cities. *Atmospheric Chemistry and Physics*, *16*(5), 3289–3309. https://doi.org/10.5194/ACP-16-3289-2016

Amnuaylojaroen, T., & Parasin, N. (2024). Pathogenesis of PM2.5-Related Disorders in Different Age Groups: Children, Adults, and the Elderly. *Epigenomes 2024, Vol. 8, Page 13*, *8*(2), 13. https://doi.org/10.3390/EPIGENOMES8020013

Athanasopoulou, E., Tombrou, M., Pandis, S. N., & Russell, A. G. (2008). The role of sea-salt emissions and heterogeneous chemistry in the air quality of polluted coastal areas. *Atmos. Chem. Phys*, *8*, 5755–5769. www.atmos-chem-phys.net/8/5755/2008/

Bhargava, S., & Bhargava, S. (2013). Ecological consequences of The Acid rain. *IOSR Journal of Applied Chemistry (IOSR-JAC*, *5*(4), 19–24. DOI: 10.9790/5736-0541924

Baron, P. A., & Willeke, K. (2001). *Aerosol Measurement: Principles, Techniques, and Applications* (2nd ed.). Wiley.

Bahadur, R., Habib, G., & Russell, L. M. (2009). Climatology of PM2.5 organic carbon concentrations from a review of ground-based atmospheric measurements by evolved gas analysis. *Atmospheric Environment*, *43*(9), 1591–1602. https://doi.org/10.1016/J.ATMOSENV.2008.12.018

Bertram, T. H., Cochran, R. E., Grassian, V. H., & Stone, E. A. (2018). Sea spray aerosol chemical composition: elemental and molecular mimics for laboratory studies of heterogeneous and multiphase reactions. *Chemical Society Reviews*, *47*(7), 2374–2400. https://doi.org/10.1039/C7CS00008A

Bučinskas, L., Garbarienė, I., Mašalaitė, A., Šapolaitė, J., Ežerinskis, Ž., Jasinevičienė, D., & Garbaras, A. (2024). Evaluating the Impact of Increased Heavy Oil Consumption on Urban Pollution Levels through Isotope (δ13C, δ34S, 14C) Composition. *Atmosphere*, *15*(8), 883. https://doi.org/10.3390/ATMOS15080883/S1

Cao, J., Chow, J. C., Lee, F. S. C., & Watson, J. G. (2013). Evolution of PM 2.5 Measurements and Standards in the U.S. and Future Perspectives for China. *Aerosol and Air Quality Research*, *13*, 1197–1211. https://doi.org/10.4209/aaqr.2012.11.0302

Charron, A., Polo-Rehn, L., Besombes, J. L., Golly, B., Buisson, C., Chanut, H., Marchand, N., Guillaud, G., & Jaffrezo, J. L. (2019). Identification and quantification of particulate tracers of exhaust and non-exhaust vehicle emissions. *Atmospheric Chemistry and Physics*, *19*(7), 5187–5207. https://doi.org/10.5194/ACP-19-5187-2019

Chen, S. L., Chang, S. W., Chen, Y. J., & Chen, H. L. (2021). Possible warming effect of fine particulate matter in the atmosphere. *Communications Earth and Environment*, *2*(1), 1–9. https://doi.org/10.1038/S43247-021-00278-5;SUBJMETA=106,172,35,4081,704,823;KWRD=ATMOSPHERIC+DYNAMICS,ENVIRONMENTAL+IMPACT

Chong-Neto, H. J., & Filho, N. A. R. (2025). How does air quality affect the health of children and adolescents? *Jornal de Pediatria*, *101*(Suppl 1), S77. https://doi.org/10.1016/J.JPED.2024.11.009

Chow, J. C., Watson, J. G., Wang, X., Abbasi, B., Reed, W. R., & Parks, D. (2022). Review of Filters for Air Sampling and Chemical Analysis in Mining Workplaces. *Minerals*, *12*(10), 1314. https://doi.org/10.3390/MIN12101314/S1

Corbin, J. C., Mensah, A. A., Pieber, S. M., Orasche, J., Michalke, B., Zanatta, M., Czech, H., Massabò, D., Buatier De Mongeot, F., Mennucci, C., El Haddad, I., Kumar, N. K., Stengel, B., Huang, Y., Zimmermann, R., Prévôt, A. S. H., & Gysel, M. (2018). Trace Metals in Soot and PM2.5 from Heavy-Fuel-Oil Combustion in a Marine Engine. *Environmental Science and Technology*, *52*(11), 6714–6722. https://doi.org/10.1021/ACS.EST.8B01764/ASSET/IMAGES/LARGE/ES-2018-01764R_0003.JPEG

Dai, W., Cheng, K., Huang, X., & Xie, M. (2024). Modeling Analysis of Nocturnal Nitrate Formation Pathways during Co-Occurrence of Ozone and PM2.5 Pollution in North China Plain. *Atmosphere 2024, Vol. 15, Page 1220*, *15*(10), 1220. https://doi.org/10.3390/ATMOS15101220

Diapouli, E., Fetfatzis, P., Panteliadis, P., Spitieri, C., Gini, M. I., Papagiannis, S., Vasilatou, V., & Eleftheriadis, K. (2022). *PM2.5 Source Apportionment and Implications for Particle Hygroscopicity at an Urban Background Site in Athens, Greece*. *13*, 1685. https://doi.org/10.3390/atmos13101685

Deike, L., Garcia, M., & van Vledder, G. (2022). A mechanistic sea spray generation function based on the coupling of surface statistics and bubble bursting physics. *AGU Advances*, *3*(5), e2022AV000750. https://doi.org/10.1029/2022AV000750

Dzubay, T. G., & Stevens, R. K. (1991). Sampling and Analysis Methods for Ambient PM-10 Aerosol. *Data Handling in Science and Technology*, *7*(C), 11–44. https://doi.org/10.1016/S0922-3487(08)70125-4

EPA, US. Exposure Research Laboratory, N. (n.d.). *EPA Positive Matrix Factorization (PM F) 5.0 Fundamentals and User Guide*. Retrieved September 3, 2025, from www.epa.gov

Ghermandi, G., Cecchi, R., Lusvarghi, L., Laj, P., Zappoli, S., & Ceccato, D. (2005). Internal/external mixing of aerosol particles elemental composition retrieved from microPIXE and PIXE. *Nuclear Instruments and Methods in Physics Research Section B: Beam Interactions with Materials and Atoms*, *240*(1–2), 313–320. https://doi.org/10.1016/J.NIMB.2005.06.222

Giannoni, M., Martellini, T., Del Bubba, M., Gambaro, A., Zangrando, R., Chiari, M., Lepri, L., & Cincinelli, A. (2012). The use of levoglucosan for tracing biomass burning in PM2.5 samples in Tuscany (Italy). *Environmental Pollution*, *167*, 7–15. https://doi.org/10.1016/J.ENVPOL.2012.03.016

Grigoratos, T., & Martini, G. (2015). Brake wear particle emissions: a review. *Environmental Science and Pollution Research*, *22*(4), 2491–2504. https://doi.org/10.1007/S11356-014-3696-8/TABLES/5

Han, C. H., Pak, H., Lee, J. M., & Chung, J. H. (2022). : Short-term effects of exposure to particulate matter on hospital admissions for asthma and chronic obstructive pulmonary disease. *Medicine*, *101*(35), e30165. https://doi.org/10.1097/MD.0000000000030165

Harrison, R. M., Allan, J., Carruthers, D., Heal, M. R., Lewis, A. C., Marner, B., Murrells, T., & Williams, A. (2021). Non-exhaust vehicle emissions of particulate matter and VOC from road traffic: A review. *Atmospheric Environment*, *262*, 118592. https://doi.org/10.1016/J.ATMOSENV.2021.118592

He, C., Jiang, W., Xiao, Q., Xing, C., Yuan, D., Lu, R., & Wu, W. (2024). A review of non-exhaust emissions on pavement area: Sources, compositions, evaluation and mitigation. *Journal of Traffic and Transportation Engineering (English Edition)*, *11*(6), 1243–1258. https://doi.org/10.1016/J.JTTE.2023.07.012

Hinds, W. C. . (1999). *Aerosol technology : properties, behavior, and measurement of airborne particles*.

Hooftman, N., Messagie, M., Van Mierlo, J., & Coosemans, T. (2018). A review of the European passenger car regulations – Real driving emissions vs local air quality. *Renewable and Sustainable Energy Reviews*, *86*, 1–21. https://doi.org/10.1016/J.RSER.2018.01.012

Hopke, P. K., Dai, Q., Li, L., & Feng, Y. (2020). Global review of recent source apportionments for airborne particulate matter. *Science of The Total Environment*, *740*, 140091. https://doi.org/10.1016/J.SCITOTENV.2020.140091

Hopke, P. K., Chen, Y., Rich, D. Q., Watson, J. G., & Chow, J. C. (2023). Issues with the Organic and Elemental Carbon Fractions in Recent U.S. Chemical Speciation Network Data. *Aerosol and Air Quality Research*, *23*(6), 230041. https://doi.org/10.4209/AAQR.230041

Hopke, P. K., Chen, Y., Rich, D. Q., Mooibroek, D., & Sofowote, U. M. (2023). The application of positive matrix factorization with diagnostics to BIG DATA. *Chemometrics and Intelligent Laboratory Systems*, *240*, 104885. https://doi.org/10.1016/J.CHEMOLAB.2023.104885

Ianniello, A., Spataro, F., Esposito, G., Allegrini, I., Hu, M., & Zhu, T. (2011). Chemical characteristics of inorganic ammonium salts in PM2.5 in the atmosphere of Beijing (China). *Atmospheric Chemistry and Physics*, *11*(21), 10803–10822. https://doi.org/10.5194/ACP-11-10803-2011

Jang, E., Choi, S., Yoo, E., Hyun, S., & An, J. (2023). Impact of shipping emissions regulation on urban aerosol composition changes revealed by receptor and numerical modelling. *Npj Climate and Atmospheric Science*, *6*(1), 1–13. https://doi.org/10.1038/S41612-023-00364-9;SUBJMETA=169,172,4081,704,895;KWRD=ENVIRONMENTAL+IMPACT,ENVIRONMENTAL+MONITORING

Jeong, J. I., Seo, J., & Park, R. J. (2022). Compromised Improvement of Poor Visibility Due to PM Chemical Composition Changes in South Korea. *Remote Sensing 2022, Vol. 14, Page 5310*, *14*(21), 5310. https://doi.org/10.3390/RS14215310

Jiang, K., Xing, R., Luo, Z., Huang, W., Yi, F., Men, Y., Zhao, N., Chang, Z., Zhao, J., Pan, B., & Shen, G. (2024). Pollutant emissions from biomass burning: A review on emission characteristics, environmental impacts, and research perspectives. *Particuology*, *85*, 296–309. https://doi.org/10.1016/J.PARTIC.2023.07.012

Kim, K. H., Kabir, E., & Kabir, S. (2015). A review on the human health impact of airborne particulate matter. *Environment International*, *74*, 136–143. https://doi.org/10.1016/j.envint.2014.10.005

Kumar, S., Saha, N., Amir Mohana, A., Sabbir Hasan, M., Safiur Rahman, M., Elmes, M., MacFarlane, G. R., Kumar, S., MacFarlane, G. R., Saha, N., Mohana, A. A., Hasan, M. S., Rahman, M. S., & Elmes, M. (2024). *Atmospheric Particulate Matter and Associated Trace Elements Pollution in Bangladesh: A Comparative Study with Global Megacities*. *235*, 222. https://doi.org/10.1007/s11270-024-07021-8

Kumar, V., & Behera, S. N. (2024). Characterization of trace elements of size-resolved particulate matter, development of emission factors and human health impacts associated with stationary diesel engine exhausts. *Journal of Hazardous Materials Advances*, *14*, 100432. https://doi.org/10.1016/J.HAZADV.2024.100432

Li, J., Pósfai, M., Hobbs, P. V., & Buseck, P. R. (2003). Individual aerosol particles from biomass burning in southern Africa: 2, Compositions and aging of inorganic particles. *Journal of Geophysical Research: Atmospheres*, *108*(D13), 8484. https://doi.org/10.1029/2002JD002310

Li, J., Zhang, M., Ge, Y., Wen, Y., Luo, J., Yin, D., Wang, C., & Wang, C. (2023). Emission Characteristics of Tyre Wear Particles from Light-Duty Vehicles. *Atmosphere 2023, Vol. 14, Page 724*, *14*(4), 724. https://doi.org/10.3390/ATMOS14040724

Lindsley, W. G. (n.d.). *NIOSH Manual of Analytical Methods (NMAM), 5th Edition Filter Pore Size and Aerosol Sample Collection*.

Lunden, M. M., Revzan, K. L., Fischer, M. L., Thatcher, T. L., Littlejohn, D., Hering, S. V., & Brown, N. J. (2003). The transformation of outdoor ammonium nitrate aerosols in the indoor environment. *Atmospheric Environment*, *37*(39–40), 5633–5644. https://doi.org/10.1016/J.ATMOSENV.2003.09.035

Ma, P., Quan, J., Dou, Y., Pan, Y., Liao, Z., Cheng, Z., Jia, X., Wang, Q., Zhan, J., Ma, W., Zheng, F., Wang, Y., Zhang, Y., Hua, C., Yan, C., Kulmala, M., Liu, Y., Huang, X., Yuan, B., … Liu, Y. (2023). Regime-Dependence of Nocturnal Nitrate Formation via N2O5 Hydrolysis and Its Implication for Mitigating Nitrate Pollution. *Geophysical Research Letters*, *50*(24). https://doi.org/10.1029/2023GL106183

Manousakas, M., Papaefthymiou, H., Diapouli, E., Migliori, A., Karydas, A. G., Bogdanovic-Radovic, I., & Eleftheriadis, K. (2017). Assessment of PM2.5 sources and their corresponding level of uncertainty in a coastal urban area using EPA PMF 5.0 enhanced diagnostics. *Science of The Total Environment*, *574*, 155–164. https://doi.org/10.1016/J.SCITOTENV.2016.09.047

Manousakas, M. I., Florou, K., & Pandis, S. N. (2020). Source apportionment of fine organic and inorganic atmospheric aerosol in an urban background area in Greece. *Atmosphere*, *11*(4). https://doi.org/10.3390/ATMOS11040330

Marple, V. A., & Willeke, K. (1976). Impactor design. *Atmospheric Environment (1967)*, *10*(10), 891–896. https://doi.org/10.1016/0004-6981(76)90144-X

Mateus, R., Reis, M. A., Jesus, A. P., & Ribeiro, J. P. (2006). Quantitative analysis of light elements in aerosol samples by PIGE. *Nuclear Instruments and Methods in Physics Research Section B: Beam Interactions with Materials and Atoms*, *249*(1–2), 784–788. https://doi.org/10.1016/J.NIMB.2006.03.139

Mendonça da Silva, L. F., Gioda, A., Massone, C. G., Nascimento, M. M., Guarieiro, L. L. N., de Andrade, J. B., da Rocha, G. O., Faria Campos, M. W., Ferreira, R. S., Canela, M. C., & Carreira, R. da S. (2025). Tracing organic pollutants in particulate Matter: Source identification and implications for air quality and public health. *Chemosphere*, *386*, 144643. https://doi.org/10.1016/J.CHEMOSPHERE.2025.144643

Miyamoto, C., Iizuka, Y., Matoba, S., Hattori, S., & Takahashi, Y. (2022). Gypsum formation from calcite in the atmosphere recorded in aerosol particles transported and trapped in Greenland ice core sample is a signature of secular change of SO2 emission in East Asia. *Atmospheric Environment*, *278*, 119061. https://doi.org/10.1016/J.ATMOSENV.2022.119061

Morakinyo, O. M., Mokgobu, M. I., Mukhola, M. S., & Hunter, R. P. (2016). Health Outcomes of Exposure to Biological and Chemical Components of Inhalable and Respirable Particulate Matter. *International Journal of Environmental Research and Public Health 2016, Vol. 13, Page 592*, *13*(6), 592. https://doi.org/10.3390/IJERPH13060592

Moubarz, G., Saad-Hussein, A., Shahy, E. M., Mahdy-Abdallah, H., Mohammed, A. M. F., Saleh, I. A., Abo-Zeid, M. A. M., & Abo-Elfadl, M. T. (2022). Lung cancer risk in workers occupationally exposed to polycyclic aromatic hydrocarbons with emphasis on the role of

DNA repair gene. *International Archives of Occupational and Environmental Health*, *96*(2), 313. https://doi.org/10.1007/S00420-022-01926-9

Neuman, J. A., Nowak, J. B., Brock, C. A., Trainer, M., Fehsenfeld, F. C., Holloway, J. S., Hübler, G., Hudson, P. K., Murphy, D. M., Nicks, D. K., Orsini, D., Parrish, D. D., Ryerson, T. B., Sueper, D. T., Sullivan, A., & Weber, R. (2003). Variability in ammonium nitrate formation and nitric acid depletion with altitude and location over California. *Journal of Geophysical Research: Atmospheres*, *108*(17), 4557. https://doi.org/10.1029/2003JD003616;WGROUP:STRING:PUBLICATION

Nichols, S. C., Mitchell, J. P., Shelton, C. M., & Roberts, D. L. (2013). Good cascade impactor practice (GCIP) and considerations for "in-use" specifications. *AAPS PharmSciTech*, *14*(1), 375–390. https://doi.org/10.1208/S12249-012-9905-1/TABLES/8

Nowak, S., Lafon, S., Caquineau, S., Journet, E., & Laurent, B. (2018). Quantitative study of the mineralogical composition of mineral dust aerosols by X-ray diffraction. *Talanta*, *186*, 133–139. https://doi.org/10.1016/J.TALANTA.2018.03.059

Paatero, P. (1999). The Multilinear Engine: A Table-Driven, Least Squares Program for Solving Multilinear Problems, including the n-Way Parallel Factor Analysis Model. *Journal of Computational and Graphical Statistics*, *8*(4), 854. https://doi.org/10.2307/1390831

Paatero, P., & Tapper, U. (1994). Positive matrix factorization: A non-negative factor model with optimal utilization of error estimates of data values. *Environmetrics*, *5*(2), 111–126. https://doi.org/10.1002/ENV.3170050203

Papagiannis, S., Sabur, ·, Abdullaev, F., Vasilatou, V., Manousos, ·, Manousakas, I., Eleftheriadis, K., & Diapouli, E. (2024). Air quality challenges in Central Asian urban areas: a PM2.5 source apportionment analysis in Dushanbe, Tajikistan. *Environmental Science and Pollution Research 2024*, 1–14. https://doi.org/10.1007/S11356-024-33833-6

Patel, P., & Aggarwal, S. G. (2022). On the techniques and standards of particulate matter sampling. *Journal of the Air & Waste Management Association*, *72*(8), 791–814. https://doi.org/10.1080/10962247.2022.2048129

Patra, P., & Roy, A. (2022). Brownian coagulation of like-charged aerosol particles. *Physical Review Fluids*, *7*(6), 064308. https://doi.org/10.1103/PHYSREVFLUIDS.7.064308/FIGURES/9/MEDIUM

Pecorari, E., Squizzato, S., Longo, A., Visin, F., & Rampazzo, G. (2014). Secondary inorganic aerosol evaluation: Application of a transport chemical model in the eastern part of the Po Valley. *Atmospheric Environment*, *98*, 202–213. https://doi.org/10.1016/J.ATMOSENV.2014.08.045

Pio, C., Cerqueira, M., Harrison, R. M., Nunes, T., Mirante, F., Alves, C., Oliveira, C., Sanchez de la Campa, A., Artíñano, B., & Matos, M. (2011). OC/EC ratio observations in Europe: Re-thinking the approach for apportionment between primary and secondary organic carbon. *Atmospheric Environment*, *45*(34), 6121–6132. https://doi.org/10.1016/J.ATMOSENV.2011.08.045

Rauber, M., Salazar, G., Yttri, K. E., & Szidat, S. (2023). An optimised organic carbong/gelemental carbon (OCg/gEC) fraction separation method for radiocarbon source apportionment applied to low-loaded Arctic aerosol filters. *Atmospheric Measurement Techniques*, *16*(3), 825–844. https://doi.org/10.5194/AMT-16-825-2023

Reff, A., Eberly, S. I., & Bhave, P. V. (2007). Receptor modeling of ambient particulate matter data using positive matrix factorization: Review of existing methods. *Journal of the Air and Waste Management Association*, *57*(2), 146–154. https://doi.org/10.1080/10473289.2007.10465319

Roberts, D. L. (2009). Theory of multi-nozzle impactor stages and the interpretation of stage mensuration data. *Aerosol Science and Technology*, *43*(11), 1119–1129. https://doi.org/10.1080/02786820903204060

Roy, A., Mandal, M., Das, S., Popek, R., Rakwal, R., Agrawal, G. K., Awasthi, A., & Sarkar, A. (2024). The cellular consequences of particulate matter pollutants in plants: Safeguarding the harmonious integration of structure and function. *Science of The Total Environment*, *914*, 169763. https://doi.org/10.1016/J.SCITOTENV.2023.169763

Safera. (2025). *Fine particles PM2.5 have a significant impact on health – Safera's sensor system measures fine particles reliably*. Retrieved September 2, 2025, from https://www.safera.com/fine-particles-pm25-are-significant-health-risk/

Sangkham, S., Phairuang, W., Sherchan, S. P., Pansakun, N., Munkong, N., Sarndhong, K., Islam, M. A., & Sakunkoo, P. (2024). An update on adverse health effects from exposure to PM2.5. *Environmental Advances*, *18*, 100603. https://doi.org/10.1016/J.ENVADV.2024.100603

Seinfeld, J.H. and Pandis, S.N. (2006) Atmospheric Chemistry and Physics: From Air Pollution to Climate Change. 2nd Edition, John Wiley & Sons, New York.

Smorodin, V. Y., & Hopke, P. K. (2006). Relationship of heterogeneous nucleation and condensational growth on aerosol nanoparticles. *Atmospheric Research*, *82*(3–4), 591–604. https://doi.org/10.1016/J.ATMOSRES.2006.02.015

Stefancova, L., Schwarz, J., Makela, T., Hillamo, R., & Smolik, J. (2011). Comprehensive characterization of original 10-stage and 7-stage modified berner type impactors. *Aerosol Science and Technology*, *45*(1), 88–100. https://doi.org/10.1080/02786826.2010.524266

Su, B., Wang, T., Zhang, G., Liang, Y., Lv, C., Hu, Y., Li, L., Zhou, Z., Wang, X., & Bi, X. (2022). A review of atmospheric aging of sea spray aerosols: Potential factors affecting chloride depletion. *Atmospheric Environment*, *290*, 119365. https://doi.org/10.1016/J.ATMOSENV.2022.119365

Subramanian, R., Khlystov, A. Y., Cabada, J. C., & Robinson, A. L. (2004). Evaluation of Measurement Methods Positive and Negative Artifacts in Particulate Organic Carbon Measurements with Denuded and Undenuded Sampler Configurations. *Aerosol Science and Technology*, *38*(S1), 27–48. https://doi.org/10.1080/02786820390229354

Toohey, M., Jia, Y., Khanal, S., & Tegtmeier, S. (2025). Stratospheric residence time and the lifetime of volcanic stratospheric aerosols. *Atmospheric Chemistry and Physics*, *25*(6), 3821–3839. https://doi.org/10.5194/ACP-25-3821-2025

U.S. Environmental Protection Agency (EPA). (2021). *Integrated Science Assessment (ISA) for Particulate Matter* (EPA/600/R-19/188). U.S. Environmental Protection Agency, Washington, DC. Retrieved from https://www.epa.gov/system/files/documents/2022-08/PM_2021.pdf

Vasilatou, V., Manousakas, M., Gini, M., Diapouli, E., Eleftheriadis, K., & Scoullos, M. (2017). Long term flux of Saharan dust to the Aegean Sea around the Attica region, Greece. *Frontiers in Marine Science*, *4*, 230831. https://doi.org/10.3389/FMARS.2017.00042/BIBTEX

Viana, M., Kuhlbusch, T. A. J., Querol, X., Alastuey, A., Harrison, R. M., Hopke, P. K., Winiwarter, W., Vallius, M., Szidat, S., Prévôt, A. S. H., Hueglin, C., Bloemen, H., Wåhlin, P., Vecchi, R., Miranda, A. I., Kasper-Giebl, A., Maenhaut, W., & Hitzenberger, R. (2008). Source apportionment of particulate matter in Europe: A review of methods and results. *Journal of Aerosol Science*, *39*(10), 827–849. https://doi.org/10.1016/J.JAEROSCI.2008.05.007

Wang, H.-C., & John, W. (1988). Characteristics of the Berner Impactor for Sampling Inorganic Ions. *Aerosol Science and Technology*, *8*(2), 157–172. https://doi.org/10.1080/02786828808959179

Wang, X., Deane, G. B., Moore, K. A., Ryder, O. S., Stokes, M. D., Beall, C. M., Collins, D. B., Santander, M. V., Burrows, S. M., Sultana, C. M., & Prather, K. A. (2017). The role of jet and film drops in controlling the mixing state of submicron sea spray aerosol particles. *Proceedings of the National Academy of Sciences, 114*(27), 6978–6983. https://doi.org/10.1073/pnas.1702420114

Wang, T., Liu, Y., Cheng, H., Wang, Z., Fu, H., Chen, J., & Zhang, L. (2022). Significant formation of sulfate aerosols contributed by the heterogeneous drivers of dust surface. *Atmospheric Chemistry and Physics*, *22*(20), 13467–13493. https://doi.org/10.5194/ACP-22-13467-2022

World Health Organization. (2024, October 24). Ambient (outdoor) air pollution and health. Retrieved September 2, 2025, from https://www.who.int/news-room/fact-sheets/detail/ambient-%28outdoor%29-air-quality-and-health

Wyer, K. E., Kelleghan, D. B., Blanes-Vidal, V., Schauberger, G., & Curran, T. P. (2022). Ammonia emissions from agriculture and their contribution to fine particulate matter: A review of implications for human health. *Journal of Environmental Management*, *323*, 116285. https://doi.org/10.1016/J.JENVMAN.2022.116285

Wyslouzil, B. E., & Wölk, J. (2016). Overview: Homogeneous nucleation from the vapor phase - The experimental science. *Journal of Chemical Physics*, *145*(21), 211702. https://doi.org/10.1063/1.4962283/15519310/211702_1_ACCEPTED_MANUSCRIPT.PDF

Ye, C., Lu, K., Song, H., Mu, Y., Chen, J., & Zhang, Y. (2023). A critical review of sulfate aerosol formation mechanisms during winter polluted periods. *Journal of Environmental Sciences*, *123*, 387–399. https://doi.org/10.1016/J.JES.2022.07.011

Zhu, W., Shi, J., Guo, S., Wang, Q., Chen, J., Lou, S., & Hu, M. (2025). Comparative analysis of methods for seasonal particulate organic nitrate estimation in urban areas. *Npj Climate and Atmospheric Science*, *8*(1), 1–10. https://doi.org/10.1038/S41612-025-00904-5;SUBJMETA=169,172,4081,704;KWRD=ENVIRONMENTAL+CHEMISTRY,ENVIRONMENTAL+IMPACT

Section B. Introduction to X-Ray emission spectroscopies

8. X-Ray Fluorescence

X-ray Fluorescence (XRF) is an analytical technique widely used for determining the elemental composition of materials. It is a rapid, non-destructive, and safe method that applies to a broad range of substances, including metals, cement, ceramics, polymers, and plastics (Beckhoff et al., 2006; Klockenkämper and Bohlen. 2015). XRF analysis can be performed on samples in solid, liquid, or even gaseous form. In XRF spectrometry, an X-ray source irradiates the sample under investigation. This source is usually an X-ray tube, although other sources can include radioactive materials or synchrotron facilities. When the sample is exposed to this radiation, the constituent elements emit secondary (fluorescent) X-rays at discrete energy levels that are uniquely characteristic of each element.

The XRF spectrum provides essential information for both qualitative and quantitative elemental analysis. According to Moseley's law, the energy of each characteristic emission line is directly linked to the atomic number (Z) of the emitting element, allowing for accurate elemental identification. Furthermore, the intensity—or count rate—of these lines is proportional to the concentration of the corresponding element in the sample.

Modern XRF instruments can detect nearly all elements in the Periodic Table, from sodium (Z = 11) to uranium (Z = 92), in a single measurement. The technique offers a broad dynamic range, from major constituents present at percent levels down to trace elements in the microgram-per-gram (μg/g) range. However, factors such as spectral line overlaps or matrix effects can sometimes limit sensitivity for certain elements.

8.1 The Nature of X-Rays

X-rays are a type of electromagnetic radiation, with wavelengths roughly between 0.01 and 10 nanometers and photon energies from 0.125 to 125 keV. While their behavior can often be described using wave theory, certain interactions with matter require a particle-based description. Phenomena such as the photoelectric effect and Compton scattering demonstrate the particle-like nature of X-rays, where photons interact with matter not as continuous waves but as discrete energy packets. (Cramer, 2020)

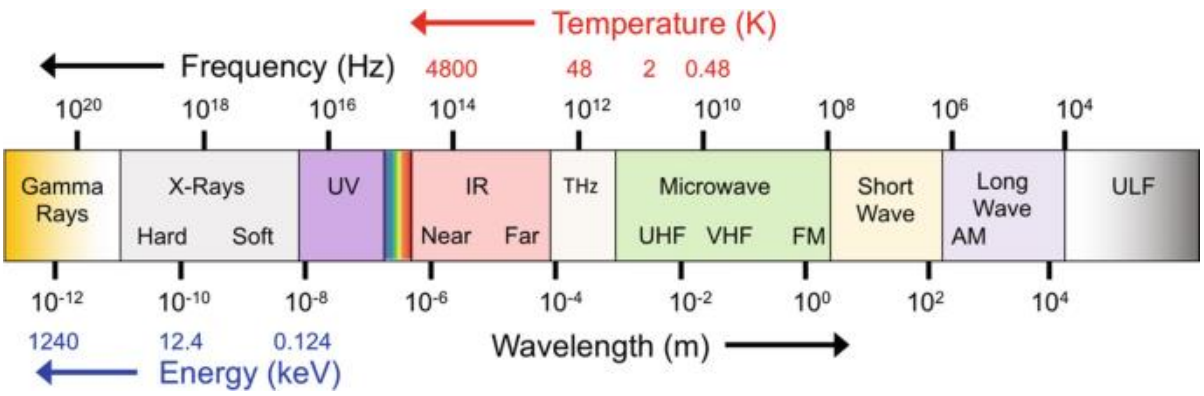

Figure 9. *Position of X-rays in the Electromagnetic Spectrum*

8.2 Interactions of X-Rays with Matter

There are three main ways in which X-rays interact with atoms: the photoelectric effect, inelastic scattering (known as Compton scattering), and elastic scattering (Rayleigh scattering). When a beam of X-ray photons interacts with matter, part of the incident radiation is absorbed—initiating the emission of fluorescent X-rays—while the rest is scattered. Scattering can occur with or without a loss of photon energy. Inelastic scattering, where the X-ray photon transfers part of its energy to an electron, is referred to as Compton scattering (**Figure 10**). In contrast, Rayleigh scattering (**Figure 10**) occurs without energy loss, where the photon is deflected by the atom as a whole but retains its original energy.

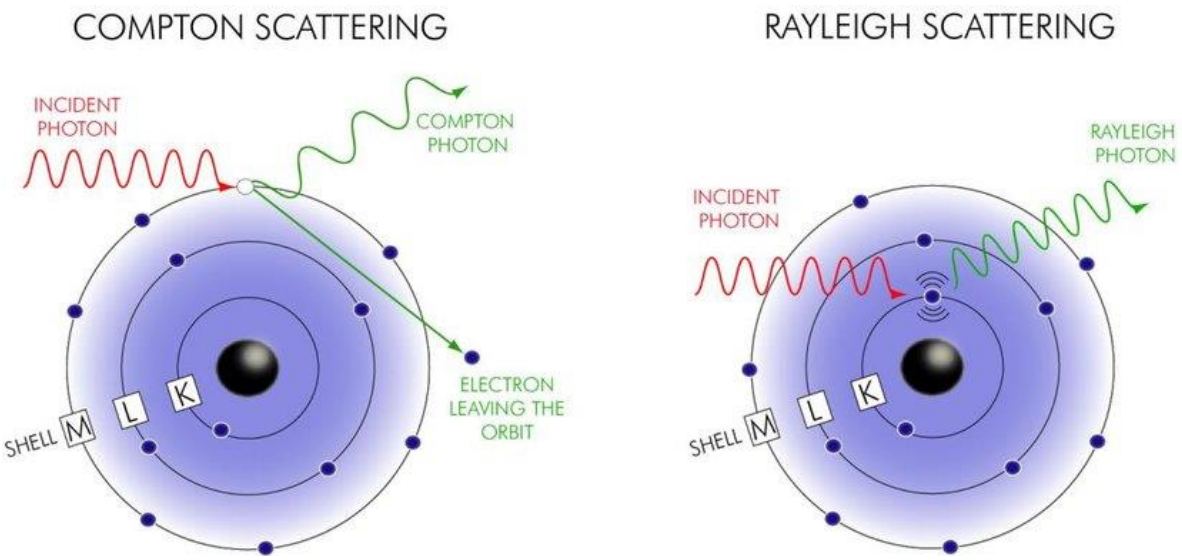

***Figure 10**. Schematic representation of photon–atom interactions. Left: Compton scattering, where an incident photon transfers part of its energy to an orbital electron, ejecting it from the atom and producing a lower-energy scattered photon. Right: Rayleigh scattering, in which the incident photon is elastically scattered by the atom without ejecting electrons, leaving the atom's structure unchanged. (Fosbinder and Orth 2011)*

In X-ray spectra, samples composed of low atomic number elements (light elements) typically exhibit strong Compton scattering and weak Rayleigh scattering. This is because their electrons are more loosely bound. In contrast, elements with higher atomic numbers (heavy elements) show a diminished Compton scattering signal, while Rayleigh scattering becomes the dominant interaction.

8.3 Production of Characteristic X-Rays

At the atomic level, the classical model describes an atom as having a dense nucleus composed of positively charged protons and neutral neutrons, surrounded by negatively charged electrons arranged in energy levels or shells. The innermost shell is the K-shell, followed by the L-, M-, and subsequent shells. The L-shell is further divided into three subshells (L_i, L_{ii}, and L_{iii}), while the M-shell comprises five subshells (M_i to M_v). The K-shell

accommodates up to 2 electrons, the L-shell up to 8, and the M-shell up to 18. When a photon with sufficient energy strikes an electron within one of these shells, the electron may be ejected from the atom, leaving behind a vacancy. The atom then seeks to return to a more stable state by filling this vacancy with an electron from a higher energy shell—such as one from the L-shell filling a vacancy in the K-shell. Since the L-electron possesses more energy than one in the K-shell, the energy difference is released in the form of an X-ray photon. This emitted radiation appears in the XRF spectrum as a characteristic spectral line.

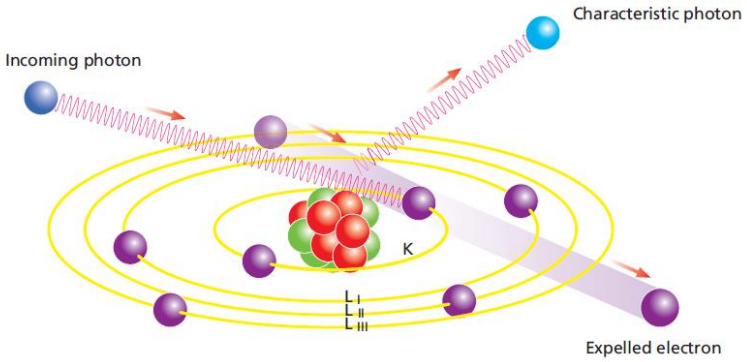

Figure 11. *Production of characteristic X-Ray radiation (Brouwer, 2003).*

The energy of X-ray photons emitted during fluorescence is determined by the difference in energy levels between the shell where an electron vacancy has formed and the shell from which an electron transitions to fill that vacancy. Since each element possesses a unique set of electron binding energies, the emitted radiation is element-specific. As a result, X-ray fluorescence provides a spectral signature—often referred to as a "fingerprint"—for each element. **Figure 12** presents a typical XRF spectrum of a multi-element reference aerosol sample.

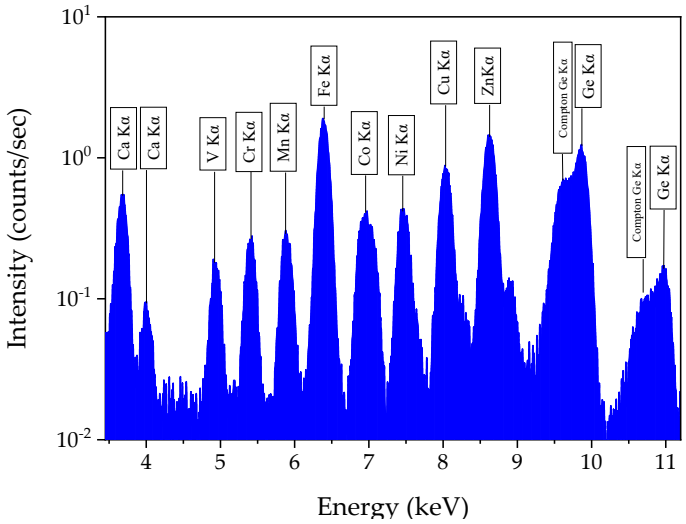

Figure 12. *XRF spectrum of a multi-element reference aerosol sample*

An atom can emit several distinct characteristic energies because vacancies can form in different electron shells, and electrons from various outer shells can transition to fill them.

For instance, a vacancy in the K-shell may be filled by an electron from any of the L- or M-shells, each producing a unique energy emission. Therefore, the full spectrum of emitted energies is specific to each element and serves as a reliable basis for elemental identification.

To eject an electron and create a vacancy, the incident X-ray photon must carry energy exceeding the binding energy of that specific electron. Once the vacancy is formed, an electron from a higher shell transition downward, releasing energy in the form of a secondary (characteristic) X-ray. The various possible transitions—for example, from L_{ii} or L_{iii} to K, or from M- or even N-shells to K—each correspond to different photon energies. The most prominent photon transitions, along with their conventional nomenclature (e.g., Kα, Kβ lines), are illustrated in **Figure 13**. The likelihood that an atom, after being excited, will emit an X-ray photon rather than undergo non-radiative processes is given by the fluorescence yield (ω_i). In non-radiative processes, the excess energy is transferred to another electron, which is then ejected from the atom—a process known as Auger electron emission. Along with Coster-Kronig transitions, these mechanisms represent alternative pathways of inner-shell relaxation that result in the emission of electrons rather than photons (Klockenkämper and Bohlen. 2015)

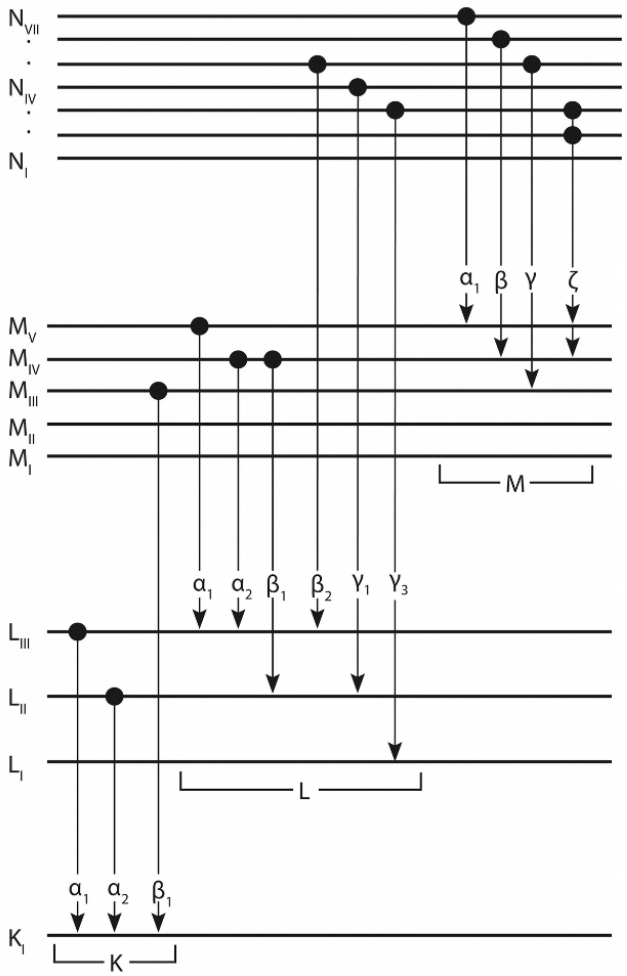

Figure 13. *Dominant photon transitions in X-ray fluorescence and the conventional nomenclature used to describe them (Ul-Hamid, 2018)*

8.4 Attenuation of X-Rays in Matter

When an X-ray beam traverses a material, some of its photons are absorbed or scattered, reducing its intensity. This process is known as X-ray attenuation and is quantitatively described by the differential equation (differential Beer-Lambert equation):

$$dI = I\mu_m \rho dt \tag{9}$$

where:

- I is the initial photon flux (number of photons per unit area per unit time),
- μ_m is the mass attenuation coefficient (expressed in cm²/g),
- ρ is the density of the material,
- dt is an infinitesimal thickness element,
- and dI is the reduction in photon flux after passing through the layer.

For a finite thickness of material, t, this relation integrates to the Beer-Lambert law:

$$I = I_0 e^{-\mu_m \rho t} = I_0 e^{-\mu_m \xi} \tag{10}$$

with:

- I_0 and I being the incident and transmitted photon flux, respectively,
- and $\xi = m/A$ being the mass (m) per unit area (A) in g/cm². (Note that $t \cdot \rho = m/A$)

This law applies strictly to monochromatic radiation, as the attenuation coefficient μ_m strongly depends on the photon energy E as well as the atomic number Z of the absorbing material. The total mass attenuation coefficient μ_m encompasses all primary photon-matter interactions (**Figure 14**) and can be expressed as:

$$\mu_m = \tau_m + \sigma_m \tag{11}$$

where:

- τ_m is the photoelectric absorption, which is the dominant mechanism in XRF and leads to the ejection of inner-shell electrons,
- σ_m is the total scattering coefficient ($\sigma_m = \sigma_{coh} + \sigma_{inc}$), consisting of:
  - σ_{coh} , the contribution from coherent (Rayleigh) scattering, and
  - σ_{inc} , the contribution from incoherent (Compton) scattering.

While scattering events do contribute to attenuation, their effect is typically much smaller than that of photoelectric absorption—especially within the energy range relevant to XRF applications (Beckhoff et al., 2006).

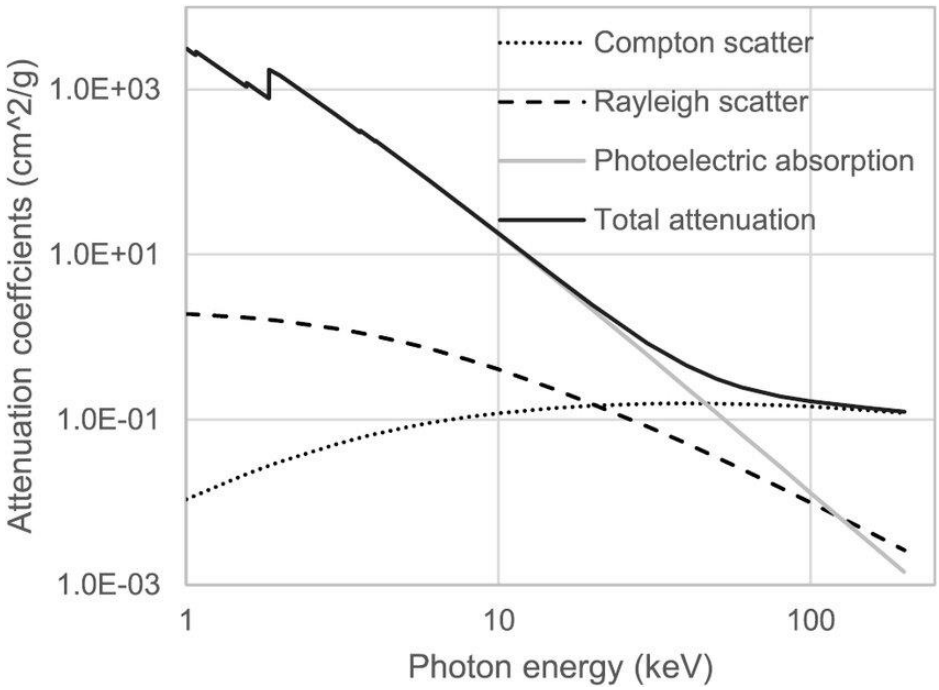

Figure 14. *Graph of photon cross sections for Compton and Rayleigh scattering, photoelectric absorption and total attenuation coefficient for borosilicate glass of composition 72%SiO_2, 12%B_2O_3, 7%Al_2O_3, 6%Na^2O, 2% K_2O, 1%CaO. (Lifton and Carmignato, 2017)*

8.5 Energy Dependence of Fluorescence Excitation Cross Sections

The photoelectric absorption cross-section of the target element fundamentally governs the intensity of characteristic X-ray fluorescence lines observed in a spectrum. The mass absorption coefficient (τ_m), which is directly related to the photoelectric cross-section, shows a strong dependence on the energy of the incident photons. This relationship is approximately given by:

$$\tau_m \approx constant \times \frac{Z^n}{E^{3.5}} \tag{12}$$

where E is the photon energy, Z is the atomic number of the absorbing element, and n varies approximately between 4 and 5 over the energy region of interest (Knoll, 2010). This expression highlights that photoelectric absorption is more significant for elements with higher atomic numbers and for photons with lower energies.

Figure 15 presents the mass-absorption coefficient as a function of excitation energy for Mo, highlighting the contributions from different electron shells. Notably, abrupt increases (absorption edges) appear at characteristic energies corresponding to the ionization thresholds of M, L, and K shells. At these edges, the incoming photons gain just enough energy to efficiently eject electrons, making them ideal for exciting the specific atomic shells.

For the example of molybdenum (Mo), the generation of characteristic X-ray emission requires excitation energies exceeding its K-shell binding energy, which lies around 20 keV. If the incident photon energy falls below this threshold, it cannot remove an inner-shell electron, resulting in the absence of observable fluorescence from the corresponding shell.

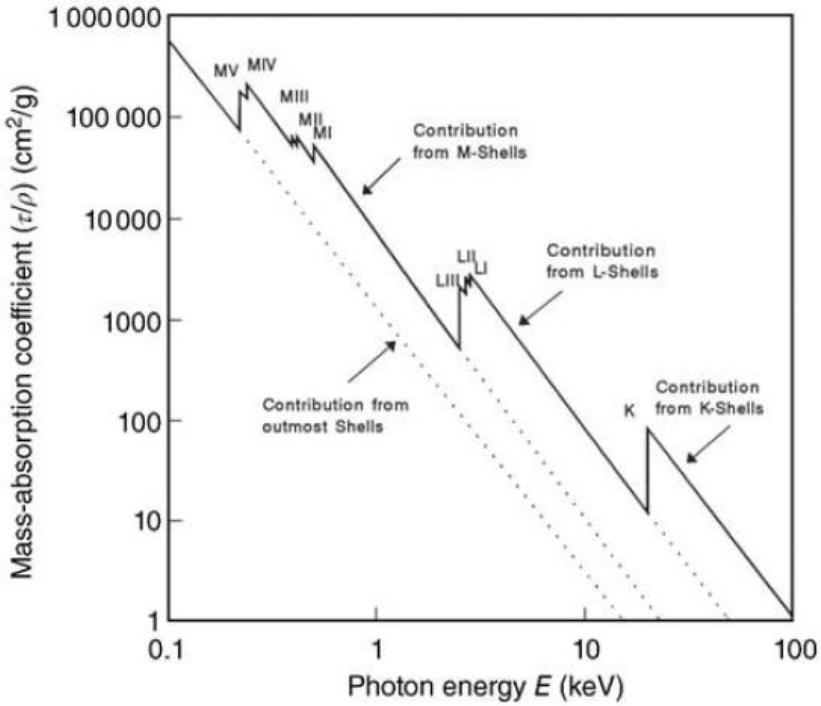

Figure 15. *Variation of the total photoelectric mass absorption coefficient (τ/ρ) of molybdenum (Mo) as a function of photon energy (keV) (Tsampa, 2020)*

To maximize fluorescence signal for Mo K-lines, an excitation source with an energy slightly above the K-absorption edge is preferred. However, in practical applications, the choice of X-ray tube anode material is often limited by availability and engineering constraints. For instance, although materials with photon energies just above Mo's K-edge would offer optimal excitation, such configurations may not be technically feasible. Therefore, compromises are made by using anodes such as Rh, Ag, or W, which emit bremsstrahlung spectra that extend beyond the Mo K-edge, although their excitation efficiency is lower (Chatoutsidou et al., 2022; Asvestas et al., 2024).

Implementing secondary target systems can alleviate some of these limitations by tailoring the spectral distribution of the excitation beam. Nevertheless, for elemental analysis where high sensitivity is required, two fundamental conditions must be satisfied:

- The photon energy of the excitation source must exceed the absorption edge of the target shell.
- The closer the photon energy is to the absorption edge (without being below it), the more efficient the excitation will be, thereby enhancing the fluorescence yield

8.6 Introduction to Quantitative Analysis with XRF

The intensity of characteristic X-ray emissions detected from a specific element in a sample depends on a complex form of variables (Van Grieken and Markowicz, 2001). These include:

- the atomic properties of the element,
- the presence and nature of surrounding elements (the matrix), the physical form of the specimen (e.g., bulk, powder, thin film, or liquid),
- its dimensions and surface preparation, the geometry of the measurement system, the spectral profile of the incident radiation, and
- the properties of the detection system.

To determine elemental concentrations from measured fluorescence intensities, both theoretical modeling and empirical strategies are employed.

The theoretical approach relies on physical models that describe atomic excitation and de-excitation mechanisms, the attenuation of X-rays within the sample, and interactions between different elements (matrix effects). To make the calculations easier, the models usually rely on simplified assumptions — such as treating the sample as flat, uniform, and evenly exposed to the X-ray beam.

On the other hand, the empirical parameter method is a more practical way to link X-ray intensity to the amount of an element in a sample. It uses simpler math, usually in the form of calibration curves, to describe this relationship by utilizing standard reference materials (Cirelli et al., 2022).

8.7 Fundamental parameters method

The fundamental parameters (FP) approach in (XRF) calibration is based on a theoretical relationship between the measured X-ray intensities and the concentrations of the elements present in the sample. This relationship relies on the physics of X-rays and on known values of fundamental atomic parameters— such as absorption and attenuation coefficients, transition probabilities, and fluorescence yields. In XRF spectroscopy, the characteristic radiation emitted by the sample is measured to determine the concentration of each element. The theoretical link between intensity and concentration was first developed in the mid-1950s (Sherman, 1956) and forms the foundation of the fundamental parameter method. This approach enables quantitative analysis by using the intrinsic X-ray properties of the elements involved.

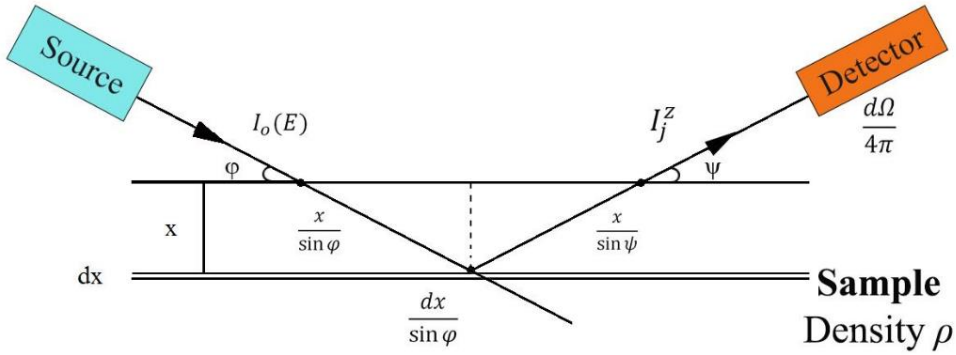

Figure 16. *Geometry of the incident and emitted X-ray beams on the sample.*

The intensity of fluorescent radiation $I_{Z,j}^{E}(x, x+dx)$ emitted from a thin film layer of thickness dx at depth x is given by the following equation

$$\underbrace{I_{Z,j}^{\#,E_i}(x,x+dx)}_{\substack{\text{Measured}\\ \text{fluoerescence}\\ \text{intensity}}} = \underbrace{I^{E_i}}_{\substack{\text{Incident}\\ \text{Beam}\\ \text{Intensity}}} \cdot \underbrace{\left(e^{-\mu^{\#}(E_i)\cdot\rho\cdot\frac{x}{\sin\varphi}}\right)}_{\substack{\text{Probablity of a}\\ \text{photon entering at depth x}\\ \text{and at an angle } \varphi}} \cdot \underbrace{\left(C_Z^{\#}\cdot\rho\cdot\frac{dx}{\sin\varphi}\right)}_{\substack{\text{mass surface}\\ \text{density of Z}\\ \text{in beam direction}}} \cdot \underbrace{\left(\tau_{Z,sh}^{E_i}\cdot\bar{\omega}_Z^{sh}\cdot\omega_Z^{j}\right)}_{\substack{\text{Emmision probability}\\ \text{of a photon from the}\\ \text{j transition}}} \cdot \underbrace{\left(e^{-\mu^{\#}\left(E_j^Z\right)\cdot\rho\cdot\frac{x}{\sin\psi}}\right)}_{\substack{\text{Probability of a}\\ \text{photon exiting from depth x}\\ \text{and at an angle } \psi}} \cdot \underbrace{\frac{d\Omega}{4\pi}}_{\substack{\text{Solid}\\ \text{Angle}}} \cdot \underbrace{\varepsilon_{E_Z^j}}_{\substack{\text{detection}\\ \text{system}\\ \text{efficiency}}} \tag{13}$$

where,

- φ *is the angle between the incident photon beam and the surface of the target,*
- ψ *is the angle between the emitted photons (toward the detector) and the surface of the target,*
- Ω *is the solid angle of the detector,*
- $\varepsilon(E)$ *is the probability that an emitted photon from the sample is detected at energy E*
- E_κ^Z *is the binding energy of the K-shell for element Z,*
- E_j^K *is the photon energy corresponding to the* $\boldsymbol{j}$ *characteristic transition of element Z*
- ω_κ^Z *is the K-shell fluorescence yield of the element with atomic number Z,*
- ω_j^K *is the partial fluorescence yield for the j photon transition of element Z,*
- $\mu_m(E)$ *is the mass attenuation coefficient as a function of photon energy E,*
- $\tau_K^Z(E)$ *is the photoelectric mass absorption coefficient for K-shell ionization of the element with atomic number Z at incident photon energy E,*
- ρ *is the density of then sample,*
- C_z *is the weight fraction of element Z in the target (equal to 1 for a pure element target)*

By rearranging the terms in equation (5), we gain:

$$I_{Z,j}^{\#,E_i}(x,x+dx) = I^{E_i}\cdot \underbrace{(C_Z\cdot\rho\cdot dx)}_{\substack{mass\\ surfacedensity}} \cdot \left(\tau_{Z,sh}^{E_i}\cdot\bar{\omega}_Z^{sh}\cdot\omega_Z^{j}\right)\cdot e^{-M^{\#}\cdot\rho\cdot x}\cdot\frac{d\Omega/4\pi}{\sin\varphi}\cdot\varepsilon_{E_Z^j} \tag{14}$$

where,

$$\hat{\mu}(E_i, \varphi, E_o, \psi) \equiv \frac{\mu(E_i)}{sin\,\varphi} + \frac{\mu(E_o)}{sin\,\psi} \tag{15}$$

In the case of a target with finite thickness ξ, the intensity of the 'j' transition of element Z is given by the following expression

$$I_{Z,j}^{\#,E_i}(\xi) = C_Z^{\#} \cdot I^{E_i} \cdot \left(\frac{\tau_{Z,sh}^{E_i} \cdot \bar{\omega}_Z^{sh} \cdot \omega_Z^j}{\hat{\mu}} \right) \cdot \frac{1 - e^{-\hat{\mu}\cdot\rho\cdot\xi}}{\hat{\mu}} \cdot \frac{d\Omega/4\pi}{sin\,\varphi} \cdot \varepsilon_{E_Z^j} \tag{16}$$

8.7.1 Fundamental parameters method – Bulk targets

In the case of a sample with infinite thickness (ξ →∞) (bulk/thick targets), the intensity of the j transition of element Z in target # is given by the following expression:

$$I_{Z,j}^{\#,E_i}(\xi \to \infty) = C_Z^{\#} \cdot I^{E_i} \cdot \frac{\tau_{Z,sh}^{E_i} \cdot \bar{\omega}_Z^{sh} \cdot \omega_Z^j}{\hat{\mu}} \cdot \frac{d\Omega/4\pi}{sin\,\varphi} \cdot \varepsilon_{E_Z^j} \tag{17}$$

According to equation (8), the target can be considered to have infinite thickness when:

$$\hat{\mu} \cdot \rho \cdot \xi >> 1 \quad \Rightarrow \rho \cdot \xi >> \frac{1}{\hat{\mu}} \tag{18}$$

8.7.2 Fundamental parameters method – Thin targets

In the case of a thin film (ξ → 0 or ξ ≪ 1), the intensity $I_{Z,j}^{\#|E_i}$ of the j transition of element Z of thin film # is given by the following expression:

$$I_{Z,j}^{\#,E_i}(\xi \to 0) = \underbrace{\left(C_Z^{\#} \cdot \rho \cdot \xi\right)}_{\substack{mass \\ surfacedensity}} \cdot I^{E_i} \cdot \tau_{Z,sh}^{E_i} \cdot \bar{\omega}_Z^{sh} \cdot \omega_Z^j \cdot \frac{d\Omega/4\pi}{sin\,\varphi} \cdot \varepsilon_{E_Z^j} \tag{19}$$

The intensity is proportional to the film thickness ξ and its density ϱ, or equivalently, to the areal density. Moreover, no factor appears to be related to the matrix of the film.

$$\hat{\mu} \cdot \rho \cdot \xi << 1 \quad \Rightarrow \quad \rho \cdot \xi \ll \frac{1}{\hat{\mu}} \tag{20}$$

8.8 Quantitative analysis of PM samples with XRF

PM samples, when collected onto substrates such as thin foils or filters, are generally considered 'thin' specimens for the purposes of X-ray fluorescence (XRF) analysis (Van Grieken and Markowicz, 2001). Because PM samples typically have thicknesses in the micrometer range, they generally satisfy the conditions for being treated as 'thin' in XRF analysis (Chiari et al., 2018). However, this assumption may not hold in cases where the sample has a high mass loading. Additionally, it is important that the sample maintains adequate homogeneity, as this is a fundamental requirement for reliable XRF measurements. As mentioned earlier in the case of a thin film the intensity $I_{Z,j}^{E_i}$ of the j transition of element Z of thin film is given by Eq (**19**). This expression shows that the intensity is proportional to the mass surface density $(C_z \cdot \rho \cdot \xi)$ of the element in the sample. Under the assumption that the specimen is thin, homogeneous, and satisfies all ideal conditions (e.g., no self-absorption, uniform excitation, and well-characterized detection), the equation can be simplified to:

$$I_{Z,j}^{\#,E_i}(\xi \to 0) = \left(C_z^{\#} \cdot \rho \cdot \xi\right) \cdot S \tag{21}$$

where S is the element-specific sensitivity factor. This sensitivity factor S can be experimentally determined as the slope of the calibration line constructed from well-characterized thin film standards of known surface mass concentrations (Abiye et al.,2021; Chatoutsidou et al., 2022) .

While the simplified (monochromatic) expression assumes a single excitation energy, this is often not the case in practical applications. For example, X-ray tubes typically emit a continuous spectrum (bremsstrahlung) in addition to characteristic lines. As a result, the actual excitation of the sample arises from a range of photon energies rather than a single energy. Therefore, the sensitivity factor should be expressed as an integral over the entire incident energy spectrum, accounting for the efficiency with which photons of each energy contribute to fluorescence production.

$$S = \left(\int_{Emin}^{Emax} I^{E_i} \cdot \tau_{Z,sh}^{E_i} \cdot \, dE \right) \cdot \bar{\omega}_Z^{sh} \cdot \omega_Z^j \cdot \frac{d\Omega/4\pi}{\sin\varphi} \cdot \varepsilon_{E_Z^j} \tag{22}$$

8.9 Energy Dispersive XRF spectrometry (ED-XRF)

Energy Dispersive X-ray Fluorescence (ED-XRF) is an analytical technique for both qualitative and quantitative elemental analysis (Beckhoff et al., 2006). In ED-XRF, an X-ray tube irradiates the sample, producing characteristic X-rays from the elements present. The characteristic photons are detected by a semiconductor detector, typically a Silicon Drift

Detector (SDD), which directly converts the energy of incoming X-ray photons into an electrical signal proportional to the photon energy. The detector converts incoming X-ray photons into electrical pulses proportional to their energy. The electronics and signal-processing system then compiles these pulses into an energy spectrum, where the position of each peak corresponds to the photon energy (and thus the element), and the peak area is proportional to the element's concentration.

ED-XRF instrumentation generally comprises the following components:

1. **X-ray Source:** Typically, an X-ray tube with a fixed anode material (e.g., Rh, Ag, W) producing a continuous bremsstrahlung spectrum with additional characteristic lines. Secondary targets may be used to enhance excitation of specific elements.

2. **Collimators and Filters:** These define the X-ray beam geometry, reduce background radiation, and optimize excitation for target elements.

3. **Solid-State Detector:** The intensity of photons as a function of energy is recorded by X-ray detectors. In ED-XRF spectroscopy, usually, solid-state detectors are employed. When a photon strikes the detector, it generates an electrical pulse proportional to the photon's energy. Detector resolution is critical for peak separation; typical SDDs achieve 120–150 eV FWHM at Mn-Kα.

4. **Electronics and Signal Processing:** Amplification, pulse shaping, and multichannel analysis are employed to translate detector signals into a digital spectrum suitable for quantitative analysis.

Figure 17 illustrates a typical ED-XRF configuration, highlighting the fixed geometry and simultaneous energy detection.

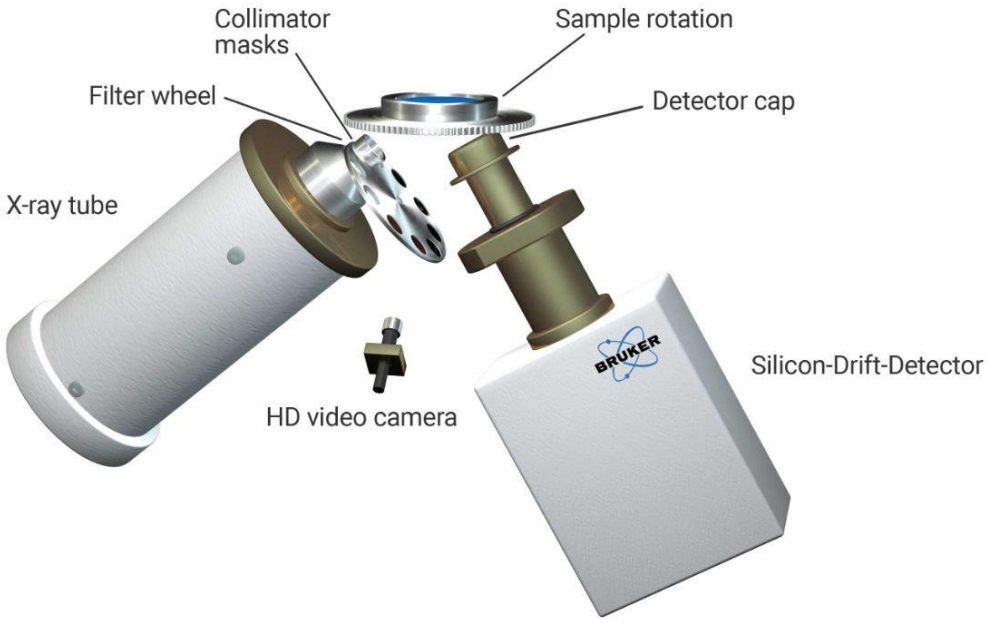

Figure 17. *Schematic diagram of a typical Energy Dispersive X-ray Fluorescence (ED-XRF) Spectrometer geometry. The system illustrates the fixed, close-coupled arrangement common to ED-XRF. X-rays are generated by the X-ray tube and pass through a filter wheel and collimator masks before striking the sample. The characteristic fluorescent X-rays emitted by the sample are then simultaneously detected by the Silicon-Drift-Detector (SDD) (Bruker, 2025).*

The energy resolution of an ED-XRF system is primarily determined by the detector properties and the associated electronics. While ED-XRF detectors offer the advantage of collecting the full spectrum in a single acquisition, their energy resolution is lower than that of WD-XRF, particularly for closely spaced peaks in the low-energy region. Consequently, spectral overlaps can occur, especially among light elements, requiring advanced deconvolution algorithms to accurately resolve individual contributions (Sole et al., 2007).

8.10 Wavelength Dispersive XRF spectrometry (WD-XRF)

Wavelength Dispersive X-ray Fluorescence (WD-XRF) is an analytical technique for qualitative and quantitative elemental analysis that relies on the diffraction of X-rays by a crystal to separate the characteristic fluorescence emitted by the sample (Beckhoff et al., 2006). This process follows Bragg's Law:

$$n\lambda = 2d\ sin\theta \tag{23}$$

, where n is the diffraction order, λ is the X-ray wavelength, d is the lattice spacing of the crystal, and θ is the diffraction angle. By varying θ, the spectrometer selects specific wavelengths corresponding to different elements.

In WD-XRF, a single crystal or synthetic multilayer serves as the dispersive element, acting as a monochromator to isolate X-rays of a single wavelength. This is achieved through

Bragg diffraction, where the goniometer adjusts the diffraction angle (θ) according to Bragg's Law, directing only the desired wavelength into the detector at any given moment. Because the scanning is sequential, each element is measured under optimal diffraction conditions, resulting in high spectral resolution (typically 5–20 eV) and effective separation of overlapping peaks—particularly in the low-energy (long-wavelength) region.

From a geometry perspective, WD-XRF employs a variable-angle configuration, with the relative positions of the sample, crystal, and detector changing to satisfy diffraction conditions for each wavelength. In contrast, Energy Dispersive X-ray Fluorescence (ED-XRF) uses a fixed geometry, with a solid-state detector collecting the entire spectrum simultaneously. While this enables faster multi-element analysis, the energy resolution is lower (typically 120–150 eV at Mn-Kα), making WD-XRF superior for resolving closely spaced peaks and analyzing complex or light-element-rich samples.

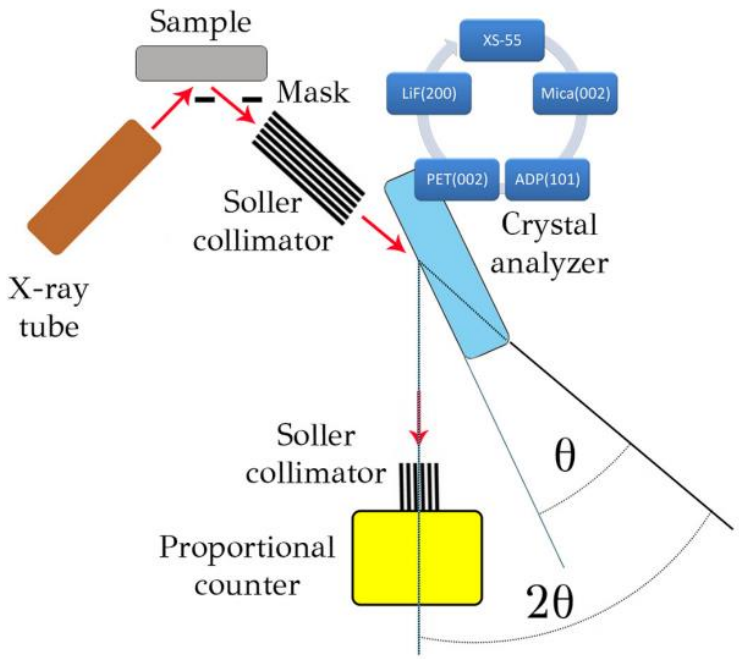

Figure 18. *In this arrangement, the X-ray tube serves as the ionization source for the sample. The effective illuminated area of the sample is defined by the mask size. The emitted fluorescence spectrum from the sample passes through a Soller collimator, which restricts the acceptance angle to a narrow range, before striking the crystal analyzer. Only photons with wavelengths satisfying the Bragg condition Eq.(23) are diffracted at the scattering angle 2θ. A proportional counter, positioned along the path of the diffracted beam, records the photon intensity. To obtain the fluorescence spectrum, both the crystal analyzer and detector are sequentially rotated in a θ–2θ scanning mode. A crystal changer mechanism enables the remote selection and replacement of the crystal analyzer when needed (Anagnostopoulos, 2018; Anagnostopoulos et al., 2018).*

The energy resolution for a given photon energy E is defined by the ratio E/ΔE, where ΔE is the full width at half maximum (FWHM) of the measured spectral line. In WD-XRF, the energy broadening is given by:

$$\Delta E = E \cos\theta_B \Delta\theta \tag{24}$$

, where θ_B is the Bragg angle and $\Delta\theta$ is the angular FWHM of the recorded line. The Bragg angle is determined by the crystal lattice spacing d and the order of reflection n using the Bragg Law:

$$\sin\theta_B = \frac{h \cdot c}{E} \cdot \frac{n}{2 \cdot d} \tag{25}$$

where, h is Planck's constant and c is the speed of light. By combining Eqs. (16) and (17), the energy broadening as a function of the transition energy, the crystal-plane spacing, and the reflection order is expressed as:

$$\Delta E = E\sqrt{\left(\frac{E}{h \cdot c} \cdot \frac{2 \cdot d}{n}\right)^2 - 1} \cdot \Delta\theta \tag{26}$$

The above relationships indicate that the performance of a WD-XRF system is strongly influenced by the Bragg angle, crystal spacing, and diffraction order. Operating at higher Bragg angles, improves spectral resolution, enabling more precise discrimination between closely spaced peaks (Chen et al., 2008) . Crystals with larger lattice spacings are particularly advantageous for analyzing low-energy X-rays, as they allow efficient diffraction at higher angles. Additionally, using lower diffraction orders increases the intensity of the detected signal, although this comes at the expense of a slight reduction in resolution. Under typical operating conditions, WD-XRF systems achieve an energy resolution in the range of 5–20 eV, which is sufficient to resolve complex spectral overlaps and provide accurate elemental identification.

In contrast, ED-XRF separates and measures photons by their energy using a solid-state detector, such as a Silicon Drift Detector (SDD). All detectable elements are measured simultaneously, which allows for rapid multi-element analysis. However, the spectral resolution is lower, typically in the range of 120–150 eV at Mn-Kα, which can make it challenging to resolve overlapping peaks, particularly in the low-energy range (Beckhoff et al., 2006). The background is generally higher compared to WD-XRF, and the sensitivity to very light elements is limited, with practical detection thresholds starting at sodium (Z = 11) in air, or slightly lighter when operating in helium or vacuum.

9. Particle-Induced X-Ray Emission (PIXE)

9.1 Ion Beam Analysis of PM samples

Ion Beam Analysis (IBA) encompasses a group of analytical techniques that utilize interactions between high-energy charged particles (typically MeV-range) and solid matter to investigate the elemental composition and structure of surface layers, generally ranging from the surface up to around 100 micrometers in depth. These techniques extract information from the detection of emitted X-rays, gamma rays, and scattered charged particles (Nastasi et al., 2014).

IBA methods are inherently multi-elemental, spanning a wide range of atomic numbers from hydrogen (H) to uranium (U), and can detect trace concentrations down to microgram per gram (μg/g) levels. They are also highly quantitative, with typical uncertainties of only a few percent, and are traceable and non-destructive, allowing for additional complementary analyses to be performed on the same sample. Another significant advantage is that no chemical preparation or digestion is required (Johansson, 1998).

In studies involving PM samples, IBA techniques are particularly effective, enabling the generation of large datasets of elemental concentrations from the small sample masses typically collected in air pollution studies. These data are valuable for both source identification and quantitative characterization, offering critical insights for environmental monitoring agencies and policymakers.

The main IBA techniques applied in aerosol analysis include Particle Induced X-ray Emission (PIXE), Particle Induced Gamma-ray Emission (PIGE), and elastic scattering techniques such as Elastic Backscattering Spectrometry (EBS) and Particle Elastic Scattering Analysis (PESA). Among these techniques, PIXE is the most commonly used method, capable of detecting all elements heavier than Na, including anthropogenic pollutants like S, V, Ni, Cu, Zn, As, and lead (Pb), as well as key crustal elements such as Al, Si, K, Ca, Ti, and Fe (Chiari et al., 2005; Lucarelli et al., 2018).

9.2 Particle Induced X-Ray Emission (PIXE)

Particle-Induced X-ray Emission (PIXE) is a technique that relies on the ejection of inner-shell electrons from atoms in a target material by high-energy incident particles (protons). The resulting characteristic X-ray emission, that are produced as the electrons from higher shells fill these vacancies, is detected with X-ray detectors to determine the elemental composition of the investigated sample (Nastasi et al., 2014). The basic principle of PIXE of the inner-shell ionization and X-ray emission is presented on **Figure 19**.

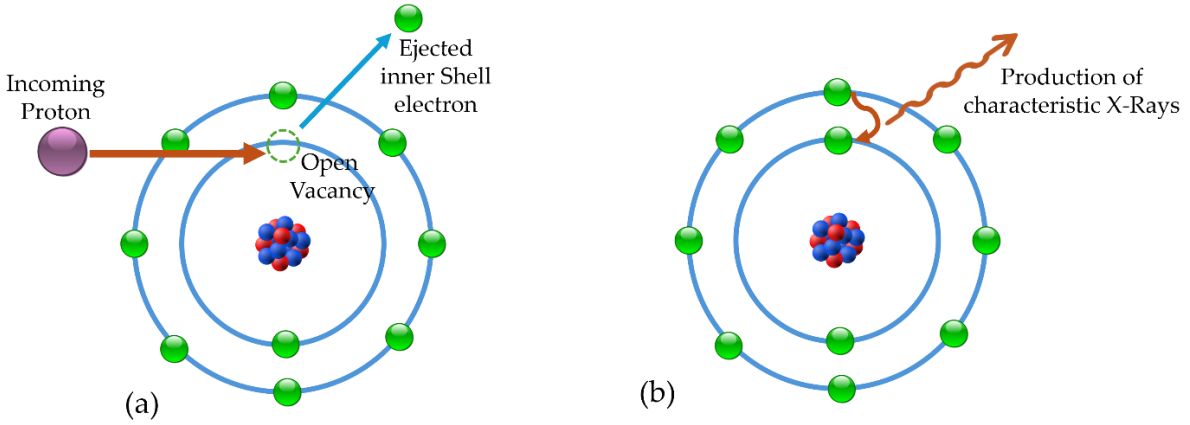

***Figure 19**. Basic principle of PIXE. (**a**) Inner-shell ionization (**b**) X-ray emission*

Since its early development, the Particle-Induced X-ray Emission (PIXE) technique has played a central role in the elemental analysis of atmospheric aerosols, historically serving as the leading method in this field (Artaxo et al., 1999). Over the years, however, newer and techniques such as Inductively Coupled Plasma Atomic Emission Spectroscopy (ICP-AES) and Inductively Coupled Plasma Mass Spectrometry (ICP-MS) have gained popularity for their ability to analyze trace elements with high precision (Nimmo et al., 1994; Low et al., 1990). Simultaneously, advances in XRF instrumentation — including the development of synchrotron radiation-based XRF — have significantly improved the performance of ED-XRF systems (Manousakas et al., 2018; Gunchin et al., 2019).

Despite these developments, PIXE continues to offer key advantages, particularly in aerosol research. It requires only a short irradiation time — typically between 2 and 10 minutes — to detect a broad range of elements, from sodium (Na) to lead (Pb) (Chiari, 2021). These elements serve as tracers for various sources of particulate matter: marine aerosols (Na, Cl), mineral dust (Al, Si, Ca, Ti, Fe, Sr), secondary sulphates (S), biomass burning (K, Zn, Rb), heavy oil combustion (V, Ni), incineration (K, Zn, Pb), and emissions from traffic or industry (Mn, Ni, Cu, Zn, Pb).

PIXE's high detection efficiency is especially beneficial when large numbers of samples — often hundreds — must be analyzed, which is a common requirement in air quality studies. Compared to ED-XRF, PIXE provides significantly greater sensitivity (often an order of magnitude higher) and requires far less sample material (Chiari, 2021). A typical PIXE spectrum is shown below.

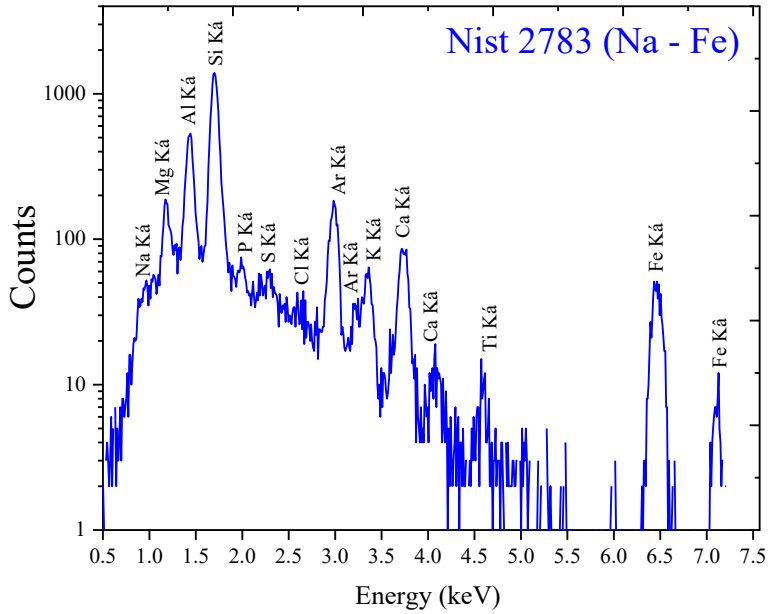

Figure 20. *PIXE spectrum of the NIST 2783 standard reference material for airborne particulate matter (APM), displaying Kα and Kβ peaks for elements ranging from sodium (Na) to iron (Fe). The sample was analyzed using a 3.05 MeV proton beam at a beam current of 7 nA.*

9.3 PIXE Quantitative Analysis Fundamentals

For a typical PIXE setup (**Figure 21**) involving a homogeneous target that is sufficiently thick to completely stop the incoming ion beam, the yield Y_z of the principal characteristic X-ray line (e.g., Kα or Lα) of an element Z can be expressed as (Nastasi et al., 2014):

$$Y_z = \frac{N_{av} \cdot \omega_z \cdot b_z \cdot t_z \cdot \varepsilon_z \cdot (\Omega/4\pi)}{A_z} \cdot N_p \cdot C_z \cdot \int_{E_0}^{E_f} \frac{\sigma_z(E) \cdot T_z(E)}{S_M(E)}\, dE \qquad (27)$$

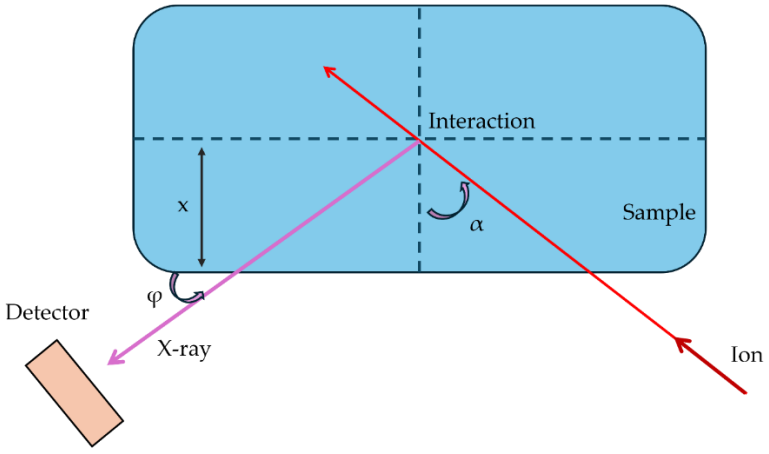

Figure 21. *Typical PIXE geometry.*

With the explanation of each term and their physical meaning given in

Table 1.

Table 1. *Notation and physical meaning of terms in the PIXE quantification formula.*

Symbol	Description
Y_z	**X-ray yield** (The total number of characteristic X-ray photons of a specific line (e.g., Kα or Lα) from element Z that are successfully detected during the measurement.
N_{av}	**Avogadro's number** (6.022×10^{23} mol^{-1}).
ω_z	**Fluorescence yield**: The probability that an inner-shell vacancy (typically K or L) in an atom of element Z will be filled by an electron transition that results in the emission of an X-ray, rather than by an Auger electron. It increases with atomic number.
b_z	**Branching ratio**: is the branching fraction of the principal line within the particular x-ray series (e.g., Kα within the K-series.)
t_z	**Transmission factor:** The fraction of emitted X-rays that pass through any intervening material (e.g., air, detector window, or filter) without being absorbed or scattered.
ε_z	**Detector intrinsic efficiency**: The probability that an X-ray photon of the characteristic energy from element Z is actually detected by the detection system. It depends on detector material, thickness, and the photon energy.
Ω	**Solid angle of detection**: The angular extent of the detector as "seen" from the sample surface, measured in steradians. It quantifies the fraction of the emitted X-rays that geometrically reach the detector. A larger solid angle means more photons are collected.
A_z	**Atomic mass of element Z**
N_p	**Number of incident protons:** The total number of protons that hit the sample during the irradiation. It defines the amount of excitation delivered to the sample and is proportional to the primary beam current and measurement duration.
C_z	**Concentration of Element Z**: The mass fraction (e.g., in μg/g or %) of element Z in the sample. It describes the amount of that element present in the irradiated volume.
$\sigma_z(E)$	**Ionization cross section**: The energy-dependent probability that a proton with energy E will ionize the target atom's inner shell (e.g., K or L) of element Z, triggering X-ray emission.
$T_z(E)$	**Self-Absorption Correction (In-Sample Transmission)**: The fraction of X-rays produced within the sample that successfully escape without being absorbed by the sample itself. This accounts for self-absorption effects, especially important in thick or dense samples.
$S_M(E)$	**Stopping Power of the Matrix:** The rate of energy loss of the incident proton per unit path length as it travels through the sample matrix. It determines how the proton slows down inside the sample.

E_0, E_f **Initial and final of the proton energies**: as it enters (E_0) and exits (E_f) the sample

Although the X-ray yield (Y_z) is mostly proportional to the concentration C_z of an element in the sample, this relationship is modified by a matrix correction term that accounts for the absorption of X-rays inside the sample before they reach the detector. This correction depends on the full elemental composition of the sample, because all elements contribute to the attenuation of both the incident beam and the emitted X-rays (Nastasi et al., 2014). The matrix term is expressed as:

$$T_z(E) = \exp\left(-\mu \cdot \frac{cosa}{sin\varphi} \cdot \int_{E_0}^{E} \frac{1}{S_M(E)} dE\right) \quad (28)$$

where μ is the matrix mass attenuation coefficient, defined as the concentration-weighted sum of the mass attenuation coefficients of all elements in the matrix. This term determines how strongly the matrix absorbs characteristic X-rays on their way out of the sample.
The geometry of the measurement also affects the degree of absorption:

- α is the angle between the *incident proton beam* and the sample surface normal.
- ϕ is the angle between the *emitted X-rays* and the sample surface.

These angles determine the effective path length that both the incident particles and the outgoing X-rays travel inside the sample. Longer path lengths lead to greater attenuation, which decreases the detected X-ray yield.

9.4 PIXE Quantitative analysis for thin targets

When the sample is sufficiently thin — as is often the case with PM aerosol deposits — both proton energy loss and X-ray absorption within the material become negligible. Under these conditions, matrix effects can be ignored, and the integral term in the yield equation simplifies accordingly (Nastasi et al., 2014). The relationship between the X-ray yield Yz and the element concentration Cz becomes linear and is expressed as:

$$Y_z = S_z \cdot N_p \cdot C_z \cdot x \quad (29)$$

Where,

- x is the sample thickness along the beam direction (x/cosα) and,
- $S_z = \frac{N_{av} \cdot \omega_z \cdot b_z \cdot t_z \cdot \varepsilon_z \cdot (\Omega/4\pi)}{A_z \cdot \cos a}$, is the sensitivity factor for element Z, defined as the X-ray yield per incident proton per unit areal density

The sensitivity factor S_z can be empirically determined for a specific PIXE setup using thin-film standards. By measuring the Kα or Lα X-ray intensity as a function of areal concentration across different elements, a calibration curve of sensitivity versus atomic

number Z can be established. This curve captures all physical and instrumental factors in the theoretical model (Eq. (29) and allows direct comparison between unknown samples and standards.

The accuracy of concentration measurements in unknown samples mainly depends on two things:

1. The quality and well-known composition of the reference standards used, and
2. The precision of the spectral fitting, which refers to how accurately the X-ray peaks are analyzed in the spectrum.

For this method to work reliably, the sample must be deposited on a thin, clean substrate that doesn't contain interfering elements. Polycarbonate foils or Teflon filters of a few micrometers thick are commonly used for this purpose. In PIXE, a sample is typically considered "thin" if its mass per unit area is less than 1 mg/cm². This condition is often met when analyzing aerosol samples with 3 MeV proton beams, which is standard in many environmental studies (Nastasi et al., 2014; Chiari, 2021).

When the assumptions of the simplified model no longer hold, such as in thick-target conditions, the equation is expanded to include matrix corrections, detector efficiency, and beam–sample geometry.

$$Y_z = H \cdot C_z \cdot Y_1(z) \cdot N_p \cdot \varepsilon_z \cdot t_z \tag{30}$$

where,

- $Y_1(z)$ is the theoretical X-ray yield per unit solid angle, per unit concentration, and per unit beam charge for element Z and,
- H is a single system-specific constant that includes the solid angle of the detector and all matrix correction contributions. Once H is calibrated using thin-film standards, the system can account for detector geometry and setup, including matrix effects for thick samples, and maintain accuracy without needing standards that perfectly match the matrix of every unknown sample.

This approach simplifies the quantification process while ensuring accurate concentration results, provided the database values and calibration standards are reliable. It also makes PIXE flexible for multi-elemental analysis, particularly when analyzing a large number of samples in environmental studies.

10. References for Section B

Abiye, O. E., Ugwumadu, C. E., Kamara, A. J., Felizardo, J. P., & Sannoh, A. (2021). Sensitivity Calibrations of K- and L-shell X-ray Lines for Elemental Analysis of Air Particulate Samples Using a Handheld XRF Spectrometer. *Aerosol Science and Engineering*, *5*(2), 127–135. https://doi.org/10.1007/s41810-021-00089-3

Anagnostopoulos, D. F. (2018). X-ray emission spectroscopy optimization for chemical speciation in laboratory. *Spectrochimica Acta Part B: Atomic Spectroscopy*, *148*, 83–91. https://doi.org/10.1016/J.SAB.2018.06.004

Anagnostopoulos, D. F., Siozios, A., & Patsalas, P. (2018). Characterization of aluminum nitride based films with high resolution X-ray fluorescence spectroscopy. *Journal of Applied Physics*, *123*(6). https://doi.org/10.1063/1.5013281/155032

Asvestas, A., Chatzipanteliadis, D., Gerodimos, T., Mastrotheodoros, G. P., Tzima, A., & Anagnostopoulos, D. F. (2024). Real-Time Elemental Analysis Using a Handheld XRF Spectrometer in Scanning Mode in the Field of Cultural Heritage. *Sustainability (Switzerland)*, *16*(14), 6135. https://doi.org/10.3390/SU16146135/S1

Artaxo, P., Castanho, A. D., Yamasoe, M. A., Martins, J. V., & Longo, K. M. (1999). Analysis of atmospheric aerosols by PIXE: the importance of real time and complementary measurements. *Nuclear Instruments and Methods in Physics Research Section B: Beam Interactions with Materials and Atoms*, *150*(1–4), 312–321. https://doi.org/10.1016/S0168-583X(98)01007-63

Beckhoff, B., Kanngießer, B., Langhoff, N., Wedell, R., & Wolff, H. (Eds.). (2006). *Handbook of practical X-ray fluorescence analysis*. Springer. https://doi.org/10.1007/978-3-540-36722-2

Brouwer P., THEORY OF XRF Getting acquainted with the principles, 2003. www.panalytical.com (accessed September 01, 2025).

Bruker. (2025). *How does XRF work?* Retrieved November 30, 2025, from https://www.bruker.com/en/products-and-solutions/elemental-analyzers/xrf-spectrometers/how-does-xrf-work.html

Chatoutsidou, S. E., Papagiannis, S., Anagnostopoulos, D. F., Eleftheriadis, K., Lazaridis, M., & Karydas, A. G. (2022). Application of a handheld X-ray fluorescence analyzer for the quantification of air particulate matter on Teflon filters. *Spectrochimica Acta Part B: Atomic Spectroscopy*, *196*, 106517. https://doi.org/10.1016/J.SAB.2022.106517

Chen, Z. W., Gibson, W. M., & Huang, H. (2008). High Definition X-Ray Fluorescence: Principles and Techniques. *X-Ray Optics and Instrumentation*, *2008*(1), 318171. https://doi.org/10.1155/2008/318171

Chiari, M., Lucarelli, F., Mazzei, F., Nava, S., Paperetti, L., Prati, P., Valli, G., & Vecchi, R. (2005). Characterization of airborne particulate matter in an industrial district near Florence by PIXE and PESA. *X-Ray Spectrometry*, *34*(4), 323–329. https://doi.org/10.1002/xrs.825

Chiari, M., Yubero, E., Calzolai, G., Lucarelli, F., Crespo, J., Galindo, N., Nicolás, J. F., Giannoni, M., & Nava, S. (2018). Comparison of PIXE and XRF analysis of airborne particulate matter samples collected on Teflon and quartz fibre filters. *Nuclear Instruments and Methods in Physics Research Section B: Beam Interactions with Materials and Atoms*, *417*, 128–132. https://doi.org/10.1016/j.nimb.2017.07.031

Chiari, M. (2021, June). *Elemental analysis of atmospheric particulate matter samples with Ion Beam Analysis techniques* [Unpublished measurement guideline]. ACTRIS – CAIS-ECAC. Retrieved from https://www.actris-ecac.eu/pmc-elements.html

Cirelli, P., Bilo, F., Tsuji, K., Matsuyama, T., Siviero, G., Pisani, L., Zacco, A., Depero, L. E., Eichert, D., & Borgese, L. (2022). Assessment of calibration methods for Pb-loaded aerosol filters analysed with X-ray fluorescence under grazing incidence. *Spectrochimica Acta Part B: Atomic Spectroscopy*, *192*, 106414. https://doi.org/10.1016/J.SAB.2022.106414

Cramer, S. P. (2020). *X-Ray Spectroscopy with Synchrotron Radiation*. https://doi.org/10.1007/978-3-030-28551-7

Fosbinder, Robert, and Orth Denise. 2011. *Essentials of Radiologic Science*. Philadelphia: Lippincott Williams & Wilkins.

González, M. F., Saadatkhah, N., & Patience, G. S. (2024). Experimental methods in chemical engineering: X-ray fluorescence—XRF. *The Canadian Journal of Chemical Engineering*, *102*(6), 2004–2018. https://doi.org/10.1002/CJCE.25218

Gunchin, G., Streli, C., Darby, I., Karydas, A. G., Eleftheriadis, K., Lodoysamba, S., Shagjjamba, D., Migliori, A., Padilla-Alvarez, R., Manousakas, M., & Osan, J. (2019). Three-Year Long Source Apportionment Study of Airborne Particles in Ulaanbaatar Using X-Ray Fluorescence and Positive Matrix Factorization. *Aerosol and Air Quality Research*, *19*(5), 1056–1067. https://doi.org/10.4209/aaqr.2018.09.0351

Johansson, S. A. E. (1989). PIXE: a novel technique for elemental analysis. *Endeavour*, *13*(2), 48–53. https://doi.org/10.1016/0160-9327(89)90002-1

Klockenkämper, R., & Bohlen, A. von. (2015). *Total-reflection X-ray fluorescence analysis and related methods*. John Wiley and Sons, Inc.

Knoll, G. F. (2010). Radiation detection and measurement (4th ed.). Wiley.

Lifton, J. J., & Carmignato, S. (2017). Simulating the influence of scatter and beam hardening in dimensional computed tomography. *Measurement Science and Technology*, *28*(10), 104001. https://doi.org/10.1088/1361-6501/AA80B2

Low, P. S., & Hsu, G. J. (1990). Direct determination of atmospheric lead by Zeeman solid sampling graphite furnace atomic absorption spectrometry (GFAAS). *Fresenius' Journal of Analytical Chemistry 1990 337:3*, *337*(3), 299–305. https://doi.org/10.1007/BF00321978

Lucarelli, F., Calzolai, G., Chiari, M., Nava, S., & Carraresi, L. (2018). Study of atmospheric aerosols by IBA techniques: The LABEC experience. *Nuclear Instruments and Methods in Physics*

Research Section B: Beam Interactions with Materials and Atoms, *417*, 121–127. https://doi.org/10.1016/J.NIMB.2017.07.034

Manousakas, M., Diapouli, E., Papaefthymiou, H., Kantarelou, V., Zarkadas, C., Kalogridis, A.-C., Karydas, A.-G., & Eleftheriadis, K. (2018). XRF characterization and source apportionment of PM10 samples collected in a coastal city. *X-Ray Spectrometry*, *47*(3), 190–200. https://doi.org/10.1002/xrs.2817

Nastasi, M., Mayer, J. W., & Wang, Y. (2014). *Ion Beam Analysis: Fundamentals and Applications* (1st ed.). CRC Press. https://doi.org/10.1201/b17310

Nimmo, M., & Fones, G. (1994). Application of adsorptive cathodic stripping voltammetry for the determination of Cu, Cd, Ni and Co in atmospheric samples. *Analytica Chimica Acta*, *291*(3), 321–328. https://doi.org/10.1016/0003-2670(94)80027-8

Sherman, J. (1955). The theoretical derivation of fluorescent X-ray intensities from mixtures. *Spectrochimica Acta*, *7*(C), 283–306. https://doi.org/10.1016/0371-1951(55)80041-0

Solé, V. A., Papillon, E., Cotte, M., Walter, P., & Susini, J. (2007). A multiplatform code for the analysis of energy-dispersive X-ray fluorescence spectra. *Spectrochimica Acta Part B: Atomic Spectroscopy*, *62*(1), 63–68. https://doi.org/10.1016/J.SAB.2006.12.002

Tsampa, K. (2020). *Characterization of platinum group mineral inclusions in archaeological gold objects using X-ray imaging spectrometry* (Master's thesis). National Technical University of Athens, http://dx.doi.org/10.26240/heal.ntua.19890.

Ul-Hamid, A. (2018). *A beginners' guide to scanning electron microscopy*. Springer. https://doi.org/10.1007/978-3-319-98482-7

Van Grieken, R. E., & Markowicz, A. (Eds.). (2001). *Handbook of X-Ray Spectrometry* (2nd ed.). Boca Raton: CRC Press. https://doi.org/10.1201/9780203908709

Section C. Instrumentation

11.1 ED-XRF spectrometer with secondary targets

The Panalytical Epsilon-5 is an ED-XRF spectrometer that features a fully integrated and self-shielded measurement chamber, where both the X-ray tube exit window and the beryllium entrance window of the detector are enclosed within the radiation-safe housing. This design ensures operator safety without the need for external shielding (PANalytical B.V., 2014).

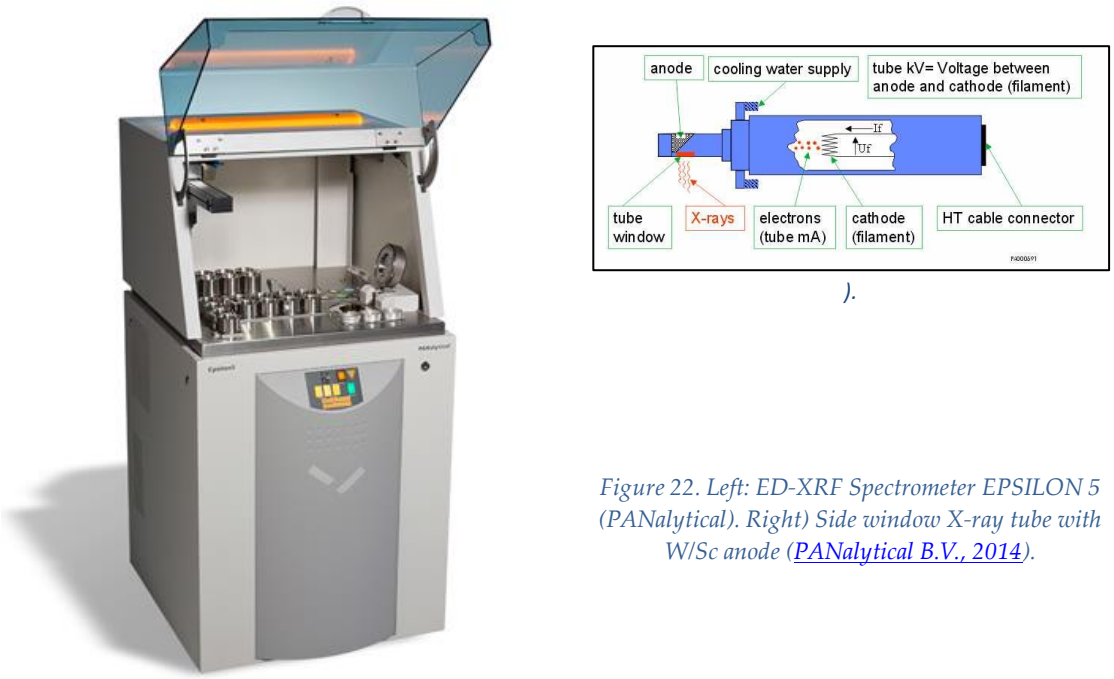

Figure 22. Left: ED-XRF Spectrometer EPSILON 5 (PANalytical). Right) Side window X-ray tube with W/Sc anode (PANalytical B.V., 2014).

The X-ray tube is a side-window capable of operating at high voltages up to 100 kV, with a maximum power output of 600 W. The voltage–current relationship is inversely scaled to maintain power limits: for instance, at 100 kV, the tube operates with a current of 6 mA, while at 25 kV, the current can be increased to 24 mA to preserve the same power output. The anode material consists of a Scandium-Tungsten (Sc/W) composite design where a thin Sc layer is deposited over a W base. The Sc/W anode, is optimized for the excitation of light elements. The presence of scandium enhances the excitation efficiency of corresponding secondary targets, making this configuration particularly well-suited for the elemental analysis of PM samples (Papagiannis et al., 2024; Manousakas et al., 2018).

A rotating secondary target carousel (**Figure 23**) is integrated into the system, allowing different secondary targets to be precisely positioned in the beam path. Each selectable configuration corresponds to a specific combination of X-ray tube voltage and secondary target material, tailored to optimize the excitation efficiency for particular groups of elements.

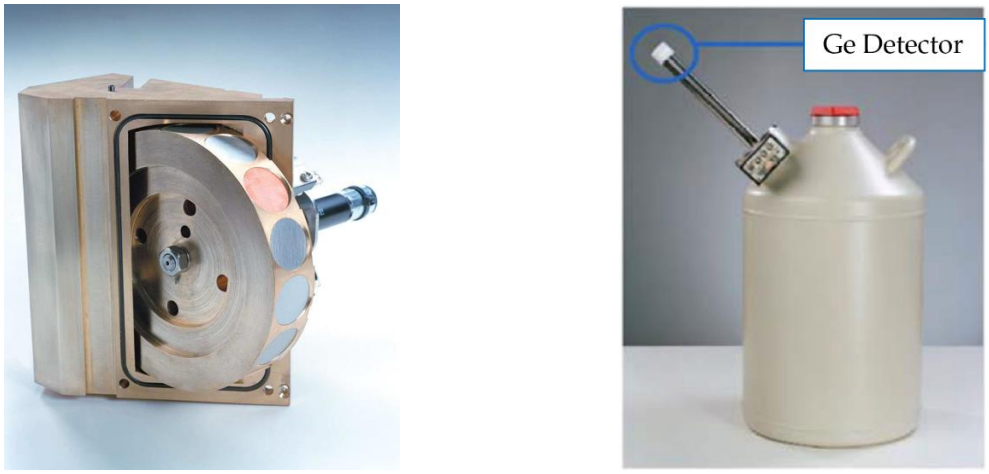

Figure 23. *Left) Rotating secondary target carousel of the ED-XRF Epsilon 5 (Panalytical) spectrometer. Right) The Ge detector and liquid N2 Dewar of the Epsilon 5 spectrometer (PANalytical B.V., 2014).*

The characteristic X-ray radiation emitted from the sample is subsequently detected by a high-purity germanium (Ge) detector with an energy resolution of approximately 150 eV full width at half maximum (FWHM) at the Mn-Kα line (5.89 keV). The detector is cooled using liquid nitrogen to maintain optimal performance and reduce electronic noise.

Table 2*. Features of the ED-XRF spectrometer Epsilon 5.*

X-Ray Tube Parameters	
Anode Element	W/Sc
Tube Window Element	Be
Tube Window Thickness (mm)	150
Min / Max Voltage (kV)	25 / 100
Min / Max Current (mA)	0.5 / 24
Maximum Power (W)	600
Detector Parameters	
Detector Element	Ge
Detector Thickness (mm)	5
Detector Window Element	Be
Detector Window Thickness	8 mm
Active Area (mm^2)	30
Geometry Parameters	
Excitation Angle (Tube → Target)	45
Scatter Angle (Target → Sample)	45
Detection Angle (Sample → Det.)	45
Sample Incidence Angle	45

11.1.1 The Role of Secondary Target Materials

In conventional ED-XRF spectrometry set-ups, the sample is excited directly by the full spectrum of the X-ray tube. For example, when using a W anode tube, the spectrum includes both a broad continuum and the characteristic lines of W. The entire spectrum contributes to excitation, and the resulting signal must be integrated from the absorption edge of the element of interest up to the tube's maximum energy (set by the applied high voltage) (Manousakas et al., 2018). This direct-excitation method has two challenges:

- Uneven excitation efficiencies: Elements with absorption edges just below the characteristic lines of the anode material are excited much more efficiently than those that can only be excited by the continuum.
- High background signal**:** Both the continuum and characteristic lines from the tube are strongly scattered by the sample, producing a broad spectral background underneath the element peaks. This background can be especially problematic for samples with complex or "dark" matrices, lowering detection limits and making trace analysis difficult.

To overcome these limitations, the Epsilon-5 spectrometer uses secondary targets positioned between the X-ray tube and the sample (**Figure 24**). These targets are typically pure-element metal foils or pressed compounds placed in reflection geometry. When irradiated by the X-ray tube, the secondary targets emit two characteristic lines (Kα and Kβ), which are then used to excite the sample.

This approach has several advantages:

- Simplified excitation spectrum: Instead of the full continuum, the sample is excited by only one or two well-defined characteristic lines. This greatly reduces the need for complex integrations over the tube's full spectral distribution.
- Lower spectral background: Secondary targets scatter much less radiation than the original tube spectrum, particularly because they are made of elements with high atomic numbers. This improves signal-to-background ratios and lowers detection limits.
- Optimized sensitivity for each element: By selecting the appropriate secondary target, the excitation lines can always be placed just above the absorption edge of the element(s) of interest. This ensures maximum excitation efficiency, even for elements that are poorly excited by the tube's continuum.

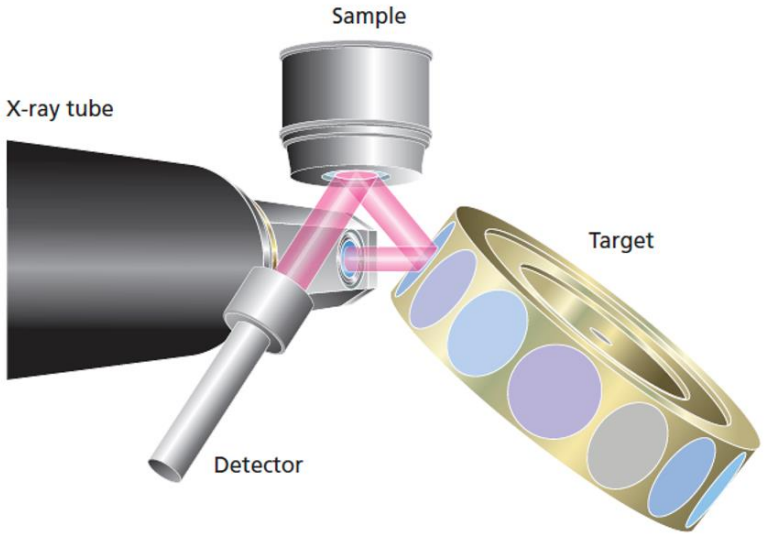

***Figure 24**. Secondary target geometry of the Epsilon 5 ED-XRF spectrometer (Brouwer, 2010).*

The installed secondary tagerts of the Epsilon 5 ED-XRF spectrometer are the following: Al_2O_3, CaF_2, Fe Ge, Mo, Zr, KBr, Ag, CeO_2 and LaB_6.

11.2 Handheld ED-XRF spectrometer

The handheld ED-XRF spectrometer (Tracer 5i, Bruker) is equipped with a 50 kV–4 W rhodium (Rh) anode X-ray tube (**Figure 25**, Left). The characteristic X-ray radiation emitted by the sample is detected by a 20 mm² silicon drift detector (SDD) with an energy resolution of approximately 140 eV FWHM at the Mn-Kα line (5.89 keV). The instrument is capable of detecting elements ranging from sodium (Na) to uranium (U) (Bruker, 2021). Voltage and current values are pre-set by the manufacturer and vary between 6–50 kV and 4.5–195 μA, respectively, with limitations imposed by the instrument's power constraints (Chatoutsidou et al., 2022; Asvestas et al., 2024). The analyzer offers two selectable collimators producing measurement spot sizes of 3 mm and 8 mm (**Figure 25**, Right), along with four automatic filter positions. While routine measurements are usually performed in air, the instrument supports vacuum operation (or helium purging) to enhance sensitivity for light elements. Measurements can also be carried out using a desktop stand, with the spectrometer positioned in a fixed, upward-facing configuration to ensure consistent measurement geometry. For vacuum operation, an external pump is connected to the instrument chamber through a dedicated tube, enabling the exact same geometry to be maintained as in air measurements.

Figure 25. Left) *The HH-XRF spectrometer, Tracer 5i (Bruker) along with the benchtop stand kit and the safety cover in place.* ***Right****) The port for inserting the 3 mm and 8 mm collimators (Bruker, 2021).*

The instrument is also equipped with absorption filters (filter wheel) that are positioned between the Rh X-ray source and the sample under analysis. These filters modify the spectrum of the incident ionizing radiation. When the X-ray beam passes through a thin filter, part of the radiation interacts with the atoms of the filter material. At the same time, the

remainder is transmitted without interaction, in accordance with the Beer–Lambert law. The instrument is supplied with four pre-installed filters that can be automatically selected during analysis to optimize excitation conditions for specific elements. The key features of the HH-XRF Tracer 5i analyzer are presented on **Table 3**.

Table 3. *Features of the Handheld ED-XRF analyzer Tracer 5i (Bruker, 2021).*

Parameter	Specification
Detection	Silicon Drift Detector (SDD) with beryllium (Be) window; typical energy resolution <140 eV at 450,000 cps
Detector Geometry	Sample incident angle: 45°; sample take-off angle: 63°– 65°
Detector Construction	Silicon thickness: 0.46 mm; effective area: 20 or 30 mm^2; beryllium (Be) window thickness: 8 μm; sample-to-detector face distance: 8.5 mm
Excitation	Rhodium (Rh) thin-window X-ray tube (transmission tube, 90° electron incidence); X-ray generator: 6–50 kV, 4.5–200 μA, max output 4 W; operator-adjustable current and voltage
X-ray Tube Geometry	Tube take-off angle: 45°; beryllium window thickness: 125 μm; target element: Rh (Z=45); target thickness: 0.6 μm; sample-to-tube face distance: 29 mm
Aperture	User-changeable apertures; supplied apertures with 3 mm and 8 mm spot sizes
Filters (5 positions)	Position 1: Ti 25 μm, Al 300 μm Position 2: No filter Position 3: Cu 75 μm, Ti 25 μm, Al 200 μm Position 4: Cu 100 μm, Ti 25 μm, Al 300 μm Position 5: Al 38 μm
Beam Path	Selectable helium or air beam path
Elemental Range (Detection)	In air: Sodium (Na) to Uranium (U); with helium purge: Fluorine (F) to Uranium (U)
Measurement Window	Air configuration: 3 μm Prolene $(C_3H_6)_n$ window
CMOS Color Camera	Internal VGA CMOS camera (640 × 480 pixels) with capability to store up to 5 images per test
Dimensions (L × W × H)	27.3 × 9.4 × 29.5 cm (10.75 × 3.7 × 11.6 in)
Weight	1.9 kg (4.1 lbs) with battery; 1.6 kg (3.6 lbs) without battery
Display	9.4 cm (3.7 in) LCD (TFT active matrix), 640 × 480 pixels, resistive touchscreen
Software	Full control on analyzer and PC software; control of all excitation parameters and live spectrum display directly on the analyzer
Data Storage & Transfer	Direct USB thumb drive storage; data transfer to PC via USB or Wi-Fi; Bluetooth connectivity for accessories
Power Supply	Li-Ion battery (7.2 V nominal), battery charger, AC adapter (9 V DC @ 3 A)
System Safety	Password protection, sample proximity sensor, low count-rate (backscatter) shutdown
Operating Environment	-10 °C to 50 °C (14 °F to 122 °F); humidity: 10–90% relative humidity (non-condensing); IP54 protection from dust and splashes
Optional Accessories	Tripod kit, benchtop stand with safety interlock, desktop base kit, manual filter kit and accessories, helium purge kit, field sample preparation kit

11.3 Large-scale μ-XRF scanner

The M6-JETSTREAM (Bruker) is an ED-XRF spectrometer (**Figure 26**) specifically designed for elemental analysis of small areas on large scale, heterogeneous samples. As an ED-XRF instrument, it employs a detector capable of measuring the energy distribution of the characteristic X-ray radiation emitted directly from the sample. This spectrometer has been developed for non-destructive elemental mapping of both large and small areas (Bruker Nano GmbH, 2021). It is most applied in the analysis of valuable cultural heritage objects, large geological specimens, and industrial quality control. Its micro-XRF imaging capabilities allow the analysis of very small regions, typically less than 20 μm, on large samples. The key advantages of the micro-XRF approach include:

- Identification of the spatial distribution of elements within the sample,
- Suitability for highly heterogeneous materials,
- Minimal or no sample preparation, and
- Flexible measurement conditions to accommodate a wide range of sample types and analytical requirements.

***Figure 26**. The large-scale μ-XRF spectrometer M6 Jetstream (Bruker) (Bruker Nano GmbH, 2021).*

The main features of the M6 Jetstream spectrometer are presented in **Table 4**:

Table 4. Main features of M6 Jetstream (Bruker Nano GmbH, 2021).

Category	Specification
Operating Conditions	- Optimum temperature range: 22 – 28 °C - Working temperature range: 17 – 33 °C - Relative humidity: 20 – 80%
X-ray Tube	- Ceramic side-window focus tube, 50 × 50 µm, with 0.1 mm Be window - Max. excitation: 50 kV / 600 µA (30 W), Rh anode - Equipped with polycapillary lens (min. spot size: 100 µm – Mo Kα)
Primary Filters	- Position 1: Empty - Position 2: Al 12.5 µm - Position 3: Al 25 µm - Position 4: Al 100 µm - Position 5: Al 100 µm / Ti 25 µm - Position 6: Al 100 µm / Ti 50 µm / Cu 25 µm - Position 7: Al 200 µm / Ti 200 µm - Position 8: Al 100 µm / Cu 68 µm / Zr 15 µm / Mo 50 µm - Position 9: Al 100 µm / Cu 125 µm / Zr 30 µm / Mo 100 µm
Sample Positioning	- Motorized X-Y-Z stage - Travel range: 800 × 620 × 90 mm - Max. speed X & Y: 100 mm/s - Max. speed Z: 10 mm/s
Detection System	- Si SDD with 30 mm² detector area - Energy resolution: <145 eV (Mn Kα) - Take-off angle: 60°
Optical System	- Focal distance: 13.3 mm - Color camera system: - High magnification: field of view approx. 1.1 mm × 8 mm - Low magnification: field of view approx. 31 mm × 22 mm
Ultrasonic Sensor	Minimum sample distance: >3 mm (material dependent)

The M6 JETSTREAM system consists of the following components (**Figure 27**):

1. **Base unit (1):** Equipped with four lockable wheels and four adjustable leveling feet for stable support of the instrument.
2. **Spacer block (2):** Required for horizontal operation; can also be used to adjust the height during vertical operation.
3. **Middle section (3):** Contains the electronic control unit and interfaces for PC operation, the kinematic system, the warning light, the measurement head, and the power supply.
4. **Upper section (4):** Includes the kinematic system, track for the measurement head (5), and tilt unit. The **measurement head** (5) integrates the X-ray source, X-ray optics, a silicon drift detector (SDD), two CCD cameras (one with adjustable focal length), sample illumination, and ultrasonic collision sensors.
5. **Safety interlock connector (6):** For remote activation and control of safety functions.
6. **Instrument computer (7):** Dedicated PC with keyboard and monitor for instrument control and data acquisition.

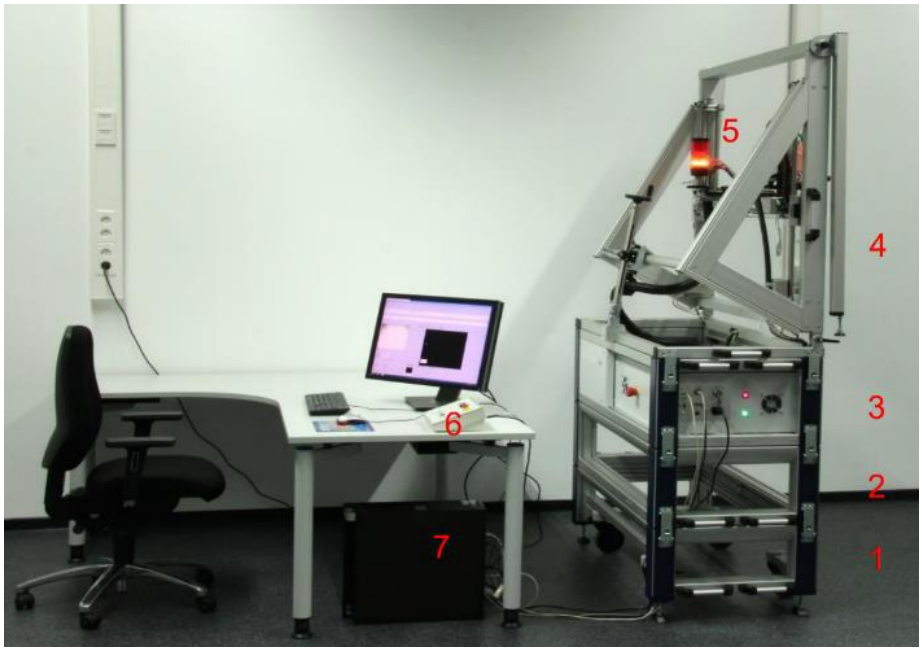

Figure 27. *System components of M6 Jetstream (Bruker Nano GmbH, 2021).*

11.3.1 The XYZ scanning unit

The XYZ scanning unit of the M6 JETSTREAM (**Figure 28**) is a four-axis servo-driven system designed for precise movement and positioning of the measurement head. It employs two electronically synchronized Y-axis drives to support and balance the weight of the measurement head. All movements of the X, Y, and Z axes are coordinated through a dedicated four-axis servo controller (

Table *5*).

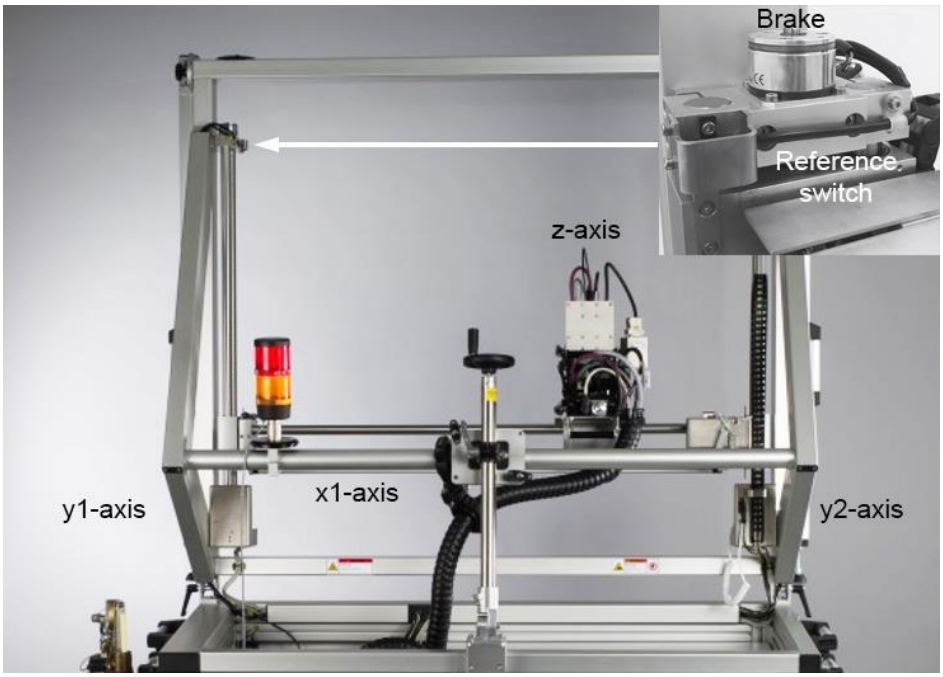

Figure 28. *Scanning unit of the M6 JETSTREAM (Bruker Nano GmbH, 2021)*

Table 5. The XYZ scanning unit of M6 Jetstream (Bruker Nano GmbH, 2021).

Parameter	Value
Scanning directions	x, y, z
Number of motorized axes	4
Drive mechanism	Ball screws driven by DC motors with 2:1 belt ratio, encoder-controlled
Ball screw pitch	x/y: 2 mm; z: 1 mm
Travel range	x: 800 mm; y: 600 mm; z: 95 mm
Maximum speed	x/y: 100 mm/s; z: 20 mm/s
Reference switches	Two optical reference switches per axis
Brakes	Electromagnetic brakes on the y and z axes

11.3.2 Measure head

The measurement head (**Figure 29**) serves as the core functional unit of the M6 JETSTREAM. Mounted on the kinematic system, it houses the X-ray source, detector, camera system, sample illumination, and ultrasonic collision sensors (Bruker Nano GmbH, 2021).

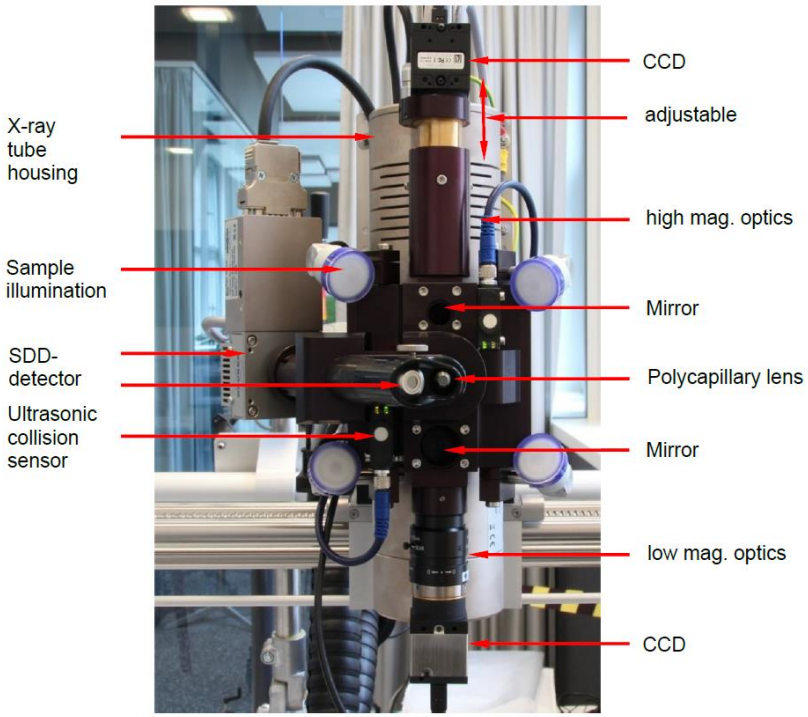

Figure 29. Measure head of M6-Jetsream (Bruker Nano GmbH, 2021).

The main functions of the different components of the spectrometer's measurement head are summarized in **Table 6**:

Table 6. Components of the measure head of M6-Jetsream (Bruker Nano GmbH, 2021).

Module	Function
Tube housing	Mechanical integration of all components, routing of cooling air, shielding of X-rays
X-ray tube	Generates the primary X-ray radiation
Tube and cooling element	Provides primary shielding, dissipates heat, and positions the X-ray tube
Shutter module	Releases the excitation beam during measurement
Filter wheel	Holds five filters and one empty position for modifying the excitation spectrum
Tube housing controller	Regulates tube temperature and stores operating parameters
Fans	Cools the X-ray tube
Mechanical interface	Attaches and positions the X-ray source on the measurement head
Warning lamps	Displays the instrument's operational status
Polycapillary X-ray optics	Defines and shapes the beam geometry

11.3.3 The role of Polycapillary X-ray optics

Polycapillary X-ray lenses are positioned between the X-ray tube and the sample to achieve optimal focusing of the X-ray beam (**Figure 30**). These lenses have a spindle-like geometry and are composed of thousands of hollow glass capillaries. Their operation relies on the principle of total external reflection of photons along the smooth inner surfaces of the capillaries. When the incident angle of the X-rays is lower than the critical angle ($\theta \leq \theta_{critical}$), the reflection coefficient approaches 100%, allowing the X-ray photons to propagate through the capillaries with minimal losses (Beckhoff et al., 2006).

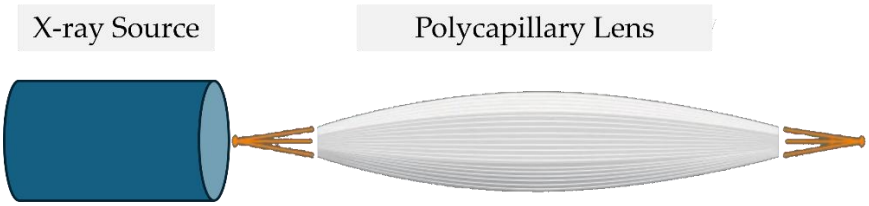

Figure 30. Schematic representation of polycapillary lens geometry.

The reflecting material primarily determines the critical angle and is inversely proportional to the X-ray photon energy. As a result, high-energy X-rays are less efficiently transmitted

through these lenses. Due to the extremely low roughness of the glass reflective surfaces, only a small fraction of the radiation is scattered, enabling highly efficient X-ray transmission through the capillaries. The X-ray spot-size measured with Molybdenum foil (Mo Kα) in dependence of measuring distance is presented in **Table 7**:

Table 7. *Spot Size and Working Distance Settings for the M6 Jetstream (Bruker Nano GmbH, 2021).*

Position Number	Spotsize	Distance
position 1	100 µm	13.3 mm
position 2	210 µm	16.5 mm
position 3	330 µm	19.7 mm
position 4	460 µm	22.9 mm
position 5	580 µm	26.1 mm

11.4 Wavelength Dispersive XRF Spectrometer

The Rigaku ZSX Primus IV is a high-performance Wavelength Dispersive X-ray fluorescence (WD-XRF) spectrometer (**Figure 31**). Its design and functionality enable rapid, accurate quantitative elemental analysis, from Be through uranium U, across a wide variety of sample types including solids, liquids, powders, alloys, and thin films (Rigaku Corporation, 2018).

Figure 31. Right) *The ZSX Primus IV WD-XRF spectrometer. Left) Inserting samples on the WD-XRF spectrometer.*

The ZSX Primus IV spectrometer features a dual-detector configuration that optimizes detection efficiency across the periodic table. It combines a proportional counter (PC), ideal for the measurement of light elements, with a scintillation counter (SC), optimized for heavier elements. This arrangement allows the instrument to perform quantitative analysis of elements ranging from beryllium (Be) to uranium (U) with high sensitivity and precision.

The proportional counter operates by filling its detection chamber with P10 gas (a mixture of argon and methane). When incident X-ray photons enter the detector through a very thin window, they ionize the argon atoms, producing positive argon ions and free electrons—collectively referred to as ion pairs. These electrons are accelerated toward an anode wire under an applied electric field, triggering further ionization events in a process known as gas multiplication. The resulting electrical pulses are proportional to the energy of the incoming X-rays, hence the name "proportional" counter. The thin entrance window is critical for minimizing attenuation of low-energy photons, making the PC particularly well suited for detecting light elements, whose characteristic X-rays are easily absorbed in thicker window materials (Rigaku Corporation, 2018).

The scintillation counter, on the other hand, is designed to measure higher-energy X-rays, typically from heavier elements. Its detection principle relies on a sodium iodide crystal doped with thallium [NaI(Tl)], which scintillates—i.e., emits visible light photons—when struck by incident X-rays. This light is then collected and amplified by a photomultiplier tube, producing a measurable electronic signal. Unlike the PC, the SC employs a beryllium entrance window. While robust, this window absorbs a significant fraction of low-energy X-rays, limiting the SC's suitability for light-element detection. However, its high stopping power and

stability make it highly efficient for heavier elements, where photon energies are sufficiently large to penetrate the Be window without significant loss.

From a geometric perspective, the ZSX Primus IV employs a tube-above geometry, which places the X-ray tube above the sample chamber. This arrangement safeguards optical components from sample debris and reduces the need for maintenance, thereby minimizing instrument downtime. The excitation source is a 3–4 kW Rh-anode end-window X-ray tube with an ultra-thin 30 μm beryllium window, specifically designed to enhance light-element detection. The instrument supports advanced measurement capabilities such as mapping and multi-spot analysis, aided by a high-resolution camera that enables precise sample positioning and detection of inclusions or heterogeneities (Rigaku Corporation, 2018).

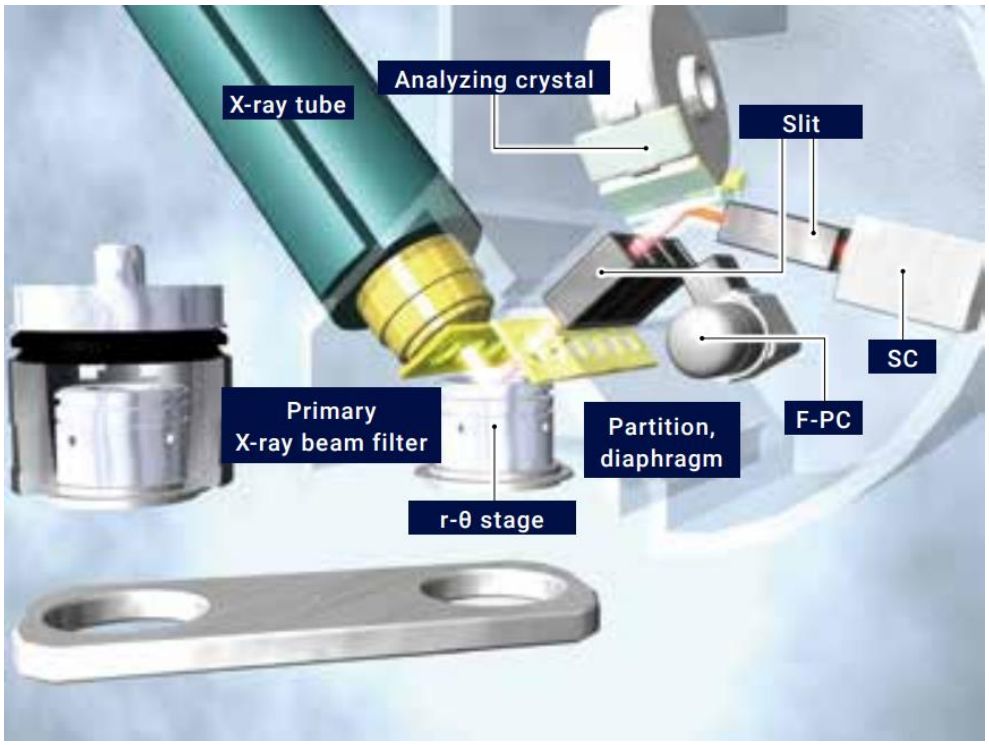

***Figure 32**. Schematic diagram of the optical geometry of the Rigaku Primus IV WD-XRF spectrometer (Rigaku Corporation, 2018). The major components of the wavelength-dispersive XRF system are shown, including the X-ray tube, and the primary X-ray beam filter used to shape the incident spectrum. The sample is positioned on the r-θ stage. Emitted fluorescence is collimated and directed through the partition/diaphragm toward the analyzing crystal, where spectral dispersion occurs according to Bragg's law. A soller slit defines the acceptance angle before detection. The characteristic radiation is measured by either the scintillation counter (SC) or the proportional counter (PC), depending on the energy range of interest.*

Operational versatility is further enhanced by the ZSX Guidance expert system, which automates the setup of quantitative analyses, and the EZ Scan function, which minimizes the need for user input. The integrated SQX fundamental parameters (FP) software corrects for matrix effects, spectral overlaps, and atmospheric variations, ensuring reliable results even in complex samples. The sample-handling system includes a standard autosampler accommodating up to 48 samples (expandable), and capable of accepting specimens up to approximately 51 mm in diameter and 30 mm in height.

For spectral conditioning, the ZSX Primus IV is equipped with a range of standard filters (Ni-400, Ni-40, Al-125, Al-25), selectable collimators (0.5–35 mm in diameter), slits, and curved analyzing crystals for enhanced sensitivity. The instrument's dual-chamber vacuum design, with optional helium purge, ensures optimal performance for light-element detection, while nitrogen can be used as an alternative purge gas when required. **Table 8** presents all the features of the ZSX Primus IV WD-XRF spectrometer.

Table 8. *Features of the ZSX Primus IV WD-XRF spectrometer (Rigaku Corporation, 2018).*

Feature Category	Specifications
Technique & Element Range	Tube-above WDXRF; quantitative analysis of elements from Be through U
Optics Configuration	Tube-above design; safeguards optics from sample debris; shorter maintenance and reduced downtime.
X-Ray Tube	3–4 kW Rh-anode end-window tube; ultra-thin 30 μm Be window for improved light-element detection
Detector & Count System	Dual detectors: scintillation counter (SC) for heavy elements, proportional counter (F-PC or optional sealed S-PC LE) for light elements; includes Digital Multi-Channel Analyzer (D-MCA) for high throughput
Mapping & Multi-Spot Analysis	Supports mapping and multi-spot analyses; high-resolution camera for precise sample location and homogeneous/inclusion detection
Software Suite	ZSX Guidance expert system automates quant set-up; EZ-scan requires minimal user input; SQX FP corrects for matrix, overlaps, and variation in atmosphere
Sample Handling	Standard autosampler accommodates up to 48 samples (expandable); uses r-θ goniometer stage; sample size up to ~Ø51 mm × 30 mm
Primary Filters & Optics	Standard filters include Ni400, Ni40, Al125, Al25; selectable collimators (up to Ø0.5 mm–35 mm), slits, and curved analyzing crystals for enhanced sensitivity
Environment & Gas Control	Dual-chamber vacuum design with optional helium purge for optimal light element performance; nitrogen can also be used

11.5 Particle Induced X-Ray Emission (PIXE) Setup

The PIXE ion beam experimental setup (**Figure 33**) has been designed so that it can be adapted to one of the existing experimental beamlines of the Tandem accelerator at the Institute of Nuclear and Particle Physics, NCSR "Demokritos". The beamline begins with a quadrupole magnet for beam focusing, followed by an electropneumatic gate valve for isolating the beamline from the experimental apparatus, as well as a switching valve connected to the analyzing magnet. The beam then travels through a 3.3 m-long beam pipe, which is coupled to a beam collimator and subsequently to the RBS/NRA experimental chamber.

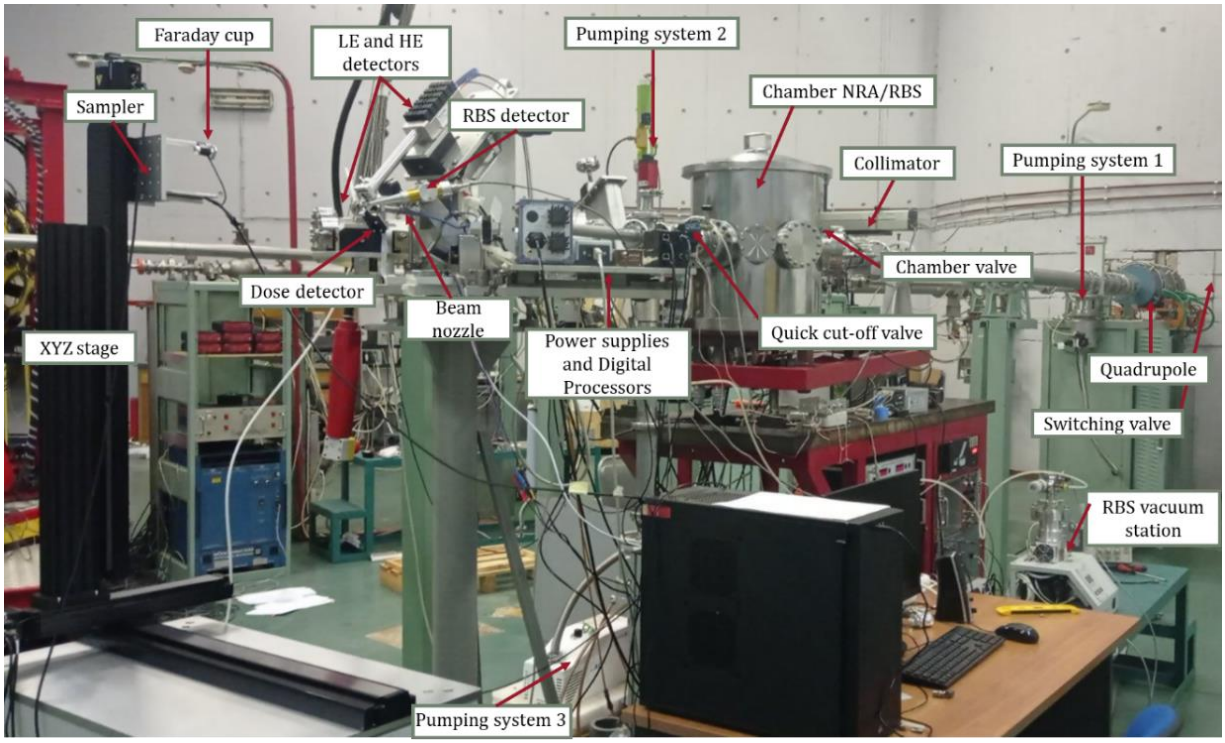

Figure 33. *Layout of the external ion beam (PIXE).*

From the RBS/NRA chamber and downwards, the beamline connects to a quick cut-off valve, followed by a 1 m-long tube ending in a specially designed detachable beam nozzle equipped with an internal collimator approximately 750 μm in diameter. Through precise alignment, the ion beam nozzle restricts the beam size to about 1 mm at the analysis point. At the nozzle exit, a thin silicon nitride (Si_3N_4) film (~100 nm, Silson, Northampton, UK) is mounted. This serves two main purposes: (1) to minimize energy loss of the ion beam, and (2) to maintain high-vacuum conditions in the setup.

The samples under investigation are placed in a dedicated sample holder (with interchangeable front plates depending on the sample type and size) mounted on a precision XYZ stage driven by stepper motors. The beam path within the irradiation line is maintained under high vacuum (~10^{-6} mbar), achieved using vacuum pumps installed at various points along the beamline.

The detector geometry has been optimized to allow the simultaneous use of two silicon drift detectors (SDDs) for PIXE measurements. One SDD operates in a helium atmosphere, while the other is equipped with a "hard" filter, enabling combined detection of major, minor, and trace elements across an energy range of 1–30 keV. Additionally, a surface barrier silicon detector (Si SBD) is positioned inside a custom-built vacuum chamber for RBS measurements. To accurately normalize the ion beam dose, the Si–Kα signal from the 100 nm Si_3N_4 exit window is monitored by a dedicated SDD (dose detector).

Finally, the control computer is equipped with all necessary software for operating the stepper motors, acquiring, processing, and analyzing spectra, as well as enabling optical monitoring of the analysis area via an integrated camera. The individual components of the experimental setup are described in detail in the following sections.

11.5.1 Vacuum System of the Experimental Setup

The pressure within the external ion beam setup and the rest of the beamline (specifically, the sections between the Switching Valve, the Chamber Valve, and the Quick Cut-off Valve) is regulated by three independent vacuum systems. Each system consists of a mechanical vacuum pump, used to evacuate the chamber from atmospheric pressure down to approximately 10^{-2} mbar, and a turbomolecular ("turbo") pump capable of achieving pressures as low as 10^{-6} mbar.

Both pumps are essential: the mechanical pump alone cannot reach the ultra-low pressures required, while the turbo pump can only operate at pressures below 10^{-2} mbar. Therefore, the evacuation process begins with the mechanical pump to reach a suitable pressure for turbo pump operation. Once the pressure has dropped to around 10^{-2} mbar, the mechanical pump is isolated from the experimental setup via a valve, and pumping continues with the turbo pump. During turbo pump operation, the mechanical pump serves as a backing pump, supporting the turbo pump's performance (**Figure 34**).

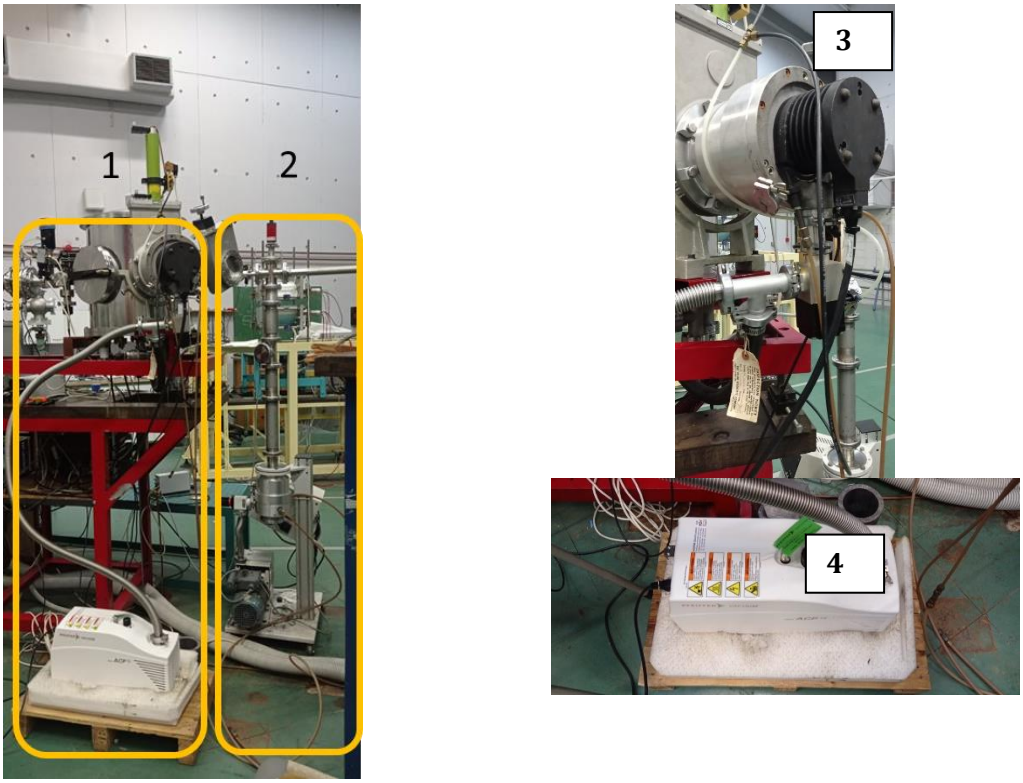

Figure 34. *The vacuum systems: [1] for the RBS/NRA chamber and [2] for the external ion beam. (3) Turbo pump of the RBS/NRA chamber. (4) Mechanical pump of the RBS/NRA chamber.*

The two vacuum systems—[1] for the RBS/NRA chamber and [2] for the external ion beam—can operate independently because they are separated by an electropneumatic quick cut-off valve (**Figure 35**). This valve offers two operating modes: "Manual" and "Auto". In *Manual* mode, the user can choose whether the valve remains open or closed. In *Auto* mode, the valve is automated and connected to a vacuum gauge so that, if the pressure rises above approximately 10^{-4} mbar, it closes automatically, isolating the two systems.

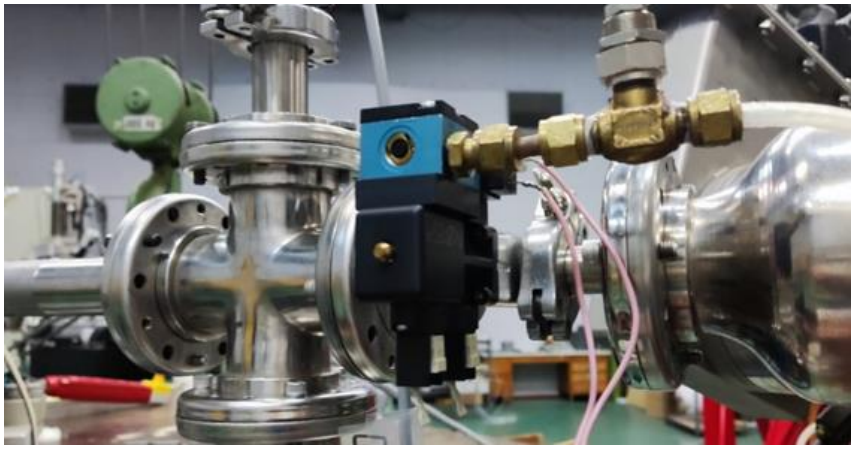

Figure 35. *The quick cut-off valve attached to the experimental setup*

11.5.2 Detection Systems

The experimental setup of the external ion beam includes four detectors: two dedicated to the Particle-Induced X-ray Emission (PIXE) application, one for Rutherford Backscattering Spectrometry (RBS), and one X-ray detector specifically for monitoring the beam dose.

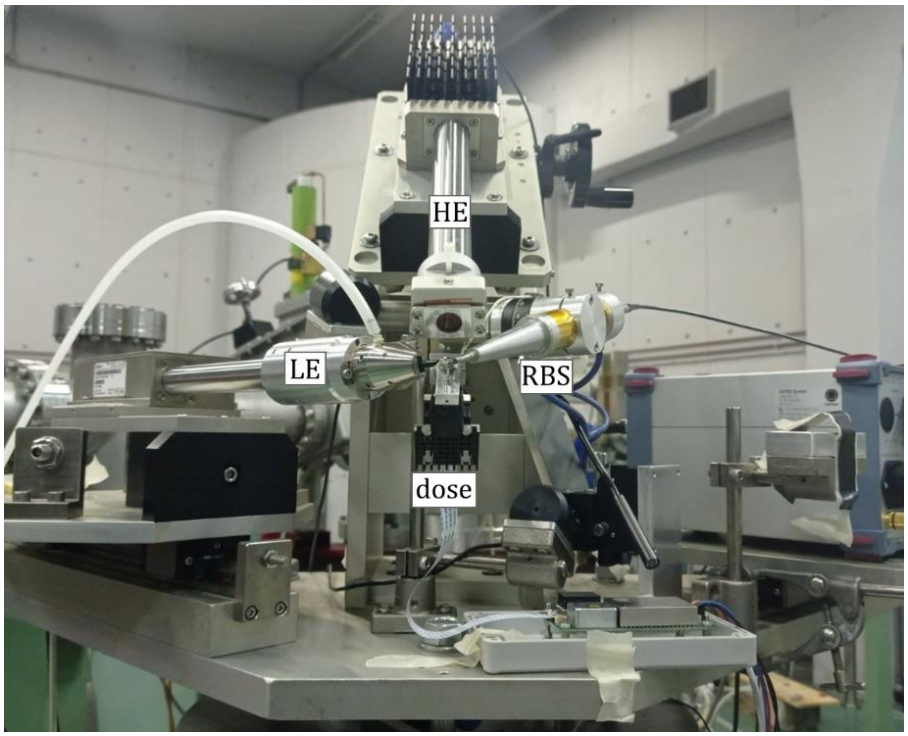

Figure 36. *The detection system of the external ion beam setup consists of four detectors. The "LE" and "HE" detectors are used for capturing the X-rays emitted from the sample, the "RBS" detector is dedicated to detecting backscattered charged particles, and the "dose" detector is employed for beam dose normalization.*

The PIXE measurements were carried out using two Silicon Drift Detectors (SDDs) simultaneously, enabling the detection of major, minor, and trace elements over an energy range of 1–30 keV.

The Low Energy (LE) Detector - AXAS-D

The first SDD, an AXAS-D H30 model from KETEK (30 mm² active area, 128 eV resolution at Mn-Kα, 8 μm Be window) (**Figure 37**) (KETEK GmbH, n.d), is optimized for detecting low-energy X-rays in the 1–8 keV range, which typically correspond to the major and minor elements in the sample. This detector—referred to as the *Low Energy (LE)* detector—is mounted on a movable cart that allows horizontal movement up to 150 mm toward or away from the focal point, enabling precise adjustment of the detector–sample distance. It is positioned at a 135° angle relative to the horizontal plane defined by the beam axis.

At the detector's front end, a detachable nosepiece houses rare-earth permanent magnets (*magnet deflector*), designed to block backscattered charged particles from reaching the detector crystal. The nosepiece also features a 3.5 mm aperture to limit the solid angle of detection. To minimize attenuation of low-energy X-rays in air, the nosepiece is connected to a plastic tube supplying a continuous helium flow (~1.5 L/min). Between the nosepiece and the Be window, a high-purity copper disk with a 2.5 mm central aperture allows the insertion of a filter.

The Be window of the detector is located approximately 46 mm from the sample, while the nosepiece is only about 3 mm away from it. The detector operates with its dedicated KETEK APS-L power supply and is connected to a DANTE Digital Pulse Processor (DPP) for spectrum acquisition and signal processing.

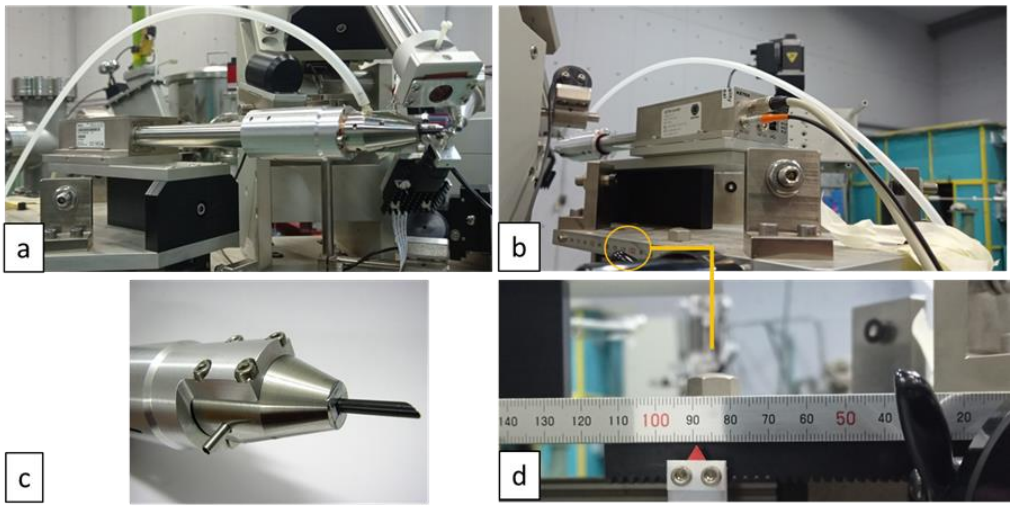

Figure 37. *The LE detector mounted on its base within the experimental setup: (a) the front view, (b) the rear view, (c) the detachable front assembly of the detector (magnet deflector), and (d) the position indicator of the LE detector base at the measurement position.*

The High Energy (HE) Detector - AXAS-M

The second Silicon Drift Detector (SDD), the AXAS-M H150 by KETEK (150 mm², 127.7 eV at Mn-Kα, 25 µm Be window)) (KETEK GmbH, n.d), is dedicated to detecting higher-energy X-rays (>3 keV). Known as the *High Energy – HE* detector, it is mounted on a wheeled base that allows for horizontal movement of up to 150 mm towards or away from the focal point **Figure 38**, bottom). The detector is positioned at a 135° angle relative to the vertical plane defined by the beam propagation axis.

In front of the Be window, a 261 µm Kapton filter is mounted within a specially designed filter holder with a diameter of 13.4 mm (**Figure 38**, top). This configuration effectively absorbs low-energy X-rays and backscattered particles. Between the holding plate and the aperture, a 1 mm-thick tin sheet with a 13.4 mm hole is inserted to ensure proper definition of the solid detection angle. The distance from the detector's Be window to the sample is approximately 46 mm.

The AXAS-M consists of two main components: the main detector unit (M1) and its power supply (M2). These are connected via a 16-pin Lemo cable (type FGG.2B.316). For signal processing, the AXAS-M1 is linked through a Lemo cable (type FFS.00.250) to its own dedicated digital pulse processor (DANTE DPP), which is separate from that of the LE detector.

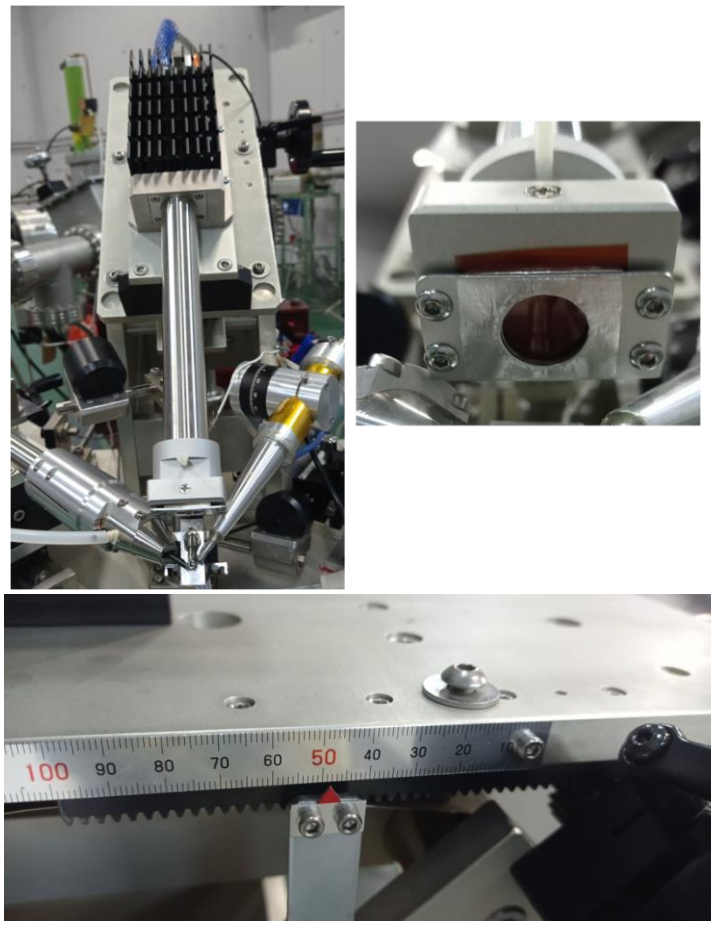

***Figure 38**.Top: The HE detector mounted on the base of the experimental setup (left) and the specialized filter holder equipped with a Kapton filter (right). Bottom: Distance scale indication on the HE detector base in its measurement position.*

11.5.3 Monitoring and Verification of Proper Sample Positioning

The visual monitoring of the analysis area is achieved using a high-definition webcam (Logitech HD Pro Webcam C920) in combination with two precisely aligned laser pointers. This setup enables easy and reproducible positioning of the sample relative to the ion beam and the detection systems (**Figure 39**). The alignment of the optical devices can be carried out with high accuracy when a visibly fluorescing target (e.g., ZnS) is irradiated at the designated reference analysis point (**Figure 40**).

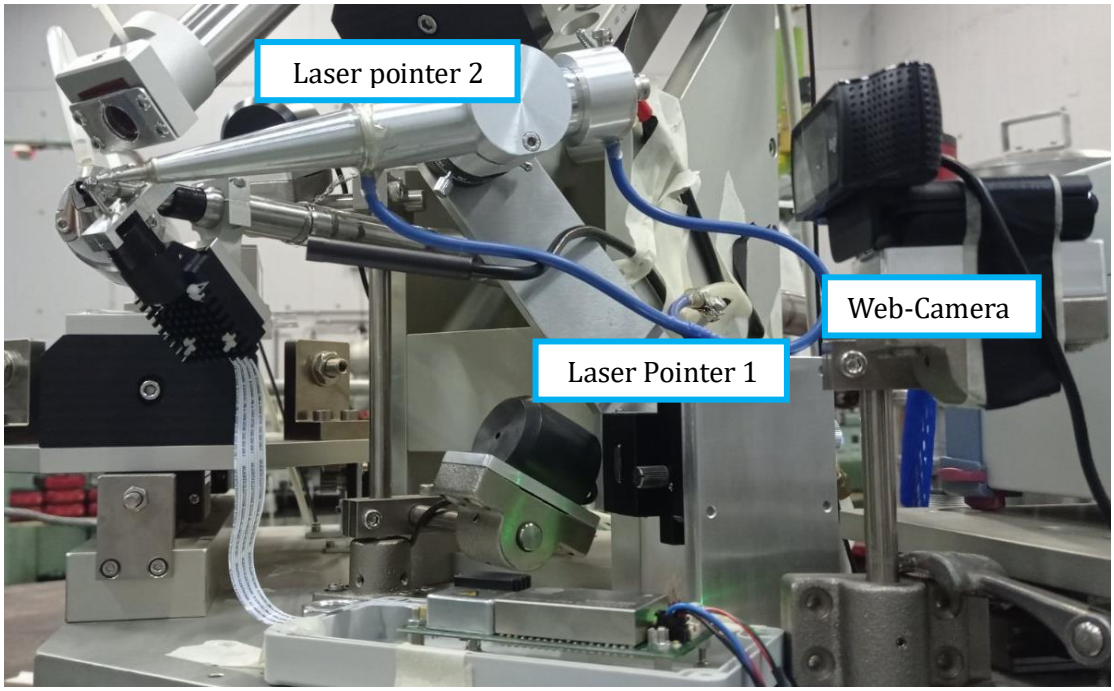

Figure 39. *The monitoring camera and laser alignment system of the experimental setup.*

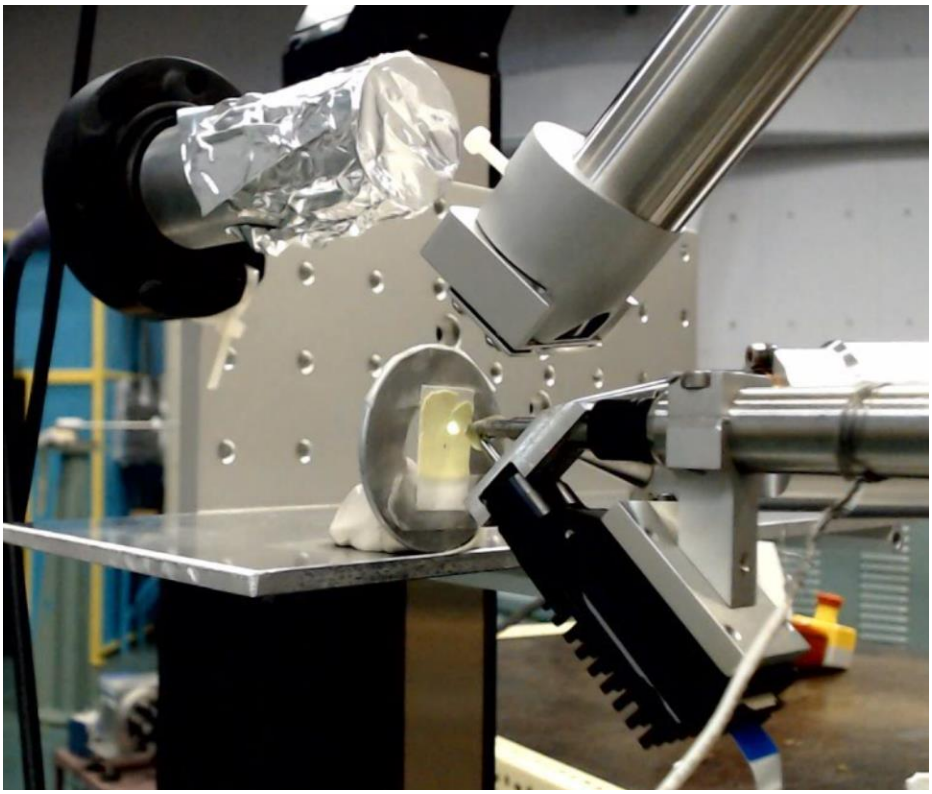

Figure 40. *Irradiation of a fluorescent ZnS sample at the intersection point of the two laser beams.*

11.5.4 The XYZ Scanning System

The XYZ scanning system enables the analysis of large-scale objects within the experimental line of the external ion beam. System control is supported through a dedicated user interface, enabling precise, reproducible positioning of the sample. The scanning system is mounted on a specially designed support table that ensures minimal tolerances in the accuracy and reproducibility of the XYZ movements, while also allowing flexible height adjustment (Zaber Technologies Inc., n.d.). This versatility enables the system to be positioned either at the ion beam reference plane (176 cm from the floor) or at alternative levels (e.g., 80 cm or 130 cm from the floor), facilitating the analysis of objects of various sizes.
The scanning system includes:

- **Three orthogonally arranged stages** with an extensive travel range (500 × 500 × 75 mm), powered by stepper motors with integrated motion controllers.
- **A variable-height support table**, portable for ease of positioning within the experimental setup.
- **A dedicated sample holder** for the automated analysis of atmospheric aerosol filters.
- **A custom support platform** for the analysis of paintings or other large artifacts placed on the XYZ stage.
- **User interface software** for complete control of motion parameters and automated scanning routines.

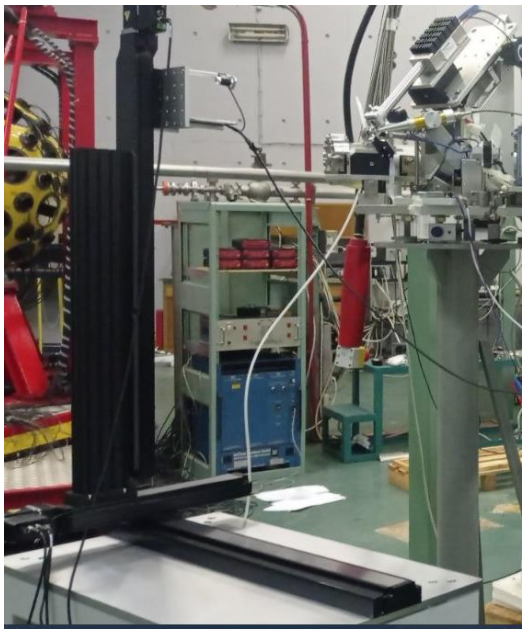

Figure 41. *The XYZ scanning system of the PIXE experimental setup.*

11.5.5 Placement of Atmospheric Aerosol Filters in a Sample Holder

A specially designed sample holder, with a maximum capacity of 15 filters, has been developed for the placement of atmospheric aerosol filters. Each filter is positioned onto its designated slot and secured using metal rings and screws to ensure that it remains taut and

stable throughout the measurement process (**Figure 43**). This design guarantees minimal warping or movement, which could otherwise affect the accuracy and reproducibility of the analysis. The sample holder's configuration allows for easy filter replacement and quick preparation for sequential measurements. Its robust construction ensures that the filters are held firmly in place even during extended experimental runs, while also facilitating precise alignment with the ion beam and detection systems. The detailed design of the aerosol filter holder is illustrated in **Figure 42**.

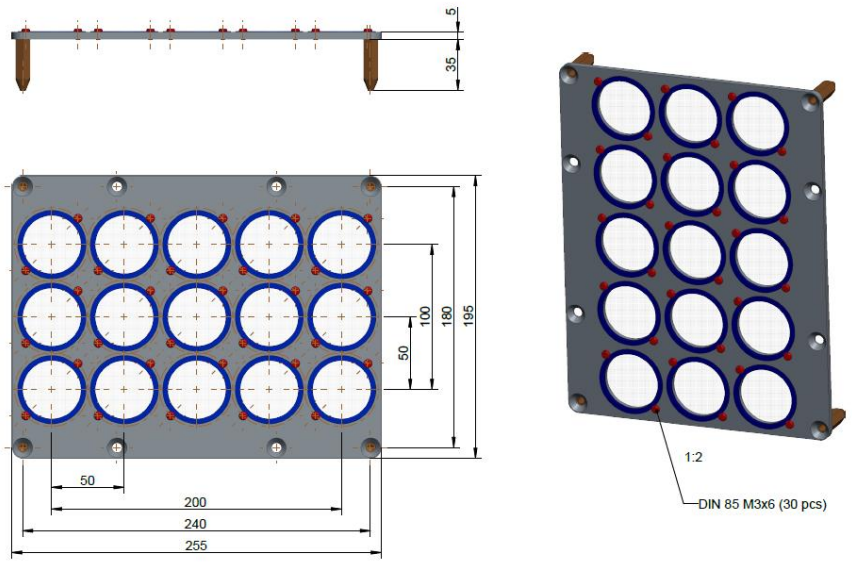

Figure 42. *Design of a special sample holder for atmospheric aerosol filter measurements. The sample holder is removable and can be easily detached using the four screws.*

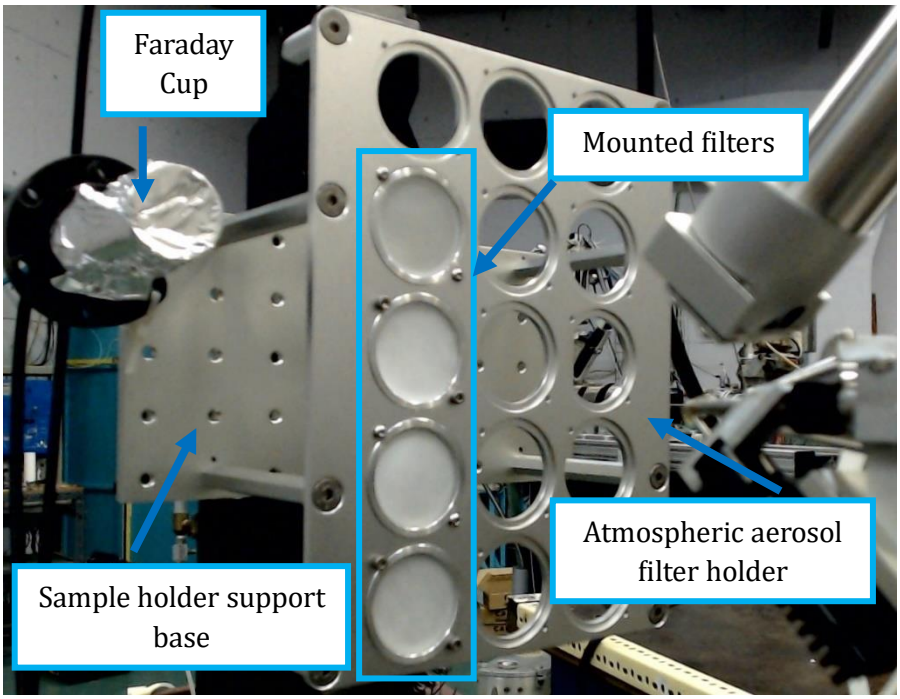

Figure 43. *The atmospheric aerosol filter holder attached to the special support base.*

11.5.6 PIXE Measurement Procedure – Beam Current Selection

Before the start of the experiment, the beam current used for irradiation is selected. Depending on the sample type and thickness, a specific current value is chosen to ensure non-destructive effects on the specimen. The table below presents the beam current values applied to a range of samples of interdisciplinary interest.

Sample type	Ion beam current (nA)
Aerosol filters	3-5
Glasses	15
Geological samples	15
Biological samples	15
Metals	5-10

11.5.7 Faraday Cup

Before each measurement cycle, the beam current is determined using a Faraday cup positioned at the sample location. The signal from the Faraday cup is sent to the Current Integrator on the console, which converts the current into digital counts. In this system, the selected current scale (e.g., 20 nA) corresponds to a full-scale output of 100 counts, meaning that each count represents 1/100 of the chosen scale. Using Equation (31), the collected charge Q can be obtained by converting the counter reading into nanocoulombs using:

$$Q(nC) = \frac{current\ scale\ (nA)}{100} \cdot Number\ of\ counts \tag{31}$$

11.6 Near real-time XRF (NRT-XRF) spectrometer

The Xact analyzer (SailBri Cooper, Inc., n.d.) is designed for the continuous determination of elemental concentrations in ambient PM. Its operation combines reel-to-reel filter tape collection with on-line X-ray fluorescence (XRF) analysis, enabling near real-time elemental monitoring (**Figure 44**).

The system functions in a two-stage semi-continuous cycle. During the sampling phase, ambient air is drawn through a Teflon filter tape at a constant volumetric flow of 16.7 L min^{-1} (equivalent to 1 m^3 h^{-1}) using a diaphragm vacuum pump. The air is sampled for a user-defined period (typically 15–240 min), generating a localized PM deposit on the tape (≈1.228 cm^2). Particle size fraction (PM_{10}, $PM_{2.5}$, or PM_1) is selected by attaching the appropriate inlet head and cyclone upstream of the sampling line (**Figure 45**) (Manousakas et al., 2025).

Figure 44. *The NRT-XRF spectrometer Xact 625i (SailBri Cooper, Inc., n.d.).*

To ensure stability and accuracy, the instrument is equipped with temperature and pressure sensors that regulate volumetric flow and ensure the correct aerodynamic size cut. A controlled heating system keeps the sample stream at 45% relative humidity, preventing condensation on the tape surface. The inlet geometry promotes uniform deposition, while approximately 90% of each PM spot is analyzed to reduce the effects of inhomogeneous loading.

During the analysis phase, the tape is automatically advanced by ~5 cm after each sampling interval, transferring the exposed PM spot into the XRF chamber. Here, non-

destructive elemental analysis is performed, while the following sample is simultaneously collected on a fresh tape section. This design enables the instrument to function nearly continuously, as sampling and analysis occur simultaneously with only brief interruptions. These interruptions last approximately 20 seconds for tape advancement and about 30 minutes each day for automated quality assurance (QA) routines.

For each interval, the instrument determines the elemental surface concentrations (ng/cm^2) and converts them into atmospheric concentrations (ng/m^3) by normalizing to the corresponding air volume. All data are automatically processed and stored by the onboard computer, providing time-resolved elemental concentration records.

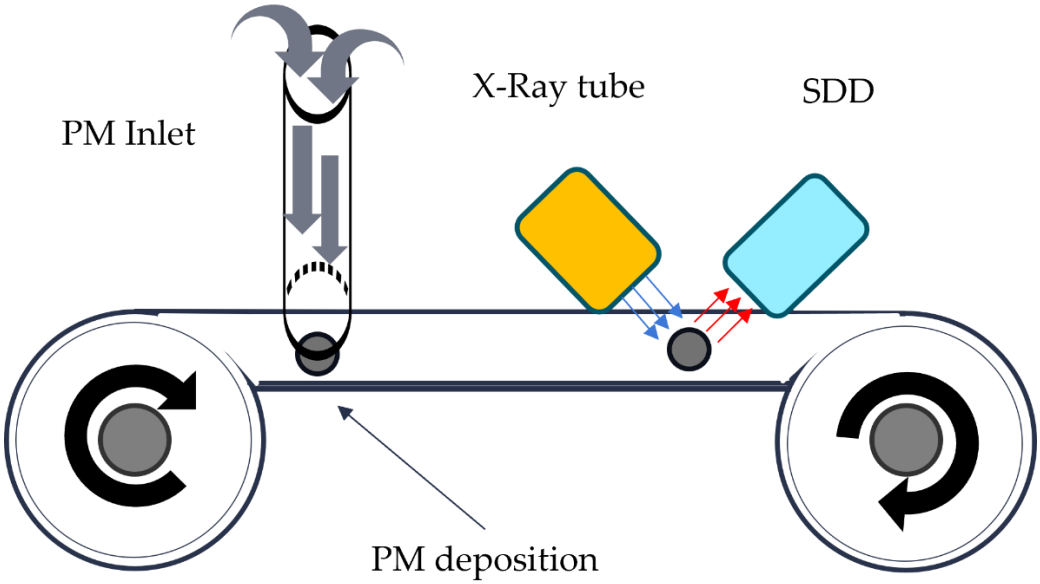

Figure 45. *Schematic representation of the operating principle of the Xact 625i.*

For continuous elemental monitoring, the NRT-XRF spectrometer employs a Teflon filter tape instead of quartz, offering several key benefits. The use of Teflon enables the detection of silicon and ensures more uniform deposition across the tape with better limits of detection. The filter tape rolls used in the instrument are typically 30–40 m in length and must be manually loaded into the system. The replacement interval depends on the chosen sampling resolution; for instance, with a 1-hour cycle, a 30 m tape provides approximately 25 days of operation (Rai, 2020). **Table 9** presents the main technical specifications and operating features of the Xact 625i for real-time elemental monitoring of ambient PM.

Table 9. *Technical specifications and operational parameters of the Xact 625i NRT-XRF spectrometer(SailBri Cooper, Inc., n.d.).*

Specification	Details
Measurement method	Based on U.S.A Environmental Protection Agency Method IO 3.3: Determination of Metals in Ambient PM Using XRF
Sampling and analysis times	Every 5, 15, 30, 60, 120, 180, or 240 minutes (user defined)
Calibration stability check frequency	Automatically with each sample analyzed
Estimated recalibration frequency	Annually, when manufacturer's operating recommendations are followed
Sample flow rate	16.7 L/min
Linearity	Correlation coefficient > 0.99
Size and weight	19″ W × 20″ D × 30″ H, 130 lbs; 19 inch (483 mm) rack-mountable or tabletop
Required operating environment	Laboratory environment with temperature controlled to 20 ± 5 °C (68 °F)
Power requirements	120 VAC, 50/60 Hz @ 4 amp OR 120 VAC, 50/60 Hz @ 20 amp (with small AC enclosure) 220 VAC, 50/60 Hz @ 2.1 amp OR 220 VAC, 50/60 Hz @ 11 amp (with small AC enclosure)
Outputs	RS-232 or TCP/IP, Modbus protocol CSV (comma-separated value) file Reporting of metals, operational parameters, alarms, and warnings
Options	Change or add elements Enclosures (NEMA 4, 4x, 12, or 12x) Inlets (PM_{10}, $PM_{2.5}$, PM_1, Low Vol TSP, and Industrial Hygiene inlets) Automatic PM_{10} and $PM_{2.5}$ inlet switcher

12. References for Section C

Asvestas, A., Chatzipanteliadis, D., Gerodimos, T., Mastrotheodoros, G. P., Tzima, A., & Anagnostopoulos, D. F. (2024). Real-Time Elemental Analysis Using a Handheld XRF Spectrometer in Scanning Mode in the Field of Cultural Heritage. *Sustainability (Switzerland)*, *16*(14), 6135. https://doi.org/10.3390/SU16146135/S1

Beckhoff, B., Kanngießer, B., Langhoff, N., Wedell, R., & Wolff, H. (Eds.). (2006). *Handbook of practical X-ray fluorescence analysis*. Springer. https://doi.org/10.1007/978-3-540-36722-2

Brouwer, P. (2010). *Theory of XRF: Getting acquainted with the principles*. https://www.chem.purdue.edu/xray/docs/Theory%20of%20XRF.pdf

Bruker. (2021). *S1 TITAN and TRACER 5i User Manual* (Doc. No. 030.0112.02.0). Bruker, Kennewick, WA, USA.

Bruker Nano GmbH. (2021). *M6 JETSTREAM: Mobile Micro-XRF Spectrometer, User Manual* (Version 3, Order no. DOC-M81-EXX021, September 24, 2021). Bruker Nano GmbH, Berlin, Germany

Chatoutsidou, S. E., Papagiannis, S., Anagnostopoulos, D. F., Eleftheriadis, K., Lazaridis, M., & Karydas, A. G. (2022). Application of a handheld X-ray fluorescence analyzer for the quantification of air particulate matter on Teflon filters. *Spectrochimica Acta Part B: Atomic Spectroscopy*, *196*, 106517. https://doi.org/10.1016/J.SAB.2022.106517

KETEK GmbH. (n.d.). *AXAS-M analytical X-ray acquisition system – modular user's manual* (Version 2.1). KETEK GmbH.

KETEK GmbH. (n.d.). *AXAS-A/D analytical X-ray acquisition system – analog/digital user's manual*. KETEK GmbH.

Manousakas, M., Diapouli, E., Papaefthymiou, H., Kantarelou, V., Zarkadas, C., Kalogridis, A.-C., Karydas, A.-G., & Eleftheriadis, K. (2018). XRF characterization and source apportionment of PM10 samples collected in a coastal city. *X-Ray Spectrometry*, *47*(3), 190–200. https://doi.org/10.1002/xrs.2817

Manousakas, M. I., Zografou, O., Canonaco, F., Diapouli, E., Papagiannis, S., Gini, M., Vasilatou, V., Tobler, A., Vratolis, S., Slowik, J. G., Daellenbach, K. R., Prevot, A. S. H., & Eleftheriadis, K. (2025). Implementation of real-time source apportionment approaches using the ACSM–Xact–Aethalometer (AXA) setup with SoFi RT: the Athens case study. *Atmospheric Measurement Techniques*, *18*(16), 3983–4002. https://doi.org/10.5194/AMT-18-3983-2025

PANalytical B.V. (2014). *Epsilon 5 User's Guide* (Edition 6). Almelo, The Netherlands: PANalytical B.V.

Papagiannis, S., Sabur, ·, Abdullaev, F., Vasilatou, V., Manousos, ·, Manousakas, I., Eleftheriadis, K., & Diapouli, E. (2024). Air quality challenges in Central Asian urban areas: a PM2.5 source apportionment analysis in Dushanbe, Tajikistan. *Environmental Science and Pollution Research 2024*, 1–14. https://doi.org/10.1007/S11356-024-33833-6

Rai, P. (2020). *Analysis of major and trace elements in ambient aerosols and their sources in European and Asian cities* (Doctoral dissertation, ETH Zurich). ETH Zurich Research Collection. https://doi.org/10.3929/ethz-b-000440336

Rigaku Corporation. (2018). *ZSX Primus Series Instruction Manual* (Document No. ME0B-10, April 26, 2018). Rigaku Corporation.

SailBri Cooper, Inc. (n.d.). *Xact® 625i ambient continuous multi-metals monitor*. Retrieved September 9, 2025, from https://sci-monitoring.com/product/xact-625i-ambient-continuous-multi-metals-monitor/

Zaber Technologies Inc. (n.d.). *Zaber Console manual*. Retrieved August 28, 2025, from https://www.zaber.com/w/Software/Zaber_Console

Section D. Results from Experimental Studies

13. Application of a Handheld X-Ray Fluorescence Analyzer for the Quantification of Air Particulate Matter on Teflon filters

Published as:

Chatoutsidou, S. E., **Papagiannis, S**., Anagnostopoulos, D. F., Eleftheriadis, K., Lazaridis, M., and Karydas, A. G.: Application of a handheld X-ray fluorescence analyzer for the quantification of air particulate matter on Teflon filters, Spectrochima. Acta Part B At. Spectrosc., 196, 106517, https://doi.org/10.1016/j.sab.2022.106517

15.1 Abstract

Elemental characterization of air particulate matter samples through the application of X-ray fluorescence (XRF) spectrometry is a widespread analytical technique. This work presents the optimization and calibration methodology of a handheld XRF spectrometer and its subsequent application in elemental quantification of unknown particulate matter samples. The optimization of the handheld spectrometer was conducted through investigation of the elemental sensitivities and Limits of Detection (LoD) at variable excitation conditions (voltage, filter). Accordingly, five optimum operating conditions were obtained each one targeted in different elemental range: 1) Z=11-12, 2) 12<Z<17, 3) 16<Z<23, 4) 22<Z<31 and 5) 30<Z<92. Subsequently, a number of reference (5 multi-element and 42 compound/single-element) materials were used to obtain calibration curves for 24 elements (Na, Mg, Al, Si, P, S, Cl, K, Ca, Ti, V, Cr, Mn, Fe, Co, Ni, Cu, Zn, As, Se, Br, Rb, Sr, Pb). Weighted least-square regression analysis was implemented to best fit the experimentally measured intensities with mass loadings resulting for the most of the elements to high correlations (Pearson r>0.78) and low statistical error. In addition, intercomparison of the elemental concentrations from 28 unknown particulate matter samples between the handheld and a benchtop XRF spectrometer showed good agreement.

13.2 Introduction

The quantitative elemental characterization of particulate matter (PM) provides useful information about the origin, primary sources and health hazard impact (Kelly & Fussell, 2012; Chen et al., 2021) through source apportionment analysis, as well as gives insights for air quality control (Viana et al., 2008; Karagulian et al., 2015). PM are suspended tiny particles that are released in the air by both natural and anthropogenic sources (Hinds, 1999). In principle, they are a complex mixture of chemical compounds characterized by variable concentrations of their components, with their properties being a direct consequence of the different production sources. The elemental quantification can be performed with ion beam analytical techniques such as the Particle Induced X-ray Emission (PIXE) (Johansson et al., 1995; Lucarelli et al., 2018) and Particle Induced Gamma-ray Emission (PIGE) which can probe efficiently some light elements (Na, Mg, Al) of interest (Lucarelli et al., 2018; Calzolai et al., 2014). Those techniques are complementary to each other, and only a few minutes of measuring are sufficient to detect over 20 elements (Na–Pb), including both anthropogenic

and crustal elements (Lucarelli et al., 2018). However, there are also other techniques which are widely used nowadays, such as the inductively coupled plasma mass spectrometry (ICP-MS) (Su et al., 2013), the graphite furnace atomic absorption (GF-AAS) (Nimmo & Fones, 1994; Low & Hsu, 1990), and the energy dispersive X-ray fluorescence (ED-XRF) (Manousakas et al., 2018; Gunchin et al., 2019; Shaltout et al., 2018; Shaltout et al., 2020; Yatkin et al., 2012). ICP-MS and GF-AAS are methods that require a great deal of work with regard to sample preparation, which is both expensive and time consuming. For that reason, a lot of researchers explore different analytical techniques such as X-ray fluorescence (XRF), which has the advantage of not requiring an accelerator facility or any sample pre-treatment and it is much more affordable. By now, several works have evaluated the performance of the aforementioned techniques (Ogrizek et al., 2022), identified limitations and conducted inter-comparison tests (Gini et al., 2021; Chiari et al., 2018; Hyslop et al., 2019). For example, the comparison between PIXE and ED-XRF techniques by Chiari et al. (2018) demonstrated generally good agreement for a wide range of elemental concentrations collected both on Teflon and quartz fibre filters.

XRF analysis is an established spectroscopic technique for non-destructive qualitative, screening and quantitative elemental characterization of materials. It is interesting, however, that the analytical performance and features of XRF spectrometers is continuously improved following relevant developments in X-ray instrumentation. In particular, over the past two decades handheld XRF (HHXRF) spectrometers have started to gain ground as a routine and research analytical tool in quite different scientific disciplines (West et al., 2008), including for example cultural heritage (Shugar & Mass, 2012; Bezur et al., 2020) or geology (Young et al., 2016). The remarkable features of HHXRF analyzers include the minimum overall size and weight, versatility in the field or even at laboratory use, short acquisition times of few minutes, user-friendly on-board software allowing targeted quantification of different kind of (mostly) bulk samples, automatic change of exciting beam filters/apertures, broad analytical range (Na–U) with typical analytical sensitivities down to μg/g for the optimum analyzed elements. The portability and versatility of HHXRF analyzers have obviously found direct applicability in different environmental applications such as the in-situ analysis of toxic heavy metals/metalloids in soils (Brent et al., 2017; Kazimoto et al., 2018), sediments (Kazimoto et al., 2018), paints (Turner et al., 2016; Ytreberg et al., 2017), in marine plastic litter (Turner, 2016), in food ingredients/dietary supplements (Palmer et al., 2009) or in the monitoring of waste electrical and electronic equipment (WEEE) (Aldrian et al., 2015). The use of HHXRF analyzers for the elemental analysis of PM is very limited. Abiye et al. (2021) have calculated the limits of detection and obtained calibration curves for elements ranging from K (Z = 19) to Pb (Z = 82). However, the study could not gain insight for lower Z elements Na (Z = 11) to Cl (Z = 17), missing important analytes that play a significant role on source apportionment analysis.

From an analytical perspective, the most important challenge to overcome in tube-excited XRF analysis of PM samples is the lack of monochromatic excitation, which poses a certain difficulty to cope with increased spectral background. ED-XRF spectrometers utilizing either monochromatic or polarized beams attained by means of triaxial polarization geometry with

a set of secondary fluorescence or Barkla scattering targets have demonstrated excellent analytical sensitivity, precision, and accuracy at the low ng/cm² range of analytes (Amaro et al., 2017; Heckel et al., 1992; Van Grieken & Markowicz, 2002). On the other hand, handheld or even modern benchtop/mobile XRF analyzers equipped with latest technology silicon drift detectors, optimized signal processors and miniature X-ray tubes have the benefit of producing high fluorescence intensities. Thus, allowing to intervene in the excitation path with different combination and variety of filter materials, to minimize or even eliminate the intensity of certain exciting beam spectral regions and utilize the rest of the spectrum for selective excitation purposes. The composite spectrum produced by the miniature transmission X-ray tubes, including the continuum (bremsstrahlung) and discrete part (anode K or/and L anode characteristic lines) with relevant contributions tuned by the applied operating high voltage, offers certain but nevertheless remarkable flexibility to convert the complexity to analytical opportunities and succeed to optimize both analytical sensitivity and precision. Towards this challenge, specific evaluation for each particular analytical problem is required.

The objective of the present work was to demonstrate that commercial HHXRF analyzers are suitable for elemental quantification of unknown particulate matter samples. Primarily, the goal was to determine the optimum operating conditions (e.g. sensitivity, limit of detection) for different groups of elements. Secondarily, calibration curves for 24 elements (Na, Mg, Al, Si, P, S, Cl, K, Ca, Ti, V, Cr, Mn, Fe, Co, Ni, Cu, Zn, As, Se, Br, Rb, Sr, Pb) were obtained by applying a least-squares model. To achieve the aforementioned goals several compounds, single- and multi-element reference materials were used whereby elemental intensities, sensitivities and limits of detection were examined. At the end, a well-established benchtop energy dispersive XRF spectrometer was employed for intercomparison between the two analyzers.

13.3 Materials and methods

13.3.1 The handheld ED-XRF spectrometer

The present work employed a handheld energy dispersive X-ray fluorescence (ED-XRF) spectrometer equipped with a 50kV-4W rhodium (Rh) anode to generate X-rays (Tracer 5i, Bruker). The characteristic X-ray radiation emitted by the sample is detected by a 20 mm² silicon drift detector (SDD) with a measured energy resolution of approximately 140 eV FWHM at Mn-Kα (5.89 keV). The analyzer is able to identify elements from sodium (Na) to uranium (U). The voltage and current cover a range pre-appointed by the instrument at 6 - 50 kV and 4.5 - 195 μA respectively with certain power consumption limitations, which lead to

the following high voltage (kV)/maximum current (μA) values: 15/155, 20/142, 25/135, 30/130, 35/113, 40/100, and 50/35.

The analyzer offers a choice of two collimators (3 mm or 8 mm) along with a selection among 4 automatic filters (**Table 10**). Herein, a collimator of 8 mm was selected to ensure analysis of the maximum possible area of the samples in order to minimize the influence of heterogeneous deposition on the filter media. Typically, measurements are conducted in air, however, increased sensitivity for light elements can be achieved through the implementation of vacuum (or helium atmosphere).

Measurement set-up included the use of a desktop stand whereby the instrument was placed in a fixed position with the examination window looking upwards. Thus, the measurement geometry was always reproducible. In addition, the creation of vacuum was achieved with an external vacuum pump connected to the instrument through a tube. Therefore, vacuum was created inside the chamber of the instrument with the geometry of the measurement remaining exactly the same as the one without the vacuum.

Table 10. *Automatic filters installed in the HHXRF analyzer and abbreviations used in this work (the numbers in the abbreviations represent mils=1/1000 inch). The quoted thicknesses (μm or mils) represent the nominal ones as given by the manufacturer.*

Filters	Abbreviation
Al 38 μm	Al1.5
Ti 25 μm/Al 300 μm	Ti1Al12
Cu 75 μm/Ti 25 μm/Al 200 μm	Cu3Ti1Al8
Cu 100 μm/Ti 25 μm/Al 300 μm	Cu4Ti1Al12

13.3.2 The benchtop ED-XRF spectrometer

The benchtop analyzer is a high-resolution energy dispersive X-ray fluorescence 3-D optics spectrometer (Epsilon 5, PANalytical). The spectrometer consists of a side-window X-ray tube with a W/Sc anode (Manousakas et al., 2018; Gunchin et al., 2019) with a beam spot size of 18 mm. The characteristic X-ray radiation emitted by the sample is detected by a Ge detector with a measured energy resolution of approximately 150 eV FWHM at Mn-Kα (5.89 keV).

The spectrometer provides a selection of 5 secondary targets (CaF_2, Ge, KBr, Mo and Al_2O_3) that can polarize the X-ray beam with a very low background (the scattered tube radiation cannot reach the detector). The selected measuring conditions for optimal analysis of particulate matter samples are given in **Table 11**. All measurements were conducted under vacuum and the total acquisition time was approximately 40 minutes per sample.

Table 11. *Operating conditions for elemental analysis of atmospheric PM samples with benchtop XRF spectrometer (PANalytical Epsilon 5).*

	Secondary Target	Detected elements	Voltage (kV)	Current (mA)
1	CaF_2	Na-K	40	15
2	Ge	Ca-Zn	75	8
3	KBr	Ga-As	75	8
4	Mo	Se–Sr and Pt-Pb	75	8
5	Al_2O_3	Ag-Ce	75	8

13.3.3 Reference materials and PM samples

Several reference materials (RMs) were used for the calibration methodology: one Standard Reference Material (NIST 2783), 4 multi-element reference materials (UCD-47-ME-H, UCD-47-MTL-ME-155, UCD-47-ME-L, AXO) and another 42 compounds/single-element reference materials (Yatkin et al., 2016; Yatkin et al., 2016; Yatkin et al., 2018; Yatkin et al., 2020; Karydas et al., 2018). A detailed list of the used reference materials with their nominal concentrations is provided in **Table 12**, **Table 13** and **Table 14**. The use of multi-element and single/compound RMs is crucial as they were explicitly developed to mimic deposited material on filter media similar to those collected by gravimetric sampling of particulate matter. For the generation of these RMs, several multi-element solutions were used containing elements usually found in PM samples with variable mass loadings (Yatkin et al., 2018). Similarly, single-compound RMs were generated on Polytetrafluoroethylene (PTFE) filters using high purity salts or nanoparticles, whereas mass loadings were determined with gravimetric measurements and verified by ED-XRF, ICP-MS and ion chromatography IC (Yatkin et al., 2020). These RMs are intended to be used for calibration or quality checks for XRF analysis of PM samples.

In addition, 28 particulate matter samples were used as unknowns to be determined by both spectrometers (handheld and benchtop). Sampling was conducted through the use of a low volume sampler (Leckel, LVS6-RV) that collected the deposited material on Teflon filters of 47 mm (Zefluor PTFE, Pall) and 2 μm pore size. The sampling time was 24 h for all measurements, with 19 of them correspond to PM10 and the remaining 9 to PM2.5. The measurements were conducted in different environments so variable PM samples were collected. Specifically, all PM2.5 measurements were performed outdoors in a suburban site with medium traffic (Chatoutsidou et al., 2019), whilst PM10 measurements were performed both indoors and outdoors in the same location.

Table 12. *Nominal concentrations of UC Davis multi-element reference materials (PTFE membrane filter (Teflon, 47 mm, 2.0 μm pore size).*

	UCD-47-MTL-ME-155		UCD-47-ME-H		UCD-47-ME-L	
	Loading (μg/cm²)	Uncertainty (%)	Loading (μg/cm²)	Uncertainty (%)	Loading (μg/cm²)	Uncertainty (%)
Na	0.874	9.2	1.57	10		
Mg	0.233	18.8	0.98	10		
Al	0.281	3.8	0.97	10	0.31	10
Si	0.413	1.8				
S	1.533	0.8	3.19	10	1.07	10
Cl	0.039	4.8				
K	0.269	0.7	1.07	10	0.37	10
Ca	0.219	1.8	1.1	10	0.37	10
Ti	0.021	8.1				
V	0.040	2.8	0.17	10	0.09	10
Cr	0.016	4.9	0.21	10	0.07	10
Mn	0.022	7.7	0.2	10	0.07	10
Fe	0.222	1.8	1.18	10	0.4	10
Co	0.029	5.5	0.19	10	0.06	10
Ni	0.012	6.4	0.17	10	0.06	10
Cu	0.038	2.9	0.32	10	0.07	10
Zn	0.016	5.7	0.48	10	0.11	10
As	0.095	3.4	0.5	10	0.1	10
Se	0.016	6.2	0.18	10	0.07	10
Br	0.014	32.9				
Rb	0.027	7				
Sr	0.030	5.4	0.2	10	0.2	10
Pb	0.041	8.6	0.5	10	0.16	10

Table 13. *Nominal concentrations of multi-element reference materials NIST2783 and AXO.*

	NIST2783		AXO	
	Loading (μg/cm²)	Uncertainty (%)	Loading (μg/cm²)	Uncertainty (%)
Mg	0.865	6	10.79	4
Al	2.33	2.3		
Si	5.88	2.7		
S	0.105	24.9		
K	0.53	9.9		
Ca	1.33	12.8		
Ti	0.15	16	8.4	4
V	0.00487	12.4		
Cr	0.0136	18.5	9.45	4
Mn	0.0321	3.8		
Fe	2.66	6		
Co	0.000773	15.6		
Ni	0.00683	17.6	9.04	4
Cu	0.0406	10.4	9.7	4
Zn	0.18	7.3		
As	0.00118	10.2		
Pb	0.0318	17		

Table 14. *Nominal concentrations of compounds and single-element certified reference materials.*

Micromatter			UC Davis		
	Loading (μg/cm²)	Uncertainty (%)		Loading (μg/cm²)	Uncertainty (%)
NaCl	17.7		NaCl	0.7	10
MgF2	3.28	5	NaCl	3	5
SiO	9.9	5	NaCl	5.9	5
GaP	11.57	5	AlCeO3	0.7	10
KCl	13.93	5	AlCeO3	2.4	5
CaF2	21.95	5	AlCeO3	5.5	5
V	45.8	5	SiO2	0.8	10
Cr	45.6	5	SiO2	3.2	5
Fe	39.9	5	SiO2	7.6	5
Co	39.4	5	S	0.8	10
Ni	38.4	5	S	3	5
CuSx	31.69	5	S	5.5	5
CuSx	40.7	5	KCl	0.5	10
ZnTe	31.1	5	KCl	2.2	5
CdSe	13.2	5	KCl	6.1	5
Se	50	5	Pb(CH3COO)2	0.5	10
CsBr	13.5	5	Pb(CH3COO)2	0.9	5
RbI	17.7	5	Pb(CH3COO)2	1.9	5
SrF2	26.6	5			
Pb	52.2	5			

Custom		
	Loading (μg/cm²)	Uncertainty (%)
KCl	43	5
Mn	408	5
GaP	6.5	5
GaP	10.3	5

15.3.4 Sensitivity and Limits of Detection

The elemental sensitivity S_a is usually employed to express the efficiency of a XRF spectrometer to excite different elements through the periodic table. It is defined as the analyte number of characteristic X-rays normalized per unit of live time (t_l, s), tube current ($i_t, \mu A$) and element areal density ($C_a, g/cm^2$). It can be deduced in a straightforward way for a sample of infinitely small thickness, namely when the condition $\mu_a \rho t/sin\theta << 1$ (as first approximation) is fulfilled for the characteristic X-rays of all analytes, where μ_a is the mass

attenuation coefficient of the main characteristic X-ray of analyte a (cm^2/g), θ is the outgoing angle (i.e. the angle formed between the sample surface and detector axis), ρ is the sample density (g/cm^3) and t is the sample thickness (cm) (Klockenkämper & von Bohlen, 2015):

$$S_a\left(\frac{cps/\mu A}{g/cm^2}\right) = \frac{I_a(cps/\mu A)}{C_a(g/cm^2)} \tag{32}$$

where

$$I_a = \frac{N_{ref,a} - N_{bl,a}}{t_l \cdot i_t} \tag{33}$$

with statistical uncertainty given by:

$$\delta I_a = \frac{\sqrt{{\sigma_{ref,a}}^2 + {\sigma_{bl,a}}^2}}{t_l \cdot i_t} \tag{34}$$

where $N_{ref,a}$, $N_{bl,a}$ represent the peak areas of element a principle characteristic X-rays (Kα or Lα) in the case of standard reference and blank sample (similar substrate but with no deposited material) respectively, measured under live time t_l; $\sigma_{ref,a}$, $\sigma_{bl,a}$ are the standard deviations of the peak area for the reference material and blank sample, respectively.

The limit of detection (LoD, µg/cm²) for an element a can be determined as follows (Álvarez et al., 2007):

$$(LoD)_a \cong \frac{3\sqrt{B_{ref,a}+N_{bl,a}}}{N_{ref,a} - N_{bl,a}} \cdot C_\alpha \tag{35}$$

or

$$(LoD)_a \cong \frac{3\sqrt{B_{ref,a}+N_{bl,a}}}{S_a \cdot t_l \cdot i_t} = \frac{3\sqrt{I^B_{ref,a} + I_{bl,a}}}{S_\alpha \cdot i_t} \cdot \frac{1}{\sqrt{t_l}} \tag{36}$$

where $B_{ref,a}$ represents the background counts below the peak area of element a for the standard reference and blank sample, respectively, and $I^B_{ref,a}$ denotes the background intensity.

At the end, analysis of the samples was conducted for 24 elements (Na, Mg, Al, Si, P, S, Cl, K, Ca, Ti, V, Cr, Mn, Fe, Co, Ni, Cu, Zn, As, Se, Br, Rb, Sr, Pb), where peak areas were evaluated by the on-board software provided by the manufacturer of the handheld analyzer (ARTAX), and by a freely available software (PyMca) (Solé et al., 2007).

13.4 Results and discussion

13.4.1 Handheld XRF optimization

The first step of optimizing experimental conditions was the selection of an appropriate multi-element RM, imitating as much as possible the real PM samples including the maximum possible number of certified analytes with typical PM elemental areal densities). For light element analysis, vacuum was tested to investigate the relative improvement in the respective elemental sensitivities (**Figure 46**).

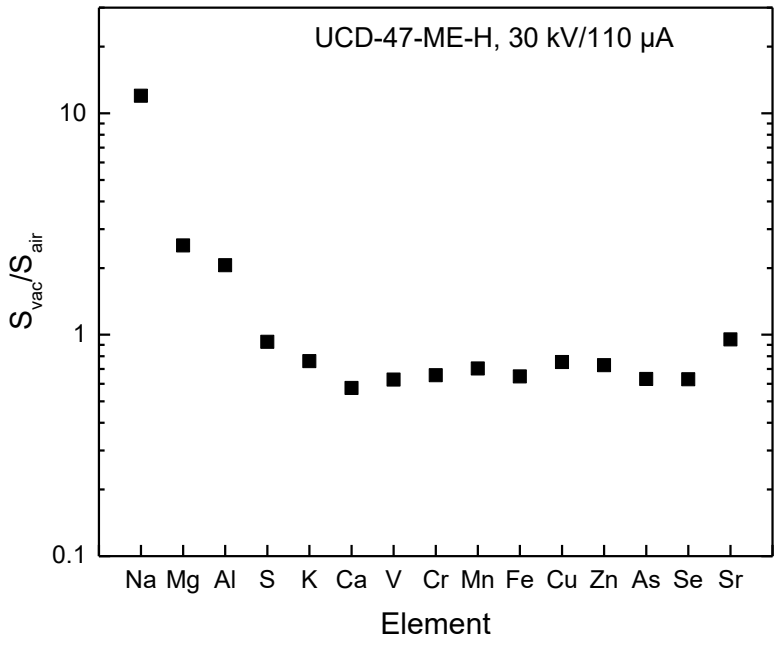

Figure 46. *Ratio of the sensitivities obtained for vacuum and air atmosphere at the same operating conditions (30 kV/110 µA, no-filter use and 180s acquisition time) for reference material UCD-47-ME-H.*

It was evidenced that vacuum enhanced the fluorescence emission of elements with atomic number Z< 20 (Ca). On the contrary, a relative constant ratio but <1 was obtained for

elements with Z>19. It should be noted here that for producing the vacuum environment inside the HH analyzer, an Ultralene (TM) gridded window was applied, different than the pure Ultralene used under the air atmosphere. Therefore, there was significant gain due to vacuum in the fluorescence intensity of the soft characteristic X-rays. However, the gridded pattern incorporated less X-ray transparent area and larger thickness of the polymer window, thus enhanced the attenuation of tender characteristic X-rays. Another and perhaps more important factor that should be considered in evaluating the appropriateness of a window material, is related with its trace elements contaminants which might "pollute" the acquired spectra with enhanced blank contribution. In fact, **Figure 47** presents typical instrument blank spectra (no sample) acquired under vacuum and air environments (30kV/110μA, 180s). It is evident that the window used for vacuum measurement generated in the whole energy region higher spectral background because of its larger thickness. With respect to contaminated peaks, below the Rh-L lines, higher blank intensities were observed for Al, Si and S and particularly for P. For this reason, vacuum was selected only for Na and Mg analysis, whereas for Al, Si, P and S analysis air atmosphere was preferred.

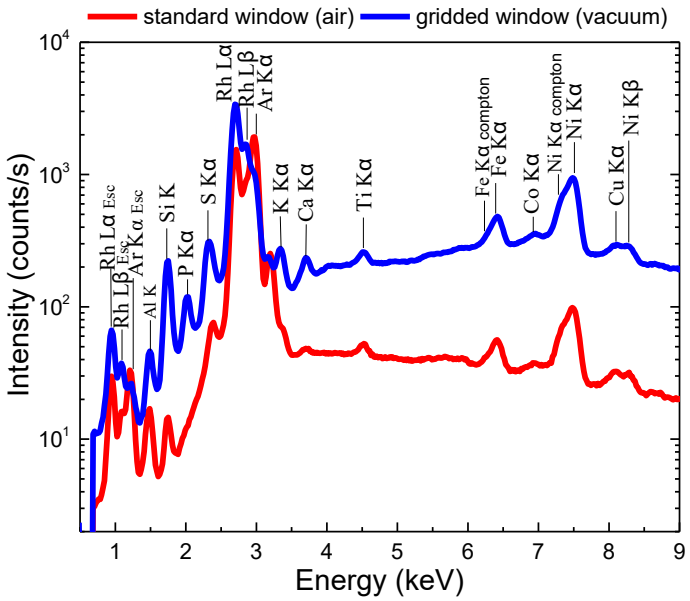

Figure 47. Comparison of instrument blanks between air and vacuum environment. Operating condition was 30 kV/110 μA and 180s acquisition time.

Few more observations need to be further commented: under vacuum, the enhanced detection of Rh-Lα/Rh-Lβ X-rays resulted to higher intensities for their respective escape peaks that interfered with Na-K (1.04keV) and Mg-K (1.25keV) respectively. However, the

gain from the relative intensity enhancement by the Rh-L component of the tube excitation spectrum under vacuum generated better detection capabilities for Na and Mg. Further on, under vacuum, the elimination of Ar-Kα from the spectrum improved significantly the analysis of Mg-K as it reduced the interfering contribution by its Kα escape peak. Above 4 keV, significant blank peak contributions were mostly produced by the Ni-K and Fe-K peaks. Both peaks are accompanied by low energy tails which can be explained due to the presence of their respective Compton scattered peaks. Thus, it can be further suggested that these peaks are produced within the tube excitation path. Small contributions by Ti and Ta peaks are also observable. The handheld spectrometer background contribution in the measured spectra is a particular feature which introduced difficulties in spectra analysis of ultra-thin samples. In contrast, spectrum background and blank contributions of the benchtop ED-XRF spectrometer were significantly lower (**Figure 48**).

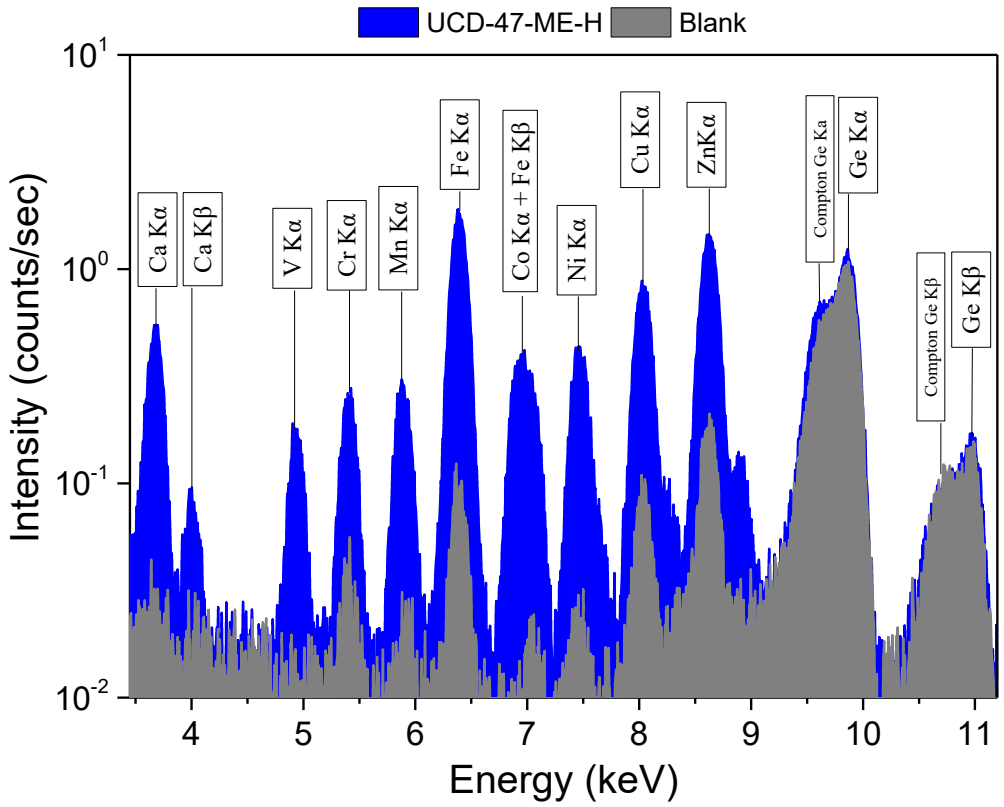

Figure 48. *XRF spectrum obtained by the benchtop spectrometer (Epsilon 5) for reference material UCD-47-ME-H using the Ge secondary target (75 kV, 8 mA, 400 s). The blue colored area represents the reference material and the grey the blank Teflon filter.*

Concerning the exciting beam filters, we must recall some basic properties of X-ray tube excitation. The exciting spectrum includes apart from the continuum (bremsstrahlung) component, the anode discrete K and L-lines. Actually, the anode Rh L-lines are located within

the 2.7-3.0 keV region, thus, producing selective and enhanced excitation of elements with absorption edges at lower energies, i.e. for Na, Mg, Al, Si, P, S and partly for Cl. **Figure 49** presents spectra of the reference material NIST2783 measured in vacuum without filter, in air without filter, and in air with the "lighter" filter Al1.5 at operating conditions 30kV/110μA and 180s.

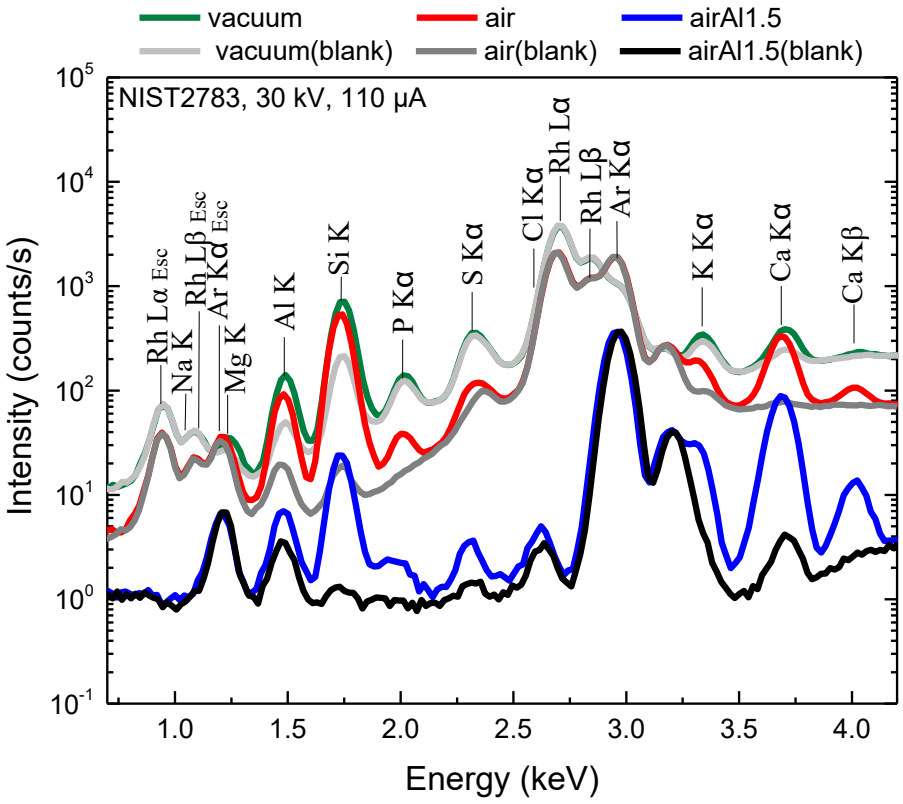

Figure 49. *XRF spectra obtained by the handheld spectrometer for reference material NIST2783 and its blank filter under varying environments (vacuum (no-filter), air (no-filter) and air (Al1.5)). Operating conditions were at 30 kV/110 μA and 180 s in all spectra.*

It can be observed that the attenuation by the filter of Rh-L lines consequently results to much lower peak intensities for light elements (Na, Mg, Al, Si, P and S). Thus, for this group of elements no filter was selected, whereas, an optimum choice for the tube high voltage value still needs to be investigated. **Figure 50** presents a systematic comparison of the obtained LoDs for selected tube high voltages (15kV – 50kV), under vacuum (Na, Mg) or air atmosphere (Al, Si, S), setting the tube current approximately at 90% of its maximum value with no filter in the excitation path. It can be observed that the lower voltage value (15 kV) exhibited the optimum LoDs for Na and Mg. On the other hand, for the rest of the elements (Al - S) minimal

differences were observed for the rest of the tube voltage values (except for 50kV), with some trend for minimum LoDs for tube voltages 25kV and 30kV, respectively.

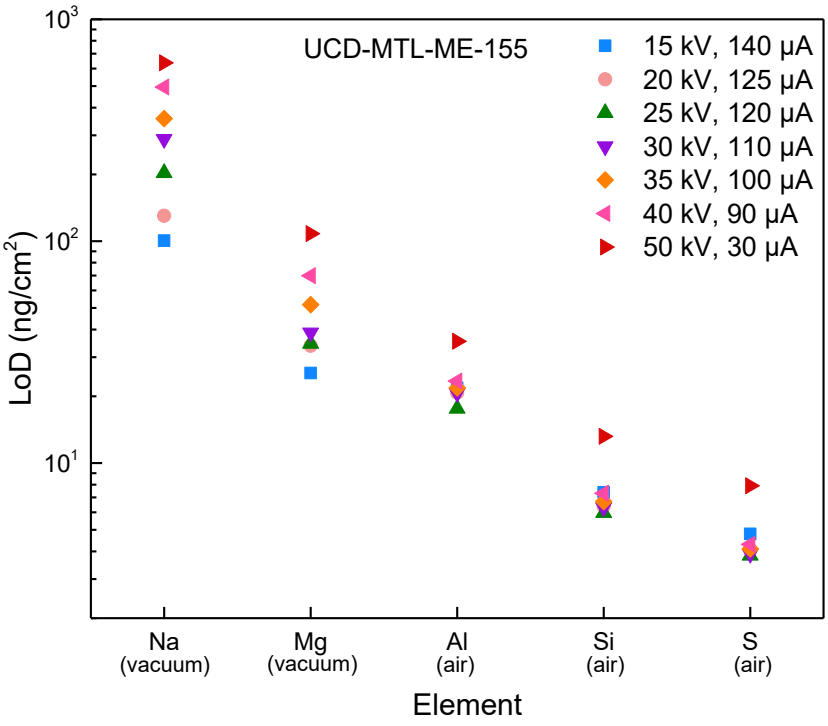

Figure 50. *Comparison of LoDs (ng/cm2) using different operating conditions by varying the voltage (15 - 50 kV) for elements with Z=11-16. All measurements were conducted with reference material UCD-47-MTL-ME-155, without any filter under vacuum (Na, Mg) or air atmosphere (Al, Si, S) within 180 s acquisition time. The tube current was varied according to voltage selection presented in section 2.1 approximately at 90% of its maximum value.*

A useful and effective test to pre-evaluate the influence of different operational voltages in the excitation of different elements is to compare their respective elemental sensitivities. **Figure 51** presents the obtained sensitivities (UCD-47-MTL-ME-155) for elements from Z=11 (Na) to Z=38 (Sr) under air atmosphere and at different high voltages (30kV/110 μA, 35kV/100 μA, 40kV/90 μA and 50 kV/30 μA) without the use of any filter. The results demonstrate almost undistinguishable sensitivities for 30kV to 40kV voltages, but generally lower elemental sensitivities were obtained for 50 kV. These findings indicate that 50 kV is likely an unfavorable tube voltage condition for the purpose of the present application as it will also enhance, as expected, the spectral background.

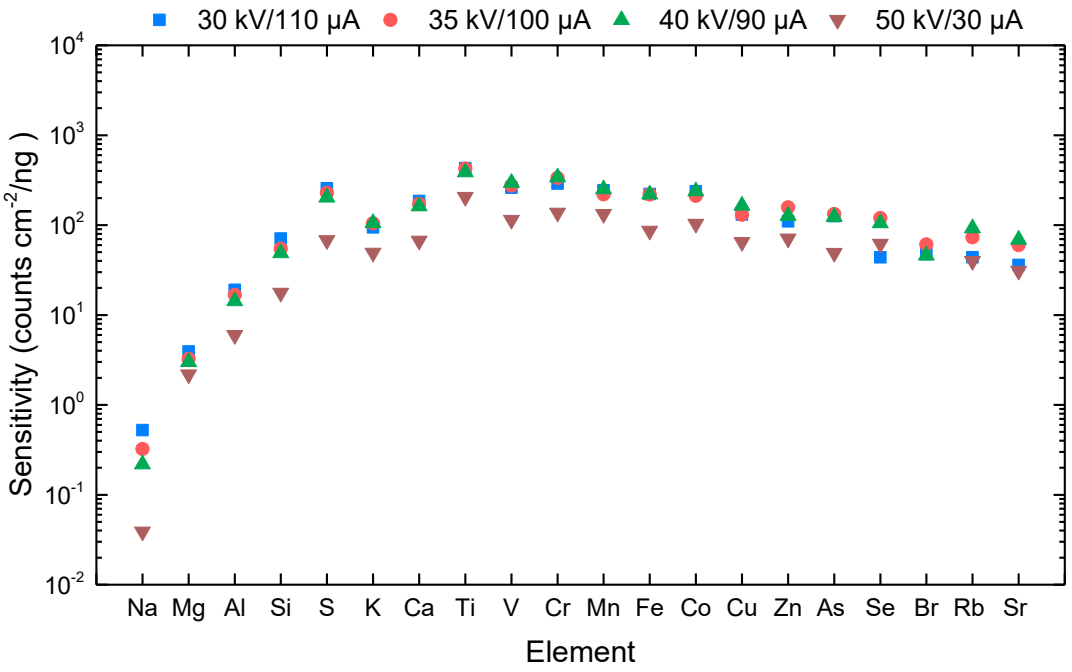

Figure 51. *Sensitivities (counts cm^{-2}/ng) of multi-element reference material (UCD-47-MTL-ME-155) at air atmosphere, no-filter use and acquisition time of 180s. Comparison between different pairs of voltage/current.*

To further investigate if the use of specific filters improves the LoD for different group of elements, three pre-installed automatic filters were comparatively evaluated for high voltages from 30kV to 40kV. From the selected results of **Figure 51** (detailed LoDs for all elements are given in **Figure 52**), it can be observed that for most of the elements the excitation condition of 30 kV and 110 μA generally resulted in lower LoD. Particularly, lighter elements (Al – S) exhibited lower LoD without the use of any of the automatic filters, whereas, the Al1.5 filter was found to provide lower LoD for Cl, K, Ca and Ti. For the elements with atomic numbers from Z=23 (V) up to Z=30 (Zn), lower LoDs were obtained using the Ti1Al12 filter. Lastly, elements with atomic number higher than Z=30 (Ga) have demonstrated lower limits of detection when the tube voltage was set at 40 kV using the Cu3Ti1Al8 filter (As-Sr in **Figure 51**). In summary, the optimal operating conditions used for elemental quantification are listed in **Table 15**, whereas the respective HHXRF spectra of the RM UCD-47-MTL-ME-155 are shown in **Figure 54**.

Table 15. *Optimal operating conditions for each element.*

Element	Voltage (kV)	Current (μA)	Atmosphere	Filter
Na, Mg	15	140	vacuum	no-filter
Al – S	30	110	air	no-filter
Cl – Ti	30	110	air	Al1.5
V – Zn	30	110	air	Ti1Al12
Ga – Zr, Pb	40	90	air	Cu3Ti1Al8

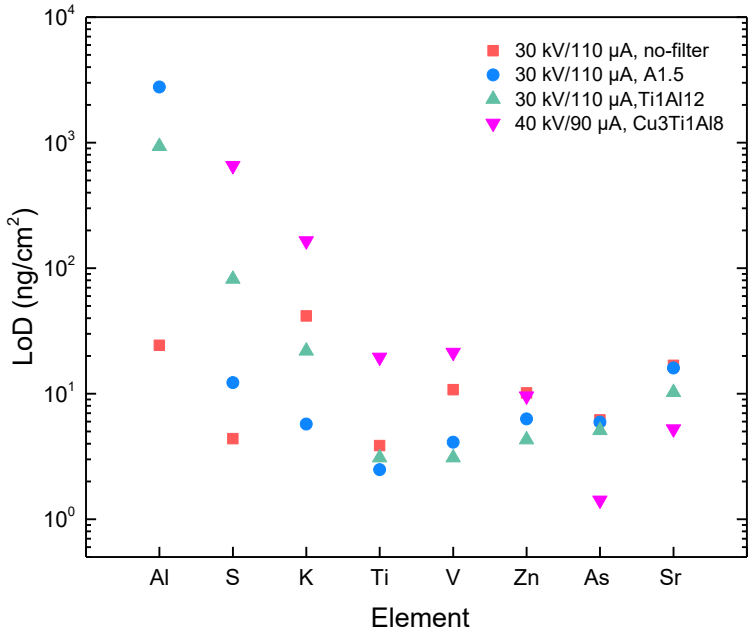

Figure 52. *Limits of detection (ng/cm²) of multi-element reference material UCD-47-MTL-ME-155 for selected elements. Comparison between different operating conditions at 30 kV and 40 kV.*

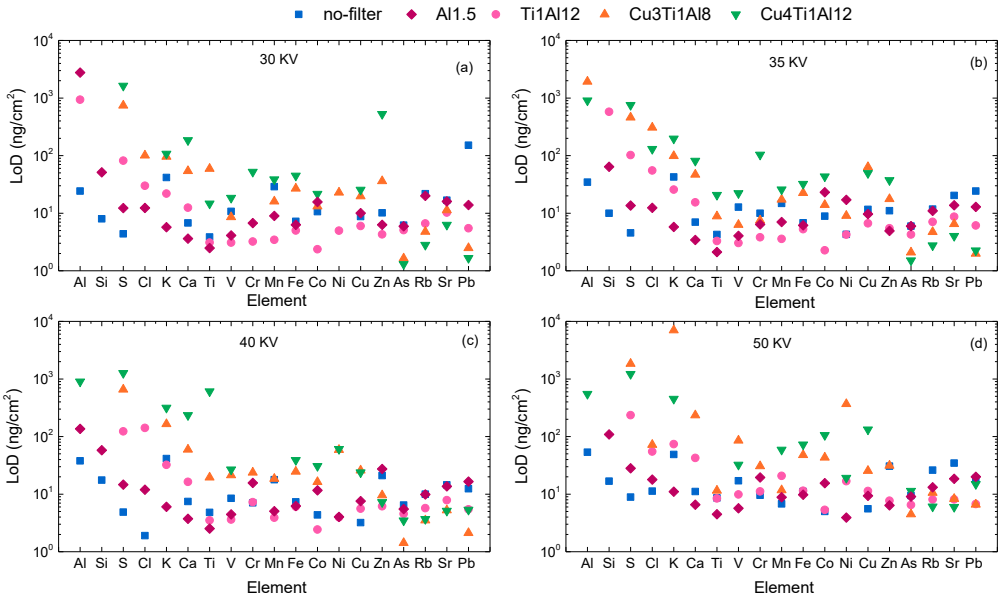

Figure 53. *Limits of detection (ng/cm²) of multi-element reference material UCD-47-MTL-ME-155 for conducted iterations under air atmosphere sorted by excitation condition: (a) 30 kV/110 μA, (b) 35 kV/110 μA, (c) 40/90 μA kV, and (d) 50/30 μA kV.*

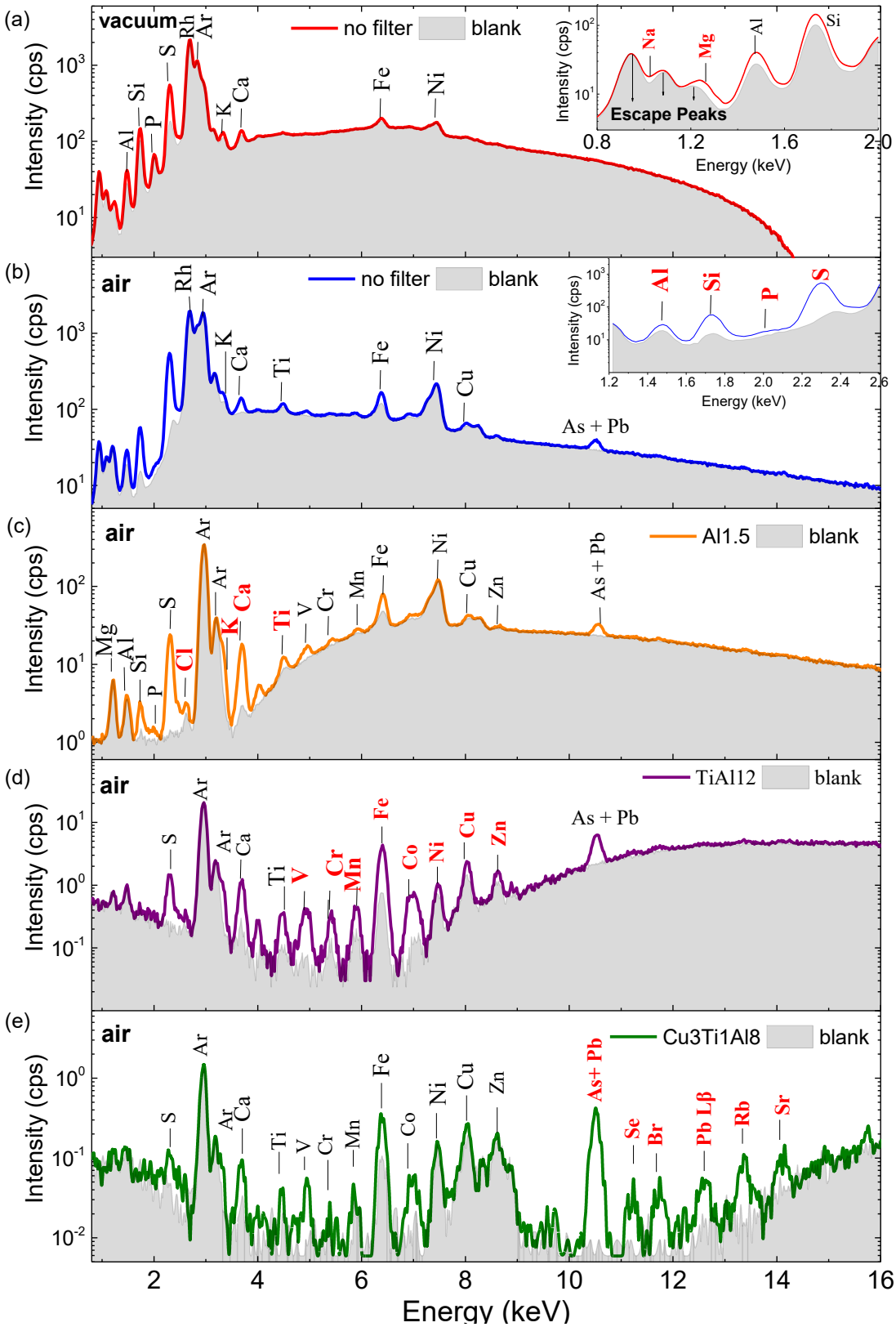

***Figure 54**. HHXRF spectra of the RM UCD-47-MTL-ME-155 measured for an acquisition time of 180 s using the optimal operating conditions. At each spectrum only elements designated in red are considered for analysis*

13.4.2 Calibration methodology

The least-squares regression models a linear curve that best describes the data points by minimizing the squared distance of the data points from the curve. Herein, weighted linear regression was adopted in order to incorporate errors of the experimental procedure (Wu & Yu, 2018). Each calibration curve was constructed by evaluating the element under investigation from the available single- and multi-element materials. Particularly, regression through the origin ($intercept = 0$) was adopted as background contributions -induced from the instrument or the blank filter- were omitted prior to the fit. Intensity and standard error for each data point were obtained using Equations (33) and (34). In this way, all calibrations curves were in the form of $y = ax$, where y is the intensity (counts/s/μA), x is the aerial density of the element under investigation (μg/cm²) and the slope represents the respective sensitivity S_a (cps/μA/μg cm²) of the element *a*.

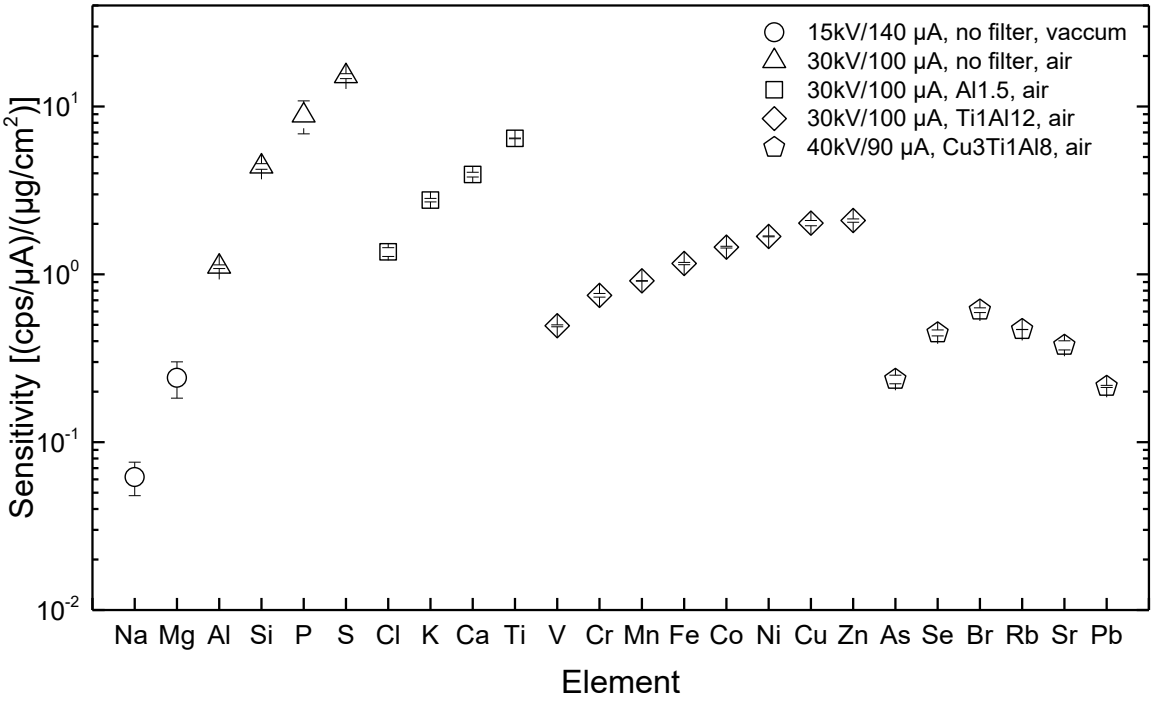

Figure 55. *Sensitivity (and st.error) for each element as obtained from the calibration curves (**Table 16**)*

The statistics of the regression model are given in **Table 16**, where the slope was used to construct **Figure 55**: it represents the elemental sensitivities as obtained from the calibration curves. In more detail, the vast majority of $p - value$ was substantially lower than 0.05 and high correlations (>0.778) were obtained from all fitted lines with lower correlations

correspond to Na, Mg and P. These results validate the correctness of the methodology used to obtain elemental sensitivities. The latter exhibited a characteristic dependence with atomic number (**Figure 55**), whereby each curve corresponding to each of the five operating conditions was characterized by different starting point as a direct result of the particular excitation mode used in each case.

Table 16. *Statistics of the calibration curves for all investigated elements obtained under the optimum conditions provided in* ***Table 15****.*

Element	Number of points	Slope (cps/μA)/(μg/cm²)	st.error	$p-value$	R^2
Na	6	0.062	0.014	0.01	0.778
Mg	4	0.242	0.059	0.01	0.886
Al	8	1.111	0.027	<<0.05	0.995
Si	6	4.397	0.171	<<0.05	0.991
P	3	8.844	1.970	0.046	0.864
S	7	15.18	0.509	<<0.05	0.992
Cl	9	1.361	0.081	<<0.05	0.968
K	9	2.770	0.067	<<0.05	0.994
Ca	5	3.929	0.125	<<0.05	0.995
Ti	3	6.451	0.031	<<0.05	0.999
V	5	0.493	0.006	<<0.05	0.999
Cr	6	0.750	0.019	<<0.05	0.996
Mn	5	0.914	0.003	<<0.05	0.999
Fe	5	1.160	0.019	<<0.05	0.998
Co	5	1.451	0.017	<<0.05	0.999
Ni	6	1.683	0.010	<<0.05	0.999
Cu	6	2.021	0.072	<<0.05	0.992
Zn	5	2.092	0.049	<<0.05	0.997
As	3	0.236	0.013	0.003	0.989
Se	5	0.448	0.018	<<0.05	0.991
Br	2	0.611	0.020	0.021	0.998
Rb	2	0.468	0.0005	<<0.05	1
Sr	4	0.377	0.023	<<0.05	0.985
Pb	8	0.215	0.003	<<0.05	0.998

13.4.3 PM sample analysis and spectrometer intercomparison

Each one of the 28 PM samples was measured twice at two distinct spots (each with 8 mm in diameter) in order to produce more representative measurements and to minimize the influence of possible inhomogeneity of the deposited material. The average measured

intensities together with the estimated uncertainties were used as input variables to the calibration equation for each element. Apart from the sampled particulate matter, two blank filters of the same manufacturer were used as reference blanks.

Three types of uncertainties were considered in order to incorporate those originating from the measurement and the analytical methodology: u_{sta} the statistical uncertainty of each analyte peak area Equation (34), u_{cal} the uncertainty in the calibration curve, and u_{ad} the quoted uncertainties within the nominal areal densities of RM analytes. Namely, the calibration uncertainty u_{cal} was estimated as the ratio of the slope to the standard error of the slope of each calibration curve, whilst, the u_{ad} uncertainty was assumed to be 5% for all reference materials. Eventually, the total uncertainty was estimated as:

$$u_{tot} = \sqrt{u_{sta}^2 + u_{cal}^2 + u_{ad}^2} \tag{37}$$

Table 17 reports the LoDs obtained from the blank Zefluor PTFE filters at optimal operating conditions for each analyte. Due to the larger thickness of the PTFE filter, the respective LoDs are quite elevated with respect to the ones obtained from the RM UCD-47-MTL-ME-155. However, comparable LoDs between the handheld and the benchtop analyzers were obtained, suggesting the good analytical response of the HHXRF spectrometer. Moreover, elemental concentrations determined from the handheld analyzer were classified into two groups: those between LoD and LoQ (Limit of Quantitation=3·LoD) and those above LoQ. The latter shows that the number of detected elements is considerably reduced when evaluating LoQs for trace elements or heavy metals (V, Mn, Ni, Cu, Sr, Br, Pb) which are usually found in very low concentrations in airborne particles. On the contrary, elements which are primarily characterized by their crustal origin (Al, Si, K, Ca, Ti, Fe) exhibited concentrations higher than LoQ Overall, by comparing the estimated concentrations between the two analyzers showed that 14 (out of the 19 identified) elements differed by average with less than 40% (Seeger et al., 2021).

Table 17. *Limits of detection (ng/cm2) for handheld and benchtop ED-XRF spectrometers, and number of samples between LoD and LoQ, and above LoQ (total number of unknown samples was 28). The % (average) concentration difference obtained from* $100 * \frac{(c_{benc} - c_{hand})}{c_{benc}}$ *between the two spectrometers is also given. Measuring time for the handheld spectrometer was 180 s for each of the five conditions used, whilst for the benchtop spectrometer measuring time was 800 s for the first condition and 400 s for the rest four conditions applied.*

	LoD (ng/cm²)		LoD<n<LoQ	n>LoQ	% difference
	Handheld	Benchtop	Handheld	Handheld	Handheld vs Benchtop
Na	321.0	192.0	12	16	-24
Mg	85.0	115.0	10	18	-10
Al	39.8	54.8	6	22	22
Si	10.7	39.4	1	27	-44
P	6.2	8.8	6	11	-
S	5.9	11.8	0	28	-12
Cl	14.8	4.4	4	24	-75
K	9.0	2.8	0	28	-8
Ca	7.7	26.4	0	28	9
Ti	7.1	25.0	4	20	12
V	10.2	18.4	13	0	16
Cr	7.0	8.8	4	5	28
Mn	5.8	9.4	9	7	16
Fe	6.5	5.3	0	28	1
Co	4.1	8.3	0	0	-
Ni	6.3	3.4	5	5	24
Cu	8.3	4.1	2	3	59
Zn	8.9	4.8	10	17	48
As	9.4	4.7	0	0	-
Se	5.6	7.5	0	0	-
Br	4.9	5.3	13	5	13
Rb	10.0	3.6	0	0	-
Sr	17.5	5.5	5	0	-74
Pb	10.6	10.1	15	7	29

Furthermore, **Figure 56** presents a comparison of the elemental concentrations which are above the respective LoQs for both XRF spectrometers. All plots imply good correlations between the concentrations estimated by the two analyzers. Specifically, Pearson correlations ranged between 0.88 - 0.99 with the lower estimate correspond to Mg. Comparisons also indicate an underestimation of the HHXRF measured concentrations for Cu and Zn (shift of the data below the 1:1 line). This observation is attributed to -typically- low environmental

concentrations associated with these heavy metals and enhanced by the elevated blank contributions.

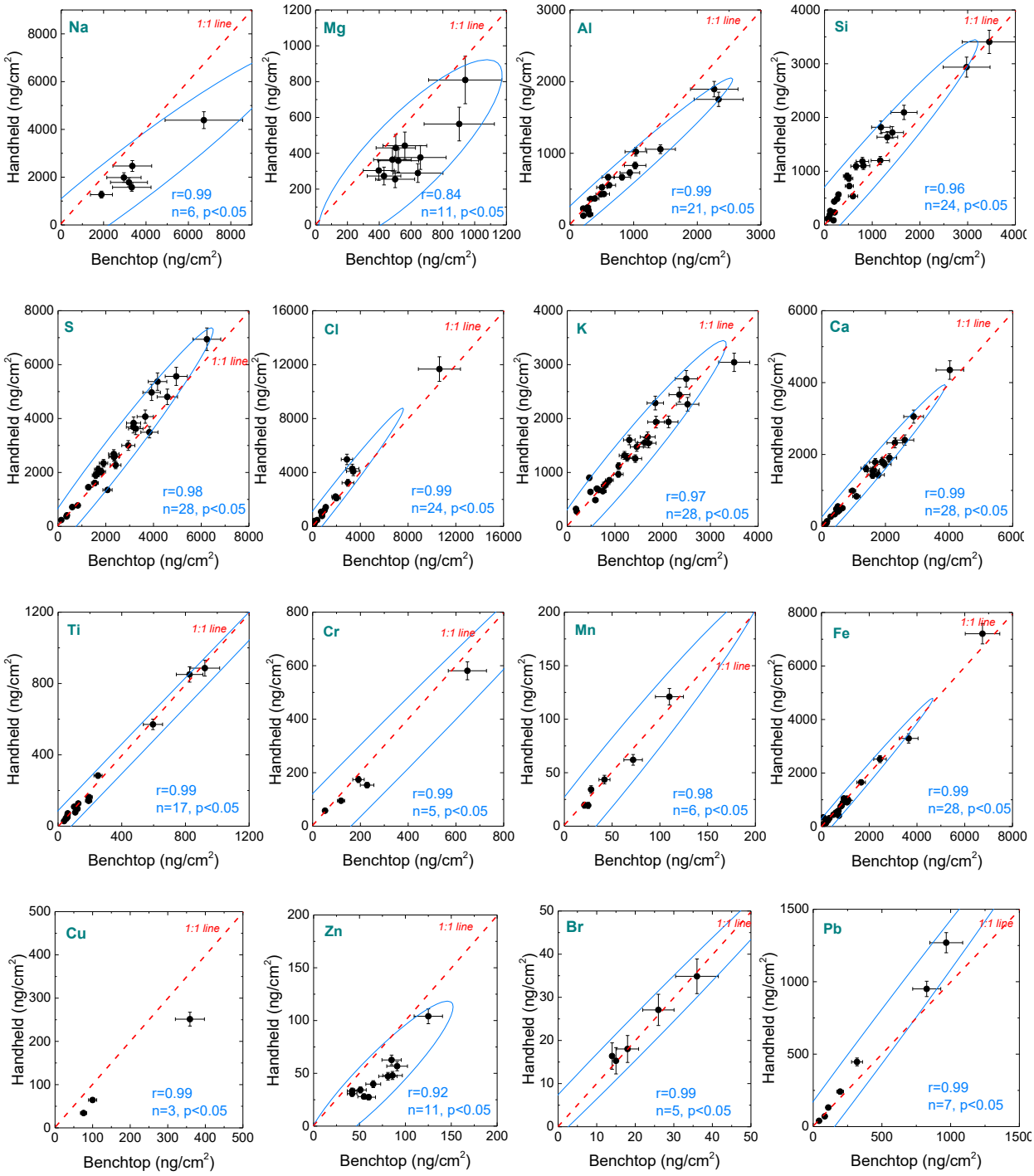

Figure 56. *Comparison of elemental concentrations (ng/cm²) above LoQ between the handheld and the benchtop ED-XRFs spectrometers. Pearson correlation and the 95% confidence ellipse are also given.*

13.5 Conclusions

This work shows that present-day handheld XRF spectrometers have the potentiality, under the appropriate optimization, to be used for the elemental characterization of air particulate matter samples, which are characterized by their multi-elemental composition and low concentrations. Investigation of the response of the analyzer has shown certain limitations of the analytical technique, nevertheless, demonstrated the applicability of HHXRF in determining a broad range of elements successfully with sufficient analytical sensitivity.

These limitations, arising from instrument blank contributions to the acquired spectra, have shown the necessity to investigate the appropriate excitation conditions for optimum quantification of the variable elements (from light to heavy metals – Na to Pb; 24 in total). Blank contributions were provoked by the presence of parasitic instrument contributions or elevated spectral background. The analytical response of the instrument was examined under variable excitation conditions (current, voltage, filter, atmosphere, acquisition time) and by using several multi-element RMs. In this way, an experimental protocol for quantification of elemental concentrations was determined, whereby 5 optimum operating conditions were obtained each one targeted in different elemental range. The comparison of LoDs between the handheld and a benchtop analyzer has shown comparable values with lower values obtained by the handheld XRF in some cases (e.g. Al, Si, Ca, Ti etc). In addition, the quantification of elemental concentrations of real particulate matter samples by the handheld XRF was in good agreement with the corresponding concentrations determined by the benchtop XRF analyzer. The percentage difference of 14 (out of the 19) identified elements was lower than 40%, as well as the elemental concentrations higher than LoQ were strongly correlated ($r=0.88 – 0.99$).

13.6 References

Abiye, O. E., Ugwumadu, C. E., Kamara, A. J., Felizardo, J. P., & Sannoh, A. (2021). Sensitivity calibrations of K- and L-shell X-ray lines for elemental analysis of air particulate samples using a handheld XRF spectrometer. *Aerosol Science and Engineering*, *5*(2), 127–135. https://doi.org/10.1007/s41810-021-00089-3

Aldrian, A., Ledersteger, A., & Pomberger, R. (2015). Monitoring of WEEE plastics in regards to brominated flame retardants using handheld XRF. *Waste Management*, *36*, 297–304. https://doi.org/10.1016/j.wasman.2014.10.025

Álvarez, R. P., Markowicz, A., Wegrzynek, D., Cano, E. C., Bamford, S. A., & Torrres, D. H. (2007). Quality management and method validation in EDXRF analysis. *X-Ray Spectrometry*, *36*(1), 27–34. https://doi.org/10.1002/xrs.923

Amaro, P., Santos, J. P., Samouco, A., Adão, R., Martins, L. S., Weber, S., Tashenov, S., Carvalho, M. L., & Pessanha, S. (2017). Validation of the Geant4 Monte Carlo package for X-ray fluorescence spectroscopy in triaxial geometry. *Spectrochimica Acta Part B: Atomic Spectroscopy*, *130*, 60–66. https://doi.org/10.1016/j.sab.2017.02.012

Bezur, A., Lee, L., Loubser, M., & Trentelman, K. (2020). XRF in cultural heritage: A practical workbook for conservators. Getty Conservation Institute. http://www.getty.edu/conservation

Brent, R. N., Wines, H., Luther, J., Irving, N., Collins, J., & Drake, B. L. (2017). Validation of handheld X-ray fluorescence for in situ measurement of mercury in soils. *Journal of Environmental Chemical Engineering*, *5*(1), 768–776. https://doi.org/10.1016/j.jece.2016.12.056

Calzolai, G., Chiari, M., Lucarelli, F., Nava, S., Taccetti, F., Becagli, S., Frosini, D., Traversi, R., & Udisti, R. (2014). PIXE–PIGE analysis of size-segregated aerosol samples from remote areas. *Nuclear Instruments and Methods in Physics Research Section B*, *318*, 125–129. https://doi.org/10.1016/j.nimb.2013.05.097

Chatoutsidou, S. E., Kopanakis, I., Lagouvardos, K., Mihalopoulos, N., Tørseth, K., & Lazaridis, M. (2019). PM10 levels at urban, suburban and background locations in the eastern Mediterranean: Local versus regional sources with emphasis on African dust. *Air Quality, Atmosphere & Health*, *12*(11), 1359–1371. https://doi.org/10.1007/s11869-019-00750-4

Chen, J., Rodopoulou, S., de Hoogh, K., Strak, M., Andersen, Z. J., Atkinson, R., Bauwelinck, M., … Hoek, G. (2021). Long-term exposure to fine particle elemental components and natural and cause-specific mortality—a pooled analysis of eight European cohorts within the ELAPSE project. *Environmental Health Perspectives*, *129*(4), 047009. https://doi.org/10.1289/EHP8368

Chiari, M., Yubero, E., Calzolai, G., Lucarelli, F., Crespo, J., Galindo, N., Nicolás, J. F., Giannoni, M., & Nava, S. (2018). Comparison of PIXE and XRF analysis of airborne particulate matter samples collected on Teflon and quartz fibre filters. *Nuclear Instruments and Methods in Physics Research Section B*, *417*, 128–132. https://doi.org/10.1016/j.nimb.2017.07.031

Gini, M., Manousakas, M. I., Kantarelou, V., Karydas, A. G., Chiari, M., Migliori, A., Civici, N., Veleva, B., Šega, K., Samek, L., Samara, C., Kertesz, Z., Osan, J., & Eleftheriadis, K. (2021).

Inter-laboratory comparison of ED-XRF/PIXE analytical techniques in the elemental analysis of filter-deposited multi-elemental certified reference materials representative of ambient particulate matter. *Science of the Total Environment, 780,* 146449. https://doi.org/10.1016/j.scitotenv.2021.146449

Gunchin, G., Manousakas, M., Osan, J., Karydas, A. G., Eleftheriadis, K., Lodoysamba, S., Shagjjamba, D., Migliori, A., Padilla-Alvarez, R., Streli, C., & Darby, I. (2019). Three-year long source apportionment study of airborne particles in Ulaanbaatar using X-ray fluorescence and positive matrix factorization. *Aerosol and Air Quality Research, 19*(5), 1056–1067. https://doi.org/10.4209/aaqr.2018.09.0351

Heckel, J., Haschke, M., Brumme, M., & Schindler, R. (1992). Principles and applications of energy-dispersive X-ray fluorescence analysis with polarized radiation. *Journal of Analytical Atomic Spectrometry*, *7*(2), 281–286. https://doi.org/10.1039/ja9920700281

Hinds, W. C. (1999). *Aerosol technology* (2nd ed.). John Wiley & Sons.

Hyslop, N. P., Trzepla, K., Yatkin, S., White, W. H., Ancelet, T., Davy, P., Butler, O., Gerboles, M., Kohl, S., McWilliams, A., Saucedo, L., Van Der Haar, M., & Jonkers, A. (2019). An inter-laboratory evaluation of new multi-element reference materials for atmospheric particulate matter measurements. *Aerosol Science and Technology, 53*(7), 731–742. https://doi.org/10.1080/02786826.2019.1606413

Johansson, S. A. E., Campbell, J. L., & Malmqvist, K. G. (1995). *Particle-induced X-ray emission spectrometry (PIXE).* Wiley.

Karagulian, F., Belis, C. A., Dora, C. F. C., Prüss-Ustün, A. M., Bonjour, S., Adair-Rohani, H., & Amann, M. (2015). Contributions to cities' ambient particulate matter (PM): A systematic review of local source contributions at global level. *Atmospheric Environment, 120,* 475–483. https://doi.org/10.1016/j.atmosenv.2015.08.087

Karydas, A. G., Czyzycki, M., Leani, J. J., Migliori, A., Osan, J., Bogovac, M., … Kaiser, R. B. (2018). An IAEA multi-technique X-ray spectrometry endstation at Elettra Sincrotrone Trieste: Benchmarking results and interdisciplinary applications. *Journal of Synchrotron Radiation, 25*(1), 189–203. https://doi.org/10.1107/S1600577517016332

Kazimoto, E. O., Messo, C., Magidanga, F., & Bundala, E. (2018). The use of portable X-ray spectrometer in monitoring anthropogenic toxic metals pollution in soils and sediments of urban environment of Dar es Salaam, Tanzania. *Journal of Geochemical Exploration, 186,* 100–113. https://doi.org/10.1016/j.gexplo.2017.11.016

Kelly, F. J., & Fussell, J. C. (2012). Size, source and chemical composition as determinants of toxicity attributable to ambient particulate matter. *Atmospheric Environment, 60,* 504–526. https://doi.org/10.1016/j.atmosenv.2012.06.039

Klockenkämper, R., & von Bohlen, A. (2015). *Total-reflection X-ray fluorescence analysis and related methods* (2nd ed.). John Wiley & Sons.

Low, P. S., & Hsu, G. J. (1990). Direct determination of atmospheric lead by Zeeman solid sampling graphite furnace atomic absorption spectrometry (GFAAS). *Fresenius' Journal of Analytical Chemistry, 337*(3), 299–305. https://doi.org/10.1007/BF00321978

Lucarelli, F., Calzolai, G., Chiari, M., Nava, S., & Carraresi, L. (2018). Study of atmospheric aerosols by IBA techniques: The LABEC experience. *Nuclear Instruments and Methods in Physics Research Section B, 417,* 121–127. https://doi.org/10.1016/j.nimb.2017.07.034

Manousakas, M., Diapouli, E., Papaefthymiou, H., Kantarelou, V., Zarkadas, C., Kalogridis, A.-C., Karydas, A.-G., & Eleftheriadis, K. (2018). XRF characterization and source apportionment of PM10 samples collected in a coastal city. *X-Ray Spectrometry, 47*(3), 190–200. https://doi.org/10.1002/xrs.2817

Nimmo, M., & Fones, G. (1994). Application of adsorptive cathodic stripping voltammetry for the determination of Cu, Cd, Ni and Co in atmospheric samples. *Analytica Chimica Acta, 291*(3), 321–328. https://doi.org/10.1016/0003-2670(94)80027-8

Ogrizek, M., Kroflič, A., & Šala, M. (2022). Critical review on the development of analytical techniques for the elemental analysis of airborne particulate matter. *TrAC Trends in Environmental Analytical Chemistry, 35,* e00155. https://doi.org/10.1016/j.teac.2022.e00155

Palmer, P. T., Jacobs, R., Baker, P. E., Ferguson, K., & Webber, S. (2009). Use of field-portable XRF analyzers for rapid screening of toxic elements in FDA-regulated products. *Journal of Agricultural and Food Chemistry, 57*(7), 2605–2613. https://doi.org/10.1021/jf803285h

Seeger, S., Osan, J., Czömpöly, O., Gross, A., Stosnach, H., Stabile, L., Ochsenkuehn-Petropoulou, M., Tsakanika, L. A., Lymperopoulou, T., Goddard, S., Fiebig, M., Gaie-Levrel, F., Kayser, Y., & Beckhoff, B. (2021). Quantification of element mass concentrations in ambient aerosols by combination of cascade impactor sampling and mobile total reflection X-ray fluorescence spectroscopy. *Atmosphere, 12*(3), 309. https://doi.org/10.3390/atmos12030309

Shaltout, A. A., Hassan, S. K., Karydas, A. G., Zaki, Z. I., Mostafa, N. Y., Kregsamer, P., Wobrauschek, P., & Streli, C. (2018). Comparative elemental analysis of fine particulate matter (PM2.5) from industrial and residential areas in Greater Cairo-Egypt by means of a multi-secondary target energy dispersive X-ray fluorescence spectrometer. *Spectrochimica Acta Part B, 145,* 29–35. https://doi.org/10.1016/j.sab.2018.04.003

Shaltout, A. A., Harfoushe, M., Ali, S. S. M., Karydas, A. G., Kregsamer, P., Wobrauschek, P., Streli, C., Abd-Elkader, O. H., Yassin, M. A., & El Orabi, N. F. (2020). Elemental composition and source apportionment of atmospheric aerosols collected from urban and residential areas of Jordan using multi-secondary targets energy dispersive X-ray fluorescence. *Spectrochimica Acta Part B, 170,* 105900. https://doi.org/10.1016/j.sab.2020.105900

Shugar, A. N., & Mass, J. L. (2012). *Handheld XRF for art and archaeology.* Leuven University Press. https://doi.org/10.2307/j.ctt9qdzfs

Solé, V. A., Papillon, E., Cotte, M., Walter, P., & Susini, J. (2007). A multiplatform code for the analysis of energy-dispersive X-ray fluorescence spectra. *Spectrochimica Acta Part B, 62*(1), 63–68. https://doi.org/10.1016/j.sab.2006.12.002

Su, Y. Y., Li, Z. M., Li, M., Yi, X. W., Zhou, G. Q., Xu, J., Zhai, L. H., Wei, G. Y., & Zhu, F. R. (2013). Development of aerosol sample introduction interface coupled with ICP-MS for direct introduction and quantitative online monitoring of environmental aerosol. *Aerosol Science and Technology*, *48*(1), 99–7. https://doi.org/10.1080/02786826.2013.861894

Turner, A. (2016). Heavy metals, metalloids and other hazardous elements in marine plastic litter. *Marine Pollution Bulletin*, *111*(1–2), 136–142. https://doi.org/10.1016/j.marpolbul.2016.07.020

Turner, A., Kearl, E. R., & Solman, K. R. (2016). Lead and other toxic metals in playground paints from South West England. *Science of the Total Environment*, *544*, 460–466. https://doi.org/10.1016/j.scitotenv.2015.11.078

Van Grieken, R., & Markowicz, A. (Eds.). (2002). *Handbook of X-ray spectrometry* (2nd ed.). Marcel Dekker.

Viana, M., Kuhlbusch, T. A. J., Querol, X., Alastuey, A., Harrison, R. M., Hopke, P. K., Winiwarter, W., Vallius, M., Szidat, S., Prévôt, A. S. H., Hueglin, C., Bloemen, H., Wåhlin, P., Vecchi, R., Miranda, A. I., Kasper-Giebl, A., Maenhaut, W., & Hitzenberger, R. (2008). Source apportionment of particulate matter in Europe: A review of methods and results. *Journal of Aerosol Science*, *39*(10), 827–849. https://doi.org/10.1016/j.jaerosci.2008.05.007

West, M., Ellis, A. T., Potts, P. J., Streli, C., Vanhoof, C., & Wobrauschek, P. (2008). *Portable X-ray fluorescence spectrometry.* RSC Publishing. https://doi.org/10.1039/9781847558640

Wu, C., & Yu, Z. (2018). Evaluation of linear regression techniques for atmospheric applications: The importance of appropriate weighting. *Atmospheric Measurement Techniques*, *11*(2), 1233–1250. https://doi.org/10.5194/amt-11-1233-2018

Yatkin, S., Armin, H. S., Trzepla, K., & Dillner, A. M. (2016). Preparation of lead (Pb) X-ray fluorescence reference materials for the EPA Pb monitoring program and the IMPROVE network using an aerosol deposition method. *Aerosol Science and Technology*, *50*(4), 309–320. https://doi.org/10.1080/02786826.2016.1150956

Yatkin, S., Belis, C. A., Gerboles, M., Calzolai, G., Lucarelli, F., Cavalli, F., & Trzepla, K. (2016). An interlaboratory comparison study on the measurement of elements in PM10. *Atmospheric Environment*, *125*(A), 61–68. https://doi.org/10.1016/j.atmosenv.2015.10.084

Yatkin, S., Gerboles, M., & Borowiak, A. (2012). Evaluation of standardless EDXRF analysis for the determination of elements on PM10 loaded filters. *Atmospheric Environment*, *54*, 568–582. https://doi.org/10.1016/j.atmosenv.2012.02.062

Yatkin, S., Trzepla, K., White, W. H., & Hyslop, N. P. (2018). Generation of multi-element reference materials on PTFE filters mimicking ambient aerosol characteristics. *Atmospheric Environment*, *189*, 41–49. https://doi.org/10.1016/j.atmosenv.2018.06.034

Yatkin, S., Trzepla, K., White, W. H., Spada, N. J., & Hyslop, N. P. (2020). Development of single-compound reference materials on polytetrafluoroethylene filters for analysis of aerosol samples. *Spectrochimica Acta Part B*, *171*, 105948. https://doi.org/10.1016/j.sab.2020.105948

Young, K. E., Evans, C. A., Hodges, K. V., Bleacher, J. E., & Graff, T. G. (2016). A review of the handheld X-ray fluorescence spectrometer as a tool for field geologic investigations on Earth and in planetary surface exploration. *Applied Geochemistry, 72,* 77–87. https://doi.org/10.1016/j.apgeochem.2016.07.003

Ytreberg, E., Lagerström, M., Holmqvist, A., Eklund, B., Elwing, H., Dahlström, M., & Dahl, P. (2017). A novel XRF method to measure environmental release of copper and zinc from antifouling paints. *Environmental Pollution, 225,* 490–496. https://doi.org/10.1016/j.envpol.2017.03.014

14. Quantitative micro-XRF imaging for assessing elemental inhomogeneity in multi nozzle cascade impactor aerosol filters

14.1 Abstract

This study presents a method for quantitatively analyzing atmospheric aerosols collected using a 10-stage Berner cascade impactor with micro-XRF imaging. The method addresses key challenges like uneven particle deposition and the balance between spatial resolution and data quality. We developed a rigorous calibration procedure using reference materials, which enabled the quantification of 29 elements with detection limits as low as a few ng/m^3. In total, we analyzed over 400 impaction spots, providing statistically representative data across coarse, fine, and ultrafine size ranges. Our analysis revealed that crustal elements, such as silicon (Si), calcium (Ca), titanium (Ti), and iron (Fe), were predominantly found in the coarse fraction. Potassium (K) and sulfur (S) displayed a bimodal distribution, indicating a mix of natural and anthropogenic sources. Vanadium (V) was detected exclusively in the fine fraction, confirming its role as a combustion marker. Generally, the concentrations measured were consistent across impaction spots, with a relative standard deviation (RSD) of less than 30%, except for very low concentrations or the largest particle sizes. Elemental mapping also revealed significant spatial variability within individual spots. This highlights the limitations of traditional single-point measurement techniques and supports the use of imaging for reliable, non-destructive analysis of aerosols. Overall, this approach serves as a robust diagnostic tool for aerosol source apportionment and exposure assessment.

14.2 Introduction

Particulate matter (PM) is widely recognized as a major atmospheric pollutant, originating from both natural processes and a wide range of human activities, such as industry, energy generation, transportation, household activities, and biomass burning. Due to its complex chemical composition—often including carbonaceous, ionic, and elemental species—PM poses serious risks to both the climate Chen et al., 2021) and public health (Ostro et al., 2015; Samoli et al., 2013). Analyzing the elemental composition of atmospheric aerosols provides essential insights into pollution sources and the associated health risks (Manousakas et al., 2021; Hopke et al., 2020). This information is critical for source apportionment studies, exposure risks (Megido et al., 2017; Caggiano et al., 2019), and the development of effective air quality management strategies.

Cascade impactors are widely employed for size-segregated sampling of atmospheric aerosols, providing essential information on particle size distributions (Stefancova et al., 2011). This data is critical for evaluating both health risks—since particle size governs respiratory deposition—and the climatic effects of aerosols. Elemental characterization of these samples is typically performed using a range of analytical techniques. Traditional methods include Particle-Induced X-ray Emission (PIXE) (Maenhaut et al., 1996; Calzolai et al., 2014), and destructive bulk analysis techniques such as Inductively Coupled Plasma Mass Spectrometry

(ICP-MS) (Conca et al., 2022) and Graphite Furnace Atomic Absorption Spectrometry (GF-AAS) (Alver Şahin et al., 2013), which require complete digestion of the collected filter material. More recent approaches have turned to Total Reflection X-ray Fluorescence (TXRF), which enables direct analysis of aerosol deposits on quartz reflectors without extensive sample preparation (Seeger et al., 2021; Crazzolara et al., 2024).

Despite the diversity of techniques, a critical and often overlooked limitation concerns the spatial inhomogeneity of aerosol deposition on filter substrates, particularly in multi-nozzle cascade impactors where particles accumulate in discrete impaction spots. When using broad-beam techniques like PIXE or TXRF, the assumption of uniform deposition across the irradiated area can lead to significant quantification errors if the beam overlaps both loaded and unloaded regions. Stelcer et al., (2011) demonstrated this clearly in MOUDI cascade impactor samples, showing that small-diameter particle deposits analyzed with large-diameter proton beams can distort elemental mass concentrations unless beam-spot corrections are applied. Similarly, Robinson et al. (2017) showcased the potential of LA-ICP-MS for spatially resolved analysis of cascade impactor samples, enabling detailed elemental mapping across filter substrates. However, while LA-ICP-MS provides excellent resolution, it is destructive and lacks the capability to determine absolute concentrations due to the absence of size-resolved calibration standards.

In this study, we applied Micro-XRF imaging as a non-destructive method to scan filter areas and evaluate the spatial distribution of elements collected across cascade impactor stages. This technique enables a detailed assessment of elemental inhomogeneity, providing critical information into sample uniformity and helping to identify potential biases in quantitative analysis procedures. Micro-XRF imaging offers spatially resolved elemental information without compromising the integrity of the sample (Gerodimos et al., 2024), making it particularly suitable for evaluating complex deposition patterns. Although this technique has been widely adopted in disciplines such as cultural heritage, forensics, biomedicine, and materials analysis, its application in atmospheric aerosol research remains limited (Cabal et al., 2017).

This is the first study to investigate the spatial distribution of elemental composition in aerosol samples collected using a 10-stage Berner Impactor (aerodynamic diameters: 0.026 to 13.7 μm) on Tedlar foils. Using the M6 Jetstream large scale Micro-XRF spectrometer (Bruker), we mapped the aerosol deposition spots across the collection substrates and generated elemental heatmaps for Si, S, K, Ca, Ti, V, and Fe. The results revealed inhomogeneity patterns in the elemental distribution across several stages, especially at larger particle sizes, indicating uneven particle deposition. Factors such as non-ideal internal airflow, particle bounce and re-entrainment, and filter overloading may contribute to this effect. These findings underline the importance of evaluating deposition homogeneity prior to conducting non-destructive elemental analyses on cascade impactor samples.

14.3 Materials and methods

14.3.1 The large-scale micro-XRF spectrometer

Measurements were performed using the M6-Jetstream scanning system (Bruker Nano GmbH, Berlin, Germany), featuring a 30 W Rhodium (Rh) anode X-ray source, polycapillary focusing optics, and a silicon drift detector with a 30 mm² active area (*Gerodimos et al., 2024*). The system utilizes a polycapillary lens to concentrate the X-ray beam onto the sample. During the analysis, the X-ray tube operated at 50 kV and 600 μA. The scanning head was aligned at the instrument's focal distance, yielding a nominal spot size of 100 μm for Mo Kα. Spectral data were processed and converted into elemental distribution maps using the integrated ESPRIT software provided with the M6-Jetstream system. All measurements were carried out in regular air conditions, using a custom stand to securely hold the aerosol samples in place during scanning.

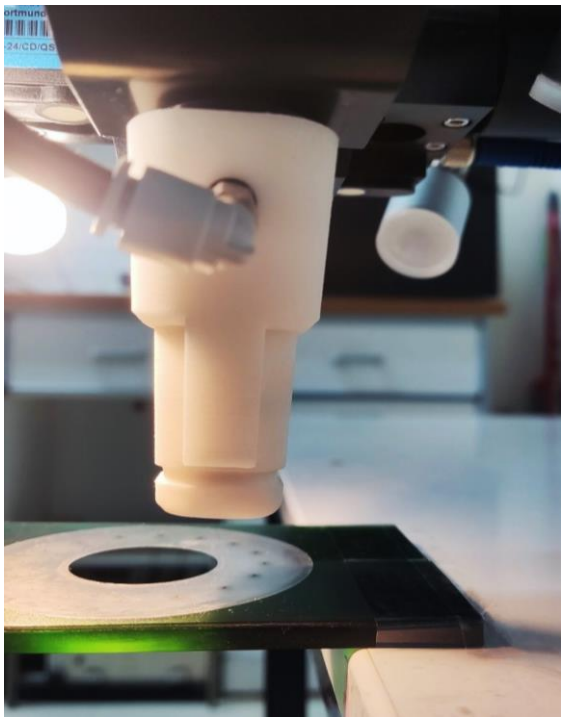

Figure 57. *The large-area micro-XRF spectrometer (M6 Jetstream, Bruker) scanning a Berner cascade impactor Tedlar aerosol filter. The filter is mounted on a custom 3D-printed stand with a hollow center (6.5 cm in diameter) to prevent background signal contributions from the support. This setup ensured that only the deposited aerosol particles contributed to the detected signal.*

14.3.2 Reference materials

For the calibration of the XRF spectrometer, we utilized infinitely thin, single-element or compound reference materials (RMs). Specifically, we employed 25 thin RMs from Micromatter, deposited on 6.3 μm Mylar films, including Al, SiO, GaP, KCl, CaF_2, V, Cr, Fe, Co, Ni, CuS_x, ZnTe, Ge, GaAs, Se, CsBr, RbI, SrF_2, YF_3, AgHg (x2), BaF_2, Pt, Au, and Pb. In

addition, two custom-made RMs (Mn and Ti) were prepared on Kapton films. We also used 17 certified single-compound RMs on polytetrafluoroethylene (PTFE) filters obtained from UC Davis, specifically UCD-47-Al&Ce (x2), UCD-47-Si (x3), UCS-47-S (x3), UCD-47-KCl (x3), UCD-47-NaCl (x3), and UCD-47-Pb. The UC Davis RMs were prepared on PTFE filters using high-purity salts or nanoparticles (Yatkin et al, 2018). Mass loadings were determined gravimetrically and verified by energy-dispersive X-ray fluorescence (ED-XRF), inductively coupled plasma mass spectrometry (ICP-MS), and ion chromatography (IC) (Yatkin et al., 2020). The uncertainty associated with the Micromatter standards is specified at 5%, while for the remaining materials it is estimated at 10%.

14.3.3 Sensitivity and limits of detection

The elemental sensitivity S_α is commonly used to quantify the efficiency of an XRF spectrometer in exciting various elements across the periodic table. It is defined as the number of characteristic X-ray photons emitted by an analyte, normalized by the live time (t_l, in seconds), and the surface density of the element (Ca, in μg/cm²). The measured intensity of the characteristic X-ray line of an analyte is denoted as I_α (counts per second, cps). For a sample of negligible thickness—where the condition $\mu_\alpha \rho x / sin\theta \ll 1$ is satisfied for the characteristic X-rays of all target elements—this sensitivity can be derived in a straightforward manner. In this expression, μ_α is the mass attenuation coefficient (cm²/g) of the characteristic X-ray of an analyte, ρ is the sample's density (g/cm³), x is the thickness (cm), and θ is the take-off angle, defined as the angle between the sample surface and the detector axis (Chatoutsidou et al., 2022):

$$S_\alpha \left(\frac{cps}{\mu g/cm^2} \right) = \frac{I_\alpha (cps)}{C_\alpha \ (\mu g/cm^2)} \tag{38}$$

Where,

$$I_\alpha (cps) = \frac{N_{ref,\alpha} - N_{bl,a}}{t_l} \tag{39}$$

with, $N_{ref,\alpha}$ and $N_{bl,\alpha}$ are the net peak areas of the principal characteristic X-rays (Kα or Lα) of element α, measured in the reference material and the corresponding blank sample (i.e., the same substrate without deposited analyte), respectively, measured under live time t_l. The statistical uncertainty represented by,

$$\sigma_{I_\alpha} = \frac{\sqrt{N_{ref,\alpha}}}{t_l} \tag{40}$$

The limit of detection (LoD in μg/cm²) for element α can be calculated using the equation:

$$(LoD)_a \cong \frac{3\sqrt{Bkg_{ref}}}{t_l}\frac{1}{S} \quad (41)$$

, where Bkg_{ref} denotes the integrated background counts in the spectral region under the characteristic peak of element α. In total, 29 elements were analyzed in the samples—Al, Si, P, S, Cl, K, Ca, Ti, V, Cr, Mn, Fe, Co, Ni, Cu, Zn, Ga, Ge, As, Se, Br, Rb, Sr, Y, Ce, Ba, Pt, Au and Pb. The corresponding peak and background areas were evaluated using the Artax 8.0 software (Bruker).

14.3.4 Operating Conditions of the experimental Set-Up

The spectrometer has a motorized filter wheel with eight main filter settings, allowing optimization of the X-ray ionization spectrum for specific analytical tasks. The main purpose of these filters is to reduce scattered radiation by absorbing selectively the bremsstrahlung component of the X-ray tube spectrum above the absorption edges of the filter materials. Thicker filters composed of higher-Z elements provide stronger suppression, improving the signal-to-background ratio. Filters can be also used to minimize Bragg reflections in the acquired spectra, if polycrystalline samples are measured.

To identify a suitable filter configuration, we initially employed a multi-element reference material (UCD-47-ME-H) (Yatkin et al, 2018), which was selected to closely resemble real PM samples. This reference material (RM) included a wide range of elements at areal densities typical of atmospheric aerosol loadings. It was solely used for qualitative evaluation of the fluorescence elemental response under different filter conditions, not for system calibration.

Based on this evaluation, no filter (NF condition) was used for the detection of light elements from Al to Ca, while the $Al_{100}Ti_{25}$ filter was selected for elements from Ti to Pb. This configuration delivered good performance across the entire elemental range of interest and minimized filter switching, enhancing time efficiency. The beam spot size was fixed at 100 μm for all measurements.

The XRF spectra of the UCD-47-ME-H multi-element reference material, acquired with no filter condition and with the $Al_{100}Ti_{25}$ filter, are presented in **Figure 58**. Clear and intense peaks are observed for light elements (Al, S, K, and Ca), in the energy range below ~4 keV (light blue color). The absence of a filter (NF condition) allows maximum transmission of low-energy characteristic X-rays, improving the respective elemental sensitivities. The application of the $Al_{100}Ti_{25}$ reduces the low-energy Bremsstrahlung background, thereby improving the signal-to-background ratio for transition metals and heavier elements. This is expected and desired when analyzing mid- to high-Z elements. In the filtered spectrum (magenta color), peaks for elements such as (V, Cr, Mn, Fe, Ni, Cu, Zn, As, Sr, and Pb) are well defined with a

noticeable reduction in background noise across the mid-energy range (~5–20 keV). The filter effectively suppresses bremsstrahlung, improving the peak-to-background ratio for heavier elements. The optimal operating conditions are presented in **Table 18.**

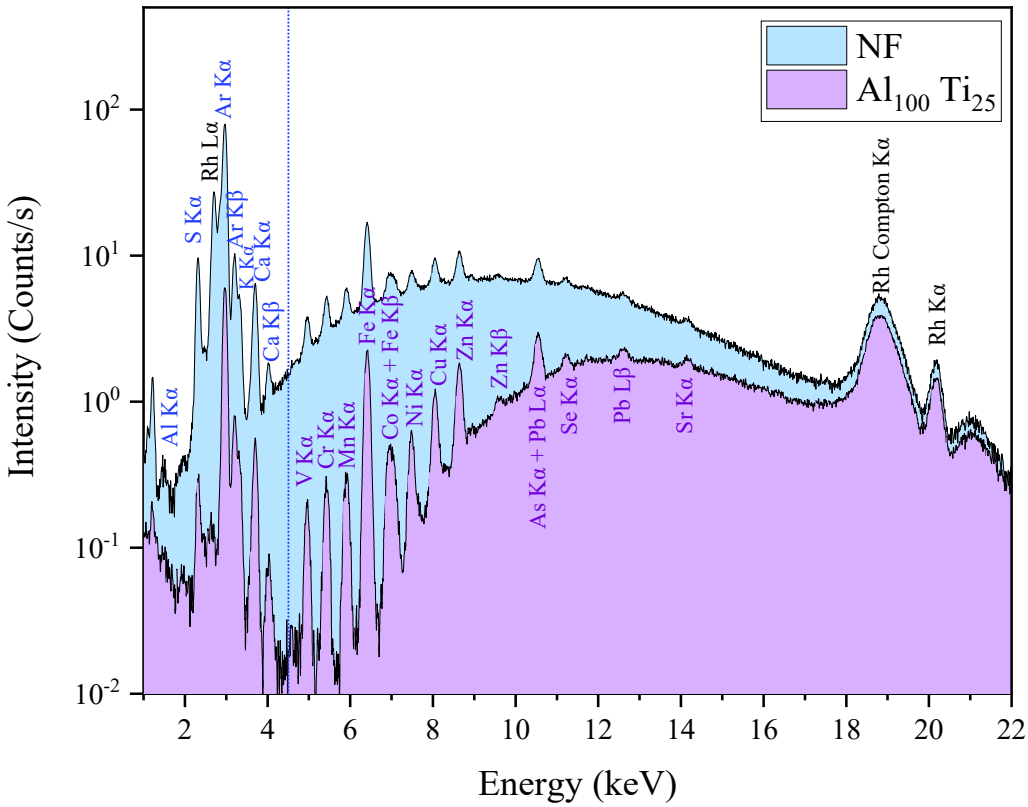

***Figure 58**. Comparison of the UCD-47-ME-H XRF spectra under two filter conditions: NF and $Al_{100}Ti_{25}$. The X-ray tube operated at a voltage of 50 kV and a current of 600 μA, with an acquisition time of 300 seconds.*

***Table 18.** Optimal operating conditions for each element*

Element	Voltage (kV)	Current (μA)	Atmosphere	Filter
Al - Ca	50	600	air	No filter (NF)
Ti - Pb	50	600	air	$Al_{100}Ti_{25}$

14.3.5 Calibration Methodology

To quantify elemental sensitivity, calibration curves were established using a weighted least-squares regression, which minimizes the squared deviations between observed data points and the fitted line while accounting for measurement uncertainties. This approach incorporates the experimental error associated with each data point, following the methodology described by Wu and Yu, 2018. For each element, calibration was performed using data obtained from both single and compound reference materials.

A regression through the origin (with intercept set to zero) was applied, as the spectra of the reference materials were free from background interference and showed no visible spectral artifacts. The intensity values and their associated uncertainties were derived according to Eqs. (39) and (40). As a result, all calibration lines followed the form $y = a \cdot x$, where y denotes the measured intensity (in $counts/s$), x is the areal density of the analyte (in µg/cm²), and Sa corresponds to the elemental sensitivity S_a, in ($(counts/s)/(\mu g/cm^2)$). **Figure 59** presents the elemental sensitivities and corresponding limits of detection based on a 120-second measurement time as a function of atomic number for the two measurement conditions.

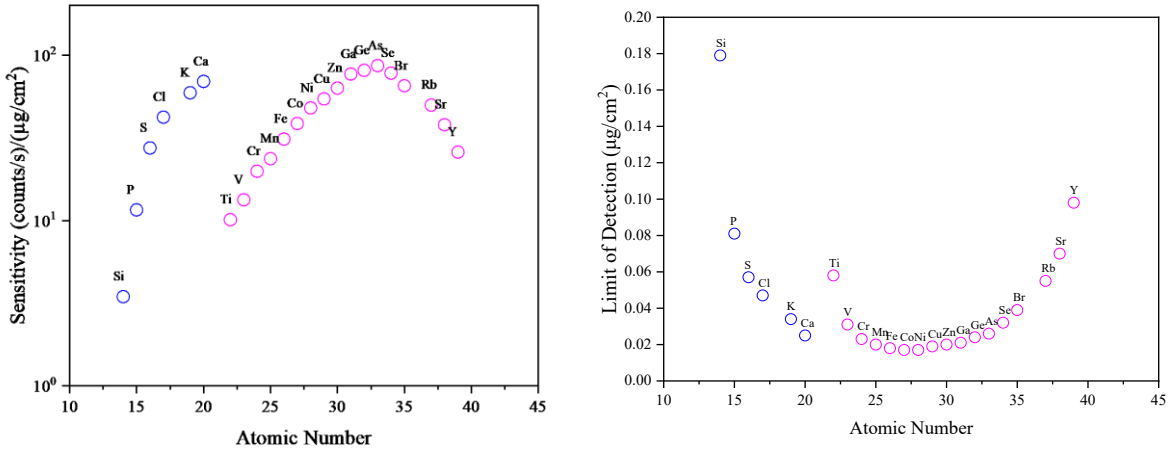

Figure 59. Elemental sensitivities and corresponding limits of detection (µg/cm2) as a function of atomic number for the two measurement conditions: no filter (used for light elements from Si to Ca, shown in blue) and the Al100Ti25 filter (used for heavier elements from Ti to Y, shown in magenta.

14.3.6 Spatial Resolution

To assess the spatial resolution of the micro-XRF spectrometer, a USAF 1951 resolution test chart was measured (Romano et al., 2017; Gerodimos et al., 2024). Each group in the USAF 1951 chart consists of six elements, with each element containing two blocks of parallel vertical and horizontal lines (Wikipedia contributors, n.d.). Elements 1–6 from Group 1 were examined using a resolution chart printed in-house with a CeraPrinter F-Series (Ceradrop®). In this process, AGFA PRELECT SPS201 nano-silver ink was applied onto Powercoat HD-coated paper through a 5 µm-thick deposition of silver (Ag) (Gerodimos et al., 2024). The line widths of these elements ranged from 250 µm (Element 1) to 140 µm (Element 6), providing a benchmark for evaluating the system's spatial resolving ability.

The scanned area was 3.54 × 8.00 mm² with a pixel size of 100 µm. The study was conducted under two different ionization beam conditions (without a beam filter and with the $Al_{100}Ti_{25}$ beam filter) and two different dwell times (50 ms and 600 ms). The Ag Lα distribution maps are shown in **Figure 60**. In the absence of a beam filter, increasing the dwell time by an order of magnitude yields a slight improvement in spatial resolution. The application of the $Al_{100}Ti_{25}$ filter suppresses the low-energy background but also reduces the emission rate of the

Ag Lα (2.98 keV) line, resulting in noisy images at short dwell times. With the longer dwell time of 600 ms, the combination of background reduction and higher counting statistics yielded maps with improved definition, particularly in the finer structures (Elements 5 and 6).

The results show that the chosen setup can detect variations in particle deposition on the Tedlar substrates while ensuring statistical meaningful analysis across various impactor stages. This evaluation was not intended to resolve individual aerosol particles (<10 μm), but to confirm that the chosen setup has sufficient spatial resolution to capture within-spot inhomogeneities and to provide representative coverage even for the smallest impaction spots.

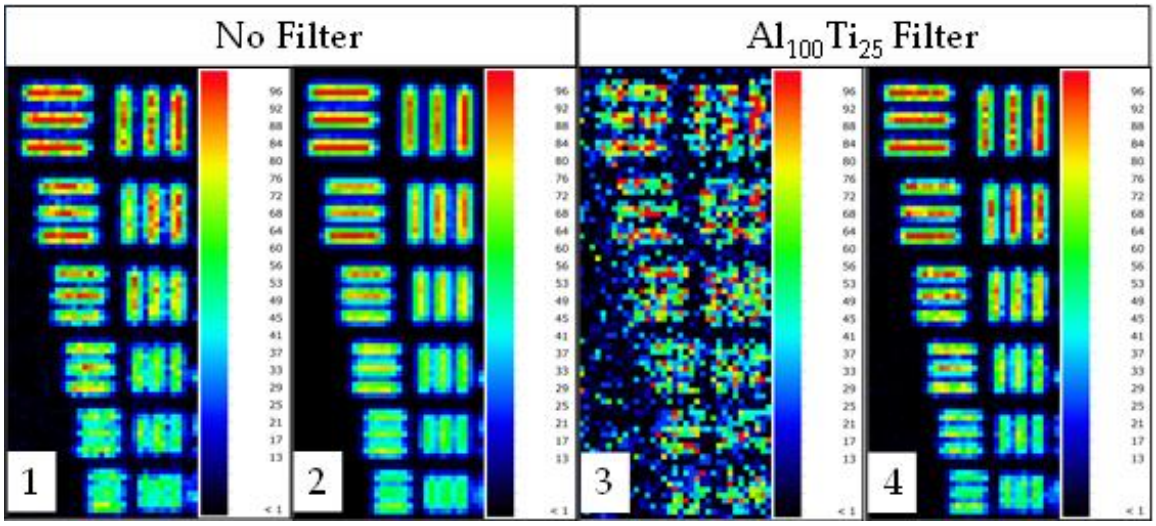

Figure 60. *Ag Lα distribution maps scanning the Group 1, Elements 1–6 of a silver printed USAF 1951 resolution test chart. The line widths range from 250 to 140 μm. The scanned area was 3.54 × 8.00 mm² with a pixel size of 100 μm. The distributions for four different conditions are shown: (1) No beam filter, dwell time 50 ms; (2) No filter, dwell time 600 ms; (3) $Al_{100}Ti_{25}$ beam filter, dwell time 50 ms; (4) $Al_{100}Ti_{25}$ beam filter, dwell time 600 ms.*

14.3.7 Study area and sample collection

As part of a dedicated measurement campaign conducted in July 2024, three representative 24-hour PM aerosol filter sets were collected using a 10-stage Berner cascade impactor at the atmospheric monitoring site located within the National Centre for Scientific Research "Demokritos" in Athens, Greece (**Figure 61**). This site, commonly referred to as the Demokritos station, is situated in a green area at the base of Mount Hymettus, approximately 8 km northeast of the Athens city center. The station operates as an urban background site, representative of suburban aerosol conditions within the greater Athens Metropolitan Area. It is routinely influenced by pollution transport from the urban core, while it can also receive regional aerosol contributions depending on prevailing wind directions (Eleftheriadis et al., 2021). The station is part of the ACTRIS and PANACEA research infrastructures and is affiliated with the Global Atmosphere Watch (GAW) program (Zografou et al, 2022).

Figure 61. *The Atmospheric Aerosol Monitoring Station located at the Demokritos Research Center in Athens, Greece.*

The PM samples were collected using a low-pressure Berner-type cascade impactor, operated at a nominal flow rate of 25.5 L·min^{-1} (Gini et al., 2022). The impactor consists of 11 stages, each designed to separate particles based on their aerodynamic diameter, with cut-off sizes spanning from 13.35 μm down to 0.03 μm. This design enables the classification of airborne particles across a wide size range, from coarse to ultrafine fractions. The separation of particles is achieved through inertial impaction. As the aerosol-laden air passes through progressively narrower nozzles at each stage, particles with sufficient inertia deviate from the airflow and strike the collection substrates, while smaller particles continue to follow the airflow to the lower stages. This mechanism allows size-segregated collection, where larger particles are deposited on the upper stages and smaller-finer particles are retained on the lower ones. The operational characteristics of the low-pressure Berner cascade impactor used in this study are summarized in **Table 19**. Each impactor stage is designed to collect particles within a specific aerodynamic diameter range, enabling classification by size through inertial impaction. The table includes the nozzle diameter, D_{Nozzle}, which refers to the diameter of the individual orifices through which air is drawn; the number of nozzles per stage ($N_{Nozzles}$); and the jet-to-plate distance ($S_{Jet\text{-}to\text{-}Plate}$), which is the gap between the nozzle outlet and the impaction surface. Also included are the Reynolds number at the nozzle Re_{Nozzle}, which indicates the flow regime (i.e., laminar, transitional or turbulent), and the upstream pressure (P_{up}, kPa), corresponding to the pressure conditions at the entrance of each nozzle, the Stokes number at 50% collection efficiency (Stk_{50}), which describes the inertial behavior of particles, and the aerodynamic cut-off diameter (D_{50}, μm), defined as the particle size for which the collection efficiency is 50%. The final row includes the pre-impactor stage, which removes coarse particles with diameters larger than 13.7 μm prior to entry into the cascade stages.

Table 19. *Operational characteristics of the low-pressure Berner cascade impactor.*

Stage	D_{Nozzle} (mm)	$N_{Nozzles}$	$S_{Jet\text{-}to\text{-}Plate}$ (mm)	Re_{Nozzle}	P_{up} (kPa)	Stk_{50}	D_{50} (μm)
1	0.289	262	0.99	461	17.74	0.198	0.026
2	0.315	127	0.95	872	29.90	0.213	0.062
3	0.343	65	0.74	1565	47.34	0.234	0.11
4	0.426	25	1.01	3275	77.19	0.235	0.173
5	0.531	16	1.24	4106	95.23	0.204	0.262
6	0.686	16	1.70	3178	100.47	0.194	0.46
7	0.711	46	2.28	1066	101.11	0.19	0.89
8	1.21	33	2.96	874	101.26	0.202	1.77
9	2.18	20	3.48	800	101.3	0.202	3.40
10	5.15	6	5.98	1129	101.32	0.190	6.80
Preimpactor	14.6	1	—	—	101.32	0.200	13.7

To improve collection efficiency and reduce particle rebound, the substrates used for impaction were Tedlar foils uniformly coated with a thin layer of Apiezon-L grease, prepared by dissolving the compound in toluene. This coating facilitates particle adhesion and reduces the likelihood of particle bounce-off, which could otherwise bias the size distribution and mass loading.

14.3.8 Micro-XRF Imaging of PM Samples

To evaluate the elemental inhomogeneity across the impactor stages and obtain quantitative data from the PM samples, micro-XRF imaging was employed on each collected filter substrate. The analysis was performed in a systematic three-step procedure:

- *Initial Filter Scanning and Visual Assessment*: Each filter, corresponding to a specific stage of the cascade impactor, was initially scanned using the micro-XRF spectrometer. A large-area mosaic (stitched) image was generated using the instrument's acquisition software, which enabled a visual inspection of the full deposition area and an assessment of the spatial distribution of particles. This preliminary scan facilitated the identification of regions containing distinct impaction spots.

- *Selection and Scanning of Impaction Spots (Active Surface Spot Area)*: Impaction spots were selected from each filter for detailed elemental mapping. The scanned area for each spot was defined based on the aerodynamic characteristics of the respective impactor stage. Specifically, the selected area was set to be 1.5 times the surface area of the nozzle opening for that stage. This choice ensured adequate coverage of the particle deposition region, capturing the entire spot impaction zone. The factor of 1.5 was

empirically chosen based on preliminary tests that demonstrated reliable coverage of the deposited aerosol while minimizing interference from surrounding blank areas.

– *Spectral Evaluation and Quantification*: Following each individual spot scan, the sum spectrum of all acquired pixels per spot was extracted and analyzed using the Artax 8.0 software (Bruker), which performed spectral deconvolution and peak fitting of the characteristic X-ray lines.

The scanning parameters of the micro-XRF spectrometer were optimized according to the impactor stage analyzed. This ensured a balance between spatial resolution, signal quality, and acquisition time, reflecting the variability in particle deposition across stages. Upper stages, which collect larger particles, displayed wider deposition areas, enabling quicker stage movement and reducing dwell times without sacrificing data quality. In contrast, lower stages exhibited smaller, denser spots with lower mass loading. To ensure sufficient counting statistics in these regions, scans were performed at slower stage speeds and longer dwell times. **Figure 62** shows a preliminary areal scan of a Tedlar filter from stage 8, conducted at a high stage speed (6.7 mm/s) and short dwell time (30 ms). The purpose of this quick scan was to obtain a quick qualitative overview of the elemental distribution of Si, Ca, S, K, and Fe. **Table 20** summarizes the measuring parameters applied for the systematic spot analyses.

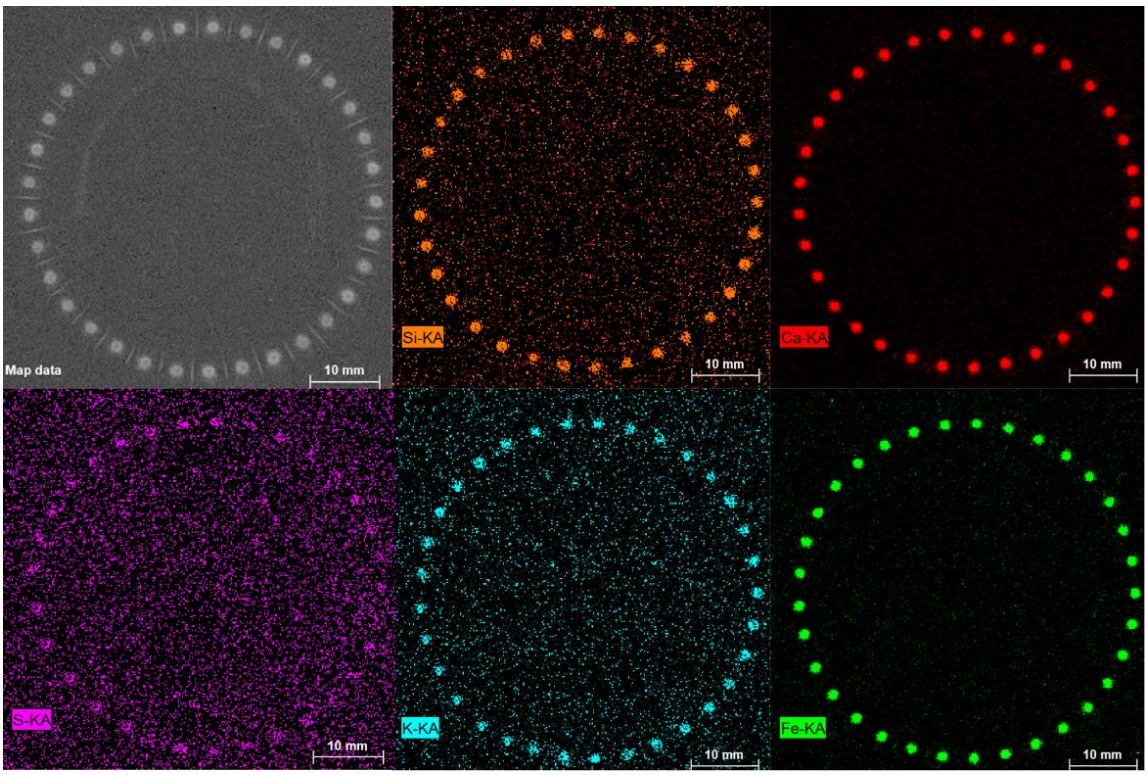

Figure 62. *Elemental distribution maps of a Tedlar filter collected from stage 8 of a Berner impactor. The maps represent the elemental distributions of Si-Kα (orange), Ca-Kα (red), S-Kα (purple), K-Kα (cyan), and Fe-Kα (green). Only 2% of the scanned area is covered by particle deposition.*

Table 20. *Measuring parameters of Set A. Pixel size (µm): dimension of each pixel. Summed area per spot (mm²): total square pixel grid used to cover each impaction spot. No. of pixels per spot: total pixels used to scan one impaction spot at each stage. No. of measured spots per stage: total spots analyzed per stage. Time per pixel (ms/pixel): integration time per pixel. Measuring time per spot (s): acquisition time for a single spot. Total time on spots (s): overall time for all spots in a given stage.*

		Stage Number									
	Measuring parameters	**10**	**9**	**8**	**7**	**6**	**5**	**4**	**3**	**2**	**1**
General	*Pixel Size (µm)*	200	100	100	100	100	100	100	100	100	100
	Summed area per spot (mm²)	64	11.6	3.2	1.2	1.0	0.81	0.49	0.36	0.25	0.25
	No. of pixels per spot	1600	1156	324	121	100	81	49	36	25	25
	No. of measured spots per stage	6	11	15	46	16	16	25	65	41	161
No Filer	*Time per pixel (ms/pixel)*	50	50	80	600	600	650	650	100	1200	1200
	Measuring time per spot (s)	80	58	26	73	60	53	32	36	30	30
	Total time on spots (s)	480	636	389	3340	960	842	796	2340	1230	4830
Filer $Al_{100}Ti_{25}$	*Time per pixel (ms/pixel)*	70	70	200	600	600	650	650	1000	-	-
	Measuring time per spot (s)	112	81	65	73	60	53	32	16	-	-
	Total Time on spots (s)	660	900	960	3360	960	840	780	1020	-	-

14.3.9 Estimating Elemental Concentration, Uncertainty and Inhomogeneity

Elemental concentrations from the micro-XRF spot scans were quantified by treating each scanned spot as an independent measurement with its associated statistical uncertainty. The fitted sum spectra provided elemental intensities, from which net intensities were obtained by subtracting the corresponding blank spectrum (greased Tedlar foil scanned under identical conditions). This procedure ensured that background contributions from the substrate and coating were removed prior to quantification. The corrected net intensities were then expressed as surface concentrations (x_{surf}, ng/cm²) based on the instrument calibration.

To calculate atmospheric concentrations (x, ng/m³), surface values were scaled by the summed area per spot and normalized to the corresponding sampled air volume:

$$x = x_{surf} \cdot \frac{Spot\ Area}{\left(\frac{Total\ Sampled\ Air\ Volume}{N_{nozzles}}\right)} \tag{42}$$

where,

- Total sampled air volume is the volume of air drawn through the impactor during sampling equal to 35.78 m³, and
- $N_{nozzles}$ is the total number of impaction nozzles per stage.

This formulation considers the effective air volume for each spot by assuming even flow distribution across the nozzles and equal deposition efficiency.

For each impaction stage, the atmospheric weighted mean concentration ($\overline{x_w}$) of an element was then calculated from the individual spot concentrations x_i and their statistical uncertainties (σ_i) using the following formula:

$$\overline{x_w} = \frac{\sum_{i=1}^{n} \frac{x_i}{\sigma_i^2}}{\sum_{i=1}^{n} \frac{1}{\sigma_i^2}} \tag{43}$$

with n representing the number of measured spots per stage. The corresponding uncertainty of the weighted mean was given by:

$$\sigma_{\overline{x_w}} = \frac{1}{\sqrt{\sum \left(\frac{1}{\sigma_i^2} \right)}} \tag{44}$$

To characterize the spatial inhomogeneity of elemental deposition across scanned spots, we employed the spot-to-spot Relative Standard Deviation (RSD%), calculated by:

$$RSD\ (\%) = 100 \times \frac{SD_{spot}}{\bar{x}} \tag{45}$$

where SD_{spot} is the standard deviation of the spot concentrations and $\bar{x}$ is the corresponding arithmetic mean. The RSD% indicates the level of spatial variability between spots and serves as a measure of inhomogeneity.

Limits of detection (LoDs) for each element were estimated at each stage based on background signal measurements from a large area of a blank Tedlar filter pre-coated with collection grease, using the same sample preparation method as for loaded filters. The LoD_{Bl} of the blank area was calculated based on Eq. (41). To determine the background signal, two large-area scans of the greased blank Tedlar filter were conducted under both measurement conditions. The no-filter and the $Al_{100}Ti_{25}$ filter conditions were used with identical pixel sizes, although the latter required longer integration times. These scans served as the reference background signals for LoD estimation, ensuring consistency with the conditions used in the sample analyses (**Table 21**).

Table 21. *Measuring parameters for the area scan of the greased blank Tedlar filter under no-filter and $Al_{100}Ti_{25}$ filter conditions. These scans were used to determine the background signal for LoD estimation.*

Measuring parameters	**Blank Area**	
	No Filter	**$Al_{100}Ti_{25}$**
Pixel Size (μm)	100	100
Time per pixel (ms/pixel)	50	70
Total Number of Pixels	12980	12980
Pixel width	110	110
Measuring Time (sec)	600	840

To account for the variation in dwell time between the reference blank and the individual sample spots, the LoD for each spot per stage was scaled as:

$$LoD_{spot} = LoD_{Bl}\sqrt{\frac{\Delta t_{Bl}}{\Delta t_{spot}}} \tag{46}$$

where Δt_{spot} is the dwell time per spot on the actual sample scan, and $\Delta t_{Bl\,total}$ is the total dwell time used for the blank scan. The areal LoDs were then converted to atmospheric units as well using Eq. (42).

Figure 63 presents the calculated detection limits in ng/m^3 for Si, S, K, Ca, Ti, V, and Fe across the ten stages of the Berner impactor. Each LoD value corresponds to measurements taken on a greased blank Tedlar filter and reflects the conditions used in actual sample analysis. The detection limits differ at each stage due to variations in acquisition time, scanned area, and measurement conditions.

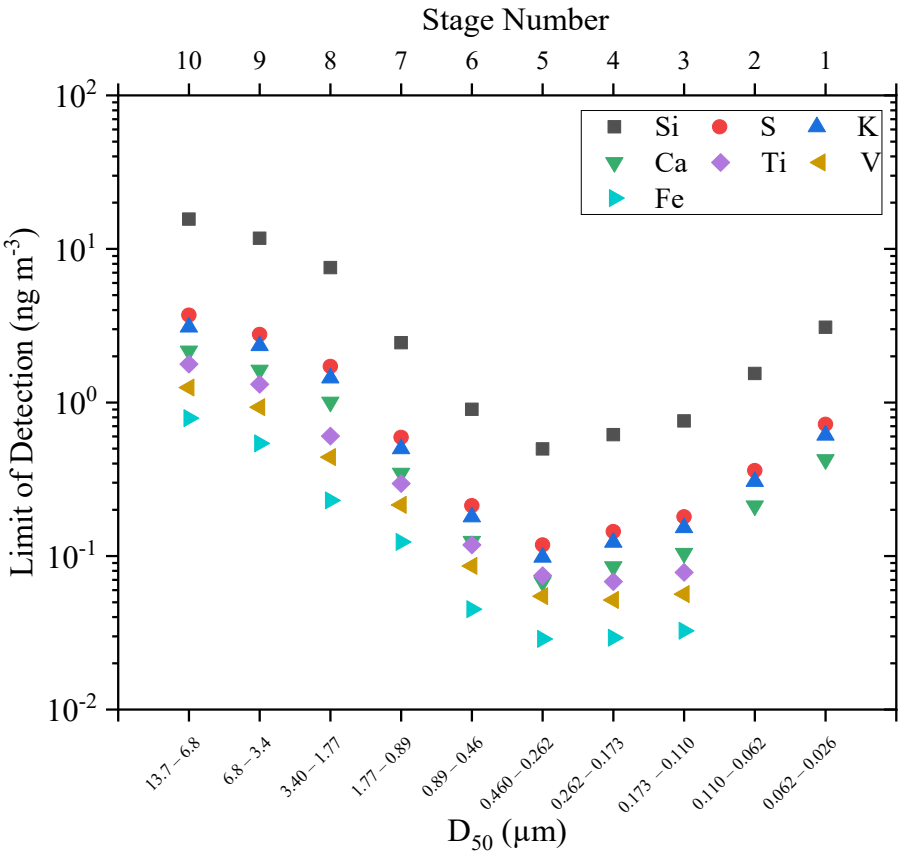

Figure 63. Element-specific detection limits (ng/m³) across aerodynamic particle sizes from Blank Tedlar filter scanning.

14.4 Results

14.4.1 High-Coverage Elemental Mapping Results (Filter set A)

Across all stages of the Berner impactor, a total of 402 impaction spots were analyzed out of 611 available in filter Set A (Stage 10 to Stage 1). This coverage provided a robust and representative view of elemental deposition across the full-size range of the impactor.

Figure 64 presents the size-resolved concentrations of all quantified elements detected in the Berner impactor stages, represented as box plots. The x-axis reflects the nominal cut-off diameter for each impactor stage (**Table 19**) while the y-axis reports elemental concentrations in ng m^{-3}. **Table 22** reports the underlying statistical parameters, including weighted mean concentrations ($\overline{x_w}$), their associated uncertainties ($\sigma_{\overline{x_w}}$), the LoD and LoQ values in ng/m³, and the relative standard deviations RSD (in %) that describe spot-to-spot inhomogeneity for each element and stage. **Figure 65** and **Figure 66** illustrate representative elemental distribution maps of Si, S, K, Ca, Ti, and Fe obtained from a large section of the Tedlar filter at Stage 9, together with the corresponding sum spectra from selected impaction spots and a blank area.

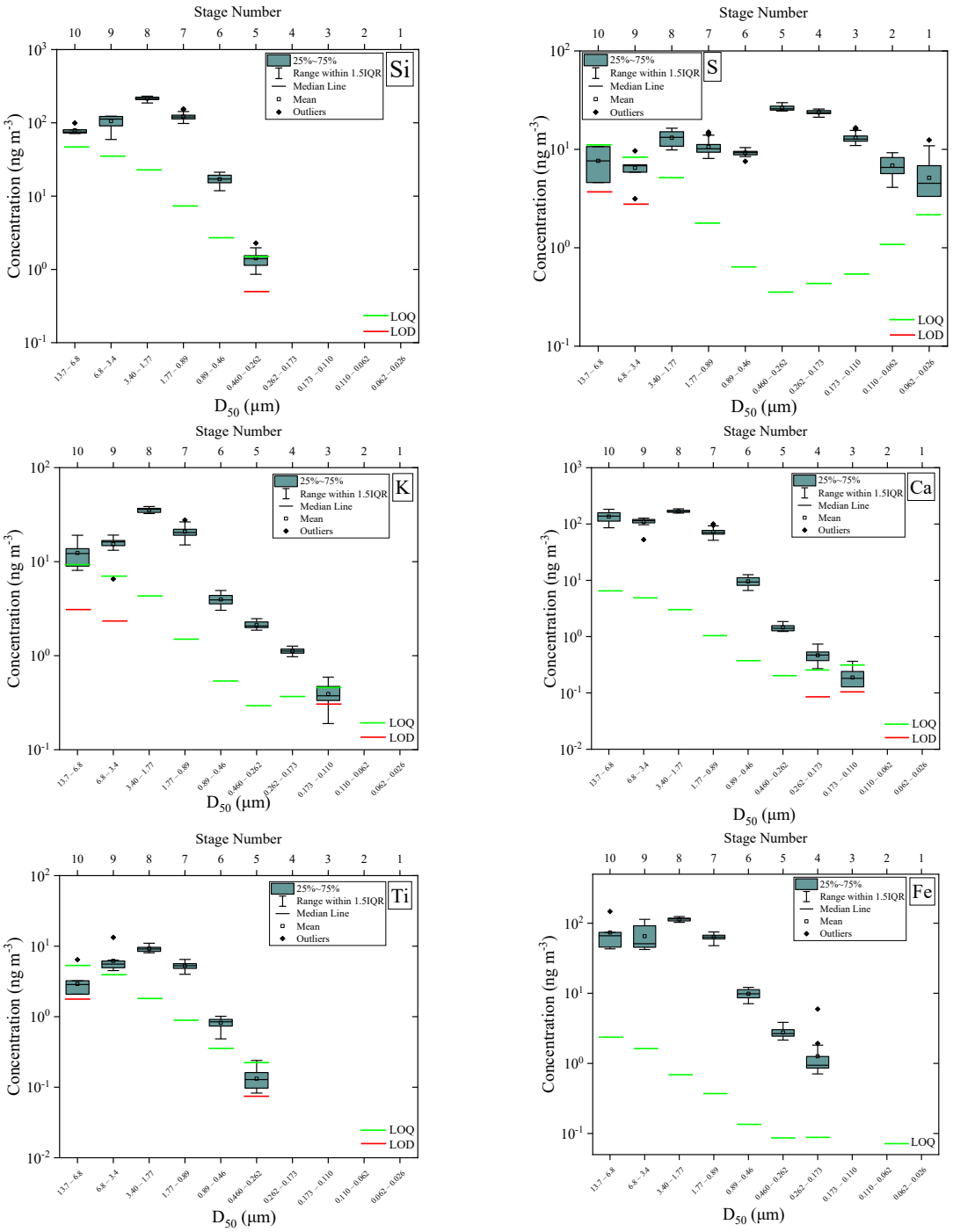

Figure 64. *Size-resolved elemental concentrations (ng/m³) of Si, S, K, Ca, Ti, and Fe from filter Set A are shown as box plots. Each box represents the interquartile range (25–75%), which contains the middle 50% of the data (from Q1 to Q3). The horizontal line inside the box indicates the median, while the square marker shows the mean concentration. Whiskers extend to the lowest and highest data points within 1.5 times the IQR from the box, including most data points. Values beyond this range are plotted as outliers. This format clearly visualizes the dataset's variability and highlights potential anomalies in elemental concentrations across particle sizes. The green and red lines represent the LoQ and LoD values, respectively. The LoD values are shown only in stages where concentrations are close or below LOQ values.*

Table 22. *Weighted mean atmospheric concentrations ($\overline{x_w}$, ng/m³) and their associated uncertainty ($\sigma_{\overline{x_w}}$, ng/m³), along with LOD (ng/m³), LOQ (ng/m³), and spot-to-spot variability (RSD) of selected elements across the stages of the Berner impactor. RSD (%) represents the relative standard deviation of analyzed impaction spots, indicating spot-to-spot variation. No values are provided when the elemental concentration is below the detection limit.*

Element	Stage	10	9	8	7	6	5	4	3	2	1
Si	$\overline{x_w}$	78.4	98.7	213.8	117.7	25.1	1.4	-	-	-	-
	$\sigma_{\overline{x_w}}$	3.4	2.2	2.0	0.4	0.2	0.1	-	-	-	-
	LOD	15.6	11.7	7.6	2.5	0.9	0.5	0.6	0.8	1.5	3.1
	LOQ	46.9	35.2	22.7	7.3	2.7	1.5	1.9	2.3	4.6	9.3
	RSD %	13	18	6	10	17	30	-	-	-	-
S	$\overline{x_w}$	7.6	6.4	13.1	10.2	13.8	26.4	22.7	12.6	6.5	4.5
	$\sigma_{\overline{x_w}}$	1.3	0.6	0.3	0.1	0.1	0.1	0.1	0.1	0.1	0.1
	LOD	3.71	2.78	1.72	0.59	0.21	0.12	0.14	0.18	0.36	0.72
	LOQ	11.12	8.33	5.16	1.78	0.64	0.35	0.43	0.54	1.08	2.16
	RSD %	56	35	16	16	8	7	5	12	21	46
K	$\overline{x_w}$	12.3	14.3	35.4	20.1	5.90	2.10	1.10	0.40	-	-
	$\sigma_{\overline{x_w}}$	0.7	0.4	0.3	0.1	0.03	0.01	0.01	0.01	-	-
	LOD	3.10	2.34	1.44	0.50	0.18	0.10	0.12	0.15	0.31	0.61
	LOQ	9.29	7.02	4.32	1.50	0.54	0.29	0.37	0.46	0.92	1.84
	RSD %	32	22	6	12	15	9	7	28	-	-
Ca	$\overline{x_w}$	131.7	98.7	167.6	69.3	13.9	1.4	0.4	0.2	-	-
	$\sigma_{\overline{x_w}}$	0.7	0.4	0.4	0.1	0.03	0.1	0.1	0.1	-	-
	LOD	2.17	1.63	1.01	0.35	0.12	0.07	0.09	0.10	0.21	0.42
	LOQ	6.50	4.88	3.02	1.04	0.37	0.20	0.26	0.31	0.64	1.27
	RSD %	25	19	5	14	21	15	26	30	-	-
Ti	$\overline{x_w}$	3.0	5.8	9.1	5.20	1.20	0.13	-	-	-	-
	$\sigma_{\overline{x_w}}$	0.2	0.2	0.1	0.04	0.02	0.01	-	-	-	-
	LOD	1.78	1.31	0.60	0.30	0.12	0.07	0.07	0.08	-	-
	LOQ	5.33	3.94	1.81	0.89	0.35	0.22	0.20	0.23	-	-
	RSD %	35	37	12	15	27	47	-	-	-	-
V	$\overline{x_w}$	-	-	-	0.44	0.14	0.18	0.20	0.11	-	-
	$\sigma_{\overline{x_w}}$	-	-	-	0.01	0.01	0.01	0.01	0.01	-	-
	LOD	1.25	0.93	0.44	0.22	0.09	0.05	0.05	0.06	-	-
	LOQ	3.75	2.79	1.32	0.65	0.26	0.16	0.15	0.17	-	-
	RSD %	-	-	-	74	51	28	75	97	-	-
Fe	$\overline{x_w}$	62.8	58.2	112.9	62.6	14.4	2.7	1.00	-	-	-
	$\sigma_{\overline{x_w}}$	0.5	0.3	0.3	0.1	0.04	0.1	0.01	-	-	-
	LOD	0.79	0.54	0.23	0.12	0.04	0.03	0.03	-	-	-
	LOQ	2.37	1.62	0.69	0.37	0.13	0.09	0.09	-	-	-
	RSD %	51	39	6	8	17	18	34	-	-	-

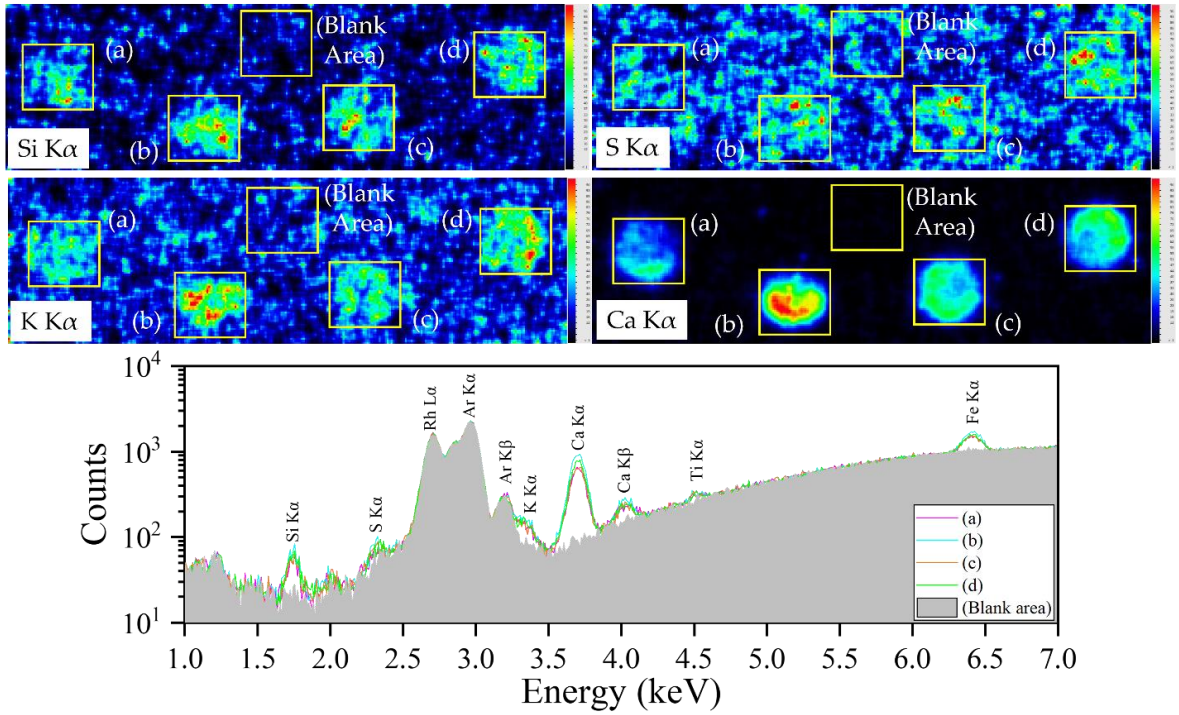

***Figure 65**. Elemental distributions of Si Kα, S Kα, K Kα, and Ca Kα measured with no filter conditions from a section (27.9mm×8.35 mm) of the Tedlar filter collected on Stage 9. The area was scanned with a pixel size of 100 µm and a dwell time of 50 ms per pixel. The total scan duration was 21 minutes. The XRF sum spectra of the four impaction spots (a-d) and blank area, marked with yellow rectangle areas are displayed.*

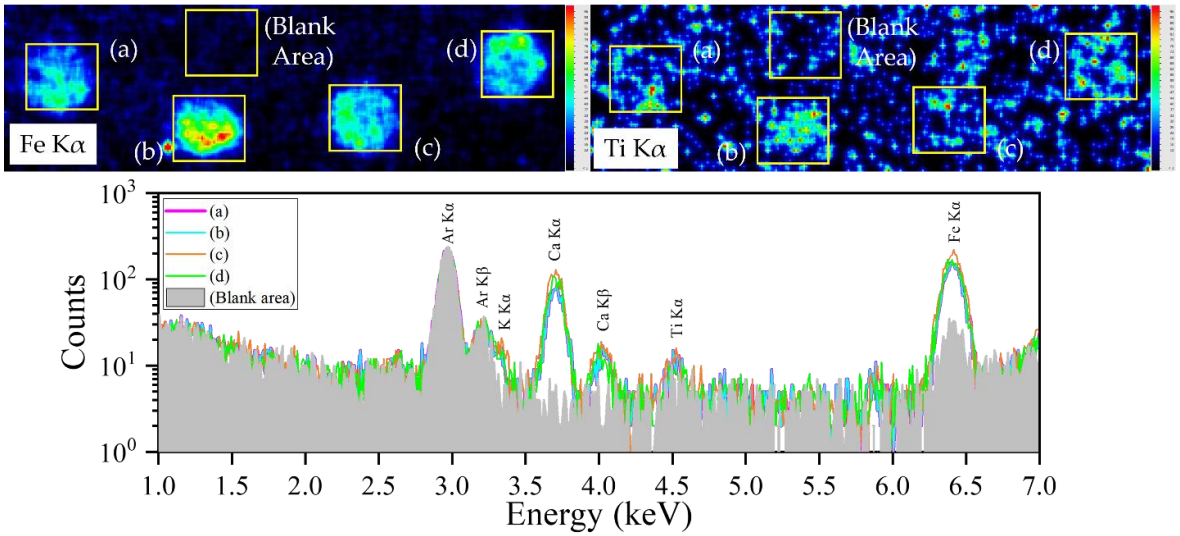

***Figure 66**. Elemental distributions of Fe Kα and Ti Kα measured with the $Al_{100}Ti_{25}$ filter conditions from a section of the Tedlar filter collected on Stage 9. The area was scanned with a pixel size of 100 µm, a dwell time of 50 ms per pixel. The total scan duration was 26 minutes. The XRF sum spectra of the four impaction spots (a-d) and blank area, marked with yellow rectangle areas are displayed.*

Silicon (Si) atmospheric concentrations are listed in **Table 22** and shown in **Figure 64**. Silicon was detected at all stages between 10 and 5. In these stages, except stage 5, the mean concentrations were above the LoQ value. No silicon was detected in stages 4 through 1. The highest mean concentration was observed at stage 8, reaching 214(2) ng/m³, followed by stage

9 with 99(2) ng/m³. As particle size decreased, Si concentrations diminished, dropping below 2.0 ng/m³ at stage 5. Overall, the presence of high concentrations in coarse stages aligns with the expected behavior of Si-rich aerosols from mineral dust or resuspended soil particles. (Viana et al., 2008, Gini et al., 2022).

Concerning the spot inhomogeneity, the RSD values for each stage are presented in **Table 22**, complemented by a quantitative overview in **Figure 64**. Coarse-mode stages 10 and 9 exhibited RSDs of 13% and 18%, respectively. The Si Kα distribution map for four spots of stage 9, and the corresponding average spectra, are shown in **Figure 65**. Stage 8, with the highest Si concentration, exhibited the most uniform spatial distribution, characterized by an RSD of 6%, indicating minimal spot-to-spot variation (min–max: 183–227 ng/m³). Overall, the RSD values for stages 10 to 6 range from 6% to 17%, indicating small spot-to-spot variability (good spot-to-spot homogeneity). The highest RSD value of 30% is observed at stage 5, which can be attributed to the fact that the extracted mean value is smaller than the LOQ value.

Calcium (Ca) concentrations exhibited a well-defined size-dependent trend, with significantly elevated levels in the coarse particle fraction and a progressive decrease toward finer stages, like Si (**Figure 64**). In stage 3, the detected concentration is above the LOD value but below the LOQ, while no calcium was detected in stages 1 and 2. The extracted concentration values for the remaining stages are higher than the LOQ levels (**Table 22**). The highest weighted mean concentration was observed at stage 8, with a value of 167.6 (4) ng/m³. The extracted concentrations for stages 5 and 4 were found to be as low as 1.4(1) and 0.4(1) ng/m³, respectively, indicating negligible contribution to the fine-mode fraction. These results collectively support the view that Ca is dominantly coarse in nature, consistent with mineral dust origin (Manousakas et al., 2018), and that its deposition tends to be markedly non-uniform in stages where mass loading is higher.

Regarding the spot-to-spot inhomogeneity, the RSD values for each stage are presented in **Table 22**, accompanied by a quantitative overview in **Figure 64**. Coarse-mode stages 10 (**Figure 67**) and 9 (**Figure 65**) showed RSDs of 25% and 19%, with min–max ranges of 86-182 ng/m³ and 119–285 ng/m³, respectively, indicating moderate spot-to-spot homogeneity across the coarse stages. Stage 7 had an RSD of 14%, with concentrations ranging from 51 to 100 ng m^{-3}. Overall, the RSD values range from 6% to 30%, indicating good to moderate spot-to-spot homogeneity.

Besides spot-to-spot variability, the elemental maps of Ca at stages 10 (**Figure 67**) and 9 (**Figure 65**) show substantial inhomogeneity within each spot. Individual impaction spots exhibit uneven Ca distributions, characterized by distinct shapes and localized enrichment zones. Such heterogeneity shows that particle deposition occurs in clusters rather than forming a uniform layer. This observation is especially important for micro-analytical techniques with very narrow beam sizes, such as micro-PIXE techniques (Angyal et al, 2024; Usui et al., 2023), when a single sub-area is scanned. In such cases, results may be biased if the probed region overlaps with either a hot spot or a depleted area. In contrast, micro-XRF imaging systematically covers the entire spot, averaging local heterogeneities and yielding more representative elemental concentrations.

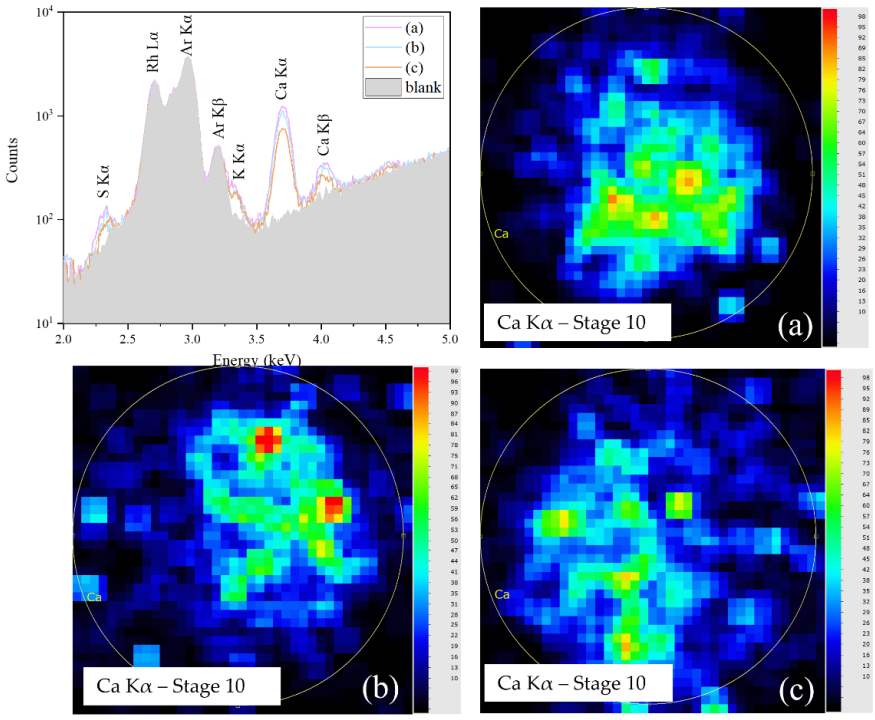

Figure 67. *XRF sum spectra (top left) from three scanned spots on Stage 10, showing variations in Ca Kα intensity among the spots (8.0 mm×8.0 mm, yellow circles with a diameter of 7.7 mm). The Ca Kα intensity distribution maps reveal uneven spatial deposition of Ca. The elemental maps were acquired with a pixel size of 200 µm, a dwell time of 50 ms per pixel. The total acquisition time for each scanned area is 80 seconds.*

Potassium (K) atmospheric concentrations are listed in **Table 22** and shown in **Figure 64**. Potassium was detected nearly at all stages, ranging from 10 to 3. In these stages, except for stage 3, the concentrations were above the LOQ value. No potassium was detected in stages 2 and 1. The highest mean concentration was observed at stage 8, reaching 35.4(3) ng/m³. As particle size decreased, K concentrations reduced significantly, dropping to 1.1(1)g/m³ at stage 4. The value of 0.4(1)g/m³ at stage 3 is higher than the LOD value, but lower than the LOQ. These results indicate that K is present in both coarse and fine particle fractions, though with a clear dominance in the coarser stages. Its presence is due to anthropogenic sources (e.g., biomass combustion, industrial processes) and natural inputs (e.g., resuspended soil or ash) (Diapouli et al., 2017; Papagiannis et al., 2024).

Regarding the spot-to-spot inhomogeneity, the RSD values for each stage are presented in **Table 22**, accompanied by a quantitative overview in **Figure 64**. At stage 8, where concentrations were highest, the RSD was only 6%, indicating tightly clustered values (33–39 ng/m³) and consistent deposition (**Figure 68**). In contrast, stage 9 showed a higher RSD of 22%, as also demonstrated by the elemental distribution maps in **Figure 65**, which indicate significant variability among the four scanned impact spots. The highest RSD value of 32% was observed in stage 10, with values ranging from 8 to 19 ng/m³. Overall, the RSD values range from 6% to 32%, indicating moderate to good spot-to-spot homogeneity.

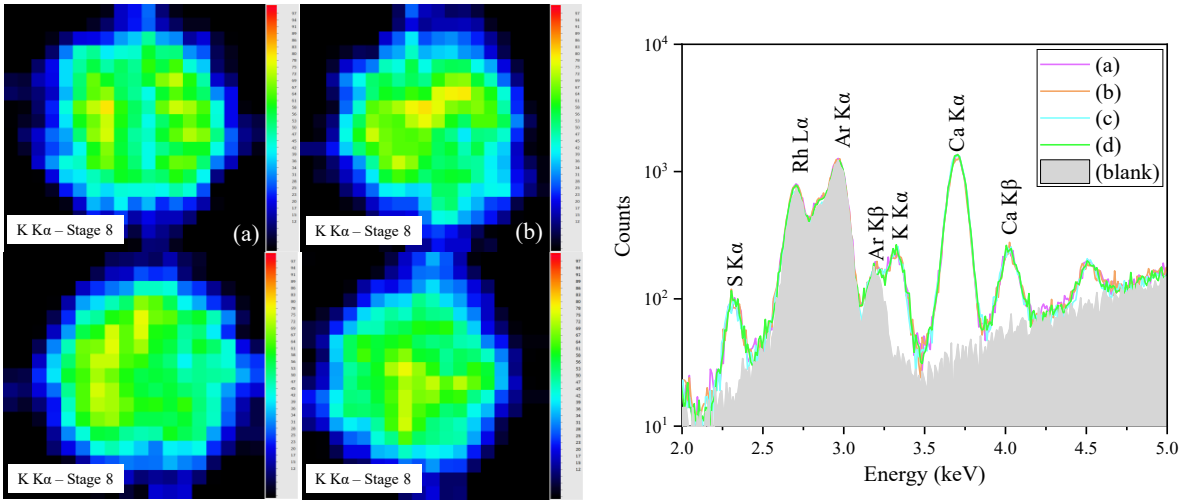

Figure 68. *K Kα elemental distribution maps from four individual impaction spots collected on Stage 8 of the Tedlar filter (a–d). Each scanned spot measures 1.9 mm × 1.9 mm. The corresponding XRF mean sum spectra for each spot are shown on the right side, confirming the presence of consistent Kα intensities (RSD 6%). The elemental maps were collected with a pixel size of 100 µm, a dwell time of 80 ms per pixel, and a total acquisition time of 40 seconds per spot.*

Sulfur (S) exhibited a broader size distribution than other crustal-related elements, being consistently detected across all stages of the cascade impactor. The highest weighted mean concentrations were observed at Stage 5 (26.4(1) ng/m³) and Stage 4 (22.7(1) ng/m³), corresponding to aerodynamic diameters of approximately 0.26 µm and 0.17 µm, respectively. These were followed by moderate levels at Stage 8 (13.1(3) ng/m³) and Stage 7 (10.2(1) ng/m³). Even at the finest stages, sulfur remained detectable, with concentrations of 6.5(1) ng/m³ at Stage 2 and 4.5(1) ng/m³ at Stage 1. These values, though lower in magnitude, remained above the respective detection limits, confirming sulfur's presence even in the sub-100 nm fraction. It has to be noted that Sulfur was the only element consistently detected in both of the final stages, underlining its fine-mode dominance and distinct behavior compared to other elements. This pattern reflects its diverse sources and atmospheric processing: fine sulfur primarily originates as secondary sulfate aerosols from SO_2 oxidation, while coarse contributions may arise from marine aerosols or heterogeneous reactions on mineral dust (Galindo et al., 2008; Groma et al., 2022).

Concerning the spot-to-spot inhomogeneity, the RSD values for each stage are presented in **Table 22**, and they are displayed in **Figure 64**. Coarse-mode stages 10 and 9 showed high variability, with RSDs of 56% and 35% (min–max: 5–11 ng/m³ and 7–22 ng/m³, respectively). The fine-mode stages 2 and 3 also exhibited RSDs of 21% and 12%, while Stage 1 reached 46%, reflecting stronger variability at very small particle sizes (**Figure 69**). By contrast, Stages 4, 5, and 6 showed low variability, with RSD values below 10% and narrow min–max ranges (e.g., 25–30 ng/m³ at Stage 5), indicating good spot-to-spot uniformity.

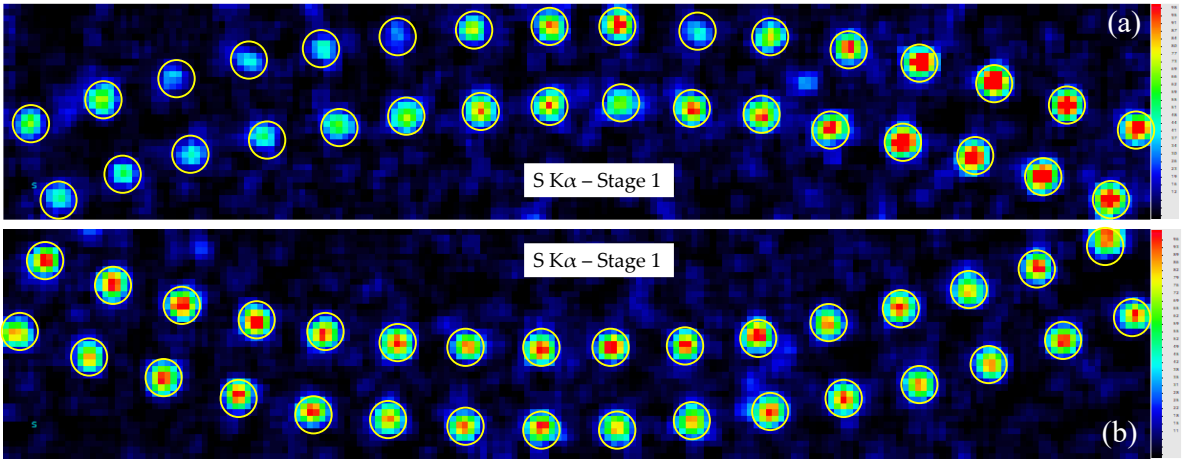

Figure 69. *S Kα elemental distribution maps from two sections of the Tedlar filter collected on Stage 1, the lowest aerodynamic size range of the cascade impactor. The scanned areas' dimensions are 18.6 mm×3.5 mm, and individual impaction spots are highlighted with yellow circles of 0.43 mm diameter. Each map was acquired with a pixel size of 100 μm and a dwell time of 1.2 sec per pixel. The total scan duration for each section is 140 minutes. Notable inhomogeneities are visible at section (a).*

Titanium (Ti) was detected from stage 10 down to stage 5. At stages 9 and 8, the extracted concentrations were above the LoQ, reaching weighted mean values of 5.8(2) and 9.1(1) ng/m³, respectively. Stage 7 also showed a mean concentration of 5.20(4) ng/m³, clearly above the LoQ, while stage 6 presented a lower but still quantifiable value of 1.20(2) ng/m³. Stage 10, in contrast, yielded a concentration of 3.0(2) ng/m³, which lies above the LoD but below the LoQ. Finally, stage 5 exhibited a very low concentration of 0.13(1) ng/m³, which is above the LoD but below the LoQ. No Ti was detected in the finer stages 4–1. The highest atmospheric weighted mean concentration was recorded at stage 8, closely followed by stage 9, indicating a dominant contribution from the coarse-mode fraction, consistent with mineral dust origin and crustal material inputs. (Manousakas et al., 2017).

Concerning the spot-to-spot inhomogeneity, the RSD values for each stage are presented in **Table 22**, complemented by a qualitative overview in **Figure 64**. The coarse-mode stages showed relatively high variability, with RSDs of 35% and 37% for stages 10 and 9, respectively. Stage 8 exhibited lower variability (RSD = 12%), while stages 7 and 6 had higher scatter, with RSDs of 27% and 47%, respectively. The elemental maps of Stage 6 Ti deposition in **Figure 70** offer an explicit visual confirmation of this variability. The Ti Kα distribution across the three scanned impaction spots shows substantial intensity differences and uneven morphologies, consistent with the elevated RSD. This heterogeneous deposition is also visible at Stage 9 (**Figure 66**), where large-scale elemental distribution maps show localized enrichment zones and uneven particle deposition. These results show that Ti is marked by significant spatial inhomogeneity across coarse-mode spots, especially at stages with concentrations near the LOQ.

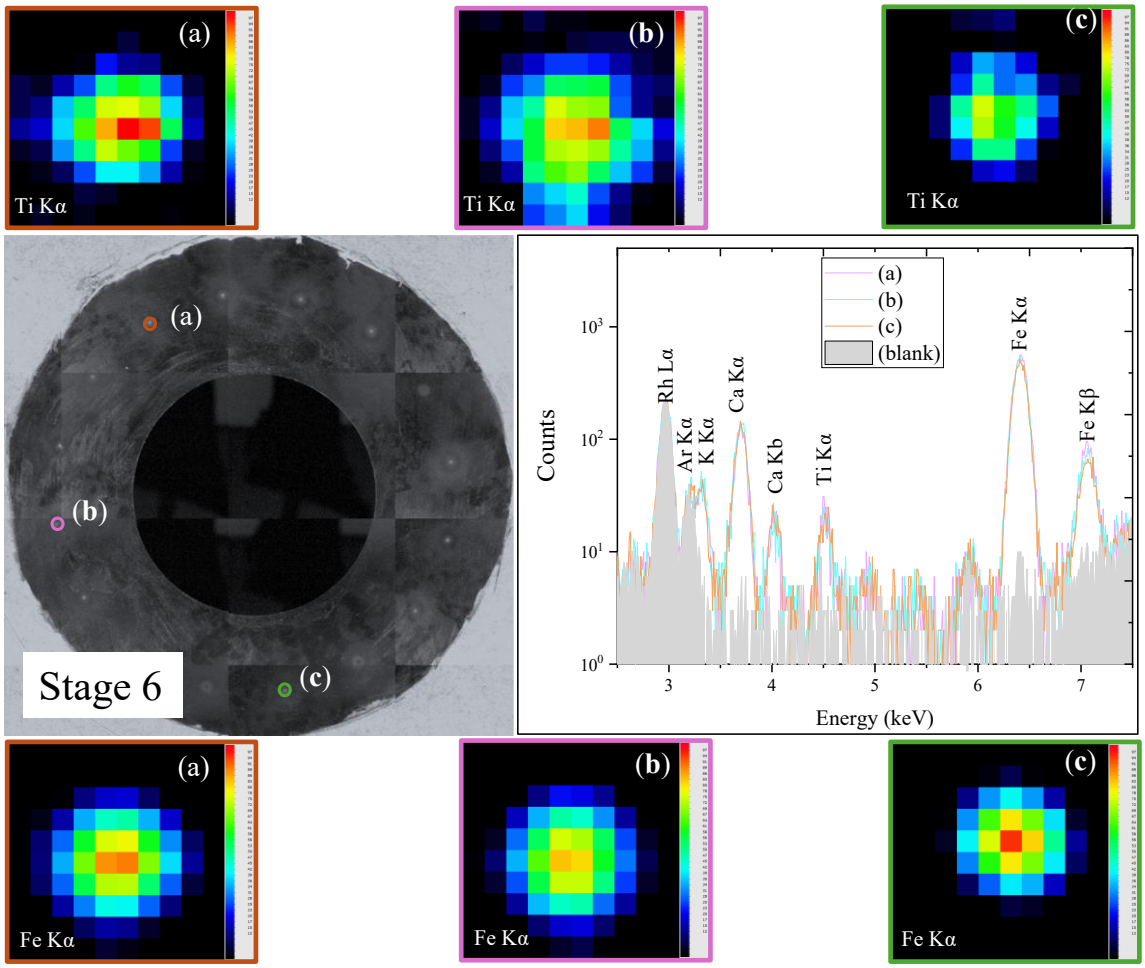

Figure 70. *Overview of the full filter from Stage 6, reconstructed from stitched optical scans generated by the micro-XRF system software. Highlighted regions (a), (b), and (c) indicate selected areas where localized elemental distribution maps of titanium (Ti Kα, upper panels) and iron (Fe Kα, lower panels) were extracted (Height: 1.0 mm, Width: 1.0 mm). Each map is paired with its corresponding summed XRF spectrum. Elemental mapping was performed using a pixel size of 100 µm, a dwell time of 600 ms per pixel, a stage speed of 167 µm/s, and a total acquisition time of 60 seconds per mapped area.*

Iron (Fe) was by far the most abundant of the measured elements, with concentrations consistently exceeding those of titanium and vanadium across all impactor stages (**Table 22**, **Figure 64**). The highest atmospheric weighted mean concentration was observed at Stage 8, reaching 112.9(3) ng/m³, followed by Stage 10 with 62.8(5) ng/m³, Stage 7 with 62.6(1) ng/m³, and Stage 9 with 58.2(3) ng/m³. Stage 6 showed lower but still significant concentrations of 14.40(4) ng/m³, while contributions from the fine mode decreased gradually, with Stage 5 and Stage 4 resulting in 2.7(1) ng/m³ and 1.00(1) ng/m³, respectively. No Fe was detected in the three smallest stages (3–1). Overall, Fe is mainly associated with crustal aerosols, originating from mineral dust, resuspended soil, and mechanical abrasion processes. (Viana et al., 2008; Grigoratos & Martini 2015).

Regarding spot inhomogeneity, the RSD values for each stage are listed in **Table 22** and are displayed in **Figure 64**. The coarse stages exhibited moderate-to-high variability, with RSDs of 51% and 39% for Stages 10 and 9, respectively. This heterogeneity is clearly reflected in the elemental distribution maps of Stage 9 (**Figure 66**), where the four scanned impaction spots display substantial differences in Fe intensity and morphology. Within-spot inhomogeneity is also evident, with Fe distributions inside individual deposits and the

presence of a small additional spot outside the marked rectangles (adjacent to spot b), confirming the irregularity of particle deposition. By contrast, Stages 8 and 7 showed considerably lower scatter (RSDs of 6% and 8%), indicating a relatively uniform deposition of Fe across impaction spots. Variability increased again at smaller sizes, with Stages 6, 5, and 4 recording RSDs of 17%, 18%, and 34%, respectively. The elemental maps from Stage 6 (**Figure 70**) confirm this trend, showing differences in Fe Kα distribution between the three scanned spots.

Vanadium (V) was detected at trace levels in the intermediate stages of the Berner impactor, specifically between Stages 7 and 3 (**Table 22**). The highest weighted mean concentration was observed at Stage 7 with 0.44(1) ng/m³, while the lowest was measured at Stage 3 with 0.11(1) ng/m³. The concentrations at Stages 4–6 remained within a narrow range (0.14–0.20 ng/m³). In all cases, the extracted values were above the LODs but remained below the LOQs, except for Stage 4, which approached the quantification threshold. A box plot for V is shown in **Figure 71** (left), illustrating these near-threshold levels. No V was detected in the coarse particle fraction (Stages 10–8) or the two finest stages (2–1). Although concentrations were very low, the detection of V in the fine fraction is noteworthy given its toxicological relevance (Rojas-Lemus et al., 2021) and its role as a marker of combustion-related aerosols (Almeida et al., 2020).

Concerning the spot-to-spot variability, the RSD values for Stages 7–3 were very high, ranging from 28% (Stage 5) to 97% (Stage 3). Such significant variability is primarily an artifact of the extremely low concentration levels, which are below the LOQ levels. **Figure 71** (right) presents an elemental distribution map from a single spot at Stage 4. Despite the very low concentrations, the V Kα signal is clearly visible, demonstrating the capability of micro-XRF imaging to detect and spatially resolve elemental deposition even at very low concentrations.

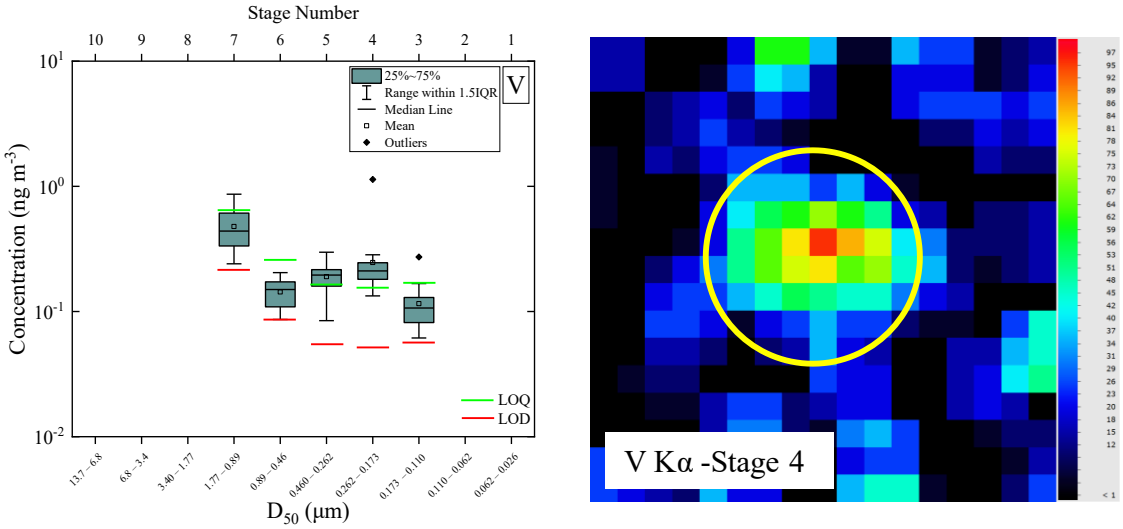

Figure 71. Left) Size-resolved elemental concentrations (ng/m³) of V from filter Set A are shown as box plots. Right) V Kα elemental distribution map collected on Stage 4. The scanned area dimensions are 1.7 mm × 1.7 mm, and the impaction spot is indicated with a yellow circle of 0.64 mm diameter. The map was acquired with a pixel size of 100 µm, a dwell time of 650 ms per pixel, a stage speed of 154 µm/s, and a total scan duration of approximately 3 minutes.

14.4.2 Filter Sets B and C

To verify the results drawn from Filter Set A, we extended the micro-XRF analysis to two additional sets of Berner impactor Tedlar filters, referred to as Filter Sets B and C. Although these two sets were scanned with lower spatial coverage, they provided valuable confirmation of the main trends observed in Set A, particularly regarding elemental size distributions and the degree of deposition inhomogeneity. The results from both sets aligned well with the patterns seen previously.

Silicon concentrations were highest in the coarse-mode stages 10 to 8, confirming its crustal origin. Spatial variability appeared lower in B and C, as reflected in the RSD values. For example, RSD% at stage 10 reached 47% in Set B and 173% in Set C, compared to Set A where values were more moderate.

The behavior of Ca was also consistent across all sets. Set A showed dominant peaks in stages 8 to 10, accompanied by high spatial variability. This was matched by Set B, where coarse-mode concentrations reached 135.7 ng m^{-3}, and by Set C, where RSD values reached up to 77% at stage 10, confirming that coarse Ca deposition remains highly uneven.

K also followed a similar distribution across all filters. In Set A, it was most abundant in the coarser stages, with localized variability. This was confirmed in Set B, where variability remained high, and in Set C, where despite lower absolute concentrations, the spread was still significant (e.g., RSD = 20% at stage 7).

S again showed fine-mode dominance, with stage 5 registering the highest values in Sets B and C (71.2 and 69.4 ng m^{-3}, respectively), similar to Set A. Inhomogeneity remained high, particularly in the finer stages. For example, RSD% reached 132% at stage 4 (B) and 28% at stage 1 (C).

Ti was most prominent in the coarse stages, especially stage 8, with concentrations around 5–9 ng m^{-3} across all sets. Variability remained moderate, with RSD values between 21% and 37%, showing some inhomogeneity but less extreme than for other elements.

V remained in the finer stages across all filters, mostly below 1 ng m^{-3}. RSD values were sometimes very high (e.g., above 100% in stage 3 of Set B), likely reflecting low signal levels and detection challenges rather than true spatial inhomogeneity.

Fe was again the most abundant element in all three sets, with clear peaks in the coarse stages. In Set B, stage 10 reached 105.1 ng m^{-3}, and in Set C, 47.8 ng m^{-3}. Variability was also pronounced, with RSD values exceeding 60% in some higher, confirming highly uneven deposition such as in the case of Set A.

14.4.3 Elemental Size Distributions

The elemental mass size distributions for Si, S, K, Ca, Ti, and Fe are presented in **Figure 72**. The graphs display the normalized mass concentration (dM/dlogdp, in ng m^{-3}) as a function of the aerodynamic diameter (d_a, in µm). In this notation, dM represents the differential mass concentration measured within a specific size bin, and dlogdp denotes the logarithmic width of that size interval (where dp corresponds to the particle diameter). This normalization is essential to compensate for the varying widths of the impactor stages, ensuring that the area under the curve accurately represents the total atmospheric mass concentration of the element. The term d_a refers to the aerodynamic diameter of the sampled aerosol particles.

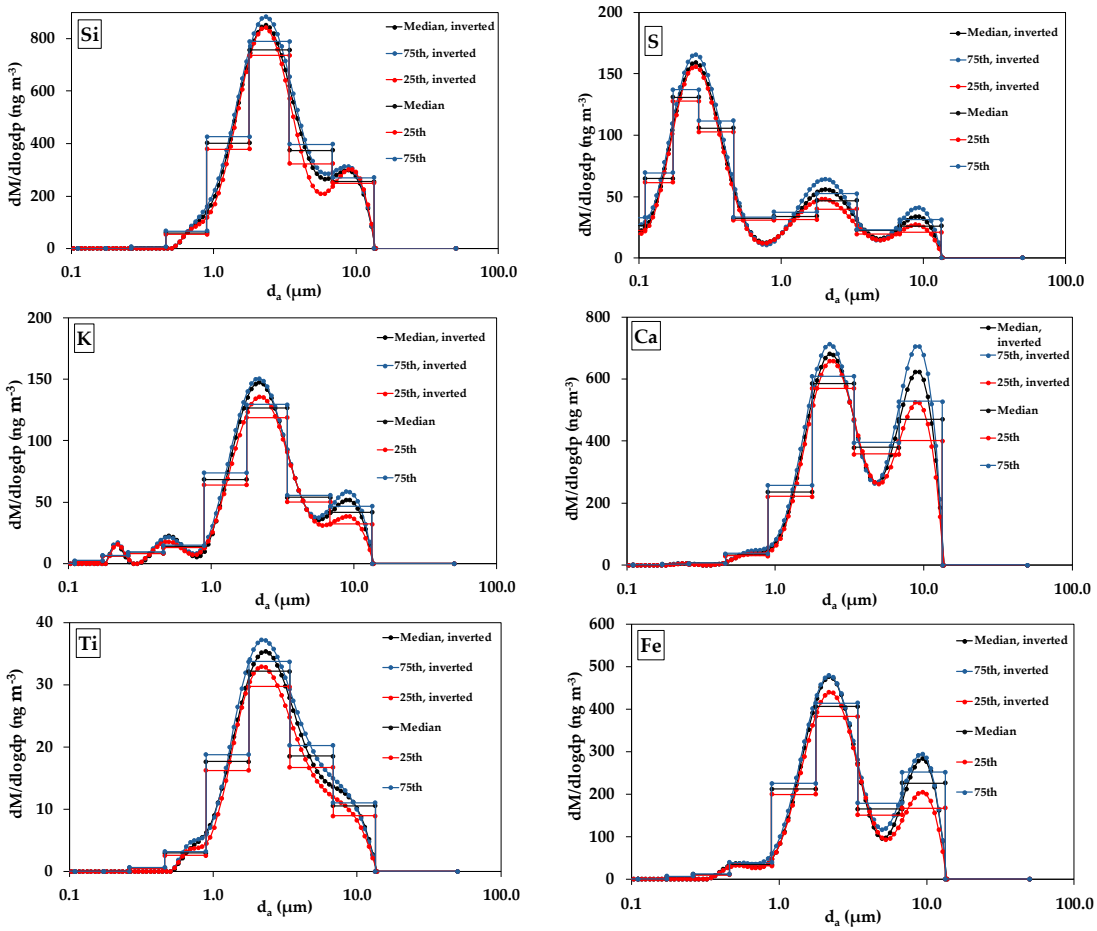

Figure 72. Elemental mass size distributions for Si, S, K, Ca, Ti and Fe.

The histograms (stepped lines) in the figures represent the raw experimental data derived from the Berner impactor stages, while the smooth curves represent the numerically inverted distributions. Taking into account the collection efficiency curves of the Berner low-pressure impactor, the initial mass and elemental size distributions (step function) were inverted into smooth size distributions using the MICRON (Multi-Instrument-inversion using

Constrained Regularization) inversion algorithm (Wolfenbarger and Seinfeld, 1990; Gini et al., 2022). These inverted curves correct for the specific collection efficiency functions of the impactor, providing a physically continuous representation of the aerosol size fractions. The black curve (Median) represents the typical elemental distribution, calculated from the multiple impaction spots measured on each stage. The blue (75th percentile) and red (25th percentile) curves indicate the upper and lower range of concentrations found among these spots. The characteristics of the size distributions confirm the distinct source origins of the analyzed elements

Silicon (Si) and Titanium (Ti): These elements exhibit a unimodal distribution with a dominant peak in the coarse mode range (2–6 μm). This profile is characteristic of mechanically generated particles, such as soil resuspension and mineral dust.

Calcium (Ca): The size distribution of calcium is bimodal within the coarse fraction. It displays a primary peak centered at approximately 2–3 μm and a secondary, distinct peak in the larger coarse range around 8–10 μm. This structure suggests contributions from different mechanical generation processes or mineralogical sources within the dust fraction.

Iron (Fe): While Fe largely follows the crustal pattern with a dominant coarse mode peak at roughly 3 μm, it notably displays a secondary shoulder in the fine particle size range (< 1 μm). This fine-mode contribution suggests an anthropogenic component, likely associated with combustion processes or non-exhaust traffic emissions such as brake wear.

Sulfur (S): The sulfur distribution is dominated by a fine mode peak centered at 0.3–0.4 μm. This is consistent with secondary inorganic aerosols (sulfates, SO_4), formed through the chemical aging and oxidation of gaseous precursors like SO_2 from anthropogenic emissions. A minor coarse mode is also observed, potentially attributable to sulfates formed via heterogeneous reactions on mineral dust particles or sea-salt interactions.

Potassium (K): Potassium displays a clear bimodal distribution. The fine mode peak (approx. 0.4 μm) serves as a tracer for biomass burning, while the coarse mode peak is associated with crustal dust and soil resuspension.

14.5 Conclusions

Non-destructive micro-XRF imaging is employed to analyze the spatial distribution of elements in size-segregated atmospheric aerosols collected with a 10-stage Berner cascade impactor. The aim is to determine the atmospheric mass concentration of the detected elements at each stage. Furthermore, the variability of deposition within each spot and between different spots on filter surfaces is analyzed.

The spectrometer's elemental sensitivity was optimized by using different X-ray ionization photon distributions to improve its detection capabilities. The background was measured with blank samples. Each spot was analyzed under both beam conditions. The atmospheric mass concentration of light elements, such as silicon, was measured. Additionally, the spatial resolution was assessed. The spatial resolution of the scans was sufficient to detect variations within individual impaction spots, enabling the identification of localized enrichments and uneven deposition patterns.

Three sets of impactor samples were analyzed, each comprising ten Tedlar filters designed to capture particles ranging from 13.7 μm (Stage 10) to 0.026 μm (Stage 1), covering nearly four orders of magnitude. Filter Set A served as the primary dataset, as roughly 80% of its impact sites were studied. Although fewer impact sites were examined in Sets B and C, the trends in elemental concentration and deposition properties were mainly consistent with those observed in Set A.

The atmospheric mass concentration of each element was measured according to the impactor stage. Detection limits (LoQ) were noted for concentrations as low as a few ng/m^3. Key findings indicate a strong coarse-mode enrichment of crustal elements, such as silicon, calcium, titanium, and iron, particularly in the upper stages of the impactor (stages 10–8). Sulfur exhibited a broad size distribution and maintained elevated concentrations across both fine and mid-sized particles. Anthropogenic tracers, including sulfur and vanadium, were mainly found in finer particle size ranges. Potassium was distributed across both coarse and fine fractions, with higher levels in the coarser stages but measurable amounts in finer ones as well, indicating its dual origin from both natural resuspension and anthropogenic combustion sources.

Beyond spot-to-spot differences, elemental maps also revealed within-spot inhomogeneity, where individual impaction spots displayed non-uniform morphologies and localized enrichments. This highlights that single-spot measurements are likely to be significantly biased when compared to scanning methods, as they might only detect local enrichment or depletion zones. In contrast, systematic scanning averages over the entire spot area, offer more accurate and representative results.

The uniform deposition on filter surfaces was accomplished by evaluating the relative standard deviation (RSD). The RSD values range from 5% to 30%, indicating good to moderate homogeneity between spots. However, there are cases where the RSD value exceeds 30%. which occur when the extracted concentrations are near the limit of quantitation (LoQ).

Interestingly, we observe high RSD values in some cases, even when concentrations are several orders of magnitude above the LoQ, especially at stage 10. This may be related to the coarse impactor stages, where particles across a very broad size range (up to the maximum cut-off) are deposited. The wide variability in particle diameters and morphologies at these stages can lead to heterogeneous elemental distributions across spots

The study emphasizes the crucial role of spatial inhomogeneity in aerosol analysis, particularly when using multi-nozzle cascade impactors. Our findings indicate that assuming a uniform sample load can lead to biased results, especially when employing micro- or sub-millimeter techniques that evaluate only small areas of a filter's surface. Consequently, it is essential to consider spatial variation before conducting any quantitative analysis. Future work should focus on improving the analytical technique by increasing the spectrometer's detection efficiency, enhancing spatial resolution, and refining the measurement strategy.

14.6 References

Almeida, S. M., Manousakas, M., Diapouli, E., Kertesz, Z., Samek, L., Hristova, E., Šega, K., Alvarez, R. P., Belis, C. A., Eleftheriadis, K., Albania, Civici, N., Radic, R., Vukic, L., Hristova, E., Veleva, B., Šega, K., Bešlic, I., Davila, S., … Karydas, A. G. (2020). Ambient particulate matter source apportionment using receptor modelling in European and Central Asia urban areas. *Environmental Pollution*, *266*. https://doi.org/10.1016/J.ENVPOL.2020.115199

Alver Şahin, Ü., Onat, B., & Polat, G. (2013). Trace element concentrations of size-fractionated particulate matter in the atmosphere of Istanbul, Turkey. *WIT Transactions on Ecology and the Environment*, *174*, 137–147. https://doi.org/10.2495/AIR130121

Angyal, A., Szoboszlai, Z., Major, I., Molnár, M., Varga, T., Török, Z., Papp, E., Enikő, F., Gini, M., Manousakas, M. I., Szikszai, Z., & Kertész, Z. (2024). Characterisation of urban aerosol size distribution by radiocarbon and PIXE analyses in a middle-European urban environment for source identification: a pilot study. *Environmental Science and Pollution Research*, *31*(34), 47258–47274. https://doi.org/10.1007/S11356-024-34215-8/FIGURES/2

Cabal, A., Legrand, S., Van den Bril, B., Toté, K., Janssens, K., & Van Espen, P. (2017). Study of the uniformity of aerosol filters by scanning MA-XRF. *X-Ray Spectrometry*, *46*(5), 461–466. https://doi.org/10.1002/xrs.2767

Ceradrop. (n.d.). *CeraPrinter F-Serie*. Retrieved August 26, 2025, from https://www.ceradrop.com/en/products/f-serie/

Chatoutsidou, S. E., Papagiannis, S., Anagnostopoulos, D. F., Eleftheriadis, K., Lazaridis, M., & Karydas, A. G. (2022). Application of a handheld X-ray fluorescence analyzer for the quantification of air particulate matter on Teflon filters. *Spectrochimica Acta Part B: Atomic Spectroscopy*, *196*, 106517. https://doi.org/10.1016/J.SAB.2022.106517

Grigoratos, T., & Martini, G. (2015). Brake wear particle emissions: a review. *Environmental Science and Pollution Research*, *22*(4), 2491–2504. https://doi.org/10.1007/S11356-014-3696-8/TABLES/5

Calzolai, G., Chiari, M., Lucarelli, F., Nava, S., Taccetti, F., Becagli, S., Frosini, D., Traversi, R., & Udisti, R. (2014). PIXE–PIGE analysis of size-segregated aerosol samples from remote areas. *Nuclear Instruments and Methods in Physics Research Section B: Beam Interactions with Materials and Atoms*, *318*(PART A), 125–129. https://doi.org/10.1016/J.NIMB.2013.05.097

Chen, S.-L., Chang, S.-W., Chen, Y.-J., & Chen, H.-L. (2021). Possible warming effect of fine particulate matter in the atmosphere. Communications Earth & Environment 2021 2:1, 2(1), 1–9. https://doi.org/10.1038/s43247-021-00278-5

Conca, E., Malandrino, M., Diana, A., Abollino, O., Giacomino, A., Bartrolí, R., Moreno, T., Querol, X., & Amato, F. (2022). Methods for Elemental Analysis of Size-Resolved PM Samples Collected on Aluminium Foils: Results of an Intercomparison Exercise. *Molecules*, *27*(21). https://doi.org/10.3390/molecules27217442

Crazzolara, C., & Held, A. (2024). Development of a cascade impactor optimized for size-fractionated analysis of aerosol metal content by total reflection X-ray fluorescence spectroscopy (TXRF). *Atmospheric Measurement Techniques*, *17*(7), 2183–2194. https://doi.org/10.5194/amt-17-2183-2024

Diapouli, E., Manousakas, M., Vratolis, S., Vasilatou, V., Maggos, T., Saraga, D., Grigoratos, T., Argyropoulos, G., Voutsa, D., Samara, C., & Eleftheriadis, K. (2017). Evolution of air pollution source contributions over one decade, derived by PM10 and PM2.5 source apportionment in two metropolitan urban areas in Greece. *Atmospheric Environment*, *164*, 416–430. https://doi.org/10.1016/j.atmosenv.2017.06.016

Eleftheriadis, K., Gini, M. I., Diapouli, E., Vratolis, S., Vasilatou, V., Fetfatzis, P., & Manousakas, M. I. (2021). Aerosol microphysics and chemistry reveal the COVID19 lockdown impact on urban air quality. *Scientific Reports 2021 11:1*, *11*(1), 1–11. https://doi.org/10.1038/s41598-021-93650-6

Galindo, N., Nicol´as, J.F., Yubero, E., Caballero, S., Pastor, C., Crespo, J., 2008. Factors affecting levels of aerosol sulfate and nitrate on the Western Mediterranean coast. Atmos. Res. 88 (3–4), 305–313 https://doi.org/10.1016/j.atmosres.2007.11.024

Gerodimos, T., Patakiouta, I. V., Papadakis, V. M., Exarchos, D., Asvestas, A., Kenanakis, G., Matikas, T. E., & Anagnostopoulos, D. F. (2024). Scanning Micro X-ray Fluorescence and Multispectral Imaging Fusion: A Case Study on Postage Stamps. *Journal of Imaging*, *10*(4), 95. https://doi.org/10.3390/JIMAGING10040095/S1

Gini, M., Manousakas, M., Karydas, A. G., & Eleftheriadis, K. (2022). Mass size distributions, composition and dose estimates of particulate matter in Saharan dust outbreaks. *Environmental Pollution*, *298*, 118768. https://doi.org/10.1016/J.ENVPOL.2021.118768

Groma, V., Alföldy, B., Börcsök, E., Czömpöly, O., Füri, P., Horváthné Kéri, A., Kovács, G., Török, S., & Osán, J. (2022). Sources and health effects of fine and ultrafine aerosol particles in an urban environment. *Atmospheric Pollution Research*, *13*(2), 101302. https://doi.org/10.1016/J.APR.2021.101302

Maenhaut, W., Hillamo, R., Mäkelä, T., Jaffrezo, J. L., Bergin, M. H., & Davidson, C. I. (1996). A new cascade impactor for aerosol sampling with subsequent PIXE analysis. *Nuclear Instruments and Methods in Physics Research, Section B: Beam Interactions with Materials and Atoms*, *109–110*, 482–487. https://doi.org/10.1016/0168-583X(95)00955-8

Manousakas, M., Papaefthymiou, H., Diapouli, E., Migliori, A., Karydas, A. G., Bogdanovic-Radovic, I., & Eleftheriadis, K. (2017). Assessment of PM2.5 sources and their corresponding level of uncertainty in a coastal urban area using EPA PMF 5.0 enhanced diagnostics. *Science of The Total Environment*, *574*, 155–164. https://doi.org/10.1016/J.SCITOTENV.2016.09.047

Manousakas, M., Diapouli, E., Papaefthymiou, H., Kantarelou, V., Zarkadas, C., Kalogridis, A.-C., Karydas, A.-G., & Eleftheriadis, K. (2018). XRF characterization and source apportionment of PM10 samples collected in a coastal city. *X-Ray Spectrometry*, *47*(3), 190–200. https://doi.org/10.1002/xrs.2817

Seeger, S., Osan, J., Czömpöly, … Beckhoff, B. (2021). *Quantification of Element Mass Concentrations in Ambient Aerosols by Combination of Cascade Impactor Sampling and Mobile Total Reflection X-ray Fluorescence Spectroscopy*. Atmosphere. https://doi.org/10.3390/ATMOS12030309

Ostro, B., Tobias, A., Karanasiou, A., Samoli, E., Querol, X., Rodopoulou, S., Basagaña, X., Eleftheriadis, K., Diapouli, E., Vratolis, S., Jacquemin, B., Katsouyanni, K., Sunyer, J., Forastiere, F., Stafoggia, M., Alessandrini, E., Angelini, P., Berti, G., Bisanti, L., … Pascal, M. (2015). The risks of acute exposure to black carbon in Southern Europe: results from the MED-PARTICLES project. Occupational and Environmental Medicine, 72(2), 123–129. https://doi.org/10.1136/OEMED-2014-102184

Papagiannis, S., Sabur, ·, Abdullaev, F., Vasilatou, V., Manousos, ·, Manousakas, I., Eleftheriadis, K., & Diapouli, E. (2024). Air quality challenges in Central Asian urban areas: a PM2.5 source apportionment analysis in Dushanbe, Tajikistan. *Environmental Science and Pollution Research 2024*, 1–14. https://doi.org/10.1007/S11356-024-33833-6

Robinson, M. S., Grgić, I., Šelih, V. S., Šala, M., Bitsui, M., & Van Elteren, J. T. (2017). Laser ablation ICP-MS of size-segregated atmospheric particles collected with a MOUDI cascade impactor: A proof of concept. *Atmospheric Measurement Techniques*, *10*(5), 1823–1830. https://doi.org/10.5194/amt-10-1823-2017

Rojas-Lemus, M., López-Valdez, N., Bizarro-Nevares, P., González-Villalva, A., Ustarroz-Cano, M., Zepeda-Rodríguez, A., Pasos-Nájera, F., García-Peláez, I., Rivera-Fernández, N., & Fortoul, T. I. (2021). Toxic Effects of Inhaled Vanadium Attached to Particulate Matter: A Literature Review. *International Journal of Environmental Research and Public Health 2021, Vol. 18, Page 8457*, *18*(16), 8457. https://doi.org/10.3390/IJERPH18168457

Romano, F. P., Caliri, C., Nicotra, P., Di Martino, S., Pappalardo, L., Rizzo, F., & Santos, H. C. (2017). Real-time elemental imaging of large dimension paintings with a novel mobile macro X-ray fluorescence (MA-XRF) scanning technique. *Journal of Analytical Atomic Spectrometry*, *32*(4), 773–781. https://doi.org/10.1039/C6JA00439C

Samoli, E., Stafoggia, M., Rodopoulou, S., Ostro, B., Declercq, C., Alessandrini, E., Díaz, J., Karanasiou, A., Kelessis, A. G., Tertre, A. Le, Pandolfi, P., Randi, G., Scarinzi, C., Zauli-Sajani, S., Katsouyanni, K., Forastiere, F., Alessandrini, E., Angelini, P., Berti, G., … Pascal, M. (2013). Associations between fine and coarse particles and mortality in Mediterranean cities: Results from the MED-PARTICLES project. Environmental Health Perspectives, 121(8), 932–938. https://doi.org/10.1289/EHP.1206124

Stefancova, L., Schwarz, J., Makela, T., Hillamo, R., & Smolik, J. (2011). Comprehensive Characterization of Original 10-Stage and 7-Stage Modified Berner Type Impactors. Aerosol Science and Technology, 45(1), 88–100. https://doi.org/10.1080/02786826.2010.524266

Stelcer, E., Morrison, A. L., Atanacio, A. J. and Cohen, D. D. (2011). PIXE analysis of MOUDI filters. Presentation to the 20th International Clean Air and Environment Conference

(CASANZ 2011), 31 July-2nd August 2011, Auckland, New Zealand, https://apo.ansto.gov.au/dspace/handle/10238/4234

S. Yatkin, K. Trzepla, W.H. White, N.P. Hyslop, Generation of multi-element reference materials on PTFE filters mimicking ambient aerosol characteristics, Atmos. Environ. 189 (2018) 41–49, https://doi.org/10.1016/j. atmosenv.2018.06.034.

S. Yatkin, K. Trzepla, W.H. White, N.J. Spada, N.P. Hyslop, Development of single-compound reference materials on polytetrafluoroethylene filters for analysis of aerosol samples, Spectrochim. Acta B 171 (2020), 105948, https://doi.org/10.1016/j.sab.2020.105948

Usui, K., Kikuchi, R., Nakatsu, S., Imayoshi, T., Kumagai, K., Tago, H., Satoh, T., Ishii, Y., & Kada, W. (2023). Characterization of hourly-collected airborne particulate matters from an automated sampling unit of the atmospheric environmental regional observation system by in-air micro-PIXE analysis. *Nuclear Instruments and Methods in Physics Research Section B: Beam Interactions with Materials and Atoms*, *544*, 165106. https://doi.org/10.1016/J.NIMB.2023.165106

Viana, M., Kuhlbusch, T. A. J., Querol, X., Alastuey, A., Harrison, R. M., Hopke, P. K., Winiwarter, W., Vallius, M., Szidat, S., Prévôt, A. S. H., Hueglin, C., Bloemen, H., Wåhlin, P., Vecchi, R., Miranda, A. I., Kasper-Giebl, A., Maenhaut, W., & Hitzenberger, R. (2008). Source apportionment of particulate matter in Europe: A review of methods and results. *Journal of Aerosol Science*, *39*(10), 827–849. https://doi.org/10.1016/J.JAEROSCI.2008.05.007

Wikipedia contributors. (n.d.). *1951 USAF resolution test chart*. In *Wikipedia*. Retrieved August 26, 2025, from https://en.wikipedia.org/wiki/1951_USAF_resolution_test_chart

Wolfenbarger, K., & Seinfeld, J. H. (1990). Inversion of aerosol size distribution data. *Journal of Aerosol Science*, *21*(2), 227–247. https://doi.org/10.1016/0021-8502(90)90007-K

Wu C, Yu Z., Evaluation of linear regression techniques for atmospheric applications: the importance of appropriate weighting, Atmos, Meas. Tech. 11 (2018) 1233–1250, https://doi.org/10.5194/amt-11-1233-2018.+

Zografou, O., Gini, M., Manousakas, M. I., Chen, G., Kalogridis, A. C., Diapouli, E., Pappa, A., & Eleftheriadis, K. (2022). Combined organic and inorganic source apportionment on yearlong ToF-ACSM dataset at a suburban station in Athens. *Atmospheric Measurement Techniques*, *15*(16), 4675–4692. https://doi.org/10.5194/AMT-15-4675-2022

15. Calibration of a WD-XRF Spectrometer for Environmental Aerosol Quantitative Studies

15.1 Introduction

In this study, the Rigaku ZSX Primus IV WD-XRF spectrometer (Section C, 11.4) was calibrated for the quantitative analysis of PM filters. A key advantage of WD-XRF is its superior spectral resolution compared to energy-dispersive systems, achieved through the use of analyzing crystals (Beckhoff et al., 2006). This enables reliable separation of overlapping peaks, which is particularly important for environmental aerosol samples that contain multiple elements at varying concentrations.

The aim of the calibration was to ensure accurate quantification across a broad range of elements relevant to particulate matter (PM) studies, from light species such as Na, Mg, and Al to heavier metals including Pb. The calibrated WD-XRF setup provides robust and reproducible measurements directly on filter samples, ensuring reliable elemental analysis of environmental aerosols.

Permission to use the Rigaku ZSX Primus IV WD-XRF spectrometer was granted by the School of Mining and Metallurgical Engineering at the National Technical University of Athens.

15.2 Materials and Methods

17.5.1 Reference Materials

For the calibration of the WD-XRF spectrometer, three categories of reference materials were employed (**Table 14**):

- **Micromatter thin films (MM):** A set of single-element or compound thin films from Micromatter were used as primary standards. These included: NaCl, MgF_2, Al, SiO, KCl, CaF_2, CuS_x, GaP, V, Fe, Cr, Ni, ZnTe, Co, GaAs, Ge, RbI, SrF_2, Se, CdSe, CsBr, BaF_2, Pt, Au, and Pb. Thin deposits of Ti and Mn were also available on Kapton substrates, as well as CeF_3.
- **Custom-made standards:** Custom made reference foils prepared for the PIXE calibration (Ti and Mn on Kapton) were also employed here, to ensure consistency between techniques. (Karydas, personal communication, 2022)
- **Reference aerosol samples (UCDavis Teflon Filters):** To replicate realistic filter conditions, a suite of aerosol reference materials from UC Davis (deposited on PTFE substrates) was additionally analyzed. These included multiple loadings of Si, S, KCl, AlCe, Pb, and NaCl, with nominal areal concentrations ranging from 0.5 to 7.6 μg/cm² (e.g., UCD47-Si-0.8, -3.2, 7.6; UCD47-S-0.8, 3.0, 5.0; UCD47_KCl_0.5, 2.2, 6.1; UCD47_AlCe_0.7, 2.4, 5.5; UCD47_Pb_0.5, 0.9, 1.9; UCD47_NaCl_0.7, 3.0, 5.9).

The combination of thin-film standards and aerosol-filter references offered extensive elemental coverage from light to heavy elements and enabled calibration and validation under conditions similar to actual atmospheric aerosol filters.

17.5.2 Measurement Conditions / Optimization

All measurements were performed under vacuum conditions to minimize absorption of low-energy X-rays by air. A beam diameter of 20 mm was selected to cover a significant fraction of the filter surface, thereby reducing the impact of inhomogeneous particle deposition on the calibration results. The excitation conditions were fixed at 40 kV and 15 mA for all measurements, providing sufficient excitation for both light and heavy elements while ensuring stable tube performance.

The spectrometer is equipped with multiple crystals, each optimized for a specific energy range of characteristic X-rays. The choice of crystal is determined by Bragg's law, where the diffraction angle depends on the lattice spacing, d, of the crystal. Crystals with larger d-spacings (e.g., RX25, PET) are well suited for low-energy X-rays, while those with smaller d-spacings (e.g., LiF(200)) are used for higher energies. In this study, the RX25 crystal was used for Na and Mg, the PET crystal for Al and Si, and the Ge crystal for P, S, and Cl. For all other elements (K to Pb), the LiF(200) crystal was selected, as it provides excellent resolution for medium- and high-energy X-rays. This combination ensured optimal peak separation across the periodic table.

Two types of detectors were employed: the proportional counter (PC) and the scintillation counter (SC). The PC detector, filled with P10 gas and equipped with a thin entrance window, was used for light elements (Na to Ca). It offers high efficiency for low-energy photons, which are easily absorbed in thicker detector windows. The SC detector, consisting of a NaI(Tl) scintillation crystal coupled to a photomultiplier tube, was used for medium- to high-energy elements (Ti to Pb). While the SC is less efficient for low-energy X-rays due to absorption in its Be window, it provides excellent stability and stopping power at higher photon energies. The use of different detectors for light and heavy elements thus maximized detection efficiency across the full elemental range.

For most elements, the S4 Soller slit was employed, providing a consistent balance between intensity and resolution. For chlorine, however, the spectrometer automatically selected the S2 slit, which is narrower. The choice of a smaller slit improves the spectral resolution at the expense of intensity and is particularly important in this case because the Cl Kα line (2.62 keV) lies close to the Rh L lines from the anode. By reducing spectral broadening, the S2 slit enhances peak separation and minimizes interference, thereby ensuring more reliable quantification of chlorine. **Table 23** presents the measurement conditions that were used for the calibration of the WD-XRF spectrometer.

Table 23. *Measurement conditions used for the calibration of the WD-XRF spectrometer. The table lists the analyzed elements in ascending order of atomic number, along with the Soller slit, analyzing crystal, detector, and measuring time employed for each line. A proportional counter (PC) was used for light elements (Na–Ca), while a scintillation counter (SC) was selected for medium- to heavy-weight elements (Ti–Pb). Measuring times were 40 s for light elements (Na–Ca) and 20 s for medium to heavy-weight elements (Ti–Pb).*

Atomic No.	Element	Slit	Crystal	Detector	Measuring time (s)
11	Na	S4	RX25	PC	40
12	Mg	S4	RX25	PC	40
13	Al	S4	PET(002)	PC	40
14	Si	S4	PET(002)	PC	40
15	P	S4	Ge(111)	PC	40
16	S	S4	Ge(111)	PC	40
17	Cl	S2	Ge(111)	PC	40
19	K	S4	LiF(200)	PC	40
20	Ca	S4	LiF(200)	PC	40
22	Ti	S2	LiF(200)	SC	20
23	V	S2	LiF(200)	SC	20
24	Cr	S2	LiF(200)	SC	20
25	Mn	S2	LiF(200)	SC	20
26	Fe	S2	LiF(200)	SC	20
27	Co	S2	LiF(200)	SC	20
28	Ni	S2	LiF(200)	SC	20
29	Cu	S2	LiF(200)	SC	20
30	Zn	S2	LiF(200)	SC	20
31	Ga	S2	LiF(200)	SC	20
32	Ge	S2	LiF(200)	SC	20
33	As	S2	LiF(200)	SC	20
34	Se	S2	LiF(200)	SC	20
35	Br	S2	LiF(200)	SC	20
37	Rb	S2	LiF(200)	SC	20
38	Sr	S2	LiF(200)	SC	20
56	Ba	S2	LiF(200)	SC	20
58	Ce	S2	LiF(200)	SC	20
78	Pt	S2	LiF(200)	SC	20
79	Au	S2	LiF(200)	SC	20
82	Pb	S2	LiF(200)	SC	20

For each element, both the characteristic X-ray peak and two background positions (BG1 and BG2) were measured. The background positions, recorded at fixed offsets from the peak angle, are used to subtract the continuum background. Measurement times were optimized according to element energy: light elements (Na to Ca) were measured for 40 seconds per peak to compensate for their relatively weak fluorescence yields, while heavier elements (Ti to Pb) were measured for 20 seconds per peak. The background was measured for 10 seconds at each position for all elements.

The spectrometer records spectra as a function of the scattering angle (2θ). Converting to photon energy (keV) is necessary to directly compare the measured peaks with X-ray line energies. To convert the measured scattering angles (2θ) into photon energies (keV), the Bragg condition was applied in combination with the photon energy–wavelength relationship. According to Bragg's law:

$$n\lambda = 2d_{hkl}\sin\theta \tag{47}$$

where n is the diffraction order of reflection (here n=1), d_{hkl} is the lattice spacing of the crystal planes (hkl) of the analyzing crystal. The corresponding photon energy is then obtained through the fundamental relation Anagnostopoulos, 2018; Anagnostopoulos et al., 2018:

$$E(keV) = \frac{hc}{\lambda} = \frac{12.39}{\lambda[\text{Å}]} \tag{48}$$

Combining both equations yields:

$$E(keV) = \frac{12.39}{2d_{hkl}\,[\text{Å}]\sin\theta} \tag{49}$$

with θ being the Bragg angle (the half of the measured scattering angle 2θ). The numerical constant 12.39 keV·Å arises from fundamental constants, specifically Planck's constant (h) and the speed of light (c).

This transformation allows direct comparison between the measured angular spectra and the X-ray line energies. For instance, the Al Kα line (1.49 keV) is observed near 2θ ≈ 144.7° on the PET(002) crystal, the S Kα line (2.31 keV) near 110.8° on the Ge(111) crystal, and the Mn Kα line (5.90 keV) around 63.0° on the LiF(200) crystal. **Figure 73** presents representative WDXRF spectra of Al, S, and Mn recorded with the ZSX Primus IV spectrometer. The spectra are displayed as a function of scattering angle (2θ) and converted into photon energy (keV) using Bragg's law and the lattice spacings of the analyzing crystals

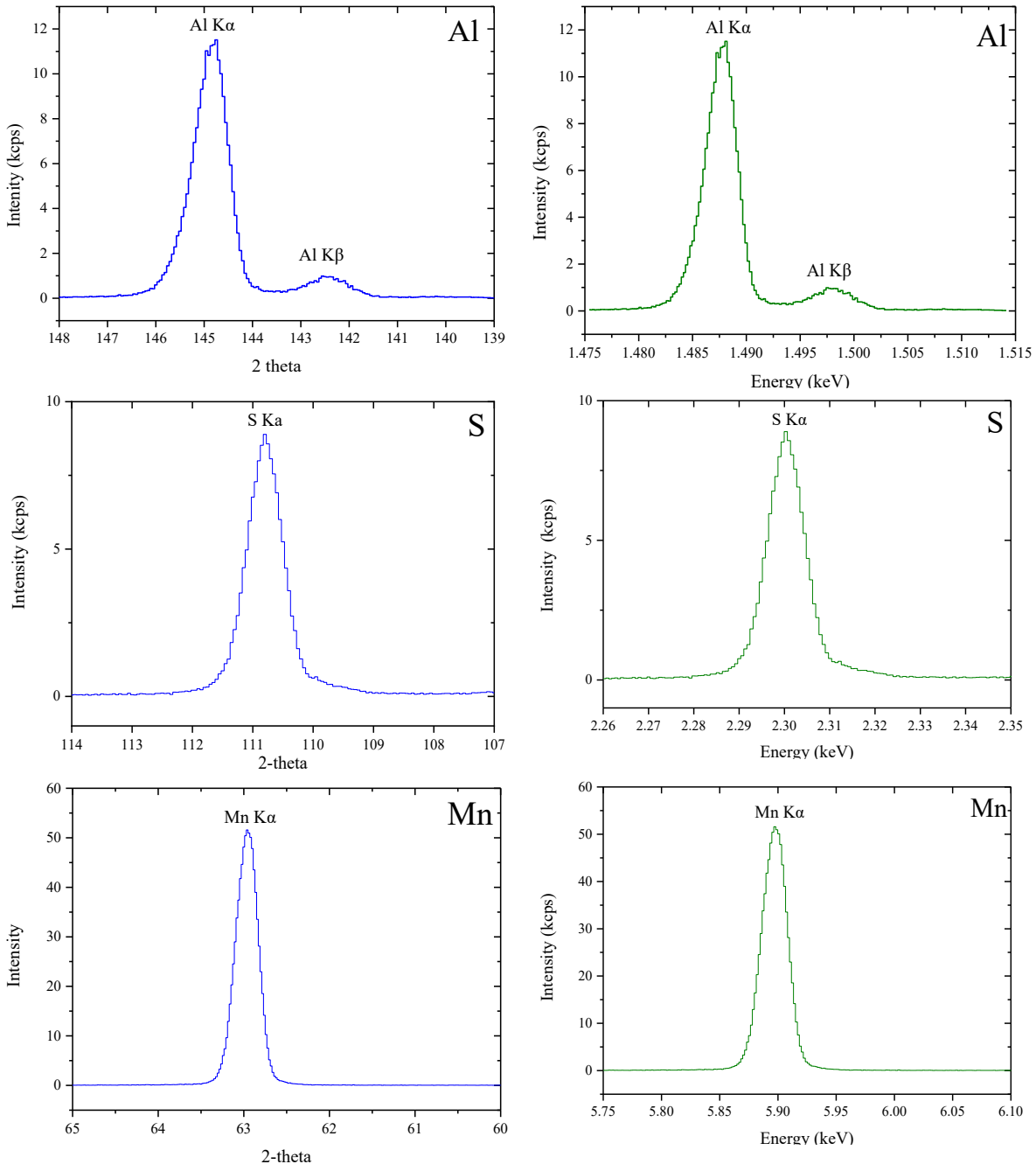

***Figure 73**. Representative WDXRF spectra of Al, S, and Mn recorded with the ZSX Primus IV, WD-XRF spectrometer from Micromatter thin-film reference standards. The spectra are shown as a function of scattering angle (2θ) and converted into photon energy (keV) using Bragg's law and the corresponding lattice spacings of the analyzing crystals. For the conversions, the following d values were applied: PET (002) = 4.371 Å, Ge (111) = 3.266 Å, and LiF (200) = 2.013 Å.*

15.2.3 Sensitivity, Limits of detection and Uncertainty

Following the same approach described in Sections D (15.3.4 and 16.3.3), the elemental sensitivities and limits of detection were calculated based on the same principles and employing blank subtraction methodology. **Figure 74** presents representative calibration curves for selected elements (Na, Al, Fe, Pb) obtained with the WD-XRF spectrometer, while **Figure 75** illustrates all the elemental sensitivities (counts s^{-1} mA^{-1} μg^{-1} cm^2) as a function of atomic number. **Figure 76** presents the corresponding limits of detection (μg cm^{-2}). For elements from Na to Ca, measurements were carried out with the flow proportional counter (PC), whereas for Ti to Pb the scintillation counter (SC) was used. The choice of analyzing crystal depended on the element: RX25 (Na, Mg), PET (Al, Si), Ge (P, S, Cl), and LiF(200) (K–Pb). Slit S4 was employed for all cases except Cl, where slit S2 was selected.

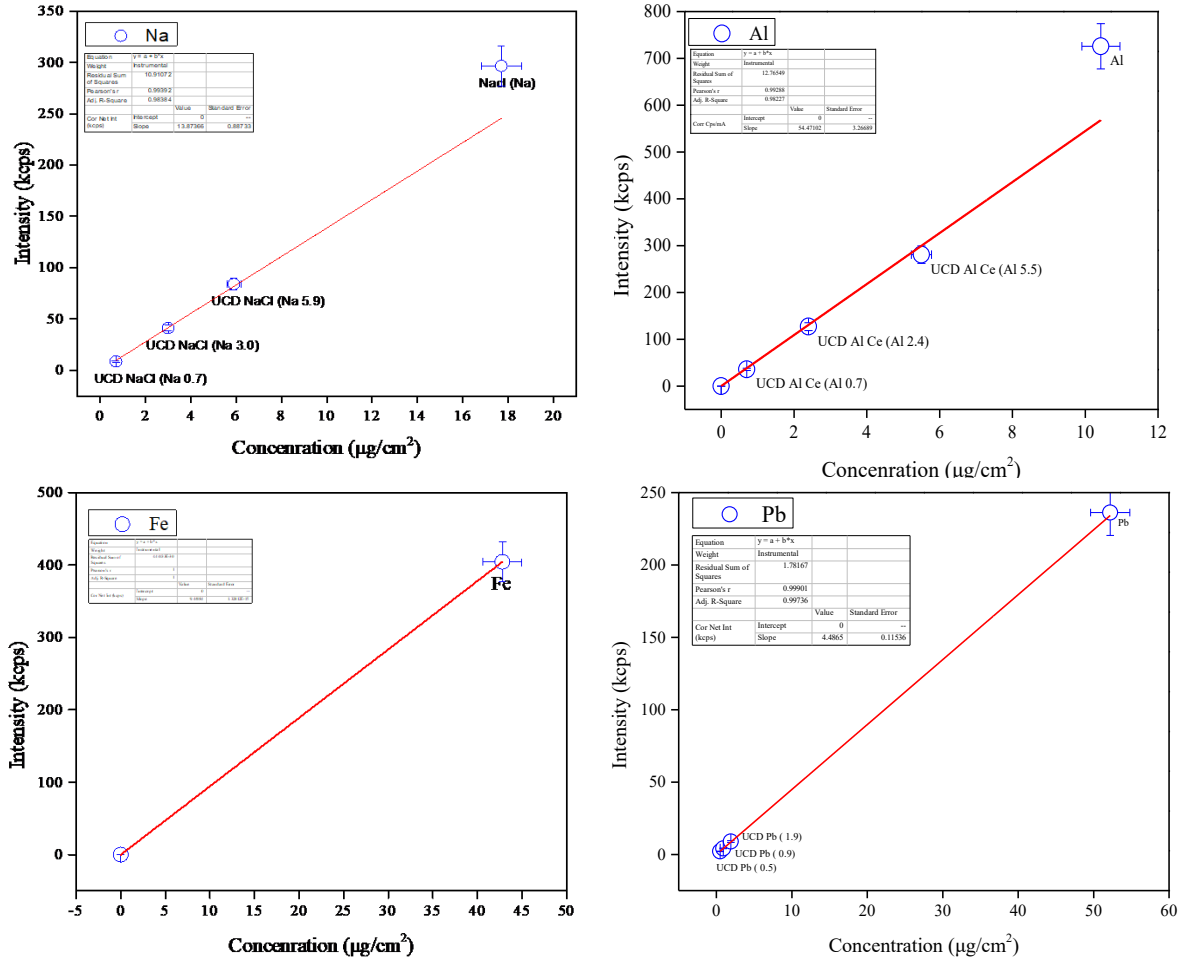

Figure 74. Calibration curves for Na, Al, Fe, and Pb obtained with the WD-XRF spectrometer. The red lines represent linear regressions between elemental concentration (µg/cm²) and measured X-ray intensity (kcps). Error bars indicate measurement uncertainties, while the inset tables summarize the calibration parameters for each element.

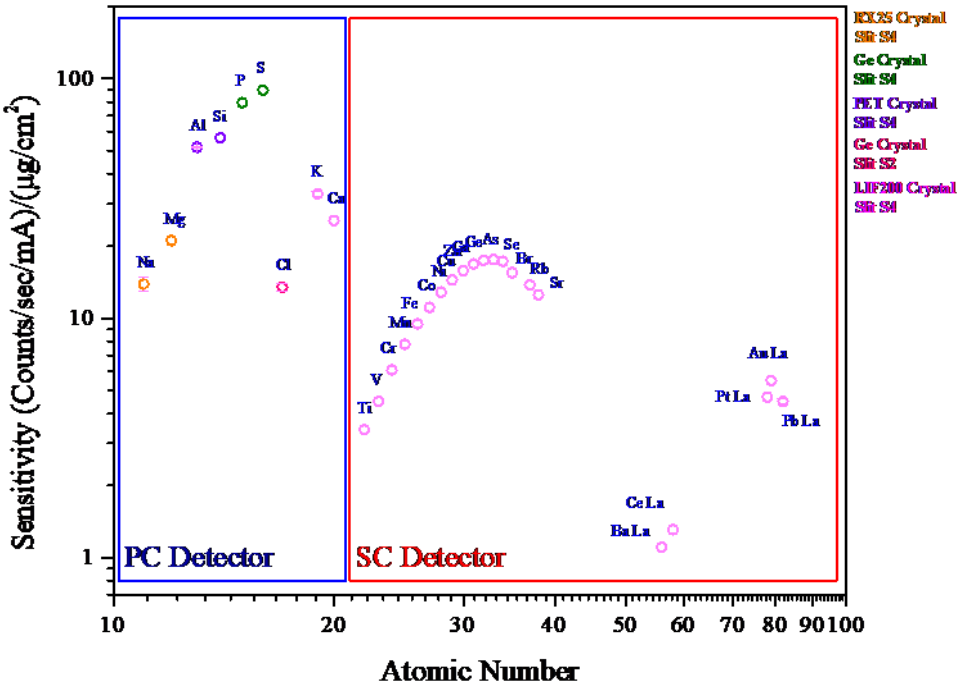

Figure 75. *Elemental sensitivities of the WD-XRF spectrometer as a function of atomic number, expressed in (counts/sec/mA)/(µg/cm²). Measurements for Na–Ca were performed using the proportional counter (PC), while elements from Ti to Pb were analyzed with the scintillation counter (SC). Different analyzing crystals were employed depending on the element: RX25 (Na, Mg), PET (Al, Si), Ge (P, S, Cl), and LiF(200) (K–Pb). Slit S4 was used for all elements except Cl, where slit S2 was applied to minimize spectral overlaps with Rh L lines.*

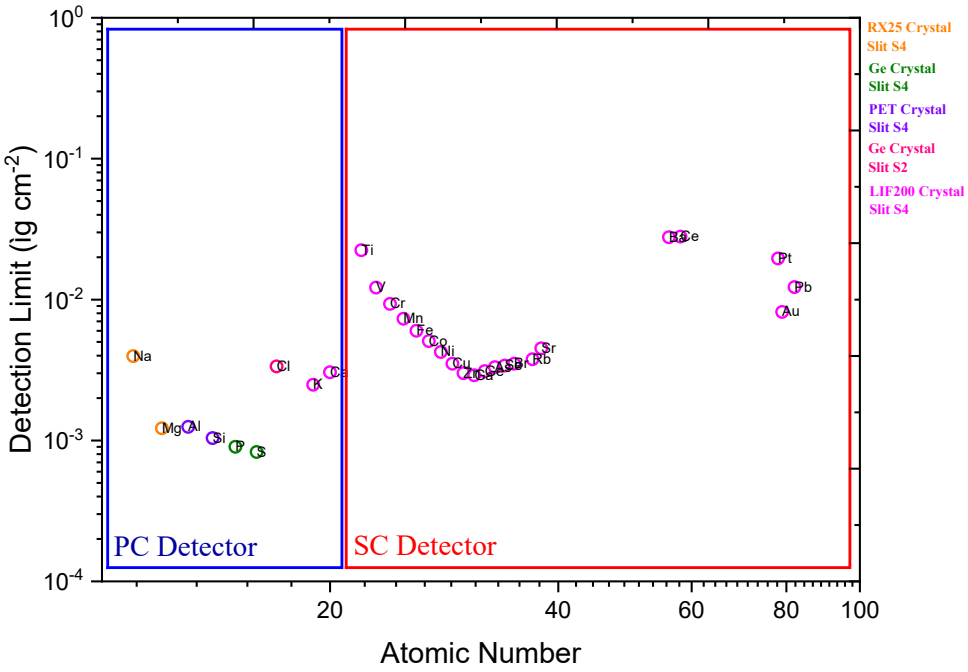

Figure 76. *Limits of detection (LoDs) of the WD-XRF spectrometer, expressed in µg cm⁻², as a function of atomic number. Measurements for Na–Ca were performed using the flow proportional counter (PC), while Ti–Pb were analyzed with the scintillation counter (SC). Different analyzing crystals were employed depending on the element: RX25 (Na, Mg), PET (Al, Si), Ge (P, S, Cl), and LiF(200) (K–Pb). Slit S4 was used for all elements except Cl, where slit S2 was applied.*

For the calculation of elemental concentrations in the unknown PM samples, uncertainties were treated according to the methodology outlined in Section 15.4.3. Three sources of uncertainty were considered: (i) the statistical uncertainty of the analyte peak area, (ii) the calibration uncertainty, and (iii) the uncertainty in the nominal areal densities of the reference materials. The calibration uncertainty was derived from the standard error of the slope obtained from each calibration curve, while the uncertainty in the nominal areal densities was set at 5% for all reference materials. The total uncertainty for each element in the aerosol samples was then obtained by combining these components according to Eq (37).

15.3 Results and Discussion

15.3.1 Measurements on PM Aerosol Samples

The comparison presented in **Table 24** highlights the performance of the WD-XRF (Rigaku ZSX Primus IV) and ED-XRF (Panalytical Epsilon 5) spectrometers across two PM_{10} samples. These samples were collected at the N.C.S.R. "Demokritos" urban background station in Athens (Agia Paraskevi), situated on the campus at the foot of Mount Hymettus. Sampling was conducted over 24-h periods using a low-volume sampler (2.3 m^3 h^{-1}) with Teflon filters suitable for XRF analysis. Prior to WD-XRF measurements, the filters had also been analyzed with the well-established Epsilon 5 ED-XRF spectrometer equipped with secondary targets, in order to evaluate the performance of the WD-XRF system (Papagiannis et al., 2024; Manousakas et al., 2018).. For major elements, particularly Al, Si, Ca, Ti, Mn, Fe, Cl, K, and S, the agreement between the two systems was very good, with concentration differences mostly within 5–20%. This consistency demonstrates the reliability of both setups for quantifying medium- and high-Z elements in particulate matter.

For lighter elements, the comparison shows more variability. Sodium (Na) and Magnesium (Mg) exhibit notable differences between the two systems, a trend commonly observed in XRF analysis of light elements. Nevertheless, the fact that both instruments detect these elements consistently suggests that relative trends can still be monitored, even if absolute values differ.

Trace elements (Ni, Cu, Zn, Br, Pb) were detected at very low areal densities, often close to the limit of detection. In this range, differences between instruments are expected because small variations in background subtraction, excitation efficiency, and spectral fitting strongly affect accuracy. Still, both setups confirmed the presence of several key trace species (e.g., Ni, Cu, Pb), demonstrating their capability to characterize trace metal signals. Overall, the results confirm that WD-XRF spectrometer produces results consistent with the well-established ED-XRF one for the main aerosol constituents.

Table 24. *Comparison between elemental concentrations (in μg/cm²) between the WD-XRF spectrometer (ZSX-Primus IV) and the ED-XRF spectrometer (Panalytical Epsilon 5) for two PM_{10} aerosol samples.*

	Sample 1		Sample 2	
El.	**WD-XRF**	**ED-XRF**	**WD-XRF**	**ED-XRF**
Na	2.54 ± 0.48	9.92 ± 2.70	1.10 ± 0.21	0.77 ± 0.21
Mg	4.88 ± 0.71	6.64 ± 1.62	0.240 ± 0.040	-
Al	14.4 ± 4.2	14.1 ± 2.3	0.140 ± 0.040	0.130 ± 0.021
Si	24.0 ± 6.1	35.0 ± 5.8	0.250 ± 0.060	-
P	0.16 ± 0.03	-	0.020 ± 0.001	-
S	1.98 ± 0.33	2.75 ± 0.26	2.92 ± 0.49	3.70 ± 0.34
Cl	7.24 ± 0.91	7.06 ± 1.17	0.330 ± 0.040	0.43 ± 0.07
K	4.37 ± 0.41	3.98 ± 0.37	0.990 ± 0.090	1.06 ± 0.10
Ca	17.4 ± 1.6	17.6 ± 1.9	0.710 ± 0.070	0.70 ± 0.08
Ti	1.28 ± 0.10	1.20 ± 0.12	0.010 ± 0.001	0.010 ± 0.001
Mn	0.140 ± 0.010	0.120 ± 0.016	-	-
Fe	10.97 ± 0.85	10.62 ± 1.14	0.820 ± 0.060	0.530 ± 0.057
Ni	0.030 ± 0.002	-	-	0.010 ± 0.001
Cu	0.015 ± 0.002	-	0.020 ± 0.002	0.020 ± 0.002
Zn	-	-	-	0.070 ± 0.009
As	-	-	0.010 ± 0.001	-
Br	0.030 ± 0.001	-	0.010 ± 0.001	-
Rb	-	-	-	-
Sr	0.100 ± 0.010	-	-	-
Ce	0.010 ± 0.001	-	-	-
Pb	0.020 ± 0.002	-	0.030 ± 0.002	-

15.5 Conclusions

The calibration and validation of the Rigaku ZSX Primus IV WD-XRF spectrometer demonstrated its suitability for quantitative analysis of aerosol filter samples across a broad range of elements. The use of thin-film standards and reference aerosol filters ensured accurate calibration under conditions representative of real atmospheric samples. Optimized selection of analyzing crystals, detectors, and Soller slits provided high spectral resolution and efficient detection for both light and heavy elements, while the application of background correction methods improved signal reliability.

The sensitivity and detection limit analysis confirmed that the setup can detect both major and trace elements in PM samples with robust performance. Comparison with the ED-XRF (Epsilon 5) spectrometer revealed very good agreement for medium- and high-Z aerosol elements (Al, Si, S, Cl, K, Ca, Ti, Mn, Fe), with concentration differences typically within 5–20%. Variability was larger for light elements such as Na and Mg, yet both systems consistently detected them, allowing relative concentration trends to be monitored.

For trace metals close to their detection limits, such as Ni, Cu, Zn, Br, and Pb, both spectrometers provided consistent qualitative identification, although small differences in absolute values were observed. Overall, the WD-XRF configuration presented here offers reliable, reproducible, and high-resolution elemental analysis of aerosol filters, making it a powerful complement to established ED-XRF systems for atmospheric studies.

15.6 References

Anagnostopoulos, D. F. (2018). X-ray emission spectroscopy optimization for chemical speciation in laboratory. *Spectrochimica Acta Part B: Atomic Spectroscopy*, *148*, 83–91. https://doi.org/10.1016/J.SAB.2018.06.004

Anagnostopoulos, D. F., Siozios, A., & Patsalas, P. (2018). Characterization of aluminum nitride based films with high resolution X-ray fluorescence spectroscopy. *Journal of Applied Physics*, *123*(6). https://doi.org/10.1063/1.5013281/155032

Beckhoff, B., Kanngießer, B., Langhoff, N., Wedell, R., & Wolff, H. (Eds.). (2006). *Handbook of practical X-ray fluorescence analysis*. Springer. https://doi.org/10.1007/978-3-540-36722-2

Karydas, A. (2022). Personal communication regarding the preparation of Ti and Mn reference foils on Kapton for PIXE and XRF calibration.

Manousakas, M., Diapouli, E., Papaefthymiou, H., Kantarelou, V., Zarkadas, C., Kalogridis, A.-C., Karydas, A.-G., & Eleftheriadis, K. (2018). XRF characterization and source apportionment of PM10 samples collected in a coastal city. *X-Ray Spectrometry*, *47*(3), 190–200. https://doi.org/10.1002/xrs.2817

Papagiannis, S., Sabur, ·, Abdullaev, F., Vasilatou, V., Manousos, ·, Manousakas, I., Eleftheriadis, K., & Diapouli, E. (2024). Air quality challenges in Central Asian urban areas: a PM2.5 source apportionment analysis in Dushanbe, Tajikistan. *Environmental Science and Pollution Research 2024*, 1–14. https://doi.org/10.1007/S11356-024-33833-6

16. PIXE Quantitative characterization of environmental aerosol filters

16.1 Introduction

The PIXE ion-beam experimental setup of the Tandem accelerator at the Institute of Nuclear and Particle Physics (INPP), NCSR "Demokritos", was used for the quantitative analysis of atmospheric PM aerosol filters. As mentioned in Chapter 9.2, PIXE is a powerful, non-destructive technique widely applied for the elemental characterization of aerosol samples, offering high sensitivity for trace and minor elements and the capability of multi-elemental analysis with minimal sample preparation (Chiari et al., 2005; Lucarelli et al., 2018).

The use of a dedicated beam line provides a controlled and reproducible experimental environment, ensuring stable beam conditions, accurate energy tuning, and optimized detection geometry. These factors are essential for reliable quantification, especially when working with low-mass aerosol deposits on thin filter substrates. In addition, the PIXE setup at INP allows for systematic calibration using standard reference materials, enabling the determination of elemental concentrations in the collected PM filters with high precision.

A key step in this process is the determination of the H-values, which are energy-dependent calibration parameters that link the measured X-ray yields (intensities) to elemental areal concentrations by accounting for the effective solid angle, detector efficiency, and instrumental constants. In this study, H-values for aerosol analysis were established using thin-film standards and implemented in the GUPIX software, which was used for spectrum fitting, quantification, and the subsequent quantitative characterization of the aerosol samples.

16.2 Materials and Methods

16.2.1 Experimental Setup

The PIXE measurements were performed using two Silicon Drift Detectors (SDDs), which enhance the effective solid angle of detection, provide superior energy resolution, support higher count rates, and enable lower limits of detection compared to conventional detectors. Both detectors were positioned at a scattering angle of 135° relative to the incident proton beam direction, optimizing detection efficiency and minimizing scattering effects.

The first detector (AXAS-D H30, KETEK; 30 mm² active area, 8 μm Be window) was equipped with a helium flow system and rare-earth permanent magnets to suppress backscattered charged particles. This setup allowed for the detection of low-energy X-rays, extending down to sodium. The second detector (AXAS-M H150, KETEK; 150 mm² active area, 25 μm Be window) was fitted with a 261 μm Kapton filter to selectively record medium- and high-energy X-rays (> 5 keV). Both detectors exhibited an energy resolution of 128 eV full width at half maximum (FWHM) at the Mn Kα line.

The proton beam, with an energy of 3.005 MeV, exited the accelerator vacuum (approximately 5.5 x 10^{-5} mbar) through a 100 nm-thick Si_3N_4 window. After collimation (~0.8 mm) and passing through a short air path (~2 mm), the beam spot at the sample position was estimated to be approximately 1 mm in diameter. Precise sample alignment was achieved using a pair of cross-mounted laser pointers, combined with a Logitech webcam for visual inspection. A newly integrated motorized XYZ stage, controlled via Zaber Console software, enabled fine positioning of the samples with high reproducibility. Samples were mounted on a specially designed holder placed to a rigid support base in front of the beam exit.

To monitor the beam charge transmitted through the samples, a Faraday cup was placed approximately 10 cm downstream of the filter position, behind the sample holder stage. The signal from the Faraday cup is directed to the Current Integrator on the console and then to a counter. This configuration ensured accurate charge collection during each irradiation. **Figure 77** presents the PIXE experimental setup for aerosol filter analysis. The main specifications of the PIXE experimental setup, including detector configuration, beam properties, and sample handling, are summarized in **Table 25.**

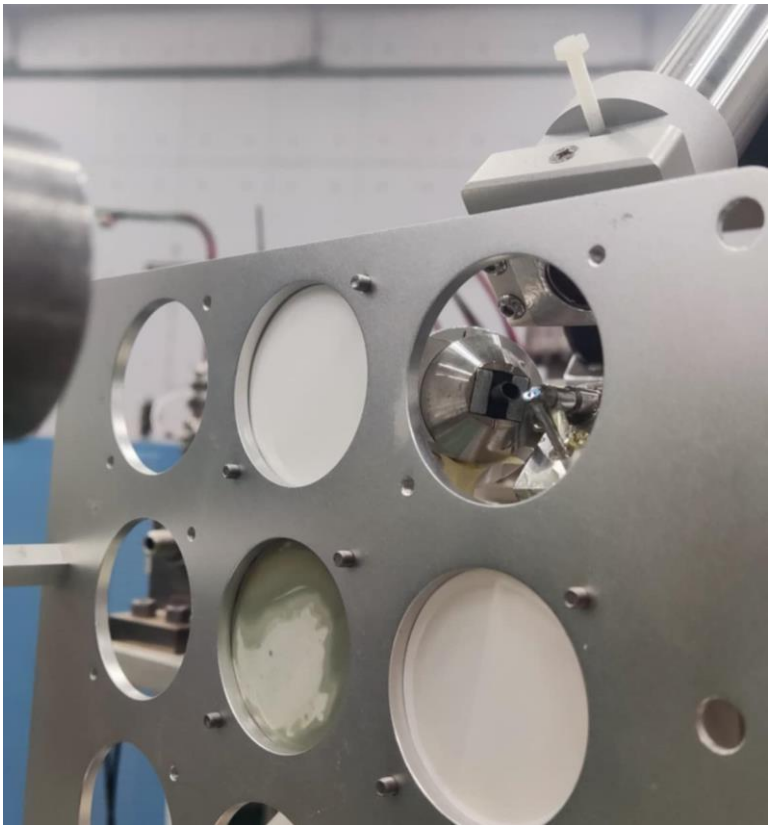

Figure 77. *Sample holder of the PIXE experimental setup at NCSR "Demokritos". The image shows the specially designed sample holder loaded with aerosol filters. Prior to each measurement, an empty slot of the holder was irradiated so that the Faraday cup positioned directly behind the stage could collect the transmitted charge. This procedure ensured accurate charge determination for the subsequent quantitative analysis of the aerosol filters.*

Table 25. *Specifications of the PIXE experimental setup at NCSR "Demokritos", including detector characteristics, proton beam properties, and sample alignment system.*

Component	Specification / Description
Detector 1	AXAS-D H30 (KETEK); 30 mm² active area; 8 μm Be window; helium flow system; rare-earth permanent magnets; optimized for low-energy X-rays (positioned at 135° relative to the incident proton beam).
Detector 2	AXAS-M H150 (KETEK); 150 mm² active area; 25 μm Be window; fitted with 261 μm Kapton filter; optimized for medium- and high-energy X-rays (> 5 keV) (positioned at 135° relative to the incident proton beam).
Energy Resolution	Both detectors: 128 eV FWHM at Mn Kα line.
Proton Beam	Energy: 3.050 MeV; exit vacuum ~5.5×10^{-5} mbar via 100 nm Si_3N_4 window; collimated (~0.8 mm); ~2 mm air path; ~1 mm beam spot at sample.
Sample Alignment	Cross-mounted laser pointers + Camera for visual inspection.
Sample Positioning	Motorized XYZ stage (Zaber Console software) for precise positioning; reproducibility ensured.
Sample Holder	Specially designed rigid holder, mounted directly in front of the beam exit.

16.2.2 Reference Materials

For the calibration and validation of the PIXE setup, a series of thin reference targets was employed: the Micromatter standards consisted of thin, homogeneous elemental or compound layers deposited on 6.3 μm Mylar substrates with well-characterized areal densities (μg/cm²). These are widely used in ion beam analysis due to their stability, reproducibility, and traceable nominal concentrations. Custom standards (Ti, Mn) were also used to complement the Micromatter collection for elements of high analytical relevance to the present study. Finally, the NIST SRM 2783 was used as a certified reference material (CRM) to validate the overall quantification accuracy under experimental conditions closely resembling real aerosol samples. The complete list of Micromatter standards and Custom-made targets used in this study, along with their nominal areal concentrations, is presented on **Table 14**. The nominal areal concentrations of the NIST 2783 reference material are also presented on **Table 13**.

16.2.3 Calibration Strategy

To perform quantitative analysis, the PIXE setup was calibrated by determining the H-values. The H-value is an empirical, energy-dependent calibration parameter that links the measured X-ray yields to elemental concentrations by incorporating all instrumental and geometrical constants, such as the effective solid angle of detection, detector efficiency, and matrix correction terms. The general expression for the measured X-ray yield of an element z is (Nastasi et al., 2014):

$$Y_z = H \cdot C_z \cdot Y_1(Z) \cdot N_p \cdot \varepsilon_z \cdot t_z \quad (50)$$

Where:

- Y_z is the measured X-ray yield (number of counts recorded),
- H is the calibration factor (H-value), which includes solid angle, detector efficiency, and setup geometry,
- C_z is the areal concentration of element z in the sample (μg/cm²),
- $Y_1(Z)$is the theoretical X-ray yield per unit solid angle, per unit concentration, and per unit charge for element z,
- N_p is the number of incident protons (related to the integrated beam charge),
- ε_z is the detector intrinsic efficiency for the X-ray line of element z, and
- t_z is the transmission factor accounting for absorption by filters, detector window, and air path.

The H-value is determined experimentally using thin film standards of known composition, where all other terms in the above equation are either known or calculated. Once established, it allows for the accurate quantification of unknown samples without requiring matrix-matched standards. By relying on H-values, the calibration captures the complete response of the PIXE system, ensuring reliable multi-element quantification across a broad atomic number range (Fernandes et al., 2018).

Calibration was performed using thin-film standards. Spectra were recorded with both detectors and fitted with the GUPIX software (Campbell et al., 2021). GUPIX calculates the theoretical yields Y1(z) and normalizes them to the measured values by adjusting the H-factor. By repeating this process across several elements, an H-value curves as a function of atomic number were established. **Figure 78** shows the PIXE spectra of reference material NIST 2783 obtained with the low- and high-energy SDD detectors.

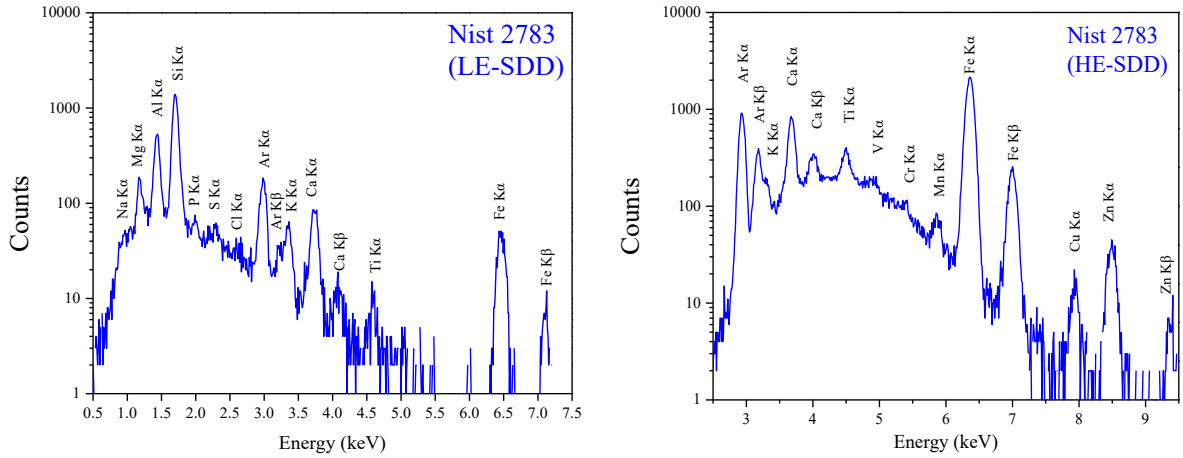

Figure 78. *PIXE spectra of the reference material NIST 2783 recorded with the two-detector setup. Left: low-energy SDD (30 mm² active area, 8 µm Be window, helium purge), optimized for low-energy X-rays. Right: high-energy SDD (150 mm² active area, 25 µm Be window, 261 µm Kapton filter), optimized for higher elements with characteristic X-rays above 5 keV.*

16.3 Results and Discussion

16.3.1 H-value Determination

The calculated H-values for both detectors are shown in **Figure 79** as a function of atomic number. For the low-energy SDD, K-line H-values were obtained from Na to Fe, while the high-energy SDD covered elements from Ca to Mo using K-lines and extended to heavier elements (Ba to Pb) using L-lines. Some fluctuations that are observed for certain elements can be attributed in the uncertainties of the certified areal densities of the thin-film standards. Such variations are typical in PIXE calibration and do not affect the overall quality of the quantification.

After determining the H-values, the spectra of the reference standards were re-analyzed in GUPIX using the newly established calibration. The elemental concentrations obtained in this way showed good agreement with the certified values, thereby confirming the reliability of the H-factors. This validation step ensured that the calibration was robust and suitable for subsequent quantification of the aerosol filters.

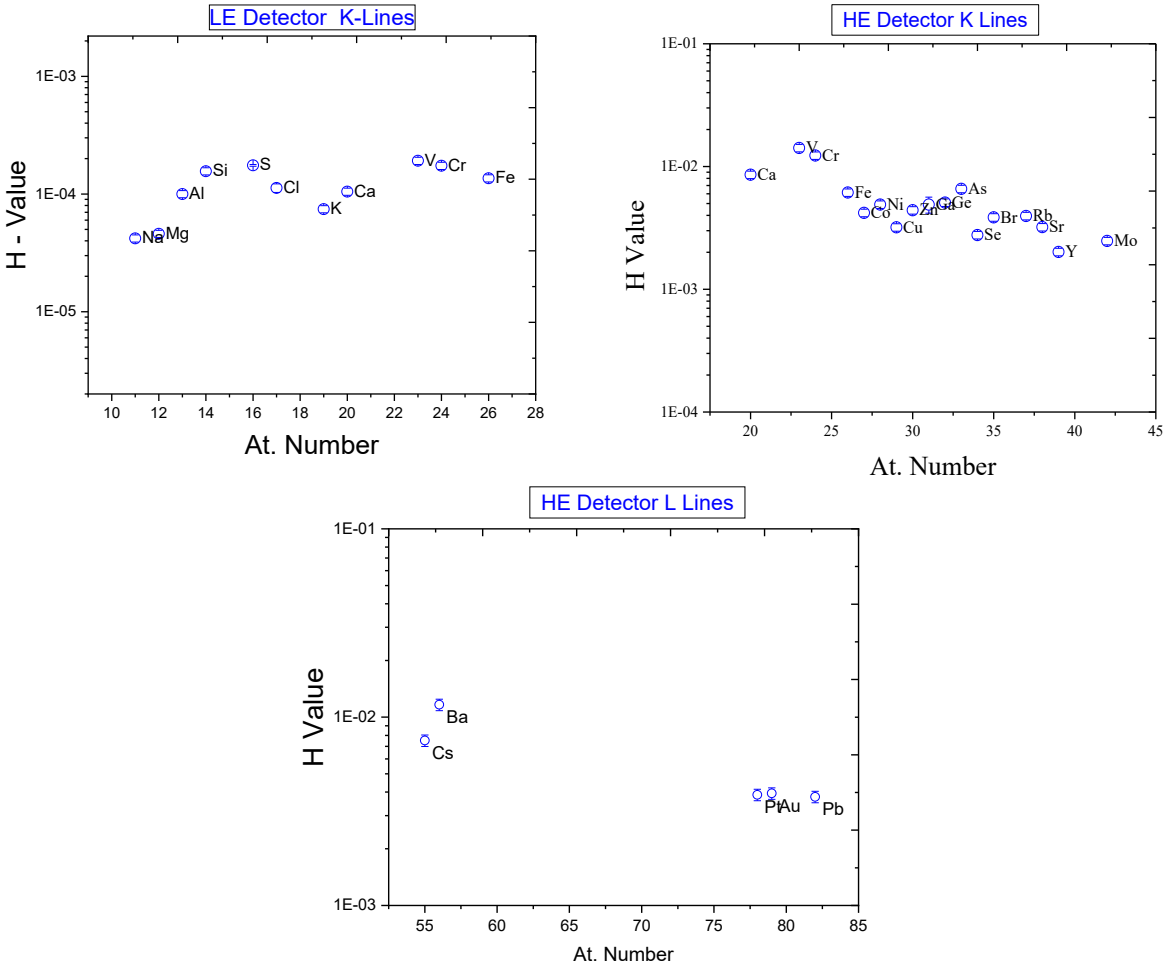

Figure 79. *Energy-dependent H-factors as a function of atomic number for the two SDD detectors. Top left: Low-energy detector, K-lines from Na to Fe. Top right: High-energy detector, K-lines from Ca to Mo. Bottom: High-energy detector, L-lines from Ba to Pb.*

16.3.2 Limit of Detection for the PIXE setup

The analytical limits of detection (LODs) of the PIXE setup were determined for each element by relating the background fluctuations under the characteristic X-ray peak to those derived from thin-film standards. The LOD for element z is expressed as:

$$LOD\left(\frac{\mu g}{cm^2}\right) = \frac{3 \cdot \sqrt{Bkg}}{Net} C_z^{std} \tag{51}$$

where:

- Bkg is the background counts within the peak region of element z,
- Net is the net peak counts measured for element z in the standard spectrum, and
- C_z^{std} is the certified areal concentration of element z in the thin-film standard.

LOD values were calculated for all elements under identical acquisition conditions. The results demonstrate the enhanced sensitivity of the LE-SDD for low-energy elements (Na–Ca) and the HE-SDD for medium-Z elements (V–Zn). A summary of the calculated LODs is provided in **Figure 80**.

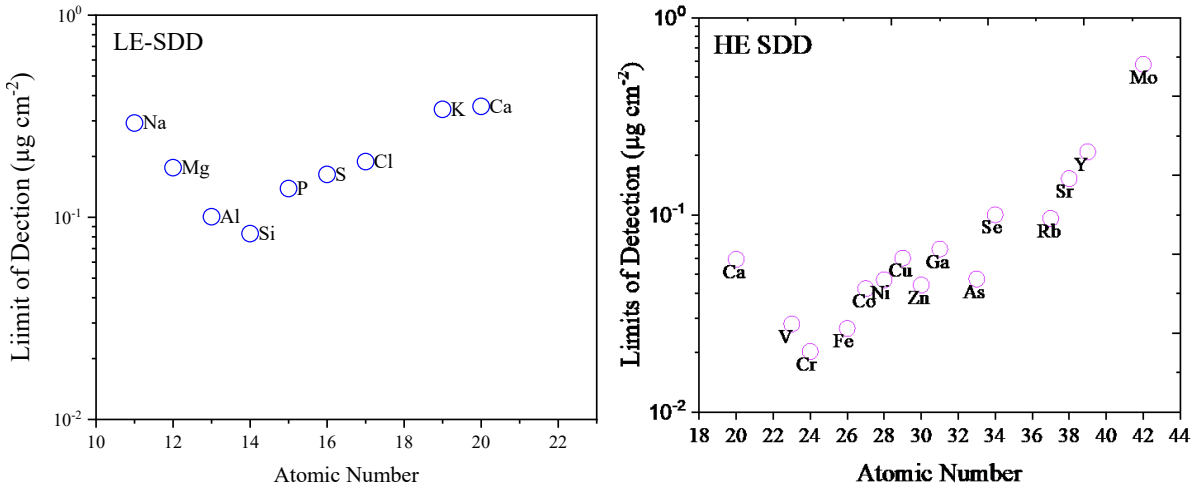

Figure 80. *Limits of detection (LODs) for elements measured with the two SDD detectors of the PIXE setup. Left: low-energy SDD (LE-SDD), optimized for light elements (Na–Ca). Right: high-energy SDD (HE-SDD), optimized for medium-Z elements (V–Zn). LODs were determined from thin-film standards).*

16.3.3 Measurements of environmental aerosol samples

The representative PIXE spectra for two $PM_{2.5}$ filters, acquired with the low-energy (LE-SDD) and high-energy (HE-SDD) detectors, illustrate the complementary coverage of the setup. The LE-SDD (8 μm Be window, He purge) is most effective below ~5 keV, where air/window absorption is critical: it resolves the light-element K lines Na–Si–P–S–Cl–K–Ca and still records Fe K lines with adequate statistics. In contrast, the HE-SDD (25 μm Be + 261 μm Kapton) intentionally suppresses photons below ~5 keV, enhancing detection of medium-Z K lines (Ti–V–Cr–Mn–Fe–Ni–Cu–Zn) (**Figure 81**).

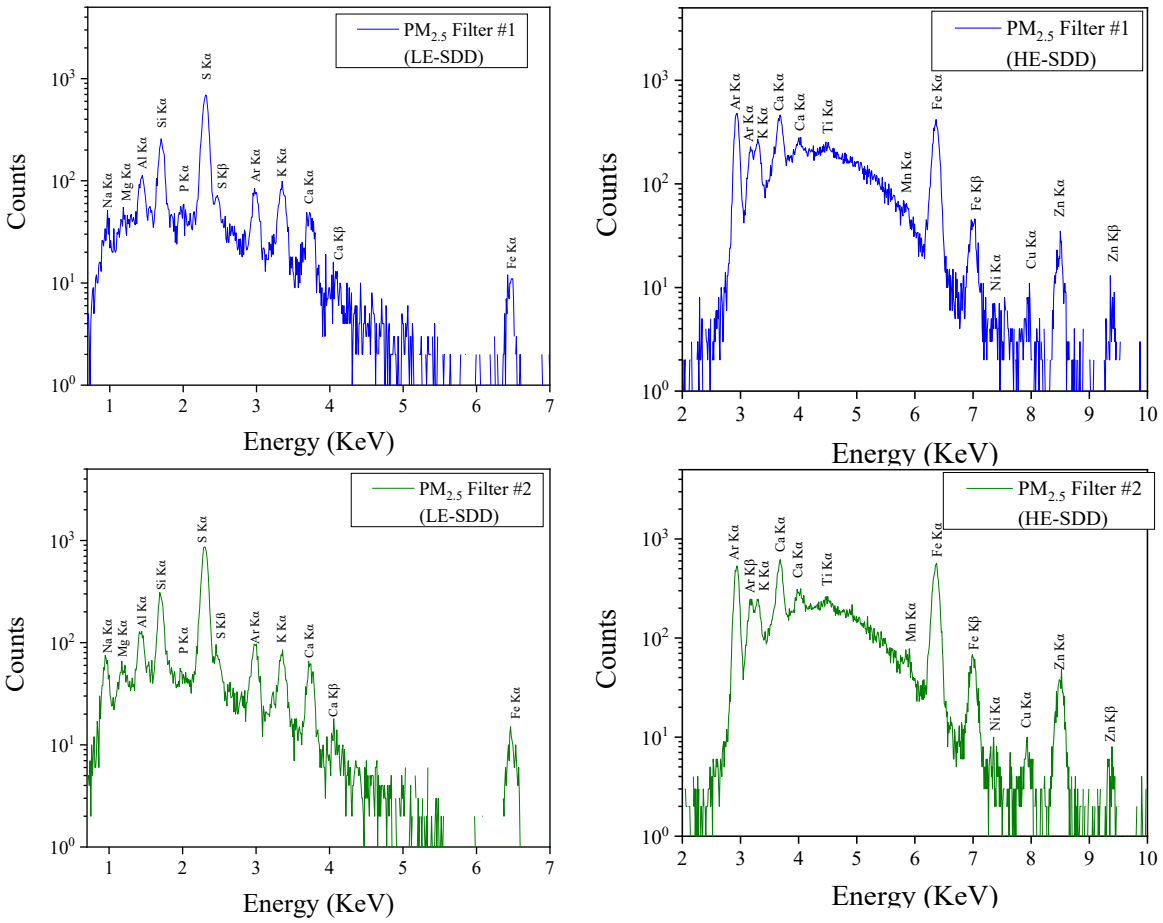

Figure 81. *Representative PIXE spectra of two $PM_{2.5}$ aerosol filters acquired with the low-energy SDD (LE-SDD, left) and the high-energy SDD (HE-SDD, right). The LE-SDD is optimized for light elements (Na–Ca), while the HE-SDD is suited for medium-Z elements (Ti–Zn). Elemental K lines are indicated. The highest-Z element detected with the present setup was Zn.*

The spectra shown correspond to acquisition times of 500 s with an integrated beam charge of approximately 2.6 μC per sample. The filters were collected at the N.C.S.R. "Demokritos" urban background station in Agia Paraskevi, Athens (37.99° N, 23.80° E, 270 m a.s.l.), located ~7 km northeast of the city center within a 600-acre pine forest at the foot of Mount Hymettus. The site is part of the ACTRIS European infrastructure and the PANACEA

National Research Infrastructure in Greece. It is considered representative of the urban background air quality in Athens, being away from direct local emission sources (Eleftheriadis et al., 2014; Triantafyllou et al., 2016). The PM samples were collected on Teflon filters over 24 h sampling periods with a low volume sampler operated at operational flow rate of 2.3 m^3h^{-1}.

The quantitative analysis of the two representative $PM_{2.5}$ filters is summarized in **Table 26**. A broad range of elements was quantified, covering both light and medium-Z species, demonstrating the wide applicability of the PIXE setup for environmental aerosol characterization. The uncertainties presented in the table originate from the GUPIX software, which provides two separate error estimates for each element: the statistical uncertainty associated with the counting statistics of the X-ray peak area (Stat error %), and the fitting uncertainty associated with the spectral deconvolution procedure (Fit error %). Since these two sources of error are independent, they were combined using the root-sum-of-squares method (e.g. Chapter 15.4.3).

Table 26. *Elemental concentrations and associated uncertainties for two representative $PM_{2.5}$ aerosol filters (Filter #1 and Filter #2), analyzed by PIXE. Concentrations are expressed in ng/cm². "BDL" indicates elements below detection limit.*

		$PM_{2.5}$ Filter #1		**$PM_{2.5}$ Filter #2**	
Z	**Element**	**Conc (ng/cm²)**	**Unc (ng/cm²)**	**Conc (ng/cm²)**	**Unc (ng/cm²)**
11	Na	241.2	51.7	866.8	93
12	Mg	137.4	38.5	262.9	59.6
13	Al	151.3	21.6	362.8	33.8
14	Si	289.7	18.1	664	28.8
15	P	*BDL*	–	*BDL*	–
16	S	1258.2	39.8	2772.8	54.5
17	Cl	*BDL*	–	*BDL*	–
19	K	630.4	59.7	804.8	81.7
20	Ca	622.2	35	985	59
22	Ti	20.9	9.6	45.1	10.6
25	Mn	11.6	4.6	17	5.2
26	Fe	379.3	12.7	726.5	16.6
28	Ni	2.6	3.7	BDL	–
29	Cu	6.9	5.8	23.2	7.2
30	Zn	41.1	7.5	100.2	10.8

For Sample 1, the dominant components included S (1258 ng/cm²), K (630 ng/cm²), and Ca (622 ng/cm²), with significant contributions also from Si (290 ng/cm²), Na (241 ng/cm²), Mg (137 ng/cm²), and Al (151 ng/cm²). Trace amounts of Mn, Ti, Fe, Ni, Cu, and Zn were detected,

while P and Cl were below the detection limit. The results highlight the sensitivity of the method to both major crustal and secondary aerosol elements.

For Sample 2, the concentration levels were generally higher. The sample was dominated by S (2773 ng/cm²), Na (867 ng/cm²), K (805 ng/cm²), Ca (985 ng/cm²), and Fe (727 ng/cm²), with notable amounts of Si, Al, and Mg. Trace metals such as Mn, Ti, Cu, and Zn were also quantified. Ni was below the detection limit in this case.

Comparison of the two filters confirms the robustness of the PIXE method, with consistent detection of major components such as S, K, Ca, and Si, which are key constituents of secondary inorganic aerosols, mineral dust, and biomass burning emissions (Viana et al., 2008). Sodium, magnesium, and calcium further reflect the contribution of marine and crustal sources (Adebiyi & Kok, 2020; Adebiyi et al., 2023), while transition metals such as Fe, Mn, Cu, and Zn are associated with anthropogenic activities, including traffic and industrial emissions (Manousakas et al., 2020; Diapouli et al., 2022).

These results demonstrate that the established calibration and H-factor approach allow reliable quantification across a wide atomic number range, down to ng/cm² levels. Despite minor differences in concentrations between the two filters, the overall elemental profiles are consistent with those typically reported for urban background aerosols in Athens, supporting the suitability of PIXE for routine multi-elemental characterization of $PM_{2.5}$.

16.4 Conclusions

This chapter presented the calibration and application of the PIXE setup at NCSR "Demokritos" for the quantitative analysis of atmospheric $PM_{2.5}$ filters. The use of two complementary detectors, a low-energy SDD and a high-energy SDD, enabled continuous elemental coverage from sodium to zinc. The low-energy detector proved particularly effective for the determination of light elements such as Na, Mg, Al, Si, P, S, Cl, K, and Ca, while the high-energy detector allowed reliable quantification of medium-Z elements, including V, Cr, Mn, Fe, Ni, Cu, and Zn. Calibration of the system was performed through the determination of energy-dependent H-factors using thin-film standards. The resulting H-values curves exhibited the expected smooth dependence on atomic number, with only minor fluctuations that can be attributed to uncertainties in the certified areal densities of the reference standards and to statistical effects

The calculated limits of detection reached ng/cm² levels for several elements. The low-energy detector provided the best performance for light elements, while the high-energy detector offered superior sensitivity for transition metals, consistent with the design characteristics of the system. Application of the method of representative $PM_{2.5}$ filters collected at the urban background site in Athens demonstrated the ability of PIXE to quantify both major aerosol components—such as S, K, Ca, Si, Na, Mg, and Al—and trace elements including Mn, Ti, Fe, Cu, Zn, and Ni. The elemental profiles obtained are consistent with

known contributions from secondary inorganic aerosols, crustal dust, marine sources, and anthropogenic activities.

Overall, the results confirm that the calibration strategy and dual-detector configuration provide reliable, multi-elemental quantification of $PM_{2.5}$ filters. The PIXE setup at NCSR "Demokritos" has thus been shown to be a powerful and sensitive tool for environmental aerosol research, capable of supporting detailed studies on elemental composition and subsequent source apportionment analysis.

16.5 References

Adebiyi, A. A., & Kok, J. F. (2020). Climate models miss most of the coarse dust in the atmosphere. *Science Advances*, *6*(15). https://doi.org/10.1126/SCIADV.AAZ9507/SUPPL_FILE/AAZ9507_SM.PDF

Adebiyi, A., Kok, J. F., Murray, B. J., Ryder, C. L., Stuut, J. B. W., Kahn, R. A., Knippertz, P., Formenti, P., Mahowald, N. M., Pérez García-Pando, C., Klose, M., Ansmann, A., Samset, B. H., Ito, A., Balkanski, Y., Di Biagio, C., Romanias, M. N., Huang, Y., & Meng, J. (2023). A review of coarse mineral dust in the Earth system. *Aeolian Research*, *60*, 100849. https://doi.org/10.1016/J.AEOLIA.2022.100849

Campbell, J. L., Cureatz, D. J. T., Flannigan, E. L., Heirwegh, C. M., Maxwell, J. A., Russell, J. L., & Taylor, S. M. (2021). The Guelph PIXE Software Package V. *Nuclear Instruments and Methods in Physics Research Section B: Beam Interactions with Materials and Atoms*, *499*, 77–88. https://doi.org/10.1016/J.NIMB.2021.05.004

Chiari, M., Lucarelli, F., Mazzei, F., Nava, S., Paperetti, L., Prati, P., Valli, G., & Vecchi, R. (2005). Characterization of airborne particulate matter in an industrial district near Florence by PIXE and PESA. *X-Ray Spectrometry*, *34*(4), 323–329. https://doi.org/10.1002/xrs.825

Diapouli, E., Fetfatzis, P., Panteliadis, P., Spitieri, C., Gini, M. I., Papagiannis, S., Vasilatou, V., & Eleftheriadis, K. (2022). *PM2.5 Source Apportionment and Implications for Particle Hygroscopicity at an Urban Background Site in Athens, Greece*. *13*, 1685. https://doi.org/10.3390/atmos13101685

Fernandes, F., Niekraszewicz, L. A. B., Amaral, L., & Dias, J. F. (2018). Evaluation of detector efficiency through GUPIXWIN H value. *Nuclear Instruments and Methods in Physics Research Section B: Beam Interactions with Materials and Atoms*, *417*, 56–59. https://doi.org/10.1016/J.NIMB.2017.07.035

Lucarelli, F., Calzolai, G., Chiari, M., Nava, S., & Carraresi, L. (2018). Study of atmospheric aerosols by IBA techniques: The LABEC experience. *Nuclear Instruments and Methods in Physics Research Section B: Beam Interactions with Materials and Atoms*, *417*, 121–127. https://doi.org/10.1016/J.NIMB.2017.07.034

Manousakas, M. I., Florou, K., & Pandis, S. N. (2020). Source apportionment of fine organic and inorganic atmospheric aerosol in an urban background area in Greece. *Atmosphere*, *11*(4). https://doi.org/10.3390/ATMOS11040330

Nastasi, M., Mayer, J. W., & Wang, Y. (2014). *Ion Beam Analysis: Fundamentals and Applications* (1st ed.). CRC Press. https://doi.org/10.1201/b17310

Viana, M., Kuhlbusch, T. A. J., Querol, X., Alastuey, A., Harrison, R. M., Hopke, P. K., Winiwarter, W., Vallius, M., Szidat, S., Prévôt, A. S. H., Hueglin, C., Bloemen, H., Wåhlin, P., Vecchi, R., Miranda, A. I., Kasper-Giebl, A., Maenhaut, W., & Hitzenberger, R. (2008). Source apportionment of particulate matter in Europe: A review of methods and results. *Journal of Aerosol Science*, *39*(10), 827–849. https://doi.org/10.1016/J.JAEROSCI.2008.05.007

17. Near Real-Time & Benchtop XRF Intercomparison for PM Elemental Analysis on Quartz and Teflon Filters: A Case Study Across Three European Cities

Published as:

Papagiannis, S., Manousakas, M. I., Anagnostopoulos, D. F., Pipkridas, M., Baalbaki, R., Sciare, J., O'Sullivan, N., Hellebust, S., Wenger, J., Fossum, K. N., Ovadnevaite, J., Tremper, A., Green, D., Eleftheriadis, K., and Diapouli, E (2026). Near Real-Time & Benchtop XRF Intercomparison for PM Elemental Analysis on Quartz and Teflon Filters: A Case Study Across Three European Cities, EGUsphere [preprint], https://doi.org/10.5194/egusphere-2025-5977

17.1 Abstract

This study presents an extensive intercomparison between a benchtop X-ray fluorescence (XRF) system and near real-time XRF monitors (Xact 625 and 625i) for measuring elemental concentrations in ambient aerosols. The measurements were conducted across three locations: Athens (Greece, March 2024), Nicosia (Cyprus, March–January 2023), and Dublin (Ireland, December 2022–February 2023). The focus was on evaluating the chemical composition of particulate matter (PM) and the impact of filter substrate choice on measurement consistency. The study specifically examines the elements Si, S, Cl, K, Ca, V, Ti, Mn, Fe, Cu, Ni, Zn, Sr, and Pb. The results highlight that filter type plays a crucial role in ensuring accurate measurements when utilizing the benchtop XRF system. At the Athens site, where PTFE filters were used, the agreement between the Xact 625i and the benchtop XRF system was stronger, with slopes generally closer to unity for most elements. In contrast, quartz fiber filters at the Dublin and Nicosia sites led to systematic deviations, especially for light elements such as S, Cl, and K, even after applying correction factors. For heavier elements like Fe, Mn, and Cu, the filter effect was less pronounced, though some variation across sites remained. Zn consistently showed good agreement, while Pb exhibited weaker correlation, possibly due to differences in the calibration curves of the two systems. Overall, this study not only evaluates instrument performance across multiple environments but also provides practical guidance for mitigating filter-related artifacts to enhance consistency in elemental aerosol measurements.

17.2 Introduction

Particulate matter (PM) is a well-known major atmospheric pollutant, originating from both natural and anthropogenic sources, with significant impacts on health (Ostro et al., 2015; Samoli et al., 2013) and climate (Chen et al., 2021). Composed of a complex blend of chemical components, such as carbonaceous, ionic, and elemental species, the PM's composition varies widely depending on sources and environmental conditions, which contributes to its diverse chemical and physical characteristics.

The elemental analysis of atmospheric aerosols can offer information of critical value for health and source apportionment studies, which are vital for understanding pollution sources (Manousakas et al., 2021; Hopke et al., 2020), assessing population exposure risks (Megido et al., 2017; Caggiano et al., 2019), and implementing effective air quality management strategies. Exposure to certain elements, including As, Ni, Cr, Cd, and Pb, has been associated with an elevated cancer risk via inhalation (Aldekheel et al., 2023). These trace elements are also implicated in disrupting respiratory health by impairing mucociliary clearance, weakening barrier functions, inducing airway inflammation, promoting oxidative stress, and triggering cell apoptosis (Skalny et al., 2020).

Although elemental species do not substantially contribute to the overall mass of PM, they are crucial for accurately identifying pollution sources. The chemical signatures of the processes are mirrored in the emitted aerosol particles, enabling the use of specific elements to trace and allocate the sources of ambient aerosols effectively (Viana et al., 2008; Amato et al., 2016; Diapouli et al., 2017). For example, crustal elements like Al, Si, Ca and Fe serve as indicators of mineral dust (Viana et al., 2008; Jain et al., 2020); Cu and Zn are markers of brake and tire wear (Rhodes et al. 2012; Huang et al. 2018; Thorpe and Harrison 2008); Br and Cl are indicators of coal combustion (Papagiannis et al., 2024); and V and Ni may point to heavy oil combustion (Jang et al., 2007; Healy et al., 2009).

Clearly, the accurate assessment of the elemental composition of ambient aerosols is of vital importance. PM emissions and atmospheric dynamics, influenced by factors like wind direction and precipitation, can fluctuate within hours, affecting aerosol concentration and composition. Sampling on an hourly timescale (or at even higher time resolution) allows for a more detailed understanding of emission, transport, and deposition processes, enabling the capture of rapid source impacts. The recent advancements in high-time-resolution elemental analysis, especially by energy dispersive X-ray fluorescence (ED-XRF) spectrometers such as the Xact 625 and Xact 625i (SailBri Cooper, Inc.), have significantly enhanced the ability to identify and trace pollution sources with greater precision (Manousakas et al., 2022; Rai et al., 2020). In addition, those near real-time XRF spectrometers (NRT-XRF) also allow automated sampling of both PM10 and PM2.5 which greatly enhances the information regarding aerosol composition (Furger et al., 2020).

A focused comparison of benchtop ED-XRF and NRT-XRF spectrometers, specifically regarding the measured elemental concentrations, is essential to determine their effectiveness in elemental monitoring of ambient aerosols. While past studies have evaluated the performance of NRT-XRF instruments, specifically the Xact 625 and 625i (Windell et al., 2025), these comparisons primarily involved ICP-MS (Furger et al., 2017; Tremper et al., 2018; Bhowmik et al., 2022) and, in only one case, the comparison of a benchtop ED-XRF spectrometer with an earlier Xact 625i model (Cadeo et al., 2025). This limited research underscores the need for a direct, updated comparison between current NRT and benchtop ED-XRF instruments to validate their performance in real-world conditions and to assess whether NRT-XRF could potentially replace traditional methodologies.

In addition to the need for direct instrument comparison, the choice of filter substrate significantly affects quantitative PM analysis in ED-XRF spectrometry (Unga et al., 2025). Within many air quality monitoring networks, high-volume samplers routinely employ quartz fiber filters because of their compatibility with subsequent analyses of organic and ionic species. When extending these existing measurements to include elemental or metal characterization, it is often more practical to use the already collected quartz filters rather than perform additional co-located sampling on Teflon filters. However, this approach requires careful consideration of substrate-related effects. While many studies have examined Teflon and quartz fiber filter differences for organic and ionic species (Vecchi et al., 2009; Khuzestani et al., 2017; Aikawa and Hiraki 2010), there is limited literature regarding elemental

characterization (Chiari et al., 2018; Yatkin et al., 2012). (Chiari et al., (2018) emphasized the challenges when working with quartz fiber filters, which can introduce self-absorption and matrix effects due to their thickness, potentially leading to very high inaccuracies in concentration measurements, especially for lighter elements. Corrective methods are therefore essential when using quartz fiber filters to obtain accurate elemental concentrations.

For the reasons above, this study focuses on a detailed comparison between a benchtop ED-XRF and near real-time (NRT) XRF spectrometers (specifically the Xact 625 and 625i models) for measuring elemental concentrations in ambient aerosols, alongside an evaluation of filter substrate performance. Measurement campaigns were conducted in Athens, Greece (March 2024), Nicosia, Cyprus (March 2022–January 2023), and Dublin, Ireland (December 2022–February 2023), including quartz fiber and Teflon substrates for the comparison. Additionally, a dedicated filter substrate campaign was performed in January 2024. The results will compare the two instrument types across different environments and timeframes, providing insights into their consistency and applicability. Furthermore, the filter substrate comparison will assess the impact of Teflon and quartz fiber filters on elemental quantification and offer practical recommendations for corrective procedures in aerosol studies.

17.3 Experimental

17.3.1 Sampling and Study area

Athens N.C.S.R. "Demokritos" station (ATH-DEM):

Measurements in Athens, specifically in Agia Paraskevi, were conducted at the urban background monitoring station located on the N.C.S.R. "Demokritos" campus (37°59'42.0"N, 23°48'57.6"E; 270 m above sea level) (**Figure 82**). This station is approximately 7 km northeast of central Athens and is situated at the base of Mount Hymettus. The station is part of the PANACEA National Infrastructure for Greece and provides representative data to the ACTRIS European infrastructure on urban background air quality due to its location, which is largely unaffected by direct emissions from urban PM sources (Zografou et al., 2022, Eleftheriadis et al., 2021).

A 24-hour sampling campaign took place from March 5 to March 25, 2024, resulting in 21 PM2.5 samples. These samples were collected using Teflon filters (PTFE Pall R2PJ047 with PMP support ring, 47 mm diameter, 2 μm pore size) on a low-volume sampler (Sequential 47/50-CD, Sven Leckel GmbH, Berlin, Germany) operating at a flow rate of 2.3 m^3/h. In addition, an earlier campaign was conducted from January 13 to January 31, 2024, to investigate potential differences in elemental composition when using different filter substrates. This included 21 PM10 samples collected on Teflon filters (WHATMAN – PTFE,

polypropylene-backed, pore size 1.0 μm, diameter 47 mm) and 21 PM10 samples collected on quartz fiber filters (PALLFLEX Tissue Quartz).

Cyprus Atmospheric Observatory (CAO-NIC):

Sampling was conducted at the Cyprus Atmospheric Observatory (CAO-NIC) urban background station of the Cyprus Institute premises in Nicosia (Athalassa Campus; 35°08'27.6"N 33°22'51.6"E; 174 m above seal level) (**Figure 82**). The site is located in a low-density residential area and is approximately 800 meters from the nearest major road and far from other significant anthropogenic sources. The Athalassa Forest Park lies to the southeast of the institute, further contributing to the minimal local pollution influences. Source apportionment studies (Bimenyimana et al., 2025; Bimenyimana et al., 2023; Christodoulou et al., 2023) show that PM at the site originates from a complex blend of local and regional sources. Regional air masses vary seasonally, bringing sulfate-rich air from Turkey and Eastern Europe in summer and dust mixed with anthropogenic pollutants from the Middle East and North Africa during other seasons. Local sources include biomass burning, traffic, power generation, and shipping activities.

PM2.5 particles were collected on 47-mm diameter quartz filters (Tissuquartz 2500QUAT-UP, Pall) at 10 m above ground level (AGL)using a Leckel SEQ47/50 sampler operating at a flow rate of 2.3 m^3/h and utilizing. After collection, the filters were placed in petri dishes and stored at -18 °C until further analysis. To ensure the proper functioning of the sampler, regular flow checks were performed throughout the campaign. A total of 256 filters were utilized over the course of the measurement period, from March 18, 2022, to January 17, 2023. Most samples were taken over 24-hour intervals, from 00:00 to 00:00 UTC. However, between December 16, 2022, to January 17, 2023, the sampling frequency was increased to every 8 hours corresponding to three collection periods: 02:00 – 10:00, 10:00 – 18:00, and 18:00 – 02:00.

Dublin Port Station (DUB-P):

Measurements were conducted in Dublin Port from 16 December 2022 to 7 February 2023 as part of the research project Source Apportionment of Air Pollution in the Dublin Port Area (PortAIR) (Fossum et al., 2025). Aerosol physicochemical properties and gaseous pollutants were measured using a suite of instrumentation housed in two containers. The monitoring site (53°20'54.4"N 6°11'40.8"W) (**Figure 82**) was selected to be downwind of most port activity and close to the ferries, which are a major daily source of shipping emissions (Fossum et al., 2024). A total of 54 PM2.5 samples were collected onto quartz fiber filters (Pallflex, 150 mm diameter), pre-baked for 3 hours at 850°C, using a high-volume sampler (model DHA 80, Digitel) operating at a flow rate of 500 L min^{-1}. Following collection, the filters were individually packed and stored in a freezer at −18°C. until analysis.

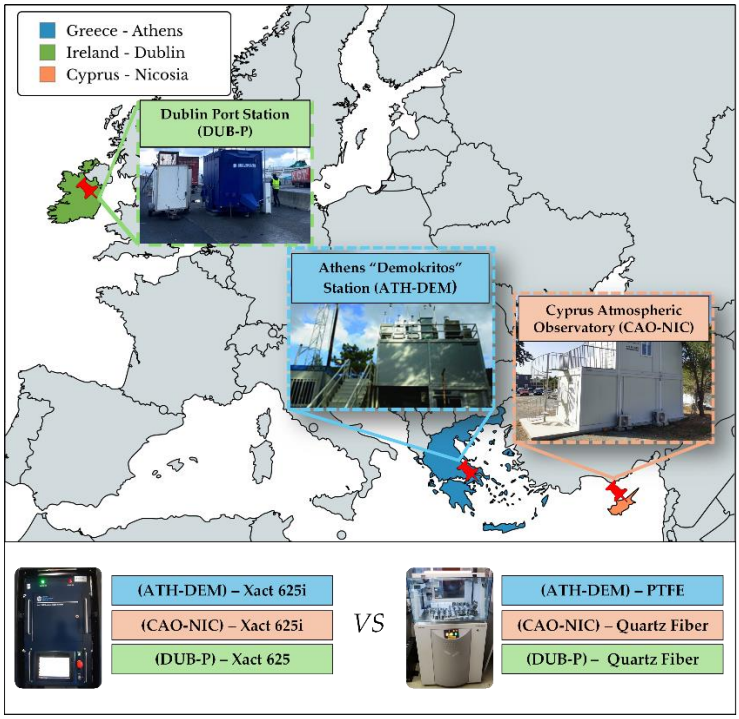

Figure 82. *Locations of the measurement campaigns conducted in this study.*

17.3.2 Benchtop ED-XRF spectrometer

PM2.5 samples were analysed for major and trace elements using a high-resolution energy-dispersive X-ray fluorescence (ED-XRF) spectrometer with advanced 3-D optics, the Epsilon 5 (PANalytical). The spectrometer features a side-window, low-power X-ray tube equipped with a tungsten/scandium (W/Sc) anode. The characteristic X-ray radiation emitted by the samples is detected by a germanium (Ge) detector, offering an energy resolution of approximately 150 eV full-width at half-maximum (FWHM) at the Mn-Kα line (5.89 keV). To enhance measurement precision, the system employs six secondary targets (CaF_2, Ge, Mo, KBr, Al_2O_3, and LaB_6) that polarize the X-ray beam, allowing for six optimized measurement conditions tailored to the analysis of aerosol samples.

Calibration of the ED-XRF spectrometer was performed using a range of reference standards, including infinitely thin, single-element, compound, and multi-element materials. Specifically, 27 Micromatter thin-film standards deposited on 6.3 μm Mylar substrates were utilized, encompassing materials such as NaCl, MgF_2, GaP, SiO, KCl, CaF_2, V, Fe, Cr, Co, CuS_x, Al, Ni, CsBr, RbI, SrF_2, Ge, Se, Ag, Sn, Sb, Pt, AgHg, CdSe, Pb, Au, BaF_2, and Ce. Additionally, 22 multi-element standards were used, including one SRM 2783 standard and 21 UCDAVIS standards on polycarbonate and Teflon substrates. The reported uncertainty for Micromatter standards is 5%, while for multi-element standards, it is 10%. Each sample underwent a 60-minute analysis. The detection limits are calculated using the equation (Manousakas et al., 2018):

$$LoD = \frac{3\sqrt{Bkg}}{I\,t}\,\frac{1}{S} \tag{52}$$

here, LoD represents the detection limit in μg/cm², Bkg denotes the background counts of a field blank filter over a FWHM region centered at the element's principal peak centroid, I is the tube current in mA, t is the measurement time in seconds (s), and S refers to the sensitivity in $(\frac{counts}{s\ mA})/(\frac{\mu g}{cm^2})$. **Figure 83a** presents the detection limits for the measured elements on PTFE and quartz fiber blank filters in ng m^{-3}. To express the concentrations and detection limits in volumetric units (ng/m³), values in μg/cm² were first multiplied by the effective area of the filter (cm²) and then divided by the total sampled air volume (m³). This conversion accounts for the sampled air mass per unit volume and allows for direct comparison with ambient air quality standards.

The Quality Assurance/Quality Control (QA/QC) protocol for analysis includes a series of procedures to ensure high data quality and reliable instrument performance. The procedures involve: a) Weekly calibration of the Ge detector – The XRF software automatically fine-tunes the energy channels to maintain optimal detector performance; b) Regular performance evaluation using SRM 2783 – Weekly analyses of the multi-element reference material are conducted to verify analytical accuracy and precision for each analyte; c) Daily monitoring with PTFE blanks – Selected PTFE blank samples are systematically analyzed to assess long-term reproducibility and ensure consistency across measurements.

17.3.3 Near real-time (NRT) XRF spectrometers

The study utilized near real-time XRF spectrometers at three locations: Athens, Greece (ATH-DEM station, Xact 625i, Cooper Environmental Services (CES), Beaverton, OR, 129 USA), Dublin, Ireland (DUB-P station, Xact 625 Cooper Environmental Services (CES), Beaverton, OR, 129 USA), and Nicosia, Cyprus (CAO-NIC station, Xact 625i, Cooper Environmental Services (CES), Beaverton, OR, 129 USA).

The Xact systems (625 and 625i) used in this study operate at a flow rate of 1 m³/h through a $PM_{2.5}$ cyclone, collecting particles on Teflon filter tape and analyzing them hourly. During each cycle, the collected sample is irradiated using a 50 kV, 50 W Rh-anode X-ray tube, and the resulting fluorescence is recorded by a silicon drift detector. Spectra are processed using the manufacturer's software to quantify elemental concentrations. The instruments run continuously, with simultaneous sampling and analysis, and routine QA checks (flow, calibration stability) performed daily and at campaign start/end. The Xact 625 deployed in Dublin (16 December 2022–7 February 2023) reported up to 24 elements (Si–U) and used a heated inlet (45 °C) when relative humidity exceeded 45%. The Xact 625i instruments in Athens (5–25 March 2024) and Nicosia (18 March 2022–17 January 2023) measured up to 35 elements (Al–Pb) under otherwise similar operating conditions.

The limits of detection for the Xact 625i and 625 are determined for each element using its sensitivity and the background counts from a blank, unused section of the tape. The reported values correspond to 1σ interference-free detection limits. For this study, a 60-minute time resolution was used. The limits of detection for Xact 625 and 625i are calculated using the equation (Rai, 2020):

$$LoD_{\sigma_0} = \frac{\sigma_0}{V} = \frac{\sqrt{Bkg\ t\ I}}{S\ t\ I}\ \frac{1}{V} \tag{53}$$

Where, σ_0 represents the 68% confidence level detection limit, Bkg is the background count rate in $counts/(s\ \mu A)$, t is the live time in seconds (s), I is the current in μA, S is the sensitivity in $(\frac{counts}{s\ mA})/(\frac{\mu g}{cm^2})$ and V is the sample volume in m^3. **Figure 83b** presents the LoDs of the Xact Xact625i XRF spectrometers in ng/m^3

Quality assurance procedures for the Xact 625i included daily energy calibration using Cr- and Nb-coated rods, response stability checks for Cd, Cr, and Pb, and independent flow rate verifications. Tape blanks spectra were collected before and after filter tape changes to ensure accuracy.

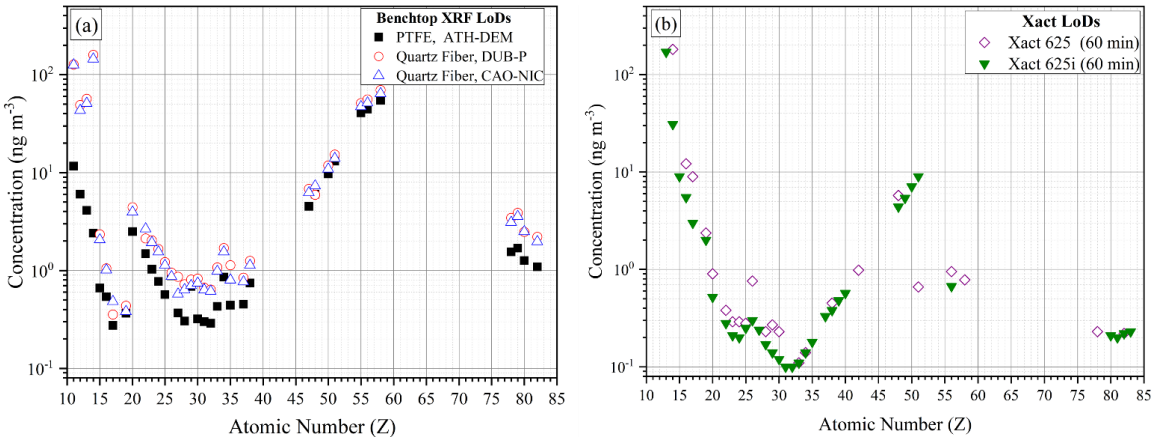

Figure 83. a) Limits of detections for the benchtop XRF spectrometer (Epsilon 5), for PTFE filters in ng m^{-3}. b) Limits of detections for the Xact 625i for 60-minute time resolution.

17.4 Results

17.4.1 Impact of PTFE and Quartz fiber filter substrates on aerosol elemental analysis with ED-XRF

In this study, benchtop ED-XRF measurements were performed on quartz fiber filters at the CAO-NIC and DUB-P sites. Because the characteristic X-ray signal response can depend on the filter matrix and thickness, it is essential to assess substrate-related effects prior to comparing data from the two systems. Evaluating the behavior of PTFE versus quartz fiber filters therefore provides a necessary basis to ensure that observed differences between the benchtop XRF and the Xact originate from instrument performance and aerosol characteristics, rather than from substrate-induced analytical bias.

The comparison of ED-XRF measurements on PTFE and quartz fiber filters underscores the influence of aerosol penetration into the quartz matrix, particularly affecting low-energy X-rays (light elements). PTFE filters, with a typical thickness of 40–50 μm, retain particles on the surface and are thus considered "infinitely thin" for XRF analysis (Chiari et al., 2018). In contrast, quartz filters— with thickness approximately at 400–600 μm —act as bulk substrates, with particles depositing both on the surface and up to ~20 μm deep (Castaneda et al., 1998; Žitnik et al., 2008). Additionally, SEM analysis by Suárez-Peña et al. (2016) confirmed the isotropic structure of quartz fibers, showing non-uniform voids and deep particle penetration, especially for submicron aerosols. Particles <1 μm can reach depths beyond 300 μm, with those 0.1–0.5 μm accumulating in the inner layers (300–600 μm) due to Brownian diffusion, while larger particles are captured in the outer layers via interception and impaction.

When using quartz fiber filters, attenuation effects impact the measurement of light elements by weakening low-energy X-rays. Aerosol particles that penetrate the filter matrix experience filter attenuation, where emitted X-rays are absorbed by the filter material before escaping. Additionally, the strong Si signal from quartz fiber filters not only hinders the precise measurement of lighter elements (Na, Mg, and Al) but also significantly enhances the spectral background which further complicates the detection of these elements, reducing measurement accuracy and sensitivity. In contrast, PTFE filters, which retain particles on the surface, minimize this effect.

To assess the impact of filter type on ED-XRF measurements, we compared elemental concentrations from 21 quartz fiber and 21 Teflon 24-hour PM_{10} filters (Section 2.1), evaluating differences due to particle penetration and X-ray attenuation. Although this comparison was performed on PM_{10} samples, it remains highly relevant to our PM2.5 dataset, as the elements most affected by attenuation — S, Cl, K—are primarily associated with fine fraction aerosols. Gini et al. (2022) reported that fine elemental Sulfur, mainly present as sulfate (SO_4^{2-}), originates from anthropogenic sources and is predominantly found in the submicron range (0.1–1 μm). Similarly, potassium exhibits a bimodal distribution, but its fine fraction—linked to biomass burning—remains the dominant one.

Linear regressions through the origin (y = ax) were performed to capture the proportional attenuation caused by the quartz filters, without introducing a baseline offset, because both filters were exposed to the same aerosol loading. The comparison between PTFE and Quartz fiber filters yielded strong correlations ($R^2 \geq 0.95$) across all analyzed elements. Slopes represent the ratio of Teflon to quartz fiber concentrations, with values above unity indicating attenuation by the quartz filter. S exhibited the highest slope (1.87 ± 0.05), followed by Cl (1.51 ± 0.08) and K (1.48 ± 0.06), suggesting enhanced attenuation (**Table 27**). In contrast, elements such as Ca (1.00 ± 0.01), Fe (0.95 ± 0.08), showed slopes near unity, consistent with minimal filter-induced effects for heavier elements.

Table 27. Linear regression slopes for each element comparing quartz fiber and Teflon filters.

Element	Slope
S	1.87 ± 0.05
Cl	1.51 ± 0.08
K	1.48 ± 0.06
Ca	1.00 ± 0.01
Ti	0.95 ± 0.02
Fe	0.95 ± 0.01
Ni	1.04 ± 0.04
Cu	0.98 ±0.02
Zn	1.07 ± 0.01

Based on these results, correction factors of 1.87, 1.51, and 1.48 were applied to S, Cl, and K measurements, respectively, while no corrections were applied to Ca, Ti, Fe, Ni, Cu, and Zn due to slopes close to unity and negligible substrate influence.

Additionally, from the recent study of Unga et al. (2025) on PM10 filters, it is shown that quartz fiber filters systematically yield lower concentrations for light elements such as S, Cl, and K compared to Teflon substrates (~0.6–0.7 Cquartz/CTeflon ratios). Our results agree with this trend, as the Teflon/quartz fiber slopes obtained here for S (1.87), Cl (1.51), and K (1.48) (**Table 27**) correspond to inverse ratios of approximately 0.5–0.7, confirming similar attenuation effects in quartz fiber substrates for light elements. **Figure 84** displays the comparison of elemental concentrations between Teflon and quartz fiber filters for S, K, Ca, and Fe.

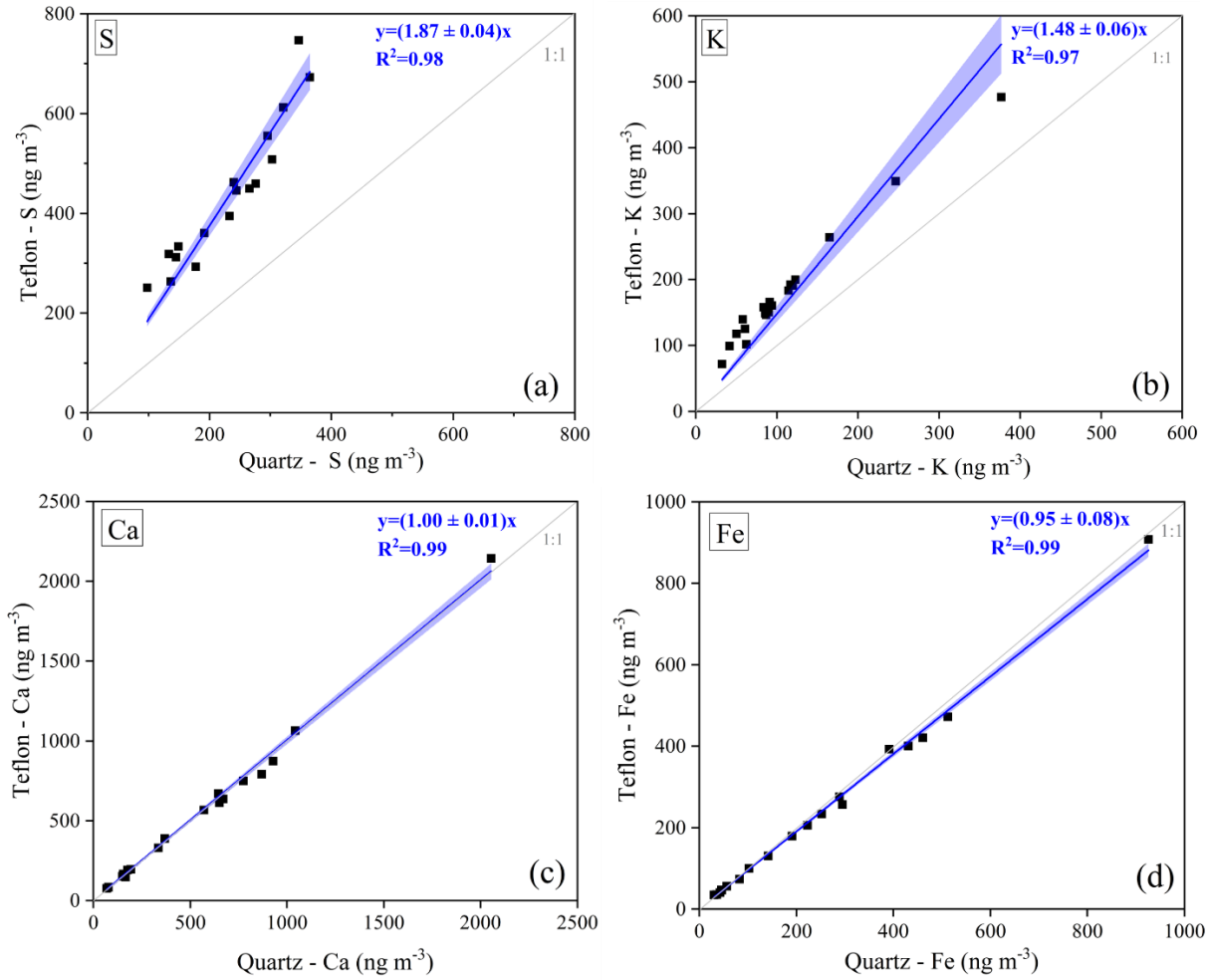

Figure 84. *Comparison of Elemental Concentrations: Teflon vs. Quartz Filters of S (a), K (b), Ca (c) and Fe (d).*

To further investigate attenuation effects, we simulated the characteristic intensities of S, Cl and K as a function of quartz fiber thickness utilizing the XMI-MSIM code (Schoonjans et al., 2013). The simulation incorporated the X-ray excitation energy (3.69 keV), spectrometer geometry, and detector characteristics of the Panalytical Epsilon 5 ED-XRF system. For quartz fiber thicknesses ranging from 1 to 450 µm, the normalized X-ray intensity showed a marked decrease due to absorption within the filter matrix. At 100 µm, the transmitted intensity dropped to approximately 0.30 for S, 0.36 for Cl, and 0.46 for K, confirming significant attenuation for lighter elements as the thickness of the quartz fiber filter increases **Figure 85**).

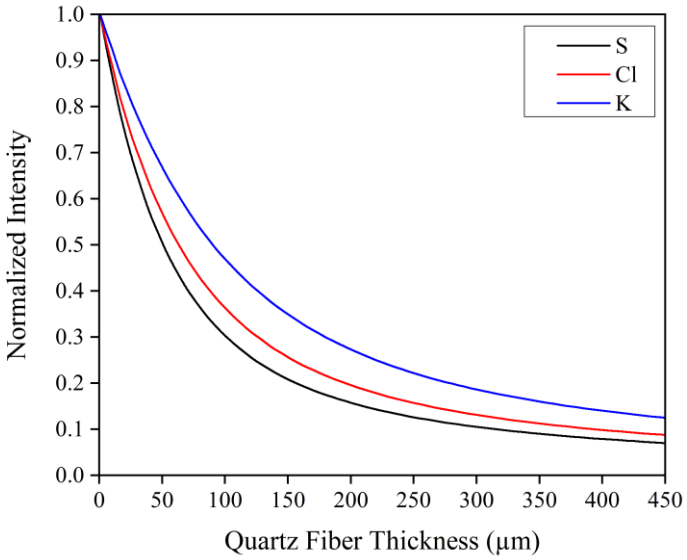

Figure 85. *Normalized intensity of S, Cl and K as a function of quartz fiber thickness filter using the XMI-MSIM simulation code.*

17.3.2 Comparative Analysis of NRT-XRF Monitors and Benchtop XRF Spectrometer: Data Processing

For the comparison between the NRT-XRF monitors (Xact 625 and Xact 625i) and the filter samples analyzed by the benchtop XRF spectrometer, the hourly Xact measurements from corresponding days were averaged to match the 24-hour filter sample periods. Each 24-hour cycle included 23.5 hourly values from the Xact instruments, while the remaining half hour is utilized for the system's calibration check. For calculating the 24-hour average value, any hourly values reported below the LOD were substituted with LOD/2 Additionally, when quartz fiber filters were used, the measured concentrations of S, Cl, and K were multiplied by correction factors of 1.87, 1.51, and 1.48, respectively (**Table 27**. Linear regression slopes for each element comparing quartz fiber and Teflon filters.).

For the quantitative analysis only values above the limit of quantification (LOQ) were used in the comparison, to ensure accuracy and reliability. The LOQ, defined as three times the limit of detection, represents the lowest concentration that can be quantified with acceptable precision and accuracy.

Linear regressions were performed using the model $y=ax+b$, as including an intercept allows detection of systematic offsets between instruments and avoids biasing the slope, consistent with best practice in instrument inter-comparison studies. In addition, 95% confidence intervals from the least-squares fit were included in the regression plots to illustrate the uncertainty in the relationship between the instruments.

17.3.3 Benchtop XRF (PTFE) vs Xact 625i

Teflon filter samples analyzed using the benchtop XRF system were compared with the corresponding Xact 625i measurements for eight elements (Si, S, Cl, K, Ca, Ti, Fe, and Zn). The linear regression slope and coefficient of determination (R^2) for each element are summarized in **Table 28**. **Figure 86** presents the regression curves for Si, S, Fe, and Zn, while **Figure 87** shows the time series graphs for S and Fe.

Table 28. *Summary of linear regression slopes and R^2 values for each element at the ATH-DEM, CAO-NIC, and DUB-P stations.*

	ATH-DEM station		CAO-NIC station		DUB-P station	
Element	**Slope**	**R^2**	**Slope**	**R^2**	**Slope**	**R^2**
Si	0.94 ± 0.19	0.88	–	–	–	–
S	0.97 ± 0.01	0.99	1.20 ± 0.07	0.49	1.58 ± 0.06	0.93
Cl	1.18 ± 0.09	0.95	3.10 ± 0.18	0.62	2.63 ± 0.13	0.89
K	0.66 ± 0.03	0.94	0.89 ± 0.02	0.83	0.78 ± 0.13	0.42
Ca	0.54 ± 0.04	0.88	1.72 ± 0.03	0.93	2.03 ± 0.30	0.66
Ti	0.72 ± 0.13	0.84	1.43 ± 0.03	0.94	–	–
V	–	–	–	–	1.37 ± 0.06	0.96
Mn	–	–	1.05 ± 0.06	0.81	–	–
Fe	0.66 ± 0.03	0.94	1.47 ± 0.03	0.91	1.63 ± 0.37	0.29
Ni	–	–	–	–	1.25 ± 0.12	0.78
Cu	–	–	0.67 ± 0.05	0.72	–	–
Zn	0.89 ± 0.10	0.77	1.02 ± 0.03	0.87	1.36 ± 0.13	0.81
Sr	–	–	0.63 ± 0.17	0.51	–	–
Pb	–	–	0.46 ± 0.14	0.15	–	–

Only four measurements for silicon (Si) were above the limit of quantification (LOQ) for the Xact 625i, reflecting the spectrometer's limited sensitivity for this element. This highlights one of the key limitations of the Xact 625i compared to the benchtop XRF system—its generally higher limits of detection (LoDs) in the lighter elements like Si, which can hinder accurate quantification, particularly for elements with low ambient concentrations. Nevertheless, for the Si data points above the LOQ, a slope of 0.94 ± 0.19 (R^2 = 0.88) was observed, indicating strong agreement between the instruments. In contrast, sulfur (S) exhibited excellent performance across both systems, with a slope of 0.97 ± 0.01 and an R^2 of 0.99, demonstrating a near-perfect correlation and underscoring the Xact 625i's robustness in measuring this element. Chlorine (Cl) demonstrated a slope of 1.18 ± 0.09 (R^2 = 0.95), indicating a strong correlation with a slight deviation from unity. Potassium (K) showed a slope of 0.66 ± 0.03 (R^2 = 0.94), suggesting consistent trends despite a systematic difference in concentrations. Calcium (Ca) and titanium (Ti) exhibited slopes of 0.54 ± 0.04 (R^2 = 0.88) and 0.72 ± 0.13 (R^2 = 0.84), respectively. Iron (Fe) displayed a slope of 0.66 ± 0.03 (R^2 = 0.94), indicating strong agreement. Although the slopes below unity suggest systematic underestimation by the Xact 625i for some elements, the consistently high R^2 values confirm reliable and reproducible trends across both systems. Zinc (Zn), with a slope of 0.89 ± 0.10

($R^2 = 0.77$), showed moderate correlation, where the slope near unity reflected comparable measurements, while the lower R^2 indicated greater variability.

The average slope of 0.82 and average R^2 of 0.91 indicated a strong overall correlation between the benchtop XRF spectrometer and the Xact 625i, suggesting that both instruments produced consistent measurements across most elements. The slope slightly below 1 implied a systematic difference in quantification, where the Xact 625i tended to report lower values compared to the benchtop XRF.

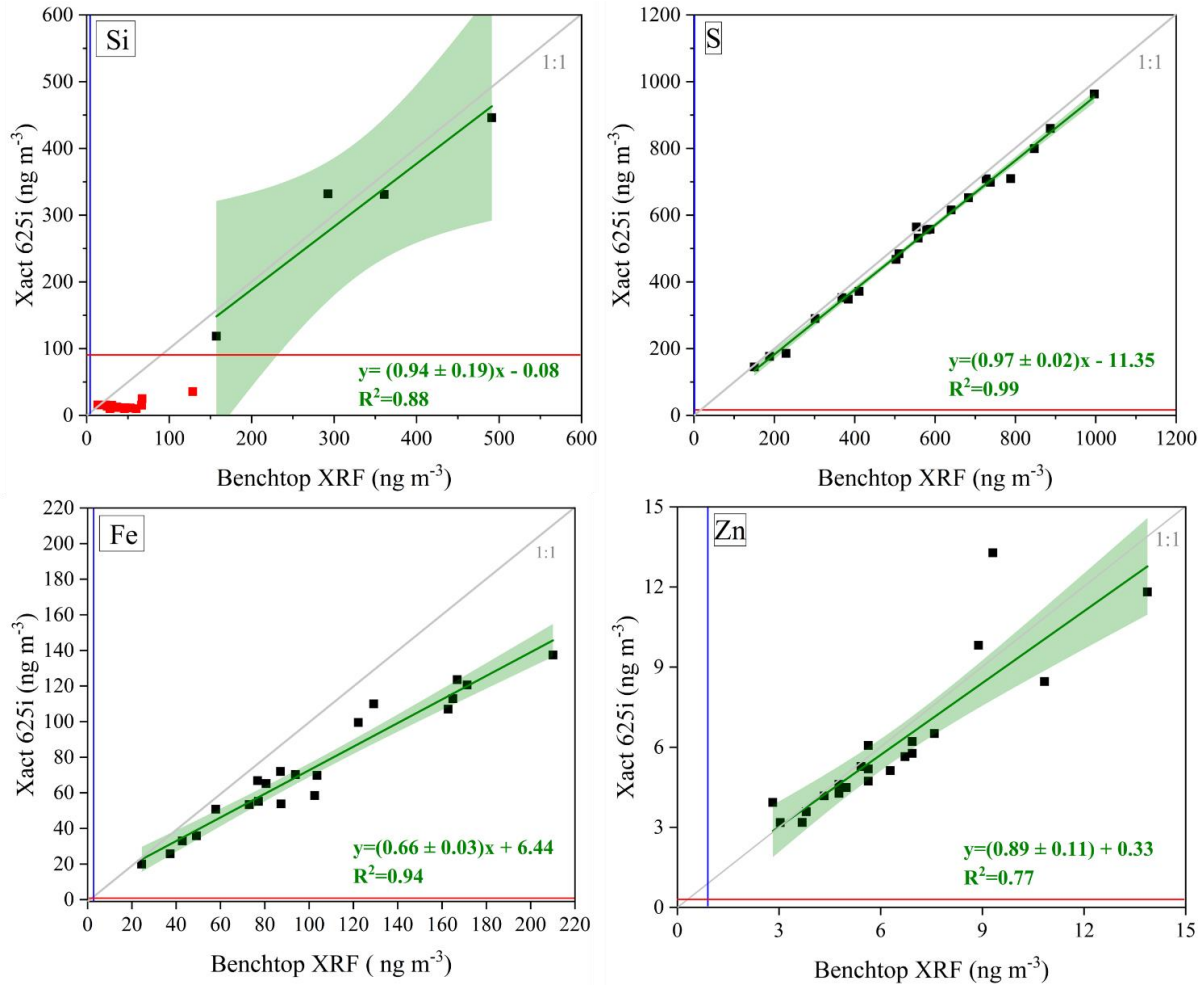

Figure 86. *Comparison of elemental concentrations in ng m^{-3} for Si, S, Fe, and Zn for the ATH-DEM station. The blue lines indicate the LOQ threshold for the benchtop XRF spectrometer, while the red lines represent the corresponding threshold for the Xact 625i continuous elemental monitor. The grey line represents the 1:1 reference line, while the green line represents the linear regression fit. Data points below the LOQ were excluded from the analysis to ensure accurate comparison between the two instruments and are highlighted in red, distinguishing measurements with higher uncertainty.*

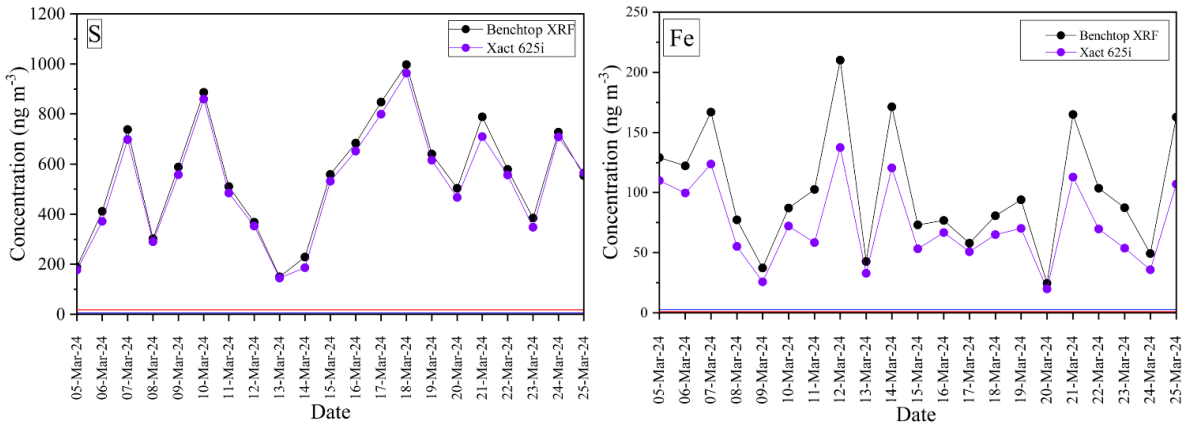

Figure 87. *Time series graphs comparing S and Fe concentrations (ng m⁻³) from March 5 to 25, 2024, show strong agreement for S, while Fe exhibits a consistent deviation, with lower values reported by the Xact 625i. This suggests differences in the calibration curves for heavier elements between the instruments. The red and blue lines indicate the LOQ thresholds for the Xact 625i and the benchtop XRF spectrometer, respectively.*

17.3.4 Benchtop XRF (Quartz Fiber) vs Xact 625i

At the CAO-NIC site, benchtop XRF measurements were performed on quartz fiber filters. Table 2 presents the linear regression slopes and R^2 values for each element, compared with the corresponding Xact 625i measurements. **Figure 88** presents the regression curves for S, Cl, K and Zn, while **Figure 89** shows the time series graphs comparing K and Zn

Sulfur (S) exhibited a slope of 1.20 ± 0.15 (R^2 = 0.49), reflecting moderate agreement between the instruments and some remaining variability after correction. Chlorine (Cl) presented a slope of 3.10 ± 0.18 (R^2 = 0.62), indicating a moderate relationship with higher variability relative to unity, which may relate to particle penetration and absorption within the quartz matrix as well as potential chloride volatility (e.g., ammonium chloride loss). Potassium (K) showed a slope of 0.89 ± 0.07 (R^2 = 0.83), demonstrating good agreement between systems. While the applied correction factors substantially improved the comparability of light-element measurements, minor residual differences remain. These are likely linked to the heterogeneous structure and variable porosity of quartz fiber filters, which can influence attenuation differently between batches, along with instrument-specific and site-dependent aerosol characteristics. Thus, small deviations are expected, but overall, the applied corrections significantly enhance consistency and reliability across the two platforms.

Calcium (Ca) and titanium (Ti) displayed slopes of 1.72 ± 0.03 (R^2 = 0.93) and 1.43 ± 0.03 (R^2 = 0.94), respectively, both showing high correlation and comparable measurements. Manganese (Mn) had a slope of 1.05 ± 0.06 (R^2 = 0.81), indicating strong agreement. Iron (Fe) exhibited a slope of 1.47 ± 0.03 (R^2 = 0.91), reflecting a consistent trend between instruments. Copper (Cu) had a slope of 0.67 ± 0.05 (R^2 = 0.72), suggesting a moderate correlation with some variability. Zinc (Zn) presented a slope of 1.02 ± 0.03 (R^2 = 0.87), indicating highly comparable measurements. Strontium (Sr) exhibited a slope of 0.63 ± 0.17 (R^2 = 0.51), indicating moderate

agreement with some residual variability, while lead (Pb) remained lower at 0.46 ± 0.14 (R^2 = 0.15), reflecting weaker correlation and higher measurement uncertainty.

In addition to the overall agreement, several distinct events were observed where elemental concentrations peaked simultaneously in both the Xact 625i and the benchtop XRF measurements, particularly for calcium (Ca), titanium (Ti), iron (Fe) and manganese (Mn). During these events, the time series from both instruments showed consistent patterns, indicating that they captured the same atmospheric variability. However, the Xact 625i consistently reported higher concentrations, which is likely attributable to differences in the calibration procedures between the two instruments.

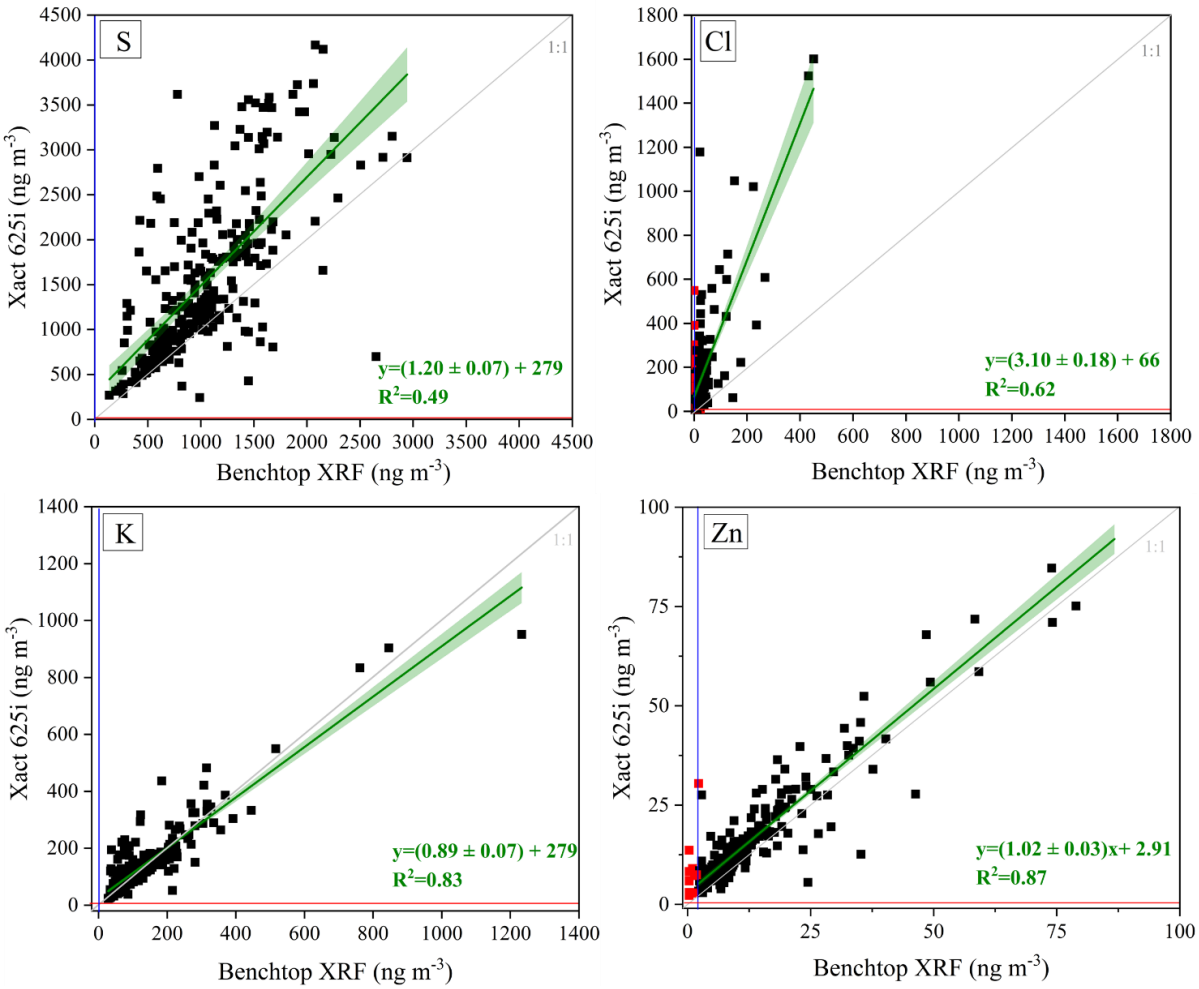

Figure 88. *Comparison of elemental concentrations in ng m^{-3} for S, Cl, K and Zn for the CAO-NIC station. The blue lines indicate the LOQ thresholds for the benchtop XRF spectrometer, while the red lines represent the corresponding thresholds for the Xact 625i continuous elemental monitor. The grey line represents the 1:1 reference line, while the green line represents the linear regression fit. Data points below the LOQ were excluded from the analysis to ensure accurate comparison between the two instruments and are highlighted in red, distinguishing measurements with higher uncertainty.*

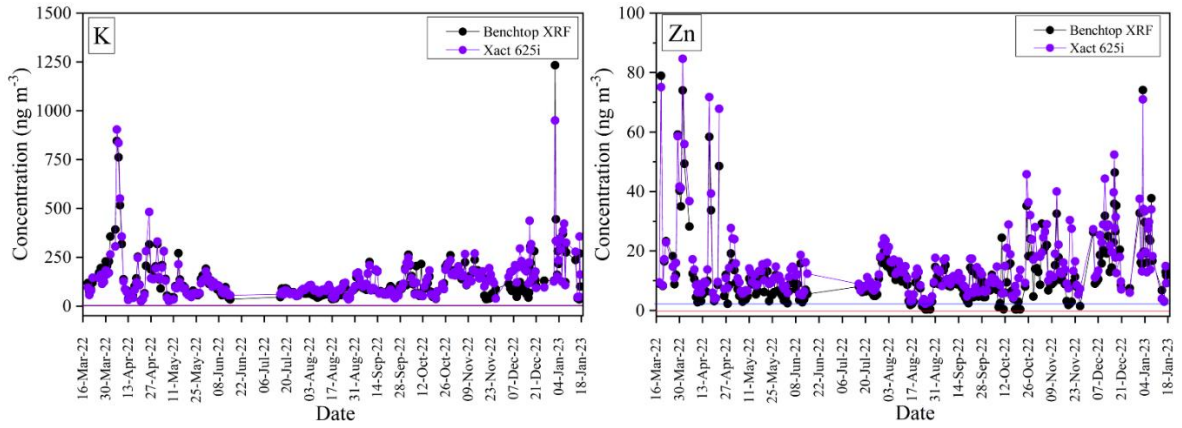

Figure 89. *Time series graphs comparing K and Zn concentrations in ng m^{-3} from 16 March 2022 to 18 January 2023. The red and blue lines indicate the LOQ thresholds for the Xact 625i and the benchtop XRF spectrometer, respectively.*

17.3.5 Benchtop XRF (Quartz Fiber) vs Xact 625

Figure 90 presents the regression curves for the elements S, Cl, V, and Ni, while **Figure 91** shows the time series graphs for Cl and Zn. Benchtop XRF measurements were performed on quartz fiber filters collected at the DUB-P site. Sulfur (S) displayed a slope of 1.58 ± 0.06 (R^2 = 0.93), indicating strong agreement between the instruments. Chlorine (Cl) showed the highest slope at 2.63 ± 0.13 (R^2 = 0.89), suggesting a systematic difference while maintaining a strong correlation. Potassium (K) had a slope of 0.78 ± 0.13 (R^2 = 0.42), reflecting a weaker correlation and more variability in the measurements. Calcium (Ca) demonstrated a slope of 2.03 ± 0.30 (R^2 = 0.66), indicating a notable deviation from unity with moderate agreement. Vanadium (V) exhibited a slope of 1.37 ± 0.06 (R^2 = 0.96), reflecting excellent correlation and comparable measurements. Iron (Fe) showed a slope of 1.63 ± 0.37 (R^2 = 0.29), indicating substantial variability and a weaker relationship. Nickel (Ni) had a slope of 1.25 ± 0.12 (R^2 = 0.78), representing reasonable agreement with some deviation. Zinc (Zn) displayed a slope of 1.36 ± 0.13 (R^2 = 0.81), showing a strong correlation between the two instruments.

The average slope of 1.6 and average R^2 of 0.7 for the DUB-P campaign indicated a moderate overall agreement between the benchtop XRF spectrometer and the Xact 625. Although the correlation varies across elements, the results highlight consistent trends for most elements, with stronger agreement for sulfur (S), vanadium (V), and zinc (Zn), while potassium (K) and iron (Fe) exhibited greater variability.

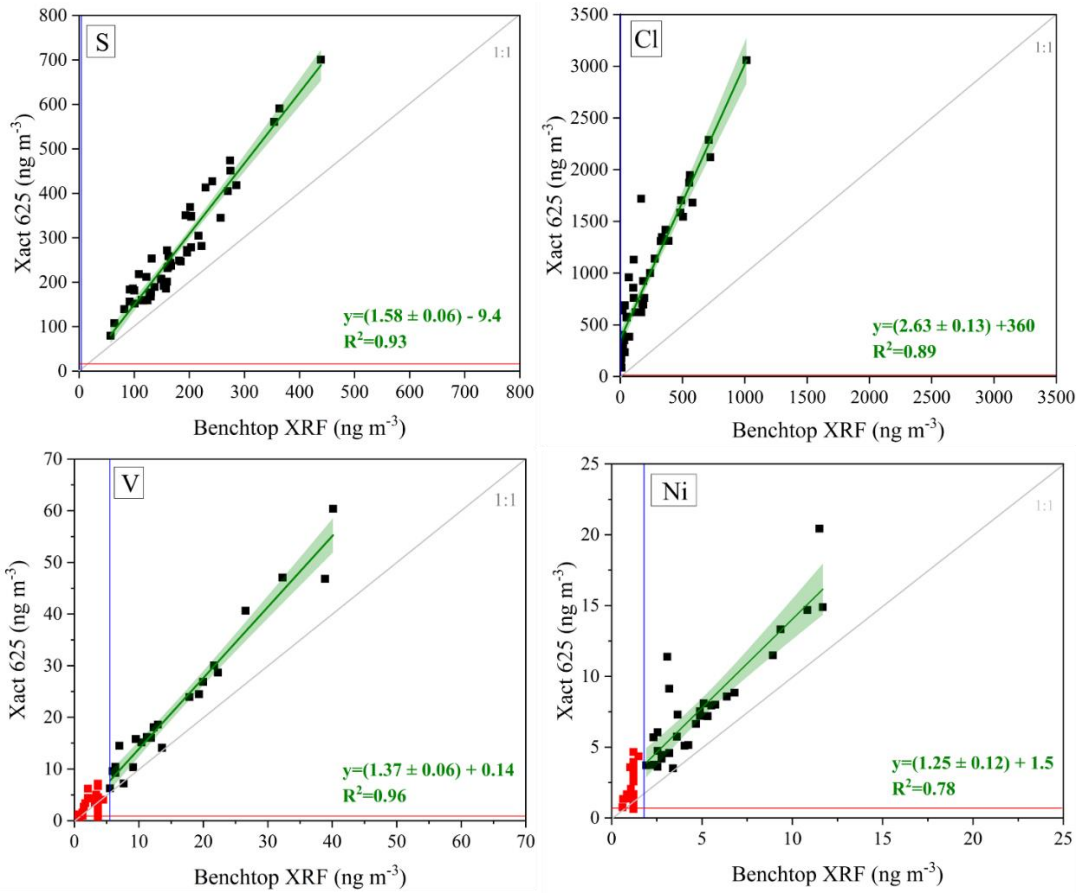

Figure 90. *Comparison of elemental concentrations in ng m^{-3} for S, Cl, V and Ni for the DUB-P station. The blue lines indicate the LOQ thresholds for the benchtop XRF spectrometer, while the red lines represent the corresponding thresholds for the Xact 625 continuous elemental monitor. The grey line represents the 1:1 reference line, while the green line represents the linear regression fit. Data points below the LOQ were excluded from the analysis to ensure accurate comparison between the two instruments and are highlighted in red, distinguishing measurements with higher uncertainty.*

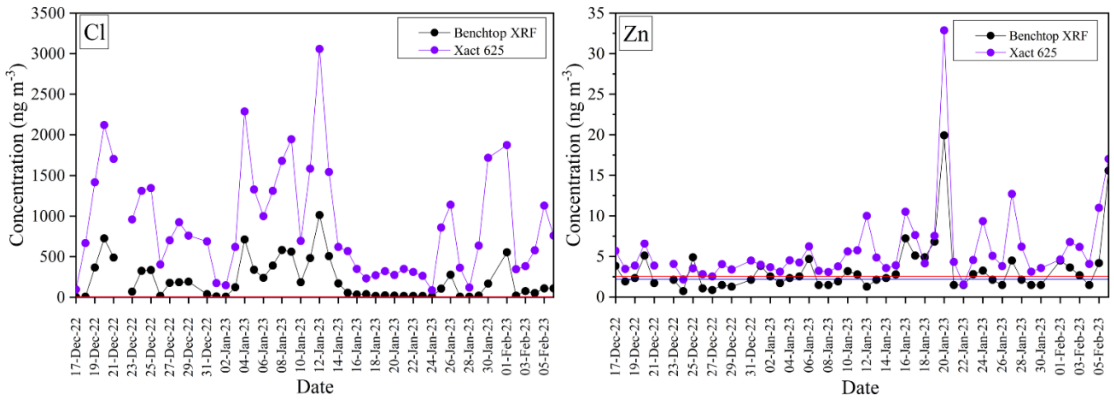

Figure 91. *Time series graphs comparing Cl and Zn concentrations (ng m^{-3}) at the Dub-P station, show a systematic difference, with the benchtop XRF consistently reporting lower concentrations than the Xact 625. This suggests that the quartz fiber filter may introduce systematic deviations, particularly for light elements, while differences in calibration curves between the instruments could also play a role. The red and blue lines indicate the LOQ thresholds for the Xact 625 and the benchtop XRF spectrometer, respectively.*

17.4 Discussion

The effect of filter type on measurement consistency is evident across the three sites. At ATH-DEM (PTFE filters) the comparison between the Xact 625i and the benchtop XRF spectrometer shows slopes consistently closer to unity for most elements. The consistently high R^2 values (≥ 0.77) across most elements suggest minimal variability, meaning the continuous XRF monitors provides results comparable to those from the benchtop XRF. However, it has to be noted that while the agreement for Si is encouraging, it also highlights the generally higher limits of detection (LoDs) of the Xact 625i for lighter elements (K and below), which can limit its sensitivity in low-concentration environments. Other elements, such as chlorine (Cl), iron (Fe), and potassium (K), also show high R^2 values (≥ 0.77) despite deviations in slope, suggesting systematic differences rather than random variability. These systematic deviations are likely due to differences in instrument calibration, as each system may utilize distinct reference standards. Overall, the better alignment at ATH-DEM is likely aided by the lower X-ray attenuation associated with PTFE filters. Cadeo et al., (2025) recently reported strong agreement between the Xact 625i and benchtop XRF using Teflon filters in Milan, with R^2 values up to 0.99 and slopes generally near unity for most elements, particularly metals. Similarly, our Athens comparison using PTFE filters showed high consistency across eight elements (average slope = 0.82, average R^2 = 0.91), with S and Si near unity and K, Ca, Ti and Fe showing slopes below one but strong correlations (R^2 > 0.84). Both studies therefore confirm that the Xact 625i performs robustly on Teflon substrates, providing reliable elemental time-series information with element-specific slope differences.

Despite the application of correction factors, the quartz fiber filter sites (DUB-P and CAO-NIC) continue to exhibit systematic deviations, particularly for lighter elements such as S, Cl, and K. Notably, S shows substantial higher concentrations at DUB-P, with a corrected slope of 1.58 ± 0.06, compared to a closer-to-unity value of 1.20 ± 0.07 at CAO-NIC. This difference is notable, especially considering the strong correlation at DUB-P (R^2 = 0.93), which implies consistent tracking of variability but a persistent offset in absolute values. One possible explanation for this discrepancy lies in the instrumental differences between the two sites: DUB-P employed the Xact 625, while CAO-NIC used the newer Xact 625i. This suggests a potential improvement in calibration or measurement accuracy in the upgraded version. Additionally, iron (Fe) shows poorer agreement at DUB-P, whereas elements like vanadium (V), nickel (Ni), and zinc (Zn) display relatively better performance. This contrast may reflect slight calibration mismatches or performance limitations specific to the older Xact 625 model.

At the CAO-NIC site, the comparison with the Xact 625i reveals both strong correlations and systematic differences across elements. Several elements, including Ca, Ti, Fe, Mn, and zinc (Zn), exhibit high R^2 values (≥ 0.81) and slopes near unity, indicating good agreement between the continuous and benchtop XRF systems. In contrast, chlorine (Cl) shows an elevated slope of 3.10± 0.18 (R^2 = 0.70), continuing the pattern seen at DUB-P, where the slope is 2.63 ± 0.13 (R^2 = 0.89). Cl is the most noteworthy element, with substantial

deviations in slope at both sites, even after the application of correction factors. Despite efforts to account for the attenuation effects, the difference in slope for Cl is far more significant than for other light elements. This suggests that there may be an underlying issue with the Cl measurement itself, which may be attributed to the volatility of the element. Additionally, peak events in elemental concentrations—particularly for Ca, Ti, Fe, and Mn—were observed in both instruments, confirming their ability to track atmospheric variability. However, the Xact 625i systematically reported higher concentrations, further supporting the role of calibration differences. Despite those differences, the overall strong average R^2 of 0.73 and the robust agreement for many mid-to-heavy elements underscore the utility of the Xact 625i, while reinforcing the need for caution when interpreting light elements on quartz filters.

Overall, the filter type significantly influences measurement consistency. PTFE filters, as used at ATH-DEM, result in stronger agreement and more stable measurements across most elements. Quartz fiber filters, used at DUB-P and CAO-NIC, exhibit greater variability for light elements; however, correction efforts mitigate these effects and improve overall comparability, especially for S and K. **Figure 92** presents the comparative concentration plots for the elements S, Cl, K, Ca, Ti, Fe and Zn between the continuous and benchtop XRF systems.

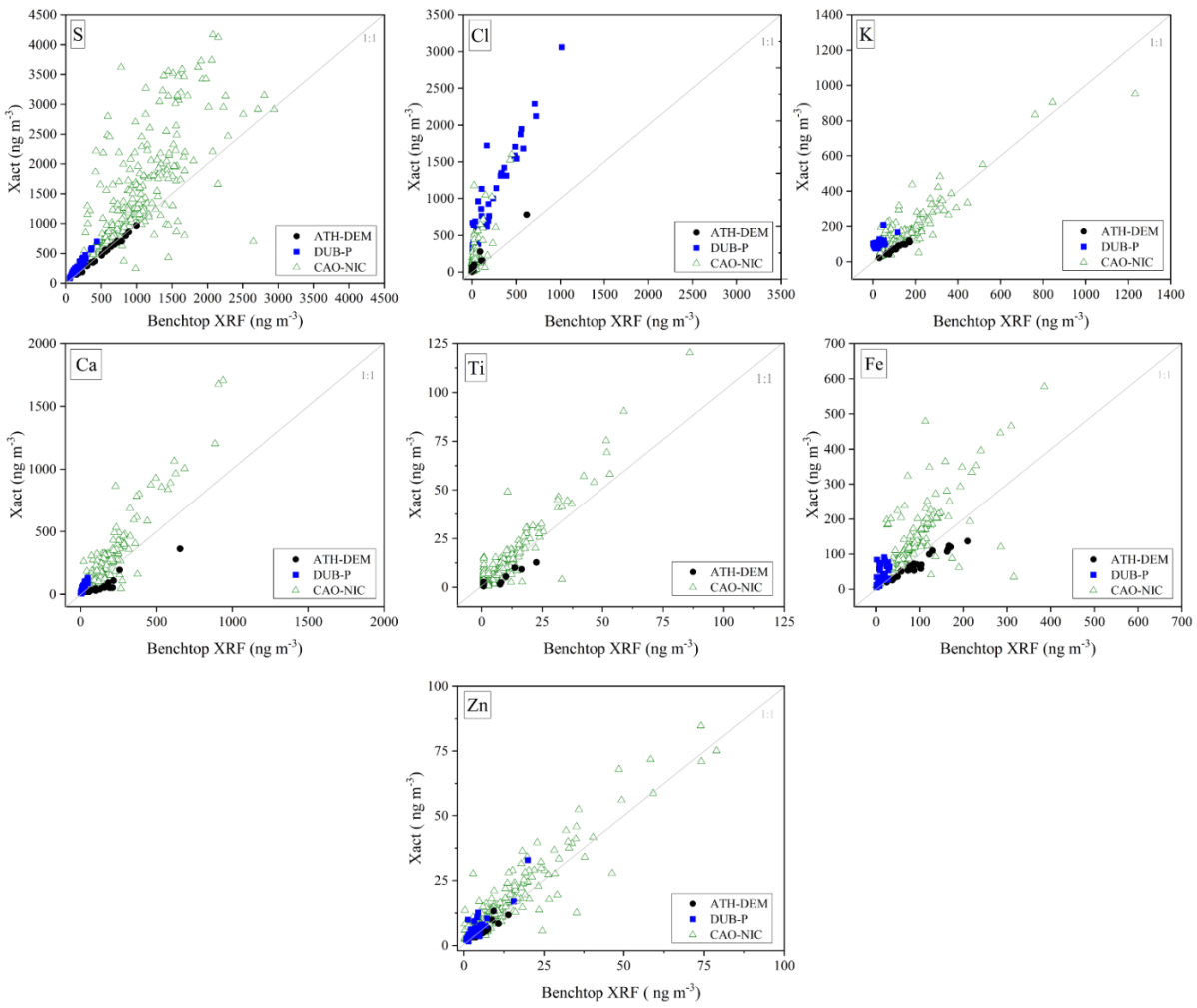

Figure 92. *Comparison of elemental concentrations of S, Cl, K, Ca, Ti (Ti was not detected in DUB-P), Fe, Zn in ng m^{-3} for all stations.*

17.5 Conclusions

This study conducted an extensive intercomparison between a benchtop ED-XRF and NRT-XRF spectrometers (Xact 625 and 625i) to evaluate their performance in measuring elemental concentrations in ambient aerosols across three locations: Athens (Greece), Dublin (Ireland), and Nicosia (Cyprus). A key focus was the influence of filter substrate of measurement results.

The findings highlight that filter type plays a critical role in the quantification of light elements. At the Athens site, where PTFE filters were used, the agreement between instruments was stronger, with slopes closer to unity and high R^2 values, indicating stable and consistent performance. In contrast, at the Dublin and Nicosia sites, which used quartz fiber filters, deviations were observed for sulfur (S), chlorine (Cl), and potassium (K) due to X-ray attenuation in the quartz matrix. Applying correction factors substantially improved agreement for S and K, demonstrating their effectiveness in mitigating substrate-related effects. For Cl, however, a residual positive bias remained likely influenced by both quartz interactions and chloride volatility. In addition, variability in quartz fiber filter composition, porosity, and thickness across filter batches may introduce inconsistent attenuation behavior, complicating the application of a universal correction factor. Overall, while corrections enhanced comparability, quartz substrates still present challenges for light-element quantification. For heavier elements such as iron (Fe), manganese (Mn), and copper (Cu), the impact of filter type was less pronounced, but variations were still present across sites. Zinc (Zn) maintained good agreement across all locations, whereas lead (Pb) exhibited weaker correlation, suggesting additional influencing factors beyond filter type. Differences in the use of different calibration standards of the two instruments may have contributed to these discrepancies.

Overall, this study underscores the complexity of intercomparisons between different XRF instrument types and filter substrates, particularly for light elements. Quartz fiber filters, in particular, introduce greater variability due to enhanced X-ray attenuation. Therefore, when using quartz fiber filters in ambient aerosol studies, it is essential to implement element-specific correction protocols and consider substrate-related uncertainties during data interpretation. For more reliable and consistent measurements, especially of light elements, PTFE filters are recommended. Additionally, harmonization of calibration procedures across instruments may help reduce discrepancies. These findings highlight the importance of carefully selecting both instrumentation and filter media in XRF-based aerosol analysis to ensure data comparability across monitoring networks.

17.6 References

Aikawa, M., & Hiraki, T. (2010). Difference in the use of a quartz filter and a PTFE filter as first-stage filter in the four-stage filter-pack method. Water, Air, and Soil Pollution, 213(1–4), 331–339. https://doi.org/10.1007/S11270-010-0388-Y/FIGURES/7

Aldekheel, M., Farahani, V. J., & Sioutas, C. (2023). Assessing Lifetime Cancer Risk Associated with Population Exposure to PM-Bound PAHs and Carcinogenic Metals in Three Mid-Latitude Metropolitan Cities. Toxics, 11(8), 697. https://doi.org/10.3390/TOXICS11080697/S1

Amato, F., Alastuey, A., Karanasiou, A., Lucarelli, F., Nava, S., Calzolai, G., Severi, M., Becagli, S., Gianelle, V. L., Colombi, C., Alves, C., Custódio, D., Nunes, T., Cerqueira, M., Pio, C., Eleftheriadis, K., Diapouli, E., Reche, C., Minguillón, M. C., Manousakas, M.-I., Maggos, T., Vratolis, S., Harrison, R. M., & Querol, X. (2016). AIRUSE-LIFE+: A harmonized PM speciation and source apportionment in five southern European cities. Atmospheric Chemistry and Physics, 16(5), 3289–3309. https://doi.org/10.5194/acp-16-3289-2016

Bhowmik, H. S., Shukla, A., Lalchandani, V., Dave, J., Rastogi, N., Kumar, M., Singh, V., & Tripathi, S. N. (2022). Inter-comparison of online and offline methods for measuring ambient heavy and trace elements and water-soluble inorganic ions (NO3-, SO42-, NH4+, and Cl-) in PM2.5over a heavily polluted megacity, Delhi. Atmospheric Measurement Techniques, 15(9), 2667–2684. https://doi.org/10.5194/amt-15-2667-2022

Bimenyimana, E., Pikridas, M., Oikonomou, K., Iakovides, M., Christodoulou, A., Sciare, J., & Mihalopoulos, N. (2023). Fine aerosol sources at an urban background site in the Eastern Mediterranean (Nicosia; Cyprus): Insights from offline versus online source apportionment comparison for carbonaceous aerosols. Science of The Total Environment, 893, 164741. https://doi.org/10.1016/J.SCITOTENV.2023.164741

Bimenyimana, E., Sciare, J., Pikridas, M., Oikonomou, K., Iakovides, M., Vasiliadou, E., Savvides, C., & Mihalopoulos, N. (2025). Persistent high PM pollution in the Eastern Mediterranean and Middle East: Insights from long-term observations and source apportionment in Cyprus. *EGUsphere*, 1–23. https://doi.org/10.5194/EGUSPHERE-2025-3234

Cadeo, L., Biffi, B., Chazeau, B., Colombi, C., Cosenza, R., Manousakas, M.-I., Daellenbach, K. R., & H Prévôt, A. S. (2025). Intercomparison of online and offline XRF spectrometers for determining the PM10 elemental composition of ambient aerosol. https://doi.org/10.5194/egusphere-2025-110

Caggiano, R., Sabia, S., & Speranza, A. (2019). Trace elements and human health risks assessment of finer aerosol atmospheric particles (PM1). Environmental Science and Pollution Research, 26(36), 36423–36433. https://doi.org/10.1007/S11356-019-06756-W/TABLES/5

Castaneda, C. M., Cahill, T. A., Romero, J. L., & King, R. S. (1998). Depth profiling of hydrogen in amorphous media and applicable to quartz air filters. Nuclear Instruments and Methods in Physics Research Section B: Beam Interactions with Materials and Atoms, 145(4), 553–561. https://doi.org/10.1016/S0168-583X(98)00506-0

Chen, S.-L., Chang, S.-W., Chen, Y.-J., & Chen, H.-L. (2021). Possible warming effect of fine particulate matter in the atmosphere. Communications Earth & Environment 2021 2:1, 2(1), 1–9. https://doi.org/10.1038/s43247-021-00278-5

Chiari, M., Yubero, E., Calzolai, G., Lucarelli, F., Crespo, J., Galindo, N., Nicolás, J. F., Giannoni, M., & Nava, S. (2018). Comparison of PIXE and XRF analysis of airborne particulate matter samples collected on Teflon and quartz fibre filters. Nuclear Instruments and Methods in Physics Research Section B: Beam Interactions with Materials and Atoms, 417, 128–132. https://doi.org/10.1016/J.NIMB.2017.07.031

Christodoulou, A., Stavroulas, I., Vrekoussis, M., Desservettaz, M., Pikridas, M., Bimenyimana, E., Kushta, J., Ivančič, M., Rigler, M., Goloub, P., Oikonomou, K., Sarda-Estève, R., Savvides, C., Afif, C., Mihalopoulos, N., Sauvage, S., & Sciare, J. (2023). Ambient carbonaceous aerosol levels in Cyprus and the role of pollution transport from the Middle East. Atmospheric Chemistry and Physics, 23(11), 6431–6456. https://doi.org/10.5194/ACP-23-6431-2023

Diapouli, E., Manousakas, M. I., Vratolis, S., Vasilatou, V., Pateraki, S., Bairachtari, K. A., Querol, X., Amato, F., Alastuey, A., Karanasiou, A. A., Lucarelli, F., Nava, S., Calzolai, G., Gianelle, V. L., Colombi, C., Alves, C., Custódio, D., Pio, C., Spyrou, C., Kallos, G. B., & Eleftheriadis, K. (2017). AIRUSE-LIFE+: Estimation of natural source contributions to urban ambient air PM_{10} and $PM_{2.5}$ concentrations in southern Europe – Implications to compliance with limit values. Atmospheric Chemistry and Physics, 17(5), 3673–3685. https://doi.org/10.5194/acp-17-3673-2017

Fossum, K. N., Lin, C., O'Sullivan, N., Lei, L., Hellebust, S., Ceburnis, D., Afzal, A., Tremper, A., Green, D., Jain, S., Byčenkienė, S., O'Dowd, C., Wenger, J., & Ovadnevaite, J. (2024). Two distinct ship emission profiles for organic-sulfate source apportionment of PM in sulfur emission control areas. Atmospheric Chemistry and Physics, 24(18), 10815–10831. https://doi.org/10.5194/ACP-24-10815-2024

Fossum, K., O'Sullivan, N., Jain, S., Lei, L., Lin, C., Ceburnis, D., Hellebust, S., O'Dowd, C., Ovadnevaite, J., & Wenger, J. (2025). Source Apportionment of Air Pollution in the Dublin Port Area (PortAIR). Research 495. Environmental Protection Agency. ISBN 978-1-80009-314-0. https://www.epa.ie/publications/research/air/research-495-source-apportionment-of-air-pollution-in-the-dublin-port-area-portair.php

Furger, M., Minguillón, M. C., Yadav, V., Slowik, J. G., Hüglin, C., Fröhlich, R., Petterson, K., Baltensperger, U., & Prévôt, A. S. H. (2017). Elemental composition of ambient aerosols measured with high temporal resolution using an online XRF spectrometer. Atmospheric Measurement Techniques, 10(6), 2061–2076. https://doi.org/10.5194/amt-10-2061-2017

Furger, M., Rai, P., Slowik, J. G., Cao, J., Visser, S., Baltensperger, U., & Prévôt, A. S. H. (2020). Automated alternating sampling of PM10 and PM2.5 with an online XRF spectrometer. Atmospheric Environment: X, 5, 100065. https://doi.org/10.1016/J.AEAOA.2020.100065

Eleftheriadis, K., Gini, M. I., Diapouli, E., Vratolis, S., Vasilatou, V., Fetfatzis, P., & Manousakas, M. I. (2021). Aerosol microphysics and chemistry reveal the COVID19 lockdown impact on urban air quality. *Scientific Reports 2021 11:1*, *11*(1), 14477-. https://doi.org/10.1038/s41598-021-93650-6

Gini, M., Manousakas, M., Karydas, A. G., & Eleftheriadis, K. (2022). Mass size distributions, composition and dose estimates of particulate matter in Saharan dust outbreaks. Environmental Pollution, 298, 118768. https://doi.org/10.1016/J.ENVPOL.2021.118768

Hopke, P. K., Dai, Q., Li, L., & Feng, Y. (2020). Global review of recent source apportionments for airborne particulate matter. Science of The Total Environment, 740, 140091. https://doi.org/10.1016/J.SCITOTENV.2020.140091

Healy, R. M., O'Connor, I. P., Hellebust, S., Allanic, A., Sodeau, J. R., & Wenger, J. C. (2009). Characterisation of single particles from in-port ship emissions. Atmospheric Environment, 43(40), 6408–6414. https://doi.org/10.1016/J.ATMOSENV.2009.07.039

Huang, R. J., Cheng, R., Jing, M., Yang, L., Li, Y., Chen, Q., Chen, Y., Yan, J., Lin, C., Wu, Y., Zhang, R., El Haddad, I., Prevot, A. S. H., O'Dowd, C. D., & Cao, J. (2018). Source-Specific Health Risk Analysis on Particulate Trace Elements: Coal Combustion and Traffic Emission As Major Contributors in Wintertime Beijing. Environmental Science and Technology, 52(19), 10967–10974. https://pubs.acs.org/doi/10.1021/acs.est.8b02091

Jain, S., Sharma, S. K., Vijayan, N., & Mandal, T. K. (2020). Seasonal characteristics of aerosols (PM2.5 and PM10) and their source apportionment using PMF: A four year study over Delhi, India. Environmental Pollution, 262, 114337. https://doi.org/10.1016/j.envpol.2020.114337

Jang, H. N., Seo, Y. C., Lee, J. H., Hwang, K. W., Yoo, J. I., Sok, C. H., & Kim, S. H. (2007). Formation of fine particles enriched by V and Ni from heavy oil combustion: Anthropogenic sources and drop-tube furnace experiments. Atmospheric Environment, 41(5), 1053–1063. https://doi.org/10.1016/J.ATMOSENV.2006.09.011

Khuzestani, R. B., Schauer, J. J., Wei, Y., Zhang, Y., & Zhang, Y. (2017). A non-destructive optical color space sensing system to quantify elemental and organic carbon in atmospheric particulate matter on Teflon and quartz filters. Atmospheric Environment, 149, 84–94. https://doi.org/10.1016/J.ATMOSENV.2016.11.002

Manousakas, M., Diapouli, E., Papaefthymiou, H., Kantarelou, V., Zarkadas, C., Kalogridis, A.-C., Karydas, A.-G., & Eleftheriadis, K. (2018). XRF characterization and source apportionment of PM10 samples collected in a coastal city. X-Ray Spectrometry, 47(3), 190–200. https://doi.org/10.1002/xrs.2817

Manousakas, M., Diapouli, E., Belis, C., Vasilatou, V., Gini, M., Lucarelli, F., Querol, X., & Eleftheriadis, K. (2021). Quantitative assessment of the variability in chemical profiles from source apportionment analysis of PM10 and PM2.5 at different sites within a large metropolitan area. Environmental Research, 192, 110257. https://doi.org/10.1016/J.ENVRES.2020.110257

Manousakas, M., Furger, M., Daellenbach, K. R., Canonaco, F., Chen, G., Tobler, A., Rai, P., Qi, L., Tremper, A. H., Green, D., Hueglin, C., Slowik, J. G., El Haddad, I., & Prevot, A. S. H. (2022). Source identification of the elemental fraction of particulate matter using size segregated, highly time-resolved data and an optimized source apportionment approach. Atmospheric Environment: X, 14, 100165. https://doi.org/10.1016/J.AEAOA.2022.100165

Megido, L., Suárez-Peña, B., Negral, L., Castrillón, L., & Fernández-Nava, Y. (2017). Suburban air quality: Human health hazard assessment of potentially toxic elements in PM10. Chemosphere, 177, 284–291. https://doi.org/10.1016/J.CHEMOSPHERE.2017.03.009

Ostro, B., Tobias, A., Karanasiou, A., Samoli, E., Querol, X., Rodopoulou, S., Basagaña, X., Eleftheriadis, K., Diapouli, E., Vratolis, S., Jacquemin, B., Katsouyanni, K., Sunyer, J., Forastiere, F., Stafoggia, M., Alessandrini, E., Angelini, P., Berti, G., Bisanti, L., … Pascal, M. (2015). The risks of acute exposure to black carbon in Southern Europe: results from the MED-PARTICLES project. Occupational and Environmental Medicine, 72(2), 123–129. https://doi.org/10.1136/OEMED-2014-102184

Papagiannis, S., Sabur, ·, Abdullaev, F., Vasilatou, V., Manousos, ·, Manousakas, I., Eleftheriadis, K., & Diapouli, E. (2024). Air quality challenges in Central Asian urban areas: a PM2.5 source apportionment analysis in Dushanbe, Tajikistan. Environmental Science and Pollution Research 2024, 1–14. https://doi.org/10.1007/S11356-024-33833-6

Park, S. S., Cho, S. Y., Jo, M. R., Gong, B. J., Park, J. S., & Lee, S. J. (2014). Field evaluation of a near-real time elemental monitor and identification of element sources observed at an air monitoring supersite in Korea. Atmospheric Pollution Research, 5(1), 119–128. https://doi.org/10.5094/APR.2014.015

Rai, P. (2020). Analysis of major and trace elements in ambient aerosols and their sources in European and Asian cities (Doctoral dissertation, ETH Zurich). ETH Zurich Research Collection. https://doi.org/10.3929/ethz-b-000440336

Rai, P., Furger, M., Slowik, J. G., Canonaco, F., Fröhlich, R., Hüglin, C., Minguillón, M. C., Petterson, K., Baltensperger, U., & Prévôt, A. S. H. (2020). Source apportionment of highly time-resolved elements during a firework episode from a rural freeway site in Switzerland. Atmospheric Chemistry and Physics, 20(3), 1657–1674. https://doi.org/10.5194/ACP-20-1657-2020

Rhodes, E. P., Ren, Z., & Mays, D. C. (2012). Zinc leaching from tire crumb rubber. Environmental Science and Technology, 46(23), 12856–12863. https://doi.org/10.1021/ES3024379/SUPPL_FILE/ES3024379_SI_001.PDF

Sailbri Cooper, Inc. - INNOVATION IN MONITORING. (n.d.). Retrieved November 15, 2024, from https://sci-monitoring.com/

Samoli, E., Stafoggia, M., Rodopoulou, S., Ostro, B., Declercq, C., Alessandrini, E., Díaz, J., Karanasiou, A., Kelessis, A. G., Tertre, A. Le, Pandolfi, P., Randi, G., Scarinzi, C., Zauli-Sajani, S., Katsouyanni, K., Forastiere, F., Alessandrini, E., Angelini, P., Berti, G., … Pascal, M. (2013). Associations between fine and coarse particles and mortality in Mediterranean cities: Results

from the MED-PARTICLES project. Environmental Health Perspectives, 121(8), 932–938. https://doi.org/10.1289/EHP.1206124

Schoonjans, T., Solé, V. A., Vincze, L., Sanchez Del Rio, M., Appel, K., & Ferrero, C. (2013). A general Monte Carlo simulation of energy-dispersive X-ray fluorescence spectrometers — Part 6. Quantification through iterative simulations. Spectrochimica Acta Part B: Atomic Spectroscopy, 82, 36–41. https://doi.org/10.1016/J.SAB.2012.12.011

Skalny, A. V., Lima, T. R. R., Ke, T., Zhou, J. C., Bornhorst, J., Alekseenko, S. I., Aaseth, J., Anesti, O., Sarigiannis, D. A., Tsatsakis, A., Aschner, M., & Tinkov, A. A. (2020). Toxic metal exposure as a possible risk factor for COVID-19 and other respiratory infectious diseases. Food and Chemical Toxicology, 146, 111809. https://doi.org/10.1016/J.FCT.2020.111809

Suárez-Peña, B., Negral, L., Castrillón, L., Megido, L., Marañón, E., & Fernández-Nava, Y. (2016). Imaging Techniques and Scanning Electron Microscopy as Tools for Characterizing a Si-Based Material Used in Air Monitoring Applications. Materials 2016, Vol. 9, Page 109, 9(2), 109. https://doi.org/10.3390/MA9020109

Thorpe, A., & Harrison, R. M. (2008). Sources and properties of non-exhaust particulate matter from road traffic: A review. Science of The Total Environment, 400(1–3), 270–282. https://doi.org/10.1016/J.SCITOTENV.2008.06.007

Tremper, A. H., Font, A., Priestman, M., Hamad, S. H., Chung, T.-C., Pribadi, A., Brown, R. J. C., Goddard, S. L., Grassineau, N., Petterson, K., Kelly, F. J., & Green, D. C. (2018). Field and laboratory evaluation of a high time resolution x-ray fluorescence instrument for determining the elemental composition of ambient aerosols. Atmos. Meas. Tech, 11, 3541–3557. https://doi.org/10.5194/amt-11-3541-2018

Unga, F., Calzolai, G., Chiari, M., Cuccia, E., Colombi, C., Franciosa, M., Dinoi, A., Merico, E., Pennetta, A., Gómez-Sánchez, N., Mapelli, C., Pareti, S., Perrino, C., Yubero, E., & Contini, D. (2025). Determination of aerosol composition by ED-XRF on Teflon and quartz substrates: potentialities and limits. Aerosol Res, 3, 405–415. https://doi.org/10.5194/ar-3-405-2025

Vecchi, R., Valli, G., Fermo, P., D'Alessandro, A., Piazzalunga, A., & Bernardoni, V. (2009). Organic and inorganic sampling artefacts assessment. Atmospheric Environment, 43(10), 1713–1720. https://doi.org/10.1016/J.ATMOSENV.2008.12.016

Viana, M., Kuhlbusch, T. A. J., Querol, X., Alastuey, A., Harrison, R. M., Hopke, P. K., Winiwarter, W., Vallius, M., Szidat, S., Prévôt, A. S. H., Hueglin, C., Bloemen, H., Wåhlin, P., Vecchi, R., Miranda, A. I., Kasper-Giebl, A., Maenhaut, W., & Hitzenberger, R. (2008). Source apportionment of particulate matter in Europe: A review of methods and results. Journal of Aerosol Science, 39(10), 827–849. https://doi.org/10.1016/J.JAEROSCI.2008.05.007

Windell, L. C., Mbengue, S., Pokorná, P., Schwarz, J., Manousakas, M. I., Papagiannis, S., Ondráček, J., & Ždímal, V. (2025). Xact625i vs PX-375: A Comparative Study of Online XRF Ambient Multi-Metal Monitors. https://doi.org/10.5194/egusphere-2025-2350

Yatkin, S., Gerboles, M., & Borowiak, A. (2012). Evaluation of standardless EDXRF analysis for the determination of elements on PM10 loaded filters. Atmospheric Environment, 54, 568–582. https://doi.org/10.1016/J.ATMOSENV.2012.02.062

Žitnik, M., Pelicon, P., Grlj, N., Karydas, A. G., Sokaras, D., Schütz, R., & Kanngießer, B. (2008). Three-dimensional imaging of aerosol particles with scanning proton microprobe in a confocal arrangement. Applied Physics Letters, 93(9), 94104. https://doi.org/10.1063/1.2976163/764942

Zografou, O., Gini, M., Manousakas, M. I., Chen, G., Kalogridis, A. C., Diapouli, E., Pappa, A., & Eleftheriadis, K. (2022). Combined organic and inorganic source apportionment on yearlong ToF-ACSM dataset at a suburban station in Athens. *Atmospheric Measurement Techniques*, *15*(16), 4675–4692. https://doi.org/10.5194/AMT-15-4675-2022

18. Air Quality Challenges in Central Asian urban areas: A $PM_{2.5}$ Source Apportionment Analysis in Dushanbe, Tajikistan

Published as:

Papagiannis, S., Abdullaev, S.F., Vasilatou, V., Manousakas, M. I. Eleftheriadis, K., & Diapouli, E. (2024). Air quality challenges in Central Asian urban areas: a PM2.5 source apportionment analysis in Dushanbe, Tajikistan. *Environmental Science and Pollution Research 2024*, 31, 39588–39601 (2024). https://doi.org/10.1007/S11356-024-33833-6

18.1 Abstract

This work presents the first comprehensive assessment of PM pollution sources in Dushanbe, Tajikistan. A total of 138 $PM_{2.5}$ samples were collected during 2015-2016 and 2018-2019 and were analyzed through gravimetric, ED-XRF, and multi-wavelength absorption techniques. The results show that $PM_{2.5}$ concentrations were substantially higher than the European annual limit value and WHO Air Quality Guidelines annual average value, with an average of 90.9 ± 68.5 μg m^{-3}. The PMF application identified eight sources of pollution that influenced $PM_{2.5}$ concentration levels in the area. Coal burning (21.3%) and Biomass burning (22.3%) were the dominant sources during the winter, while Vehicular traffic (7.7%) contributed more during the warm season. Power plant emissions (17.5%) showed enhanced contributions during the warm months, likely due to high energy demand. Cement industry emissions (6.9%) exhibited significant contribution during the cold period of 2018-2019, while Soil dust (11.3%) and Secondary sulphates (11.5%) displayed increased contribution during the warm and cold months, respectively. Finally, Waste burning (1.5%) displayed the lowest contribution, with no significant temporal variation. Our results highlight the significant impact of anthropogenic activities, and especially the use of coal burning for energy production (both in power plants and for residential heating), and the significant contribution of biomass burning during both warm and cold seasons.

18.2 Introduction

Many cities and metropolitan areas around the world are experiencing rapid growth due to the expansion of the urban population, industrialization, and intensive human activities. This can lead to increased energy consumption and combustion emissions, which contribute to the deterioration of air quality and human health.

Suspended Particulate Matter (PM) is one of the most important atmospheric pollutants, originating from both natural and anthropogenic sources; many studies have demonstrated the detrimental effects on the environment, human health (Samoli et al., 2013; Katsouyanni et al., 2001; Beelen et al., 2015), and climate change (Chen et al., 2021; Tai et al., 2010; Yang et al., 2022). Atmospheric particles consist of many different chemical components, depending on their sources. Among the major anthropogenic sources contributing to PM concentrations levels are traffic, biomass burning, industry, coal burning, while natural sources include local dust resuspension, long-range dust transport events and sea salt (Manousakas et al., 2018; Diapouli et al., 2017). In addition to primary sources, PM concentration levels may be impacted by secondary aerosol formation (e.g., secondary inorganic and organic aerosol).

The process of identifying air pollution sources and quantifying their contribution to pollutants' concentration levels is an important step in managing air quality, as it may assist

towards developing targeted effective air pollution mitigation strategies. Positive matrix factorization (PMF) is a mathematical receptor modeling tool that has been used widely for source apportionment analysis (Belis et al., 2020; Gunchin et al., 2019; Hopke, 2016). PMF aims to quantify the contribution of the major aerosol sources to the PM concentration levels recorded at a receptor site, based on the PM chemical composition and its temporal variability.

The escalating issue of the poor air quality across Central Asia is raising significant concerns among researchers and the general populace alike. A study in Almaty, Kazakhstan (Kerimray et al., 2020) reveals increasing trends in PM concentrations from 2013 to 2017. Winter peaks highlight coal combustion's significant contribution. Coal-fired power plants are a potential culprit, highlighting the need for stricter regulations and cleaner energy sources. Bishkek, Kyrgyzstan, faces similar struggles (Dzushupov et al., 2022). Over 40% of the urban population relies on poor quality coal for heating, resulting in deteriorating air quality throughout the city. Traffic is another significant contributor to PM pollution, with old vehicles running on low-quality fuel dominating the streets, intensified by insufficient public transport options. Air quality challenges are evident in Uzbekistan as well (Salomova et al., 2022). While industrial activity has decreased, a rise in car ownership has led to increased traffic emissions. Dust storms from surrounding deserts further complicate the issue along with landfill burning, particularly during the summer. Despite some progress in implementing cleaner technologies and waste management, air pollution remains a serious public concern.

Tajikistan also faces similar struggles since it has grown significantly in recent decades in terms of population, industrialization, and urbanization, which has led to declining air quality, due to increased anthropogenic emissions, such as biomass and coal burning (Chen et al., 2022). Tajikistan is also affected by frequent dust transport events, which further contribute to the increase of PM in the atmosphere and air quality deterioration (Abdullaev et al., 2019; Hofer et al., 2017). In the study conducted by Tursumbayeva et al. (2023), it is highlighted that Central Asian countries, including Tajikistan's capital, Dushanbe, rank very high in IQAir's air quality index (IQAir 2022). The researchers also highlight that, when it comes to research publications, the number is significantly lower compared to other countries worldwide.

Although a few studies have investigated crustal and organic aerosols in the region Chen et al., 2022; Abdullaev et al., 2019), it is important to note the scarcity of scientific literature addressing the source apportionment of PM pollution in Central Asian countries. In fact, only one study provided insight into $PM_{2.5}$ source apportionment across multiple countries, including Dushanbe (Tajikistan) and Kurchatov (Kazakhstan) (Almeida et al., 2020); nevertheless, this study did not specifically delve into the unique characteristics and PM sources in the different countries, while no data on carbonaceous species was available for Central Asian countries.

In this framework, the present work aims to cover the need for a better understanding of the air quality challenges Central Asian urban centers face. For this purpose, two measuring campaigns were performed during 2015-2016 and 2018-2019 in order to characterize $PM_{2.5}$ concentration levels and major chemical components. The chemical

composition database was used for the application of PMF, in order to identify the major PM sources and to quantify their contribution to $PM_{2.5}$ concentrations. The importance of research on Dushanbe's air quality extends beyond the city itself. Central Asian nations share many of the same air quality challenges, and findings from Dushanbe can contribute knowledge to other urban centers in the region. By understanding the unique sources and characteristics of $PM_{2.5}$ in Dushanbe, policy makers can develop more effective strategies for tackling PM air pollution across Central Asia, leading to improved public health outcomes for millions of people. It should be noted that this is the first source apportionment study in Dushanbe that includes data on carbonaceous aerosol, a critical parameter for the identification of combustion sources.

18.3 Experimental

18.3.1 Sampling and study area

Two $PM_{2.5}$ sampling campaigns were carried out in Dushanbe, Tajikistan (38º 33´34´´N, 68º 51´23´´E, elevation 867 m; **Figure 93**), specifically at an urban background site situated on a hill within the campus of the Physical-Technical Institute of the Academy of Sciences of Tajikistan (Hofer et al., 2017). The sampling site, located about 7.5 km away from the city center of Dushanbe, is surrounded by residential buildings. It should be noted that the city is characterized by significant industrial activities, including a cement plant - OJSC "Tochikcement" - (Location C) and a large 400-Megawatt coal-fired power station (Location B), with the addition of small-sized heating enterprises and construction sites (Figure 1). Moreover, in close proximity to the sampling area, there is a municipal waste landfill (Location A), situated approximately 850 meters away.

The campaigns were conducted during two periods: from August 2015 to May 2016, and from October 2018 to February 2019, including both warm and cold seasons. Specifically, in the 2015-2016 period, the warm period extended from August 2015 to Mid-October 2015 and from Mid-April 2016 to the end of May 2016. Conversely, the cold period of 2015-2016 spanned from the second half of October 2015 to mid-April 2016. Similarly, in the 2018-2019 period, the cold period extended from October 2018 to February 2019.

Sampling was performed with the low volume sampler MVS6D D-10623 (Berlin, Germany Kleinfiltergerät). 24h $PM_{2.5}$ samples were collected onto Teflon membrane filters (PTFE Whatman), 47mm in diameter, with 1μm pore size. On average, 9 samples were collected per month, leading to a total of 138 filters, with 88 filters obtained during the 2015-2016 period and 50 filters collected during the 2018-2019 period. The filters were used for the gravimetric determination of $PM_{2.5}$ mass concentration, as well as for PM chemical speciation.

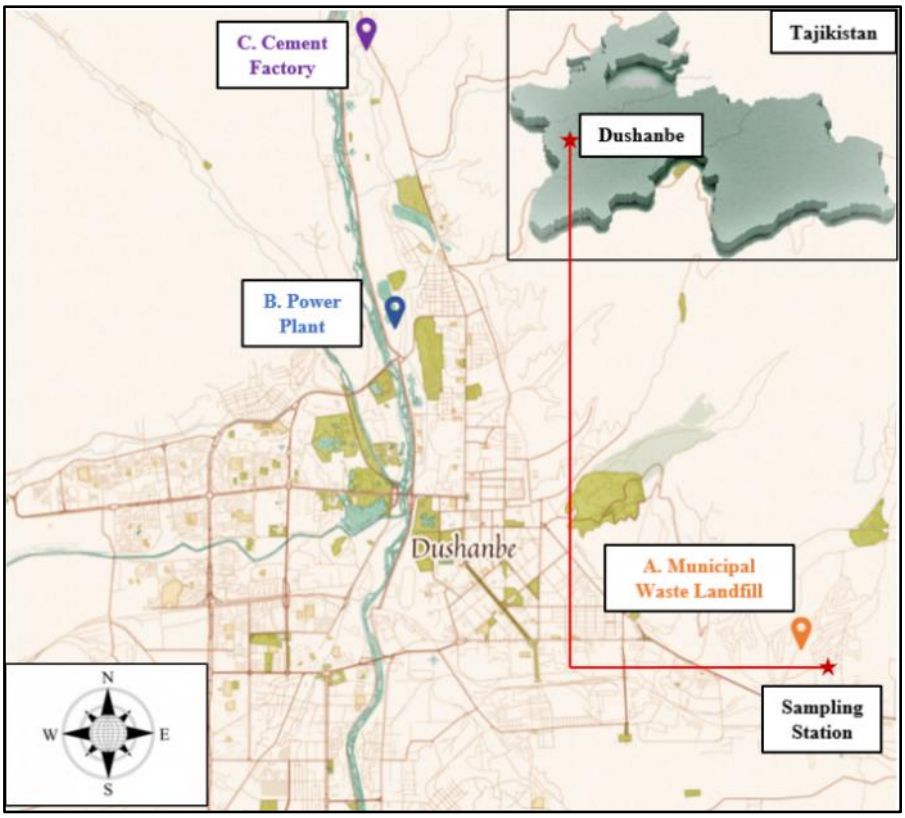

Figure 93. *Study area of Dushanbe.*

18.3.2 PM Chemical Characterization

18.3.2.1 Elemental Analysis

$PM_{2.5}$ samples were analysed for major and trace elements using the high-resolution energy dispersive X-Ray fluorescence 3-D optics spectrometer Epsilon 5 (PANanalytical). The spectrometer consists of a side-window low power X-ray tube with a W/Sc anode. The characteristic X-ray radiation emitted by the sample is detected by a Ge detector with a measured energy resolution of approximately 150 eV FWHM at Mn-Kα (5.89 keV). The spectrometer provides a selection of 9 secondary targets (Al, CaF_2, Fe, Ge, Zr, Mo, KBr, Al_2O_3, LaB_6), that can polarize the X ray beam and therefore 9 measuring conditions were selected for the optimal analysis of the aerosol samples.

For the calibration of the XRF spectrometer, we utilized infinitely thin, single-element, compound, or multi-elemental standards. Specifically, we employed various reference materials including 27 Micrommater thin reference materials deposited on 6.3 µm Mylar (such as NaCl, MgF_2, GaP, SiO, KCl, CaF_2, V, Fe, Cr, Co, CuS_x, Al, Ni, CsBr, RbI, SrF_2, Ge, Ag, Sn, Sb, Pt, AgHg, CdSe, Pb, Au, BaF_2, and Ce), seven custom-made on Kapton (including Ti, Cr, Mn × 2, Co, Cu, and BaF_2), and eight multi-standards on filter media (such as SRM 2783 and seven custom-made). The custom-made standards on filter media were devised due to the inadequate availability of certified APM materials on membrane filters covering a suitable range of concentrations. Consequently, CRMs 2584 and 2583 (indoor dust) were dispersed and collected on membrane filters (PTFE filters with PMP support ring and PTFE filters without support ring), with the dust particles of the reference material being rendered airborne in dry

form using a 220 Topas Aerosol Generator powered by compressed pure N2. The uncertainty associated with Micromatter standards is specified at 5%, while for multi-element standards, is set at 10%.

All measurements were conducted under vacuum and the total analysis time per sample was about 90 minutes. The methodology that was used for the elemental characterisation is explained in detail in Manousakas et al., (2018). 22 elements were determined by the ED-XRF method, namely Na, Mg, Al, Si, S, Cl, K, Ca, Ti, V, Cr, Mn, Fe, Co, Ni, Cu, Zn, Br, Rb, Sr, Ba and Pb. The detection limits (LOD) (ng/m^3) and the corresponding uncertainties (Unc) (%) are given in **Table 29**.

Table 29. *LOD and uncertainties for each analyzed element with ED-XRF*

El.	LOD (ng /m^3)	Unc%	El.	LOD (ng /m^3)	Unc%
Na	14.3	24	Mn	1.1	16
Mg	11.8	22	Fe	0.9	11
Al	11.8	16	Co	1.2	20
Si	13.5	24	Ni	0.5	12
S	3.0	11	Cu	0.5	11
Cl	1.3	17	Zn	0.6	11
K	0.5	11	Br	1.3	14
Ca	2.3	11	Rb	1.4	14
Ti	0.9	11	Sr	1.0	18
V	0.7	12	Ba	11.9	18
Cr	0.4	12	Pb	2.9	18

18.3.2.1 Black Carbon Analysis

$PM_{2.5}$ samples were measured by the Multi-wavelength Absorption Black carbon Instrument (MABI) (ANSTO) for the determination of their black carbon (BC) content. MABI measures the light transmission decay caused by the particles collected on a filter sample, at seven different wavelengths (405, 465, 525, 639, 870, 940, and 1050 nm).

While data from all seven wavelengths were considered, the choice of 870 nm was the prevailing choice. At 870 nm, black carbon exhibits significant absorption properties with the additional benefit of minimizing interference from other components such as brown carbon (Olson et al., 2015; Zhang et al., 2019; Liakakou et al., 2020). Secondly, the selection aligns with the operational wavelength (880 nm) of many aethalometers, which are commonly used instruments for BC monitoring (Backman et al., 2017). The detailed methodology for the calculation of BC concentrations using MABI, is explained elsewhere (Kebe et al., 2021).

18.3.2.2 Quality Assurance – Quality Control Procedure

The Quality Assurance / Quality Control (QA/QC) protocol for ED-XRF analysis incorporates various essential procedures for ensuring data quality and instrument performance. These procedures encompass: a) Weekly calibration of the Ge detector, where

the XRF software automatically adjusts energy channels to maintain optimal performance; b) Routine assessment of each analyte performance against the multi-elemental reference material SRM 2783, with daily weekly analyses to validate analytical accuracy and precision; c) Continuous evaluation of each analyte performance through the systematic analysis of selected PTFE blanks on a daily basis, aimed at assessing long-term reproducibility and consistency.

Similarly, for the Multi-wavelength Absorption Black carbon Instrument (MABI), the QA/QC procedures were the following: a) The system's calibration is checked every four samples; b) Detector calibration is conducted before every batch of measurements to ensure consistent performance; c) Regarding calibration, a visual representation is provided through a calibration chart. This chart indicates whether all measurements reside within specified tolerance levels. If the measurements meet the correct criteria, the calibration is accepted, and measurements on actual filters can proceed. If not, the calibration is rejected, and the process is repeated (Cohen et al., 2000).

18.3.3 Positive Matrix Factorization

Positive matrix factorization (PMF) is a receptor model which aims to identify the major PM sources, based on their chemical profiles, and quantify their contribution to measured PM concentration levels (Paatero and Tapper, 1994). The basic mass balance equation that is used by PMF can be expressed as:

$$X_{mn} = \sum_{p=1}^{k} g_{mp} \cdot f_{pn} + e_{mn} \tag{54}$$

where, X is the concentrations of each species (n) measured in each sample (m), g is the contribution of each source (p) in each sample (m) generated by the model, f is the contribution of each species (n) to the chemical profile of each source (p) generated also by the model, and e the residual for species (n) in sample (m).

The goal of PMF is to solve equation (24) by minimizing the sum of squared residuals (E) between the measured and predicted concentrations until a stable solution (Q) is found (Paatero, 1999):

$$Q = \sum_{m=1}^{\nu} \sum_{n=1}^{\mu} \frac{{e_{mn}}^2}{{s_{mn}}^2} \tag{55}$$

where s_{mn} is the uncertainty of each species (n) in each sample (m).

The EPA PMF 5.0 model was applied to the combined dataset from 2015-2016 and 2018-2019, which included in total 138 sampling days and 23 species (BC, Na, Mg, Al, Si, S, Cl, K, Ca, Ti, V, Cr, Mn, Fe, Co, Ni, Cu, Zn, Br, Rb, Sr, Ba and Pb).

The expanded uncertainties (including sampling and analytical uncertainties) of all measured concentrations were calculated and included in the input database. Regarding the

elemental analysis with X-Ray fluorescence, the current study considered several key factors contributing to measurement uncertainty, including uncertainties related to peak area, calibration, field operations, sampling, sample deposition, attenuation of characteristic X-rays from light elements, and the relative standard deviation of consecutive measurements (with a sample size of 3 for each sample). The total expanded uncertainty was calculated as the square root of the combined variances (Manousakas et al., 2018).

Regarding BC measurement by MABI, we considered specific factors affecting the measurements, including sample handling and instrument sensitivity. Given the challenges in precise BC quantification, we assigned a 15% expanded uncertainty to accommodate potential variability and errors.

Values below the limit of detection (LOD) were substituted with half of the LOD, and their uncertainties were set at 5/6 of the LOD. A 5% modeling uncertainty was introduced to factor in modeling inaccuracies. Three species were categorized as 'weak' (Na, Mg and Ni), while PM was included as the total variable.

18.4 Results

18.4.1 $PM_{2.5}$ Chemical Composition

The average $PM_{2.5}$ concentration measured was 90.9 ± 68.5 μg m^{-3}, which greatly exceeds the EU annual limit value (25 μg m^{-3}) and the stricter WHO annual guideline (10 μg m^{-3}). The highest average concentrations were observed during October (143.7 μg m^{-3}) and November 2015 (142.6 μg m^{-3}). The lowest $PM_{2.5}$ concentrations were recorded during April and May 2016, with average concentrations of 29.4 and 44.3 μg m^{-3} respectively. The monthly average $PM_{2.5}$ concentrations are presented in **Figure 94**. Higher PM concentration levels were recorded during 2015-2016, in comparison to 2018-2019. Specifically, the average $PM_{2.5}$ concentration during 2015-2016 was 99.5 ± 77.6 μg/m^3, significantly higher than the average concentration of 72 ± 41 μg/m^3 observed during 2018-2019. This represents a significant difference of approximately 32% between the two sampling periods (at p=0.01). While there is limited data on PM pollution in Central Asian urban areas, it should be noted that Dushanbe ranks among the most polluted cities in the area, according to 2021 data (Tursumbayeva et al., 2023), with an average $PM_{2.5}$ concentration of 59.5 μg m^{-3}, in agreement with the mean concentration measured in this study during 2018-2019 (70.8 μg m^{-3}). Almeida et al., (2020) reported on the $PM_{2.5}$ concentration levels for the same site, during 07/2014 – 05/2015. The average $PM_{2.5}$ concentration measured was 124 μg m^{-3}, which is in agreement with our results, especially with respect to the 2015-2016 campaign.

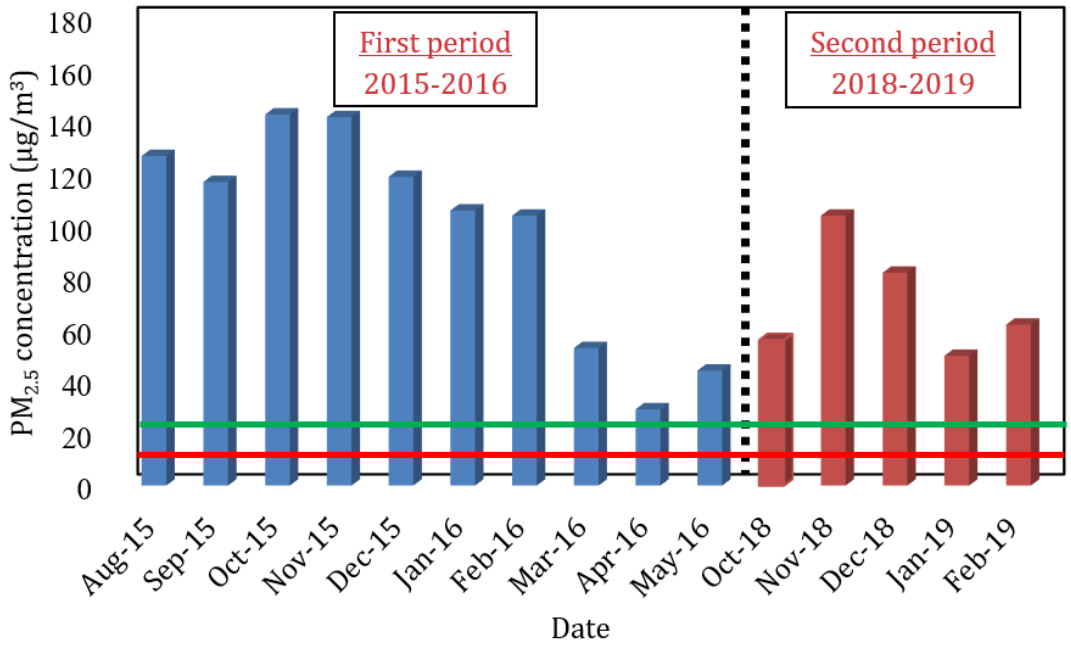

Figure 94. *Monthly average PM2.5 concentrations for the whole study period. The red line represents the WHO annual guideline and the green line the EU annual limit value.*

The average BC concentration was measured equal to 9.1 ± 6.4 μg m^{-3}. In agreement with PM mass concentrations, the highest BC concentrations were observed during October and December of 2015, with average concentration values of 14.4 and 18.0 μg m^{-3} respectively. There was a notable increasing pattern of BC concentrations from August 2015 (7.4 μg m^{-3}) to December 2015 (18.0 μg m^{-3}) (**Figure 95**). This increase in BC concentrations is likely due to residential heating. In January and February, these concentrations slightly decreased (12.5 and 9.5 μg m^{-3} respectively), reaching the lowest reported values from March to May (5.3 to 3.1 μg m^{-3}). The same trend appears to be followed during the 2018-2019 period, but with the peaking month during November 2018 (11.3 μg m^{-3}). The lowest concentrations were recorded in April and May 2016, with average concentrations of 2.7 and 3.1 μg m^{-3} respectively. A significant percentage decrease was observed during these two sampling periods (45%). This variability in BC concentrations underscores the potential impact of residential heating on the local air quality. Chen et al. (2022) similarly noted decreased concentration values of EC during the spring period compared to the winter period of their study conducted between 2018 and 2019. They reported average concentrations of 4.2 μg m^{-3} during the spring period, contrasting with 7.3 μg m^{-3} observed during the winter period.

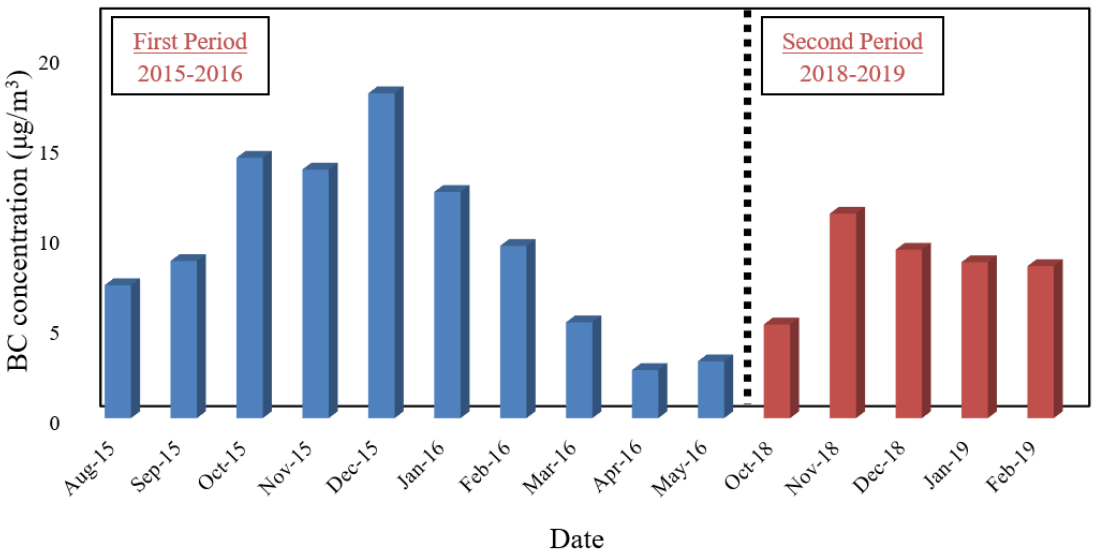

Figure 95. *BC concentrations for the whole study in µg m⁻³.*

The main elements contributing to PM mass were Si and Ca, with maximum concentrations up to 28.1 and 21.9 µg m^{-3} respectively, followed by Na, Fe, Al, and S. The high concentration levels of crustal elements indicate the increased soil dust resuspension and transport, which is frequent in central Asia (Hofer et. al., 2017).

Correlation analysis of the different elemental components was utilized to explore the similarity of their time trends. The correlation coefficients observed between various elements offer insights into potential shared sources. Al, Si, Ca, Ti, and Fe exhibited strong correlations with each other (PC > 0.82), indicative of a soil dust origin. Additionally, Zn and lead Pb displayed strong correlation (PC = 0.88), suggesting potential common sources related to vehicular traffic and waste burning activities. Moreover, V was strongly correlated with Ni, Mg, Ca, Ti, Mn, Fe, and Cr (PC > 0.85), hinting at common sources associated with industrial activities in the region.

The elements' Enrichment Factor (EF) was also calculated and is displayed in **Figure 96**. EF values greater than 10 indicate dominance by anthropogenic sources, while EF values lower than 5 suggest elements of crustal origin. EF values falling between 5 and 10 denote elements originating from both natural and anthropogenic sources (IAEA, 1992). The EF of an element for each PM sample was determined using the formula:

$$EF = \frac{(\frac{X}{C})_{PM-Sample}}{(\frac{X}{C})_{Crust}} \quad (56)$$

where, X/C is the ratio of concentration of each element over the concentration of a reference element of crustal origin, calculated for each PM sample and for the Earth's crust. The reference element is typically chosen from Al, Si, Sc, Mn, Ti, Fe. For our analysis, Si was selected as the reference element. The elemental composition of the Earth's crust was obtained from *Wedepohl (1995)*. EF analysis revealed that S, Cl, Co, Cu, Zn, Br, and Pb are mainly related

to anthropogenic sources. Additionally, Ca and Ni displayed EF values between 5 and 10, suggesting contributions from both natural and anthropogenic sources. Conversely, the remaining elements (Na, Mg, Al, K, Ti, V, Cr, Mn, Fe, Rb, Sr and Ba) analyzed exhibited EF values lower than 5, indicating primarily crustal origin. Emissions of crustal aerosols in the

study area may be related to soil dust resuspension and transport but also to industrial activities, i.e. the operation of the cement plant.

Table 30 presents the $PM_{2.5}$ concentration (in μg m^{-3}) and composition (in ng m^{-3}) during the entire study.

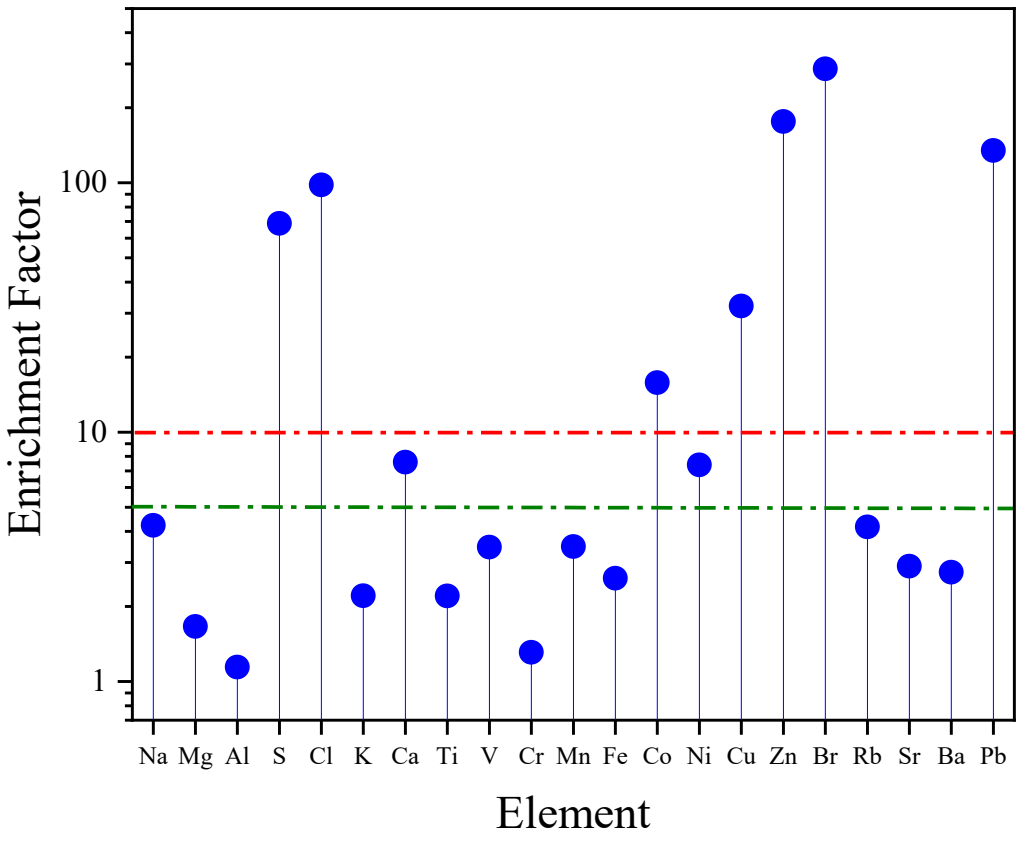

Figure 96. *Enrichment factors for the elements of the whole study period.*

Table 30. *PM2.5 concentration (in μg m^{-3}) and composition (in ng m^{-3}) during the entire study.*

Species	Average	St. Dev	Min.	Max.
$PM_{2.5}$	90.0	68.5	18.1	417.1
BC	9100.0	6400.0	1700.0	44000.0
Na	2370.0	2830.0	160.0	16200.0
Mg	490.0	580.0	10.0	2100.0
Al	1930.0	1810.0	130.0	7800.0
Si	6620.0	6560.0	250.0	28100.0
S	1430.0	1070.0	400.0	6700.0
Cl	1370.0	1420.0	40.0	8100.0
K	1380.0	1090.0	290.0	6200.0
Ca	4870.0	6240.0	110.0	21900.0
Ti	150.0	200.0	4.0	870.0
V	4.0	3.0	0.7	30.0
Cr	1.0	2.0	0.4	10.0
Mn	40.0	60.0	1.0	300.0
Fe	1750.0	2740.0	60.0	11200.0
Co	4.0	3.0	0.4	30.0
Ni	3.0	2.0	0.5	10.0
Cu	10.0	20.0	1.1	100.0
Zn	200.0	210.0	1.8	1040.0
Br	10.0	10.0	1.3	70.0
Rb	10.0	10.0	1.5	70.0
Sr	20.0	40.0	1.1	130.0
Ba	40.0	50.0	12.0	220.0
Pb	50.0	40.0	4.0	190.0

18.4.2 PM2.5 Source Apportionment

The model was run for different numbers of sources. After investigating a range of possible solutions ranging from 4 to 10 sources, the eight-source solution was selected as the optimum. The best solution was identified by the use of key performance indicators, including Q values, distribution of scaled residuals, fit of measured PM concentrations, as well as by assessing the physical meaning of the obtained source profiles and contributions (Reff et al., 2007). The final solution was selected from 100 runs, while the uncertainty of the solution was assessed by implementing the Bootstrapping and Displacement error estimation tools provided by EPA PMF 5.0 (Manousakas et al., 2017). The differences between Q_{true} and Q_{rob} was less than 1%, while between Q_{true} and Q_{theor} was less than 10%.

The assessment of the agreement between the measured $PM_{2.5}$ mass concentration and the concentration predicted by the model serves as a valuable indicator for evaluating the quality of the fit. The model-predicted concentration and the actual concentration exhibit a strong positive correlation ($y = 0.64x$, $R^2 = 0.85$), demonstrating a robust fit that effectively characterizes the true contribution of $PM_{2.5}$ sources in the studied area.

High rotational ambiguity was revealed for the base run which indicated that the solution had high uncertainty. A few constrains were then introduced to the model to achieve a more stable solution (Manousakas et al., 2017) and obtain chemical profiles that better describe the main aerosol sources identified. Specifically, the following constraints were introduced: BC was pulled up maximally in the factors of Waste burning and Traffic and set to zero in the Soil dust factor. In addition, S was pulled up maximally in the Power plant profile. The dQ% was kept in all cases at the lowest value of 0.5% ensuring that no significant changes with respect to the unconstrained results would occur. The introduction of all four constraints resulted in an overall dQ of 1.9%.

Very low rotational ambiguity was observed after applying the constraints. The Bootstrap (BS) error estimation was used to check the reproduction of the factors and the number of runs was set to 100. BS results were very good, revealing reproducibility above 80% for all factors. In addition, displacement showed no factor swaps for the solution, for all dQ levels.

The seasonal source contributions are presented in **Figure 97**. The chemical profiles of the eight-factor solution are presented in **Figure 98** and the average relative contributions of the different sources to the observed $PM_{2.5}$ concentration levels are presented in **Figure 99**.

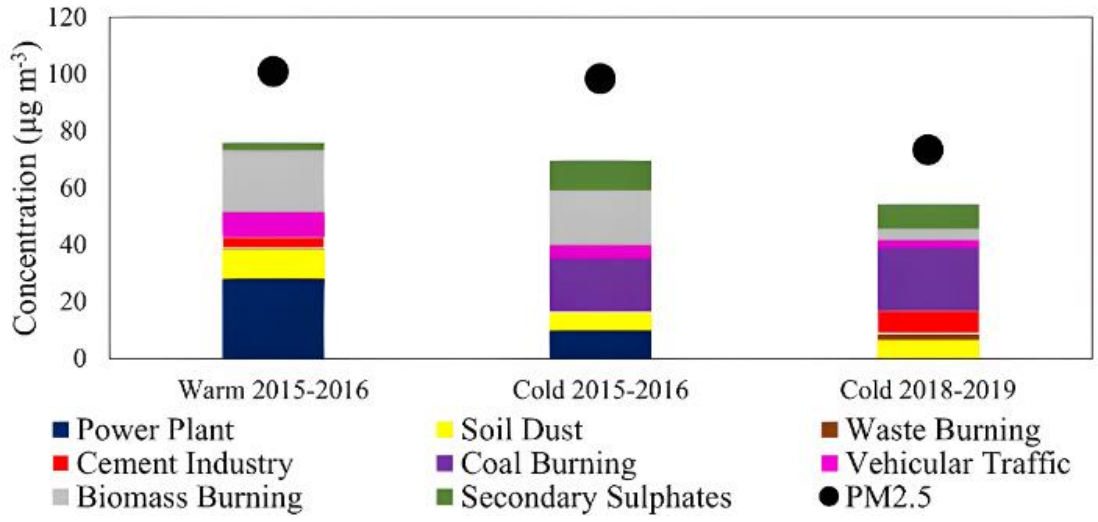

Figure 97. *Average source contribution to PM2.5 and measured PM2.5 in μg m^{-3} for the warm and cold seasons of the whole study period.*

Factor 1 is identified as Soil dust and is characterized by the high levels of Al, Si, Ca, Mg, Ti, K and Fe, elements that are related to mineral dust (Viana et al., 2008; Jain et al., 2020). The calculated ratios of Si/Al (3.31), Fe/Al (0.68), and Ti/Al (0.07) are in agreement with the upper crustal ratio values reported by Wepepohl (1995), namely 3.92, 0.40, and 0.04 respectively, further supporting the identification of this factor as Soil dust. Soil dust accounts on average for 11.3% of total $PM_{2.5}$ concentration, contributing slightly more during the warm

months (by 14% on average). This profile agrees well with the Soil dust profile reported by Almeida et al., (2020), which accounted for 14% of the total $PM_{2.5}$ concentration.

Factor 2 contains mainly S and is thus associated with the production of secondary aerosol, and specifically secondary sulfates. Secondary sulfates are major components of secondary inorganic aerosols and are known to contribute to visual degradation (Kang et al., 2004) and negatively affect respiratory health in humans (Mangia et al., 2015). They may be produced locally or transported over long distances from anthropogenic emissions of their gaseous precursor, SO_2. In general, the main tracers for secondary sulphates include the ionic species SO_4^{2-} and NH_4^+ (Viana et al., 2008; Fakhri et al., 2024). Given the absence of major ion concentrations in the database, S serves as the primary indicator, which is a methodology employed in numerous studies (Marcazzan et al., 2003; Manousakas et al., 2017; Diapouli et al., 2022). The average contribution of this factor to $PM_{2.5}$ corresponds to 11.5% and accounts for 14% of $PM_{2.5}$ during the cold months and 4% during the warm months.

Factor 3 is characterized by high levels of Ca and Fe and contribution from other crustal elements (such as, Ti, Mg, K and Na), while it accounts for a high percentage of Cr, V and Ni. The factor is identified as Cement industry. Emissions from cement facilities are associated with cement dust (crustal elements with increased presence of Ca) and combustion emissions. The profile was also compared with published cement profiles from the SPECIEUROPE (EC-JRC) repository (Pernigotti et. al., 2016). SPECIEUROPE contains particulate chemical profiles, including organic and inorganic species, derived from both measurements of emission sources and source apportionment studies carried out in Europe. Very good agreement was observed with the profiles from Yatkin and Bayram, 2008 for the crustal elements but also for elements associated with combustion processes like Ni, V and Zn. The V/Ni ratio in the profile was calculated at 1.9, which may point towards heavy fuel oil combustion. High levels of Cr have been also associated with cement industries, as all forms of cement contain a certain amount of chromate (Demir et al., 2003). Furthermore, Cr has gained significant attention in the cement industry due to its potential to cause cement eczema, a type of allergic contact dermatitis (Paone 2008). The average contribution of this source to $PM_{2.5}$ is at 6.9% and displays significant contribution during the cold period of 2018-2019 (16%).

The next factor (Factor 4) is identified as Coal burning and is traced by BC, Cl and Br; more than 40% of the mass of these species is explained by the Coal burning factor. Cl has consistently been used as a tracer for coal combustion in various studies (Zong et al., 2016; Deng et al., 2014). Additionally, Rai et al. (2020) has highlighted the use of a Cl-Br factor as a potential indicator for coal burning activities. Moreover, Peng et al. (2021) reported unprecedented levels of bromine chloride (BrCl) at a mid-latitude site in North China during winter, with widespread coal burning in rural households. The contribution of this factor is quite high during the winter periods, specifically between December 2015 – January 2016 and December 2018 – February 2019, indicating residential coal burning for heating purposes. It has been observed that Cl and Br tend to exhibit high volatility during coal combustion, as seen in the partitioning behavior of trace elements (Vassilev et al., 2000; Clarke et al., 1993).

The average contribution of Coal burning to $PM_{2.5}$ is 21.3%, and accounts for 48 % of $PM_{2.5}$ during the winter months (December to February). It should be noted that residential coal burning was also found to contribute significantly to $PM_{2.5}$ levels in Kurchatov (Kazakhstan) (Almeida et al., 2020), highlighting the need to mitigate residential heating emissions in Central Asian urban areas.

Factor 5 is identified as Waste burning, with main tracers: BC, Zn, Pb and Cl. Waste burning is a fairly common practice to dispose unwanted materials and takes place in both developing and developed countries. In Dushanbe, municipal waste management strategies have not yet been implemented, and waste separation remains unresolved (Environmental Performance Reviews: Tajikistan, 2017). Zn and Pb are trace metals that have been linked with waste incineration (Duan and Tan, 2013; Rai et al., 2020; Manousakas et al., 2022, Pant et al., 2012), and Cl is also reported to be an important elemental tracer for plastic waste burning (Li et al., 2012; Jayarathne et al., 2018). It is primarily emitted as HCl and results to a large degree from polyvinylchloride (PVC) (Christian et. al., 2010). The SPECIEUROPE database was once again used to check for similarities between municipal waste profiles and good agreement was observed with the published profile of Samara et. al., 2003, corresponding to metal scrap incinerator, especially for the elements of Zn (scrap metal incineration) and Pb (lead smelter). The closest municipal waste landfill facility is located North-West approximately 850 m away from the sampling site. This factor accounts for 1.5% of the average $PM_{2.5}$ concentration, displaying the lowest contribution between all identified sources. No seasonal variability was observed for the years 2015-2016 but the contribution of this source was significantly increased during 2018-2019 (on average 4%).

Factor 6 accounts for most of the mass of Cu and Zn (89 and 46%, respectively) and a major part of Pb mass (34%), while it is also characterized by high levels of BC. These markers, commonly associated with vehicular traffic, are identified as including both exhaust and non-exhaust emissions (Pant et al., 2012). Non exhaust emissions are comprised of brake, tire and road wear and road dust resuspension. Zn is a metal that is generally used in rubber to strengthen the tires and has been suggested for tire wear emissions (Rhodes et. al., 2012), while Cu and Pb particles are formed from friction between brake pads and disks (brake wear) (Huang et al., 2018; Thorpe et al., 2008). The average contribution of this factor to $PM_{2.5}$ corresponds to 7.7%. It should be noted that the lack of information on organic mass may have led to an underestimation of traffic exhaust emissions. This source contributed more during the warm season of 2015-2016 (8.8 $\mu g\ m^{-3}$, corresponding to 11% of $PM_{2.5}$ mass). A significant decrease was observed in the more recent years, with the cold period of 2015-2016 displaying almost double the contribution of the cold period of 2018-2019 (4.6 $\mu g\ m^{-3}$ in 2015-2016 versus 2.6 $\mu g\ m^{-3}$ in 2018-2019, corresponding to 7 and 5% of the total $PM_{2.5}$ mass, respectively).

Factor 7 is associated with most of Co, V and Ni mass (74, 53 and 40%, respectively) and a significant part of Rb, Ba and Sr mass (30 - 42%). It is also characterized by high levels of Al, Si, Ca, Fe, K, BC and Na. This factor is identified as Power plant emissions. In Dushanbe, the main power plant is the Dushanbe-2 power station. It is a 400-megawatt coal-fired facility and is located in the north-west part of the city. Coal is a complex material that is comprised

of organic matter and inorganic ash that is created over centuries by multi-layers of fallen vegetation (Vardar et al., 2010). Co has been used as a tracer for coal-fired (lignite) power plants (Vardar et al., 2010, Uyar et al., 2016). V, Ni, Mg, Si, Ca, Fe, Al and S are included in fly ash (Argyropoulos et al., 2013). Coal power plants are obligated to have electrostatic filters that retain the high percentages of fly ash, but a significant amount usually escapes those filters, and is emitted in the air. Finally, the presence of Na in this factor can be also explained by the desulfurization process of the flue gas (Manousakas et al., 2015). Flue gases are a mixture of combustion products, including water vapor, carbon dioxide, particulates, heavy metals, and acidic gases generated from direct (incineration) or indirect (gasification and pyrolysis) oxidation of RDF (Refuse-derived fuels) or intermediate syngas (Materazzi et al., 2017). The average contribution of Power plant emissions to $PM_{2.5}$ is 17.5% and accounts for 22% during the warm months, indicating the increased activity of the plant, possibly due to high energy demand.

The final factor (Factor 8) is identified as Biomass burning and is mainly traced by BC, K and S (Viana et al., 2008). 29 – 34% of the total mass of these species is associated with this factor. In addition, this source accounts for 28% of the total mass of Rb, an element that has been also suggested as tracer for Biomass burning emissions (Massimi et al., 2020). The increased contribution of S in the Biomass burning profile may be attributed to the aging process of the smoke particles. Li et al. (2003) highlights that with the aging of smoke, potassium chloride (KCl) particles from biomass burning, are converted to potassium sulfate (K_2SO_4) and potassium nitrate (KNO_3) through reactions with sulfur- and nitrogen-bearing species from biomass burning as well as other sources. This indicates that while more KCl particles occur in fresh smoke, aged smoke contains more K_2SO_4 and KNO_3. Almeida et al. (2020) also utilized S as an important marker for aged biomass burning in the profile of Skopje/MKD. The Biomass burning impact is more pronounced during 2015-2016, with similar contributions during warm and cold season, at 28% of total $PM_{2.5}$ mass. Very low contribution is observed for the cold period of 2018-2019 (7%). This factor displays the highest average contribution to $PM_{2.5}$ (22.3%). Biomass burning has also been identified by Chen et al., (2022) as a significant contributor to PM air pollution in Dushanbe.

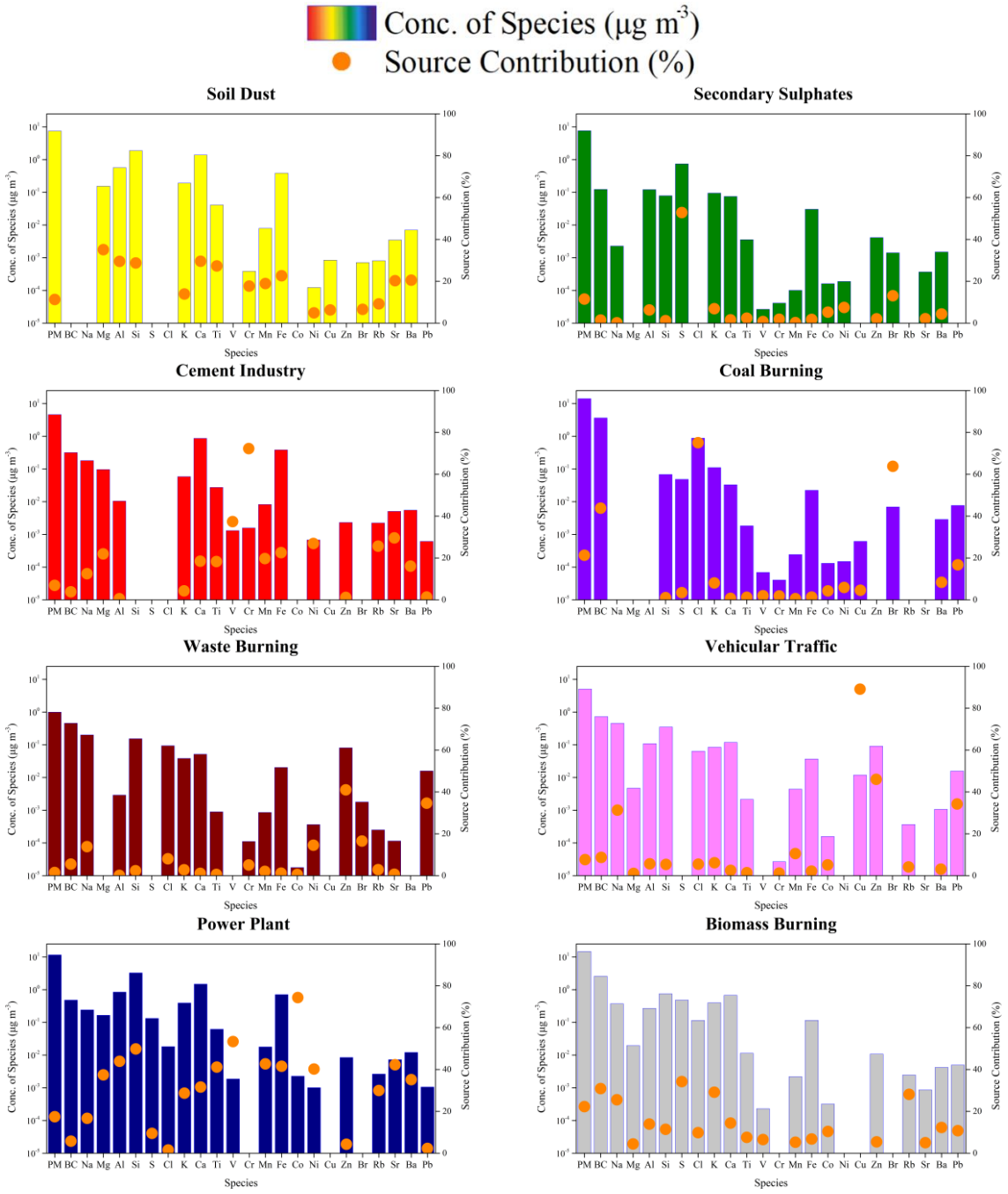

Figure 98. *The PM2.5 source profiles have been obtained by Positive Matrix Factorization (PMF) using PM, BC, and elemental concentrations. The bars express the concentrations of species (in µg m^{-3}), and the orange circles display the % contribution of the source to the average species concentration.*

0

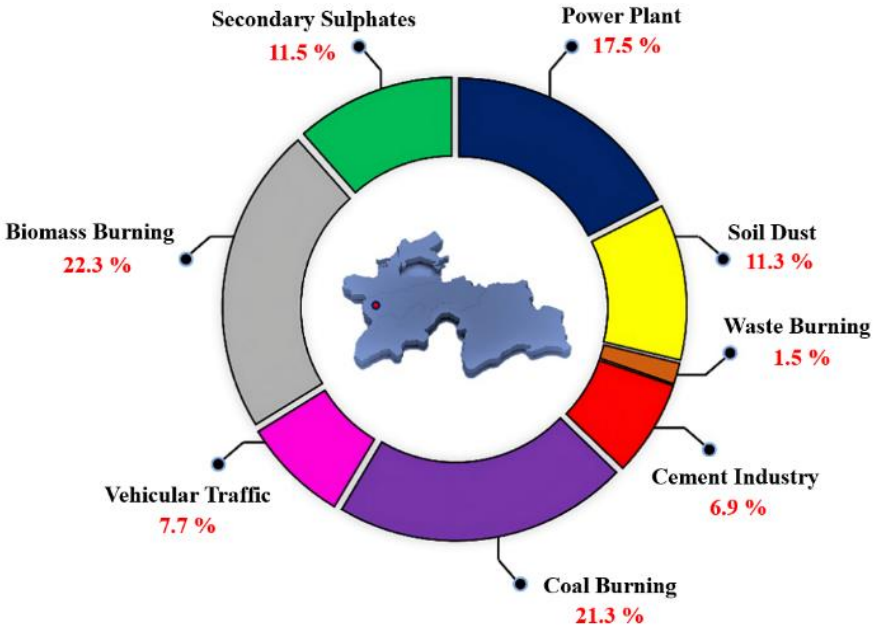

Figure 99. *Relative contribution of PM2.5 sources for the whole study period.*

The Conditional Probability Function (CPF) was also used to investigate the effects of different emission sources in different directions by integrating source apportionment information, with wind speed and direction data (Kim et al., 2012, Rai et al., 2016). The implementation of CPF proves advantageous for identifying pollution origins, provided that said origins reside within a specific range from the sampling location. The wind speed and wind direction data utilized in this study were sourced from the local monitoring network of Dushanbe (https://www.visualcrossing.com/weather/weather-data-services). Only the highest 10% of the source contributions was utilized (90^{th} percentile) in this analysis. The mathematical representation of CPF is given by the equation:

$$CPF = m_{\Delta\theta}/n_{\Delta\theta} \tag{57}$$

Here, $m_{\Delta\theta}$ represents the count of wind occurrences in sector $\Delta\theta$, that surpasses a specific threshold, while $n_{\Delta\theta}$ denotes the total number of data points within the same wind sector. It is probable that the sources are situated in the direction with relatively high values of conditional probability (**Figure 100**).

The results from the CPF analysis revealed distinct emission source patterns in relation to the sampling station's geographical location. Notably, the western - northwestern region was found to be associated with the cement industry, power plant and waste burning sources, coinciding with the locations of the Cement Plant, Dushanbe-2 coal power station and the municipal waste landfill. The southwestern direction was found to be a predominant source of soil dust, attributed to long-range transport from nearby desert regions such as Leili and Karakum deserts (Abdullaev et al., 2019). Biomass Burning was found to originate predominantly from the South, and may be also associated with long range transport, as

further supported by the high S contribution in the biomass burning profile. Vehicular traffic and secondary sulphate sources predominantly originate from the western area, pointing towards the city center. The coal burning source demonstrates a wider spatial distribution, pointing towards residential heating emissions from various locations around the study area.

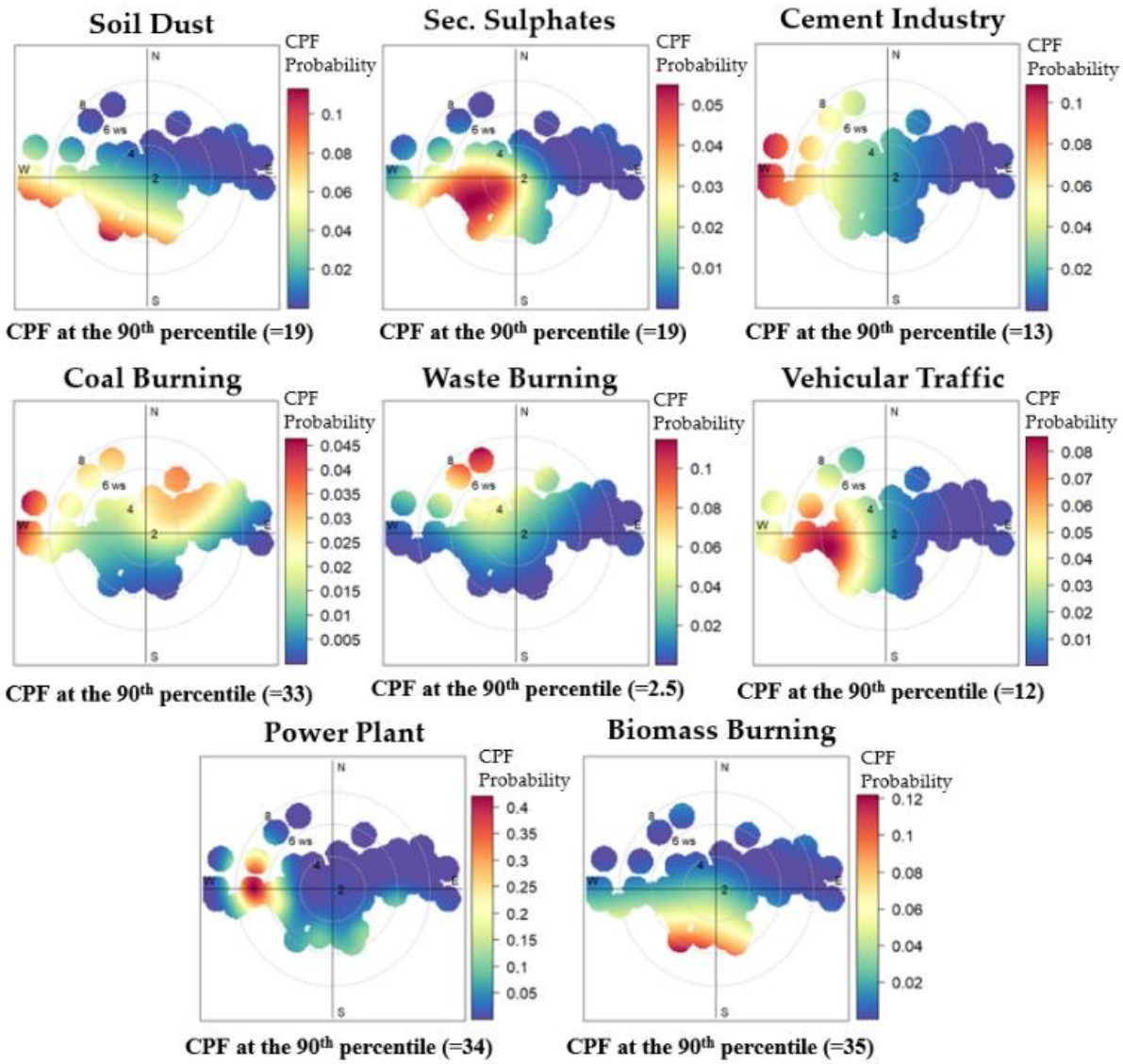

Figure 100. *CPF polar plots for source contribution.*

18.5 Conclusions

This is the first work effort to quantify pollution sources in Dushanbe, Tajikistan, an area with significant air quality issues, particularly concerning PM pollution. The measurement campaign, conducted during 2015-2016 and 2018-2019, provided valuable insights into the composition and sources of $PM_{2.5}$ in the region.

Our findings reveal alarmingly high $PM_{2.5}$ concentrations that surpass the established limits set by both European standards and WHO guidelines. The identification of eight primary sources of pollution, including coal burning, biomass burning, and cement industrial emissions, underscores the complicated nature of the PM pollution problem in Dushanbe. Furthermore, seasonal variations in source contributions highlight the dynamic nature of pollution sources, with coal burning dominating during winter months and power plant emissions peaking during warmer seasons.

Notably, this work addresses a critical gap in research by focusing on Central Asia, an often-overlooked region in air quality studies. By incorporating carbonaceous species (BC) into source apportionment analysis, we aimed to provide a better understanding of combustion sources in the area.

However, future studies should aim to delve deeper into the understanding of PM pollution in Central Asian cities. By expanding research efforts and incorporating additional source tracers, such as organic aerosols and secondary inorganic species, more effective strategies for mitigating air pollution can be developed. We hope that this study may serve as a starting point for a comprehensive characterization and source apportionment of PM pollution in central Asia, where large cities face significant environmental problems due to increasing population and economic activities.

18.6 References

Abdullaev, S. F., & Sokolik, I. N. (2019). Main Characteristics of Dust Storm sand Their Radiative Impacts: With a Focuson Tajikistan. *Journal of Atmospheric Science Research*, *2*(2). https://doi.org/10.30564/JASR.V2I2.352

Almeida, S. M., Manousakas, M., Diapouli, E., Kertesz, Z., Samek, L., Hristova, E., Šega, K., Alvarez, R. P., Belis, C. A., & Eleftheriadis, K. (2020). Ambient particulate matter source apportionment using receptor modelling in European and Central Asia urban areas. *Environmental Pollution*, *266*, 115199. https://doi.org/10.1016/j.envpol.2020.115199

Argyropoulos, G., Grigoratos, T., Voutsinas, M., & Samara, C. (2013). Concentrations and source apportionment of PM10 and associated elemental and ionic species in a lignite-burning power generation area of southern Greece. *Environmental Science and Pollution Research 2013 20:10*, *20*(10), 7214–7230. https://doi.org/10.1007/S11356-013-1721-Y

Backman, J., Schmeisser, L., Virkkula, A., Ogren, J. A., Asmi, E., Starkweather, S., Sharma, S., Eleftheriadis, K., Uttal, T., Jefferson, A., Bergin, M., Makshtas, A., Tunved, P., & Fiebig, M. (2017). On Aethalometer measurement uncertainties and an instrument correction factor for the Arctic. *Atmospheric Measurement Techniques*, *10*(12), 5039–5062. https://doi.org/10.5194/AMT-10-5039-2017

Beelen, R., Hoek, G., Raaschou-Nielsen, O., Stafoggia, M., Andersen, Z. J., Weinmayr, G., Hoffmann, B., Wolf, K., Samoli, E., Fischer, P. H., Nieuwenhuijsen, M. J., Xun, W. W., Katsouyanni, K., Dimakopoulou, K., Marcon, A., Vartiainen, E., Lanki, T., Yli-Tuomi, T., Oftedal, B., … Brunekreef, B. (2015). Natural-cause mortality and long-term exposure to particle components: an analysis of 19 European cohorts within the multi-center ESCAPE project. *Environmental Health Perspectives*, *123*(6), 525–533. https://doi.org/10.1289/EHP.1408095

Belis, C. A., Pernigotti, D., Pirovano, G., Favez, O., Jaffrezo, J. L., Kuenen, J., Denier van Der Gon, H., Reizer, M., Riffault, V., Alleman, L. Y., Almeida, M., Amato, F., Angyal, A., Argyropoulos, G., Bande, S., Beslic, I., Besombes, J. L., Bove, M. C., Brotto, P., … Yubero, E. (2020). Evaluation of receptor and chemical transport models for PM10 source apportionment. *Atmospheric Environment: X*, *5*, 100053. https://doi.org/10.1016/J.AEAOA.2019.100053

Chen, P., Kang, S., Zhang, L., Abdullaev, S. F., Wan, X., Zheng, H., Maslov, V. A., Abdyzhapar uulu, S., Safarov, M. S., Tripathee, L., & Li, C. (2022). Organic aerosol compositions and source estimation by molecular tracers in Dushanbe, Tajikistan. *Environmental Pollution*, *302*, 119055. https://doi.org/10.1016/J.ENVPOL.2022.119055

Chen, S.-L., Chang, S.-W., Chen, Y.-J., & Chen, H.-L. (2021) . Possible warming effect of fine particulate matter in the atmosphere. *Communications Earth & Environment 2021 2:1*, *2*(1), 1–9. https://doi.org/10.1038/s43247-021-00278-5

Christian, T. J., Yokelson, R. J., Cárdenas, B., Molina, L. T., Engling, G., & Hsu, S. C. (2010). Trace gas and particle emissions from domestic and industrial biofuel use and garbage burning in central Mexico. *Atmospheric Chemistry and Physics*, *10*(2), 565–584. https://doi.org/10.5194/ACP-10-565-2010

Clarke, L. B. (1993). The fate of trace elements during coal combustion and gasification: an overview. *Fuel*, *72*(6), 731–736. https://doi.org/10.1016/0016-2361(93)90072-A

Cohen, D.D., Taha, G., Stelcer, E., Garton, D., Box, G. The Measurement and Sources of Fine Particle Elemental Carbon at Several Key Sites in NSW over the Past Eight Years. *Proceedings of the 15th International Clean Air and Environment Conference 2000*, Sydney, Australia, 26–30 November 2016; Clean Air Society of Australia and New Zealand: Chirnside Park, Australia; pp. 485–490

Diapouli, E., Popovicheva, O., Kistler, M., Vratolis, S., Persiantseva, N., Timofeev, M., Kasper-Giebl, A., & Eleftheriadis, K. (2014). Physicochemical characterization of aged biomass burning aerosol after long-range transport to Greece from large scale wildfires in Russia and surrounding regions, Summer 2010. *Atmospheric Environment*, *96*, 393–404. https://doi.org/10.1016/J.ATMOSENV.2014.07.055

Diapouli, E., Manousakas, M. I., Vratolis, S., Vasilatou, V., Pateraki, S., Bairachtari, K. A., Querol, X., Amato, F., Alastuey, A., Karanasiou, A. A., Lucarelli, F., Nava, S., Calzolai, G., Gianelle, V. L., Colombi, C., Alves, C., Custódio, D., Pio, C., Spyrou, C., … Eleftheriadis, K. (2017). AIRUSE-LIFE +: Estimation of natural source contributions to urban ambient air PM10 and PM2. 5 concentrations in southern Europe - Implications to compliance with limit values. *Atmospheric Chemistry and Physics*, *17*(5), 3673–3685. https://doi.org/10.5194/acp-17-3673-2017

Diapouli, E., Fetfatzis, P., Panteliadis, P., Spitieri, C., Gini, M. I., Papagiannis, S., Vasilatou, V., & Eleftheriadis, K. (2022). PM2.5 Source Apportionment and Implications for Particle Hygroscopicity at an Urban Background Site in Athens, Greece. *Atmosphere 2022, Vol. 13, Page 1685*, *13*(10), 1685. https://doi.org/10.3390/ATMOS13101685

Demir, T. A., Berber, A., Kalyoncu, C., Isıklı, B., Demir, T. A., Urer, S. M., Berber, A., Akar, T., & Kalyoncu, C. (2003). Effects of chromium exposure from a cement factory. *Environmental Research*, *91*, 113–118. https://doi.org/10.1016/S0013-9351(02)00020-8

Deng, S., Shi, Y., Liu, Y., Zhang, C., Wang, X., Cao, Q., Li, S., & Zhang, F. (2014). Emission characteristics of Cd, Pb and Mn from coal combustion: Field study at coal-fired power plants in China. *Fuel Processing Technology*, *126*, 469–475. https://doi.org/10.1016/J.FUPROC.2014.06.009

Duan, J., & Tan, J. (2013). Atmospheric heavy metals and Arsenic in China: Situation, sources and control policies. *Atmospheric Environment*, *74*, 93–101. https://doi.org/10.1016/J.ATMOSENV.2013.03.031

Dzushupov, K. O., Buban, J. M. A., Aidaraliev, A. A., Ahmadi, A., Chahal, P., Ibrahim, M., Lin, X., & Kouwenhoven, M. B. N. (2022). Air pollution in Bishkek, Kyrgyzstan: Driving factors and state response. *Public Health Challenges*, *1*(4). https://doi.org/10.1002/PUH2.22

Environmental Performance Reviews: Tajikistan | United Nations iLibrary. (n.d.). Retrieved June 1, 2022, from https://www.un-ilibrary.org/content/books/9789210601696#chapters

Fakhri, N., Stevens, R., Downey, A., Oikonomou, K., Sciare, J., Afif, C., & Hayes, P. L. (2024). Source apportionment of PM 2.5 in Montréal, Canada, and health risk assessment for

potentially toxic elements. *Atmos. Chem. Phys*, *24*, 1193–1212. https://doi.org/10.5194/acp-24-1193-2024

Gunchin, G., Manousakas, M., Osan, J., Karydas, A. G., Eleftheriadis, K., Lodoysamba, S., Shagjjamba, D., Migliori, A., Padilla-Alvarez, R., Streli, C., & Darby, I. (2019). Three-year long source apportionment study of airborne particles in ulaanbaatar using X-ray fluorescence and positive matrix factorization. *Aerosol and Air Quality Research*, *19*(5), 1056–1067. https://doi.org/10.4209/aaqr.2018.09.0351

Hofer, J., Althausen, D., Abdullaev, S. F., Makhmudov, A. N., Nazarov, B. I., Schettler, G., Engelmann, R., Baars, H., Wadinga Fomba, K., Müller, K., Heinold, B., Kandler, K., & Ansmann, A. (2017). Long-term profiling of mineral dust and pollution aerosol with multiwavelength polarization Raman lidar at the Central Asian site of Dushanbe, Tajikistan: case studies. *Atmos. Chem. Phys*, *17*, 14559–14577. https://doi.org/10.5194/acp-17-14559-2017

Hopke, P. K. (2016). Review of receptor modeling methods for source apportionment. *Journal of the Air & Waste Management Association*, *66*(3), 237–259. https://doi.org/10.1080/10962247.2016.1140693

Huang, R. J., Cheng, R., Jing, M., Yang, L., Li, Y., Chen, Q., Chen, Y., Yan, J., Lin, C., Wu, Y., Zhang, R., El Haddad, I., Prevot, A. S. H., O'Dowd, C. D., & Cao, J. (2018). Source-Specific Health Risk Analysis on Particulate Trace Elements: Coal Combustion and Traffic Emission As Major Contributors in Wintertime Beijing. *Environmental Science and Technology*, *52*(19), 10967–10974. https://doi.org/10.1021/ACS.EST.8B02091

IAEA. (1992). Sampling and Analytical Methodologies for Instrumental Neutron Activation Analysis of Airborne Particulate Matter. *International Atomic Energy Agency*, *4*, 53.

IQAir, 2022. World's Most Polluted Countries & Regions (Historical Data 2018-2022). URL. World's Most Polluted Countries in 2022 - PM2.5 Ranking | IQAir, accessed 07.07.2023

Jain, S., Sharma, S. K., Vijayan, N., & Mandal, T. K. (2020). Seasonal characteristics of aerosols (PM2.5 and PM10) and their source apportionment using PMF: A four year study over Delhi, India. *Environmental Pollution*, *262*, 114337. https://doi.org/10.1016/j.envpol.2020.114337

Jayarathne, T., Stockwell, C. E., Bhave, P. V, Praveen, P. S., Rathnayake, C. M., Islam, M. R., Panday, A. K., Adhikari, S., Maharjan, R., Douglas Goetz, J., Decarlo, P. F., Saikawa, E., Yokelson, R. J., & Stone, E. A. (2018). Nepal Ambient Monitoring and Source Testing Experiment (NAMaSTE): emissions of particulate matter from wood-and dung-fueled cooking fires, garbage and crop residue burning, brick kilns, and other sources. *Atmos. Chem. Phys*, *18*, 2259–2286. https://doi.org/10.5194/acp-18-2259-2018

Kang, C. M., Lee, H. S., Kang, B. W., Lee, S. K., & Sunwoo, Y. (2004). Chemical characteristics of acidic gas pollutants and PM 2.5 species during hazy episodes in Seoul, South Korea. *Atmospheric Environment*, *28*(38), 4749–4760. https://doi.org/10.1016/J.ATMOSENV.2004.05.007

Katsouyanni, K., Touloumi, G., Samoli, E., Gryparis, A., Le Tertre, A., Monopolis, Y., Rossi, G., Zmirou, D., Ballester, F., Boumghar, A., Anderson, H. R., Wojtyniak, B., Paldy, A., Braunstein, R., Pekkanen, J., Schindler, C., & Schwartz, J. (2001). Confounding and effect modification in the short-term effects of ambient particles on total mortality: Results from 29 European cities within the APHEA2 project. *Epidemiology*, *12*(5), 521–531. https://doi.org/10.1097/00001648-200109000-00011

Kebe, M., Traore, A., Manousakas, M. I., Vasilatou, V., Ndao, A. S., Wague, A., & Eleftheriadis, K. (2021). *Source Apportionment and Assessment of Air Quality Index of PM 2.5-10 and PM 2.5 in at Two Different Sites in Urban Background Area in Senegal*. https://doi.org/10.3390/atmos12020182

Kerimray, A., Baimatova, N., Ibragimova, O. P., Bukenov, B., Kenessov, B., Plotitsyn, P., & Karaca, F. (2020). Assessing air quality changes in large cities during COVID-19 lockdowns: The impacts of traffic-free urban conditions in Almaty, Kazakhstan. *Science of the Total Environment*, *730*, 139179. https://doi.org/10.1016/j.scitotenv.2020.139179

Kim, E., Hopke, P. K., & Edgerton, E. S. (2012). Source Identification of Atlanta Aerosol by Positive Matrix Factorization. *Http://Dx.Doi.Org/10.1080/10473289.2003.10466209*, *53*(6), 731–739. https://doi.org/10.1080/10473289.2003.10466209

Li, G., Lei, W., Bei, N., & Molina, L. T. (2012). Contribution of garbage burning to chloride and PM 2.5 in Mexico City. *Atmospheric Chemistry and Physics*, *12*(18), 8751–8761. https://doi.org/10.5194/ACP-12-8751-2012

Li, J., Pósfai, M., Hobbs, P. V., & Buseck, P. R. (2003). Individual aerosol particles from biomass burning in southern Africa: 2, Compositions and aging of inorganic particles. *Journal of Geophysical Research: Atmospheres*, *108*(D13), 8484. https://doi.org/10.1029/2002JD002310

Liakakou, E., Kaskaoutis, D. G., Grivas, G., Stavroulas, I., Tsagkaraki, M., Paraskevopoulou, D., Bougiatioti, A., Dumka, U. C., Gerasopoulos, E., & Mihalopoulos, N. (2020). Long-term brown carbon spectral characteristics in a Mediterranean city (Athens). *Science of The Total Environment*, *708*, 135019. https://doi.org/10.1016/J.SCITOTENV.2019.135019

Mangia, C., Cervino, M., & Gianicolo, E. A. L. (2015). Secondary Particulate Matter Originating from an Industrial Source and Its Impact on Population Health. *International Journal of Environmental Research and Public Health 2015, Vol. 12, Pages 7667-7681*, *12*(7), 7667–7681. https://doi.org/10.3390/IJERPH120707667

Manousakas, M., Diapouli, E., Papaefthymiou, H., Kantarelou, V., Zarkadas, C., Kalogridis, A.-C., Karydas, A.-G., & Eleftheriadis, K. (2018). XRF characterization and source apportionment of PM10 samples collected in a coastal city. *X-Ray Spectrometry*, *47*(3), 190–200. https://doi.org/10.1002/xrs.2817

Manousakas, M., Diapouli, E., Papaefthymiou, H., Migliori, A., Karydas, A. G., Padilla-Alvarez, R., Bogovac, M., Kaiser, R. B., Jaksic, M., Bogdanovic-Radovic, I., & Eleftheriadis, K. (2015). Source apportionment by PMF on elemental concentrations obtain3qed by PIXE analysis of PM10 samples collected at the vicinity of lignite power plants and mines in Megalopolis, Greece. *Nuclear Instruments and Methods in Physics Research, Section B: Beam Interactions with Materials and Atoms*, *349*, 114–124. https://doi.org/10.1016/j.nimb.2015.02.037

Manousakas, M., Furger, M., Daellenbach, K. R., Canonaco, F., Chen, G., Tobler, A., Rai, P., Qi, L., Tremper, A. H., Green, D., Hueglin, C., Slowik, J. G., El Haddad, I., & Prevot, A. S. H. (2022). Source identification of the elemental fraction of particulate matter using size segregated, highly time-resolved data and an optimized source apportionment approach. *Atmospheric Environment: X*, *14*, 100165. https://doi.org/10.1016/J.AEAOA.2022.100165

Manousakas, M., Papaefthymiou, H., Diapouli, E., Migliori, A., Karydas, A. G., Bogdanovic-Radovic, I., & Eleftheriadis, K. (2017). Assessment of PM2.5 sources and their corresponding

level of uncertainty in a coastal urban area using EPA PMF 5.0 enhanced diagnostics. *Science of The Total Environment*, *574*, 155–164. https://doi.org/10.1016/j.scitotenv.2016.09.047

Marcazzan, G. M., Ceriani, M., Valli, G., & Vecchi, R. (2003). Source apportionment of PM10 and PM2.5 in Milan (Italy) using receptor modelling. *Science of The Total Environment*, *317*(1–3), 137–147. https://doi.org/10.1016/S0048-9697(03)00368-1

Massimi, L., Simonetti, G., Buiarelli, F., Di Filippo, P., Pomata, D., Riccardi, C., Ristorini, M., Astolfi, M. L., & Canepari, S. (2020). Spatial distribution of levoglucosan and alternative biomass burning tracers in atmospheric aerosols, in an urban and industrial hot-spot of Central Italy. *Atmospheric Research*, *239*. https://doi.org/10.1016/J.ATMOSRES.2020.104904

Materazzi, M., & Lettieri, P. (2017). Fluidized Beds for the Thermochemical Processing of Waste. *Reference Module in Chemistry, Molecular Sciences and Chemical Engineering*. https://doi.org/10.1016/B978-0-12-409547-2.12180-8

Olson, M. R., Garcia, M. V., Robinson, M. A., Van Rooy, P., Dietenberger, M. A., Bergin, M., & Schauer, J. J. (2015). Investigation of black and brown carbon multiple-wavelength-dependent light absorption from biomass and fossil fuel combustion source emissions. *Journal of Geophysical Research: Atmospheres*, *120*(13), 6682–6697. https://doi.org/10.1002/2014JD022970

Paatero, P. (1999). The Multilinear Engine: A Table-Driven, Least Squares Program for Solving Multilinear Problems, including the n-Way Parallel Factor Analysis Model. *Journal of Computational and Graphical Statistics*, *8*(4), 854. https://doi.org/10.2307/1390831

Paatero, P., & Tapper, U. (1994). Positive matrix factorization: A non-negative factor model with optimal utilization of error estimates of data values. *Environmetrics*, *5*(2), 111–126. https://doi.org/10.1002/ENV.3170050203

Pant, P., & Harrison, R. M. (2012). Critical review of receptor modelling for particulate matter: A case study of India. *Atmospheric Environment*, *49*, 1–12. https://doi.org/10.1016/J.ATMOSENV.2011.11.060

Paone, P. (2008). Heavy metals in the cement industry: A look at volatile cycles and simple mitigation techniques. *IEEE Cement Industry Technical Conference (Paper)*, 65–75. https://doi.org/10.1109/CITCON.2008.11

Peng, X., Wang, W., Xia, M., Chen, H., Ravishankara, A. R., Li, Q., Saiz-Lopez, A., Liu, P., Zhang, F., Zhang, C., Xue, L., Wang, X., George, C., Wang, J., Mu, Y., Chen, J., & Wang, T. (2021). An unexpected large continental source of reactive bromine and chlorine with significant impact on wintertime air quality. *National Science Review*, *8*(7). https://doi.org/10.1093/NSR/NWAA304

Pernigotti, D., Belis, C. A., & Spanó, L. (2016). SPECIEUROPE: The European data base for PM source profiles. *Atmospheric Pollution Research*, *7*(2), 307–314. https://doi.org/10.1016/J.APR.2015.10.007

Rai, P., Chakraborty, A., Mandariya, A. K., & Gupta, T. (2016). Composition and source apportionment of PM1 at urban site Kanpur in India using PMF coupled with CBPF. *Atmospheric Research*, *178–179*, 506–520. https://doi.org/10.1016/J.ATMOSRES.2016.04.015

Rai, P., Furger, M., El Haddad, I., Kumar, V., Wang, L., Singh, A., Dixit, K., Bhattu, D., Petit, J. E., Ganguly, D., Rastogi, N., Baltensperger, U., Tripathi, S. N., Slowik, J. G., & Prévôt, A. S. H. (2020). Real-time measurement and source apportionment of elements in Delhi's atmosphere. *Science of The Total Environment*, *742*, 140332. https://doi.org/10.1016/J.SCITOTENV.2020.140332

Reff, A., Eberly, S. I., & Bhave, P. V. (2007). Receptor Modeling of Ambient Particulate Matter Data Using Positive Matrix Factorization: Review of Existing Methods. *Journal of the Air & Waste Management Association*, *57*(2), 146–154. https://doi.org/10.1080/10473289.2007.10465319

Rhodes, E. P., Ren, Z., & Mays, D. C. (2012). Zinc leaching from tire crumb rubber. *Environmental Science and Technology*, *46*(23), 12856–12863. https://doi.org/10.1021/ES3024379/SUPPL_FILE/ES3024379_SI_001.PDF

Salomova, F. I., Ahmadalieva, N. O., Sadullaeva, K. A., & Sherkuzieva, G. F. (2022). DUST STORM AND ATMOSPHERE AIR POLLUTION IN UZBEKISTAN. *Central Asian Journal of Medicine*, *2022*(2). https://repository.tma.uz/jspui/bitstream/1/2140/1/1_Ахмадалиева_H_DUST_STORM_Central_Asian_Journal_2022.pdf

Samara, C., Kouimtzis, T., Tsitouridou, R., Kanias, G., & Simeonov, V. (2003). Chemical mass balance source apportionment of PM10 in an industrialized urban area of Northern Greece. *Atmospheric Environment*, *37*(1), 41–54. https://doi.org/10.1016/S1352-2310(02)00772-0

Samoli, E., Stafoggia, M., Rodopoulou, S., Ostro, B., Declercq, C., Alessandrini, E., Díaz, J., Karanasiou, A., Kelessis, A. G., Tertre, A. Le, Pandolfi, P., Randi, G., Scarinzi, C., Zauli-Sajani, S., Katsouyanni, K., Forastiere, F., Alessandrini, E., Angelini, P., Berti, G., … Pascal, M. (2013). Associations between fine and coarse particles and mortality in Mediterranean cities: Results from the MED-PARTICLES project. *Environmental Health Perspectives*, *121*(8), 932–938. https://doi.org/10.1289/EHP.1206124

Tai, A. P. K., Mickley, L. J., & Jacob, D. J. (2010). Correlations between fine particulate matter (PM2.5) and meteorological variables in the United States: Implications for the sensitivity of PM2.5 to climate change. *Atmospheric Environment*, *44*(32), 3976–3984. https://doi.org/10.1016/J.ATMOSENV.2010.06.060

Thorpe, A., & Harrison, R. M. (2008). Sources and properties of non-exhaust particulate matter from road traffic: A review. *Science of The Total Environment*, *400*(1–3), 270–282. https://doi.org/10.1016/J.SCITOTENV.2008.06.007

Tursumbayeva, M., Muratuly, A., Baimatova, N., Karaca, F., & Kerimray, A. (2023). Cities of Central Asia: New hotspots of air pollution in the world. *Atmospheric Environment*, *309*, 119901. https://doi.org/10.1016/j.atmosenv.2023.119901

Uyar, G., Ören, M., Bülent, Z., Üniversitesi, E., Yildirim, Y., & Ince, M. (2016). *Mosses as indicators of atmospheric heavy metal deposition around a coal-fired power plant in Turkey Samanlı Dağları (Sakarya-Kocaeli-Yalova-Bursa)'nın Briyofit Flora ve Epifitik Vejetasyonu View project MOSSES AS INDICATORS OF ATMOSPHERIC HEAVY METAL DEPOSITION AROUND A COAL-FIRED POWER PLANT IN TURKEY*. https://www.researchgate.net/publication/285982430

Viana, M., Kuhlbusch, T. A. J., Querol, X., Alastuey, A., Harrison, R. M., Hopke, P. K., Winiwarter, W., Vallius, M., Szidat, S., Prévôt, A. S. H., Hueglin, C., Bloemen, H., Wåhlin, P., Vecchi, R., Miranda, A. I., Kasper-Giebl, A., Maenhaut, W., & Hitzenberger, R. (2008). Source apportionment of particulate matter in Europe: A review of methods and results. In *Journal of Aerosol Science* (Vol. 39, Issue 10, pp. 827–849). Elsevier Ltd. https://doi.org/10.1016/j.jaerosci.2008.05.007

Vardar, N., & Yumurtaci, Z. (2010). Emissions estimation for lignite-fired power plants in Turkey. *Energy Policy*, *38*(1), 243–252. https://doi.org/10.1016/J.ENPOL.2009.09.011

Vassilev, S. V., Eskenazy, G. M., & Vassileva, C. G. (2000). Contents, modes of occurrence and behaviour of chlorine and bromine in combustion wastes from coal-fired power stations. *Fuel*, *79*(8), 923–938. https://doi.org/10.1016/S0016-2361(99)00231-8

Wedepohl, K. H. (1995). The composition of the continental crust*. *Geochimica et Cosmochimica Acta*, *59*(7), 1217–1232.

Yang, D., Zhang, H., Wang, Z., Zhao, S., & Li, J. (2022). Changes in anthropogenic particulate matters and resulting global climate effects since the Industrial Revolution. *International Journal of Climatology*, *42*(1), 315–330. https://doi.org/10.1002/JOC.7245

Yatkin, S., & Bayram, A. (2008). Source apportionment of PM10 and PM2.5 using positive matrix factorization and chemical mass balance in Izmir, Turkey. *Science of The Total Environment*, *390*(1), 109–123. https://doi.org/10.1016/J.SCITOTENV.2007.08.059

Zhang, G., Peng, L., Lian, X., Lin, Q., Bi, X., Chen, D., Li, M., Li, L., Wang, X., & Sheng, G. (2019). An Improved Absorption Ångström Exponent (AAE)-Based Method for Evaluating the Contribution of Light Absorption from Brown Carbon with a High-Time Resolution. *Aerosol and Air Quality Research*, *19*(1), 15–24. https://doi.org/10.4209/AAQR.2017.12.0566

Zong, Z., Wang, X., Tian, C., Chen, Y., Qu, L., Ji, L., Zhi, G., Li, J., & Zhang, G. (2016). Source apportionment of PM 2.5 at a regional background site in North China using PMF linked with radiocarbon analysis: insight into the contribution of biomass burning. *Atmos. Chem. Phys*, *16*, 11249–11265. https://doi.org/10.5194/acp-16-11249-2016

19. Chemical Speciation and Source Apportionment of $PM_{2.5}$ in Greek Urban and Suburban Areas: Insights from the PANACEA Initiative

19.1 Abstract

The PANhellenic infrastructure for Atmospheric Composition and climatE chAnge (PANACEA) is a significant environmental initiative in Greece, focusing on atmospheric composition and climate change. This study, conducted under PANACEA, examines chemical speciation and source apportionment of PM2.5 at three urban background sites (Athens - "Demokritos", Athens - "Thissio", Ioannina) two urban sites (Patra and Volos) and one rural site (Xanthi). Sampling was carried out from June to August 2019 and December 2019 to February 2020, with an additional campaign at the Athens - "Thissio" site from December 2018 to March 2019 and July to August 2019, resulting in over 551 24-hour $PM_{2.5}$ samples. These samples were analyzed for major and trace elements, ions, organic carbon (OC), and elemental carbon (EC). Positive Matrix Factorization (PMF) was used for source apportionment, identifying seven major sources: biomass burning (27.5–50.9%), heavy oil combustion (2.5–15.1%), industrial emissions (3.3–14.4%), mineral dust (4.8–16.4%), sea salt (1.6–11.7%), secondary sulfates and organics (7.1–33.0%), and vehicular traffic (9.7–27.6%). The variation in source contributions underscores the influence of local geography, industry, and transportation infrastructure on air quality in each city.

19.2 Introduction

Particulate matter (PM) is a well-recognized and highly concerning atmospheric pollutant, with a multitude of studies highlighting its detrimental impacts on human health (Ostro et al., 2015; Samoli et al., 2013), the environment, and climate change (Chen et al., 2021). Fine particulate matter ($PM_{2.5}$), consisting of particles with aerodynamic diameters less than 2.5 μm, is of particular concern due to its ability to deeply penetrate the lungs, leading to severe respiratory system damage (Xing et al., 2016), autoimmune conditions (Zhao et al., 2019), and even lung cancer (Nakharutai et al., 2022).

Depending on the source, many natural and anthropogenic pollutants may contribute to PM concentration levels. These types of pollution sources might include biomass burning, traffic, industry, sea salt, mineral dust, and secondary aerosol formation (Viana et al., 2008). Therefore, identification and allocation of pollutants to their sources is an important key aspect in order to moderate and manage air quality, as it can be used as a guidance for developing air pollution mitigation strategies. Positive matrix factorization (PMF) stands as one of the most useful receptor model source apportionment analyses (SA) tools (Paatero and Tapper, 1994). PMF's goal is to quantify the contribution of the major aerosol sources to the PM concentration levels recorded at a receptor site, based on the PM chemical composition and its temporal variability.

Greece, located in southeastern Europe, is a region of great significance due to its unique geographical position, diverse atmospheric conditions, and frequent dust transport

events from Africa (Vasilatou et al., 2017 a). However, there remains a notable research gap concerning the comprehensive characterization of fine PM pollution in this region. To effectively characterize source profiles in a given region, there is a pressing need for harmonized source SA from multi-city investigations. Such studies (Amato et al., 2016; Saraga et al., 2021) are crucial for accurately identifying pollution sources, understanding regional pollution patterns, and formulating effective environmental policies.

Existing studies have primarily focused on the major cities (Athens, Thessaloniki and Patras) (Diapouli, et al., 2017; Manousakas et al., 2018; Theodosi et al., 2018) highlighting the need to investigate air quality across a broader range of urban centers. This work aims to fill this research gap by conducting the first comprehensive SA analysis across three urban background locations (Athens - "Demokritos", Athens – "Thissio" and Ioannina, two urban (Patra and Volos) and 1 rural (Xanthi) for $PM_{2.5}$.

For this purpose, two measurement campaigns were carried out during the summer (June-August) and winter (December-February) seasons of 2019-2020. Additionally, a supplementary campaign was conducted at the Athens – "Thissio" station, covering the periods from December 2018 to March 2019 and from July 2019 to August 2019. By characterizing $PM_{2.5}$ concentration levels and major chemical components at urban and suburban sites, this work aims to provide a comprehensive understanding of the sources of fine PM pollution in Greece.

19.3 Methods

19.3.1 PM Sampling

- **Athens Demokritos station (ATH.DEM-UB)**: The measurements in Athens, Agia Paraskevi took place at the N.C.S.R. "Demokritos" urban background station in campus (37.99° N, 23.80° E, 270 meters above sea level (m.a.s.l.)), approximately 7 km northeast of the metropolitan center of the city and covers an area of 600 acres in a forest of pine trees, at the foot of Mount Hymettus. The station is a member of the ACTRIS European infrastructure and the PANACEA National Infrastructure in Greece. The site is not directly impacted by fresh urban PM emissions and is thus considered representative of the urban background air quality in Athens (Eleftheriadis et al., 2014; Triantafyllou et al., 2016). 24h sampling periods were performed during 06/2019 – 08/2019 and 12/2019 and 02/2020 and in total, 124 $PM_{2.5}$ samples were collected on Teflon filters, by low volume samplers at an operational flow rate of 2.3 m^3h^{-1} (**Figure 101**).
- A**thens Thissio station (ATH.THIS-UB)**: Aerosol sampling was conducted at the Thissio urban background supersite of the National Observatory of Athens (NOA) (37.97◦ N, 23.72◦ E, 105m amsl), situated on the Nymphs Hill in the historic center of

Athens, Greece. The monitoring site, surrounded by a pedestrian zone and a moderate populated residential area, is in distance from main roads, thus is not directly affected from any major anthropogenic emissions and has been previously proven suitable for capturing a variety of urban background, regional and long range transport influences (Paraskevopoulou et al., 2015; Athanasopoulou et al., 2017; Grivas et al., 2019; Dimitriou et al., 2021). 108 PM2.5 aerosol samples were collected on quartz filters (Flex Tissuquartz, 2500QAT-UP 47 mm, Pall) during 12/2018 – 03/2019 (winter period) and 07/2019 and 08/2020 (summer period) at a 24hour basis starting from 18:00 LT using low volume samplers (Dichotomous Partisol – Plus, Model 2025 Sequential Air Sampler, Rupprecht & Patashnick). The filters were pre and post equilibrated for 48 hours under controlled conditions (RH 40±5 %, T 20±3 °C) prior weighing by means of a Mettler Toledo MX5 microbalance (1 μg sensitivity) to obtain the mass concentration (Paraskevopoulou et al., 2014; Theodosi et al., 2018) (**Figure 101**).

- **Ioannina station (IOA-UB)**: The Ioannina station was located in an urban background location (39.65 N, 20.85 E, 518 m asl), at the Kiafa region. The sampling period was performed during 07/2019 – 08/2019 and 12/2019 and 02/2020 and in total, 101 $PM_{2.5}$ samples were collected onto quartz fiber filters with a high-volume Digitel DH77 sampler (**Figure 101**).
- **Xanthi station (XAN-RUR)**: The Xanthi station was located in a suburban background location (41.15° N, 24.92° E.), at the site of atmospheric electricity measurements of Demokritus University of Thrace. The sampling period was performed during 07/2019 – 08/2019 and 12/2019 and 02/2020 and in total. 101 $PM_{2.5}$ samples were collected onto quartz fiber filters a high-volume Digitel DH77 sampler (**Figure 101**).
- **Volos station (VOL-URB)**: The Volos Station was located near a busy street which is close to the harbor (39.36° N, 22.93° E) and it is representative of the atmospheric urban region. The sampling period was performed during 06/2019 – 08/2019 and 01/2020 and in total. 44 $PM_{2.5}$ samples were collected onto quartz fiber filters by a Leckel low volume sampler (2.3 m^3/h) (**Figure 101**).
- **Patra stations (PAT-URB)**: The Patra station during the warm period (07/2019 – 08/2019) was located at Institute of Chemical Engineering Sciences, ICE- HT (38.29° N, 21.80° E), which is 8 km (northeast) away from the city center and 1km (south) from the Patras – Athen's highway. During the cold period (01/2020 – 02/2020) the sampler was housed inside the campus of the Technological Educational Institute (TEI) of Patras (38◦13' N, 21◦45' E). The TEI is in the southwest of the city, surrounded by moderate-traffic streets and houses, and is considered an urban site. Both sampling sites used a low volume sampler (6.7 l/min) and 73 samples were collected in total (**Figure 101**).

Figure 101. *The six sampling locations of the PANACEA campaign.*

19.3.2 Sample treatment and chemical analysis

19.3.2.1 Elemental Analysis

Benchtop ED-XRF spectrometer with secondary targets

$PM_{2.5}$ samples underwent analysis for both major and trace elements using the Epsilon 5 (PANanalytical) high-resolution energy dispersive X-Ray fluorescence 3-D optics spectrometer. This spectrometer is comprised of a side-window X-ray tube with a W/Sc anode. The characteristic X-ray emissions from the sample were detected by a Germanium (Ge) detector, achieving a measured energy resolution of approximately 150 eV FWHM at Mn-Kα (5.89keV). The spectrometer offers a choice of 9 secondary targets (Al, CaF_2, Fe, Ge, Zr, Mo, KBr, Al_2O_3, LaB_6) capable of polarizing the X-ray beam. Consequently, 9 distinct measuring conditions were employed to optimize the analysis of the aerosol samples. All measurements were carried out on both PTFE and Quartz fiber filters, conducted under vacuum conditions, with each sample requiring an approximate total analysis time of 90 minutes. The detailed methodology employed for elemental characterization is thoroughly described in the work of Manousakas et., 2018. In total, 23 elements were identified using the benchtop ED-XRF spectrometer, including Na, Mg, Al, Si, S, Cl, K, Ca, Ti, V, Cr, Mn, Fe, Co, Ni, Cu, Zn, Br, Rb,

Sr, Cs, Ba, and Pb. The detection limits (LOD) (ng m^{-3}) for Quartz and Teflon filters are given in **Table 31**.

Table 31. *LOD in ng m^{-3} for each analyzed element with ED-XRF for Quartz and Teflon Filters.*

Element	LOD (ng m^{-3}) Quartz	LOD (ng m^{-3}) Teflon	Element	LOD (ng m^{-3}) Quartz	LOD (ng m^{-3}) Teflon
Na	12.6	9.5	**Fe**	0.9	0.7
Mg	15.0	4.3	**Co**	0.8	0.7
Al	43.2	5.6	**Ni**	0.7	0.5
Si	120.0	5.8	**Cu**	0.8	0.6
S	1.9	1.5	**Zn**	0.9	0.7
Cl	0.7	0.7	**Br**	1.5	1.2
K	0.4	0.5	**Rb**	1.6	1.0
Ca	1.6	1.1	**Sr**	1.4	1.0
Ti	1.1	0.9	**Cs**	15.6	12.3
V	0.6	0.5	**Ba**	18.2	14.4
Cr	0.6	0.4	**Pb**	2.8	2.1
Mn	1.3	1.0			

Near real time XRF spectrometer

During the summer period for the ATH.THIS-UB station (07/2019 and 08/2020), the fine aerosol elemental composition was determined using a Horiba Inc. PX-375 online ED-XRF spectrometer (Creamean et al., 2016; Grivas et al., 2020). The instrument sampled through a PM_{10} inlet followed by a very sharp-cut cyclone (VSCC) for $PM_{2.5}$ separation. Particles were drawn at a flow rate of 16.7 l min^{-1} and collected on a PTFE filter tape. Concentrations for an array of elements, including Al, Ti, V, Mn, Fe, Ni, Cu, Zn, and Pb, were determined at 3-hour intervals and then averaged over the 24-hour intervals of concurrently collected filter samples. The detection limits (LOD) for the Horiba Inc. PX-375 online ED-XRF spectrometer are given in **Table 32**in ng m^{-3}.

Table 32. LOD in ng m^{-3} for each analyzed element with Near Real Time XRF spectrometer (PX-375).

Element	LOD (ng m^{-3})
Al	3.18
Si	0.50
S	0.18
K	0.27
Ca	0.04
Ti	0.14
Mn	0.06
Fe	0.39
Ni	0.05
Cu	0.23
Zn	0.16
Pb	0.06

Inductively Coupled Plasma Mass Spectrometry (ICP-MS)

Trace elements during the winter period for the ATH.THIS-UB station (Al, Ca, Mn, Fe, V, Cr, Ni, Cu, Zn, and Pb) were determined by Inductively Coupled Plasma Mass Spectrometry (ICP-MS, Perkin Elmer, NexION 300X) after an acid microwave digestion procedure following the procedure described in Theodosi et al. (2018). Yttrium (Y) and Indium (In) were added as internal standards, and all reported concentrations were corrected for blanks. Limits of detection for ICP-MS are provided in Table S3 in ng m^{-3}.

Table 33. LOD in ng m^{-3} for each analyzed element for ICP-MS.

Element	LOD (ng m^{-3})
Al	3.4
Ca	5.0
Ti	0.2
V	0.1
Cr	0.4
Mn	0.5
Fe	1.4
Co	0.0
Ni	0.7
Cu	1.7
Zn	5.5
Pb	0.2

19.3.3 Organic and Elemental Carbon – OC & EC

For the ATH.DEM-UB database, Elemental carbon (EC) and organic carbon (OC) concentrations in $PM_{2.5}$ were measured in near-real time at three-hour intervals. This was done using the thermo-optical transmittance (TOT) technique with a semi-continuous OC-EC field analyzer (Model-4, Sunset Laboratory, Inc., Tigard, OR, U.S.A.) fitted with an in-line parallel carbon denuder to eliminate organic gases. The analysis followed the EUSAAR-2 protocol. For the rest of the database the OC and EC levels were determined using a Sunset Laboratory OC/EC Analyzer, via the Thermal-Optical Transmission (TOT) technique and following the EUSAAR-2 protocol (Cavalli et al., 2010; Paraskevopoulou et al., 2014). The detection limits for OC and EC were estimated at 0.26 and 0.05 μg m^{-3}, respectively, with uncertainties less than 10% (5% for OC and 8% for EC). All reported concentrations were blank corrected.

19.3.4 Ionic species

Ion chromatography was used to determine the levels of the inorganic species. Prior to the analysis, the filters were extracted in ultrapure water (18.2 MΩ cm at 25 °C) under sonication for 30 min. Depending on the sampling site, 9.6 mL up to 15 mL of water was used per filter sample for the extraction. The extract was filtered through a syringe filter (Labfil, PVDF, 0.45um, 25mm). The IC system used was a Shimatzu (LC-20ADsp). For the Cations, the following conditions/chemicals were used: column, Metrosep C4- 150/4.0, injection volume 120 μL, mobile phase: 1.7 mmol/L nitric acid, 0.7 mmol/L dipicolinic acid, flow: 0.9 ml min^{-1}. For the anions the respected conditions/chemicals were: column Metrosep A Supp5- 150/4.0, suppressor: SeQuant SAMS, mobile phase: 3.2 mmol L^{-1} Na_2CO_3 and 1.0 mmol L^{-1} $NaHCO_3$, flow: 0.7 ml min^{-1}, injector volume120 μL. Three replicate injections were done per sample and the average value was reported. Depending on the measurement site the limit of detection varied. Overall, the following detection limit ranges were estimated in μg m^{-3}: Na^+: 0.07-1.17, NH_4^+: 0.01-0.03, K^+: 0.03-0.06, Ca^{2+}: 0.07-0.17, Mg^{+2}: 0.07-0.17, Cl^-: 0.03-0.08, NO_3^-: 0.02-0.05, SO_4^{2-}: 0.02-0.05. The expanded uncertainties for each ion were calculated based on the three replicate injections performed per sample. For the Ath.THIS-UB database, The major aerosol cations (Ca^{2+}, Mg^{2+}, Na^+, K^+, NH_4^+) and anions (SO_4^{2-}, NO_3^-, Cl^-) were analyzed by Ion Chromatography (IC; Dionex-500; Thermo Fischer Scientific) following the methodology described in Paraskevopoulou et al. (2015). All analytical results were blank-corrected.

19.3.3 Source apportionment

Positive matrix factorization (PMF) serves as a receptor model designed to access primary sources of particulate matter (PM) based on their distinct chemical profiles and to

quantify their respective impacts on observed PM concentration levels (Paatero and Tapper, 1994). The fundamental mass balance equation utilized by PMF can be represented as follows:

$$X_{mn}=G_{mp}F_{pn}+E \tag{58}$$

Here, X denotes the concentrations of individual species (n) measured across different samples (m), g represents the contribution of each source (p) to each sample (m) as determined by the model, f denotes the contribution of each species (n) to the chemical profile of each source (p), also determined by the model, and e signifies the residual for species (n) in sample (m).The objective of PMF is to solve equation (1) by minimizing the sum of squared residuals (E) between measured and predicted concentrations until a stable solution (Q) is achieved (Paatero, 1999):

$$Q=\sum_{m=1}^{\nu}\sum_{n=1}^{\mu}\frac{{e_{mn}}^2}{{s_{mn}}^2} \tag{59}$$

where s_{mn} is the uncertainty of each species (n) in each sample (m).

19.4 Results and discussion

19.4.1 $PM_{2.5}$ levels

The observed average concentrations for $PM_{2.5}$ and all analyzed species are presented in **Table 34**. Only two sites exceeded the EU legal limit for the annual $PM_{2.5}$ concentration (25 μg m-3), while the other stations were within the permissible range. The IOA-UB station exhibited the highest average $PM_{2.5}$ concentrations (39.9 ± 35.8 μg m^{-3}) followed by the VOL-URB (29.8 ± 15.4 μg m^{-3}), ATH.THIS-UB (20.7 ± 15.3), PAT-URB (18.7 ± 9.5 μg m^{-3}), XAN-RUR (12.9 ± 5.3 μg m^{-3}) and finally ATH.DEM-UB (11.0 ± 4.1 μg m^{-3}).

Large seasonal variability in $PM_{2.5}$ concentrations was observed at nearly all monitoring stations, with notable differences between winter and summer sampling periods. The IOA-UB station recorded the most substantial change: average concentrations were at 8.0 μg m^{-3} from July to August 2019, while they rose sharply to 57.4 μg m^{-3} between December 2019 and February 2020, representing a 630% increase. At the VOL-URB station, the average concentration increased from 25.5 μg m^{-3} during the June to August 2019 period to 42.8 μg m^{-3} in January 2020. The XAN-RUR station saw minimal change, with concentrations of 13.2 μg m^{-3} in July to August 2019 and 12.8 μg m^{-3} between December 2019 and February 2020. The PAT-URB station experienced a notable increase in average $PM_{2.5}$ concentrations, rising from 14.9 μg m^{-3} in July to August 2019 to 23.7 μg m^{-3} in January to February 2020. At the ATH.THIS-UB station, concentrations nearly doubled, from 14.5 μg m^{-3} in July to August 2020 to 27.5 μg

m^{-3} during December 2018 to March 2019. Conversely, the ATH.DEM-UB station reported a decrease in $PM_{2.5}$ levels, with average concentrations falling from 12.4 μg m^{-3} between June and August 2019 to 9.0 μg m^{-3} from December 2019 to February 2020.

Table 34. *Average PM2.5 and component concentrations levels in ng m^{-3} for the six stations. NA: Not Available*

	Average concentration (ng m^{-3})					
Species	**ATH.DEM-UB**	**ATH.THIS-UB**	**IOA-UB**	**VOL-URB**	**XAN-RUR**	**PAT-URB**
$PM_{2.5}$	11032	20694	39858	29792	12940	18682
OC	2792	6465	16510	5941	3341	6101
EC	383	1344	1715	1200	300	787
Na^+	156	263	128	514	162	254
NH_4^+	629	1144	996	1386	865	878
K^+	136	245	853	366	203	389
Mg^{2+}	20	78	34	548	31	31
$Ca^{2+,}$	137	521	714	84	137	272
Cl^-	72	406	378	285	243	138
NO_3^-	181	787	1996	1674	424	763
SO_4^{2-}	2452	3445	2964	6220	1879	3049
Na	106	NA	NA	NA	NA	NA
Mg	30	NA	NA	NA	NA	NA
Al	88	129	NA	NA	NA	NA
Si	172	501	NA	NA	NA	NA
S	784	NA	529	669	372	384
Cl	18	NA	56	26	2	33
K	150	NA	486	176	105	309
Ca	120	NA	528	624	80	92
Ti	6	4.2	6.3	10	4.8	7.7
V	1	3	0.3	1.2	NA	NA
Cr	1	NA	0.4	1.9	0.6	2.8
Mn	2	7.3	2.8	22	1.1	6.5
Fe	110	181	119	416	59	54
Co	NA	NA	0.5	0.8	NA	NA
Ni	2	2	2	2	2	2
Cu	6	5	3	14	0.8	22
Zn	13	23	13	188	13	11
Br	2	NA	3	3.3	2.4	NA
Rb	NA	NA	1.5	NA	NA	NA
Sr	NA	NA	1.3	1.2	NA	NA
Cs	NA	NA	8	NA	10	NA
Ba	10	NA	NA	NA	12	NA
Pb	4	4	4	16	NA	23

Regarding carbonaceous aerosols, the average concentrations of OC and EC varied notably across different stations. At IOA-UB, the average OC concentration was at 16.5 ± 17.7 μg m^{-3}, with EC at 1.7 ± 1.7 μg m^{-3} .OC levels increased significantly from 2.6 μg m^{-3} in summer to 26.4 μg m^{-3} in winter, while EC concentrations rose from 0.4 μg m^{-3} to 2.6 μg m^{-3}. At VOL-URB, the average concentrations were 5.9 ± 4.6 μg m^{-3} for OC and 1.2 ± 0.6 μg m^{-3} for EC. Seasonal variations showed OC rising from 3.9 μg m^{-3} in summer to 12.2 μg m^{-3} in winter, and EC from 1.1 to 1.4 μg m^{-3}. XAN-RUR recorded 3.3 ± 1.6 μg m^{-3} for OC and 0.3 ± 0.2 μg m^{-3} for EC, with OC levels increasing from 2.8 to 3.8 μg m^{-3} and EC doubling from 0.2 to 0.4 μg m^{-3}. At PAT-URB, OC averaged 6.1 ± 4.7 μg m^{-3} and EC 0.8 ± 0.8 μg m^{-3}, with OC rising from 4.1 to 8.8 μg m^{-3} and EC increasing from 0.4 to 1.3 μg m^{-3}. ATH.THIS-UB had average concentrations of 6.5 ± 5.2 μg m^{-3} for OC and 1.3 ± 1.8 μg m^{-3} for EC, with seasonal changes showing OC growing from 4.2 μg m^{-3} in summer to 8.7 μg m^{-3} in winter, and EC from 0.5 to 2.1 μg m^{-3}. Lastly, at ATH.DEM-UB, OC was recorded at 2.8 ± 1.1 μg m^{-3} and EC at 0.4 ± 0.2 μg m^{-3}. OC showed a slight decrease from 2.9 μg m^{-3} in summer to 2.7 μg m^{-3} in winter, while EC increased from 0.3 to 0.5 μg m^{-3}. The observed increases in OC and EC concentrations during the winter months can likely be attributed to enhanced residential heating activities, contributing to elevated levels of PM.

The concentrations of major inorganic ions, particularly NH_4^+, NO_3^- and SO_4^{-2}, showed distinct seasonal patterns across the studied locations. At IOA-UB, the average NH_4^+ concentration was 1.0 ± 0.6 μg m^{-3}, with a slight increase from 0.94 μg m^{-3} in summer to 1.04 μg m^{-3} in winter. NO_3^- showed a significant seasonal variation, rising from 0.11 μg m^{-3} in summer to 3.34 μg m^{-3} in winter. SO_4^{-2}, however, exhibited a decrease from 3.52 μg m^{-3} in summer to 2.57 μg m^{-3} in winter. In VOL-URB, NH_4^+ concentrations averaged 1.4 ± 0.9 μg m^{-3}, increasing from 0.97 μg m^{-3} in summer to 2.63 μg m^{-3} in winter. NO_3^- also showed a marked increase, from 0.64 μg m^{-3} in summer to 4.77 μg m^{-3} in winter, indicating significant seasonal variability. SO_4^{-2} concentrations were relatively stable, with a slight decrease from 6.38 μg m^{-3} in summer to 5.72 μg m^{-3} in winter. XAN-RUR exhibited NH_4^+ levels averaging 0.9 ± 0.5 μg m^{-3}, with concentrations slightly decreasing from 1.00 μg m^{-3} in summer to 0.75 μg m^{-3} in winter. NO_3^- increased notably from 0.08 μg m^{-3} in summer to 0.69 μg m^{-3} in winter, while SO_4^{-2} remained relatively constant, averaging around 1.9 μg m^{-3} across seasons. At PAT-URB, NH_4^+ concentrations were 0.9 ± 0.4 μg m^{-3} on average, decreasing from 1.06 μg m^{-3} in summer to 0.59 μg m^{-3} in winter. NO_3^- increased from 0.45 μg m^{-3} in summer to 1.11 μg m^{-3} in winter, whereas SO_4^{-2} showed a decrease from 4.04 μg m^{-3} in summer to 1.61 μg m^{-3} in winter. In ATH.THIS-UB, NH_4^+ concentrations averaged 1.14 ± 0.57 μg m^{-3}, decreasing from 1.46 μg m^{-3} in summer to 0.83 μg m^{-3} in winter. NO_3^- levels rose from 0.16 μg m^{-3} in summer to 1.38 μg m^{-3} in winter. SO_4^{-2} concentrations decreased from 4.42 μg m^{-3} in summer to 2.50 μg m^{-3} in winter. Finally, at ATH.DEM-UB, NH_4^+ showed an average concentration of 0.63 ± 0.44 μg m^{-3}, decreasing from 0.88 μg m^{-3} in summer to 0.38 μg m^{-3} in winter. NO_3^- concentrations rose from 0.10 μg m^{-3} in summer to 0.25 μg m^{-3} in winter. SO_4^{-2} decreased from 3.22 μg m^{-3} in summer to 1.71 μg m^{-3} in winter. Overall, the data reveal significant seasonal variations, with NO_3^- concentrations rising in winter at most sites, likely due to increased emissions from residential

heating, while SO_4^{2-} levels surge in summer, driven by enhanced photochemical activity. **Figure 102** presents the seasonal and average concentrations of $PM_{2.5}$ for the six stations.

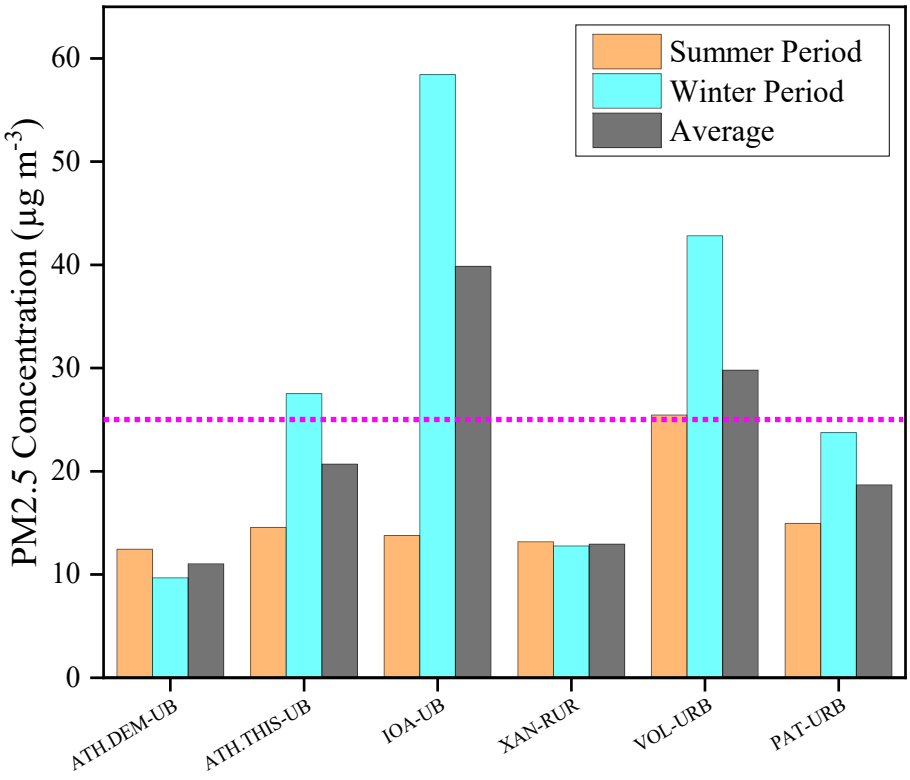

Figure 102. *Seasonal and average concentrations of PM2.5 for the six stations. The purple dotted line represents the EU annual limit value (25 µg m⁻³).*

19.4.2 Mass closure of $PM_{2.5}$ components

"Chemical mass closure" is the process of reconstructing the measured weighed mass solely based on chemical composition. This involves comparing the combined masses of various chemical species to the gravimetric PM mass. In this process, the reconstructed $PM_{2.5}$ mass comprises organic matter (OM), elemental carbon (EC), mineral dust (Min. Dust), sea salt (SS), secondary inorganic aerosol (SIA), and other trace elements excluding minerals (Chow et. al., 2015). Crustal ratios from Mason, 1966 were employed in order to assess the mineral dust component. Specifically, the crustal ratios of Na, Al and Si were used with respect to Ti.

For the calculation of the sea salt component, the main composition of sea spray (ss) was taken into account (Diapouli et al., 2017) as:

$$\text{Sea Salt (SS)} = {}_{ss}[Na] + [Cl] + {}_{ss}[Mg] + {}_{ss}[K] + {}_{ss}[Ca] + {}_{ss}[SO_4^{2-}] \quad (60)$$

, where ${}_{ss}[Na] = [Na^+]_{tot} - {}_{nss}[Na]$, ${}_{nss}[Na] = 6.4\,[Ti]$, ${}_{ss}[Mg] = 0.119\,{}_{ss}[Na]$, ${}_{ss}[K] = 0.037\,{}_{ss}[Na]$, ${}_{ss}[Ca] = 0.038\,{}_{ss}[Na]$ and ${}_{ss}[SO_4^{2-}] = 0.253\,{}_{ss}[Na]$. The highest average sea salt concentrations were

observed at the ATH.THIS-UB station (0.7 μg m^{-3}). The remaining stations had average concentration levels between 0.11 and 0.54 μg m^{-3}. On average, sea salt levels accounted for 0.5% to 3.5% of $PM_{2.5}$ contributions.

Secondary inorganic aerosol (SIA) was calculated based on Seinfeld and Pandis, 1998 as:

$$SIA = {}_{nss}[SO_4^{2-}] + [NO_3^-] + [NH_4^+] \quad (61)$$

Here, ${}_{nss}[SO_4^{2-}]$ is the non-sea-salt $[SO_4^{2-}]$ concentration where ${}_{nss}[SO_4^{2-}] = [SO_4^{2-}]_{total} - {}_{ss}[SO_4^{2}]$. The SIA concentrations varied geographically, with the highest levels observed at the VOL-URB station (9.9 μg m^{-3}), followed by the IOA-UB (5.7 μg m^{-3}), ATH.THIS-UB (5.3 μg m^{-3}), PAT-URB (4.4 μg m^{-3}), XAN-RUR (3.1 μg m^{-3}), and ATH.DEM-UB (2.3 μg m^{-3}). The high average concentration of SIA at the VOL-URB could be attributed to cement industry activity, which utilizes high-sulfur limestone resulting in increased SO_2 emissions (Zhang et al., 2019). On average, SIA levels accounted for 15.9% to 30.1% of $PM_{2.5}$ contributions. Additionally, shipping emissions in the harbor may also contribute to the observed SIA levels. SIA levels accounted on average between 15.9% and 30.1% of the $PM_{2.5}$ contributions.

Mineral dust was calculated based on Nava et al., 2012 from the contributions of crustal, non-sea salt (nss) components as:

$$\text{Min. Dust} = 1.35\ {}_{nss}[Na] + 1.66\ {}_{nss}[Mg] + 1.89\ [Al] + 2.14\ [Si] + 1.21\ {}_{nss}[K] + 1.95\ {}_{nss}[Ca] + 1.67\ [Ti] + 1.43\ [Fe] \quad (62)$$

, where ${}_{nss}[Mg] = [Mg^{2+}]_{tot} - {}_{ss}[Mg]$, $[Al] = 18.5\ [Ti]$, $[Si] = 63.0\ [Ti]$, ${}_{nss}[K] = [K]_{tot} - {}_{ss}[K]$ and ${}_{nss}[Ca] = [Ca]_{tot} - {}_{ss}[Ca]$. The average concentrations of mineral dust ranged from 1.1 μg m^{-3} at XAN-RUR station to 3.3 μg m^{-3} (VOL-URB). These levels account on average between 7.5 and 10.9 % of the $PM_{2.5}$ contributions.

As for organic matter (OM), it was calculated by multiplying OC by a factor (or multiplier) that transforms OC into OM (Chow et al., 2015):

$$OM = f \times OC \quad (63)$$

The magnitude of the factor multiplier ranged from 1.5 to 2 (Chow et al., 2015). The concentration level of organic matter varied among the studied cities, with the highest average concentration level observed at the IOA-UB station (23.2 μg m^{-3}), reaching up to 42.2 μg m^{-3} during the winter period. This may be attributed to biomass burning activities associated with household heating, as reported by Papanikolaou et al., 2022. The same situation seems to prevail at the VOL-URB, PAT-URB and ATH.THIS-UB stations as well. Average concentration of OM reaches 12.7 μg m^{-3} (VOL-URB), 6.6 μg m^{-3} (PAT-URB) and 8.6 μg m^{-3} (ATH.THIS-UB), but during the winter period of the study it rises to 19.1 μg m^{-3}, 14.1 μg m^{-3} and 13.9 μg m^{-3} respectively. On the other hand, the ATH.DEM-UB and XAN-RUR station showed lower

concentrations of OM, with an average of 4.5 and 5.8 μg m^{-3} respectively, which did not exceed 6.4 μg m^{-3} during the winter period. Overall, OM accounted for 38.5% to 64.3% of the $PM_{2.5}$ contributions.

Regarding EC and trace elements, no factor multiplier is necessary, and their average values are directly added to the $PM_{2.5}$ mass. EC levels range from 0.3 to 1.5 μg m^{-3} across all sites, while elemental tracers have even lower contributions, ranging between 0.04 and 0.22 μg m^{-3}. The unaccounted mass can be attributed to various factors, including unmeasured moisture, and possible measurement errors. In this study, the XAN-RUR and ATH.DEM-UB sites had higher unaccounted mass values, at 20.6% and 13.4% respectively, while the other sites had values below 10.5%.

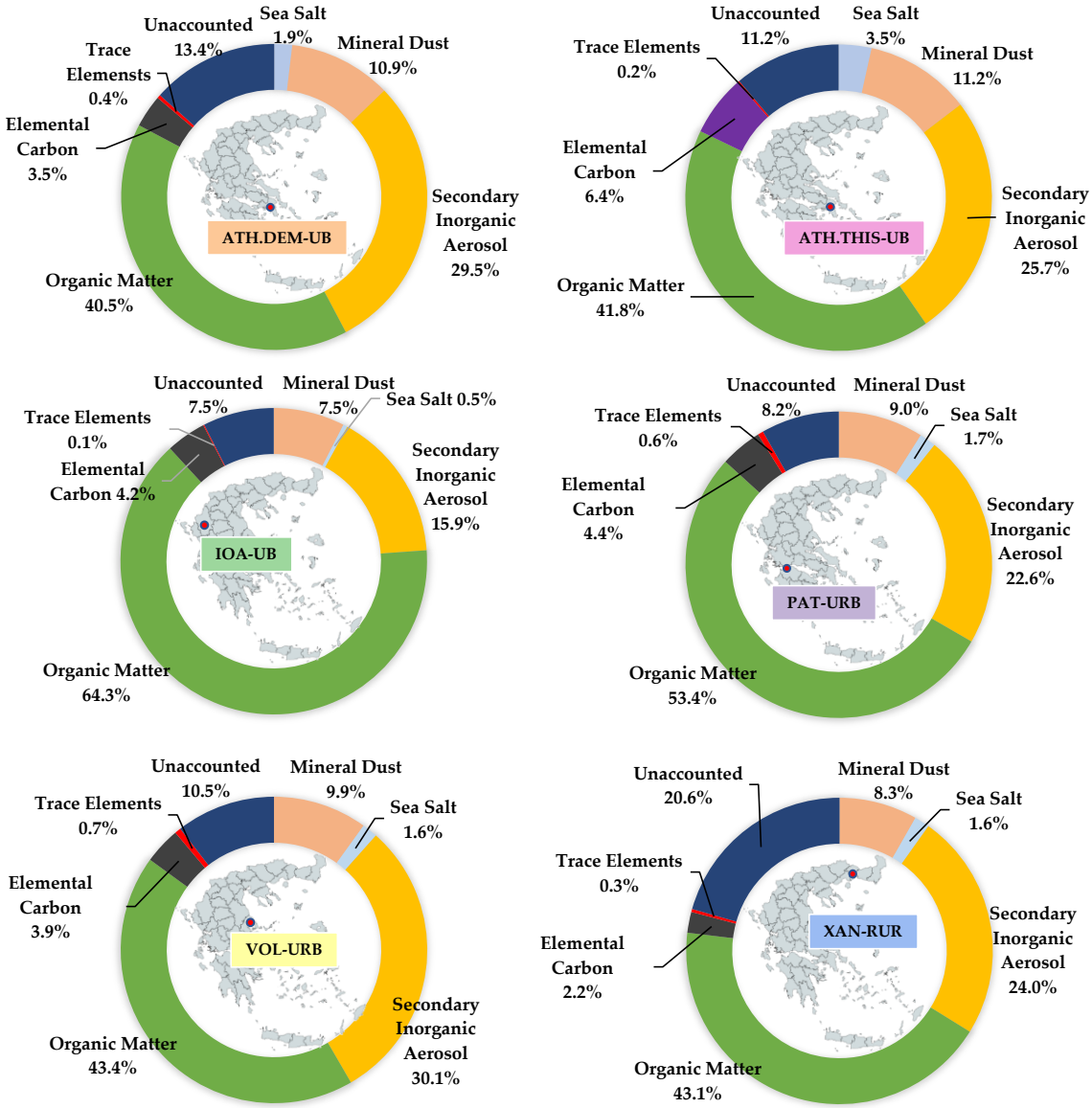

Figure 103. *Mass closure contributions for the six stations.*

19.4.3 Source apportionment results

Source apportionment was performed by the use of the EPA PMF 5.0 software. In order to address rotational ambiguity and achieve more realistic solutions, a combination of different species and model constraints were implemented depending on the specific site (Paatero and Hopke, 2008). The data below limit of detection (LOD) were replaced with ½ of the LOD and their corresponding uncertainty values with 5/6 of the LOD. The calculated expanded uncertainties for all concentration measurements, incorporating both sampling and analytical uncertainties, were included in the input database. The uncertainty estimates were based on the approaches by Manousakas et al., 2018, Paraskevopoulou et al., 2015 and Theodosi et al., 2018. Furthermore, an additional 5 to 7% uncertainty was introduced into the model to account for potential errors in the modeling process. Various variables also were identified as "weak" and were determined by applying the signal-to-noise ratio (S/N) methodology explained by Paatero and Hopke, 2003, while PM was included as the total vaiable.

Each dataset was run for a different number of sources. After an exploration of several possible solutions spanning from 4 to 10 sources, the final range of optimal solutions ranged between 6 and 7 factors for the different sites, which are identified by evaluating several key performance indicators, such as Q values, scaled residuals distributions, the goodness-of-fit of predicted PM concentrations, and an assessment of the physical plausibility and meaning of the resulting source profiles and contributions (Reff et al., 2007). To assess each final solution, 100 model runs were performed, and the uncertainty of each solution was assessed through the implementation of error estimation tools, including Bootstrapping (BS) and Displacement (DIS) given by EPA-PMF 5.0. BS results were generally good, revealing good reproducibility, above 80% for all factors. In addition, displacement showed no factor swaps for the solution, for all dQ levels.

Rotational ambiguity is a common problem that affects the solution of PMF which is more severe when datasets are small, such as in the case of VOL-URB (44 samples) which also greatly increases the overall uncertainty of the PMF solution. A common remedy for this issue, is the implementation of multiple constrains because they can reduce uncertainty, improve stability, and enhance interpretability of PMF solutions (Manousakas et al., 2017). In all cases, the differences in %dQ values were kept below 2.5%, which means that no significant changes with respect to the unconstrained results would occur. This indicates that the constraints applied were reasonable and did not distort the PMF solutions.

The identified factors of $PM_{2.5}$ have been grouped into seven categories, namely: Biomass burning, Heavy oil combustion, Industrial emissions, Mineral dust, Sea Salt, Secondary sulphates & Organics, and Vehicular traffic. There were five shared factors among all sites including: Biomass burning, Secondary sulphates & Organics, Vehicular Traffic, Mineral dust and Sea salt. Industrial sources were found at XAN-RUR and VOL-URB stations, while the Heavy oil combustion was detected at ATH.DEM-UB, ATH.THIS-UB, IOA-UB and

VOL-URB. Additionally, the Vehicular Traffic factors showed some variation among the cities. In ATH.DEM-UB, IOA-UB and PAT-URB, Vehicular Traffic was split into two components: Vehicular Exhaust and Vehicular Non-Exhaust while in ATH.THIS-UB, XAN-RUR and VOL-URB, Vehicular Traffic was kept as a single component, due to the inability of the PMF model to resolve the distinct profiles of exhaust and non-exhaust emissions. Lastly, a unique distinction of a Cement industrial factor was identified at VOL-URB separating it from the other generic industrial source at XAN-RUR. **Table 35** presents a summary of the PMF setup for each station, including the list of input species, the number of available samples, the resolved sources/factors, and the specific constraints applied during model optimization. **Figure 103** presents the contributions (%) from the chemical mass closure analysis for the six stations. **Figure 106** - **Figure 111** present the $PM_{2.5}$ source profiles derived from PMF for the six stations while **Figure 112** presents the relative contributions of the identified sources to $PM_{2.5}$ concentrations across all studied locations (top), and the average source contributions expressed in $\mu g\ m^{-3}$ (bottom).

Table 35. *Summary table of input species, number of samples, identified sources and every constraint value that was applied to the PMF model.*

Station	Input Species	No. of samples	Sources/Factors	Constraints
ATH.DEM.-UB	$PM_{2.5}$, OC, EC, Na^+, NH_4^+, Mg^{2+}, Cl^-, NO_3^-, SO_4^{2-}, Al, Si, K, Ca, Ti, V, Mn, Fe, Ni, Cu, Zn, Br, Pb	124	Sec. Sulphates & Organics, Oil Combustion, Vehicular Exhaust, Vehicular Non-Exhaust, Mineral Dust, Sea Salt and Biomass Burning.	-Vehicular Non-Exhaust, Zn Pulled Up Maximally -Vehicular Exhaust, EC Pulled Up Maximally - Oil Combustion, V and Ni pulled up maximally, - Secondary Sulphates, EC set to Zero -Biomass Burning, OC Pulled Up Maximally, EC pulled down maximally
ATH.THIS. -UB	$PM_{2.5}$, OC, EC, Na+, NH4+, K+, Mg2+, Cl-, NO3-, SO42-, Al, Ti, V, Mn, Fe, Ni, Cu, Zn, Pb	108	Sec. Sulphates & Organics, Oil Combustion, Vehicular Traffic, Mineral Dust, Sea Salt, Biomass Burning	-Sec. Sulphates, EC set top Zero, Cl- Pulled Down Maximally -Oil Combustion, OC and EC Pulled Up Maximally - Mineral Dust , EC set top Zero
IOA-UB	$PM_{2.5}$, OC, EC, Na^+, NH_4^+, Mg^{2+}, Ca^{2+}, Cl^-, NO_3^-, SO_4^{2-}, K, Ca, Ti, Mn, Fe, Ni, Cu, Zn, Br, Rb, Sr, Pb	101	Sea Salt, Biomass Burning, Mineral Dust, Vehicular Non-Exhaust, Vehicular Exhaust, Oil Combustion and Sec. Sulphates.	- Vehicular Exhaust, K pulled down maximally.
PAT-URB	$PM_{2.5}$, OC, EC, Na+, NH_4^+, K^+, Mg^{2+}, Cl^-, NO_3^-, SO_4^{2-}, Ca, Ti, Fe, Ni, Cu, Zn, Pb	73	Biomass, Burning, Vehicular Exhaust, Vehicular Non-Exhaust, Mineral Dust, Sea Salt, and Sec. Sulphates & Organics.	- Vehicular Exhaust, Fe pulled up maximally.
VOL-URB	$PM_{2.5}$, OC, EC, Na+, NH_4^+, K^+, Mg^{2+}, Cl^-, NO_3^-, SO_4^{2-}, Ca, Ti, V, Mn, Fe, Ni, Cu, Zn, Pb	44	Oil Combustion, Secondary Sulphates & Organics, Biomass Burning, Mineral Dust, Cement Industry, Sea Salt, and Vehicular Traffic.	- Vehicular Traffic, EC & OC pulled up maximally. - Secondary Sulphates, EC set to zero. - Mineral Dust, EC and V set to Zero.
XAN-RUR	$PM_{2.5}$, OC, EC, NH_4^+, Mg^{2+}, Cl^-, NO_3^-, SO_4^{2-}, K, Ca, Ti, Mn, Fe, Ni, Cu, Zn, Br, Cs, Ba	101	Sea Salt, Secondary Sulphates & Organics, Industry, Vehicular Traffic, Mineral Dust and Biomass Burning.	- Vehicular Traffic, Zn pulled up maximally.

Biomass Burning

Biomass Burning (BB) was identified in all six stations as one of the most dominant contributors of $PM_{2.5}$. BB is mainly traced by the high levels of OC, EC and K (Viana et al., 2008). The OC/EC ratio can help to distinguish between biomass burning and other sources of carbonaceous aerosols since biomass burning typically produces aerosols with a higher OC/EC ratio than other combustion sources because the burning process is not as complete, resulting in more organic matter being emitted along with elemental carbon (Zhang et al., 2013). This ratio varied from 5.7 (ATH.DEM-UB) and 4.1 (ATH.THIS-UB), 12.3 (IOA-UB), 6.0 (PAT-URB), 10.2 (VOL-URB) and 6.2 (XAN-RUR). This variability may be attributed to several factors, such as the different type of wood fuel used, the combustion processes employed, as

well as the various sampling locations that were chosen to collect aerosol samples for analysis, including background and urban areas. Cl, Zn, Br, Rb and Pb were also observed in some cases, which are typically tracers of waste burning activities (Moffet et al., 2008).

Secondary nitrates (NO_3^-) were found to be present in the BB factor at high percentages in all stations and particularly during the winter months. Secondary nitrates (NO_3^-) can be formed from the oxidation of NO_x emitted by biomass burning and other sources. The formation and stability of secondary nitrates depend on temperature, humidity, ammonia availability and aerosol composition (Fan et al., 2022). During winter, lower temperatures favor the partitioning of nitric acid (HNO_3) into particulate nitrate, while higher humidity enhances the uptake of ammonia (NH_4) by acidic aerosols. Moreover, BB produces organic aerosols that can act as seeds for nitrate condensation (Kodros et al., 2022). These factors contribute to the higher concentrations of secondary nitrates observed in winter compared to summer.

The average contributions for BB varied between 2.9 μg m^{-3} (27.5% of $PM_{2.5}$) at ATH.DEM-UB, 6.3 μg m^{-3} (39.3% of $PM_{2.5}$) at ATH.THIS-UB, 16.3 μg m^{-3} (50.9% of $PM_{2.5}$) at IOA-UB, 6.9 μg m^{-3} (37.9% of $PM_{2.5}$) at PAT-URB, 7.8 μg m^{-3} (27.8% of $PM_{2.5}$) at VOL-URB, and 1.8 μg m^{-3} (16.2% of $PM_{2.5}$) at XAN-RUR. Biomass burning emissions showed a strong impact during the winter months for all sites, likely because wood is still widely used for residential heating. This temporal variability was particularly dominant at IOA-UB, PAT-URB, VOL-URB and ATH.THIS-UB with BB contributions of 28.2 μg m^{-3} (62.2% of $PM_{2.5}$), 14.2 μg m^{-3} (58.1% of $PM_{2.5}$), 25.2 μg m^{-3} (61.2% of $PM_{2.5}$) and 10.4 μg m^{-3} (50.9% of $PM_{2.5}$) respectively. Regarding the ATH.DEM-UB and XAN-RUR stations, the increase in BB contribution was more moderate with levels of 4.2 μg m^{-3} (44.4% of $PM_{2.5}$) and 3.2 μg m^{-3} (28.0% of $PM_{2.5}$) respectively.

High levels of BB were also documented for the IOA-UB station by Kaskaoutis et al. (2022), who reported exceptionally high winter-mean OC concentrations of 26.0 μg/m^3, with an OC/EC ratio of 9.9. Their study also noted average BCwb and $PM_{2.5}$ concentrations of 4.5 μg m^{-3} and 57.5 μg m^{-3}, respectively. Additionally, they observed record-high levoglucosan (Lev) concentrations, averaging 6.0 μg m^{-3} and peaking at 15.9 μg m^{-3}, indicating a significant influence of biomass burning (BB) on the air quality. Theodosi et al. (2018) reported that biomass burning contributed 31% to PM2.5 levels at the ATH.THIS-UB station, with an average winter concentration of 19.1 μg/m^3 and an OC/EC ratio of 3.7. Similarly, Diapouli et al., 2017 (a) reported a comparable biomass burning contribution at the ATH.DEM-UB station, with an average concentration of 2.6 μg/m^3. The significant difference in biomass burning contributions between ATH.DEM-UB (27.5% of PM2.5) and ATH.THIS-UB (39.3% of PM2.5), which is approximately 2.2 times higher at the ATH.THIS-UB station, can likely be attributed to its closer proximity to the city center, where residential density is higher. Additionally, the variation may also be influenced by differences in the time periods during which the sampling was conducted.

Heavy Oil Combustion

Heavy Oil Combustion (HOC) was prevalent at ATH.DEM-UB, ATH.THIS-UB, IOA-UB, and VOL-URB stations and it is mainly characterized by the high levels of Ni, V, EC and OC (Viana et al., 2008). Heavy fuels oils are primarily used in industrial areas, refineries and in ship diesel engines.

HOC in Athens occurs outside the city, either in industrial areas on the western part of the peninsula or due to shipping emissions. Consequently, the emissions are transported to these two sites instead of originating within the urban area of Athens (Manousakas et al., 2021). In Ioannina, lake Pamvotida, home to the Ioannina Island, serves as a route for passenger ships on a daily basis that use heavy fuel oils. The industrial area of Ioannina (located at the NW outside the city) also contains various industries that utilize HOC activities (metallurgy, pellet production etc). Finally, in Volos, HOC emissions may originate from two primary contributors: shipping emissions from the harbor and the cement industry (AGET HERACLIS factory). The high presence of Ca, Mg, EC and Cu in the HOC profile of VOL-URB can be also explained by increased industrial activity of the cement factory in the area.

The average contributions of HOC varied between 1.6 μg m^{-3} (15.1% of $PM_{2.5}$) at ATH.DEM-UB, 0.4 μg m^{-3} (2.5% of $PM_{2.5}$), at ATH.THIS-UB, 2.4 μg m^{-3} (7.5% of $PM_{2.5}$), at IOA-UB and 2.5 μg m^{-3} (9.0% of $PM_{2.5}$) at VOL-URB. Higher contribution of HOC is observed at IOA-UB during the cold period (3.0 μg m^{-3}), while in ATH.DEM-UB and VOL-URB the contribution is higher during the warm period (2.5 μg m^{-3} and 3.2 μg m^{-3} respectively).

The conditional probability function (CPF) was also utilized to examine the impact of various emission sources from different directions by combining source apportionment data with wind speed and direction information (Kim et al., 2012, Rai et al., 2016). Applying CPF is beneficial for pinpointing the sources of pollution, assuming these sources are located within a certain distance from the sampling site. For this analysis, only the top 25% of the source contributions (75th percentile) were used. The mathematical formulation of CPF is expressed through the following equation:

$$CPF = m_{\Delta\theta}/n_{\Delta\theta} \quad (64)$$

In this context, $m_{\Delta\theta}$ represents the number of wind occurrences within sector $\Delta\theta$ that exceed a specified threshold, while $n_{\Delta\theta}$ indicates the total number of data points in that same wind sector. It is likely that the sources are located in the direction where the conditional probability values are relatively high.

At ATH.DEM-UB and ATH.THIS-UB, a higher probability of HOC contribution was observed in the south-east and south-west directions, which can be attributed to the presence of refineries in Elefsina and the overall emissions from shipping activities in that vicinity. In the case of IOA-UB the western direction exhibited a higher probability of HOC pollution, likely due to shipping emissions and the long-range transport of mineral dust originating from the southern regions. The industrial area located in the north-west demonstrated

significantly increased HOC emissions, making it a substantial contributor to $PM_{2.5}$ pollution in the area. Furthermore, the CPF analysis indicated a minor contribution from the north-east direction, which could be associated with passenger transportation ships to the Ioannina Island. Finally at VOL-URB, the CPF analysis highlighted distinct sources of HOC pollution from the eastern direction, where a cement factory is located. Furthermore, the south-east direction encompasses the general shipping emissions from the harbor. The CPF plots for the HOC emissions are presented in **Figure 104**.

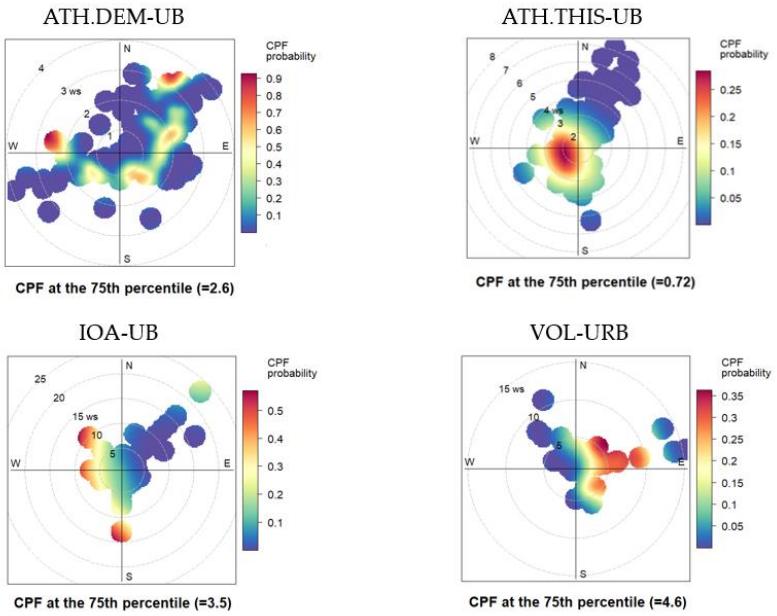

Figure 104. *CPF analysis for HOC emissions at the ATH.DEM-UB, ATH.THIS-UB, and IOA-UB and VOL-URB stations.*

Industrial Emissions

The presence of Industrial Emissions (IE) has been detected primarily in two cities, Volos and Xanthi. Specifically, in Volos, the presence of certain elements including OC, EC, Ca, Ti, Fe, V, and Ni were identified as indicators of cement industrial emissions due to the prevalence of cement dust (which contains crustal elements like Ca) and combustion emissions. The AGET HERACLIS factory located in Volos holds the position of the largest cement production facility within the HERACLIS Group and is deemed as one of the most significant cement factories within Greece.

Similarly, in Xanthi, industrial emissions were detected based on the presence of elements of Ni, Zn, Fe, OC, and Ba, which are typically associated with the industrial activities (Sharma et al., 2023). The industrial area of Xanthi features a number of different applications such as the production and processing of aluminum, batteries and plastic products. Besides OC and Fe, the presence of Ni and Zn indicate metallurgy and combustion activities. Ba also finds extensive use in various industrial applications (Peana et al., 2021). Its compounds, including nitrate and sulfate, are utilized in the production of a wide range of materials, such as plastics, ceramics, and various adhesives.

These cement industrial profile weas also compared with published cement and industrial oil profiles from the SPECIEUROPE (EC-JRC) repository (Pernigotti et al., 2016). SPECIEUROPE contains particulate chemical profiles, including organic and inorganic species, derived from both measurements of emission sources and source apportionment studies carried out in Europe. Regarding the Cement industrial factor, very good agreement was observed with the profile from Yatkin and Bayram, 2008 (Cement Kiln) for the crustal elements but also for elements associated with combustion processes like Ni, V and Zn. No typical seasonal variability was observed for any site. The average contributions of IE varied between 4.2 μg m^{-3} (14.4% of $PM_{2.5}$) at VOL-URB and 0.4 μg m^{-3} (3.3% of $PM_{2.5}$) at XAN-RUR.

Mineral Dust

Mineral Dust (MD) is predominantly composed of aerosols generated by processes arising from either natural occurrences or human actions. Natural dust occurs when wind traverses over land surfaces, causing the formation or re-suspension of particles characterized by a notable presence of naturally occurring elements found in the Earth's crust, such as Al, Si, Ca, Fe, Ti, Mn and Fe (Vasilatou et al., 2017 b). MD was identified at all six stations with contributions ranging from 1.3 μg m^{-3} (12.1% of $PM_{2.5}$) at ATH.DEM-UB, to 2.3 μg m^{-3} (14.6% of $PM_{2.5}$) at ATH.THIS-UB, 1.7 μg m^{-3} at IOA-UB (5.3% of $PM_{2.5}$), 0.9 μg m^{-3} (4.8% of $PM_{2.5}$) at PAT-URB, 3.1 μg m^{-3} (11.0% of $PM_{2.5}$) at VOL-URB, and 0.9 μg m^{-3} (4.8% of $PM_{2.5}$) at XAN-RUR.

Furthermore, the phenomenon of long-range transport originating from the northern region of Africa has been documented, in addition to the localized release of MD. Multiple stations concurrently recorded substantial contributions from this particular source (ATH.DEM-UB, IOA-UB, and XAN-RUR). By employing the Hysplit model, developed by the National Oceanic and Atmospheric Administration (NOAA), it was determined that these occurrences were linked to the extended-range dispersion of mineral dust from the North of Africa (**Figure 105**). The meteorological database used was the NCEP/NCAR Reanalysis. The calculation of backward trajectories was performed at three altitudes above ground level (AGL), namely 500m, 1000m, and 1500m. This analysis covered a time span of 120 hours, which can be recognized as a characteristic period for identifying long-range transport incidents. The episodes of long-range transport were registered on 20 to 22 December of 2019 with an increase of soil contribution of up to 16.8 μg m^{-3} at ATH.DEM-UB, 28.7 μg m^{-3} at IOA-SUB and 14.3 μg m^{-3} at XAN-RUR.

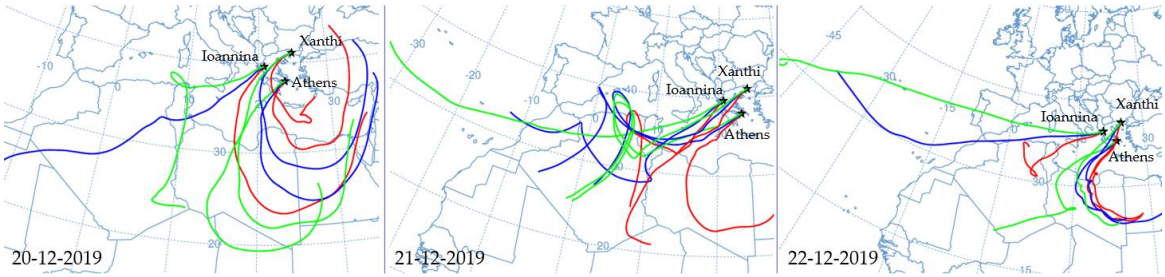

Figure 105. *Backward trajectories using Hysplit from NOAA: end at 20, 21 and 22 December 2019 (left to right) at ATH.DEM-UB, IOA-UB and XAN-RUR, indicating the long-range transport of MD from the Sahara Desert. The Green, blue and red lines refer to starting height equal to 1500 m, 1000 m and 500 m, respectively.*

Sea Salt

Sea salt (SS) was identified in all studied locations, and it is mainly traced by the high contributions of Na, Cl and Mg (Viana et al., 2008). It has to be noted that the Na^+ ion was excluded from Xanthi's database since the S/N ratio was below 0.2 (Paatero and Hopke, 2008) and the profile was traced by the high contribution of Mg^{2+}, Cl^-, SO_4^{2-}, and Br. A noteworthy characteristic of aged sea salt was consistently observed in all cases, which can be attributed to a reduction in the concentration of Cl.

The extent of chloride depletion in sea salt can be estimated by calculating the mass concentration ratio of Cl/Na, which has been reported to be typically around 1.81 Bowen 1979). The Cl/Na ratio ranged from 0.2 to 0.9 for all cities, except for XAN-RUR, where Na^+ data were excluded from the input database. Significant proportions of Bromine (Br) were observed in SS emissions at both IOA-UB (29.8%) and XAN-RUR (23.9%), in addition to the major species typically associated with these emissions. The Cl/Br ratio, a key indicator of the SS profile in Xanthi, generally ranges between 288 and 292 ((Davis et al., 1998). Notably, the measured Cl/Br ratio for Xanthi's profile was 299, which closely aligns with this expected range

The contributions of SS ranged between 0.3 μg m^{-3} (2.8% of $PM_{2.5}$) at ATH.DEM-UB, to 1.9 μg m^{-3} (11.7% of $PM_{2.5}$) at ATH.THIS-UB, 0.5 μg m^{-3} (1.6% of $PM_{2.5}$) at IOA-UB, 0.7 μg m^{-3} (3.6% of $PM_{2.5}$) at PAT-URB, 0.8 μg m^{-3} (2.7% of $PM_{2.5}$) at VOL-URB, and 0.8 μg m^{-3} (7.0% of $PM_{2.5}$) at XAN-URB. A notable seasonal variability was observed in Athens (0.6 μg m^{-3} – 6.4% of $PM_{2.5}$), Xanthi (1.2 μg m^{-3} – 10.5% of $PM_{2.5}$) and Patra (1.1 μg m^{-3} – 4.4% of $PM_{2.5}$).

Secondary Sulphates & Organics

In general, secondary aerosols are not directly emitted into the atmosphere from a single identifiable source. Instead, they form through chemical transformations of gaseous precursors originating from combustion processes. These transformations lead to the conversion of these precursors into PM over varying time scales, involving heterogeneous processes. As a result, secondary aerosols may contain marker species that are also found in

anthropogenic emissions (Viana et al., 2008). Secondary sulfates are also associated with long-range transport events and are commonly found in "aged air masses" due to the gradual oxidation of sulfur dioxide (SO_2) to sulfate (SO_4^{2-}) (Manousakas et al., 2017).

The Secondary Sulfates & Organics (SSO) factor was consistently observed in nearly all sites (Athens, Patra, Volos, and Xanthi), with the exception of Ioannina, where only a minor contribution of organic carbon (OC) was noted. The dominant components of the Secondary sulphate & organics profile were found to be SO_4^{2-}, NH_4^+, and OC. This outcome arises from the secondary formation of aerosols in the atmosphere through the photochemical oxidation of released gaseous sulfur oxides and volatile organic compounds (VOCs). Subsequently, these sulfur oxides react with ammonia (NH_3) during the process. Similar SSO profiles were also identified by Amato et al., 2016, Diapouli et al., 2017, and Paraskevopoulou et al., 2015 containing both $(NH_4)_2SO_4$ and OC urban background and suburban sites in Europe. Additionally, the presence of EC in the ATH.DEM-UB profile (10.9%) may suggest mixing with other primary sources. Notably, three sites (ATH.DEM-UB, IOA-UB, and XAN-RUR) exhibited a significant contribution of bromine (Br) ranging from 26.8% to 36.9%. Bromine is a naturally occurring element found in the Earth's crust and seawater in various chemical forms. The SSO profiles also showed a mixture of other species, including Mg^{2+} and Zn, which are characteristic elements associated with Sea Spray and industrial activities.

The contributions of Secondary Sulfates & Organics (SSO) varied across the studied sites. In more detail, SSO levels were at 3.5 μg m^{-3} (32.7% of $PM_{2.5}$) at ATH.DEM-UB, 3.2 μg m^{-3} (19.8% of $PM_{2.5}$) at ATH.THIS-UB, 2.3 μg m^{-3} (7.1% of $PM_{2.5}$) at IOA-UB, 4.8 μg m^{-3} (26.7% of $PM_{2.5}$) in PAT-URB, and 3.7 μg m^{-3} (33% of $PM_{2.5}$), 6.6 μg m^{-3} (23.3% of $PM_{2.5}$) at VOL-URB, and 3.7 μg m^{-3} (33.0% of $PM_{2.5}$) at XAN-UB. Moreover, a noticeable seasonal pattern emerged, with higher SSO concentrations observed during the warmer months. This temporal trend is likely attributed to increased photochemical activity during periods of higher solar radiation and temperature, leading to enhanced secondary aerosol formation.

Vehicular Traffic

The characteristics of Vehicular Traffic (VT) factors varied across the studied locations. At ATH.DEM-UB, IOA-UB, and PAT-UB, the VT factor was further subdivided into two distinct components: Vehicular Exhaust (VEX) and Vehicular Non-Exhaust (NEX). However, at ATH.THIS-UB, XAN-RUR, and VOL-URB, the PMF model faced challenges in distinguishing between exhaust and non-exhaust emissions, leading to the consolidation of Vehicular Traffic into a single component.

The traffic-related profiles associated with NEX were primarily traced by species originating from crustal sources, such as Fe, Mn, and Ti, representing road dust (Jandacka et al., 2023), as well as trace elements like Cu and Pb, indicative of brake wear (Huang et al., 2018; Thorpe et al., 2008). Notably, the dominance of NEX emissions was observed at IOA-UB and PAT-UB, where average concentrations ranged from 1.6 μg m^{-3} (accounting for 5.0% of $PM_{2.5}$) and 1.4 μg m^{-3} (representing 7.8% of $PM_{2.5}$), respectively. In contrast, ATH.DEM-UB exhibited

significantly lower concentrations of 0.2 μg m^{-3} (constituting only 2% of $PM_{2.5}$). The marked difference in concentration values can be attributed to the varying proximities of the sampling stations to busy traffic arteries.

The VEX sources were primarily composed of carbonaceous compounds (OC and EC). The highest OC/EC value was found at ATH.DEM-UB (12.9), which may be attributed to the reduced share of diesel vehicles in the local fleet, aligning well with the findings of Amato et al., 2016. A lower OC/EC ratio was observed at IOA-UB (5.3) and PAT-UB (5.7), suggesting a potentially higher contribution from diesel cars to the VEX profiles in those regions. In addition to OC and EC, other trace elements such as Ca, Zn, Ni, Fe, and Mn, related to lubricating oils and engine wear, were also detected, which could be emitted from vehicle tailpipes, as noted in the study by Wang et al., 2021. The concentrations of VEX emissions ranged from 0.8 μg m^{-3} (7.7% of $PM_{2.5}$) at ATH.DEM-UB, to 7.2 μg m^{-3} (22.6% of $PM_{2.5}$) at IOA-UB, and 3.5 μg m^{-3} (19.1% of $PM_{2.5}$) at PAT-URB.

Although the IOA-UB site is considered an urban background location, it is located closer to trafficked streets, leading to higher traffic density and increased exposure to PM emissions. Similarly, the PAT-URB station is near busy roads, contributing to elevated concentrations. In contrast, the ATH.DEM-UB station is situated further from the city center, within a pine forest environment, and is less directly impacted by urban PM emissions. This likely explains the lower concentrations observed at ATH.DEM-UB, as it better represents the urban background condition.

The combined vehicular traffic (VT) profiles were observed at ATH.THIS-UB, VOL-URB and XAN-RUR. These profiles comprised carbonaceous species (OC and EC) along with substances associated with brake, tire, and road wear, as well as dust resuspension, such as Cu, Zn, Pb, Ba, Ca, Fe, Mn and Cs (Viana et al., 2008; Khan et al., 2017) . In contrast to ATH.DEM-UB, the ATH.THIS-UB station exhibited a significantly lower OC/EC ratio of 4.4, suggesting a different composition of vehicular emissions in that area. This difference could be attributed to the ATH.THIS-UB station's closer proximity to the Athens city center, where traffic patterns and vehicle types may vary. At XAN-RUR, the OC/EC ratio was notably higher at 14.5, which, when compared to the ratio at VOL-URB (6.4), indicates a higher prevalence of gasoline-fueled vehicles over diesel-fueled ones in Xanthi. The concentrations of vehicular traffic (VT) ranged from 2.0 μg m^3 (12.1% of PM2.5) at ATH.THIS-UB to 2.7 μg m^3 (24.1% of PM2.5) at XAN-RUR, and 3.3 μg m^3 (11.7% of PM2.5) at VOL-URB.

ATH.DEM-UB station

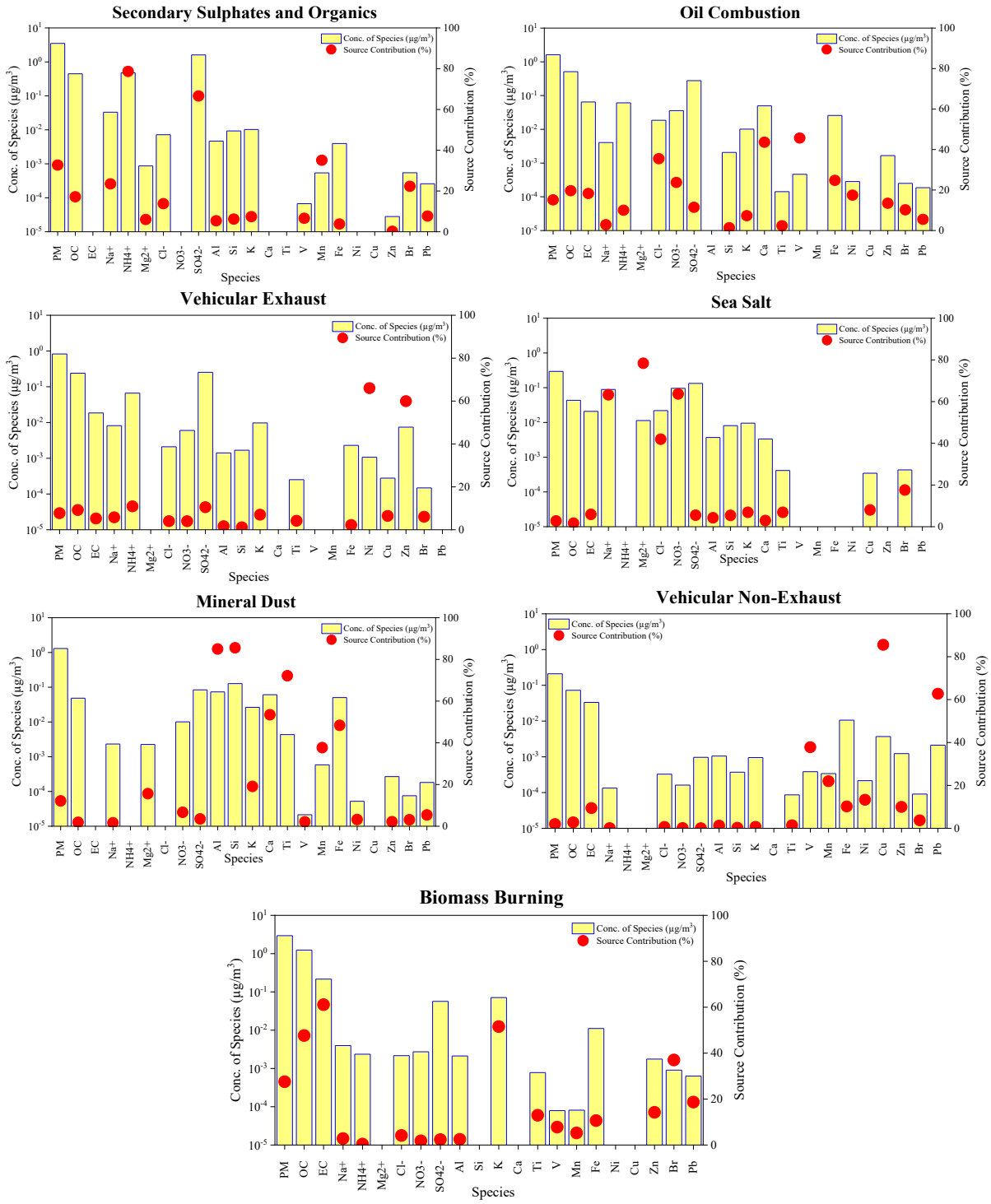

Figure 106. *$PM_{2.5}$ source profiles derived from PMF for the ATH.DEM-UB station. The bars represent species concentrations (in µg m^{-3}), while the red circles display the percentage contribution of each source to the average species concentration.*

ATH.THIS-UB station

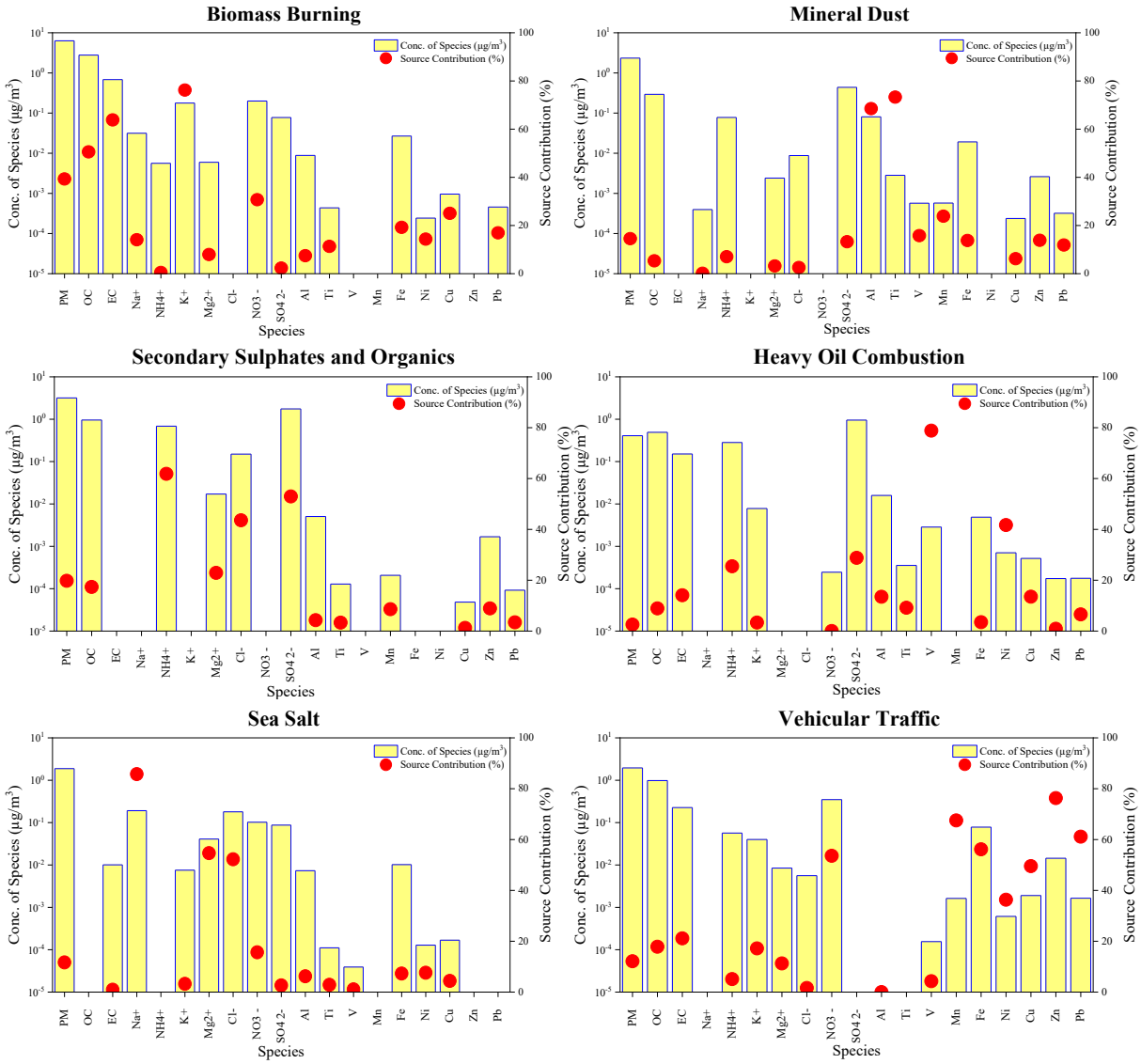

***Figure 107**. $PM_{2.5}$ source profiles derived from PMF for the ATH.THIS-UB station. The bars represent species concentrations (in μg m^{-3}), while the red circles display the percentage contribution of each source to the average species concentration.*

IOA-UB station

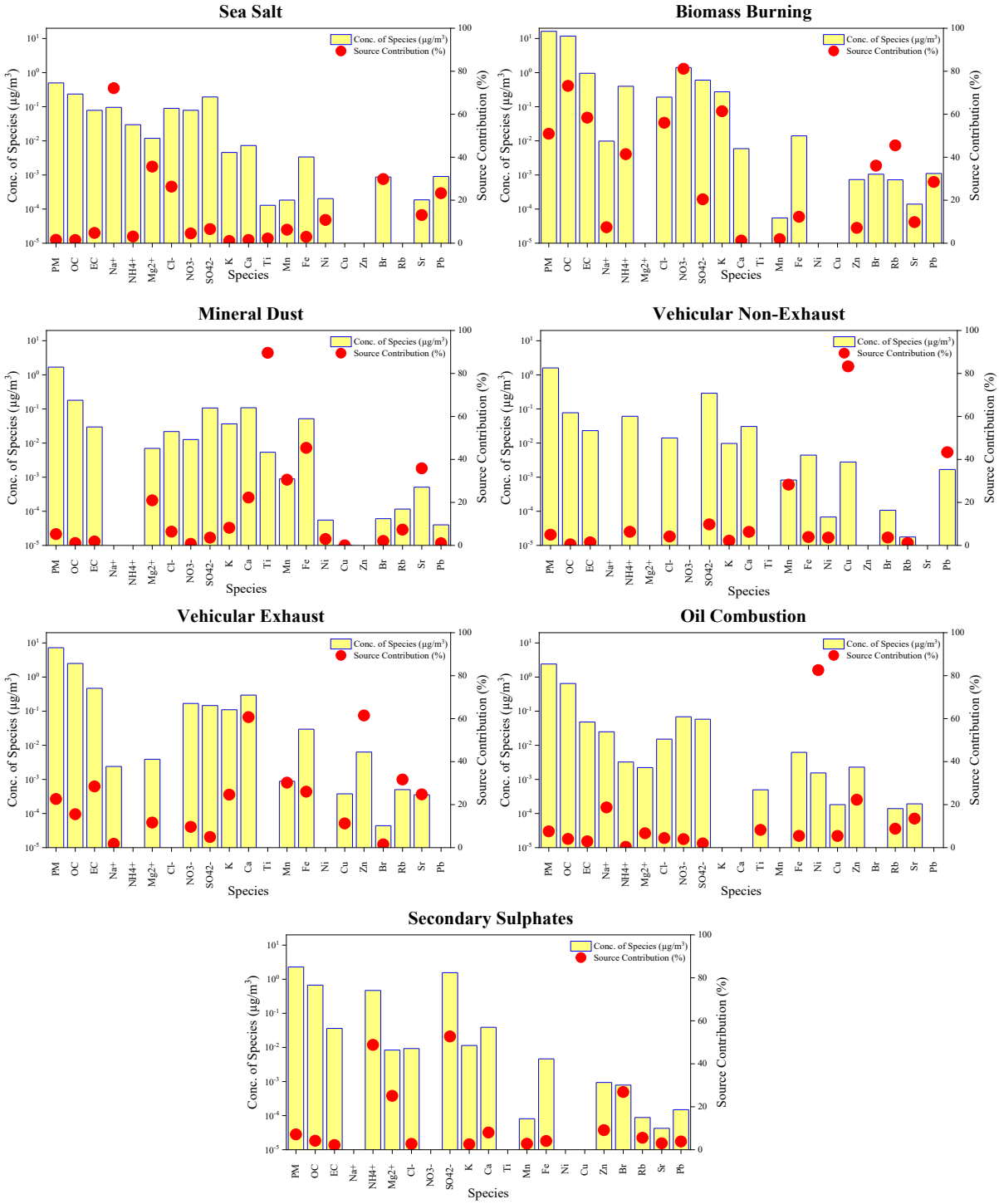

Figure 108. *$PM_{2.5}$ source profiles derived from PMF for the IOA-UB station. The bars represent species concentrations (in μg m⁻³), while the red circles display the percentage contribution of each source to the average species concentration.*

PAT-URB station

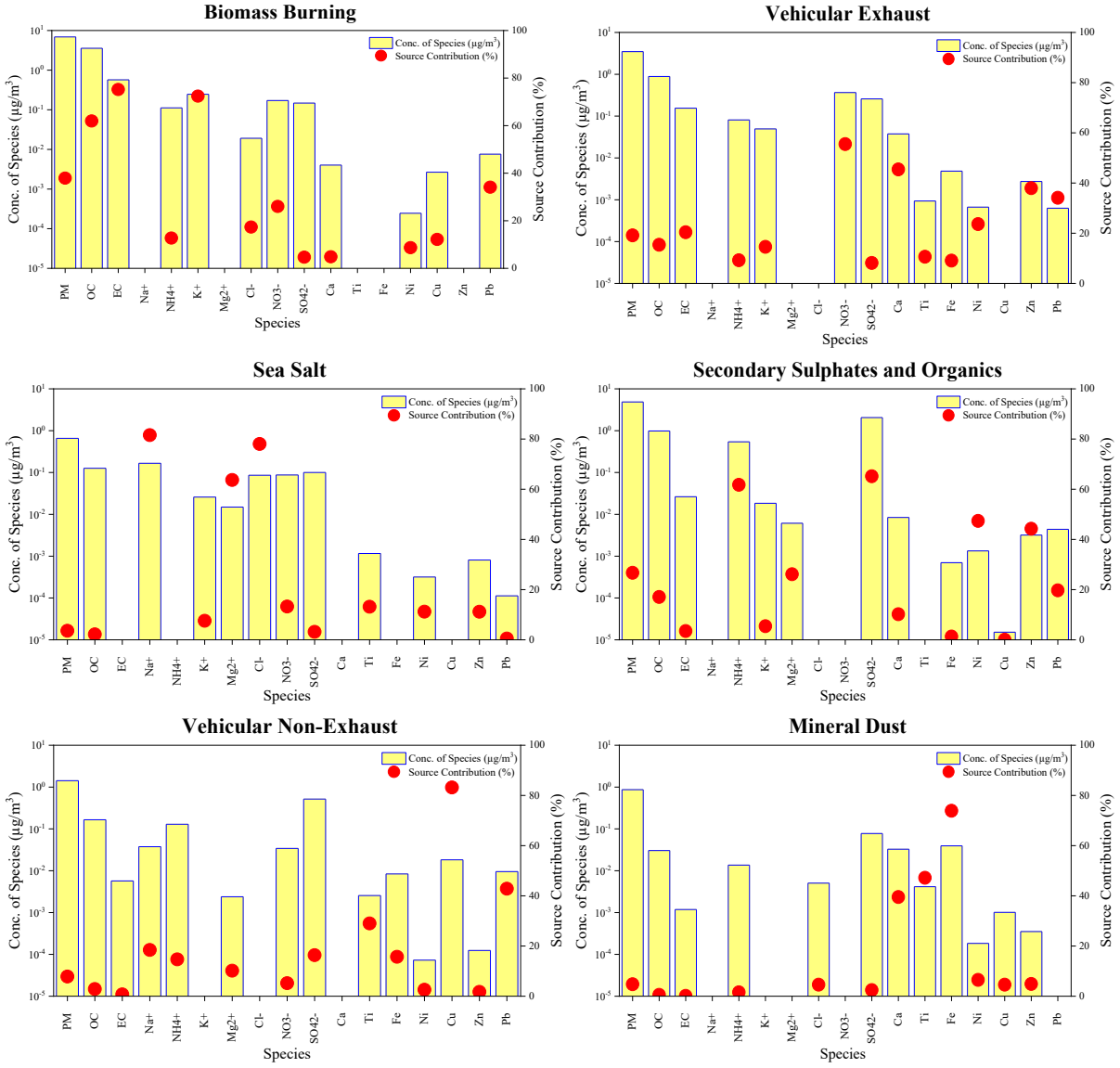

Figure 109. *$PM_{2.5}$ source profiles derived from PMF for the PAT-URB station. The bars represent species concentrations (in µg m^{-3}), while the red circles display the percentage contribution of each source to the average species concentration.*

VOL-URB station

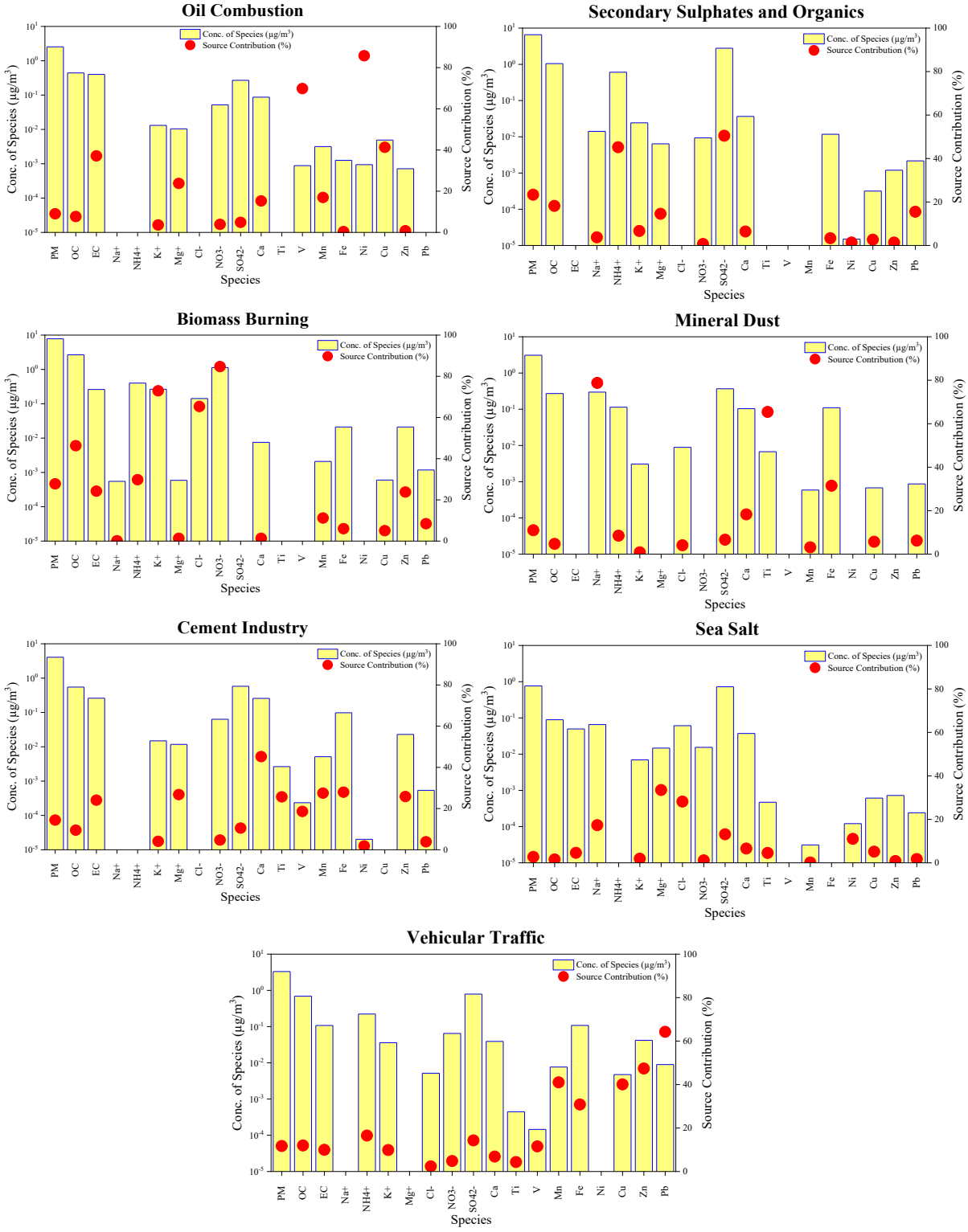

Figure 110. *$PM_{2.5}$ source profiles derived from PMF for the VOL-URB station. The bars represent species concentrations (in µg m^{-3}), while the red circles display the percentage contribution of each source to the average species concentration.*

XAN-RUR station

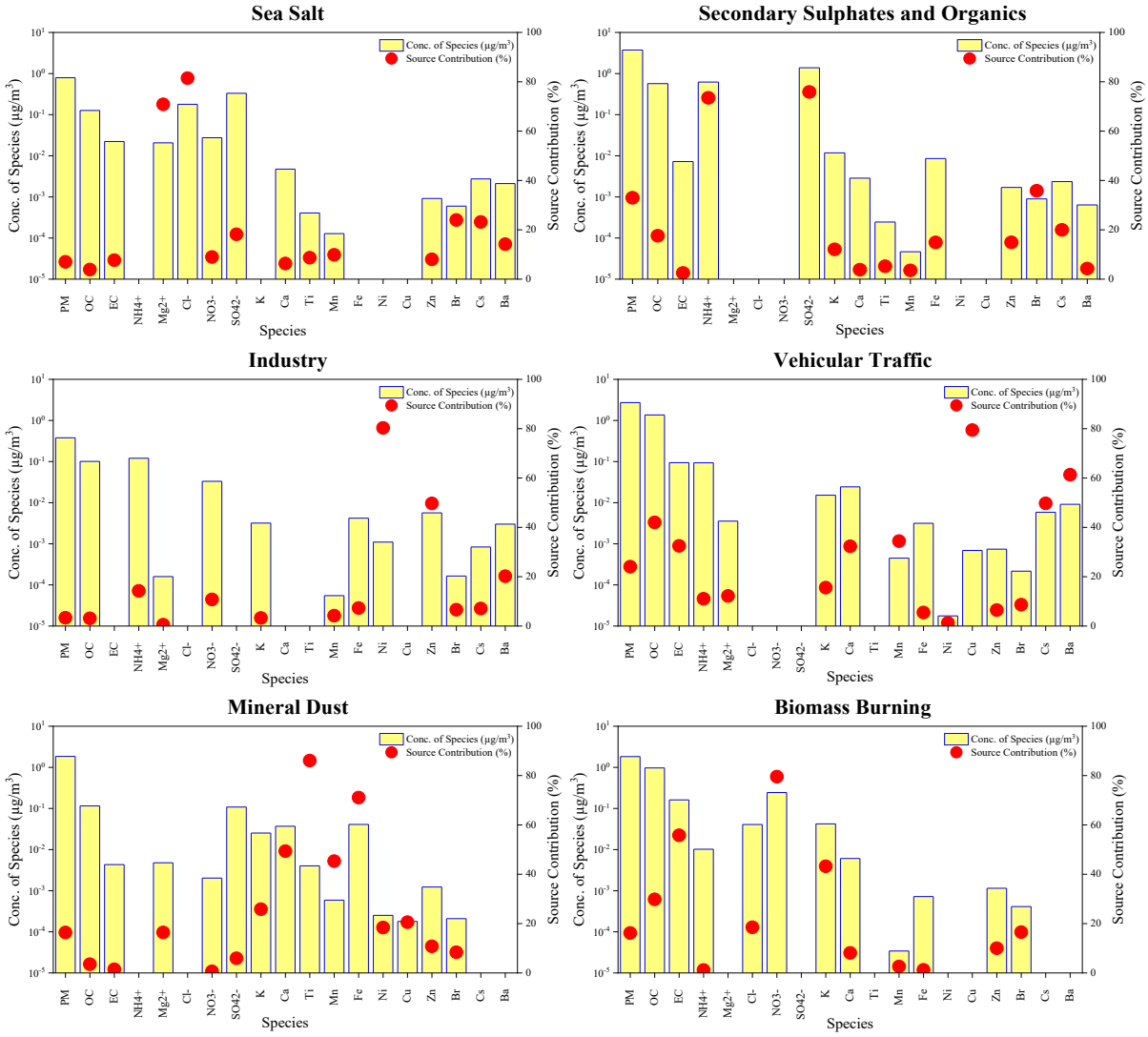

Figure 111. *$PM_{2.5}$ source profiles derived from PMF for the XAN-RUR station. The bars represent species concentrations (in µg m^{-3}), while the red circles display the percentage contribution of each source to the average species concentration.*

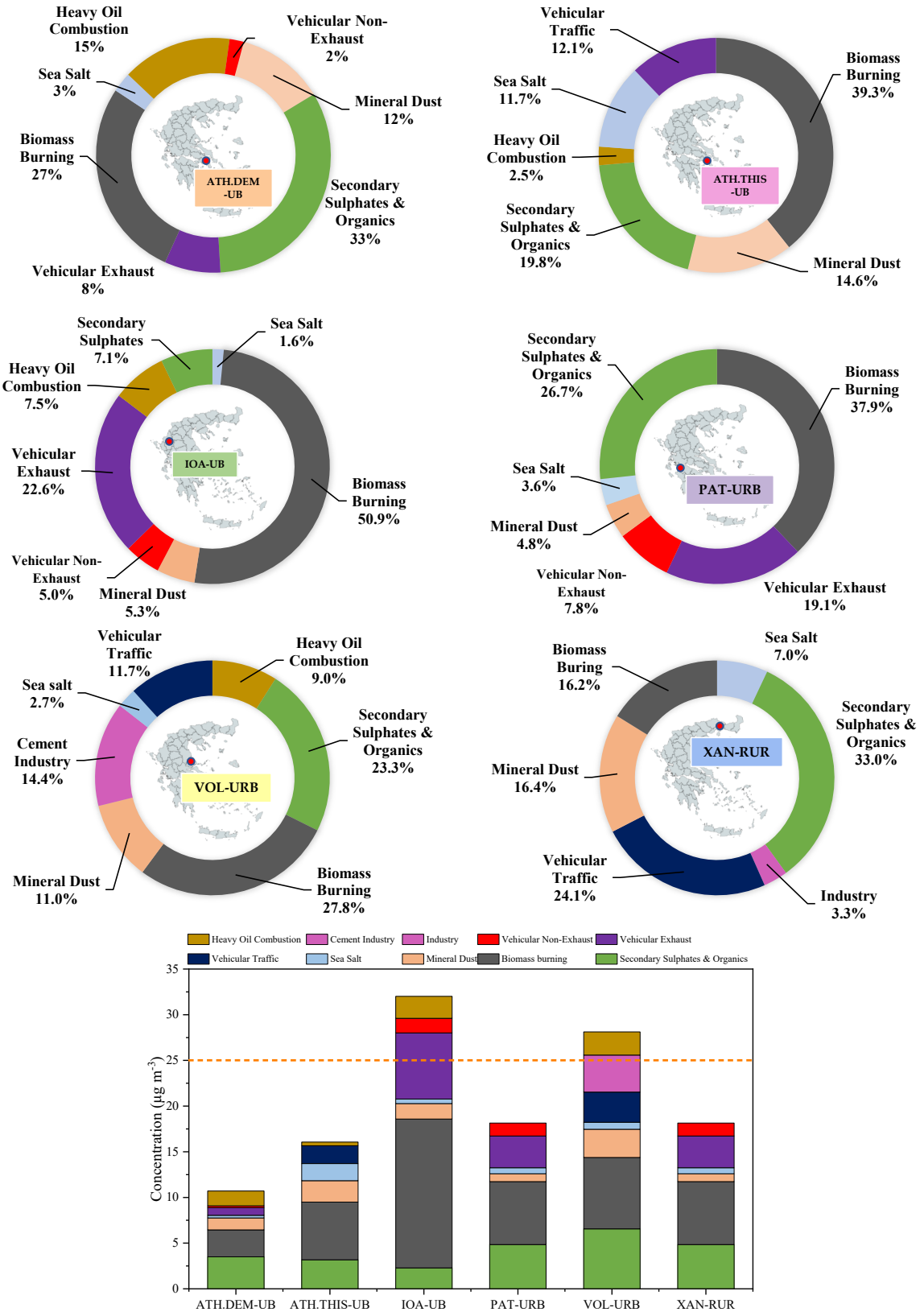

Figure 112. *Top) Relative contributions of different sources to the observed PM2.5 concentration levels for all the studied locations. Bottom) Average source contributions in μg m^{-3} to PM2.5. The orange dotted line represents the EU annual limit value (25 μg m^{-3}).*

19.5 Conclusions

In this current study, we conducted source apportionment analyses for $PM_{2.5}$ in five Greek cities—Athens, Ioannina, Xanthi, Volos, and Patra—quantifying the major sources using data from both summer (June-August) and winter (December-February) of 2019-2020. A supplementary campaign at the Athens "Thissio" station provided additional data from December 2018 to March 2019 and July to August 2019.

The observed average PM2.5 concentrations varied significantly across the studied locations, with Ioannina showing the highest levels (39.9 ± 35.8 μg m^{-3}), followed by Volos (29.8 ± 15.4 μg m^{-3}), Athens "Thissio" (20.7 ± 15.3 μg m^{-3}), Patra (18.7 ± 9.5 μg m^{-3}), Xanthi (12.9 ± 5.3 μg m^{-3}), and Athens "Demokritos" (11.0 ± 4.1 μg m^{-3}). Notably, only two sites, Ioannina and Volos, exceeded the EU legal limit for annual PM2.5 concentrations (25 μg m^{-3}), while the others remained within the permissible range.

Seven source categories were identified: biomass burning, heavy oil combustion, industrial emissions, mineral dust, sea salt, secondary sulfates, and vehicular traffic. Five of these sources—biomass burning, secondary sulfates, traffic, mineral dust, and sea salt—were consistently present across all sites, highlighting their widespread regional impact on $PM_{2.5}$ pollution in Greece.

Biomass burning was identified as a dominant source of $PM_{2.5}$ across all stations, with significant contributions, particularly during the winter, due to the continued reliance on wood for residential heating, even in recent years. This issue was especially pronounced in Ioannina and Volos, where winter BB contributions reached 28.2 μg m^{-3} (62.2% of $PM_{2.5}$) and 25.2 μg m^{-3} (61.2% of $PM_{2.5}$), respectively, highlighting the severity of the problem in these areas. The average contributions of BB ranged from 27.5 to 50.9%.

Heavy oil combustion was primarily associated with industrial activities and shipping emissions, particularly in Athens, Ioannina, and Volos. In Volos, the cement industry notably contributed to higher levels, alongside other industrial sources. Across the stations, HOC contributions to PM2.5 averaged between 2.5% and 15.1%. Similarly, industrial emissions (IE), prevalent mainly in Volos (4.2 μg m^{-3} - 14.4% of $PM_{2.5}$) and Xanthi. The contribution from IE showed no significant seasonal variation, indicating a consistent year-round impact.

Vehicular traffic (VT) emissions were diverse across the cities. In Athens, Ioannina, and Patra, the VT factor was divided into vehicular exhaust (VEX) and vehicular non-exhaust (NEX) while other cities grouped them into a single category. The dominant components of NEX emissions were traced to road dust and brake wear, with higher concentrations observed in Ioannina and Patra. VEX emissions were primarily composed of OC and EC, with Athens exhibiting a higher OC/EC ratio than Ioannina and Patra, possibly reflecting a greater presence of gasoline-fueled vehicles.

Mineral Dust was detected across all cities, with contributions from both natural sources and long-range transport events from northern Africa. Sea Salt was also present throughout, with high levels of sodium (Na), chloride (Cl), and magnesium (Mg) detected.

The Cl/Na ratio ranged from 0.2 to 0.9, indicating significant chloride depletion in aged sea salt. Secondary Sulfates & Organics (SSO) showed variable contributions linked to increased photochemical activity during warmer months.

19.6 References

Amato, F., Alastuey, A., Karanasiou, A., Lucarelli, F., Nava, S., Calzolai, G., Severi, M., Becagli, S., Gianelle, V. L., Colombi, C., Alves, C., Custódio, D., Nunes, T., Cerqueira, M., Pio, C., Eleftheriadis, K., Diapouli, E., Reche, C., Minguillón, M. C., … Querol, X. (2016). AIRUSE-LIFE+: A harmonized PM speciation and source apportionment in five southern European cities. Atmospheric Chemistry and Physics, 16(5), 3289–3309. https://doi.org/10.5194/ACP-16-3289-2016

Athanasopoulou, E., Speyer, O., Brunner, D., Vogel, H., Vogel, B., Mihalopoulos, N., & Gerasopoulos, E. (2017). Changes in domestic heating fuel use in Greece: Effects on atmospheric chemistry and radiation. *Atmospheric Chemistry and Physics*, *17*(17), 10597–10618. https://doi.org/10.5194/ACP-17-10597-2017

Barraza, F., Uzu, G., Jaffrezo, J. L., Schreck, E., Budzinski, H., Le Menach, K., Dévier, M. H., Guyard, H., Calas, A., Perez, M. I., Villacreces, L. A., & Maurice, L. (2020). Contrasts in chemical composition and oxidative potential in PM10 near flares in oil extraction and refining areas in Ecuador. *Atmospheric Environment*, *223*. https://doi.org/10.1016/J.ATMOSENV.2020.117302

Bowen, H.J.M., 1979. Environmental Chemistry of the Elements. Academic Press, London, London

Cavalli, F., Viana, M., Yttri, K. E., Genberg, J., & Putaud, J. P. (2010). Toward a standardised thermal-optical protocol for measuring atmospheric organic and elemental carbon: The EUSAAR protocol. *Atmospheric Measurement Techniques*, *3*(1), 79–89. https://doi.org/10.5194/AMT-3-79-2010

Chen, S.-L., Chang, S.-W., Chen, Y.-J., & Chen, H.-L. (2021). Possible warming effect of fine particulate matter in the atmosphere. *Communications Earth & Environment 2021 2:1*, *2*(1), 1–9. https://doi.org/10.1038/s43247-021-00278-5

Chiari, M., Yubero, E., Calzolai, G., Lucarelli, F., Crespo, J., Galindo, N., Nicolás, J. F., Giannoni, M., & Nava, S. (2018). Comparison of PIXE and XRF analysis of airborne particulate matter samples collected on Teflon and quartz fibre filters. *Nuclear Instruments and Methods in Physics Research Section B: Beam Interactions with Materials and Atoms*, *417*, 128–132. https://doi.org/10.1016/J.NIMB.2017.07.031

Chow, J. C., Watson, J. G., Kuhns, H., Etyemezian, V., Lowenthal, D. H., Crow, D., Kohl, S. D., Engelbrecht, J. P., & Green, M. C. (2004). Source profiles for industrial, mobile, and area sources in the Big Bend Regional Aerosol Visibility and Observational study. *Chemosphere*, *54*(2), 185–208. https://doi.org/10.1016/J.CHEMOSPHERE.2003.07.004

Chow, J. C., Lowenthal, D. H., Chen, L. W. A., Wang, X., & Watson, J. G. (2015). Mass reconstruction methods for PM2.5: a review. *Air Quality, Atmosphere and Health*, *8*(3), 243–263. https://doi.org/10.1007/S11869-015-0338-3/TABLES/4

Creamean, J. M., Neiman, P. J., Coleman, T., Senff, C. J., Kirgis, G., Alvarez, R. J., & Yamamoto, A. (2016). Colorado air quality impacted by long-range-transported aerosol: A set of case studies during the 2015 Pacific Northwest fires. *Atmospheric Chemistry and Physics*, *16*(18), 12329–12345. https://doi.org/10.5194/ACP-16-12329-2016

Davis, S. N., Whittemore, D. O., & Fabryka-Martin, J. (1998). Uses of Chloride/Bromide Ratios in Studies of Potable Water. *Groundwater*, *36*(2), 338–350. https://doi.org/10.1111/J.1745-6584.1998.TB01099.X

Diapouli, E., Manousakas, M., Vratolis, S., Vasilatou, V., Maggos, T., Saraga, D., Grigoratos, T., Argyropoulos, G., Voutsa, D., Samara, C., & Eleftheriadis, K. (2017). Evolution of air pollution source contributions over one decade, derived by PM10 and PM2.5 source apportionment in two metropolitan urban areas in Greece. *Atmospheric Environment*, *164*, 416–430. https://doi.org/10.1016/J.ATMOSENV.2017.06.016

Diapouli, E., Manousakas, M. I., Vratolis, S., Vasilatou, V., Pateraki, S., Bairachtari, K. A., Querol, X., Amato, F., Alastuey, A., Karanasiou, A. A., Lucarelli, F., Nava, S., Calzolai, G., Gianelle, V. L., Colombi, C., Alves, C., Custódio, D., Pio, C., Spyrou, C., … Eleftheriadis, K. (2017). AIRUSE-LIFE +: estimation of natural source contributions to urban ambient air PM10 and PM2. 5 concentrations in southern Europe – implications to compliance with limit values. *Atmospheric Chemistry and Physics*, *17*(5), 3673–3685. https://doi.org/10.5194/acp-17-3673-2017

Diapouli, E., Fetfatzis, P., Panteliadis, P., Spitieri, C., Gini, M. I., Papagiannis, S., Vasilatou, V., & Eleftheriadis, K. (2022). PM2.5 Source Apportionment and Implications for Particle Hygroscopicity at an Urban Background Site in Athens, Greece. 13, 1685. https://doi.org/10.3390/atmos13101685.

Dimitriou, K., Grivas, G., Liakakou, E., Gerasopoulos, E., & Mihalopoulos, N. (2021). Assessing the contribution of regional sources to urban air pollution by applying 3D-PSCF modeling. *Atmospheric Research*, *248*, 105187. https://doi.org/10.1016/J.ATMOSRES.2020.105187

Fan, W., Chen, T., Zhu, Z., Zhang, H., Qiu, Y., & Yin, D. (2022). A review of secondary organic aerosols formation focusing on organosulfates and organic nitrates. *Journal of Hazardous Materials*, *430*, 128406. https://doi.org/10.1016/J.JHAZMAT.2022.128406

Grivas, G., Stavroulas, I., Liakakou, E., Kaskaoutis, D. G., Bougiatioti, A., Paraskevopoulou, D., Gerasopoulos, E., & Mihalopoulos, N. (2019). Measuring the spatial variability of black carbon in Athens during wintertime. *Air Quality, Atmosphere and Health*, *12*(12), 1405–1417. https://doi.org/10.1007/S11869-019-00756-Y/FIGURES/6

Grivas, G., Athanasopoulou, E., Kakouri, A., Bailey, J., Liakakou, E., Stavroulas, I., Kalkavouras, P., Bougiatioti, A., Kaskaoutis, D. G., Ramonet, M., Mihalopoulos, N., & Gerasopoulos, E. (2020). Integrating in situ Measurements and City Scale Modelling to Assess the COVID–19 Lockdown Effects on Emissions and Air Quality in Athens, Greece. *Atmosphere 2020, Vol. 11, Page 1174*, *11*(11), 1174. https://doi.org/10.3390/ATMOS11111174

Huang, R. J., Cheng, R., Jing, M., Yang, L., Li, Y., Chen, Q., Chen, Y., Yan, J., Lin, C., Wu, Y., Zhang, R., El Haddad, I., Prevot, A. S. H., O'Dowd, C. D., & Cao, J. (2018). Source-Specific Health Risk

Analysis on Particulate Trace Elements: Coal Combustion and Traffic Emission As Major Contributors in Wintertime Beijing. *Environmental Science and Technology*, *52*(19), 10967–10974. https://doi.org/10.1021/ACS.EST.8B02091

Jandacka, D., Brna, M., Durcanska, D., & Kovac, M. (2023). Characterization of Road Dust, PMx and Aerosol in a Shopping–Recreational Urban Area: Physicochemical Properties, Concentration, Distribution and Sources Estimation. Sustainability 2023, Vol. 15, Page 12674, 15(17), 12674. https://doi.org/10.3390/SU151712674

Kaskaoutis, D. G., Grivas, G., Oikonomou, K., Tavernaraki, P., Papoutsidaki, K., Tsagkaraki, M., Stavroulas, I., Zarmpas, P., Paraskevopoulou, D., Bougiatioti, A., Liakakou, E., Gavrouzou, M., Dumka, U. C., Hatzianastassiou, N., Sciare, J., Gerasopoulos, E., & Mihalopoulos, N. (2022). Impacts of severe residential wood burning on atmospheric processing, water-soluble organic aerosol and light absorption, in an inland city of Southeastern Europe. Atmospheric Environment, 280, 119139. https://doi.org/10.1016/J.ATMOSENV.2022.119139

Khan, M. F., Hwa, S. W., Hou, L. C., Mustaffa, N. I. H., Amil, N., Mohamad, N., Sahani, M., Jaafar, S. A., Nadzir, M. S. M., & Latif, M. T. (2017). Influences of inorganic and polycyclic aromatic hydrocarbons on the sources of PM2.5 in the Southeast Asian urban sites. *Air Quality, Atmosphere and Health*, *10*(8), 999–1013. https://doi.org/10.1007/S11869-017-0489-5/FIGURES/6

Kim, E., Hopke, P. K., & Edgerton, E. S. (2012). Source Identification of Atlanta Aerosol by Positive Matrix Factorization. *Http://Dx.Doi.Org/10.1080/10473289.2003.10466209*, *53*(6), 731–739. https://doi.org/10.1080/10473289.2003.10466209

Kodros, J. K., Kaltsonoudis, C., Paglione, M., Florou, K., Jorga, S., Vasilakopoulou, C., Cirtog, M., Cazaunau, M., Picquet-Varrault, B., Nenes, A., & Pandis, S. N. (2022). Secondary aerosol formation during the dark oxidation of residential biomass burning emissions. Environmental Science: Atmospheres, 2(5), 1221–1236. https://doi.org/10.1039/D2EA00031H

Manousakas, M., Papaefthymiou, H., Diapouli, E., Migliori, A., Karydas, A. G., Bogdanovic-Radovic, I., & Eleftheriadis, K. (2017). Assessment of PM2.5 sources and their corresponding level of uncertainty in a coastal urban area using EPA PMF 5.0 enhanced diagnostics. *Science of The Total Environment*, *574*, 155–164. https://doi.org/10.1016/J.SCITOTENV.2016.09.047

Manousakas, M., Diapouli, E., Papaefthymiou, H., Kantarelou, V., Zarkadas, C., Kalogridis, A.-C., Karydas, A.-G., & Eleftheriadis, K. (2018). XRF characterization and source apportionment of PM10 samples collected in a coastal city. X-Ray Spectrometry, 47(3), 190–200. https://doi.org/10.1002/xrs.2817

Manousakas, M., Diapouli, E., Belis, C., Vasilatou, V., Gini, M., Lucarelli, F., Querol, X., & Eleftheriadis, K. (2021). Quantitative assessment of the variability in chemical profiles from source apportionment analysis of PM10 and PM2.5 at different sites within a large metropolitan area. *Environmental Research*, *192*, 110257. https://doi.org/10.1016/J.ENVRES.2020.110257

Mason B., (1966) Principles of Geochemistry (third ed.), John Wiley & Sons, Inc., New York, NY

Moffet, R. C., Desyaterik, Y., Hopkins, R. J., Tivanski, A. V., Gilles, M. K., Wang, Y., Shutthanandan, V., Molina, L. T., Abraham, R. G., Johnson, K. S., Mugica, V., Molina, M. J., Laskin, A., & Prather, K. A. (2008). Characterization of aerosols containing Zn, Pb, and Cl from an industrial region of Mexico City. *Environmental Science and Technology*, *42*(19), 7091–7097. https://doi.org/10.1021/ES7030483/SUPPL_FILE/ES7030483_SI_001.PDF

Nakharutai, N., Traisathit, P., Thongsak, N., Supasri, T., Srikummoon, P., Thumronglaohapun, S., Hemwan, P., & Chitapanarux, I. (2022). Impact of Residential Concentration of PM2.5 Analyzed as Time-Varying Covariate on the Survival Rate of Lung Cancer Patients: A 15-Year Hospital-Based Study in Upper Northern Thailand. International Journal of Environmental Research and Public Health 2022, Vol. 19, Page 4521, 19(8), 4521. https://doi.org/10.3390/IJERPH19084521

Nava, S., Becagli, S., Calzolai, G., Chiari, M., Lucarelli, F., Prati, P., Traversi, R., Udisti, R., Valli, G., & Vecchi, R. (2012). Saharan dust impact in central Italy: An overview on three years elemental data records. *Atmospheric Environment*, *60*, 444–452. https://doi.org/10.1016/J.ATMOSENV.2012.06.064

Ostro, B., Tobias, A., Karanasiou, A., Samoli, E., Querol, X., Rodopoulou, S., Basagaña, X., Eleftheriadis, K., Diapouli, E., Vratolis, S., Jacquemin, B., Katsouyanni, K., Sunyer, J., Forastiere, F., Stafoggia, M., Alessandrini, E., Angelini, P., Berti, G., Bisanti, L., … Pascal, M. (2015). The risks of acute exposure to black carbon in Southern Europe: results from the MED-PARTICLES project. *Occupational and Environmental Medicine*, *72*(2), 123–129. https://doi.org/10.1136/OEMED-2014-102184

Paatero, P. (1999). The multilinear engine: a table-driven, least squares program for solving multilinear problems, including the n-way parallel factor analysis model. J Comput Graph Stat 8(4):854. https://doi.org/10.2307/1390831

Paatero, P., & Tapper, U. (1994). Positive matrix factorization: A non-negative factor model with optimal utilization of error estimates of data values. *Environmetrics*, *5*(2), 111–126. https://doi.org/10.1002/ENV.3170050203

Paatero, P., & Hopke, P. K. (2003). Discarding or downweighting high-noise variables in factor analytic models. *Analytica Chimica Acta*, *490*(1–2), 277–289. https://doi.org/10.1016/S0003-2670(02)01643-4

Paatero, P., & Hopke, P. K. (2008). Rotational tools for factor analytic models. *Journal of Chemometrics*, *23*(2), 91–100. https://doi.org/10.1002/CEM.1197

Papanikolaou, C. A., Papayannis, A., Mylonaki, M., Foskinis, R., Kokkalis, P., Liakakou, E., Stavroulas, I., Soupiona, O., Hatzianastassiou, N., Gavrouzou, M., Kralli, E., & Anagnou, D. (2022). Vertical Profiling of Fresh Biomass Burning Aerosol Optical Properties over the Greek Urban City of Ioannina, during the PANACEA Winter Campaign. *Atmosphere 2022, Vol. 13, Page 94*, *13*(1), 94. https://doi.org/10.3390/ATMOS13010094

Paraskevopoulou, D., Liakakou, E., Gerasopoulos, E., Theodosi, C., & Mihalopoulos, N. (2014). Long-term characterization of organic and elemental carbon in the PM2.5 fraction: The

case of Athens, Greece. *Atmospheric Chemistry and Physics*, *14*(23), 13313–13325. https://doi.org/10.5194/ACP-14-13313-2014

Paraskevopoulou, D., Liakakou, E., Gerasopoulos, E., & Mihalopoulos, N. (2015). Sources of atmospheric aerosol from long-term measurements (5 years) of chemical composition in Athens, Greece. *Science of The Total Environment*, *527–528*, 165–178. https://doi.org/10.1016/J.SCITOTENV.2015.04.022

Peana, M., Medici, S., Dadar, M., Zoroddu, M. A., Pelucelli, A., Chasapis, C. T., & Bjørklund, G. (2021). Environmental barium: potential exposure and health-hazards. Archives of Toxicology, 95(8), 2605–2612. https://doi.org/10.1007/S00204-021-03049-5/FIGURES/2

Pernigotti, D., Belis, C. A., & Spanó, L. (2016). SPECIEUROPE: The European data 575 base for PM source profiles. *Atmospheric Pollution Research*, *7*(2), 307–314. 576 https://doi.org/10.1016/J.APR.2015.10.007

Querol, X., Alastuey, A., Rodriguez, S., Plana, F., Ruiz, C. R., Cots, N., Massagué, G., & Puig, O. (2001). PM10 and PM2.5 source apportionment in the Barcelona Metropolitan area, Catalonia, Spain. *Atmospheric Environment*, *35*(36), 6407–6419. https://doi.org/10.1016/S1352-2310(01)00361-2.

Rai, P., Chakraborty, A., Mandariya, A. K., & Gupta, T. (2016). Composition and source apportionment of PM1 at urban site Kanpur in India using PMF coupled with CBPF. *Atmospheric Research*, *178–179*, 506–520. https://doi.org/10.1016/J.ATMOSRES.2016.04.015

Reff, A., Eberly, S. I., & Bhave, P. V. (2007). Receptor Modeling of Ambient Particulate Matter Data Using Positive Matrix Factorization: Review of Existing Methods. Journal of the Air & Waste Management Association, 57(2), 146–154. https://doi.org/10.1080/10473289.2007.10465319

Saffari, A., Daher, N., Samara, C., Voutsa, D., Kouras, A., Manoli, E., Karagkiozidou, O., Vlachokostas, C., Moussiopoulos, N., Shafer, M. M., Schauer, J. J., & Sioutas, C. (2013). Increased biomass burning due to the economic crisis in Greece and its adverse impact on wintertime air quality in Thessaloniki. *Environmental Science and Technology*, *47*(23), 13313–13320. https://doi.org/10.1021/ES403847H/SUPPL_FILE/ES403847H_SI_001.PDF

Samoli, E., Stafoggia, M., Rodopoulou, S., Ostro, B., Declercq, C., Alessandrini, E., Díaz, J., Karanasiou, A., Kelessis, A. G., Tertre, A. Le, Pandolfi, P., Randi, G., Scarinzi, C., Zauli-Sajani, S., Katsouyanni, K., Forastiere, F., Alessandrini, E., Angelini, P., Berti, G., … Pascal, M. (2013). Associations between fine and coarse particles and mortality in Mediterranean cities: Results from the MED-PARTICLES project. *Environmental Health Perspectives*, *121*(8), 932–938. https://doi.org/10.1289/EHP.1206124

Saraga, D., Maggos, T., Degrendele, C., Klánová, J., Horvat, M., Kocman, D., Kanduč, T., Garcia Dos Santos, S., Franco, R., Gómez, P. M., Manousakas, M., Bairachtari, K., Eleftheriadis, K., Kermenidou, M., Karakitsios, S., Gotti, A., & Sarigiannis, D. (2021). Multi-city comparative PM2.5 source apportionment for fifteen sites in Europe: The ICARUS project. *Science of The Total Environment*, *751*, 141855. https://doi.org/10.1016/J.SCITOTENV.2020.141855

Seinfeld, J.H., Pandis, S.N., 1998. Atmospheric Chemistry and Physics: From Air Pollution to Climate Change. John Wiley, Hoboken, N. J, p. 443.

Sharma, S. K., & Mandal, T. K. (2023). Elemental Composition and Sources of Fine Particulate Matter (PM2.5) in Delhi, India. *Bulletin of Environmental Contamination and Toxicology*, *110*(3), 60. https://doi.org/10.1007/s00128-023-03707-7

Song, C. H., & Carmichael, G. R. (1999). The aging process of naturally emitted aerosol (sea-salt and mineral aerosol) during long range transport. *Atmospheric Environment*, *33*(14), 2203–2218. https://doi.org/10.1016/S1352-2310(98)00301-X

Theodosi, C., Tsagkaraki, M., Zarmpas, P., Grivas, G., Liakakou, E., Paraskevopoulou, D., Lianou, M., Gerasopoulos, E., & Mihalopoulos, N. (2018). Multi-year chemical composition of the fine-aerosol fraction in Athens, Greece, with emphasis on the contribution of residential heating in wintertime. *Atmospheric Chemistry and Physics*, *18*(19), 14371–14391. https://doi.org/10.5194/ACP-18-14371-2018

Thorpe, A., & Harrison, R. M. (2008). Sources and properties of non-exhaust particulate matter from road traffic: A review. Science of The Total Environment, 400(1–3), 270–282. https://doi.org/10.1016/J.SCITOTENV.2008.06.007

Vasilatou, V., Diapouli, E., Abatzoglou, D., Bakeas, E. B., Scoullos, M., & Eleftheriadis, K. (2017). Characterization of PM2.5 chemical composition at the Demokritos suburban station, in Athens Greece. The influence of Saharan dust. *Environmental Science and Pollution Research*, *24*(12), 11836–11846. https://doi.org/10.1007/S11356-017-8684-3/FIGURES/6

Vasilatou, V., Manousakas, M., Gini, M., Diapouli, E., Eleftheriadis, K., & Scoullos, M. (2017). Long term flux of Saharan dust to the Aegean Sea around the Attica region, Greece. *Frontiers in Marine Science*, *4*, 42 https://doi.org/10.3389/fmars.2017.00042

Viana, M., Kuhlbusch, T. A. J., Querol, X., Alastuey, A., Harrison, R. M., Hopke, P. K., Winiwarter, W., Vallius, M., Szidat, S., Prévôt, A. S. H., Hueglin, C., Bloemen, H., Wåhlin, P., Vecchi, R., Miranda, A. I., Kasper-Giebl, A., Maenhaut, W., & Hitzenberger, R. (2008). Source apportionment of particulate matter in Europe: A review of methods and results. In Journal of Aerosol Science (Vol. 39, Issue 10, pp. 827–849). Elsevier Ltd. https://doi.org/10.1016/j.jaerosci.2008.05.007

Wang, J. M., Jeong, C. H., Hilker, N., Healy, R. M., Sofowote, U., Debosz, J., Su, Y., Munoz, A., & Evans, G. J. (2021). Quantifying metal emissions from vehicular traffic using real world emission factors. *Environmental Pollution*, *268*, 115805. https://doi.org/10.1016/J.ENVPOL.2020.115805

Xing, Y. F., Xu, Y. H., Shi, M. H., & Lian, Y. X. (2016). The impact of PM2.5 on the human respiratory system. Journal of Thoracic Disease, 8(1), E69. https://doi.org/10.3978/J.ISSN.2072-1439.2016.01.19

Yatkin, S., & Bayram, A. (2008). Source apportionment of PM10 and PM2.5 using 632 positive matrix factorization and chemical mass balance in Izmir, Turkey. *Science* 633 *of The Total Environment*, *390*(1), 109–123. 634 https://doi.org/10.1016/J.SCITOTENV.2007.08.059

Zhang, T., Wu, C., Li, B., Wang, J., Ravat, R., Chen, X., Wei, J., & Yu, Q. (2019). Linking the SO2 emission of cement plants to the sulfur characteristics of their limestones: A study of 80 NSP cement lines in China. *Journal of Cleaner Production*, *220*, 200–211. https://doi.org/10.1016/J.JCLEPRO.2019.02.133

Zhang, Y., Obrist, D., Zielinska, B., & Gertler, A. (2013). Particulate emissions from different types of biomass burning. Atmospheric Environment, 72, 27–35. https://doi.org/10.1016/J.ATMOSENV.2013.02.026

Zhao, C. N., Xu, Z., Wu, G. C., Mao, Y. M., Liu, L. N., Qian-Wu, Dan, Y. L., Tao, S. S., Zhang, Q., Sam, N. B., Fan, Y. G., Zou, Y. F., Ye, D. Q., & Pan, H. F. (2019). Emerging role of air pollution in autoimmune diseases. Autoimmunity Reviews, 18(6), 607–614. https://doi.org/10.1016/J.AUTREV.2018.12.010

Section E. Conclusions

This doctoral thesis effectively bridged the gap between analytical instrumentation development and practical environmental monitoring, creating a solid framework for the physicochemical characterization of atmospheric aerosols. Going beyond conventional monitoring networks that rely on bulk PM mass concentrations, such as PM_{10} and $PM_{2.5}$, this work demonstrated that X-ray-based techniques can provide **precise, high-quality elemental data for accurate source apportionment**.

A significant methodological contribution was the validation of cost-effective, portable solutions for aerosol analysis. A portable methodology using a **handheld ED-XRF** was established, quantifying twenty-four elements (Na-Pb) by optimizing excitation conditions and employing weighted regression calibrations. The system achieved detection limits comparable to those of benchtop systems for elements such as Al, Si, Ca, and Ti, provided that vacuum conditions were used for low-Z elements. Results showed strong correlations with a benchtop spectrometer with secondary tarhets ($r>0.88$-0.99 for elements above the limit of quantification), validating the device for field-ready quantification and rapid screening Furthermore, **μ-XRF imaging** offered valuable insights into the spatial distribution of particles on cascade impactor filters. The analysis revealed noticeable spatial variability for some coarse-mode elements (Si, Ca, Fe, Ti) on the upper impactor stages, where relative standard deviations (RSD) could exceed 30%. These observations indicate that relying on a single measurement spot may introduce bias, highlighting the benefit of using scanning μ-XRF techniques to account for spatial variability and improve quantification accuracy.

To address the need for high spectral resolution and trace element detection, **Wavelength-Dispersive XRF (WD-XRF)** and **Particle-Induced X-ray Emission (PIXE)** systems were calibrated using thin-film standards. The Rigaku ZSX Primus IV WD-XRF demonstrated superior spectral resolution compared to a benchtop ED-XRF spectrometer with secondary targers, effectively separating overlapping peaks and achieving excellent agreement (5-20% difference) with ED-XRF. The dedicated external-beam PIXE setup at NCSR "Demokritos," utilizing dual Silicon Drift Detectors, was validated as a high-sensitivity, quantitative system for environmental filters, requiring only 5-7 minutes per filter.

Finally, an extensive intercomparison between **Near Real-Time (NRT) XRF (Xact 625i and Xact 625, Sailbri Cooper)** and **a benchtop ED-XRF (Epsilon 5, Panalytical)** spectrometers across three European sites (Athens, Dublin, Nicosia) highlighted the critical role of filter substrate in data accuracy. While robust agreement was maintained for heavier elements (e.g., Fe, Zn), quartz fiber filters introduced significant X-ray attenuation challenges for light elements (S, Cl, K), whereas PTFE filters yielded superior consistency with near-unity slopes. These findings highlight the importance of carefully selecting both instrumentation and filter media in XRF-based aerosol analysis to ensure data comparability across monitoring networks.

It has to be noted, in all intercomparison studies, measurements from the benchtop ED-XRF spectrometer with secondary targets (Epsilon 5, PANalytical) were considered the reference. This instrument served as the benchmark because it was thoroughly calibrated using certified thin-film standards, operated under optimized excitation conditions, and was routinely applied to ISO-compliant aerosol filter analyses.

These methods were applied to real-world case studies. In **Dushanbe, Tajikistan**, the thesis presented the first multi-year (2015-2016, 2018-2019), source-resolved assessment of $PM_{2.5}$. Mean $PM_{2.5}$ concentrations were nearly 91 $\mu g/m^3$, with winter monthly averages frequently exceeding 140 $\mu g/m^3$. PMF analysis identified eight sources, with coal burning and biomass burning together accounting for over 40% of the annual $PM_{2.5}$ mass.

In Greece, the PANACEA initiative—a harmonized study of six sites—identified residential biomass burning as the ubiquitous and dominant wintertime source, accounting for approximately 60% in Ioannina and Volos. Additionally, industrial and shipping signatures were strongest in coastal cities, and seasonal increases in Organic Carbon (OC) and Elemental Carbon (EC) were directly linked to residential heating. The integrated case studies confirm that residential solid-fuel combustion is the primary driver of wintertime pollution exceedances in both Central Asia and Greece.

By providing quantitative, source-specific apportionment, this thesis offers policymakers the scientific evidence needed to develop effective, targeted interventions. These include promoting clean heating options, improving building energy efficiency, enforcing shipping fuel regulations, and reducing traffic-related toxic metals (Cu, Zn, Ba, Pb) from non-exhaust sources.

This dissertation demonstrates that combining advanced X-ray fluorescence (XRF) and Particle-Induced X-ray Emission (PIXE) techniques with receptor modeling offers innovative methods and new insights into the sources of particulate matter (PM) pollution across various environments. It establishes a robust analytical framework for non-destructive aerosol analysis, which has been validated using multiple instruments and applied in case studies of significant societal importance in Europe and Central Asia. The findings confirm that residential combustion is the primary contributor to winter pollution exceedances, while maritime and industrial emissions continue to impact pollutant levels. Additionally, natural sources play a significant role in shaping background pollution levels. Overall, this work lays an evidence-based foundation for air quality management and paves the way for future studies that will be more detailed, chemically comprehensive, and focused on policy implications.

Author's Publications

Journals

1. Chatoutsidou, S. E**., Papagiannis, S.**, Anagnostopoulos, D. F., Eleftheriadis, K., Lazaridis, M., & Karydas, A. G. (2022). Application of a handheld X-ray fluorescence analyzer for the quantification of air particulate matter on Teflon filters. *Spectrochimica Acta Part B: Atomic Spectroscopy*, *196*, 106517. https://doi.org/10.1016/J.SAB.2022.106517

2. Diapouli, E., Fetfatzis, P., Panteliadis, P., Spitieri, C., Gini, M. I**., Papagiannis, S.**, Vasilatou, V., & Eleftheriadis, K. (2022). PM2.5 Source Apportionment and Implications for Particle Hygroscopicity at an Urban Background Site in Athens, Greece. *Atmosphere*, *13*(10), 1685. https://doi.org/10.3390/atmos13101685

3. Urošević, M. A., Lazo, P., Stafilov, T., Nečemer, M., Andonovska, K. B., Balabanova, B., Hristozova, G., **Papagiannis, S.**, Stihi, C., Suljkanović, M., Špirić, Z., Vassilatou, V., & Vogel-Mikuš, K. (2023). Active biomonitoring of potentially toxic elements in urban air by two distinct moss species and two analytical techniques: a pan-Southeastern European study. *Air Quality, Atmosphere and Health*, *16*(3), 595–612. https://doi.org/10.1007/S11869-022-01291-Z/TABLES/1

4. Poupkou, A., Kontos, S., Liora, N., Tsiaousidis, D., Kapsomenakis, I., Solomos, S., Liakakou, E., Athanasopoulou, E., Grivas, G., Diapouli, E., Vasilatou, V., **Papagiannis, S.**, Progiou, A., Kalabokas, P., Melas, D., Gerasopoulos, E., Eleftheriadis, K., & Zerefos, C. (2023). Evaluation of the Simulated Atmospheric Particulate Matter Chemical Composition in Athens: Organic Aerosols Formation Sensitivity Tests. *Environmental Sciences Proceedings 2023, Vol. 26, Page 32*, *26*(1), 32. https://doi.org/10.3390/ENVIRONSCIPROC2023026032

5. Ioannidou, E., **Papagiannis, S.**, Ioannis Manousakas, M., Betsou, C., Eleftheriadis, K., Paatero, J., Papadopoulou, L., & Ioannidou, A. (2023). Trace Elements Concentrations in Urban Air in Helsinki, Finland during a 44-Year Period. *Atmosphere 2023, Vol. 14, Page 1430*, *14*(9), 1430. https://doi.org/10.3390/ATMOS14091430

6. Vasilakopoulou, C. N., Matrali, A., Skyllakou, K., Georgopoulou, M., Aktypis, A., Florou, K., Kaltsonoudis, C., Siouti, E., Kostenidou, E., Błaziak, A., Nenes, A., **Papagiannis, S.**, Eleftheriadis, K., Patoulias, D., Kioutsioukis, I., & Pandis, S. N. (2023). Rapid

transformation of wildfire emissions to harmful background aerosol. *Npj Climate and Atmospheric Science 2023 6:1*, *6*(1), 218-. https://doi.org/10.1038/s41612-023-00544-7

7. Ioannidou, E., **Papagiannis, S.**, Manousakas, M. I., Vestenius, M., Eleftheriadis, K., Paatero, J., Papadopoulou, L., & Ioannidou, A. (2024). Airborne 210Pb, Si, Zn and Pb as tracers for atmospheric pollution in Helsinki metropolitan area. *Applied Radiation and Isotopes*, *206*, 111252. https://doi.org/10.1016/J.APRADISO.2024.111252

8. **Papagiannis, S.**, Abdullaev, S.F., Vasilatou, V., Manousakas, M. I. Eleftheriadis, K., & Diapouli, E. (2024). Air quality challenges in Central Asian urban areas: a PM2.5 source apportionment analysis in Dushanbe, Tajikistan. *Environmental Science and Pollution Research 2024*, 31, 39588–39601 (2024). https://doi.org/10.1007/S11356-024-33833-6

9. Poupkou, A., Kontos, S., Liora, N., Tsiaousidis, D., Kapsomenakis, I., Solomos, S., Liakakou, E., Athanasopoulou, E., Grivas, G., Bougiatioti, A., Petrinoli, K., Diapouli, E., Vasilatou, V., **Papagiannis, S.**, Progiou, A., Kalabokas, P., Melas, D., Mihalopoulos, N., Gerasopoulos, E., … Zerefos, C. (2025). Investigating the Role of Organic Aerosol Schemes in the Simulation of Atmospheric Particulate Matter in a Large Mediterranean Urban Agglomeration. *Sustainability (Switzerland)*, *17*(6). https://doi.org/10.3390/SU17062619/S1

10. Bika, P., Ioannidis, N., Tsipas, P., **Papagiannis, S.**, Gatou, M. A., Pavlatou, E. A., Karydas, A. G., Stergiopoulos, T., & Dallas, P. (2025). Detection and Selective Sorption of Copper Ions by a COF-Modified Melamine Sponge. *ACS Omega*, *10*(21), 21755–21766. https://pubs.acs.org/doi/10.1021/acsomega.5c01393

11. Tsamos, P., **Papagiannis, S**., Xarchoulakos, D., Kehagia, K., & Noli, F. (2025). The Impact of Crude Oil Facilities on the Accumulation of Heavy Metals and Radionuclides in a Coastal Environment. *Water, Air, and Soil Pollution*, *236*(10), 667-. https://doi.org/10.1007/S11270-025-08264-9/FIGURES/4

12. Manousakas, M. I., Zografou, O., Canonaco, F., Diapouli, E., **Papagiannis, S.**, Gini, M., Vasilatou, V., Tobler, A., Vratolis, S., Slowik, J. G., Daellenbach, K. R., Prevot, A. S. H., & Eleftheriadis, K. (2025). Implementation of real-Time source apportionment approaches using the ACSM-Xact-Aethalometer (AXA) setup with SoFi RT: The Athens case study. *Atmospheric Measurement Techniques*, *18*(16), 3983–4002. https://doi.org/10.5194/AMT-18-3983-2025

13. Windell, L. C., Mbengue, S., Pokorná, P., Schwarz, J., Prévôt, A. S. H., Manousakas, M. I**.,** **Papagiannis, S.**, Ondráček, J., Prokeš, R., & Ždímal, V. (2025). Xact625i vs. PX-375: a comparative study of online XRF ambient multi-metal monitors vs. ICP-MS. *Atmospheric Measurement Techniques*, *18*(22), 7021–7038. https://doi.org/10.5194/AMT-18-7021-2025

14. **Papagiannis, S.,** Manousakas, M. I., Anagnostopoulos, D. F., Pipkridas, M., Baalbaki, R., Sciare, J., O'Sullivan, N., Hellebust, S., Wenger, J., Fossum, K. N., Ovadnevaite, J., Tremper, A., Green, D., Eleftheriadis, K., and Diapouli, E (2026). Near Real-Time & Benchtop XRF Intercomparison for PM Elemental Analysis on Quartz and Teflon Filters: A Case Study Across Three European Cities, EGUsphere [preprint], https://doi.org/10.5194/egusphere-2025-5977

15. **Papagiannis S.**, Patakiouta I., Gini M., Manousakas M. I., Asvestas A., Diapouli E., Eleftheriadis K. E., Karydas A. G., Anagnostopoulos D. F., Quantitative micro-XRF imaging for assessing elemental inhomogeneity in multi nozzle cascade impactor aerosol filters, In preparation for submission

Conferences

1. *Sources of particulate related pollution in a highly populated, industrialized area of Tajikistan*. S. **Papagiannis, S**. Abdulayev, V. Vasilatou, M. Manousakas, K. Eleftheriadis, E. Diapouli. 11th Internatinal Aerosol Conference (IAC), 4-9 September 2022.

2. *Investigation of potential Sahara dust transport event indicators by means of aerosol trace metal concentration ratios in the Eastern Mediterranean for the years 2012-2021*. V. Vasilatou, E. Diapouli, M. Gini. **S. Papagiannis**, M. Manousakas, K. Eleftheriadis. 11th Internatinal Aerosol Conference (IAC), Greece, Athens, 4-9 September 2022.

3. *PM2.5 source apportionment and implications for particle hygroscopicity, at an urban background site in Athens, Greece*. E. Diapouli, C. Spitieri, M.I. Gini, P. Fetfatzis, P. Panteliadis, **S. Papagiannis**, V. Vasilatou and K. Eleftheriadis. 11th Internatinal Aerosol Conference (IAC), Greece, Athens, 4-9 September 2022.

4. *A study of PM2.5 source apportionment in five Greek cities*. **S. Papagiannis**, E. Diapouli, V. Vasilatou, M. Gini, N. Mihalopoulos, K. Eleftheriadis, PANACEA group, European Aerosol Conference (EAC), Spain, Malaga, 3 – 8 September 2023.

5. *Modelling study of PM levels and organic aerosol formation in a large Mediterranean urban centre*. A. Poupkou, S. Kontos, N. Liora, D. Tsiaousidis, I. Kapsomenakis, S. Solomos, E. Liakakou, G. Grivas, E. Athanasopoulou, E. Diapouli, V. Vasilatou, **S. Papagiannis**, A. Progiou, P. Kalabokas, D. Melas, E. Gerasopoulos, K. Eleftheriadis, C. Zerefos, European Aerosol Conference (EAC), Spain, Malaga, 3 – 8 September 2023.

6. *Evaluation of simulated atmospheric PM chemical composition in Athens - Organic aerosols formation sensitivity tests*, Anastasia Poupkou, Serafim Kontos, Natalia Liora, Dimitrios Tsiaousidis, Ioannis Kapsomenakis, Stavros Solomos, Eleni Liakakou, Eleni Athanasopoulou, Georgios Grivas, Evangelia Diapouli, Vasiliki Vasilatou, **Stefanos Papagiannis**, Athena Progiou, Pavlos Kalabokas, Dimitrios Melas, Evangelos Gerasopoulos, Konstan-tinos Eleftheriadis and Christos Zerefos, 6th International Conference on Meteorology, Climatology and Atmospheric Physics (COMECAP), 25-29 September 2023

7. *Elemental Characterization of Particulate Matter collected on Teflon filters by X-Ray Spectrometry*. **Stefanos Papagiannis**, Kalliopi Tsampa, Emmanouela Remountaki, Evangelia Diapouli, Konstantinos Eleftheriadis, Dimitrios Anagnostopoulos and Andreas Karydas. European X-ray Spectrometry Conference (EXRS), Greece, Athens, 24 – 28 June 2024.

8. *Real-time source apportionment of fine atmospheric aerosols using an online XRF system*. Manousos Manousakas, **Stefanos Papagiannis**, Olga Zografou, Maria Gini, Stergios Vratolis, Evangelia Diapouli and Konstantinos Eleftheriadis. European X-ray Spectrometry Conference (EXRS), Greece, Athens, 24 – 28 June 2024.

9. *Study of elemental distribution in cascade impactor filter samples by μ-XRF scanning*. **Stefanos Papagiannis**, Maria Gini, Theofanis Gerodimos, Anastasios Asvestas, Evangelia Diapouli, Konstantinos Eleftheriadis, Andreas Karydas and Dimitrios Anagnostopoulos. European X-ray Spectrometry Conference (EXRS), Greece, Athens, 24 – 28 June 2024.

10. *Assessment of elemental inhomogeneity in cascade impactor filter samples using MA-XRF*. **Stefanos Papagiannis**, Maria Gini, Ioanna Patakiouta, Theofanis Gerodimos, Evangelia Diapouli, Konstantinos Eleftheriadis, Andreas Karydas, Dimitrios Anagnostopoulos, European Aerosol Conference (EAC), Finland, Tampere, 25 –30 August 2024.

11. *MItigating Transport-Related Air Pollution in Europe: The MI-TRAP project*. Konstantinos Eleftheriadis, Maria Gini, Manousos Manousakas, Evangelia Diapouli, Stergios Vratolis, **Stefanos Papagiannis**, Olga Zografou, Theodore Giannakopoulos, Stasinos Konstantopoulos, Grisa Mocnik, Luka Drinovec, Veronique Riffault, Roberta Vecchi, Vladimir Zdimal, Evangelia Samoli, Costas Antoniou, Mihalis Lazaridis, Massimo Ciari, Giulia Calzolai, Chrysi Laspidou, Julie Fry, Q.T. Nguyen, Francesco Cappelluti, Jibran Khan, Andreas Massling, Marta Almeida, Andreas Nowak, Hans-Joachim Schulz, Julia Tzortzi, Martjin Schaap, Volker Diegmann, Florian Huewe, C. Castiglioni, Konstantina Vasilatou, Andre Prevot, Heekwan Lee, Claudio Crazzolara. European Aerosol Conference (EAC), Finland, Tampere, 25 –30 August 2024.

12. *Near Real-Time & Benchtop XRF Intercomparison for PM Elemental Analysis: A Case Study Across Three European Cities*. **Stefanos Papagiannis**, Manousos Ioannis Manousakas, Dimitrios Anagnostopoulos, Michael Pikridas, Rima Baalbaki, Niall O'Sullivan, John Wenger, Konstantinos Eleftheriadis, Evangelia Diapouli, 9th Metrology Conference, Greece, Athens, 20 - 21 June 2025.

13. *Airborne 210Pb and trace elements as tracers for atmospheric pollution in Helsinki metropolitan area*, Eleftheria Ioannidou, **Stefanos Papagiannis**, Manousos Ioannis Manousakas, Mika Vestenius, Konstantinos Eleftheriadis, Jussi Paatero, Alexandra Ioannidou, 8th International Conference on Environmental Radioactivity, Kraków, Polland, 14–19 Sept 2025.

Technical Reports

1. *Technical user manual for analytical experimental setups used for the elemental analysis of aerosol using ion techniques and X-ray Fluorescence technique for external users*. **Papagiannis, S** Deliverable D1.7.1, Project "CALIBRA" (MIS 5002799), Institute of Nuclear and Particle Physics, NCSR "Demokritos" (2022).

2. *SOP Manual: WD-XRF Rigaku Supermini 200 Benchtop Spectrometer for the elemental characterization of environmental aerosol filters*. **Papagiannis, S.** Greater Cairo Air Pollution Management and Climate Change Project, The World Bank Group (2023).

Short Bio

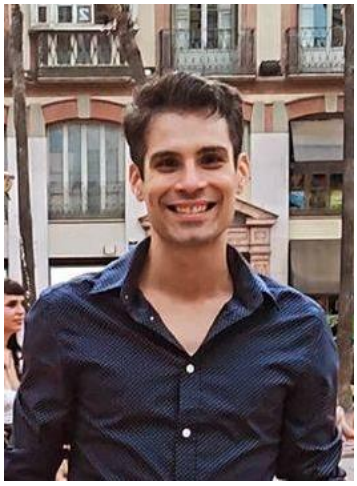

Stefanos Papagiannis was born in 1990 in Athens. He graduated in 2017 from the Department of Materials Science & Engineering at the University of Ioannina, where he also completed his MSc in 2020. He is currently a PhD candidate in the Department of Materials Science & Engineering at the University of Ioannina. His research focuses on *"Characterization of atmospheric aerosol components and sources of pollution using X-ray spectrometry techniques"* under the supervision of Dr. D.F. Anagnostopoulos, Dr. A.G. Karydas, and Dr. E. Diapouli. He has experience in elemental analysis using ED-XRF and PIXE, quantitative materials characterization, X-ray μ-imaging, and Monte Carlo simulations for X-ray applications. His research interests include X-ray fluorescence spectrometry, source apportionment of atmospheric aerosols using positive matrix factorization, and advanced characterization of environmental and material samples.